ABSTRACTS DEL VIII MEETING

DEL CAPITOLO ITALIANO

DELLA EUROPEAN SOCIETY OF BIOMECHANICS

ESB-ITA 2018

Milano, 25-27 GIUGNO 2018

ORGANIZZATO CONGIUNTAMENTE AL
VI CONGRESSO DEL GRUPPO NAZIONALE DI BIOINGEGNERIA (GNB)

Proceedings of the Sixth National Congress of Bioengineering, GNB 2018, Milan June 25-27, 2018.

Patron Editore, Bologna, ISBN 9788855534219

Selection of the papers presented at the session in collaboration with ESB-ITA.

All the other details about the conference are available at the website: www. Gnb2018. Polimi. It

Indice

Computational tools for the reliability assessment and the engineering design of procedures and devices in bariatric surgery

E.L. Carniel[1,2], C.G. Fontanella[1,3], C. Salmaso[1], I. Toniolo[1], S. Gentilotti[1], L. Polese[1,4], M. Foletto[1,4], S. Merigliano[1,4] and A.N. Natali[1,2]
[1] *Centre for Mechanics of Biological Materials, University of Padova, Italy*
[2] *Department of Industrial Engineering, University of Padova, Italy*
[3] *Department of Biomedical Sciences, University of Padova, Italy*
[4] *Department of Surgery, Oncology and Gastroenterology, University of Padova, Italy*

Abstract - **Bariatric surgery is the most effective intervention for severe obesity, as one of the most serious health problem worldwide. Laparoscopic adjustable gastric banding is one of the principal technique. Nonetheless, side effects are frequent and weight-loss is not always successful. Non-optimal intervention design, surgery invasiveness and general anesthesia are the principal cause of this situation. A more advanced approach is required, integrating bioengineering and medical competences, aiming to engineering design the procedure, to improve efficacy and to reduce the need for anesthesia.**

Computational methods can be exploited to evaluate stomach functionality after surgery and to interpret mechano-biological processes, aiming at the optimal design of the intervention. Results from coupled experimental and computational activities are here reported, showing the potentialities of the engineering approach.

Endoscopic surgery should minimize invasiveness and anesthetic requirement, but previously proposed techniques demonstrate marginal efficacy. Procedural consistent advances are required, as devices designed to provide endoscopic gastric banding. Preliminary results from computational activities are proposed, again to show the capabilities of the engineering approach to mimic and to optimize the overall surgical procedure.

Keywords **– Bariatric surgery, computational biomechanics, endoscopic surgery.**

I. Introduction

OBESITY is an epidemic disease associated with multiple co-morbidities, whose prevalence in developed countries is increasing. The United States spend million dollars annually on treatment and prevention. It has been estimated that 30% of adults in the US meet the criteria for obesity and also in Europe obesity is common [1]. Several surveys show that the prevalence of overweight among school age children is as high as 40% in parts of Europe. The World Health Organization and health agencies in most countries report epidemiological data showing an increase in morbidity and mortality because of increasing weight. Major obesity related diseases include increased risk for cardiovascular diseases, dyslipidemia, diabetes mellitus, cancer, and psychosocial impairment. These conditions are responsible for more than 2.5 million deaths per year worldwide. The loss of life expectancy is profound [2].

Bariatric surgery remains the most effective intervention for patients with body mass index (BMI) of 40 kg/m^2 or greater or those with BMI of 35 kg/m^2 or greater with specific related co-morbidities [3]. Bariatric surgery envisages different interventions, which are routinely performed by laparoscopy. Some operations reduce the stomach capacity, as gastric banding or gastrectomy, some others reduce the absorbing capacity of gastrointestinal organs, as biopancreatic diversion with duodenal switch; finally, there are operations that exploit both the effects, as gastric by-pass. Nowadays, adjustable gastric banding is one of the most common and successful operation [4]. Surgical failure and post-surgical side effects affect up to 25% of the patients [3]. Furthermore, the efficacy of bariatric surgery, as post-operative weight loss and approach to food, should be improved. Complications are mostly due to the empirical approach, surgery invasiveness and high anesthesiology risk. For this reason, there is a need for less invasive bariatric procedures, as endoscopic ones. Currently available endoscopic techniques still have limits and mostly fail because of their unsuitableness or procedural difficulties [5]. Further efforts are mandatory for a reliable definition of endoscopic methods. Coupled engineering and clinical activities are necessary for the design, as an example, of a reliable and effective endoscopic approach to gastric banding. The specific bariatric procedure and the post-surgical conformation of the operated gastrointestinal organs are usually defined on clinical basis only. A more rational approach is advocated, considering physiological and mechano-biological processes, as the physio-mechanical functionality of the gastrointestinal organs and the relationship between food intake, mechanical stimulation of gastrointestinal wall and feeling of satiety. Methods and procedures of bariatric surgery should be consequently defined by integrating competences in the areas of surgery, physiology and bioengineering. In this context, only qualitative or semi-quantitative activities have been previously performed [6,7]. Considering the specific bariatric procedure, mechanical models of the gastrointestinal tract can be developed and applied to quantitatively investigate the mechanical stimulation of the gastrointestinal wall because of food intake [8]. Physiological and mechano-biological investigations can be performed to identify quantitative relationships between mechanical stimulation of the gastrointestinal wall, volume of the ingested food and feeling of satiety.

The methods of computational biomechanics, mechano-biology, physiology and surgery can be exploited aiming at defining computational tools for the optimal design of procedures and devices for a more reliable and effective approach to bariatric surgery.

II. Materials and Methods

A. Computational model of the stomach

Aiming at providing computational tools for bariatric surgery optimization, a computational model of the stomach was developed. Model definition and validation were performed by analyzing histo-morphometric data and results from mechanical tests at both tissue and structure levels.

An inner connective layer and an outer muscular layer mainly compose the stomach wall. Collagen and muscular fibers within connective and muscular layers, respectively, show preferential orientations, leading to anisotropic behavior. Thickness measurements, histological investigations [9] and mechanical tests on wall samples [10] from the different regions of the stomach (fundus, corpus and antrum) pointed out different results. Consequently, the stomach wall can be defined as a multi-layered, anisotropic and non-homogeneous structure (Fig. 1).

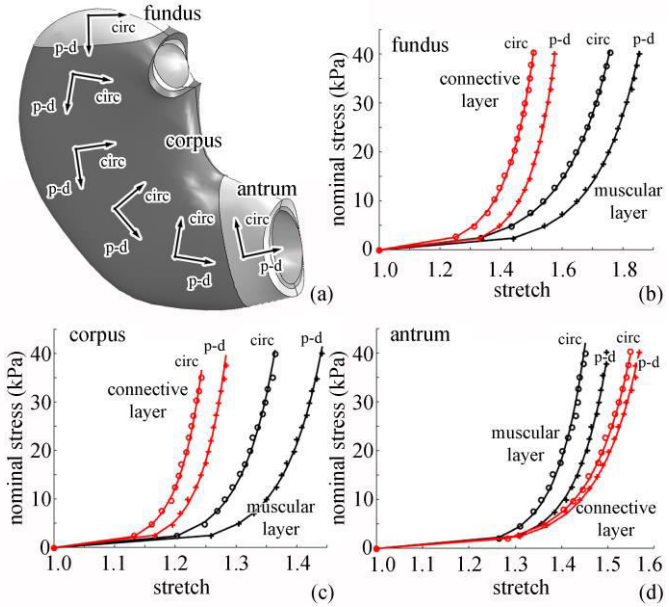

Fig. 1. Virtual solid model of the stomach with indication of the three main regions, as fundus, corpus and antrum, and the principal orientations, as proximal-distal and circumferential directions (a). Inverse analysis of tensile tests on swine stomach tissues specimens from different regions, as fundus (b), corpus (c) and antrum (d), and layers: experimental data (empty circles, as results from tests performed along circumferential direction, and crosses, as results from tests performed along proximal-distal direction) and model results (continuous lines).

Aiming at characterizing stomach tissues mechanics, results from experimental investigations suggested the assumption of a visco-hyperelastic constitutive formulation:

$$\mathbf{S}\left(\mathbf{C},\mathbf{q}^i\right)=2\frac{\partial W^0\left(\mathbf{C}\right)}{\partial\mathbf{C}}-\sum_{i=1}^{n}\mathbf{q}^i \qquad (1)$$

where $\mathbf{S}$ is the second Piola-Kirchhoff stress tensor, $\mathbf{C}$ is the right Cauchy-Green strain tensor, while W^0 is an hyperelastic potential that specifies the instantaneous response of the tissue, and was defined considering the typical fiber-reinforced configuration [11]. The evolution of viscous variables $\mathbf{q}^i$ was specified by usual differential equations:

$$\dot{\mathbf{q}}^i+\frac{1}{\tau^i}\mathbf{q}^i=2\frac{\gamma^i}{\tau^i}\frac{\partial W^0\left(\mathbf{C}\right)}{\partial\mathbf{C}} \qquad (2)$$

Hyperelastic parameters have been identified by the inverse analysis of uni-axial tensile tests (Fig. 1b,c,d), which have been performed on wall samples from pig stomachs [10]. In detail, specimens from connective and muscular layers were harvested from the fundus, the corpus and the antrum, considering both proximal-distal and circumferential directions (Fig. 1a). On the other side, viscous parameters were identified by the analysis of relaxation data from structural tests, as reported below.

Aiming at the definition and the validation of the stomach computational model, structural tests were performed considering stomach samples [8]. Stomachs of fifteen piglets (weight: 30 ± 2 Kg) were collected. Detailed stomach measurements were performed. Subsequently inflation tests allowed to evaluate the stomach structural response, as the pressure-volume behavior. Sample experimenting was performed by a multi-step inflation procedure. Each step was composed of 280 ml inflation of saline at 40 ml/s inflation rate, and subsequent 600 s of rest to allow the almost complete development of relaxation phenomena. The step was repeated up to the full filling of the stomach, leading to pressure-time data. The collection of pressure and volume data at the end of the rest stages led to pressure-volume almost equilibrium curves. The analysis of pressure-time results during the constant volume stages led to relaxation curves, entailing the identification of the viscous parameters. Experimentations were performed considering both the pre- and the post-bariatric surgery conformations. Gastric banding was provided by a silicon rubber band, evaluating also the influence of band pre-tension.

Morphometric data were processed to develop an average finite element model of the fundus, the corpus and the antrum, considering both the connective and the muscular layers. A distribution of local coordinate systems was defined to provide a mathematical description of the orientation of collagen and muscular fibers (Fig. 1a). The mechanical behavior of the stomach tissues was defined by implementing the anisotropic visco-hyperelastic formulation in the framework of the general purpose finite element code Abaqus Explicit 6.14 (Dassault Systèmes Simulia Corp., Providence, RI). Computational analyses were performed aiming to investigate the pressure volume behavior of the stomach. Subsequently, the stomach computational model was morphed according to data from measurements performed on human samples [9].

B. Investigation of stomach functionality in post-surgical conformation

The post-surgical conformation of the stomach is usually defined on the basis of the surgeon expertise and the outcome of previously performed interventions. Activities are required to prove methods for a rational pre-surgical planning of the bariatric intervention. Computational analyses can be performed to evaluate stomach functionality in the post-surgical conformation, as the pressure-volume behavior and the mechanical stimulation of gastric receptors.

As an example, the computational model of the stomach was exploited to investigate the stomach mechanical functionality after laparoscopic gastric banding, depending on the band pre-tension condition (Fig. 2). A finite element model of the silicon rubber band was developed. Band pre-tension was simulated considering a fictitious thermal contraction of the band.

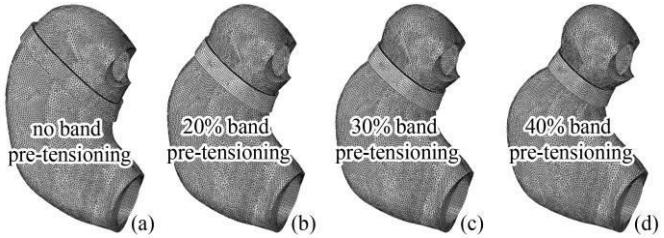

Fig. 2. Computational modeling of laparoscopic gastric banding. Models are developed considering also the influence of band pre-tensioning, as 0% (a), 20% (b), 30% (c) and 40% (d) band stretch. Models are exploited to investigate tissues response because of stomach inflation. A fluid filled cavity is defined considering the stomach inner surface and a constant fluid incoming flow is imposed. The upper and the lower extremity of the cavity, at the gastroesophageal and gastroduodenal junctions, are fixed.

C. Tools for endoscopic approach to gastric banding

Bariatric surgery is mainly developed by laparoscopic approach, which requires general anesthesia. The anesthesiology risk in obese patient is relevant. Endoscopic techniques are less invasive and sedation requirement is minor, but efforts are mandatory to define a reliable approach. Computational methods can be exploited for both the evaluation of stomach functionality in post-surgical conformation and the design of devices and instrumentations for the endoscopic methods.

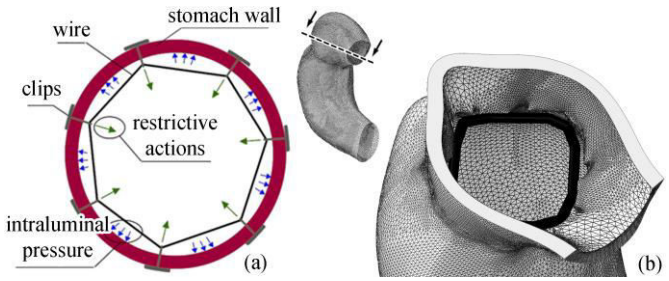

Fig. 3. Schematic representation (a) and computational investigation (b) of the endoscopic approach to gastric banding.

As an example, an endoscopic approach to gastric banding was analyzed. The intervention should be performed affixing a circular pattern of clips in the stomach fundus all around the gastroesophageal junction. Subsequently, clips must be connected by a wire. (Fig. 3).

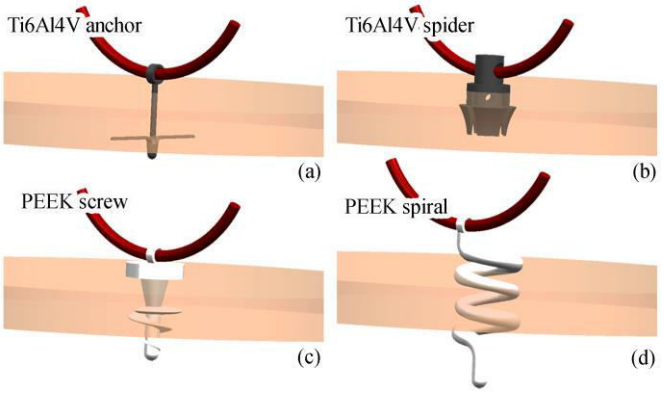

Fig. 4. Virtual solid models of different clips for endoscopic gastric banding: anchor (a), spider (b), screw (c), and spiral (d).

Computational analyses have been performed to identify a reliable design of the clips. Wire traction allows the development of the stomach pouch, which is typical of gastric banding. The major efforts pertain to design reliable surgical clips, considering both the applicability by an endoscopic tool and the capability to support wire traction. Different clips conformations have been investigated, as anchors, spiders, screws and spirals (Fig. 4).

III. Results

The reliability of the computational model of the stomach was assessed by the comparison of experimental and model results from inflation tests (Fig. 5).

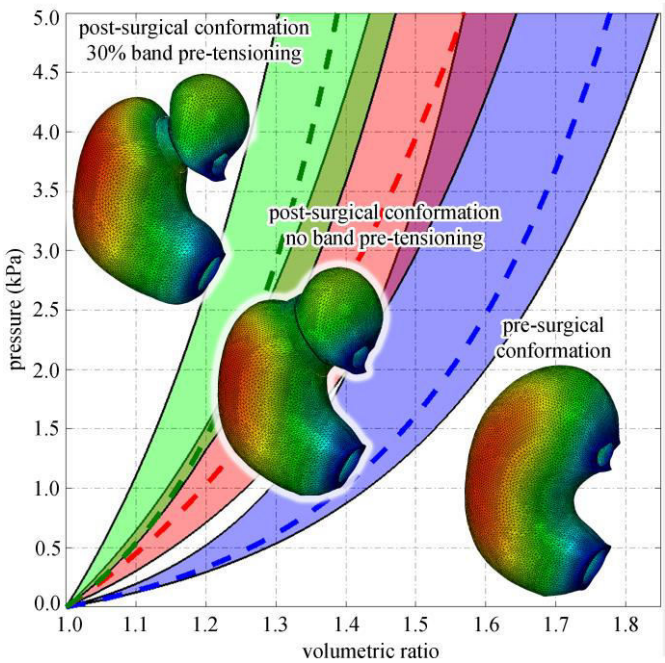

Fig. 5. Reliability assessment of the stomach computational model by the comparison of experimental (colored bands) and computational (discontinuous lines) results from inflation tests: pre-surgical conformation (blue), post surgical conformation with (green) and without (red) band pre-tensioning. Contours of displacement magnitude fields are reported for the different situations (1000 ml inflated volume).

Results are provided considering different stomach conformations, as pre-surgical one and post-surgical conditions after laparoscopic gastric banding. Subsequently, after the morphing procedure in the light of human stomach dimensions, the computational model was exploited to evaluate the influence of gastric banding parameters on stomach functionality, as the pressure-volume behavior and the mechanical loading of gastric wall, with particular regard to the fundus region where mechano-receptors are mainly localized (Fig. 6). Again, reference is made to laparoscopic gastric banding. With regard to the design of the endoscopic approach, preliminary results from the computational analysis of clips insertion are finally proposed (Fig. 7).

IV. Discussion

Preliminary outcomes were reported from activities that are under development in the research field of stomach mechanics and bariatric surgery. Results from experimental tests were exploited to develop, identify and validate a computational model of the stomach. Computational activities analyzed stomach natural configuration and different post-surgical conformations. Computational results highlighted the great influence of bariatric surgery parameters on stomach mechanics.

In detail, the surgical procedure strongly affects the stomach structural stiffness (Fig. 5) and the strain field conformation and intensity (Fig. 6).

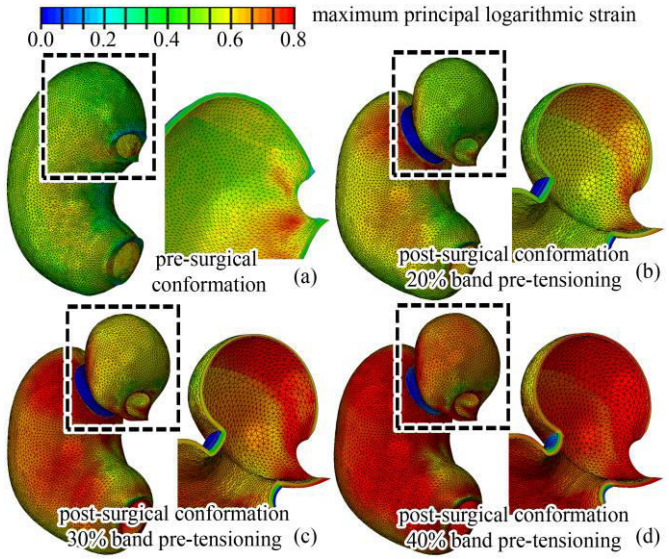

Fig. 6. Analysis of stomach functionality in pre- (a) and post- (b-d) surgical conformations depending on gastric band pre-tensioning. Distribution of tensile strain on the outer surface of the overall stomach and the inner surface of the fundus region. Results are reported at 1000 ml inflated volume.

Attention was here focused on gastric banding, because of its wide application and effectiveness. Nevertheless, the same approach can be adopted to analyze other surgical techniques and to design innovative and more reliable procedures (Figs. 3, 4 and 7). The results show the potentiality of experimental and computational biomechanics for the investigation of stomach functionality and the planning of bariatric surgery procedures and techniques.

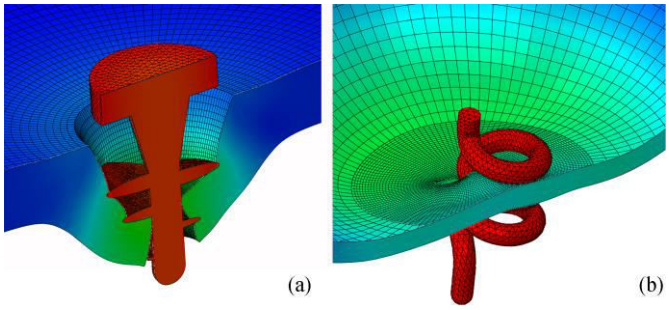

Fig. 7. Computational methods for the design of clips for endoscopic wire fixation: analysis of interaction phenomena between clips, as screw (a) and spiral (b), and stomach wall during clip insertion.

V. Conclusions

As previously reported by other authors [7], experimental activities allow evaluating stomach pressure-volume behavior depending on surgical methods and conditions. The increased stomach stiffness after surgery confirms the clinical evidence that bariatric intervention reduces the stomach capacity. On the other side, computational methods make it possible to broad experimental results to an extremely wider scenario, considering many different surgical procedures. Furthermore, computational models provide information that experimental methods cannot supply. In detail, the computational approach makes it possible to identify the strain and the stress fields in stomach tissues, whose distribution is strongly affected by the bariatric procedure. As an example, position and pre-tension value of the gastric band have a relevant impact on both the stomach capacity (Fig. 5) and the areas of gastric wall that are mainly strained and stressed (Fig. 6). Mechanical stimuli, as strain and stress, act on receptors that contribute to regulate the feeling of satiety. The relevance of this aspect is enforced by the recent trends in bariatric surgery, which aim not to restrict stomach capacity, but to induce satiety by increasing receptors stimulation [6]. Considering the mechano-transduction capabilities of gastric receptors, it follows the relevance of the proposed computational methods, which allow evaluating the intensity and the conformation of strain and stress fields depending on stomach conformation and food intake.

Further efforts are mandatory for a more exhaustive and accurate computational approach to stomach mechanics. For example, the here reported experimental activities have been developed considering biological samples from pig model only. Activities are currently under development adopting human samples that are harvested from stomach scraps from bariatric interventions. Furthermore, a more reliable investigation of stomach mechanics should consider motility, as the active contribution of muscular components, and fluid-structure interaction phenomena between bolus and stomach wall. Such approach should entail a more reliable investigation of physio-mechanical processes that develop during stomach activities.

In conclusion, computational methods enable the evaluation of bariatric intervention reliability and effectiveness, and the functional comparison between different surgical techniques. Computational tools can consequently provide a valuable aid for the pre-surgical design and the definition of novel procedures.

References

[1] S. Gallus, A. Lugo, B. Murisic, C. Bosetti, P. Boffetta, C. La Vecchia, "Overweight and obesity in 16 European countries", *Eur J Nutr*, vol. 54, pp. 679-689, 2015.

[2] G.S. Berenson, "Health Consequences of Obesity", *Pediatr Blood Cancer*, vol. 58, pp. 117-121, 2012.

[3] S.H. Chang, C.R. Stoll, J. Song, J.E. Varela, C.J. Eagon, G.A. Colditz, "The effectiveness and risks of bariatric surgery: an updated systematic review and meta-analysis, 2003-2012", *JAMA Surg*, vol. 149, pp. 275-287, 2014.

[4] A. Lazzati, M. De Antonio, L. Paolino , F. Martini, D. Azoulay, A. Iannelli, S. Katsahian, "Natural history of adjustable gastric banding: lifespan and revisional rate: a nationwide study on administrative data on 53,000 patients", *Ann Surg*, vol. 265, pp. 439-445, 2017.

[5] H.S. Choi, H.J. Chun, "Recent Trends in Endoscopic Bariatric Therapies", *Clin Endosc*, vol. 50, pp. 11-16, 2017.

[6] S.C. Woods, "Gastrointestinal satiety signals I. An overview of gastrointestinal signals that influence food intake", *Am J Physiol Gastrointest Liver Physiol*, vol. 286, pp. 7-13, 2004.

[7] F. Gao, D. Liao, J. Zhao, A.M. Drewes, H. Gregersen, "Numerical analysis of pouch filling and emptying after laparoscopic gastric banding surgery", *Obes Surg*, vol. 18, pp. 243-250, 2008.

[8] E.L. Carniel, A. Frigo, C.G. Fontanella, G.M. De Benedictis, A. Rubini, L. Barp, G. Pluchino, B. Sabbadini, L. Polese, "A biomechanical approach to the analysis of methods and procedures of bariatric surgery", *J Biomech*, vol. 56, pp. 32-41, 2017.

[9] H. Elariny, H. González, B. Wang, "Tissue thickness of human stomach measured on excised gastric specimens from obese patients", *Surg Technol Int*, vol. 14, pp. 119-124, 2005.

[10] J. Zhao, D. Liao, P. Chen, P. Kunwald, H. Gregersen, "Stomach stress and strain depend on location, direction and the layered structure", *J Biomech*, vol. 41, pp. 3441-3447, 2008.

[11] E.L. Carniel, V. Gramigna, C.G. Fontanella, C. Stefanini, A.N. Natali, "Constitutive formulations for the mechanical investigation of colonic tissues", *J Biomed Mater Res A*, vol. 102, pp. 1243-1254, 2014.

In vitro full-field strain distribution of the anterior longitudinal ligament

Ruspi M. L.[1], Galbusera F. [2], Palanca M. [1], Liebsch C. [3], Villa T. [2,4], Wilke H-J. [3], Brayda-Bruno M. [5], Cristofolini L. [1], La Barbera L. [4]

1 *Alma Mater Studiorum – Università di Bologna: marialuisa.ruspi2@unibo.it, marco.palanca2@unibo.it, luca.cristofolini@unibo.it*

2 *IRCCS Galeazzi Orthopaedic Institute, Milan, Italy: tomaso.villa@polimi.it*

3 *Institute of Orthopaedic Research and Biomechanics, University of Ulm, Ulm, Germany*

4 *Laboratory of Biological Structure Mechanics, Department of Chemistry, Materials and Chemical Engineering "G. Natta", Politecnico di Milano, Italy: luigi.labarbera@polimi.it*

5 *Department of Spine Surgery III, IRCCS Istituto Ortopedico Galeazzi, Milan, Italy*

***Abstract* – The spine is a complex structure subjected to different types of motor tasks. Some in vitro tests can give information about range of motion and stiffness of the spine reproducing pseudophysiological loading conditions. These tests provide information only related to a global description of the spine.**

In order to have local information in a point-wise way, Digital Image Correlation (DIC) is a recent toll which can obtain a contact-less and full-field measurement of the distribution of strain on a surface.

There are no studies regarding the superficial strain distribution measured on the anterior longitudinal ligament (ALL).

The present work was performed using segments of the human spine (T11-S) loaded in flexion/extension, right/left lateral bending and clockwise/anticlockwise axial torsion using a universal spine tester and DIC. To confirm that the specimens had a physiological behavior, the range of motion was preliminarily measured using a system of six optoelectronic cameras (Vicon MX13). DIC system evaluated successfully the distribution of strain on the ALL for each specimen in all the different loading conditions.

This study showed a different behaviour of the ALL in the different regions: larger deformations were measured on the ALL in correspondence with intervertebral disc (reaching values of 80000 microstrain), while smaller deformations (about 15000 microstrain) were measured on the ALL in correspondence with the mid of the vertebrae. When the intervertebral disc works in compression, it bulges and so the ALL followed this movement.

The orientation of the strain followed the deformation of the fibers of the ALL mostly in correspondence with the intervertebral disc than the vertebral bone.

This is the first time that the deformation of the ALL was measured under different loading conditions, obtaining a full-field strain distribution including the direction of strain.

***Keywords* – Biomechanics, Anterior Longitudinal Ligaments, Digital Image Correlation, Strain distribution, Spine**

I. Introduction

THE spine is a complex structure of the human body allowing, from a biomechanical point of view, the standing position and permitting the trunk flexibility in terms of combination of different motor tasks. In vitro investigations can provide basic information about the biomechanics of spine reproducing pseudophysiological loading conditions [1]. The length of spinal specimens used for in vitro tests varies depending on the purpose of the study [2], [3], [4]. Functional spine units (consisting of two adjacent vertebrae with the intervertebral disc and all the interconnecting ligaments) were tested [5].

Recently, a multisegmental vertebral unit was preferred in order to better reproduce the propagation of loads. Furthermore, many ligaments (posterior and anterior longitudinal ligaments, ligamentum flavum, and supraspinous ligaments) form continuous structures and so a multisegmental vertebral unit represents the vertebral mechanism more closely than a functional spine motion unit alone [6]. In these tests, range of motion and stiffness were evaluated under different physiological loading conditions for the different spinal levels [7]. These tests provide useful information but only related to a global description of the spine.

In order to have local information in quantitative full-field distribution way, Digital Image Correlation (DIC) is a recent tool which allows contact-less and full-field measurement of the distribution of strains on the specimen surface. DIC can be used both on hard and soft tissue [8], [9].

In literature, there are no studies about the strain distribution measured on the anterior longitudinal ligament (ALL). In fact, some studies considered the ALL as a standalone structure studying its mechanical properties, and not as a part of a multisegmental vertebral unit [10], [11], [12].

The present work wanted to investigate the strain distribution on the ALL, testing multisegmental vertebral units (T11-S) under different loading conditions. In order to obtain a complete full-field strain distribution on the different regions of the ALL (in correspondence to the vertebral bone and to the intervertebral disc), DIC was used.

II. Material and Methods

A. Specimen and Digital Image Correlation

Five human thoracolumbar spine specimens (T11-S1) were obtained through an ethically approved donation program (Science Care Inc., Phoenix, AZ). All specimens were CT-scanned to exclude major defects. All the muscles and fat were removed, keeping intact carefully the intervertebral discs and all the ligaments (except the intertransverse ligament).

Each specimen was aligned with the central intervertebral disc disposed horizontally. The extremities were potted in poly-methyl-methacrylate (PMMA) cements.

Before testing the specimens, a specific white-on-black speckle pattern was prepared on the anterior side of the specimen in order to use DIC system. The background was prepared staining the entire spine segment with methylene blue with a brush, which does not induce significant alteration of the mechanical properties [13]. The white speckle pattern, instead, was created using water-based paint sprayed with an optimized airgun [14], [13].

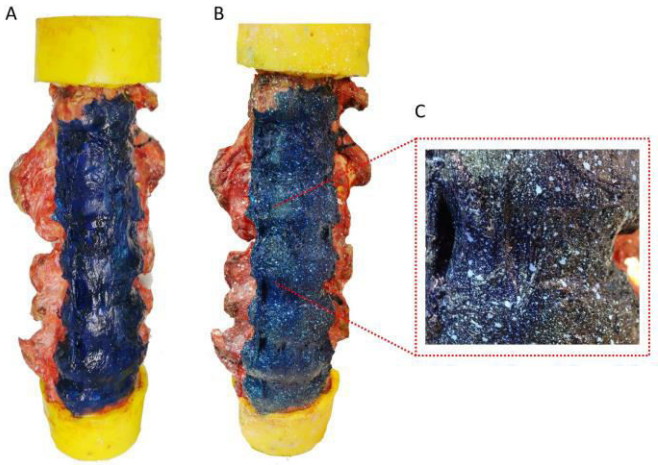

Figure 1 – Preparation of the pattern. A: Dark background (methylene blue). B: White speckle pattern. C: Zoom of the surface of ALL prepared

A commercial 3D-DIC system (Q400, Dantec Dynamics, Skovlunde, DK) with two 5MPixels cameras and 17mm lens was used in order to measure the full-field strain distribution on the ALL.

A field of view of 120x160 mm was set for the two cameras to frame the vertebra L5, the intervertebral disc between L5-L4, the vertebra L4 and the intervertebral disc between L4-L3. The pixel size was 0.08 mm and the deep field was 70 mm.

An optimization in zero strain condition allowed selecting the best compromise between the measurement spatial resolution and the measurement uncertainties. A facet size from 39 to 59 pixels, a grid spacing of 4 pixels, and a filter with a kernel size of 5x5 were set obtaining a systematic error < 10 microstrain and a random error < 100 microstrain. These errors were acceptable considering the range of strain expected in the soft tissue.

B. Mechanical testing

The load was applied using a universal spine tester for quasi-static moments [15]. The lower part of the specimens was mounted rigidly to the base of the spine tester; the upper part was fixed in a gimbal. This gimbal allowed rotation around all three coordinated axes as well as vertical translation.

The specimens were tested under pure bending moments (±7.5Nm), simulating 3.5 loading cycles of flexion/extension, right/left lateral bending and clockwise/anticlockwise axial torsion. Each direction of loading was implemented in rotation-control (1°/sec for flexion/extension and lateral bending, 0.5°/sec for axial torsion) [4].

To confirm that the specimens had a physiological behavior, the range of motion (RoM) was preliminarily measured using a system of six optoelectronic cameras (Vicon MX13).

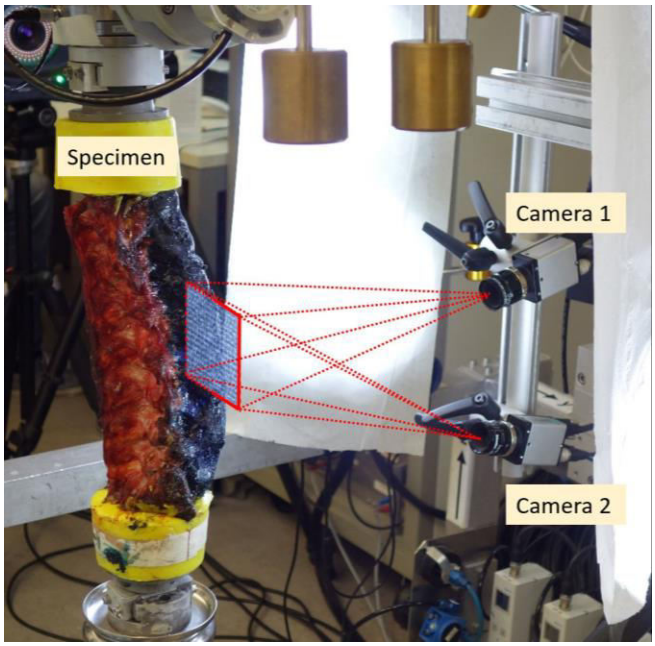

Figure 2 - Configuration of the test. View of the specimen in the spine tester. The two cameras of DIC system acquired images during the test

III. Results and Discussion

The DIC system successfully evaluated the strains of the ALL for each specimen in all the different loading conditions.

Larger deformations were measured on the ALL in correspondence with intervertebral disc (reaching values of 80000 microstrain), while smaller deformations (about 15000 microstrain) were measured on the ALL in correspondence with the mid of the vertebrae. The peak values of maximum and minimum principal strain for all conditions were about the same (+80 000/-80 000 microstrain).

During flexion, the ALL had maximum principal strain oriented horizontally in particular where the ALL crossed the intervertebral disc. In fact, when the intervertebral disc works in compression, it bulges and so the ALL is stretched in the circumferential direction.

During extension, the ALL works in traction and the maximum principal strains had a vertical direction. This distribution of values was in agreement to the directions of the fibers of the ALL. In fact, during extension, the values of strain measured in front of the vertebral bone and in front of the intervertebral disc were more homogeneus than during flexion.

For right lateral bending, compressive horizontal strains were measured on the right side of the ligament, while tensile vertical strains were measured on the left side of it. The contrary was seen during left lateral bending. Also in this type of movement, larger deformations were measured in correspondence with the intervertebral disc, while smaller deformations were measured in correspondence with the vertebral bone due to the different behavior of tissues. As in flexion, the compressed side of intervertebral disc bulged.

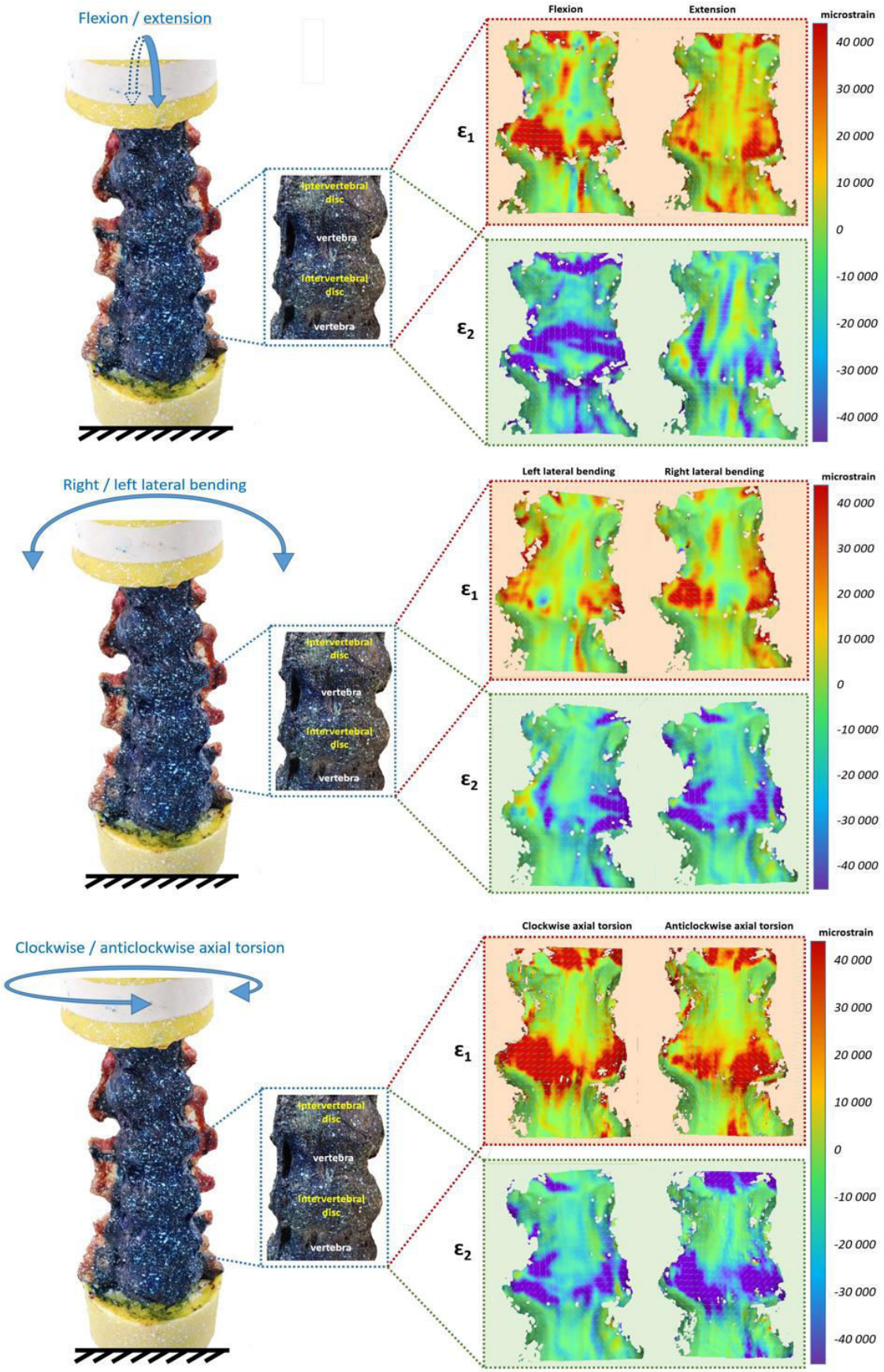

Figure 3 – The images show on the left: the anterior side of the specimen, on the right: strain distribution of maximum (ε1) and minimum (ε2) principal strain on the anterior side of the specimen (ALL) during flexion/extension, right/left lateral bending and clockwise and anticlockwise axial rotation

For clockwise and anticlockwise axial torsion, the values of maximum principal strain reached peaks of 80000 microstrain in correspondence with the intervertebral disc. Similar values were measured also for minimum principal strains (reaching -80000 microstrain).

The orientation of the strain followed the deformation of the fibers of the ALL mostly in correspondence with the intervertebral disc than with the vertebral bone.

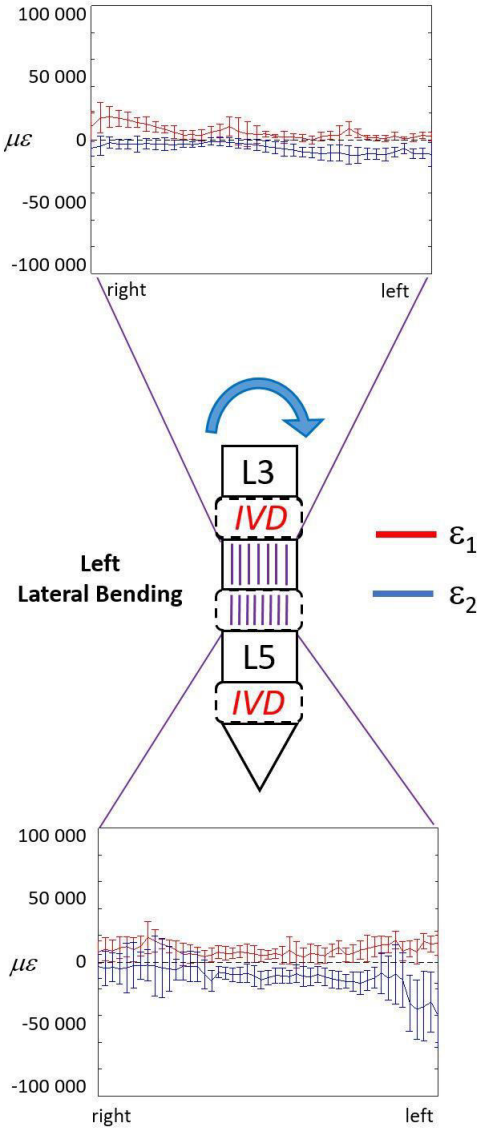

Figure 4 - Lateral bending at the maximum load (7.5Nm). To describe the strain distribution around the specimen, the median over longitudinal lines were calculated for L4 vertebra and L5-L4 IVD. The plot shows the distribution of ε_1 (red) and ε_2 (blue) around L4 and the IVD. The median and standard deviation within the sample are reported.

IV. Conclusion

This study aimed to examine human multisegmental spine units providing a full-field strain distribution.

For the first time, the deformation and the behaviour of the exterior fibers of the ALL were measured *in vitro* under different loading conditions in a full-field way.

The spine was accounted as a whole, considering the complex boundary condition and describing in details the strain distribution, with particular emphasis to the ALL, which cannot be analysed using traditional techniques.

This study showed a different behaviour of the ALL in the different regions: in correspondence with the vertebrae and the intervertebral discs.

The non-homogeneous distribution of the strain measured on the ALL showed that in front of the vertebrae the strain was smaller than in front of the intervertebral discs.

The results obtained with DIC can improve the knowledge of the role of ligaments in order to improve the surgical techniques.

References

1. Wilke, H.J., et al., *Is it Possible to Simulate Physiologic Loading Conditions by Applying Pure Moments?* SPINE, 2001. **26**: p. 636 - 642.
2. Kettler, A., et al., *Effects of Specimen Length on the Monosegmental Motion Behavior of the Lumbar Spine.* SPINE, 2000. **25**: p. 543 - 550.
3. Brandolini, N., L. Cristofolini, and M. Viceconti, *Experimental Methods for the Biomechanical Investigation of the Human Spine: A Review.* Journal of Mechanics in Medicine and Biology, 2014. **14**(01): p. 1430002.
4. J., W.H., W. K, and C. L., *Testing criteria for spinal implants: recommandations for the standardization of in vitro stability testing of spinal implants.pdf.* Eur Spine J, 1997.
5. Wilke, H.J., et al., *Spinal Segment Range of Motion As a Function of In Vitro Test Conditions: Effects of Exposure Period, Accumulated Cycles, Angular-Deformation Rate, and Moisture Condition.* Thr anatomical record, 1998. **251**: p. 15-19.
6. Behrsin, J. and C. Briggs, *Ligaments of the lumbar spine: a review.* Surgical - Radiologic Anatomy, 1988. **10**: p. 211 - 219.
7. Mayer, T.G., et al., *Spinal Range of Motion.* 1997. **22**: p. 1976 - 1984.
8. Palanca, M., G. Tozzi, and L. Cristofolini, *The use of digital image correlation in the biomechanical area: a review.* International Biomechanics, 2015. **3**: p. 1-21.
9. Palanca, M., et al., *Full-field strain distribution in multi-vertebrae spine segments: An in vitro application of Digital image correlation.* MEP, 2017.
10. Tkaczuk, H., *Tensile Properties of Human Lumbar Longitudinal Ligaments.* Acta Orthopaedica Scandinavica, 2014. **39**(sup115): p. 1-69.
11. Gillespie, K.A. and J.P. Dickey, *Biomechanical Role of Lumbar Spine Ligaments in Flexion and Extension: Determination Using a Parallel Linkage Robot and a Porcine Model.* SPINE, 2003. **29**: p. 1208 - 1216.
12. Heuer, F., H. Schmidt, and H.J. Wilke, *The relation between intervertebral disc bulging and annular fiber associated strains for simple and complex loading.* J Biomech, 2008. **41**(5): p. 1086-94.
13. Lionello, G., C. Sirieix, and M. Baleani, *An effective procedure to create a speckle pattern on biological soft tissue for digital image correlation measurements.* J Mech Behav Biomed Mater, 2014. **39**: p. 1-8.
14. Palanca, M., T.M. Brugo, and L. Cristofolini, *Use of digital image correlation to investigate the biomechanics of the vertebra.* Journal of Mechanics in Medicine and Biology, 2015. **15**.
15. Wilke, H.J., H. Schmitt, and S. Wolf, *A universal spine tester for in vitro experiments with muscle force simulation.* European Spine Journal, 1994. **3**: p. 91-97.

Investigation of the biomechanical response of infrapatellar fat pad in osteoarthritic condition

C.G. Fontanella[1,2], E.L. Carniel[1,3], V. Macchi[1,4], R. De Caro[1,4], and A.N. Natali[1,3]
[1] *Centre for Mechanics of Biological Materials, University of Padova, Italy*
[2] *Department of Biomedical Sciences, University of Padova, Italy*
[3] *Department of Industrial Engineering, University of Padova, Italy*
[4] *Institute of Human Anatomy, Department of Neuroscience, University of Padova, Italy*

Abstract - **The infrapatellar fat body (IFP) is situated between the patellar tendon, the femoral condyle and the tibial plateau of the knee. The IFP consists of adipose lobules delimited by connective septa. The structural functionality of the IFP is debated and pertains to a cushioning role in the knee joint, providing to distribute and to damp mechanical action during articular activity. In case of osteoarthritis (OA), IFP is found to be affected by inflammation and fibrosis.**

The aim of the present study is to analyze the influence of the OA on the microscopic and the structural conformation with regard to mechanical properties. The microscopic analysis of the IFP was performed through histological and ultrastructural methods. The volume of IFP was segmented from Magnetic Resonance images to identify the influence of OA. Geometrical data together with the constitutive tissue configuration of lobules and septa represent the basic data to provide numerical micro-models of the IFP. Numerical analyses were developed to evaluate the mechanical behavior considering the characteristic loading conditions as compression, torsion and shear actions.

Results from histomorphometric investigations showed that the IFP affected by OA maintains similar lobules configuration but thicker interlobular septa. At the same time, the OA determined a decrease in IFP volume. The results from numerical analysis pointed out the mechanical relevance of IFP and the loss of proper stress-strain performances of the OA IFP under mechanical loads.

Keywords - **Infrapatellar fat pad, osteoarthritis, magnetic resonance, computational biomechanics.**

I. Introduction

Recent advances in medical research address to the evidence that specific body fat tissues have not only the classic role of energy storage but also a relevant mechanical function. The infrapatellar fat pad (IFP) is located in the knee between patellar tendon, femoral condyles and tibial plateau, underneath the patella. It is covered by synovial membrane posteriorly and is closely related also to articular cartilage, being intra-capsular and extra-synovial. It is hypothesized that the IFP provides cushioning of the knee, facilitates the distribution of synovial fluid and acts to absorb forces through the knee joint [1]. Recent studies suggest that, besides synovial membrane, cartilage and subchondral bone, the IFP could be involved in knee osteoarthritis (OA), in consideration of its location and on the metabolic properties of adipose tissue as a potential source of adipokines and cytokines [2]-[5]. OA is the most common joint disease and a major cause of pain and disability, especially in the elderly population. OA has a multifactorial etiology with a combination of biomechanical, genetic, inflammatory and hormonal factors [3],[4]. Abnormal biomechanical loading is an etiological factor that can be caused by partial or total meniscectomy, malalignment, joint instability, muscle weakness, peripheral neuropathy. In addition, obesity is a risk factor for the onset of OA, because of the joint overload determined by weight and of the inflammation of the adipose tissue [4].

The IFP consists of white adipose tissue, of lobular type, with lobules delimited by thin connective septa. The presence of OA [2] suggests changes in the histological conformation, morphology and a consequent different mechanical response.

With regard to the control and OA IFP, the geometrical conformation and the composition of adipose lobules and of interlobular septa were studied through histological and ultrastructural methods [9]. Elaborations of magnetic resonance imaging (MRI) were used to evaluate the volume and other morphometric measures of the IFP and to investigate how these measurements are influenced by OA condition [6].

Results from the micro-structural configuration and composition [7], [8] made it possible to develop computational models, which allowed investigating the IFP mechanical functionality. Finite element micro-models of the fat tissue were developed by considering the specific adipose lobules dimension, fibrous septa thickness and the mechanical properties of the different sub-components. The mechanical behavior of the lobules and the fibrous septa was interpreted by hyperelastic constitutive formulations. Numerical analyses were developed taking into account of compression, torsion and shear loads, aiming at evaluating the mechanical response in typical physiological situations.

II. Materials and Methods

A. Histo-morphometric configuration

Samples of IFP were collected both from OA patients who underwent total knee replacement (TKR) at the Orthopedic Clinic of Padova University Hospital (28 subjects, 21 females, 7 males, mean age 68,9), and from bodies of the Body Donation Program 'Donation to Science' of the Padova University (8 subjects, 4 females, 4 males, mean age 81,8), with no macroscopic evidence of OA.

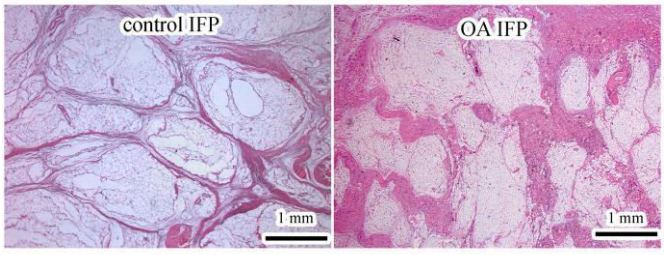

Fig. 1. Microscopic appearance of control and OA IFP.

The study was approved by the Local Ethical Committee and patients signed the informed consent. Procedures carried out on cadavers have been performed according to European guidelines [9],[10]. Thick sections of 10 μm were obtained from paraffin-embedded specimens. Different image analysis procedures allowed the identification and the quantification of the sub-components, in particular elastic and collagen fibers (Fig. 1). Using specific imaging software (Adobe Photoshop CS5, Adobe Systems Incorporated, USA), the septal walls were identified. Subsequently, images were converted to 8-bit binary images for the elaboration with a specifically developed algorithm implemented in Matlab R2012b (The MathWorks, Inc., USA). Parallel lines, with an interline distance of ~200 μm, were randomly overlaid on rotated 4x images. Orthogonal lines to the left aspect of the septal walls were drawn, leading to the measurements of the intercept length. Using a similar procedure, the dimension of adipocyte lobules was calculated [11],[12].

B. Magnetic Resonance analysis

The MRI of control and OA subjects were acquired using 1.5 tesla magnets. The DICOM images were processed by using an imaging density segmentation software. The reconstruction of the soft tissues required the elaboration of MRI images that made it possible to distinguish the different soft tissues with different grey levels [6],[13]. During segmentation of the knees, the imaging parameters, as brightness, intensity, contrast, were adjusted manually. For all slices the IFP was depicted. The same reader defined all segmentations with quality control performed by an experienced radiologist to ensure reliable measurements [13].

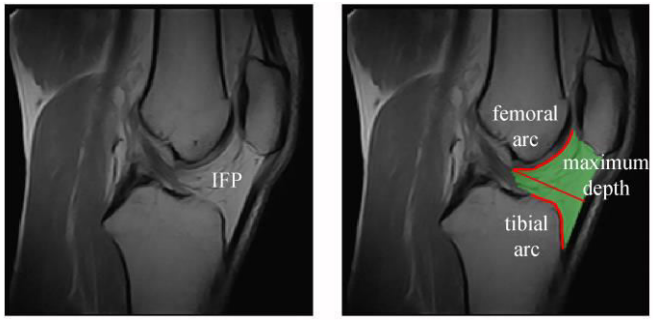

Fig. 2. Sagittal MRI of the knee joint with segmentation of the IFP with marked volume green. Indication of the measurements on the central sagittal slice of the maximum depth and the femoral and tibial arcs.

The IFP volume and the maximum depth, the femoral arc and the tibial arc of the sagittal slice located in the center of the segmented IFP (central sagittal slice) were determined (Fig. 2). The maximum depth was calculated as the length of the perpendicular segment to the patellar tendon passing through the point of the IFP more internally to the joint. The femoral and tibial arcs were calculated as the profile of the IFP adjacent to the corresponding bonehead.

C. Finite element models

Basing on the results of histo-morphometric studies, a three-dimensional micro-model of the IFP was developed. Histological data were increased of a 25% factor to correct the shrinkage that inevitably occurred during tissue processing [14]. Adipose lobules were modeled by lobules, which were separated by connective septa. The virtual solid model was composed by different layers, which were shifted each other according to a hexagonal scheme. This configuration well interprets the actual histo-morphological conformation of the tissue [7],[8]. The numerical model was developed using four node tetrahedral elements. A wedge model was assumed for the analysis of compression and torsion loading conditions [15] and a cubical shape for the shear specimen [16].

The further step of the micro-model development pertained to the definition of sub-components mechanical response. The histological conformation of control adipose chambers suggested the isotropic and almost-incompressible behavior and data from mechanical tests showed the non-linear mechanical response. Consequently, an hyperelastic isotropic constitutive formulation was assumed [8]. The performed histological examinations revealed the typical fibre-reinforced conformation of connective septa. In the IFP there was a prevalence of collagen I fibers (43%) with respect to collagen III fibers (18%), while low percentage of elastic fibers. The septa were characterized by the anisotropic configuration of fibrous components and the non linear stress-strain behavior. A fiber-reinforced hyperelastic formulation was assumed with two collagen fibres families spirally wound around the adipose chambers, running in clockwise and anticlockwise directions according to a 30 degrees angle [8]. In order to evaluate the effect of OA phenomena on the mechanical behaviour, further experimental investigations were considered. Results from compression tests performed on degraded adipose tissue showed the increase of stiffness. An hyperelastic isotropic constitutive formulation was assumed [8]. The OA IFP presented a relatively minor amount of collagen fibers (35%), with an increase of elastic fibers. Consequently, an isotropic hyperelastic constitutive model was assumed for OA IFP interlobular septa, because a minor amount of fibers was found respect to control IFP. The constitutive identification was performed considering data from mechanical tests performed on healthy and pathological tissues whose conformations are similar to human lobules and interlobular septa, as pig fat tissues and human ligaments [7],[8].

D. Numerical analysis

Numerical analyses were developed by using the general purpose finite element code Abaqus 6.14 (Dassault Systèmes Simulia Corp., Providence, RI). The constitutive formulations were implemented by specific user subroutines UMAT.

The developed wedge model was constrained to analyze the tissue compressive behavior. The bottom side of the model was fixed, the top side was moved downward up to about 40% structural compressive strain, the planar lateral faces were constrained to ensure the symmetric configuration, while the circular lateral face was unconstrained.

The shear behavior of the tissue was analyzed considering both torsion and pure shear tests. The numerical analyses of torsion loading were developed applying a rotation of 0.5 rad of the top surface of the numerical micro-model while the bottom side was fully fixed**.** Simple shear tests were developed by constraining the bottom face of the cubic model, while a purely transversal displacement was imposed to the upper face of the specimen up to about 0.5 structural shear strain [17].

III. Results and Discussion

Results from histo-morphometric analysis reported in terms of median, 25th and 75th percentile data, showed thick connective septa and a relatively small dimension of adipose lobules within OA IFP (Table 1).

	septa thickness (mm) median [25%; 75%]	lobules diameter (mm) median [25%; 75%]
Control	0.229 [0.145; 0.424]	1.160 [0.650; 1.983]
OA	0.355 [0.196; 0.689]	1.000 [0.528; 1.725]
p-value	0.004*	0.141

***p-value<0.05**

Table 1. Dimensions of interlobular septa and adipose lobules.

The comparison of results from microscopical investigations on control and OA IFP [9] highlighted the peculiar conformation and composition of IFP adipose lobules and interlobular connective septa.

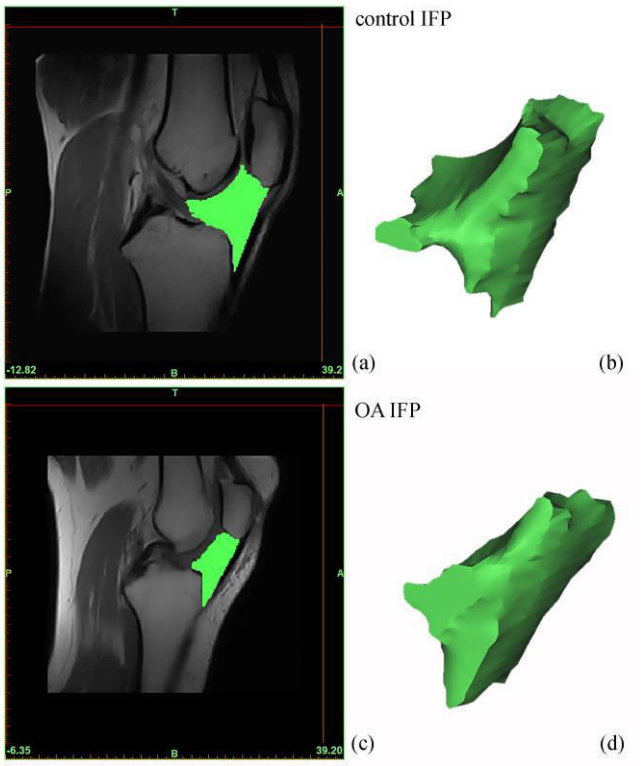

Fig. 3. Sagittal MRI of the knee joint with segmentation of the IFP with marked volume green for control (a) and OA (c) IFP. 3D reconstruction of the IFP for control (b) and OA (d) IFP.

Results from MRI analysis were reported as mean (±SD) values and ranges. Statistical analyses were performed using a t-test student. A $p<0.05$ was considered significant (GraphPad Software Inc., San Diego, CA, USA).

Considering the OA IFP volumes, the relative difference compared with controls patient was -25% (Fig. 3). In addition, other morphometric measures of IFP size appeared to be smaller in OA (Fig. 4).

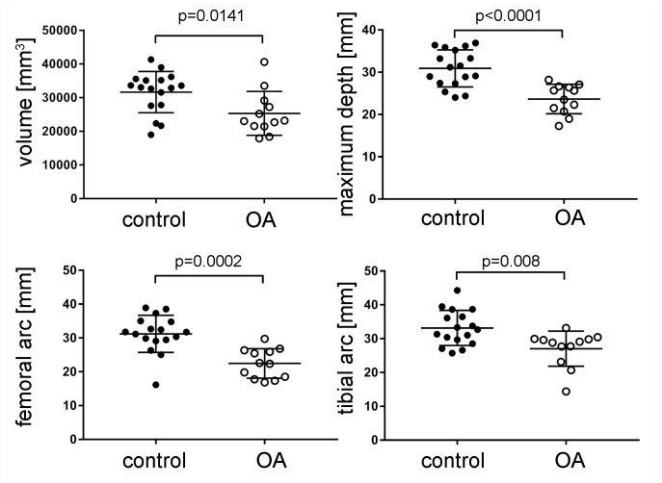

Fig. 4. Relationship between IFP volume, maximum depth, femoral arc and tibial arc in Control and OA IFP. Mean ± standard deviation and p-values are indicated.

Results from numerical analyses made it possible to compare the structural behavior of control and OA IFP considering compression, torsion and shear tests. Typical contours of tensile stress were reported (Fig. 5). Post-processing of numerical results allowed better understanding the contribution of tissue sub-components to the IFP mechanical functionality.

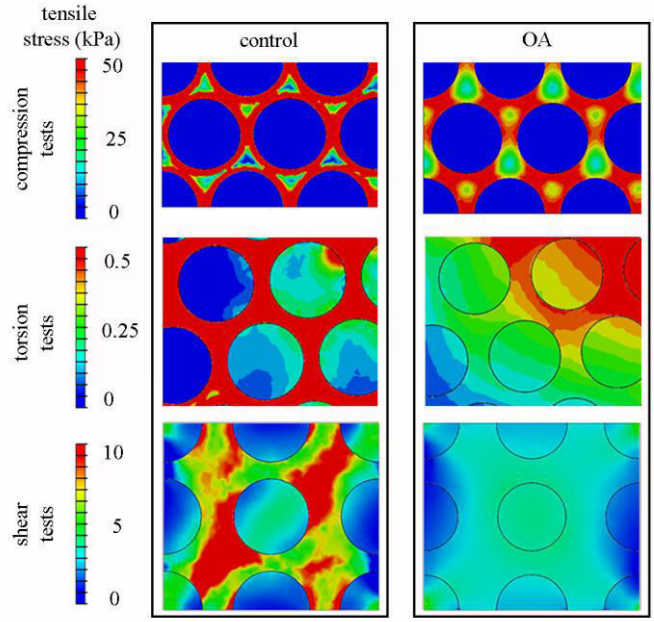

Fig. 5. Results from the numerical analysis of compression, torsion and shear tests: contours of tensile stress, as the maximum principal stress, for control and OA IFP.

The results related to the compressive loading show a homogeneous distribution of the tensile stress around the adipose lobules for the healthy IFP. In contrast, the OA IFP shows a non-organized distribution of the stresses within the interlobular septa. The mechanical behavior of the septa affects the mechanical response of the adipose lobules. The compressive stress-strain behavior of IFP shows an increase of compressive stiffness in OA condition, which reduces the capability of the tissue to adapt themselves and to redistribute loads through the adjacent biological structures (Fig. 6).

The inadequacy of OA IFP to withstand shear action is showed by numerical results under torsional and shear tests. Results from healthy IFP show a distribution of tensile stress along fibers direction, suggesting the capability of fibers to oppose to torsional actions. On the other side, circumferential distribution of tensile stresses characterizes the OA condition, because of the random distribution of fibers inside the interlobular septa. Such differences highlight the relevance of fibers contribution to shear stiffness and strength in healthy IFP. The shear response shows a larger stiffness in the IFP with respect to OA IFP under torsional and tangential loads (Fig. 6). The altered mechanical functionality of OA IFP suggests the reduced capability to redistribute loads and to dump impulsive actions, and the consequent potential damage induced on adjacent soft tissues.

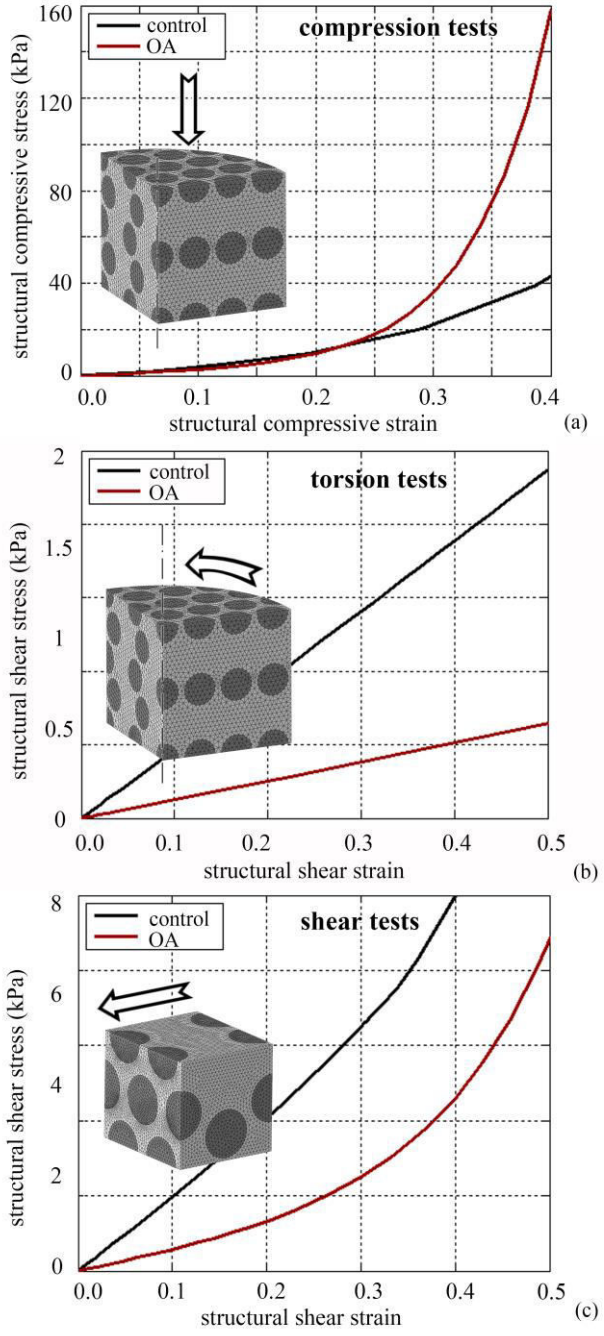

Fig. 6. Comparison of the structural behavior of the control and OA IFP for compression (a), torsion (b) and shear (c) loading conditions.

IV. Conclusion

The analysis developed represents a preliminary step in the characterization of the mechanical behavior of healthy and OA IFP. The present study describes the changes of histologicic and morphologic organization and the resulting mechanical behavior of IFP due to OA. Interlobular septa of OA IFP was thicker compared with those of control patients and presented a smaller dimension of adipose lobules. This peculiar conformation determines a decrease of IFP volume. Histo-morphometric variations determine the variation of stress-strain behavior of the OA IFP under mechanical loads.

These findings may be of interest also for the action to be taken during surgical intervention procedure and in particular in the assessment of the possible removal of the IFP in case of TKA, in consideration of pain induced by tissue high stiffness. In general, the overall mechanical functionality of knee joint is under investigation and further mechanical tests and subsequent computational investigations are in progress for a better interpretation of the mechanics of healthy and OA IFP.

References

[1] A. Hoffa, "The influence of the adipose tissue with regard to the pathology of the knee join", *J Am Med Assoc*, vol. 43, pp. 795-796, 1904.

[2] K.M. Clements, A.D. Ball, H.B. Jones, S. Brickmann, S.J. Read, F. Murray, "Cellular and histopathological changes in the infrapatellar fat pad in the monoiodoacetate model of osteoarthritis pain", *Osteoarthritis Cartilage,* vol.17, pp. 805-812, 2009

[3] S. Clockaerts, et al., 2010. "The infrapatellar fat pad should be considered as an active osteoarthritic joint tissue: a narrative review" *Osteoarthritis Cartilage,* vol.18, 876-882, 2010.

[4] A. Ioan-Facsinay and M. Kloppenburg, "An emerging player in knee osteoarthritis: the infrapatellar fat pad", *Arththerapy*, vol.15, pp. 225, 2013.

[5] M.B. Goldring and S.R. Goldring, "Osteoarthritis", *J Cell Physiol*, vol. 213, pp. 626-634, 2007.

[6] B. Burda, et al., "Variance in infra-patellar fat pad volume: does the body mass index matter?-data from osteoarthritis initiative participants without symptoms or signs of the knee disease", *Ann Anat*, vol. 213, pp. 19-24, 2017.

[7] A.N. Natali, C.G. Fontanella, and E.L. Carniel, "A numerical model for investigating the mechanics of calcaneal fat pad region", *J Mech Behav Biomed*, vol. 5, pp. 216-223, 2012.

[8] C.G. Fontanella, F. Nalesso, E.L. Carniel, and A.N. Natali, "Biomechanical behavior of plantar fat pad in control and degenerative foot conditions", *Med Biol Eng Compu,* vol. 54, pp. 653-661, 2016.

[9] R. De Caro, V. Macchi, and A. Porzionato, " Promotion of body donation and use of cadavers in anatomical education at the University of Padova", *Anat Sci Educ*, vol. 2, pp. 91-92, 2009.

[10] A. Porzionato, et al., "Quality management of Body Donation Program at the University of Padova", *Anat Sci Educ,* vol. 5, pp. 264-272, 2012.

[11] V. Macchi, et al., "The infrapatellar adipose body: an histotopographic study", *Cell Tissue Organs,* vol. 201, pp. 220-231, 2015-2016.

[12] M. Favero, et al., "Infrapatellar Fat Pad features in osteoarthritis: a histopathological and molecular study", *Rheumatology*, vol. 56(10), pp. 1784-1793, 2017.

[13] E. Steidle-Kloc, W. Wirth, A. Ruhdorfer, T. Dannhauer, and F. Eckstein, "Intra- and inter-observer reliability of quantitative analysis of the infrapatellar fat pad and comparison between fat- and non-fat-suppressed imaging – Data from the osteoarthritis initiative", *Ann Anat*, vol. 204, pp. 29-35, 2016.

[14] P-B. Dobrin, "Effect of histologic preparation on the cross-sectional area of arterial rings", *J Surgical Research,* vol. 61, pp. 413-415, 1996.

[15] W.R. Ledoux, J.J. Blevins, "The compressive material properties of the plantar soft tissue", *J Biomech*, vol. 40, pp. 2975-2981, 2007.

[16] S. Pai and W.R. Ledoux, "The shear mechanical properties of diabetic and non-diabetic plantar soft tissue", *J Biomech*, vol. 45, pp. 364-370, 2012.

[17] G. Sommer, et al., "Multiaxial mechanical properties and constitutive modeling of human adipose tissue: a basis for preoperative simulations in plastic and reconstructive surgery", *Acta Biomater*, vol. 9, pp. 936-948, 2013.

A segmentation method for OCT images of coronary arteries treated with bioresorbable stents: validation and application to numerical modelling

M. Bologna[1,2], S. Migliori[2], E. Montin[1], R. Rampat[3], D. Hildick-Smith[3], J. Cockburn[3], F. Migliavacca[2], L. Mainardi[1] and C. Chiastra[2]

[1] *Department of Electronics, Information and Bioengineering (DEIB), Politecnico di Milano, Milan, Italy*

[2] *Department of Chemistry, Materials and Chemical Engineering "Giulio Natta", Politecnico di Milano, Milan; Italy*

[3] *Sussex Cardiac Centre, Brighton and Sussex University Hospitals, Brighton, UK*

***Abstract*—This study presents an automatic segmentation method for the detection of both coronary lumen contours and polymeric stent struts from *in-vivo* optical coherence tomography images (OCT). OCT scans and angiographic projections from seventeen patients treated with a bioresorbable scaffolds were collected. Results obtained with the automatic OCT segmentation method were compared to manual delineation performed by an expert reader. Values of sensitivity coefficient were 98.4% ± 3.14% and 78.64% ± 20.10% for the lumen contours and stent struts segmentation, respectively. The obtained specificity values were 99.48% ± 0.33% and 91.42% ± 15.89% for the lumen contours and stent struts segmentation, respectively. A segmented OCT dataset was used in combination with angiographic images to create the 3D geometrical model of the stented coronary artery of one patient. A transient computational fluid dynamics simulation was then performed. The availability of OCT acquisitions at follow-up extends the application of the proposed automatic segmentation method to study the relation between post-implant altered fluid dynamics and neointimal regrowth.**

***Keywords*—Optical coherence tomography, image segmentation, bioresorbable scaffold, coronary arteries, computational fluid dynamics.**

I. Introduction

CORONARY artery disease is one of the leading cause of death worldwide. The main technique for the treatment is balloon angioplasty followed by stent implantation. In-stent restenosis (i.e. the partial or total re-occlusion of the vessel in the months after treatment) is one of the main issues of stent implantation. Among the different causes of in-stent restenosis, the alteration of the local fluid dynamics due to the stent plays an important role in the onset and evolution of this disease.

Computational fluid dynamics (CFD) is a valuable tool for the analysis of blood flow in complex geometries such as coronary arteries [1]. Medical imaging can provide realistic 3D models of the vessels that can be used as domains to perform CFD simulations [1]. Optical coherence tomography (OCT) is an infrared-based imaging technique that provides high resolution images of the coronary lumen (in-plane resolution of 10-15 μm), in which stent struts can be easily recognized [2]. OCT is often used in combination with X-ray angiography to reconstruct the 3D models [3]. Many algorithms for lumen contour segmentation from OCT images have been developed [3]. As regards the stent segmentation, the majority of the studies focus on the segmentation of metallic stents [3]. The limited number of works about the detection of bioresorbable polymeric scaffolds may be addressed to their recent introduction and the negative long-term clinical outcomes of the Absorb Bioresorbable Vascular Scaffold (BVS) (Abbott Vascular, Abbott Park, IL, USA). However, the extensive development of the bioresorbable stent technology suggests that the detection algorithm for polymeric stents will probably become more and more important in the coming years [3]. Since the bioresorbable stent optical properties are very different from the metallic stents, the techniques used for metallic stent segmentation might not be effective. Therefore, the segmentation algorithms should account for different image features.

The aim of this work is to present and validate a new segmentation algorithm for both lumen contours and polymeric stent struts from *in-vivo* OCT images. Moreover show an application of this algorithm, for one analysed case, the 3D model of the stented coronary artery is reconstructed starting from the segmentation results and it is used for a transient CFD simulation.

II. Materials and Methods

A. Clinical dataset

Seventeen *in vivo* OCT pullbacks of coronary arteries treated at the Brighton and Sussex University Hospitals (Brighton, UK) with the Absorb BVS were selected to develop and validate the segmentation algorithm. The OCT scans were performed after stent implantation in 17 patients belonging to the Absorb in Bifurcation Coronary trial (ABC-ONE), a single centre, randomized trial comparing different sizing strategies when using bioresorbable scaffolds for the treatment of coronary bifurcation disease. The study comply with the Declaration of Helsinki on human research and was approved by the South East Coast (Brighton and Sussex, UK) Research Ethics Committee. All patients gave informed consent.

OCT imaging was performed using the FastView catheter R and the Lunawave coronary imaging console (Terumo Corp., Tokyo, Japan). The OCT catheter was carefully advanced over a guidewire beyond the target region. While contrast agent was continuously injected at a rate of 4 ml/s, OCT images of the main coronary vessel were acquired at a rate of 160 frame/s with a pullback speed of 20 mm/s. OCT resolution was 15 μm (in-plane) and 125 μm (Longitudinal OCT resolution, i.e. the distance between two consecutive frames). OCT images were

saved as 8-bit RGB images. In addition to OCT, multiple angiographic projections were acquired during the stenting procedure.

B. Segmentation algorithm of OCT images

The workflow of the OCT image segmentation process, which enables the detection of both lumen contours and Absorb BVS struts, is shown in Fig. 1. Image segmentation was performed in MATLAB 2016b (Mathworks, Natick, MA, USA).

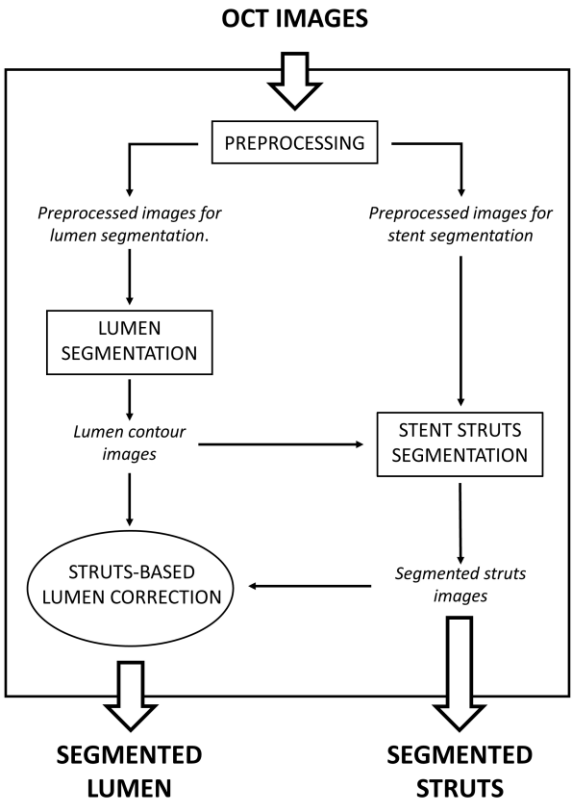

Fig. 1: Flow chart representing the main steps of the segmentation algorithm presented in this study. The operations presented in square blocks are always performed, while that in the elliptic block is optional. The output of each step is written in italic.

The *pre-processing* step is similar to that described in [4]. Briefly, the OCT images are cropped in order to remove the longitudinal vessel view and converted into grayscale. The visualization tools and the OCT catheter are removed. A further processing step, which is necessary only before lumen segmentation, is the removal of the noise inside the lumen. The image without noise is obtained by product of the original image and a binary mask. The binary mask is created through the following steps: (1) intensity thresholding, (2) morphological opening (MATLAB function *imopen*), (3) area thresholding (MATLAB function *bwareaopen*).

The *lumen segmentation* step is the same as that previously developed in [4]. Briefly, the pre-processed images are converted into polar coordinates (r, θ) and a Sobel filter is applied to detect edges. The first pixel detected as edge for each value of θ (i.e. for each A-scan) is considered as part of the lumen contour. The identified pixels are interpolated and the result is converted back to Cartesian coordinates. In Fig. 2 an example of detected lumen contour is represented in yellow.

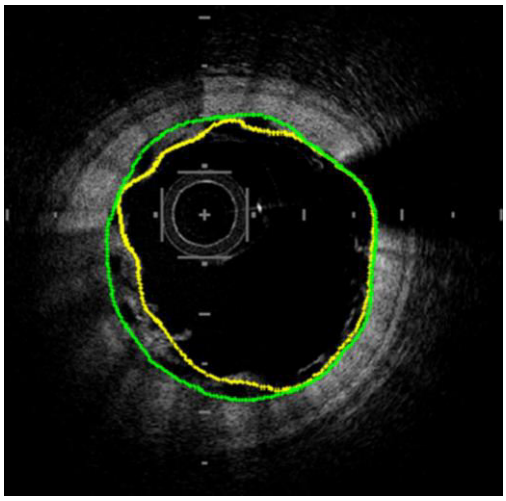

Fig. 2: Lumen contours superimposed on the original OCT image. The yellow contour represents the lumen pre-correction, while the green contour represents the lumen post-correction

The *stent struts segmentation* step is achieved by means of an innovative strategy and it is performed entirely in Cartesian coordinates. The main idea behind the segmentation is that the Absorb BVS struts appear in the OCT images as approximately rectangular regions with a low intensity core surrounded by bright pixels (Fig. 3). Ideally, such struts can be identified with three steps: (1) intensity thresholding (a pre-defined quantile of the pixel intensity distribution is used); (2) flood fill operation to close the holes in the binary image (performed with MATLAB command *imfill*); (3) boolean subtraction of the original binary image from the filled image. When the stent struts present a partially connected layer of bright pixels at their boundary (i.e. "open box" struts), the procedure described above is not able to recognise the strut. Furthermore, false positives are identified with these operations, especially close to the outer wall.

The problem introduced by the presence of "open box" struts is significantly reduced if a morphological closing as a disk structure element of 1-pixel radius is performed, after the intensity thresholding step. Although this operation cannot correct large gaps in the struts boundary, it helps to improve the sensitivity of the segmentation. A nonlinear filter (γ-filter, with γ=0.6) is also applied to the images to enhance the contrast of the image.

The false positives are removed by applying a series of filtering rules. First, the struts are bounded to have area between two thresholds A_{min} and A_{max} (in this case, 10 and 300 pixels). Then, the lumen is dilated using a disk of radius R_{dil} (in this case, 20 pixels) and all the struts outside this expanded lumen are removed. Lastly, the struts centroid must have a distance lower than D_{Max} (in this case 5 pixels) from a reference line, which is a spline that interpolates the centroids of the struts identified by a first rough segmentation. This segmentation is performed by following the points 1-3 previously described, followed by a morphological opening with a 3-pixels radius disk. This allows performing a low-sensitivity but high-specificity segmentation, which is ideal for the interpolation of the reference line. This line is interpolated

by using also the struts identified in the images adjacent to the one of interest, to account for images with a low number of struts, where the quality of the interpolation is low.

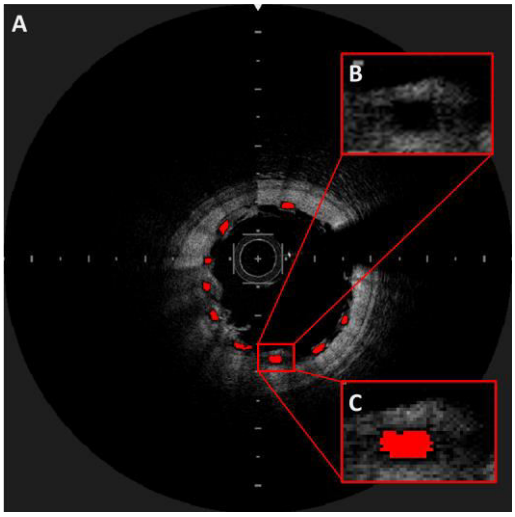

Fig. 3: Example of the Absorb BVS struts segmentation. A) Original image. B) Detail of a specific strut. C) Segmentation of the strut in B.

The *strut-based lumen correction* is the last step of the segmentation process. In case of baseline acquisitions and for well apposed struts, the adluminal wall of the strut should be on the lumen boundary. However, when two struts are in contact, or when there is residual blood close to the lumen wall (such as in the left part of Fig. 2 and 3), the lumen identified in the first part of the algorithm is not accurate. The struts-based correction provides a new lumen contour by combining the pre-correction lumen (in yellow in Fig. 2) with the line that interpolates the position of the abluminal wall of the struts. This analysis is performed in polar coordinates. For each θ, only the contour with the highest radial value is chosen. The result is shown in Fig. 2 in green.

C. *Validation of the OCT segmentation algorithm*

To validate the algorithm, the results were compared with manual segmentation performed by an expert reader using open source software MRIcro. In particular, the region of interest (ROI) for lumen segmentation is the region enclosed in the identified lumen contour in each OCT image, while for stent segmentation the ROIs are represented by the stent struts. Fifty test images were sampled for each acquisition, for a total of 850 images for the lumen and 850 images for the stent. The sampling of the images was performed uniformly through the whole acquisition for the lumen segmentation and the stented portion for the stent segmentation. The quality of the automatic segmentation was assessed through the computation of sensitivity and specificity indexes, expressed as mean and standard deviation [4], [5].

D. *3D model reconstruction*

To verify the applicability of the segmentation method for subsequent 3D reconstruction of stented coronary artery models for CFD applications, one of the investigated cases, consisting in a left anterior descending coronary artery treated with a 3.5x23 Absorb BVS, was selected for 3D reconstruction from OCT and angiographic images. The 3D reconstruction method of the stented vessel is described in detail elsewhere [5]. Briefly, the vessel lumen creation comprises the following steps: (1) creation of a 3D point cloud from the 2D segmented OCT images; (2) proper alignment of the points along the centreline obtained from the combination of two angiographic projections (Fig. 4A); (3) interpolation of the contour points of each slice to create contour lines; (4) connection of the contour lines to create the lumen surface. Steps 1-2 are also performed for the creation of the 3D stent model. These steps are followed by: (3) creation of a stent centreline from a 3D geometrical model of the stent in its expanded straight configuration; (4) morphing of the straight stent centreline on the OCT stent point cloud; (5) loft of rectangular sections along the deformed centreline. The result of the 3D reconstruction is reported Fig. 4B.

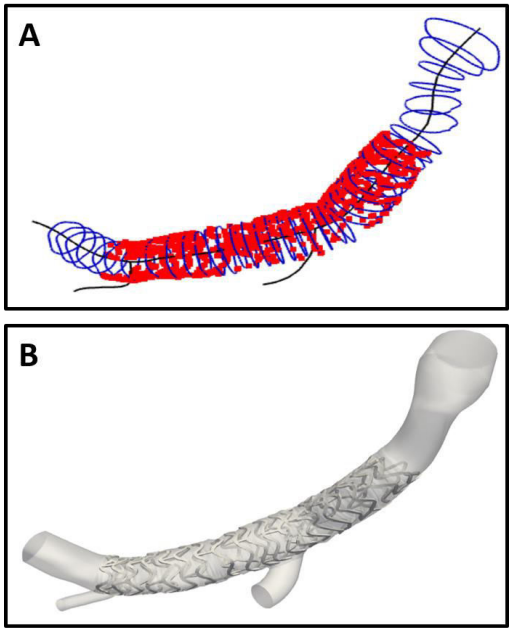

Fig. 4: 3D reconstruction of a right coronary artery treated with a 3.5x23 Absorb BVS A) Lumen contour points (blue) and stent strut centroids (red) aligned along the main vessel (black line). B) CAD geometry of the stented coronary artery suitable for CFD analyses.

E. *CFD simulation set-up*

The 3D stented model was discretized with tetrahedral elements using ICEM CFD (ANSYS Inc., Canonsburg, PA, USA). A transient CFD analysis was performed by means of Fluent (ANSYS Inc.). A typical coronary artery flow waveform [6] was imposed at the inlet as a flat velocity profile. The mean flow-rate (81.92 ml/min) was estimated by counting in the angiographic projections the number of frames required for the contrast agent to pass from the inlet to the outlets [7]. A flow-split estimated using a diameter-based scaling law was applied at the outlets [8]. The simulation settings are reported in [9].

III. Results and Discussion

A. *Validation of the segmentation algorithm*

Tables I and II show the results of the validation of the

segmentation algorithm.

The similarity indexes obtained from the validation of the lumen segmentation are high and comparable with previous studies [4], [5] (Table I). The sensitivity of the Absorb BVS strut detection algorithm is lower than the one obtained for metallic strut detection [4], but the specificity is high. Although the sensitivity to Absorb BVS struts detection is relatively low, it is high enough to detect enough struts for the 3D reconstruction phase.

To the best of the authors' knowledge, only another method for Absorb BVS struts segmentation have been proposed so far [10]. That method works only with fully "preserved box" struts. However, since in our case a significant portion of the struts appear as "open box" struts, we could not apply such algorithm.

TABLE I
SIMILARITY INDEXES FOR LUMEN SEGMENTATION

SIMILARITY INDEX	*% Value (mean ± sd)*
Sensitivity	98.4 ± 3.14
Specificity	99.48 ± 0.33

TABLE II
SIMILARITY INDEXES FOR STENT SEGMENTATION

SIMILARITY INDEX	*% Value (mean ± sd)*
Sensitivity	78.64 ± 20.10
Specificity	91.42 ± 15.89

B. Results of CFD simulation

The results of the CFD simulation are presented in Fig. 5. The region of low values of time-averaged wall shear stress (TAWSS) reflected the flow recirculation at the proximal side branch and the 39% of the scaffolded main branch segments underwent TAWSS ≤ 0.4 Pa, which is considered as potential trigger for neointimal regrowth and to cause late complications [11].

IV. CONCLUSION

A new method for the segmentation of polymeric stent struts in *in-vivo* OCT coronary images has been presented and validated. This work is one of the first attempt to automatize segmentation of bioresorbable vascular scaffold. The study also shows how the results of the segmentation, combined with the centreline obtained from angiographic images, can be used to build a 3D model of a diseased coronary artery treated with the Absorb BVS. Eventually, results of a CFD simulation performed on the model have been shown.

The presented framework has the potential of linking hemodynamics measurements to neointimal regrowth providing a way to better understand the factors that lead to success or failure of stent implantation.

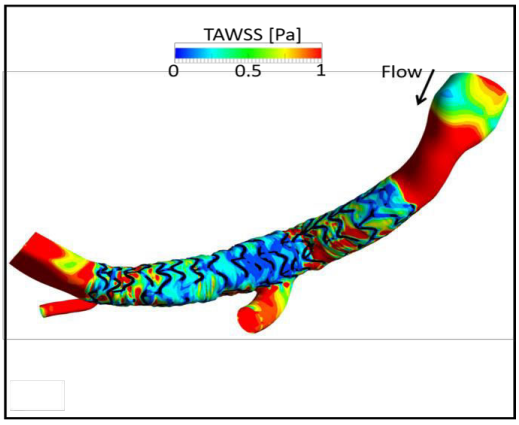

Fig. 5: Time average wall shear stress (TAWSS) contour map of the coronary artery treated with a 3.5x23 Absorb BVS.

ACKNOWLEDGEMENT

S. Migliori is supported by the European Commission through the H2020 Marie Skłodowska-Curie European Training Network H2020-MSCA-ITN-2014 VPH-CaSE, www.vph-case.eu, GA No. 642612.

REFERENCES

[1] D. A. Steinman, "Image-based computational fluid dynamics modeling in realistic arterial geometries," *Ann. Biomed. Eng.*, vol. 30, no. 4, pp. 483–497, 2002.

[2] G. Ferrante, P. Presbitero, R. Whitbourn, and P. Barlis, "Current applications of optical coherence tomography for coronary intervention," *Int. J. Cardiol.*, vol. 165, no. 1, pp. 7–16, 2013.

[3] C. Chiastra, S. Migliori, F. Burzotta, G. Dubini, and F. Migliavacca, "Patient-Specific Modeling of Stented Coronary Arteries Reconstructed from Optical Coherence Tomography: Towards a Widespread Clinical Use of Fluid Dynamics Analyses," *J. Cardiovasc. Transl. Res.*, pp. 1–17, 2017.

[4] C. Chiastra, E. Montin, M. Bologna, S. Migliori, C. Aurigemma, *et al.*, "Reconstruction of stented coronary arteries from optical coherence tomography images: Feasibility, validation, and repeatability of a segmentation method," *PLoS One*, vol. 12, no. 6, pp. 1–23, 2017.

[5] S. Migliori, C. Chiastra, M. Bologna, E. Montin, G. Dubini, *et al.*, "A framework for computational fluid dynamic analyses of patient-specific stented coronary arteries from optical coherence tomography images," *Med. Eng. Phys.*, vol. 47, pp. 105–116, 2017.

[6] J. E. Davies, Z. I. Whinnett, D. P. Francis, C. H. Manisty, J. Aguado-Sierra, *et al.*, "Evidence of a dominant backward-propagating 'suction' wave responsible for diastolic coronary filling in humans, attenuated in left ventricular hypertrophy," *Circulation*, vol. 113, no. 14, pp. 1768–1778, 2006.

[7] S. Sakamoto, S. Takahashi, A. U. Coskun, M. I. Papafaklis, A. Takahashi, *et al.*, "Relation of distribution of coronary blood flow volume to coronary artery dominance," *Am. J. Cardiol.*, vol. 111, no. 10, pp. 1420–1424, 2013.

[8] A. G. van der Giessen, H. C. Groen, P. A. Doriot, P. J. de Feyter, A. F. W. van der Steen, *et al.*, "The influence of boundary conditions on wall shear stress distribution in patients specific coronary trees," *J. Biomech.*, vol. 44, no. 6, pp. 1089–1095, 2011.

[9] C. Chiastra, S. Morlacchi, D. Gallo, U. Morbiducci, R. Cardenes, *et al.*, "Computational fluid dynamic simulations of image-based stented coronary bifurcation models," *J. R. Soc. Interface*, vol. 10, no. 84, pp. 20130193–20130193, 2013.

[10] A. Wang, S. Nakatani, J. Eggermont, Y. Onuma, H. M. Garcia-Garcia, *et al.*, "Automatic detection of bioresorbable vascular scaffold struts in intravascular optical coherence tomography pullback runs," *Biomed. Opt. Express*, vol. 5, no. 10, pp. 3589–3602, 2014.

[11] A. M. Malek, S. L. Alper, and S. Izumo, "Hemodynamic shear stress and its role in atherosclerosis.," *J. Am. Med. Assoc.*, vol. 282, no. 21, pp. 2035–2042, 1999.

Bone healing monitoring based on external fixator instrumentation: three case studies

A. Sorriento[1], F. Omar Ahmed Ba Fakih[2], C. Stefanini[1,2], L. Fabbri[3], G. Ciuti[1], M. Scaglione[3], P. Dario[1], S. Mazzoleni[1]

[1] *The BioRobotics Institute, Scuola Superiore Sant'Anna, Pisa, Italy*
[2] *Khalifa University, Abu Dhabi, United Arab Emirates*
[3] *Orthopaedics and Traumatology Unit, Pisa University Hospital, Italy*

***Abstract*— In this study an instrumented external fixator for bone healing monitoring is proposed. The frequency resonance and the amplitude of the vibration response were analyzed in three cases: healthy, fractured and healing bone.**
The results showed specific frequency peaks for each of the three cases. The quantitative discrimination in terms of amplitude and frequency resonance among different phases during the bone union process reported in this article suggests a future clinical validation.

***Keywords*— Biomechanics, fracture healing process, orthopaedic fixation system, vibration analysis.**

I. Introduction

BONE fracture healing is a complex phenomenon which involves participation of biochemical and biomechanical regulatory factors. Fracture healing process is characterized by four overlapped phases, starting with an inflammation phase, followed by two repair phases consisting of soft and hard callus formation and ended up with a remodelling phase [1]. In clinical practice one of the common surgical treatments is based on the use of external or internal fixation to restore the original properties and biomechanical functions. Approximately 5–10% of the 6.2 million fractures occurring annually in the United States are associated with impaired healing. Delayed bone healing and non-union represent the main drawbacks, associated with patients and fracture dependant risk factors [2].

The tools currently available to assess the state of bone union include imaging studies, mechanical assessment, serologic markers and clinical examination [3]. The clinical findings and radiological features remain the gold standard in the diagnosis of bone union, despite this kind of approach is subjective and not reproducible [4].

The explored methods include direct measurement, indirect measurement and vibration testing procedures. The basic concept is that bone stiffness increases as a fracture heals [3]. Direct measurement of callus stiffness consists of the calculation of the deflection at the fracture site under loading with all the fixation devices removed [5]. It is based on the concept that the degree of deflection is inversely related to the stability of the fracture [3].

In the indirect approach a load is applied and shared by the fixation device. Basing on the fact that the deformation of the frame is in inverse proportion to the stiffness of the callus, the change in load sharing, detected using strain gauges or load cells, can give information about bone stiffness [6].

Vibration analysis represents a valid means for assessing the mechanical properties of a healing fracture. When the bone is excited by mechanical signals, it changes the vibration response relating to its density and its structural stiffness [7].

Recently, some works, based on the vibration theory, have been conducted in order to monitor the state of bone fracture, treated by external fixator [8].

Previous studies proved that Whole Body Vibration (WBV) can be beneficial in improving fracture healing in animals without any safety problems reported [9].

The objective of this study is to present the vibration response on three case studies, using an instrumented external bone fixator.

II. Methods

A. The experimental set-up

Figure 1 shows the humerus model used in this experiment (Model 1028, Sawbones, Krossverksgatan, Malmoe, Sweden), whose biomechanical characterization is known [10].

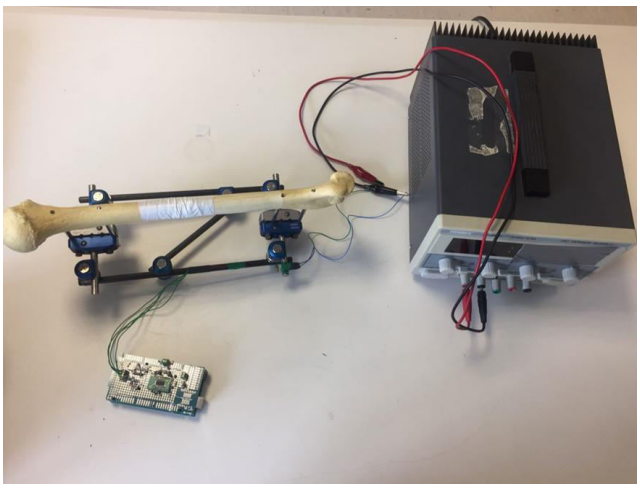

Fig. 1: The setup used in the experiment

The test bone was fixed with a Hoffmann II external fixation system (Stryker, Kalamazoo, MI, USA). It was integrated with two strain gauges (Micro-Measurements, Wendell, NC, USA), one for each side of the connecting rod and an Arduino Mega 2560 electronic board.

The input signal was generated by a vibration system, composed of a 8 mm diameter DC motor (Model 108-104, Precision Microdrives Ltd, London, UK) placed on a bar of

the external fixator and a prismatic eccentric mass made of brass alloy CW614N.

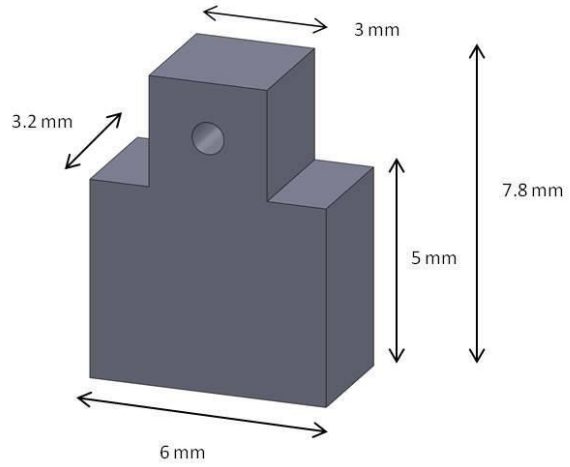

Fig. 2: Shape and dimensions of the eccentric mass used in the experiment

Three case studies and three different bone specimens were included in this experiment: healthy, fractured and healing bone as shown in Fig. 3.

The fixated saw-bone was subjected to a through-cut in the middle part to simulate a fracture. Then, foam and tape were inserted in order to reproduce the healing phase.

Fig. 3: Three bone cases: (a) healthy bone, (b) fractured bone, (c) healing bone.

Voltages from 1.0 V to 3.0 V, with a step of 0.1 V, were applied to test the whole system in a wide range of conditions.

An algorithm was implemented in order to record the frequency and amplitude of the resonance response, characterising the system stiffness.

Finally, the highest amplitude was identified and the corresponding frequency was selected as the resonance frequency of the whole system.

III. Results

A. *Experimental results*

The amplitudes of the resonance response versus the motor voltage were reported for each case study (Fig. 4).

The test on the healthy bone showed a peak of amplitude (0.13) at 2.6 V. The corresponding resonance frequency was recorded at 251.333 Hz (as shown in Fig. 4, (a)).

The results for the complete fracture presented the same value of amplitude peak at 2.3 V with a resonance frequency of 184.902 Hz (Fig. 4, (b)).

Finally, a resonance frequency of 200.646 Hz at 2.5 V was reported in the case of healing bone (Fig. 4, (c)).

The first amplitude peak observed at 1.3 V, in the fractured and healing bone results, corresponded to the intrinsic resonance frequency of the whole system.

The second amplitude peak observed at 2.3 V and 2.5 V represented the typical mechanical characteristic of the fractured saw-bone model.

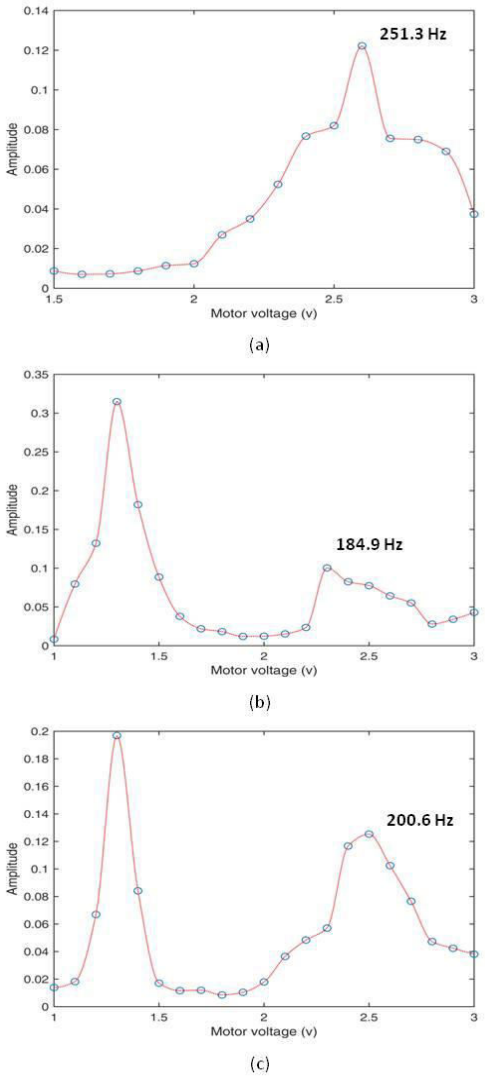

Fig. 4: Vibration amplitudes at different motor voltages for (a) healthy bone, (b) fractured bone and (c) healing bone.

IV. Discussion and Conclusion.

Despite a great deal of studies have been focused on the quantitative assessment of bone union, this still represents a complex and challenging scientific and clinical issue.

Recent studies investigated the application of a vibration analysis in the orthopaedic field for the assessment of bone union [8].

In our study the same vibrational approach was used in order to evaluate its potential application as clinical method for monitoring the bone healing process.

The recorded values showed an interesting trend across the three case studies. The fractured bone shows a decrease of the resonance frequency and voltage values compared to those recorded in the healthy bone (Table I).

TABLE I

	Motor voltage at resonance (V)	*Resonance Frequency (Hz)*
Healthy bone	2.6	251.3
Fractured bone	2.3	184.9
Healing bone	2.5	200.6

It is likely that the different stages are characterized by different resonance frequency and amplitude, thus representing the typical mechanical characteristics of the bone model. Hence the application of vibrations to the bone-fixator system may be able to provide useful information on the mechanical characteristics of the bone during the healing process.

However our preliminary study presents some limitations. The biomechanical properties of the bone model are rather different from those real. Secondly the healing process was simulated by using foam and tape, thus making a strong simplification. In fact the bone fracture healing is a complex process which has to take into account several factors for the development of a detailed biomechanical model. Finally the soft tissue representation was not involved in this study, thus not considering the signals transmission through soft tissues and their damping effect

A solution able to overcome the current limitations is represented by the realization of a new bone and soft tissues model using specific biomechanical properties that are of interest to the vibration analysis. The future models will be representative of the main steps of the fracture healing process through the reproduction of the biomechanical properties of the growing bone callus. Then the vibration response will be tested on the new set of models.

Based on this approach reference values for each stage will be recorded: such values can be used by orthopaedic surgeons and rehabilitation staff to monitor the bone healing process, even remotely.

Then the identification of an appropriate measurement protocol will be carried out in order to perform a clinical validation of the instrumented external fixator: data on different patients affected by long bone fracture will be recorded and, therefore, the proposed vibrational approach will be tested by using real clinical data.

References

[1] M. Wang, N. Yang, and X. Wang, “A review of computational models of bone fracture healing,” Med Biol Eng Comput, vol. 55, no. 11, pp. 1895-1914, Nov. 2017.

[2] I. Pountos, T. Georgouli, S. Pneumaticos, and P. V. Giannoudis, “Fracture non-union: Can biomarkers predict outcome?,” Injury, vol. 44, no. 12, pp. 1725-32, Dec. 2013.

[3] B. P. Cunningham, S. Brazina, S. Morshed, and T. Miclau, “Fracture healing: A review of clinical, imaging and laboratory diagnostic options,” Injury, vol. 48 Suppl 1, pp. S69-S75, Jun. 2017.

[4] G. E. Cook, B. D. Bates, P. Tornetta, M. D. McKee, S. Morshed, G. P. Slobogean, and E. H. Schemitsch, “Assessment of Fracture Repair,” *Journal of Orthopaedic Trauma,* vol. 29, pp. S57-S61, 2015.

[5] J. B. Richardson, J. L. Cunningham, A. E. Goodship, B. T. O'Connor, and J. Kenwright, “Measuring stiffness can define healing of tibial fractures,” J Bone Joint Surg Br, vol. 76, no. 3, pp. 389-94, May. 1994.

[6] F. Burny, W. Burny, M. Donkerwolcke, and M. Behrens, “Effect of callus development on the deformation of external fixation frames,” Int Orthop, vol. 36, no. 12, pp. 2577-80, Dec. 2012.

[7] P. Augat, M. Faschingbauer, K. Seide, K. Tobita, S. A. Callary, L. B. Solomon, and J. H. Holstein, “Biomechanical methods for the assessment of fracture repair,” Injury, vol. 45 Suppl 2, pp. S32-8, Jun. 2014.

[8] W. Ong, W. Chiu, M. Russ, and Z. Chiu, “Integrating sensing elements on external fixators for healing assessment of fractured femur,” Structural Control and Health Monitoring, vol. 23, no. 12, pp. 1388-1404, 2016.

[9] J. Wang, K. S. Leung, S. K. Chow, and W. H. Cheung, “The effect of whole body vibration on fracture healing - a systematic review,” Eur Cell Mater, vol. 34, pp. 108-127, Sep. 2017.

[10] S. Worldwide, "Biomechanical Test Materials Catalogue," *Vashon, WA*.

Combining computational and experimental methods to investigate the effect of hemodynamics on vascular tissues

M. Franzoni[1, 2], N. Aristokleous[1, 2], C. Cunnane[1, 2], R. Cahalane[1, 2], N. Alam[2], J. Lynch[1, 2], D. Moran[1, 2], D.T. O'Connor[1, 2], D. Newport[2], J.G. Houston[3] and M.T. Walsh[1, 2, 4].

[1]*Bioscience and Bioengineering Research Centre (BioSciBER), University of Limerick, Ireland.*

[2]*Bernal Institute, School of Engineering, University of Limerick, Ireland.*

[3]*Molecular & Clinical Medicine, School of Medicine, University of Dundee, Dundee, Scotland, UK.*

[4]*Health Research Institute (HRI), University of Limerick, Ireland.*

***Abstract*—Hemodynamics is strongly correlated with the occurrence and progression of vascular diseases. To provide clinicians with usable tools to predict the localisation and risk of specific hemodynamics patterns occurring in the vasculature, a multidisciplinary approach is required. Here a comprehensive methodology that aims to provide fast and accurate information employing non-invasive methods is presented.**

***Keywords*—Cardiovascular diseases, Medical imaging, Computational biomechanics, Bioreactors.**

I. Introduction

CARDIOVASCULAR diseases (CVD) are the global leading cause of death. Over 17 million people died in 2016 due to a cardiovascular pathology, accounting for the 30% of overall deaths [1]. Despite CVD having many concurrent causes such as diet, tobacco smoke and poor physical activity [2], all CVD have a biomechanical component [3]-[4]. Transmural pressure and wall shear stress (WSS) are known to have profound effects on vascular cellular components and thus on the mechanical behaviour of the vessel [5]. Pathologies such as hypertension, atherosclerosis, aneurysms and strokes are caused or promoted by the transduction of mechanical stress induced by specific hemodynamics. Confoundingly, lesion formation further negatively affects the hemodynamics in a disease promoting circular process. A clear example of this process is the development of atherosclerotic lesions [6]. These lesions are preferentially located in areas exposed to disturbed WSS, the growth of the lesions induces even more disturbed WSS that ultimately leads to vessel stenosis or plaque rupture.

To understand the effects of hemodynamics on the vasculature, it is necessary to have precise information about the geometry and the mechanical stresses in the area of interest. The limits in obtaining this data in a non-invasive and accurate manner, led to development of imaging techniques and computational methods. Furthermore, the mechanical properties of the vascular tissues in specific areas of the vasculature are also needed.

In the last four decades several studies have partially revealed the intimate relationship between hemodynamics and vascular biology. However, the extreme simplification of *in-vitro* experimental settings [7] and the intrinsic limits of *in-vivo* studies, have stunted the creation of clinical tools to predict localisation and risk of patient-specific vascular lesion formation. Moreover, the majority of studies focused on the effects of arterial hemodynamics on arterial tissues. The venous context remains very poorly addressed despite the fact that venous tissues, used for cardiac bypass or in the creation of native vascular accesses (VA) for hemodialysis, have a very high rate of stenosis probably due to the altered hemodynamics [8].

For these reasons a comprehensive, multidisciplinary approach to tackle the hemodynamics role in CVD is proposed. By using magnetic resonance images (MRI), realistic geometries are created and used for computational reconstruction of specific vascular geometries. These geometries, together with specific hemodynamics are employed to calculate local stresses. To evaluate the accuracy of these simulations, the effects of compliant tissues is evaluated by using fluid-structure interaction (FSI) techniques. To assess the feasibility of using ultrasound (US) images, which have lower resolution compared to MRI, it is also evaluated the degree to which the progressive idealisation of a patient-specific geometry impacts the computational results.

These models are also validated in *in-vitro* experimental settings using particle image velocimetry (PIV). Finally the stresses obtained are then applied to cell and tissue cultures, using different bioreactors.

Here an overall view of the methods used in our laboratory with a particular focus on the remodeling of venous tissues used in the creation of native vascular access for hemodialysis, is presented.

II. Materials and Methods

A. Imaging and computational models

STAR CCM+ is utilised to conduct computational fluid dynamic (CFD) simulations on both idealised and patient-specific arteriovenous fistulas (AVF) models. Wall shear stress (WSS) parameters are utilised to identify areas of disturbed shear (DS) that are hypothesised to lead to the development of intimal hyperplasia (IH), which can result in fistula non-maturation and AVF failure [9]-[10]. To this aim, MRI scan data from four post-operative time-points (TPs) at days 20, 41, 55, and 172, are used to reconstruct the AVF geometries. Phase-contrast MRI is used to obtain patient-

specific boundary conditions, which are applied to each model. The blood was modelled as incompressible Newtonian (ρ=1050 kg/m^3, μ=3.5 mPa·s) and the inlet flow was considered fully developed and laminar. Helical flow can lead to WSS uniformity, which can reduce areas of DS [11]. This reduction in DS is hypothesised to lead to a decrease in the incidence of AVF dysfunction by suppressing one of the main contributors to the development of IH. This work, therefore, aims to determine if helical flow is present in AVFs and is associated with a reduction in exposure to DS.

B. Fluid-Structure Interaction Simulations

A two-way FSI simulation was performed to evaluate and demonstrate the effect of wall compliance on the hemodynamics of the patient-specific AVF geometries compared to rigid models (Fig. 1). Block-structured meshes consisting solely of linear hexahedral elements were constructed using GridPro Workspace. FSI simulations were carried out using Star-CCM+ and Abaqus. The vessel wall details cannot be determined from MR images and were assumed to have constant thickness of 0.4mm, (10% of the lumen diameter [12]). Moreover, the wall was modelled as a hyperelastic material following a 3rd -order Yeoh model and the constants were provided from [13]. The blood was modelled as previously stated.

C. Effects of idealised geometries

Scanning AVF with MRI requires lengthy scans, making the acquisition difficult. In particular, a major limitation of computational studies that analyse VA is the transverse nature of such analyses. To overcome MRI limits, vascular geometries can be reconstructed using US [14] which is routinely performed. However, the spatial resolution of US is considerably lower, resulting in lower quality reconstructions. This study aimed to determine the degree to which progressive idealisation of a patient-specific AVF geometry impacts the computational results. One of the four AVF rigid models was selected. The Vascular Modelling Toolkit was utilised to compute centreline data and record diameter readings from the fistula. These readings were used to recreate a pseudo-realistic AVF model (Fig. 2B). A second model (Fig. 2C) was created using the mean diameter for the artery and vein, therefore removing tapering. Finally, planar models (Fig. 2C, D) were developed to examine the impact of torsion on hemodynamics. All geometries were discretised as previously described. To replicate pulsatile flow, a parabolic waveform was applied at the arterial inlet. The arterial and venous outlets were modelled using a flow split condition. The blood was modelled as previously stated.

D. Particle image velocimetry validation

PIV is a fluid mechanics technique commonly used to capture vascular hemodynamics and validate numerical simulations. The benefit of using PIV, over other techniques, is the possibility to provide whole field measurements with a spatial resolution that can match that of CFD. A rigid, 1:1 patient-specific AVF model was used for this PIV study. Planar PIV measurements were performed on the anastomosis region of the phantom providing in-plane velocity components. Out-of-plane velocity was extracted using integration. The setup was designed as such to allow 95% of the flow to exit the proximal vein and 5% to leave the distal artery. The working fluid used was a mixture of water, glycerol and sodium iodide (37.3%, 14.7% and 48%) seeded with 10µm fluorescent particles (ρ=1568 kg/m^3 and μ=4 mPa·s). To reduce optical distortions, the AVF phantom was submerged in refractive index matching solution. Experiments were carried out at two flow rates, steady (Re = 1742) and patient-specific pulsatile (Re_{av}=1742, Re_{max}=2156). Planar PIV measurements were performed in planes parallel to each other. Cross correlation was performed on a 100 image pairs for steady flow measurements. Pulsatile flow measurements were recorded at 15 different points on the waveform where 60 images are recorded for each point and phase averaged.

E. Mechanical properties of the venous tissue

Mechanical characterisation of venous tissues is only partially addressed in literature, compared to arterial tissues. Here, a review of the studies (e.g. [15]-[16]) conducted to evaluate the mechanical parameters of venous tissues, is presented.

F. In-vitro settings

To evaluate the effects of specific hemodynamics derived from AVF computational studies on the biology of the vascular tissues, two bioreactors have been designed and created. The first consists in a real-time controlled cone-and-plate [17] and the second in an ex-vivo perfusion system. The first device is used to elucidate the effects of WSS waveform features, such as WSS magnitude, temporal gradients (t-WSSG), frequency components and reverse phases on human umbilical vein endothelial cell (HUVEC) cultures. Waveforms ranging in WSS magnitude from 0.5 to 2.5 Pa, t-WSSG from 3 to 30 Pa/s and from 0 to 0.5 of oscillatory shear index (OSI) value were programmed and applied for 24 hours. HUVEC (5th passage) were growth to 90% confluence in commercial petri dishes (150 cm^2) using EGM2 (EGM added with bullet-kit, Lonza). Before the experiment, the culture media was replaced by fresh media supplemented with Xhantam gum to increase the viscosity to 3.5 mPa·s. At the end of the stimulation, cells were imaged, fixed and incubated with fluorescent antibodies for f-actin fibers and CD-31 in order to evaluate the morphology and KLF2 and p65 NF-kB to evaluate the activation state [18]. Immunofluorescence images were processed using open-source software.

The second system is used to perfuse freshly harvested bovine venous tissues with a 1 Hz pulsatile waveform ranging 200-1200 mL/min. Tissues where maintained in a straight configuration and exposed for 6 days using the previously described media. A roller pump is used to generate the flow insuring the sterility of the culture system. Tissues were fixed and stained with haematoxylin-eosin. Images of the tissues are compared to images obtained from the native tissues and the static controls alternatively opened longitudinally or kept closed. The comparison of the images is used to evaluate the remodeling and the development of IH induced by the perfusion.

III. Results

A. Imaging and computational models

The venous segment of each AVF was analysed for the presence of helical flow. This revealed that the AVFs that exhibited helical flow also displayed the lowest amount of DS. Comparing the results of the computational simulations to the clinical outcomes of each patient revealed that the models that displayed helical flow did not suffer from AVF dysfunction, while the remaining models developed stenosis soon after their creation. These are preliminary results from a recent study conducted on a small cohort of patients. Therefore, these findings need to be validated in a larger cohort of patients to evaluate the significance of these results.

B. Fluid-Structure Interaction Simulations

Fig. 1 shows the contour plots of time-averaged WSS (TAWSS) and relative residence time (RRT) distributions at the four investigated TPs and for both CFD and FSI simulations. TAWSS significantly increased from 1st to 2nd, and to 3rd TP, followed by a significant decrease, showing a qualitative coincide at the 1st and 4th TP. Moreover, quantitative results show that rigid wall simulations overestimate the area exposed to TAWSS >50 Pa for all four TPs. Qualitative results for RRT show high values at the swing segment indicating areas with low WSS and high OSI, in other words disturbed flow.

The comparison between hemodynamic predictions from CFD and FSI shows similar distribution patterns in all parameters investigated. These results suggest that, although different results are achieved with the use of FSI simulations, simulations assuming solid walls can reproduce the same WSS distribution patterns.

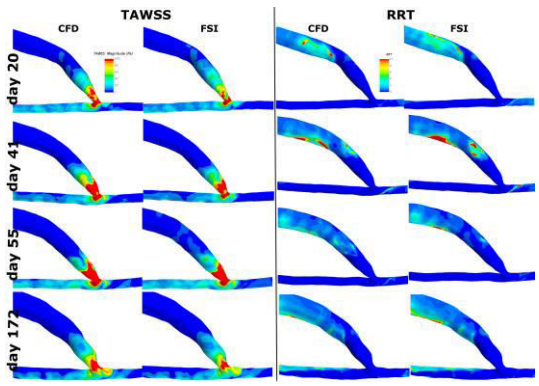

Fig. 1 Contour plots of TAWSS (Left) and RRT (right), for both CFD and FSI simulations, and at four post-operative TPs.

C. Effects of idealised geometries

This study compared 4 progressively idealised models to a patient-specific model, to determine which most accurately captured AVF hemodynamics, therefore, determining if US can be used to construct patient-specific models. As shown in Fig. 2, models (B) and (D) performed the best, suggesting tapering towards the anastomosis is the most significant geometrical feature. Notably torsion also plays a significant role in the intensity of turbulent flow within the AVF. Finally, model (B) best described the distribution and variation of disturbed flow metrics (Fig. 2).

It was concluded that model (B) adequately captured the distribution of disturbed shear metrics and displayed similar transitional to turbulent flow as the patient-specific model. This would suggest US can reproduce adequate AVF models for use in longitudinal studies. These results should be validated by reproducing an AVF geometry using US and comparing with MRI generated geometries.

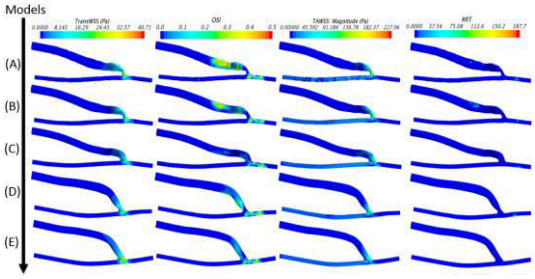

Fig. 2: Progressive geometry idealization effects on AVF hemodynamics.

D. Particle image velocimetry validation

Fig. 3 shows the flow separation occurring on the arterial floor and downstream of the anastomosis producing a large recirculation zone and a smaller zone in the proximal vein. The streamlines of pulsatile flow are similar to steady flow however the extent of the recirculation zone is greater. The results from this study determine that a complex flow structure is present. While it is clear that the flow structure in steady and pulsatile is similar there is also some difference confirming that it is necessary to model the pulsatile transient flow. These results will be used to validate numerical simulations as well as serve as a reference data set to assess the feasibility of US imaging velocimetry as an in-vivo validation technique.

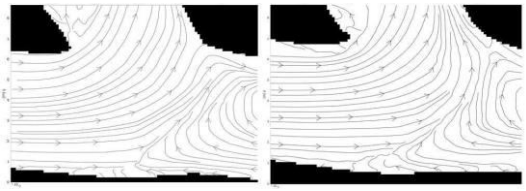

Fig. 3: Streamlines derived from PIV study. (Left: Steady, Right: Patient-Specific).

E. Mechanical properties of the venous tissue

Venous tissue can be characterised as non-linear, viscoelastic with stress increasing at higher strains. For uniaxial tensile testing of human saphenous vein tissues, mean elastic modulus values differ significantly between human samples tested in the longitudinal direction compared to the circumferential direction with a range of 19.42(5.73)-130.2(56.36) MPa and 1.22(.14)-42.62(27.76) MPa respectively. Saphenous vein samples also failed at higher stresses in the longitudinal direction with mean Cauchy stress failure values ranging from 4.82(2.25)-14.69(6.66) MPa compared to that of the circumferential direction 2.61(0.67)-4.63(1.93) MPa. However, due to a limited cohort of published studies and large variations in mechanical properties between species and locations, further investigation is required.

F. In-vitro settings

HUVEC exposed to WSS waveforms with the same maximum magnitude (1.5 Pa) but increasing maximum t-

WSSG (ranging from 10 to 18 Pa/s) increase elongation significantly. HUVEC exposed to WSS waveforms with the same t-WSSG (15 Pa/s) but increasing magnitude (0.5, 1.5, 2.5 Pa, respectively) increase in elongation significantly. F-actin fibers alignment is increased only by increasing the t-WSSG and not by magnitude. Staining for KLF2 and NF-kB, showed differences in the presence and distribution of these proteins that are known to be involved in IH development.

Bovine venous tissues were successfully perfused for 6 days. The system has demonstrated to be able to induce morphological changes in the samples. Histological images (Fig.5) show that tissues exposed to flow increased in diameter and decreased in thickness compared to native or static control tissues. The straight configuration of the tissues during the perfusion differs greatly from the realistic configuration of an AVF, this is a first step in developing a protocol to maintain viable tissues in culture for long period of time.

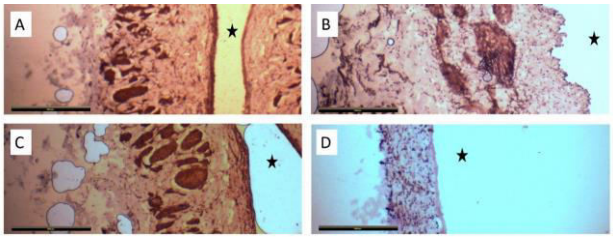

*Fig. 5: Histological images of bovine tissues. A)native, B) static open, C) static close and D) dynamic. Scale bar 1mm, * indicates the lumen.*

IV. Conclusion

A series of computational and experimental techniques have been combined to assess the effects of hemodynamics on vascular tissue remodeling. We focused mostly on the remodeling of venous tissues used in the creation of an AVF. However these techniques may be use to study other areas of the vasculature exposed to lesions. In the computational reconstruction of vascular geometries, the balance between the accuracy of the simulation and the costs is crucial. To this aim, our preliminary results show that simplifying CFD by using rigid wall conditions and idealised geometries, affects the hemodynamic reconstruction only to a certain extent. This leads to the possibility of using US images to reconstruct in-vivo vascular geometries. US evaluation is cheaper and routinely done by clinicians if compared to MRI, thus the use of these images may increase the availability of data in order to follow vascular remodeling in longitudinal studies and provide a useful tool in surgical pre-planning. A major limitation to the proposed approach is caused by the lack of information on venous tissues mechanical properties. Our literature review have found limited number of studies and poor agreement between them. This may affects the accuracy of SFI simulation and require further studies.

Finally, biological evidence obtained using the developed bioreactors, provide further information about the relationship between hemodynamics and the stenosis development in the AVF. The two proposed systems are capable of reproducing controlled mechanical stimuli in cell and tissue culture. The next steps require the perfusion of an AVF geometry created with fresh tissues to replicate more realistic conditions. This will allow to test patient-specific hemodynamics conditions and evaluate the role of geometrical configurations of the AVF of the development of IH.

In conclusion, the finely tuned biomechanical responses to specific hemodynamic patterns control health and disease in cardiovascular tissues during the entire life. The final goal of our activities is to provide clinicians with usable tools to assess and predict CVD insurgence and progression.

Acknowledgement

Supporting grants: Science Foundation Ireland grant n°15/CDA/332 and Irish Research Council for Science Engineering and Technology grant GOIPG/2014/1450.

References

[1] Abajobir AA et al. “Global, regional, and national age-sex specific mortality for 264 causes of death, 1980–2016: a systematic analysis for the Global Burden of Disease Study 2016”. Lancet (2017) Vol. 16(390) pp.1151-1210.

[2] Reamy BV, Williams PM, Kuckel DP. “Prevention of Cardiovascular Disease”. Prim Care (2018) Vol. 45(1) pp.25-44.

[3] Baeyens N and Schwartz MA. “Biomechanics of vascular mechanosensation and remodeling”. Mol Biol Cell (2016) Vol. 27(1) pp. 7-11.

[4] Baeyens N, Bandyopadhyay C, Coon BG, Yun S, Schwartz MA. “Endothelial fluid shear stress sensing in vascular health and disease”. J Clin Invest (2016) Vol. 126(3) pp. 821-828.

[5] Lu D and Kassab GS. “Role of shear stress and stretch in vascular mechanobiology”. J R Soc Interface (2011) Vol. 8(63) pp. 1379-85.

[6] Eshtehardi P et al. “High wall shear stress and high-risk plaque: an emerging concept”. Int J Cardiovasc imaging (2017) Vol. 33(7) pp.1089-1099.

[7] Franzoni M and Walsh MT. “Towards the Identification of Hemodynamic Parameters Involved in Arteriovenous Fistula Maturation and Failure: A Review”. Cardiovasc Eng Technol. (2017) Vol. 8(3) pp.342-356..

[8] Brahmbhatt A, Remuzzi A, Franzoni M, Misra S. “The molecular mechanisms of hemodialysis vascular access failure”. Kidney Int (2016) Vol 89(2) pp. 303-316.

[9] Cunnane CV, Cunnane EM, Walsh MT. “A Review of the Hemodynamic Factors Believed to Contribute to Vascular Access Dysfunction”. Cardiovasc Eng Technol (2017) Vol. 8(3) pp. 280-294.

[10] Lee T and Roy-Chaudhury P. “Advances and new frontiers in the pathophysiology of venous neointimal hyperplasia and dialysis access stenosis”. Adv Chronic Kidney Dis (2009) Vol. 16(5) pp. 329-38.

[11] Caro CG, Cheshire NJ, Watkins N. “Preliminary comparative study of small amplitude helical and conventional ePTFE arteriovenous shunts in pigs”. J R Soc Interface (2005) Vol. 2(3) pp. 261-6.

[12] Gutierrez M et al. “Automatic measurement of carotid diameter and wall thickness in ultrasound images”. Comput Cardiol (2002) Vol. 29 pp. 359-362.

[13] Decorato I et al. “Numerical simulation of the fluid structure interactions in a compliant patient-specific arteriovenous fistula”. Num Methods Biomed Eng (2014). Vol. 30(2) pp. 143-159.

[14] McGah PM, Leotta DF, Beach KW, Aliseda A. “Effects of wall distensibility in hemodynamic simulations of an arteriovenous fistula”. Biomech and modeling in mechanobiology (2014) Vol. 13(3) pp. 679-695.

[15] Donovan DL, Schmidt SP, Townshend SP, Njus GO, Sharp WV. “Material and structural characterization of human saphenous vein”. J Vasc Surg (1990) Vol. 12(5) pp. 531-7.

[16] Hamedani BA, Navidbakhsh M, Tafti HA. “Comparison between mechanical properties of human saphenous vein and umbilical vein”. BioMed Eng OnLine (2012) vol. 11(59) pp. 1-15.

[17] Franzoni M, Cattaneo I, Ene-Iordache B, Oldani A, Righettini P, Remuzzi A. “Design of a cone-and-plate device for controlled realistic shear stress stimulation on endothelial cell monolayers”. Cytotechnology (2016) Vol. 68(5) pp. 1885-96.

[18] Franzoni M, Cattaneo I, Longaretti L, Figliuzzi M, Ene-Iordache B, Remuzzi A. “Endothelial cell activation by hemodynamic shear stress derived from arteriovenous fistula for hemodialysis access”. Am J Physiol Heart Circ Physiol. (2016) Vol. 1-310(1) pp. H49-59.

Effect of the collagen fibrils architecture on the corneal mechanical response

A. Montanino[1], A. Gizzi[2], M. Vasta[3], M. Angelillo[4] and A. Pandolfi[1]
[1] *Politecnico di Milano, Dipartimento di Ingegneria Civile ed Ambientale, Milano, Italy*
[2] *Università Campus Bio-Medico di Roma, Dipartimento di Ingegneria, Roma, Italy*
[3] *Università di Chieti-Pescara, Dipartimento INGEO, Pescara, Italy*
[4] *Università di Salerno, Dipartimento di Ingegneria Civile, Fisciano (SA), Italy*

***Abstract*—We present a finite element model of the human cornea accounting for collagen fibrils distribution in the stromal tissue. With the final aim of understanding the effects of fibril architecture on the mechanical response of the cornea, we numerically simulate three different mechanical tests on the cornea (ex-vivo inflation test, in-vivo probe indentation test, and in-vivo air puff test), on five different fibril dispersion models.**

The numerical results show no marked differences in the static tests regarding global response and stress distribution, with the exception in the case of varying shear stiffness across the thickness.

We conclude that the in plane actual fibril architecture has a minor relevance on the corneal mechanical response with respect to the main fibril anisotropy currently acknowledged in the literature.

***Keywords*—Human cornea, biomechanics, distributed fibers**

I. Introduction

CORNEA consists of a matrix of proteoglycans reinforced with a complex fibril architecture, as first revealed in [1], mainly aligned in the superior-inferior (SI) and nasal-temporal (NT) directions at the center of the cornea, and in circumferential direction at the limbus. Recent advances in biomedical imaging have also revealed differences in the fibril features across the corneal thickness, providing shear stiffness on the anterior surface reaching one order of magnitude more than the posterior side [2]. Moreover, it has been shown in [3] that the fibril alignment becomes less unidirectional in the anterior surface of the cornea.

In the state-of-the-art of biomechanical modelling, there are no precise patient-specific numerical models of the fibrils dispersion, though advanced models accounting for fibril architecture in the cornea have been proposed [4-6]. Consequently, it arises the need of understanding if mechanical tests can reveal differences in the fibrils architectures.

In the view of developing a complete patient-specific material model for the human cornea, the present work aims to show how different fibril architectures influence the mechanical response of the material subjected to different mechanical tests, to understand how mechanical test can provide information about actual fibril distribution.

The paper is organized as follows: section II introduces the geometrical and material models; section III describes the mechanical tests and the numerical simulations, and in section IV we draw conclusions and future perspectives.

II. Geometry and material models

A cornea oriented finite element code has been developed in-house to simulate different mechanical tests on the cornea, as well the effects of refractive surgery interventions. Among the features of the code, there is the possibility of using the patient-specific geometry of the cornea, revealed by optical imaging; the option of using different material models, including various fibril distributions inside the stroma; a built-in algorithm for the identification of the unstressed corneal geometry.

A. Geometry

The physiological geometry of the cornea is provided by optical imaging, on which a finite element mesh is created using an ad-hoc software (Fig. 1). The physiological geometry is stressed, since fluids and gels lying in the anterior chamber of the eye exert a pressure on the posterior surface of the cornea, denoted as Intra-Ocular Pressure (IOP). In order to develop correct stress analysis on the cornea, the physiological stress state has to be determined. With this aim, an ad-hoc procedure [7] is then implemented in the code to identify the unstressed geometry of the cornea.

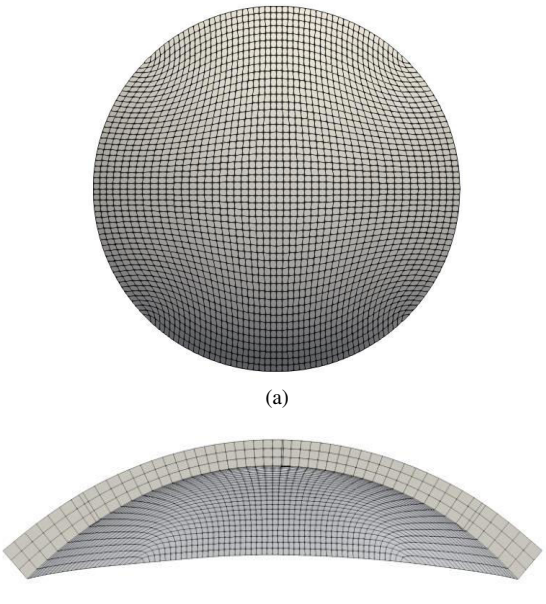

(a)

(b)

Fig. 1: Patient specific finite element mesh of the human cornea: (a) top side; (b) section in the Superior-Inferior direction

B. Material model

The material model adopted in the present study accounts explicitly for fibril distribution in the cornea. It assumes that fibrils are distributed in the stroma according to a probability density function [8]. The proteoglycan matrix is modelled as isotropic and incompressible. Consequently, the strain energy density function Ψ is the sum of three different contributions

$$\Psi = \Psi_{vol}(J) + \Psi_{iso}\,(\bar{I}_1, \bar{I}_2) + \Psi_{aniso}(I_4^*, \sigma_M^2)$$

where $\Psi_{vol}(J)$ is the volumetric part and depends only on the determinant of the deformation gradient $\boldsymbol{F}$, being $J = det\boldsymbol{F}$; $\Psi_{iso}\,(\bar{I}_1, \bar{I}_2)$ is the isotropic contribution accounting for the matrix and for the 60% of the material fibrils, not aligned on preferential directions, modelled according to Mooney-Rivlin's strain energy function, and depending on the first and second invariants ($\bar{I}_1$ and $\bar{I}_2$) of the isochoric Cauchy-Green deformation tensor.

The contribution $\Psi_{aniso}(I_4^*, \sigma_M^2)$ accounts explicitly for the fibril dispersion, and depends on the local averaged fibril stretch through the pseudo-invariant I_4^* and on the its dispersion through the variance σ_M^2.

Details about the mathematical definition of the strain energy functions are provided in [9].

A schematic draw of fibril structure and preferential fibril orientation is given in Figure 2.

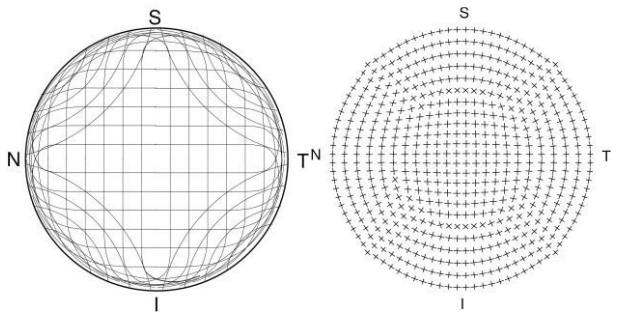

Fig. 2: (left) Fibrils organization within the cornea [10]; (right) Main orientation of the fibrils assumed in the numerical models. S is the superior point, I the inferior point, N the nasal point and T the temporal point.

In this work we focus on five different fibril architectures inside the cornea, and in particular we assume five different models:

1. Baseline model, with fully 3D dispersed fibrils with no variation across the thickness.
2. DT model: linearly varying fibril dispersion across the thickness (fiber dispersed in the posterior surface, and constant dispersion coefficient on the anterior side); no variation in the fibril stiffness.
3. SL model: variation of the stiffness and degrees of fibril dispersion between the center and the periphery of the cornea, with no variations across the thickness.
4. ST model: no variation in the fibril dispersion degree across the thickness and fibril stiffness variations of one order of magnitude across the thickness.
5. Model ALL: all models DT, SL and ST are considered jointly.

C. Static and dynamic analysis

We investigate the effects of fibril organization in the cornea simulating three different mechanical tests:

1. The ex-vivo inflation test: consisting in pressurizing the cornea in a quasi-static configuration from its posterior side up to 40 mmHg. The cornea is fixed at the limbus.
2. The probe indentation test: an in-vivo test consisting in the quasi-static pushing of a probe on the apex of the cornea, which measures the corneal reacting forces to the imposed displacement;
3. The dynamic in-vivo air puff test: a contactless tonometer consisting in a rapid air jet from the external surface of the cornea, which determines a temporary and local change in the concavity of the cornea, from which ophthalmologists are able to estimate the IOP. More recently, the test has been regarded in the literature as a possible tool to determine the mechanical properties of the cornea [11].

For all the considered tests, information about the physiological stress state is needed, and it is recovered through the identification of the unstressed geometry, according to the procedure explained in [7] which must be performed before each numerical analysis.

III. Results

A. Inflation test

Figure 3 shows the results of the inflation test in terms of the apical displacement versus the IOP. At the physiological IOP (set as 16 mmHg throughout the whole study) all models show similar behavior, and are practically indistinguishable, whereas at higher levels of IOP (40 mmHg) the ST model results stiffer than the others while the DT model is the most compliant.

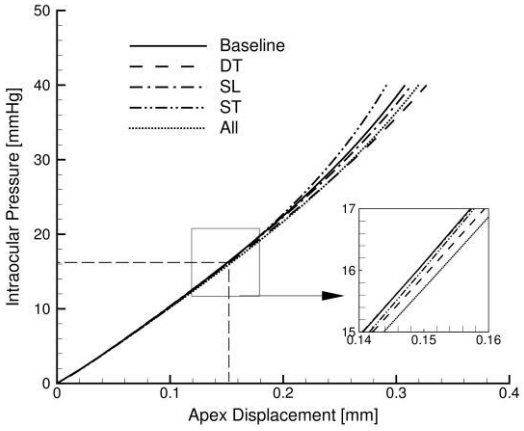

Fig. 3: Inflation test: Intraocular pressure versus the apex displacement for the five considered models.

In Figure 4 we represent the Cauchy stress distribution σ_{xx} for the baseline model and all the variations. We note that all models show a similar stress state, with the significant

exception of the ST case, which coincides with the case ALL. In this configuration, in fact, the stress is completely carried by the external layers, corresponding to the zone with significantly larger values of the shear stiffness.

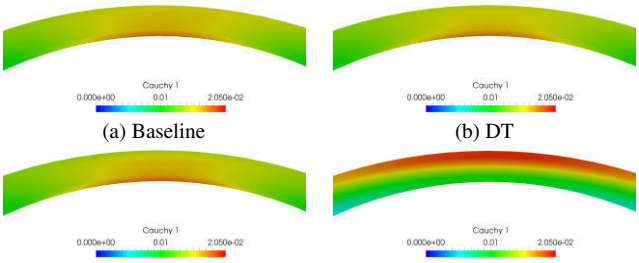

(a) Baseline (b) DT

(c) SL (d) ST and ALL

Fig. 4: Inflation test: tensile stress distribution along the SI direction for the different models investigated, at the physiological IOP. The ST and ALL model exhibit the same behavior since both include stiffness variations across the thickness.

B. *Probe test*

The results of the quasi-static probe indentation test are shown in Figures 5 and 6. In Figure 5 we show the global mechanical response of the cornea in terms of the reaction force versus the imposed displacement. In this case, we note that the Baseline and SL models are the stiffest, whereas the most compliant is the ST model, that behaves like the model ALL.

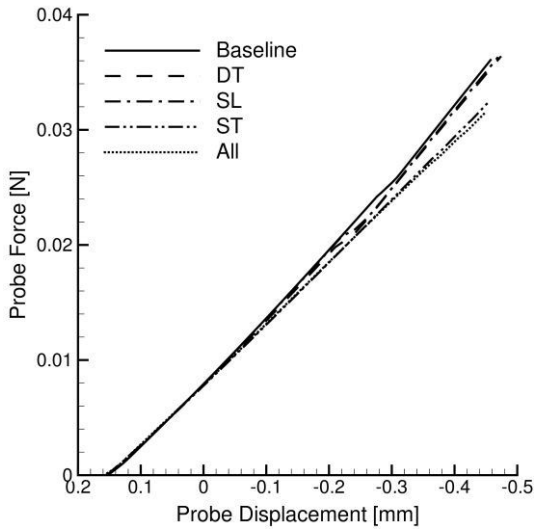

Fig. 5: Probe indentation test. Reaction forces at the probe versus the probe displacement.

Figure 6 shows the Cauchy stress component σ_{yy} distribution along the SI direction. Again, the Baseline, DT and SL models behave similarly, whereas the ST and ALL models do not show the tensile stress on the posterior surface of the cornea, exhibited by the other models.

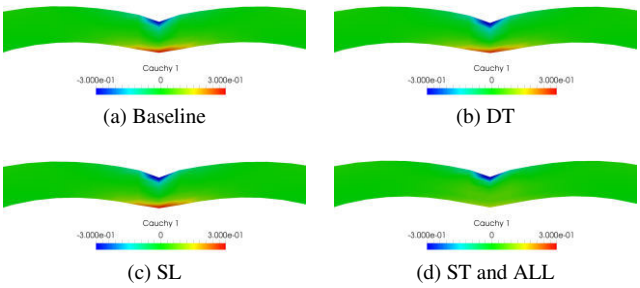

(a) Baseline (b) DT

(c) SL (d) ST and ALL

Fig. 6: Probe indentation test: tensile stress distribution along the SI direction for the different models investigated. The ST and ALL model exhibit the same behavior since the both include stiffness variations across the thickness.

C. *Air puff test*

The results of the air puff tests are reported in Figures 7 and 8. In Figure 7 we show the apex displacement time history during the air puff for all the investigated models. Differently from static tests, in this case, all architectures exhibit different characteristics in terms of the global response, the Baseline model being the stiffest and the ALL model being the most compliant.

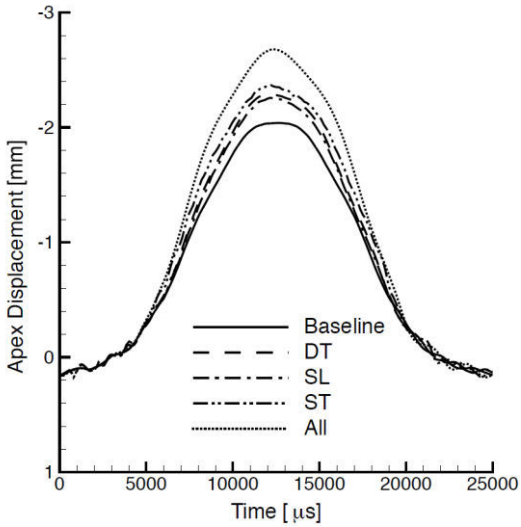

Fig. 7: Air puff test: apex displacement time history.

Figure 8 shows the stress distribution for the different architectures at the maximum apex displacement. All models exhibit compression in the SI direction, but differently from previous tests, in each architecture the stress distribution is different from the others. In particular, the ST and ALL models reveal the most extended zone under compressive stress, the DT and SL model exhibit similar stress distributions with a reduced compressed zone, and the Baseline model exhibits a more extended compressed zone than the SL and DT models, but smaller with respect to the ST and ALL cases.

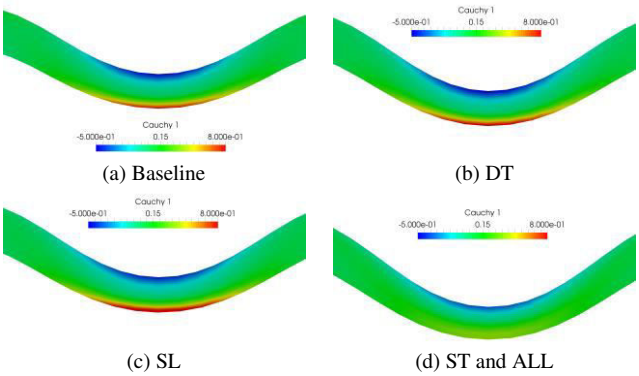

(a) Baseline (b) DT

(c) SL (d) ST and ALL

Fig. 8: Air puff test: tensile stress distribution along the SI direction for the different models investigated at the maximum apex displacement.

IV. CONCLUSIONS

In this work we have presented a material model for the cornea explicitly accounting for the local variation of the collagen fibril architecture. In particular, five different fibril dispersion models have been investigated, in which fibril distribution and thickness change both across the thickness and in plane, between the central zone and the limbus.

The different architectures have been tested with three different mechanical tests (the inflation test, the probe indentation test, and the air puff test), in order to elucidate the effects of fibril distribution on the material mechanical response and to define a practical procedure highlighting the particular fibril architecture from clinical exams.

The inflation test does not reveal significant differences among the architectures in terms of apex displacement versus IOP, while the stress analysis reveals the same behavior for all models except the ST case. For this model, the stress distribution shows higher variability across the corneal thickness due to the significant differences in the fibril stiffness across the thickness.

In the probe indentation test the force-displacement curve does not permit a clear distinction among the investigated architectures, whereas the stress analysis again reveals differences only for the ST model.

The air puff test, on the contrary, allows to distinguish the Baseline model from the other fibril architectures through the apex displacement time history, and all models are clearly distinguishable through the stress analysis, where each model exhibits stress distributions different from the other architectures.

In conclusion, the present study permits to state that the fibril dispersion across the thickness and in plane is not of primary importance in the mechanical response of the corneal material, whereas a primary role is played by the fibril stiffness variability across the corneal thickness. Moreover, we remark that the quasi-static tests do not allow a clear distinction between the different architectures while this is feasible via the dynamic air puff test.

Finally, we point out some limitations of this work: first, the anterior and posterior epithelium layers of the cornea are neglected, due to the very limited mechanical contribution to the whole corneal material; and second, the numerical model of the air puff test does not account for the interaction with the fluid filling the anterior chamber of the eye, which provides additional inertia to the cornea and also a time-varying load due to the fluid incompressibility. In our simulations, the fluid inertial effects are provided by additional masses in the nodes of the posterior surface of the corneal finite element mesh.

A first model of FSI in the air puff test has been developed in [12] considering simplifications in the material and in the geometry, while a complete 3D version of the air puff test is currently under development.

REFERENCES

[1] W. Kokott. "Über mechanisch-funktionelle Strukturen des Auges." *Albrecht von Graefes Archiv für Ophthalmologie* vol. 138.4, pp. 424-485 ,1938

[2] S.J. Petsche, D. Chernyak, J. Martiz, M. E. Levenston, and P.M. Pinsky. "Depth-dependent transverse shear properties of the human corneal stroma". *Investigative ophthalmology & visual science*, vol.53.4, pp. 873-880, 2012.

[3] M. Abahussin, S. Hayes, N. E. K. Cartwright, C. S. Kamma-Lorger, Y. Khan, J. Marshall, and K. M. Meek. "3D collagen orientation study of the human cornea using X-ray diffraction and femtosecond laser technology". *Investigative ophthalmology & visual science*, vol 50.11, pp. 5159-5164, 2009

[4] A. Elsheikh. "Finite element modeling of corneal biomechanical behavior". *Journal of Refractive Surgery*, vol. 26.4, pp. 289-300, 2010

[5] S. J. Petsche and P.M. Pinsky. "The role of 3-D collagen organization in stromal elasticity: a model based on X-ray diffraction data and second harmonic-generated images". *Biomechanics and modeling in mechanobiology*, vol. 12.6, pp. 1101-1113, 2013.

[6] C. Whitford, N. V. Movchan, H. Studer, and A. Elsheikh. "A viscoelastic anisotropic hyperelastic constitutive model of the human cornea". *Biomechanics and modeling in mechanobiology*, 1-11, 2017, **https:7//doi.org/10.1007/s1023**

[7] A. Pandolfi, G. Fotia, and F. Manganiello. "Finite element simulations of laser refractive corneal surgery". *Engineering with Computers*, vol. 25.1, 15, 2009.

[8] A. Pandolfi, and M. Vasta. "Fiber distributed hyperelastic modeling of biological tissues.", Mechanics of Materials vol. 44, pp. 151-162, 2012.

[9] A. Montanino, A. Gizzi, M. Vasta, M. Angelillo, and A. Pandolfi. "Modeling the biomechanics of the human cornea accounting for local variations of the collagen fibril architecture". ZAMM-Journal of Applied Mathematics and Mechanics/Zeitschrift für Angewandte Mathematik und Mechanik, 2018

[10] H. Aghamohammadzadeh, R.H. Newton, and K.M. Meek, "X-ray scattering used to map the preferred collagen orientation in the human cornea and limbus", *Structure* 12, 249–256, 2004

[11] S. Kling, N. Bekesi, C. Dorronsoro, D. Pascual, and S. Marcos. "Corneal viscoelastic properties from finite-element analysis of in vivo air-puff deformation". *PloS one*, vol. 9.8, e104904, 2008.

[12] A. Montanino, M. Angelillo, A. Pandolfi. "Modelling with a meshfree approach the cornea-aqueous humor interaction during the air puff test". *Journal of the mechanical behavior of biomedical materials*, vol. 77, pp. 205-216, 2018

Modelling the abdominal wall response under active muscles and effective internal pressures

S. Pianigiani[1], P.G. Pavan[1], S. Todros[1], P. Pachera[1], and A.N. Natali[1]
[1] *Department of Industrial Engineering, Centre for Mechanics of Biological Materials, University of Padova, Italy*

***Abstract*— Abdominal wall biomechanics is dependent on muscular contraction and Intra-Abdominal Pressure (IAP) which characterize different physiological functions and daily tasks. The active behaviour of muscular fibres must be considered within computational models of the abdominal wall. A three dimensional Finite Element (FE) model of a healthy abdomen is developed by implementing different constitutive models to describe the mechanical behaviour of the different structures. Fascial tissues, aponeuroses and linea alba are modelled as hyperelastic fiber-reinforced materials, while a three-element Hill's model is assumed for the muscles. IAPs are simulated by adopting an internal abdominal cavity.**

The deformation resulting from different levels of muscle activation, corresponding to different tasks has been evaluated and the results corresponding to an abdominal crunch are shown.

This model represents an advanced approach to simulate abdominal wall mechanics by considering active muscles and effective internal pressures in healthy conditions. The model described in this study can be hence used for a valid clinical support. By means of a similar numerical approach, abdominal pathologies can be properly investigated, such as potential herniated regions.

***Keywords*—Abdominal wall, active muscles, intra-abdominal pressure, FEM.**

I. Introduction

CLINICAL findings are nowadays still highlighting recurrences after practices for repairing incisional abdominal hernias [1]. Providing support in biomechanical investigations about the abdominal wall can definitely be a key factor for reducing the number of recurrences, thus improving the patient's satisfaction and reducing costs of the national health services.

Numerical analyses are nowadays increasing and can represent a possibility to integrate experimental activity, resulting less invasive and expensive, while allowing the simulation of several scenarios. Little is still known about the effects of coupling different internal abdominal pressures (IAP) and different levels of muscular activation of the abdominal muscles. In fact, active behaviour of muscular fibres is not often considered when simulating abdominal wall behaviour. The different tissues that compose human abdominal wall provide pure passive action in protecting and supporting the abdominal cavity (Linea alba (LA), aponeuroses and fasciae) and contribute with their active behaviour to the accomplishment of physiological tasks as breathing, coughing, phonation and postural control (Rectus Abdominis (RA), External Oblique (EO), Internal Oblique (IO) and Transversus Abdominis (TA)) [2].

Additionally, the abdominal wall is subjected to a variable IAP that directly depends on the volume of internal organs. IAP increases with inspiration and decreases with expiration and is affected by the activation of the muscles which determines an additional pressure. Different pathologies are related to abnormal effects of IAP and to the mechanical characteristics of abdominal wall structures highlighting the clinical interest for biomechanical properties of this region. An increase in IAP can have negative effects: decreased cardiac output due to reduced venous return, decreased renal blood flow, glomerular filtration rate and reduced splanchnic and hepatic perfusion [3]. High values of IAP have direct consequences, together with other factors, in the formation and recurrence of abdominal hernias.

As concerning this aspect, the evaluation of the forces exerted on the fascial structures in the healthy abdomen during the execution of different daily tasks represents an issue of relevant clinical interest. In fact, the forces acting on the fasciae are directly applied to surgical meshes currently adopted in the repair of abdominal hernias.

In current numerical modelling of abdominal wall, IAPs are usually simulated applying a uniform pressure on the internal fascia of muscles, without considering the effects of the internal cavity. Having regard of these limitations, this work proposes a finite element (FE) analysis of the abdominal biomechanics of a healthy human abdomen in which muscular activation is simulated and coupled with the effects of the internal abdominal pressure at different levels.

II. Materials and Methods

In the light of previous studies [4], the current model is going to extend the reproduction of the muscular structures up to the pelvis area based upon medical images, the internal abdominal cavity, and implementing a three-element Hill's model that simulates the contractile behaviour of the abdominal muscles. FE analyses are performed reproducing different levels of IAP corresponding to several daily activities to evaluate the biomechanical response of internal fascia and anterior border of the abdominal wall.

A. Finite Element model

The FE model (Fig. 1) is developed starting from a previous investigation [4] describing the abdomen biomechanics in passive condition. The abdominal wall region is modelled by means of a segmentation software (ITK-SNAP [5]), starting from CT images and histo-morphometric data from the literature. The principal abdominal components are included: LA, RA, aponeurosis, and a structure comprising all the lateral muscles (IO, TA and EO). Also an internal cavity is modelled up to the pelvis area (not shown in Fig.1).

Since fasciae cannot be precisely identified in the medical scans, they are reconstructed on the surfaces of LA, aponeuroses and muscles by considering thickness values from literature data [6]. This procedure allows the modelling of the anterior and posterior rectus sheaths and the transversalis fascia.

The model is obtained by using ABAQUS CAE software (SIMULIA, Dassault Systems), while numerical analyses are performed by means of ABAQUS Standard (SIMULIA, Dassault Systems) integrated with specific user-defined constitutive formulations. In the present model, the constitutive formulations of abdominal muscular tissues include the active behaviour as an upgrade of previous models [4,7].

B. Constitutive models

The kinematics of both connective and muscular tissues is based on the use of the right Cauchy-Green strain tensor $\mathbf{C}=\mathbf{F}^T\mathbf{F}$, where $\mathbf{F}$ is the deformation gradient. The mechanical behaviour of the connective tissues is described by adopting a hyperelastic constitutive model. This formulation [4] accounts for the mechanical properties of the connective tissues, including large strains, almost-incompressibility and presence of oriented collagen fibres. The strain energy function W_c is defined as:

$$W_c = U_{cm}(J) + \tilde{W}_{cm}(\tilde{I}_1) + \tilde{W}_{cf}(\tilde{I}_4)$$
$$U_{cm} = \frac{k_{cm}}{2}\left(J^2 - 1 - 2\ln J\right) \quad \tilde{W}_{cm} = \frac{\mu_{cm}}{2}\left(\tilde{I}_1 - 3\right)$$
$$\tilde{W}_{cf} = \frac{\alpha_{f1}}{2\alpha_{f2}}\left[\exp\left(\alpha_{f2}\left\langle \tilde{I}_4 - 1\right\rangle^2\right) - 1\right] \qquad (1)$$
$$J = det(\mathbf{F}) \quad \tilde{I}_1 = \mathrm{tr}(J^{-2/3}\mathbf{C}) \quad \tilde{I}_4 = J^{-2/3}\mathbf{C}:(\mathbf{m}_0 \otimes \mathbf{m}_0)$$

being $\mathbf{m}_0$ the unit vector defining the local orientation of the fibres in the undeformed configuration. The bulk modulus k_{cm} is adjusted to ensure the almost-incompressibility of the tissue, while μ_{cm} is the initial shear stiffness of the ground matrix. Finally, parameters α_{f1} and α_{f2} affect the nonlinear response of collagen fibres. The stress-strain response obtained from the constitutive model is fitted based on experimental data taken from the literature for each connective tissue.

The muscular tissue [8-12] is described as an isotropic and almost-incompressible hyperelastic ground matrix with strain energy function

$$W_m = U_{mm}(J) + \tilde{W}_{mm}(\tilde{I}_1)$$
$$U_{mm}(J) = \frac{k_{mv}}{2}\left(J^2 - 1 - 2\ln J\right) \qquad (2)$$
$$\tilde{W}_{mm} = \alpha_{m1}\, exp\left[\alpha_{m2}\left(\tilde{I}_1 - 3\right)\right] - \alpha_{m1}$$

embedding the muscular fibres. In terms of the first Piola-Kirchhoff stress tensor $\mathbf{P}$ the response of the fibres is:

$$\mathbf{P} = \left(P_p + P_a\right)\mathbf{F}\mathbf{m}_0 \otimes \mathbf{m}_0 \qquad (3)$$

being P_p and P_a passive and active stress response and $\mathbf{m}_0$ the unit vector corresponding to the local spatial disposition of the muscular fibres in the undeformed configuration. According to the Hill's model, the active response is described by:

$$P_a = P_0 \cdot f_a \cdot f_l \cdot f_v \qquad (4)$$

where P_0 is the maximum isometric stress and the other factors are dimensionless. The function f_a represents the level of activation of the fibres over time. The term f_l is the so-called 'force-length' function and describes the maximum stress in isometric condition depending on the initially imposed fibre stretch.

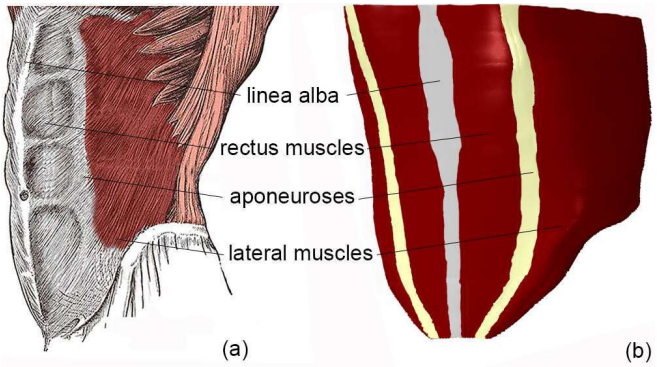

Fig. 1: Abdominal structures in an anatomical image (a) and in the solid model (b): linea alba, rectus muscles, aponeuroses and lateral muscles.

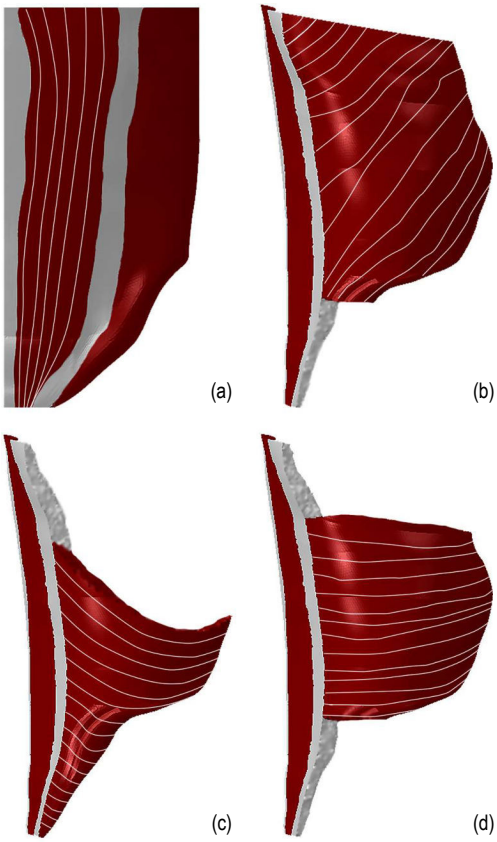

Fig. 2: Description of the orientation of the muscular fibres for the rectus three lateral muscles of the model: (a) rectus, (b) external oblique, (c) internal oblique, and (d) transversus abdominis.

Finally, the term f_v is the so-called 'force-velocity' function, describing the relation between stress and strain rate.

For all considered muscular structures, the anatomical orientation of the fibres is taken into account. In particular, the different orientations of the fibres of the rectus and the three lateral muscles are described in Fig. 2. As the lateral muscles are considered in a unique structure, their contribution during active contraction is not only simulated by the orientation of the fibres, but also considering the portion of volume with respect to the total muscular structure (Fig. 2).

C. Loading and boundary conditions

In order to account for the abdomen insertion on the xiphoid process, on the ribs and on the pelvis, the upper and the lower sides of the overall abdominal wall are considered fixed. The lateral muscles edges are fixed to represent the connections

with the iliac crest, the thoracolumbar fascia and the costal cartilages of the ribs.

A possible sliding between fascial tissues and muscles is allowed by means of frictionless contact conditions, as it is pointed out by anatomical investigation [6].

The internal pressure due to the organs of the abdominal cavity is obtained by considering a volumetric region filled with fluid elements characterized by almost-incompressible behaviour. The loading acting on the abdomen is obtained by applying a contraction of the muscles, through the activation function f_a. The shortening of muscle fibres induces a slight volume reduction of the filled region, producing a hydrostatic pressure corresponding to IAP and acting on the internal side of the abdominal wall. Therefore, the system finds a static equilibrium between the membrane forces acting on the abdominal wall and the pressure distributed on its internal side.

The literature [3] reports levels of IAP describing different daily tasks in physiological condition. The range comprising them all up to abdominal crunch (range 1.8-26.7 mm Hg) has been simulated as result of volumetric stiffness of the internal cavity and the muscular contraction.

III. RESULTS

Figure 3 shows the displacements of the abdominal wall along medial-lateral, posterior-anterior, cranio-caudal direction for the analysed IAP corresponding to an abdominal crunch. Figure 4 describes the behaviour of the abdominal wall for a section corresponding to the 12th rib along the transversal plane. It is possible to highlight the presence of two local minima, corresponding to aponeuroses. Additionally, by seeking the volume corresponding to the lateral muscles (EO, IO, TA), an increasing thickness is observed with increasing contraction.

When analysing the displacement of the rectus sheets, under active behaviour, their movement is perceptible in posterior-anterior direction. Actually, the investigation of these regions results of particular interest since they can be directly involved in mesh fixation for intraperitoneal hernia repair.

IV. DISCUSSION AND CONCLUSIONS

The model presented in this work was formerly considered in a pure passive state and validated for healthy [4] and herniated conditions [7]. In these studies, numerical results were compared with experimental data from both cadaveric and in vivo tests. Reliable outcomes were found taking into account different aspects, as the abdominal wall compliance, the membrane forces acting on the different abdominal tissues and the abdominal area variation with increasing IAP.

While the verification of the model was feasible for passive conditions, suitable experimental data that correlate IAP, muscle contraction and abdomen deformation are not at disposal at present. In fact, partial data can be extrapolated from different literature works that result in limited scenario of the observed anatomical site and cannot be suitably correlated.

The velocity of muscle contraction and the corresponding IAP rate induce in the fascial structure an increasing strain with the same rate of experimental testing adopted as reference [12] for the fitting of the constitutive model (1).

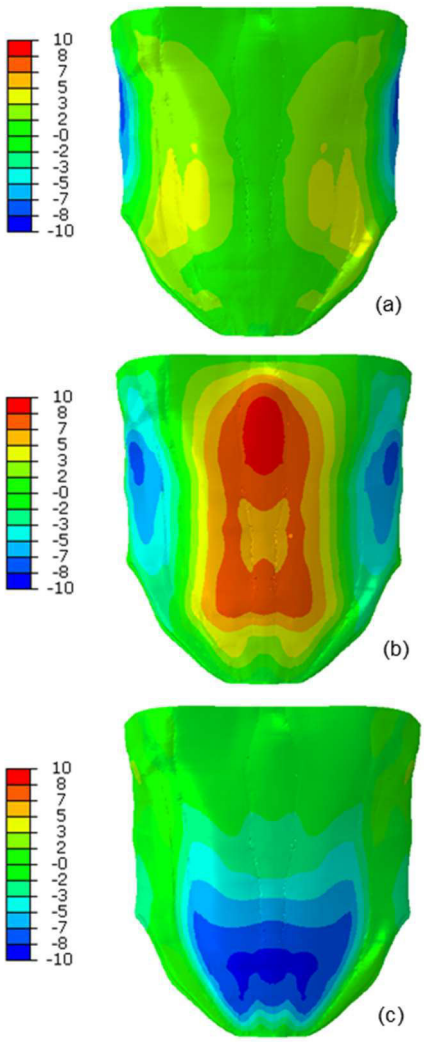

Fig. 3: Displacements contours for the analyzed IAP along: (a) medial-lateral direction, (b) posterior-anterior direction, (c) cranio-caudal direction. The legend describes the displacements in mm.

Therefore, the use of an hyperelastic model and omitting visco-elastic phenomena in the fascial tissues has marginal effects in the numerical analyses considered in this work.

Other authors [13,14] observed a similar trend of contraction by analysing the intra-abdominal pressure. In particular, an increasing displacement of the rectus on the transversal plane over the navel coupled with a reduction of the pelvis along the cranio-caudal direction is observed coherently to the results showed in this work (Fig. 3).

Another effect of the muscular contraction consists in a reduction of the membrane force acting on the fasciae. The literature usually reports the evaluation of the transversal membrane force by considering the overall abdominal wall thickness [15,16]. Differently, the numerical model developed in this work makes it possible to evaluate membrane force acting on the single tissues, in particular in the fasciae. Since surgical meshes are fixed to the fasciae in intraperitoneal hernia repair, the estimation of the mechanical states in fascial tissues could be of relevant interest in the perspective of evaluating the possible loads on the prostheses.

Additional studies should be performed to characterize the contractile behaviour of abdominal muscle fibres.

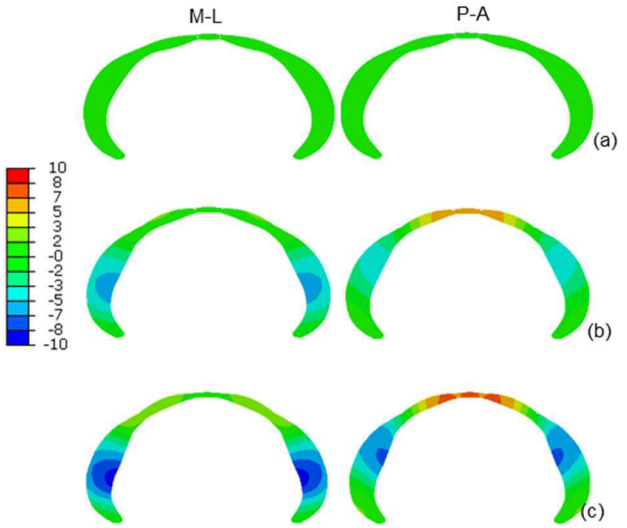

Fig. 4 Section with contours of the abdominal wall corresponding to the 12th rib along the transversal plane. Images on the left column describe the displacements in the medial-lateral direction, while the images on the right column describe the displacements in the posterior-anterior direction. The displacement values in mm are depicted in the legend. The three images for each direction refer to relaxed behavior (a), a mild contraction (b) and the contraction corresponding to an abdominal crunch (c).

Literature remarks report about the experimental characterization of different kinds of muscular fibres, both from animal [17,18] and human [19], but there is still a lack of knowledge with specific regard to the fibres of the human abdominal muscles. Moreover, for a better definition of the IAP dependence on muscular contraction, it would be useful to record simultaneously EMG data and IAP values on healthy subjects performing different tasks.

EMG results should be coupled with MRI data or ultrasound imaging and measurements of the abdomen displacement to associate the effective muscular activation level to the corresponding abdominal deformation and IAP.

The numerical model developed in this work allows a coherent representation of the abdominal wall mechanics with respect to previous approaches, which included only the passive behaviour of abdominal muscles. Based upon the obtained results, this study enforces the significance of including active muscular activation together with a proper rendering of the internal abdominal pressure when simulating abdominal wall biomechanics. In fact, when neglecting the muscular contraction, an overestimation of abdominal wall deformation and membrane force is made.

This numerical research draws the lines for searching data from experimental in-vivo tests to verify numerical results and complete the validation the model. Ongoing analyses by echo-measurements and three-dimensional scanner performed by this research team are currently tailored to this aim. The experimental data will make it possible to verify the correspondence in the FE model of the muscle thickness variation and the profile change of the abdomen at different transversal sections, from relaxed to contraction conditions.

The validation of the numerical model of healthy abdomen will be followed by the extension of this computational approach to include pathological or clinical conditions. These findings can be coupled with current updates about mechanical response of synthetic or biological meshes for hernia surgical repairing, hence providing potential guidelines to surgeon tailoring the patient-specific pre-planning for reducing recurrences during the post-operative period.

References

[1] S.V. Gopal and A. Warrier, “Recurrence after groin hernia repair-revisited”, *Int J Surg*, vol. 11, pp. 374-377, June 2013.

[2] M. Iizuka, “Respiration-related control of abdominal motoneurons”, *Resp Physiol Neurobiol,* vol.179, pp.80–88, October 2011.

[3] W.S. Cobb, J.M. Burns, K.W. Kercher, B.D. Matthews, H.J. Norton and B.T. Heniford, “Normal intraabdominal pressure in healthy adults”, *J Surg Re,s* vol. 129, pp. 231–235, December 2005.

[4] P. Pachera, P.G. Pavan, S. Todros, C. Cavinato, C.G. Fontanella and A.N. Natali, “A numerical investigation of the healthy abdominal wall structures”, *J Biomech*, vol. 49, pp.1818–1823, June 2016.

[5] P.A. Yushkevich, J. Piven H.C. Hazlett, R.G. Smith, S. Ho, J.C. Gee, and G. Gerig “User-guided 3D active contour segmentation of anatomical structures: Significantly improved efficiency and reliability”, *Neuroimage* vol. 31, pp. 1116–1128, July 2006.

[6] L. Lancerotto, C. Stecco, V. Macchi, A. Porzionato, A. Stecco and R. De Caro, “Layers of the abdominal wall: anatomical investigation of subcutaneous tissue and superficial fascia”, *Anat*, Surg Radiol Anat, vol. 33, pp. 835-842, January 2011.

[7] S.Todros,, P. Pachera, N. Baldan, P.G. Pavan, S. Pianigiani, S. Merigliano and A.N. Natali, “Computational modeling of abdominal hernia laparoscopic repair with a surgical mesh”, *Int J Comput Assist Radiol Surg* vol. 1, pp. 73-81, November 2017.

[8] S.M. Mijailovich, B. Stojanovic, A. Ko Liang, V.J. Wedeen and R.J. Gilber, “Derivation of a finite-element model of lingual deformation swallowing from the mechanics of mesoscale myofiber tracts obtained by MRI”, *J Appl Physiol*, vol. 109, pp.1500–1514, Novembre 2010.

[9] T. Joahansson, P. Meier and R. Blickhan, “A finite-element model for the mechanical analysis of skeletal muscle”, *J. Theor. Biol*, vol. 206, pp. 131–149, September 200.

[10] A.E. Ehret, M. Böl, and M. Itskov, “A continuum constitutive model for the active behaviour of skeletal muscle”, *J Mech Phys Solids,* vol. 59, pp. 625–636, March 2011.

[11] P.G. Pavan, P. Pachera, A. Forestiero and A.N. Natali, “Investigation of interaction phenomena between crural fascia and muscle by using a three-dimensional numerical model”, *Med Biol Eng Comput,* vol. 55, pp. 1683–1691,September 2017.

[12] L. Marcucci, C. Reggiani, A.N. Natali, P.G. Pavan, “From single muscle fiber to whole muscle mechanics: a finite element model of a muscle bundle with fast and slow fibers”, *Biomech Model Mechanobiol*, vol. 16, pp.1833-1843, December 2017.

[13] V.S. Tuktamyshev, “On the nature of intra-abdominal pressure,” *Russian Journal of Biomechanics*, vol. 20, pp. 169-176, March 2016.

[14] V.S. Tuktamyshev, E.Y. Kasatova, E.A. Truhacheva, A.V. Kasatov, “The study of compressibility of abdominal contents,” *Russian Journal of Biomechanics*, vol. 20, pp. 261-265, March 2016.

[15] U. Klinge, B. Klosterhalfen, J. Conze, W. Limberg, B. Obolenski, A.P. Öttinger and V. Schumpelick, “Modified mesh for hernia repair that is adapted to the physiology of the abdominal wall”, *Eur J Surg*, vol. 164, pp. 951–960, December 1998.

[16] J. Conze and U. Klinge, “Biocompatibility of biomaterials - clinical and mechanical aspects”, in: Schumpelick V, Kingsnorth AN (ed) Incisional hernia. Springer-Verlag, Berlin, pp. 169–177.

[17] Grasa, M. Sierra, N. Lauzeral, M.J. Muñoz, F.J. Miana-Mena FJ and B. Calvo, “Active behavior of abdominal wall muscles: Experimental results and numerical model formulation”, *J Mech Behav Biomed*, vol. 61, pp .444–454, August 2016.

[18] N. Lai, L.B. Gladden, P.G. Carlier and M.E. Cabrera, “Models of muscle contraction and energetics”, *Drug Discov Today* vol. 5, pp.273–288, Winter 2008.

[19] S.K. Gollapudi and D.C. Lin, “Experimental determination of sarcomere force-length relationship in type-I human skeletal muscle fibers”, *J Biomech*, vol. 42, pp.2011–2006, September 2009.

Biomechanical characterization of diaphragmatic hernia repair with FE modelling

N. de Cesare[1,2], C. Trevisan[3,4], E. Maghin[3,4], A.N. Natali[1,2], M. Piccoli[4,5] and P.G. Pavan[1,2]

[1] *Department of Industrial Engineering, University of Padova, Italy*

[2] *Centre for Mechanics of Biological Materials, University of Padova, Italy*

[3] *Department of Woman's and Child's Health, University of Padova, Italy*

[4] *Tissue Engineering Lab, Fondazione Istituto di Ricerca Pediatrica Città della Speranza, Padova, Italy*

[5] *Department of Biomedical Sciences, University of Padova, Italy*

***Abstract*—The diaphragm is a mammalian skeletal muscle that plays a fundamental role in the process of respiration. Congenital diaphragmatic hernia (CDH) compromises the respiratory functions, hence the need of surgical intervention to repair the defect and restore the physiological conditions. This study aims to characterize, the differences in the mechanical behaviour between mouse healthy diaphragm and surgically repaired diaphragm, through numerical modelling.**

In the finite element analysis (FEA) the mechanical response was featured with an isotropic hyperelastic model for the tendon and the polymeric implant, while for the muscular tissue a three-element Hill's model was adopted to characterize fibres behaviour.

FEA is useful to simulate the diaphragm contraction in eupnea condition in order to evaluate the deformation differences between the two conditions (i.e. healthy and repaired). The polymeric implant reduces the diaphragm excursion compared to the healthy condition and this explains the compromised mechanical functionality of the surgical repaired muscle.

***Keywords*—Congenital Diaphragmatic Hernia, Muscle Fibres, Constitutive Modelling, Finite Element Method.**

I. Introduction

THE thoracic diaphragm is a thin dome-shaped layer that separates the thoracic from the abdominal cavity. It is constituted by a central tendon and a portion of muscle which is subdivided in crural and costal diaphragm. The muscle is located at the base of the thorax and has insertions into the lower ribs.

Among all the respiratory muscles, the diaphragm is the most important and assists the breathing process, through the contraction, producing the double effect of increasing the chest cavity volume and pushing down the pleura, facilitating the airflow into the lungs. Furthermore, its particular curved shape influences the pumping action and the contractile properties further enhancing the process. Different pathologies can compromise its functional response, such as the Congenital Diaphragmatic Hernia (CDH).

In the west world, CDH occurs in about 1 in every 2,500 live births, mortality rate is about 30% due to insufficient lung growth and persistent pulmonary hypertension, and this accounts for 1% of the entire US infant mortality [1], [2].

Nowadays the materials used in surgical practice are less than ideal. One of the most commonly adopted implant is made of polytetrafluoroethylene (PTFE, Trademark Gore-Tex®, W. L. Gore and Associates, Flagstaff, AZ). This type of patch is soft, conformable, chemically inert and with good sealant properties [3], representing the gold standard for CDH repair. At present, the improvement of surgical procedures is studied in animal models [4], indeed some works have accounted the effects of different surgical treatments on CDH on rodents [5], [6].

This work is focused on the numerical modelling of mice diaphragm biomechanics and sets out to emphasize the differences between healthy and surgical repaired diaphragm. The investigation of the biomechanics of the two diaphragm configurations was performed with the Finite Element Method (FEM). The numerical models presented were reconstructed starting from of images and anatomical samples, instead the mechanical properties of materials were deduced by the use of experimental data retrieved from the literature.

II. Materials and Methods

A. Finite elements model

Two models were created starting from anatomical data of mouse diaphragm (Fig. 1), both built ABAQUS CAE Software (Dassault Systémes). The thickness of tendon and muscle were set to 150 μm and 300 μm, respectively [7]. In the herniated diaphragm, portions of muscle and tendon were removed in the left hemi-diaphragm and replaced with a synthetic patch elliptically shaped (150 μm thickness, 9.5 mm major axis, 5.5 mm minor axis).

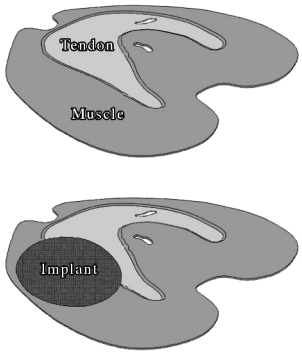

Fig. 1: Mouse diaphragm geometrical model, healthy (a) and repaired (b).

The implant is considered as perfectly bounded to the surrounding muscular and tendon tissue. This condition is a reasonable representation of the continuity between implant and tissue that takes place after post-surgery healing, with

the formation of fibrotic tissue. In fact, the model developed refers to a condition of 90 days after surgery.

B. Constitutive models

There is a total lack of experimental data about the mechanical characteristic of the central tendon of mouse diaphragm. In other species, the central tendon was found to be anisotropic [8]. In this work, considering that diaphragm deformation is almost completely due to muscle contraction, the tendon model was simplified as neo-Hookean material with the following strain energy function:

$$w_t = C_{1t}(\tilde{I}_1 - 3) + \frac{K_{vt}}{2}(J^2 - 1 - 2\ln J) \qquad (1)$$

where the scalar term $\tilde{I}_1$ is the first principal invariant of the iso-volumetric part of the right Cauchy-Green strain tensor $\tilde{\mathbf{C}}$ and the scalar term J is the Jacobian of deformation. The stress-like parameter C_{1t} is set to 75 MPa [8]. The stress-like parameter K_{1t} represents the bulk modulus of the tissue, set to 2,000 MPa, in order to obtain an almost-incompressibility.

The diaphragm muscle tissue was characterized according to three-element Hill model [9] and, in this work, the model was configured to describe the mouse's diaphragm mechanical behaviour.

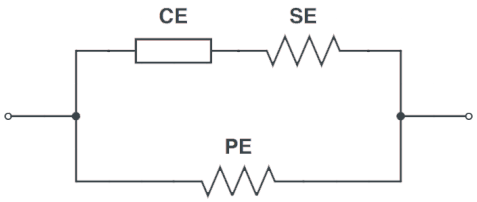

Fig. 2: Three-element Hill's model composed by a contractile element (CE), an elastic element (SE) and an elastic element (PE).

Using the nominal stress P, the equilibrium in SE-CE branch, requires the condition $P_{SE} = P_{CE}$, where the PE element describes the passive elasticity of the surrounding components and the CE element can be stretched without stiffness in a non-activated state. By this, the stress of PE element is:

$$P_{SE} = \begin{cases} 0 & \lambda_f \leq 0 \\ 4P_0(\lambda_f - 1)^2 & \lambda_f > 0 \end{cases} \qquad (2)$$

where λ_f is the stretch of the muscle fibre. The CE element describes the force generated by muscle fibre contraction, therefore the active tension P_{CE} is the following:

$$P_{CE} = P_0 f_a(t) f_l(\lambda_m) f_v(\dot{\lambda}_m) \qquad (3)$$

where the scalar value P_0 is the maximum stress of the fibre in isometric conditions; this was obtained from the literature [10] with a value of 0.267 ± 0.02 MPa (avg ± std). The scalar function $f_a(t)$ describes the activation and deactivation level of the fibre contraction over the time t [11]. Finally, the mechanical response of the SE element was described as a non-linear relationship among nominal stress and stretch [12]:

$$P_{SE} = \beta\{\exp[\alpha(\lambda_s - 1)] - 1\} \qquad (4)$$

where α and β are scalar parameters for muscle tissue of the mouse diaphragm.

The mechanical behaviour of the PTFE implant is always described with a neo-Hookean hyperplastic constitutive model, with the following strain energy function:

$$w_i = C_{1i}(\tilde{I}_1 - 3) + \frac{K_{vi}}{2}(J^2 - 1 - 2\ln J) \qquad (5)$$

where the symbols have the same meaning as in Eq. (1). Experimental test were developed on PTFE samples according to standard methods [13]. The parameters C_{1i} and K_{vi} were set up respectively to 16.7 MPa and 417.8 MPa.

C. Boundary and loading conditions

The diaphragm, in physiological conditions, is subjected to trans-diaphragmatic pressure (TDP) that can be considered as the combination of pleural pressure (PP) and intra-abdominal pressure (IPA). The effects produced by TDP are applied as uniform pressure to the caudal surface of the diaphragm muscle. According to experimental data retrieved from the literature, TDP was set to 10 cmH_2O [14], which corresponds to a diaphragm displacement of 1 mm in the cranio-caudal direction [15]. Both can be considered as reference values for eupnea conditions.

The diaphragm muscle activation level under eupnea conditions was found using a correlation between body mass (BM) of different species and other functional parameters [16]. It was shown that the respiration volume *(RV)* of mouse diaphragm, as in other species, obeys to the following exponential allometric correlation:

$$RV = 10^A \cdot BM^b \qquad (6)$$

where BM is the body mass, while A and b are suitable constants. A similar allometric exponential correlation was reported in the literature [16] for the ratio between eupnea muscle contraction stress (P) and maximum isometric stress (P_0), as shown in Fig. 3. The graph allows to relate data between different species, from which the mouse value was estimated.

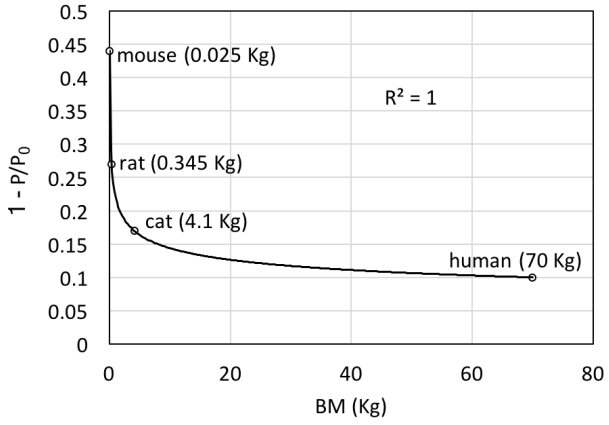

Fig. 3: Correlation of body mass and ratio between muscle stress in eupnea (P) and maximum isometric stress (P_0).

III. Results and Discussion

Figure 4 shows the TDP and the displacement in the cranio-caudal direction of healthy diaphragm versus time. TDP is close to experimental data found in the literature [14], which report a value of 9.9 ± 0.6 cmH_2O (average ± SD). Further, the maximum displacement is comparable with the range of 0.89÷1.06 mm also reported by experimental tests from the literature [15].

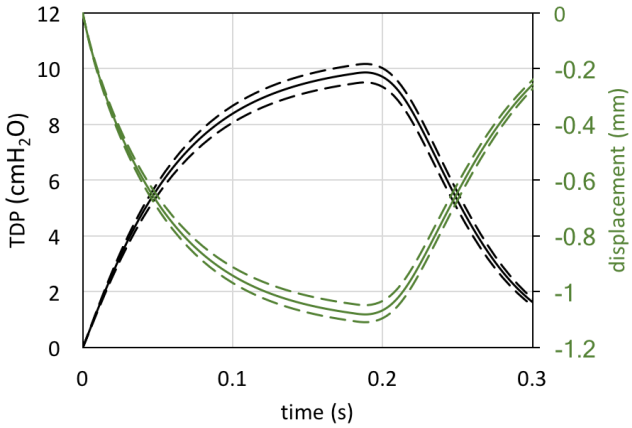

Fig. 4: Trans-diaphragmatic pressure (black curve) and displacement of healthy diaphragm (green curve), both as a function of time up to 0.3 s. Solid lines refer to the average value of maximum isometric stress (P_0), while dashed lines refer to average ±SD.

A comparison of lungs volume change (VC) and diaphragm displacement along the cranio-caudal direction on healthy and repaired diaphragm (Fig. 5), in the case of an average value of maximum isometric stress P_0, shows a reduction of 5.5% of the maximum displacement and 9.0% of VC with respect to healthy condition.

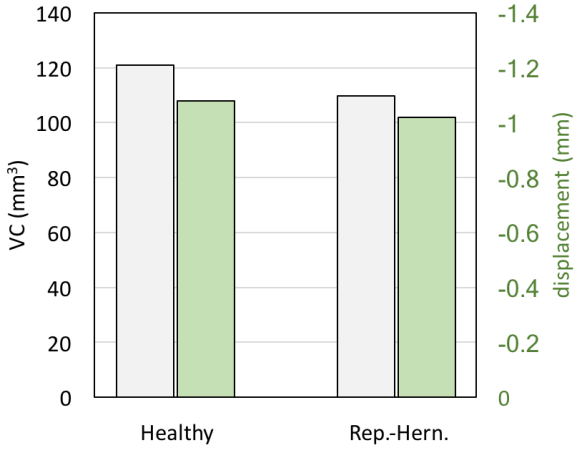

Fig. 5: Volume change (VC) in lung cavity (green bars) at the maximum excursion of the diaphragm muscle (grey bars) in healthy and repaired conditions.

The field of displacement along the cranio-caudal direction shows that the synthetic implant generates a non-physiological asymmetry on the left side of the diaphragm with respect to the right one, compared to the healthy condition.

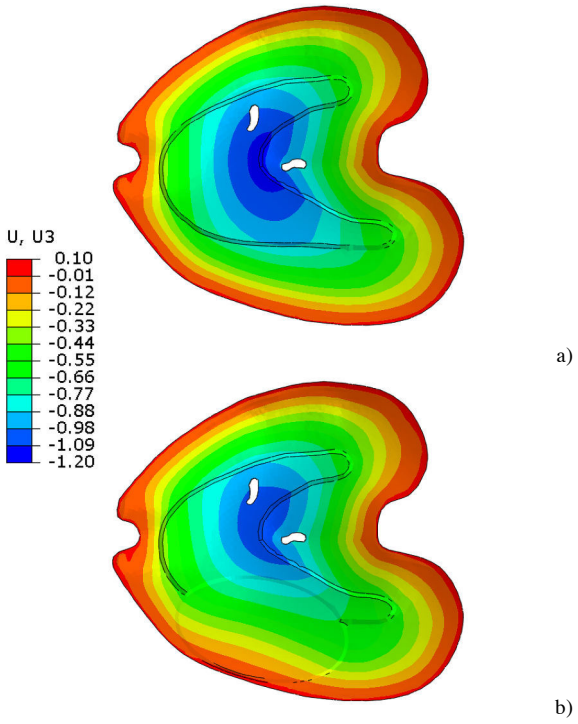

Fig. 6: Displacement field (mm) along the cranio-caudal direction for healthy (a) and repaired diaphragm (b). The non-physiological displacement on the left side diaphragm is visible.

Another interesting aspect is the change of the mechanical state of the muscle tissue around the synthetic graft, which shows an increment of strains in the repaired diaphragm. Figure 7 shows the contour of maximum and minimum principal logarithmic strains of the diaphragm at the time of maximum muscle contraction, where the logarithmic strain is defined as $\varepsilon_l = \ln(\lambda)$, being λ the stretch component. Compared to healthy diaphragm, abnormal peak values were found near the costal region of the repaired diaphragm (Fig. 7b), more precisely in the region between synthetic implant and ribs. The maximum principal nominal strain was estimated as 8.5% in healthy diaphragm and 18.9% in repaired diaphragm. On the contrary, the central tendon is minimally deformed by TDP and muscle contraction force. Similar values were found for the minimum principal nominal strain, with –8.3% in healthy diaphragm and –17.5% in repaired diaphragm. The numerical results suggest that a possible reason for hernia recurrence is the failure of muscle tissue around the graft because of excessive strain. This result is consistent with experimental data obtained in mouse.

Some limits in the present model must be pointed out. The tendon is considered as isotropic tissue. In fact, literature does not provide any data relative to the mechanical behaviour of the mouse diaphragm. Other experimental tests on animal models (i.e. dog) present that the central tendon has anisotropic properties [8]. Nonetheless, the analysis shows that the tendon is subjected to limited strain thanks to its large stiffness, therefore the assumption of the tendon as an isotropic tissue has marginal effect on the results.

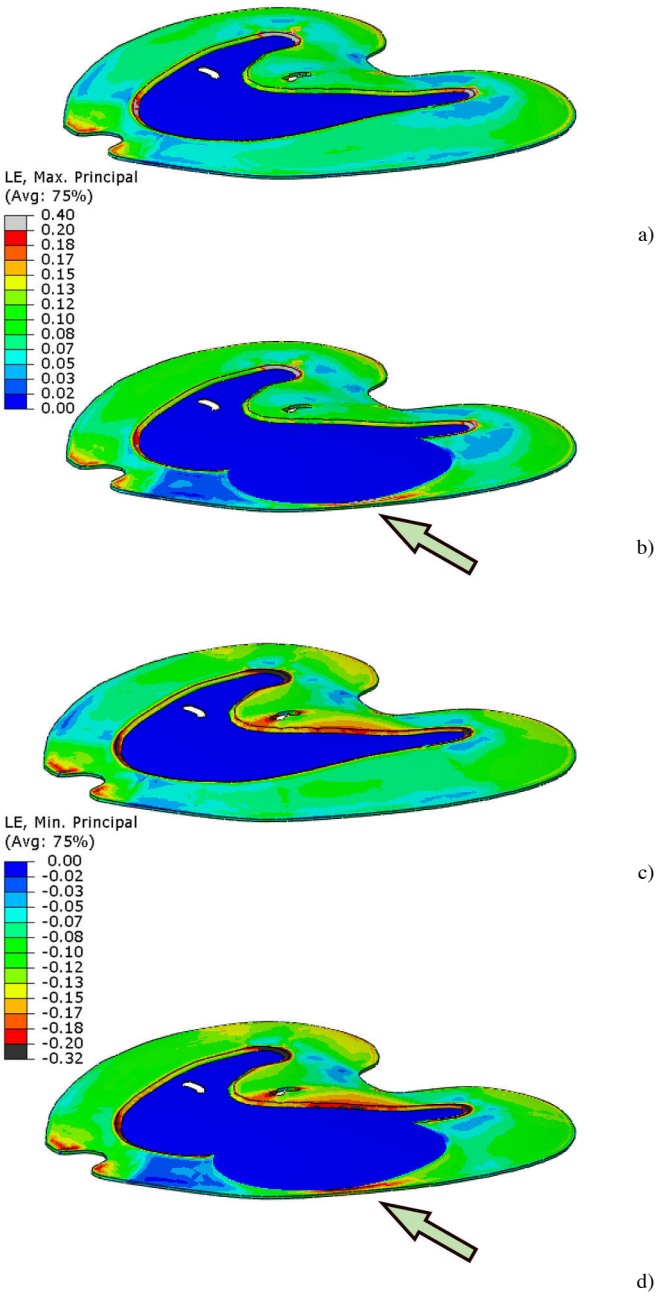

Fig. 7: Maximum principal logarithmic strains in healthy (a) and repaired (b) diaphragm. Minimum principal logarithmic strains in healthy (c) and repaired (d) diaphragm.

IV. Conclusion

The numerical analyses proposed in this work demonstrate that a synthetic implant has several consequences on the physiological functionality of the diaphragmatic muscle. In fact, its passive behaviour and its stiffness reduce muscle excursion during breathing process, therefore reducing the inhaled air volume. Additional effects are the asymmetry resulting in the excursion of repaired and contralateral emi-diaphragms. Moreover, peak strains on the muscular tissue around the synthetic graft are found. This can be considered as a reason for possible hernia recurrences.

In the perspective of surgical repair of CDH by using synthetic implant, it is clear that biomechanical alterations can be considered the main cause of frequently reported complications. Furthermore, size and shape are chosen in function of both dimension and position of the defect, therefore, the changing of these does not reduce the mismatch respect the healthy condition. This suggests to find alternatives to synthetic implants, for example adopting biological substitutes with mechanical properties more similar to diaphragmatic muscle and, above all, with the capability to undergo a remodelling, growing up with the host diaphragm.

Acknowledgement

This work has been funded by Fondazione CARIPARO (Cassa di Risparmio di Padova e Rovigo) – Bando Ricerca Pediatrica 2016-2018.

References

[1] P. De Coppi, J. Deprest, "Regenerative medicine solutions in congenital diaphragmatic hernia", *Seminars in Pediatric Surgery*, 26(3):171–177, 2017.

[2] K.P. Lally, "Congenital diaphragmatic hernia – The past 25 (or so) years", *Journal of Pediatric Surgery*, 51(5):695-698, 2016.

[3] A.C. Gasior, S.D. St. Peter, "A review of patch options in the repair of congenital diaphragm defects", *Pediatric Surgery International*, 28(4):327–33, 2012.

[4] M.P. Eastwood, L. Joyeux, S. Pranpanus, J. Van der Merwe, E. Verbeken, et al., "A growing animal model for neonatal repair of large diaphragmatic defects to evaluate patch function and outcome", *Public Library of Science*, One 12(3): e0174332, 2017.

[5] K.M. Brouwer, W.F. Daame, D. Reijnen, R.H. Verstegen, G. Lammers, et al., "Repair of surgically created diaphragmatic defect in rat with use of a crosslinked porous collagen scaffold", *Journal of Tissue Engineering*, Regen Med 7: 552–561, 2012.

[6] G.P. Liao, Y. Choi, K. Vojnits, H. Xue, K. Aroom, et al., "Tissue Engineering to Repair Diaphragmatic Defect in a Rat Model", *Stem Cells Int*, 2017:1764523, 2017.

[7] M. Piccoli, L. Urbani, M.E. Alvarez-Fallas, C. Franzin, A. Dedja, et al., "Improvement of diaphragmatic performance through orthotopic application of decellularized extracellular matrix patch", *Biomaterials,* 74:245–255, 2016.

[8] W. Hwang, N.G. Kelly, A.M. Borieck, "Passive mechanics of muscle tendinous junction of canine diaphragm", *Journal of Applied Physiology,* 98, 1328–1333, 2004.

[9] L. Marcucci, C. Reggiani, A.N. Natali, P.G. Pavan, "From single muscle fiber to whole muscle mechanics: a finite element model of a muscle bundle with fast and slow fibers", *Biomechanics and Modeling in Mechanobiology*, published online, 2017.

[10] S.M. Greising, C.B. Mantilla, B.A. Gorman, L.G. Ermilov, G.C. Sieck, "Diaphragm muscle sarcopenia in aging mice", *Experimental gerontology*, 48, 881–887, 2013.

[11] A.E. Ehret, M. Böl, M. Itskov, "A continuum constitutive model for the active behaviour of skeletal muscle", Journal of the Mechanics and *Physics of Solids*, 59:625–636, 2011.

[12] M. Kojic, S. Mijailovic, N. Zdravkovic, "Modelling of muscle behaviour by the finite element method using Hill's three-element model", *International Journal for Numerical Methods in Engineering*, 43:941–953, 1998.

[13] S. Todros, P. Pachera, N. Baldan, P.G. Pavan, S. Pianigiani, et al., "Computational modeling of abdominal hernia laparoscopic repair with a surgical mesh", *International Journal of Computer Assisted Radiology and Surgery*, accepted October 20th, 2017.

[14] S.M. Greising, D.C. Sieck, G.C. Sieck, C.B. Mantilla, "Novel method for transdiaphragmatic pressure measurements in mice", *Respiratory Physiology & Neurobiology,* 188(1):56–59, 2013.

[15] L. Zuo, W.J. Roberts, K.D. Evans, "Diagnostic Ultrasound Imaging of Mouse Diaphragm Function", *Journal of Visualized Experiments*, 86:51290, 2014.

[16] S.L. Lindstedt, P.J. Schaeffer, "Use of allometry in predicting anatomical and physiological parameters of mammals", *Laboratory Animals*, 36, 1–19, 2002.

A novel computational framework for large strain explicit solid dynamics: applications in biomechanics

Osama I. Hassan[1,2], Antonio J. Gil[1], Chun Hean Lee[1], F. Auricchio[2] and Javier Bonet[3]
[1] *Zienkiewicz Centre for Computational Engineering, College of Engineering, Swansea University, United Kingdom*
[2] *Department of Civil Engineering and Architecture (DICAR), Universitá di Pavia, Italy*
[3] *University of Greenwich, London, United Kingdom*

***Abstract*—This paper introduces a novel computational framework for the simulation of solid mechanics problems encountered in biomechanical applications of clinical, industrial and academic importance. The framework overcomes numerical challenges faced by modern–day computer simulations of medical interest. This new approach is useful in numerous scenarios such as modelling of biological soft tissues, design of biomedical shape memory polymer devices and stent deployment in balloon angioplasty. Moreover, the scheme shows great potential for handling Fluid–Structure Interaction (FSI) problems that arise in many biomechanical applications.**

***Keywords*—biomechanics, large strain, locking, stent**

I. INTRODUCTION

Computational biomechanical models have been progressing rapidly in the past few decades with a myriad of applications ranging from the smallest scale at the molecular level up to the level of cardiovascular and musculoskeletal systems. Advanced numerical approaches are constantly being developed with the aim of increasing the capabilities of such simulations; e.g. analysing complex geometries, enhancing constitutive models, handling different biological processes, etc. This endeavour faces many engineering challenges that need to be addressed using novel numerical strategies to solve the boundary– and initial–value problems of clinical, industrial, and academic interest.

One such challenge is the simulation of biological soft tissues which exhibit an inherently nonlinear mechanical behaviour over finite strains [1]. Additionally, due to the existence of high volume fraction of water inside most tissues, they exhibit a nearly incompressible behaviour under physiologic conditions. It is well known that the performance of the classical low order Finite Element displacement–based method [2] used in conjunction with tetrahedral elements behaves poorly near the incompressible limit. Low order interpolation polynomials fail to adequately represent general volume preserving displacement fields. This phenomenon is known as volumetric locking and is characterised by a severe under–prediction of the displacement field even if the mesh is of a reasonable size [3]. In the context of solid mechanics, the incompressibility constraint appears in the simulation of rubbery solids typically modelled as incompressible hyperelastic materials. Many advances in soft–tissue mechanics have come from building upon advances in rubber elasticity.

Additionally, volumetric locking could also be encountered in the simulation of biomedical Shape Memory Polymers (SMPs) devices [4]. SMPs is a class of smart materials able to store a temporary shape and recover the original shape upon the exposure to an external stimulus, such as temperature. At high temperature, the material is assumed to be in a “rubbery” phase; while at low temperature state it undergoes a “glassy” phase.

Another computational challenge that appears in many biomedical applications is the simulation of bending–dominated scenarios in thin shape structures. One example is the study of stent performance during and after deployment in balloon angioplasty where large bending deformation of the stent strut is encountered [5]. In this scenario, the difficulty arises from the inability of the elements to represent deformations in which the transverse shear should vanish; a problem known as shear locking. Traditional displacement–based Finite element formulations are known to suffer from this limitation.

Furthermore, the process of mesh generation represents another challenge as it constitutes a large portion of the overall design and analysis time. Hence, it is regarded as the main bottleneck in almost all practical simulations. In biomedical applications; unstructured tetrahedral meshes have been gaining increasing popularity due to the existence of several fast and robust automatic mesh generators. In [13], a study of a rare case of double aortic arch was conducted to determine the best surgical access. A tetrahedral mesh was used to model the complex geometry of the arch (Fig. 1).

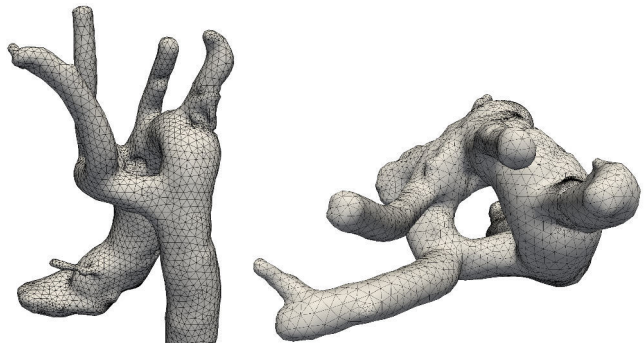

Fig. 1: Computational mesh of a double aortic arch. Tetrahedral elements were used to mesh the complex geometry.

On the contrary, producing high quality hexahedral meshes on arbitrary geometries is not an easy task and cannot be fully automated. Unfortunately, modern tetrahedral element technology in solid mechanics typically uses the traditional Finite Element based second order displacement formulation.

The use of mixed approaches [2] proved to be very efficient in solid dynamics, circumventing the above–mentioned drawbacks for the traditional displacement based techniques. A novel mixed system of first order hyperbolic conservation laws for large strain solid dynamics was introduced in [6,7,8]. Essentially, the formulation is established in terms of the linear momentum, the deformation gradient tensor and the Jacobian, and written in a Total Lagrangian formalism. The use of a Total Lagrangian description of the motion has clear advantages in the context of solid dynamics. Firstly, all the calculations are carried out based on the undeformed mesh leading to a simple algorithm. Secondly, the Lagrangian setting follows the evolution of any material particle, which is of paramount importance in history dependent constitutive laws. The algorithm is ideal near the incompressibility limit with excellent behaviour in bending dominated scenarios and highly nonlinear deformations without showing any spurious pressure oscillations. This is shown in this paper by simulating a cardiovascular SMP stent in its rubbery phase where large deformations are encountered.

Moreover, the computational domain is discretised using a Finite Volume based approach very popular within the field of Computational Fluid Dynamics (CFD). This strategy allows for the introduction of a unified discretisation methodology for both solids and fluids. This coupling is a central feature in the study of the mechanics of the heart, arteries, veins, microcirculation, and pulmonary blood flow [9]. Hence, the proposed framework has a great potential in exploring this class of Fluid-Structure Interaction (FSI) problems.

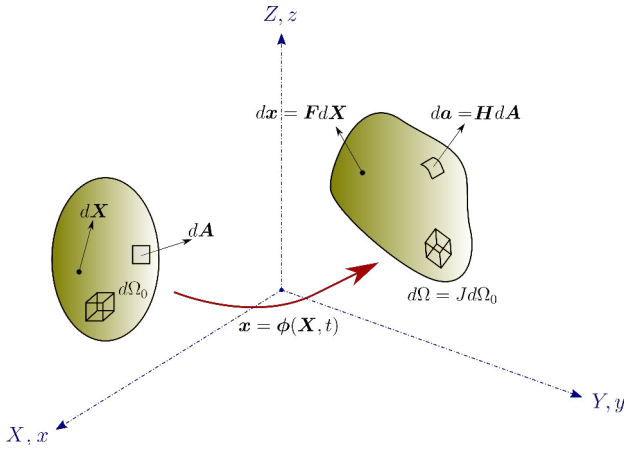

Fig. 2: Motion of a continuum domain.

II. Governing Equations

In this section, the motion of a continuum deformable body is considered (Fig. 2). The body assumes an initial reference configuration at time $t = 0$ and occupies a volume denoted as Ω_0. As the body undergoes deformation it occupies a volume Ω in the deformed configuration. The motion can be described by the following $\boldsymbol{p}$-$\boldsymbol{F}$-J mixed-based system of hyperbolic equations:

$$\frac{\partial \boldsymbol{p}}{\partial t} - \mathrm{DIV}\boldsymbol{P} = \boldsymbol{f}_0; \tag{1a}$$

$$\frac{\partial \boldsymbol{F}}{\partial t} - \boldsymbol{\nabla}_0 \left(\frac{\boldsymbol{p}}{\rho_0} \right) = \boldsymbol{0}; \tag{1b}$$

$$\frac{\partial J}{\partial t} - \mathrm{DIV} \left(\boldsymbol{H}^T \frac{\boldsymbol{p}}{\rho_0} \right) = 0. \tag{1c}$$

where $\boldsymbol{p} := \rho_0 \boldsymbol{v}$ is the linear momentum, ρ_0 is the material density, $\boldsymbol{v}$ is the velocity field, $\boldsymbol{f}_0$ is the body force per unit undeformed volume, $\boldsymbol{F}$ is the deformation gradient (or fibre map), $\boldsymbol{H} := J\boldsymbol{F}^{-T}$ is the cofactor of the deformation gradient (or area map), J is the Jacobian of the deformation (or volume map) and $\boldsymbol{P}$ represents the first Piola-Kirchhoff stress tensor. For closure, appropriate initial and boundary conditions, as well as a constitutive model, are supplemented.

III. Finite Volume Spatial Discretisation

Consider the general form of the hyperbolic system of conservation laws given in (1); by making use of the local conservation property of the finite volume method, the expression is integrated for a given control volume Ω_0^a to give:

$$\Omega_0^a \frac{d\boldsymbol{\mathcal{U}}_a}{dt} = -\int_{\partial\Omega_0^a} \boldsymbol{\mathcal{F}}\boldsymbol{N}\, dA + \int_{\Omega_0^a} \boldsymbol{\mathcal{S}}\, d\Omega_0^a. \tag{2}$$

where $\boldsymbol{\mathcal{U}}_a$ is the average value of a given conservation variable within the control volume Ω_0^a, $\boldsymbol{\mathcal{F}}$ represents the corresponding flux matrix, $\boldsymbol{\mathcal{S}}$ is a source term and $\boldsymbol{N}$ is the outward unit normal vector given on the boundary $\partial\Omega_0^a$. Notice that the divergence theorem has been used to obtain the surface integral term. A finite volume discretisation of the equation yields the following summation of a central difference term and a dissipation operator:

$$\Omega_0^a \frac{d\boldsymbol{\mathcal{U}}_a}{dt} = -\sum_{b\in\Lambda_a} \frac{1}{2}(\boldsymbol{\mathcal{F}}_a + \boldsymbol{\mathcal{F}}_b)\boldsymbol{C}_{ab} - \sum_{\gamma\in\Gamma_a^B} \boldsymbol{\mathcal{F}}_a^\gamma \boldsymbol{N}_\gamma \frac{A_\gamma}{3} + \boldsymbol{\mathcal{A}}_\mathcal{D}(\boldsymbol{\mathcal{U}}_a). \tag{3}$$

where the source term $\boldsymbol{\mathcal{S}}$ has been omitted for simplicity. Λ_a is the set of neighbouring control volumes to node a and Γ_a^B is the set of boundary faces surrounding node a. The central difference contribution consists of two terms; the first is a summation over internal edges and the second is a summation over boundary faces. In this second term, a weighted average stencil proposed in [10] is employed, computing the flux over a face γ in three dimensions as:

$$\boldsymbol{\mathcal{F}}_a^\gamma = \frac{6\boldsymbol{\mathcal{F}}_a + \boldsymbol{\mathcal{F}}_b + \boldsymbol{\mathcal{F}}_c}{8}. \tag{4}$$

The introduction of appropriate numerical dissipation $\boldsymbol{\mathcal{A}}_\mathcal{D}$ is of paramount importance in order to counterbalance the negative diffusion introduced by the central difference term. In this

paper, two alternative approaches are used to evaluate the dissipation term. The first is based on an upwind algorithm where the numerical flux is obtained as the solution of the Riemann problem established by the contact discontinuity at the faces. The second is a JST algorithm where the dissipation is added explicitly based on the Jameson-Schmidt-Turkel method [11].

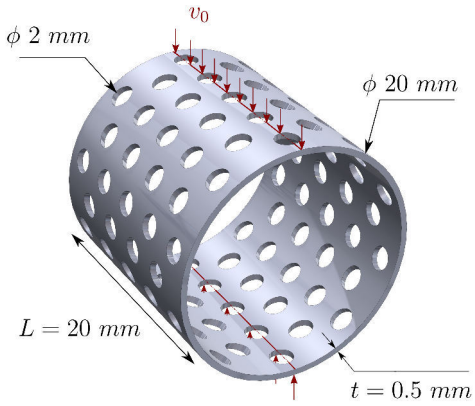

Fig. 3: Cardiovascular stent simulation. The geometry is similar to the one reported in [4].

IV. Artificial Compressibility Algorithm

The mixed–based set of governing equations for large strain solid dynamics introduced above are advanced explicitly in time using a Runge–Kutta time integrator. In nearly incompressible scenarios, the volumetric wave speed c_p takes very high values and it can even reach a degenerate value of infinity in the fully incompressible case. As the time step is controlled by the Courant–Friedrichs–Lewy number, the increase in wave speed is reflected in a very small time step size resulting in a very inefficient algorithm. Hence, it is very important to introduce an efficient algorithm for the treatment of nearly and fully incompressible scenarios.

The use of the Finite Volume scheme allows for the exploration of methods that were originally developed to solve the incompressible Navier–Stokes equations in the field of Computational Fluid Dynamics. Several methods have been developed in the past where the main differences between them comes from the way in which the incompressibility condition is satisfied numerically. Those different methods can be grouped under three main categories [12]; namely, pressure–based methods, artificial compressibility methods and techniques based on derived variables. In this paper, the artificial compressibility method is preferred.

V. Simulation of a Cardiovascular Stent

A cardiovascular stent is simulated. The geometry is similar to the one reported in [4] with external radius $r = 10$ mm, thickness $t = 0.5$ mm, length $L = 20$ mm and hole diameter $d = 2$ mm. The geometry is provided in Fig. 3. The problem is initialised with a traction–free condition at all boundaries and subjected to the following Gaussian velocity profile:

$$\boldsymbol{v}_0 = [0, 0, v_z]; \qquad v_z = \frac{ABe^{-A(t-C)}}{\left[e^{-A(t-C)} + 1\right]^2}. \tag{5}$$

where $A = 800$ s^{-1}, $B = 6 \times 10^{-3}$ m and $C = 1.5 \times 10^{-2}$ s.

The problem is run with a neo–Hookean material with density $\rho_0 = 1000$ kg/m^3, Young's modulus $E = 0.9$ MPa and Poisson's ratio $\nu = 0.45$. The maximum allowable time step is governed by the Courant–Friedrichs–Lewy (CFL) condition given as:

$$\Delta t = \alpha_{\text{CFL}} \frac{h_{\text{min}}}{c_{\text{p,max}}} \tag{6}$$

where $c_{\text{p,max}}$ is the maximum volumetric wave speed , h_{min} is the minimum characteristic length within the computational domain and α_{CFL} is the CFL stability number. For the test cases presented here, a value of $\alpha_{\text{CFL}} = 0.3$ is used to ensure both accuracy and stability.

Fig. 4 shows a comparison between the results obtained using the proposed algorithm and the traditional Bubnov–Galerkin approach. It is clear that the standard approach is unable to obtain the correct solution leading to an unstable pressure field. The dynamic behaviour of the stent is shown in Fig. 5 by depicting a series of snapshots in time for the deformation along with the pressure field. The results show a locking-free deformation with a smooth pressure field.

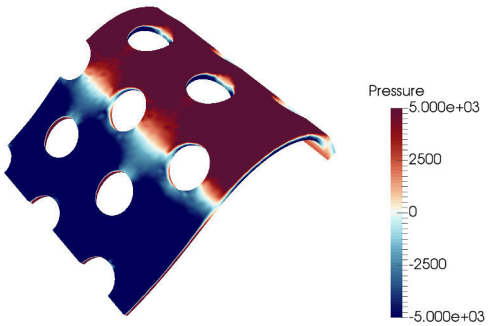

(a) Proposed $\boldsymbol{p}$-$\boldsymbol{F}$-J formulation

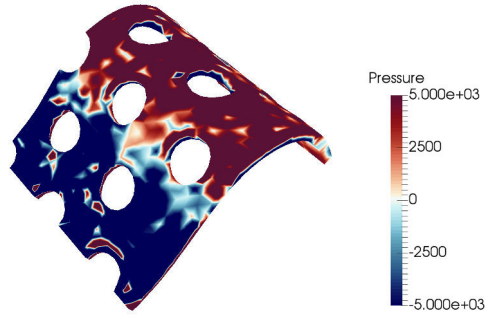

(b) Standard Bubnov–Galerkin

Fig. 4: Pressure field comparison at time t = 0.018 s. The standard Bubnov–Galerkin approach shows pressure instabilities in contrast to the proposed $\boldsymbol{p}$-$\boldsymbol{F}$-J formulation.

VI. Conclusion

This paper has introduced a second order Total Lagrangian vertex–centred finite volume algorithm for the numerical simulation of large strain solid dynamics for nearly and truly incompressible materials. A mixed formulation written in the form of a system of first order hyperbolic equations is employed. The linear momentum $\boldsymbol{p}$, the deformation gradient $\boldsymbol{F}$ and the Jacobian J are regarded as primary conservation variables. For computational efficiency, the artificial compressibility algorithm extensively used in the CFD community is employed and suitably adapted. The framework shows a great potential for biomechanical simulations in many areas of research; especially when it is important to take the effect of coupling fluids and solids in one monolithic framework.

Acknowledgement

The first author gratefully acknowledge the financial support provided by the Erasmus Mundus Program (SEED). The second, third and fifth authors gratefully acknowledge the financial support provided by the Ser Cymru National Research Network for Advanced Engineering and Materials.

References

[1] J. D. Humphrey. Review Paper: Continuum Biomechanics of Soft Biological Tissues. Proceedings: Mathematical, Physical and Engineering Sciences 459, no. 2029: 3-46, 2003.
[2] T. J. R. Hughes. The Finite element method : linear static and dynamic finite element analysis. Dover Publications, 2000.
[3] T. Belytschko, W. K. Liu, and B. Moran. Nonlinear Finite Elements for Continua and Structures. John Wiley & Sons, 2000.
[4] E. Boatti, G. Scalet, and F. Auricchio. A three–dimensional Finite–strain phenomenological model for shape–memory polymers: Formulation, numerical simulations, and comparison with experimental data. International Journal of Plasticity, 83:153–177, 2015.
[5] A. Schiavone and L. Zhao. The importance of vessel factors for stent deployment in diseased arteries. J Integr Cardiol, 1: DOI: 10.15761/JIC.1000130, 2015
[6] C. H. Lee, A.J. Gil, J. Bonet. Development of a cell centred upwind finite volume algorithm for a new conservation law formulation in structural dynamics. Computers and Structures, 118:13-38, 2013.
[7] O. I. Hassan, A.J. Gil, C.H. Lee and J. Bonet. A first order hyperbolic framework for large strain computational solid dynamics: An upwind vertex-centred Updated Lagrangian scheme. In proceedings of the 24th ACME Conference, Cardiff, United Kingdom, 31 March–1 April, 2016.
[8] M. Aguirre, A. J. Gil, J. Bonet and C. H. Lee. An upwind vertex centred finite volume solver for Lagrangian solid dynamics. JCP, 300, 387422, 2015.
[9] D. Suvranu, G. Farshid and R. K. Mofrad. Computational Modeling in Biomechanics. Springer, Dordrecht, 2010.
[10] H. Luo, J. Baum and R. Lohner, An improved finite volume scheme for compressible flows on unstructured grids, in: AIAA paper, Reston, Virigina, pp. 95–0348.
[11] A. Jameson. Origins and further development of the Jameson–Schmidt–Turkel scheme. AIAA Journal, 55(5):1487–1510, 2017.
[12] D. Kwak and C. Kiris. Computation of Viscous Incompressible Flows, volume 1, Springer, 2015.
[13] A. Finotello, S. Morganti, S. Marconi, R. Romarowski, P. Totaro and F. Auricchio. Double aortic arch: engineering support to decision making process. Proceedings of the VII Annual Meeting, Italian Chapter of the European Society of Biomechanics, 28-29 September 2017, Rome, Italy.

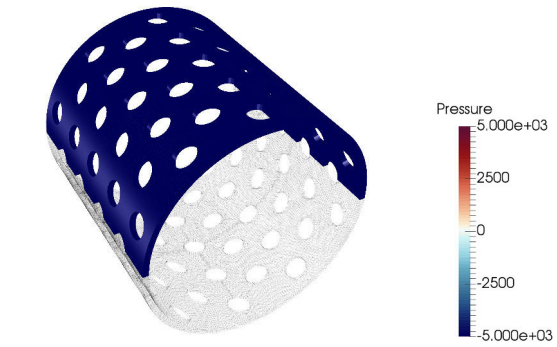

(a) t = 0 s

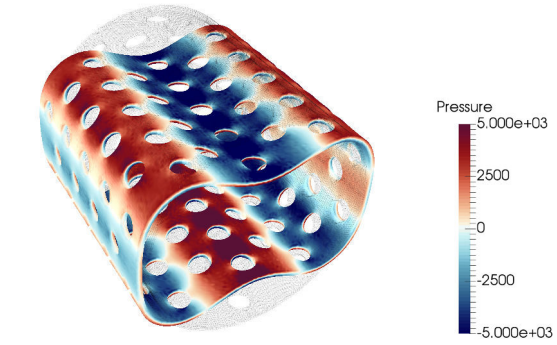

(b) t = 0.015 s

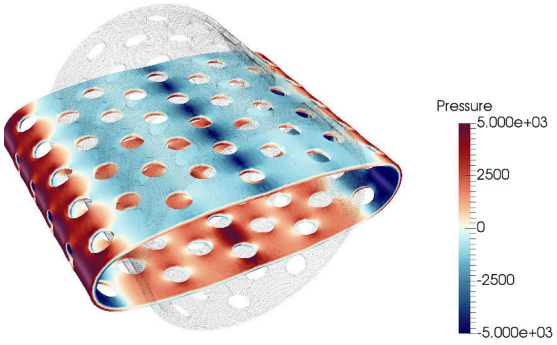

(c) t = 0.02 s

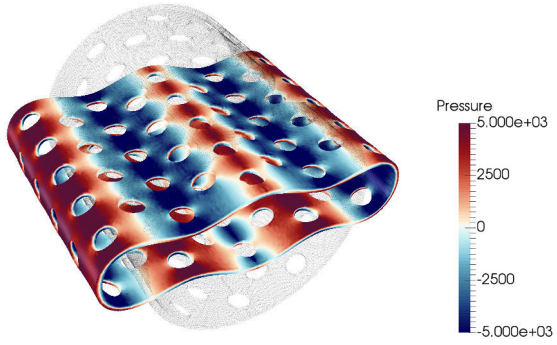

(d) t = 0.05 s

Fig. 5: Deformation of a cardiovascular stent. Several snapshots in time showing pressure distribution.

3D Finite Element Model of Osteophytes in the Human Femur Head

Andrada Pica[1], Fabiano Bini[1], Andrea Marinozzi[2], Franco Marinozzi[1]

[1] *Department of Mechanical and Aerospace Engineering, "Sapienza" University of Rome, via Eudossiana, 18–00184 Rome, Italy*

[2] *Orthopedy and Traumatology Area, "Campus Bio-Medico" University, via Alvaro del Portillo, 200-00128 Rome, Italy*

***Abstract* - Osteophytes represent abnormal osteo-cartilaginous outgrowths associated with the evolution of osteoarthritis (OA). Finite element analysis was performed on a 3D model of the proximal half of human femur in order to determine the relevance of osteophytes on the stress and strain distributions within the femur head. We assume that the model includes three linearly elastic, homogeneous and isotropic media representing the articular cartilage, the cortical and trabecular bone, respectively. Simulations were carried out for a healthy and an advanced stage OA femur. Different load distributions are considered for the two models due to the alterations of bone structure. The patterns of stress and strain within the trabecular tissue suggest that osteophytes manifestation could justify the development of bone cysts (geodes) and the formation of highly mineralized tissue (eburnation). The finite element approach presented in this work provides new insights into biomechanics of OA joint and could result useful in predicting bone behaviour towards abnormal mechanical solicitations.**

***Keywords* - hip osteoarthritis, osteophyte, 3D FEM, contact mechanics**

I. INTRODUCTION

Osteoarthritis (OA) is a degenerative debilitating joint disease which causes a significant loss of mobility, imposing burden socioeconomic consequences [1]. The physiopathology of OA is characterized by articular cartilage degeneration, joint space narrowing, modification of the structural and material properties of the subchondral bone, inflammation of the synovium tissue, osteophyte and cyst formation [2]. The importance of bone alterations in OA progression is an open issue under investigation. Recent studies [3]-[4] have analysed the relevance of abnormal bone development, e.g. osteophytes, on the structural and mechanical properties of the underlying bone.

Osteophytes are osteo-cartilaginous outgrowths that induce the generation of contact points between the bony extremes of osteoarthritic joints [5]-[6] and participate to the development of mechanical stress alterations within the diseased articulations. In the OA femur head three main arrangements of femoral head osteophytes, i.e. marginal, epiarticular and subarticular have been identified by means of standard histological techniques [5] and by computed tomography imaging [6]. The influence of osteophytes on the stress and strain distributions within the femur head has been already examined through a 2D finite element model (FEM) by Marinozzi and co-workers [3]-[4]. In these previous studies, the conformational changes were analysed under the Hertzian theory [7] of friction free contact stress between two rigid bodies, i.e. acetabulum and the altered femur head.

In the present work, the analysis of the osteophytes effect on the OA femur head is extended to a 3D model. Furthermore, we introduce the contribution of the articular cartilage, assumed as an elastic material bonded to a rigid substrate, i.e. femur head. The cartilage forms a resilient pad which allows load transfer to occur frictionless between the joint surfaces. Therefore, we present the stress and strain patterns within the femur head for a healthy condition and an advanced stage of OA [5].

II. METHODS

To be able to consider a 3D FEM of a femur head, Computed Tomography images were used. The image slices of the femur head of a 72 year old male were provided by the National Library of Medicine in Maryland (USA). The 3D FEM includes the articular cartilage, the cortical and the trabecular bone, respectively. Materials properties were assumed to be constant, linearly elastic and isotropic. We assign to the articular cartilage an average value of the Young modulus of 15 MPa [8], a Poisson's ratio of 0.1 [9] and a density of 1000 kg/m^3 [2]. For the cortical bone, a Young modulus of 22 GPa [10], a Poisson's ratio of 0.3 [11] and a tissue density equal to 2000 kg/m^3 [12] is considered. The trabecular tissue is characterized by a Young modulus of 1 GPa [13], a Poisson's ratio of 0.3 [4] and an apparent tissue density of 1000 kg/m^3 [14].

Analysis is carried out with Comsol Multiphysics 5.0 (COMSOL – Stockholm, Sweden). FEM simulations are performed for a Healthy Femur (HF) and for an advanced level of OA severity. The Advanced Stage (AS) is associated with the existence of four groups of osteophytes, i.e. epiarticular, subarticular and two marginal bone outgrowths. The centre of the Cartesian coordinate system coincides with the centre of the femur head. The femoral Z-axis is vertical, the Y-axis points in the medial-lateral direction and the X-axis points in the postero-anterior direction. The Y and Z-axes are in the coronal plane of the body, while X-axis is in the sagittal plane. In order to describe the load distribution, it is useful to introduce geometrical parameters concerning the contact surface between the acetabulum and the femur head by means of which the pressure is transmitted. The latter depends on three centre-edge angles describing the acetabular coverage of the femur angle. The extension of the main contact area (MCA) in the YZ plane is identified by the functional angle θ_F. In the HF condition, the centre edge angle of Wiberg (θ_{CE}) in the YZ plane is assumed to be equal to 30°, while the angle θ_F is set to 110°. Generally, the pathological cases are characterized by θ_{CE} values minor than 20° [15], thus we adopted a value of 10° in the AS model. We consider that in the OA case, the MCA is reduced with respect to the HF model due to the presence of four contact points introduced by the bone outgrowths. In Fig. 1b the marginal osteophytes are identified as O_1 and O_2, the

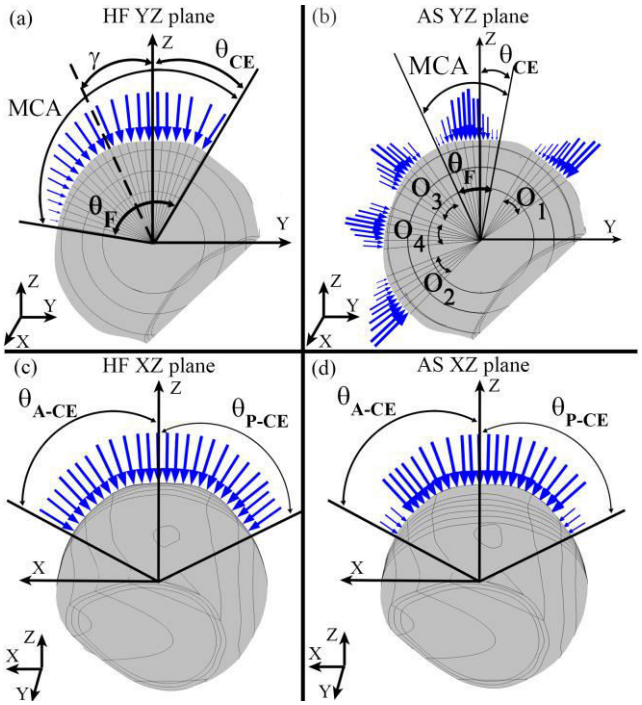

Fig. 1: Load distribution in the YZ plane, i.e. coronal plane, in the healthy femur (HF) (a) and in the advanced stage (AS) OA femur (b). In (c) and (d), the load distributions in the XZ plane, i.e. sagittal plane, are illustrated for HF and AS models. For each plane, we represent the load distribution of the most solicited sections, which are sited in correspondence of the coordinate system origin. The blue arrows are proportional with the load magnitude.

epiarticular osteophyte as O_3 and the subarticular osteophyte as O_4. Thus, in the coronal plane, we assume that the altered MCA is described by a value of θ_F equal to 35°, while the extension of each group of osteophytes is characterized by an angle of 25°. In the XZ plane, i.e. sagittal plane, the estimation of the acetabular contact surface with the femoral head is described by the anterior ($\theta_{A\text{-}CE}$) and posterior ($\theta_{P\text{-}CE}$) angles of Wiberg. According to [16], we set both $\theta_{A\text{-}CE}$ and $\theta_{P\text{-}CE}$ to 60°. In the sagittal plane, the extension of MCA is maintained constant, both in healthy and pathological conditions. In this plane, the groups of osteophytes adopt the same values for the centre edge angles $\theta_{A\text{-}CE}$ and $\theta_{P\text{-}CE}$.

Suitable assumptions were implemented to resolve the contact problem of the 3D femur head model subject to a particular load distribution within the joint. We make the hypothesis of a friction free joint so that tangential stresses are negligible compared with normal stresses, which are directed orthogonally to the contact surface [10]. Moreover, we consider a constant cartilage thickness over the whole surface of the femoral head. Since it was observed that osteophytes formation can occur without overt cartilage damage [17], we assume that the cartilage thickness remains unaltered during OA evolution. Furthermore, in the FEM simulations, the distal end of the model was fully constrained to prevent any movement in the plane [3]-[4], [10].

The resultant force (H) applied to the hip joint is associated with the stance phase of gait and it considers the effect of the partial body weight (W), obtained as total body weight diminished by the weight-bearing leg, and the abductor muscle force calculated to be two times W. The magnitude of H is approximatively 2.4 times W, in agreement with [18]. For a subject with a mass weight estimated to 65 kg, the loading force H corresponds roughly 1554 N.

In this study, the magnitude of the force H is maintained constant in both healthy and pathological conditions. In the HF, the resultant force over the MCA coincides with the total force H. In the AS model, the force is distributed between the reduced MCA and the groups of osteophytes. In accordance with [3]-[4], in the AS model, the load acting on the MCA is 25% of the total amount H, while the remaining 75% of H is equally distributed between the four groups of osteophytes.

We considered different load patterns in order to obtain contact pressure distribution. We applied the load profile as a boundary condition on each domain that composes the contact surface. In the YZ plane, we divided the contact area in circular sectors with a centre angle of 5°.

In agreement with [10], [19], in the HF condition, the load distribution in the YZ plane is implemented to be proportional to the cosine of the angle γ (Fig. 1a), which is defined as the angle between the Z-axis and the generic point on the contact surface MCA [19].

In pathological conditions, due to the structural alterations of the femur head represented by the osteophytes, punctual loads under friction free hypothesis are considered. Therefore, the pressure applied on the MCA, epiarticular and subarticular osteophytes is modelized with a symmetric parabolic distribution [20]-[21]. According to Johnson [20], the contact pressure between the acetabulum and the thin elastic layer of the cartilage, bounded to the rigid substrate constituted by the femoral head can be described as a function of the distance $\boldsymbol{r}$ from the centre of the contact area of radius $\boldsymbol{a}$ as expressed by Eq. (1) [20]-[21], where p_{max} is the maximum contact pressure:

$$\boldsymbol{p(r)} = \boldsymbol{p}_{\max} \cdot \left[1 - \left(\frac{\boldsymbol{r}}{\boldsymbol{a}}\right)^2\right]^{1/2} \quad (1)$$

Following the Johnson's parabolic distribution, the pressure is maximum in the centre of the contact area and null in the marginal zone, at the maximum distance from the centre.

In order to respect the acetabular coverage conditions and to represent the hypothesis of remarkable degenerative changes at the acetabular lateral rim [19], the marginal osteophytes are modelled as half spheres impinging on the acetabular labrum producing half parabolic load distributions in the YZ plane. Thus, the maximum magnitude of the force is considered at the extremity of the acetabular rim (Fig.1b).

In the sagittal plane, for both models, the load follows a symmetric parabolic distribution [22]. Its maximum value is achieved in the centre of the contact surface, which is assumed in correspondence of the Z axis (Fig. 1c and d).

To assess the mechanical response of bone tissue, the stress magnitude and the strain modulus are determined as follows:

$$\boldsymbol{Stress} = -\frac{1}{3} \cdot (\boldsymbol{\sigma_{xx}} + \boldsymbol{\sigma_{yy}} + \boldsymbol{\sigma_{zz}}) \quad (2)$$

$$\boldsymbol{Strain} = \left(\left(\frac{\boldsymbol{du}}{\boldsymbol{dx}}\right)^2 + \left(\frac{\boldsymbol{dv}}{\boldsymbol{dy}}\right)^2 + \left(\frac{\boldsymbol{dw}}{\boldsymbol{dz}}\right)^2 \right)^{1/2} \quad (3)$$

where σ_{xx}, σ_{yy}, σ_{zz} are the Cauchy stress tensor components and $\frac{\boldsymbol{du}}{\boldsymbol{dx}}, \frac{\boldsymbol{dv}}{\boldsymbol{dy}}, \frac{\boldsymbol{dw}}{\boldsymbol{dz}}$ the displacement gradient components.

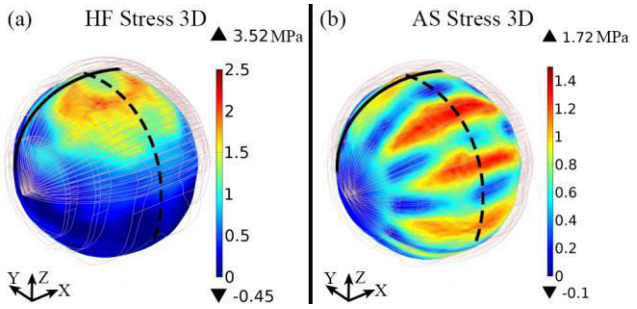

Fig. 2: Stress distribution in the trabecular region of the HF model (a) and AS model (b). The grey lighter shell corresponds to the cortical bone and the cartilage geometry. The dotted black line represents the parallel slice to the YZ plane (coronal plane) sited in correspondence of the coordinate system origin, while the continuous black line indicates the parallel slice to the XZ plane (sagittal plane), sited at a distance R = 10.5 mm on the positive Y-axis direction with respect to the coordinate system origin. The slices are analysed in Figures 3 and 4.

III. RESULTS AND DISCUSSION

Abnormal hip joint contact stress is a crucial factor accelerating the OA development. We performed FE simulations, characterized by 19582908 DOF in the HF model and 11441082 DOF in the AS model, in order to achieve stress and strain patterns of the femur head in association with OA evolution. The outcomes concern the three layers of the FE model, i.e. cartilage, cortical and trabecular bone. The results were corroborated by comparing predictions with clinical studies [23] and previous FE models [3]-[4]. Fig. 2 shows an axonometric view of the stress distribution occurring at the trabecular region of HF and AS models. The maximum stress magnitude is observed in correspondence of the contact points, i.e. the MCA in the HF case and the five points of contact in the AS model, while the central region of the femoral head results understressed in

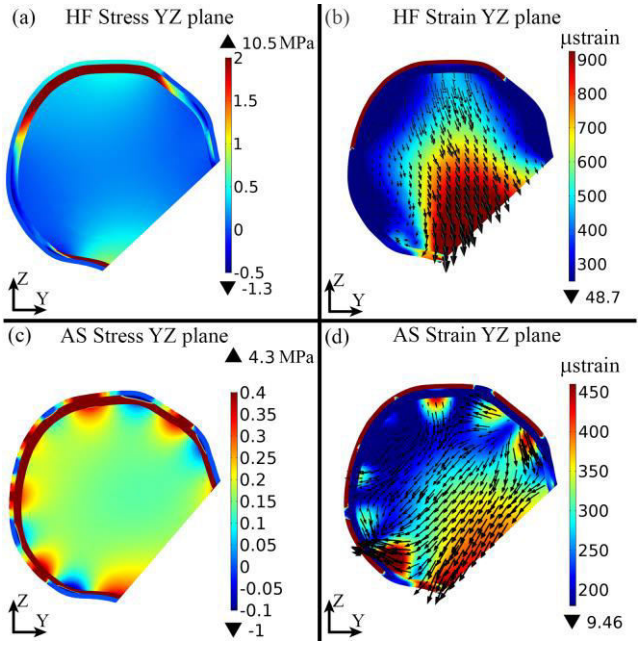

Fig. 3: Stress distribution in YZ plane (coronal plane) of the HF model (a) and AS femur head (b). In (c) and (d) the vector map and the modulus of strain in YZ plane (coronal plane) of the HF and AS models respectively, are represented for the three layers composing the femur head model (cartilage, cortical and trabecular bone).

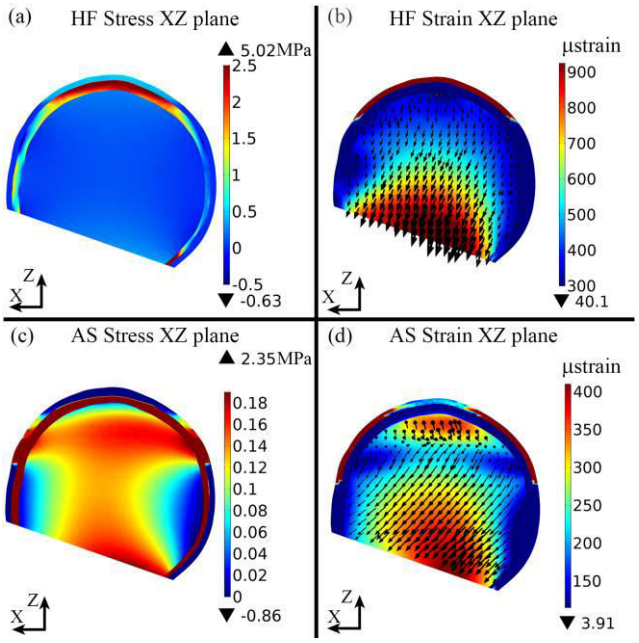

Fig. 4: Stress distribution in XZ plane (sagittal plane) of the HF model (a) and AS femur head (b). In (c) and (d) the vector map and the modulus of strain in XZ plane (sagittal plane) of the HF and AS models respectively, are represented for the three layers composing the femur head model (cartilage, cortical and trabecular bone).

both cases. The stress magnitude is in agreement with the literature data [11], [24] concerning the stance phase of gait.

In the YZ plane, the strain modulus of HF (Fig. 3b) is maximum in the cartilage layer, in correspondence of the MCA. In the cortical and trabecular tissue, the strain gradually increases its modulus from the superior region of the femur head to the femoral neck zone. Conversely, in the AS model (Fig. 3d), the strain is roughly constant in correspondence of the cartilage and in the cortical bone region. The subchondral bone is characterized by zones with elevated modulus alternated to regions of minimum strain. This pattern, also achieved in [3]-[4], allows the appearance of anomalies in bone formation, e.g. geodes. Moreover, in Fig. 3d, changes in the direction of the strain vectors can be noted in proximity of the subchondral bone, that suggest the presence of abnormal bone structure [25].

Thus, since we have determined the validity of the imposed loading conditions in the coronal plane, we assume reasonable the mechanical response of bone tissue obtained in the sagittal plane. Overall, the strain in the HF (Fig. 4b), has roughly the same pattern in both planes. In the XZ plane of the AS case (Fig. 4d), the strain distribution varies mostly in correspondence of the cartilage and in the trabecular region. The cartilage layer shows low values of strain in the inferior lateral zone since this region does not belong to the assumed MCA. In the subchondral bone region, a major fraction of tissue is subjected to a high strain with respect to the distribution in the coronal plane. The strain magnitude decreases in the peripheral zones of the section, leading to appropriate conditions for the development of geodes.

The previous investigations of Marinozzi et al. [3]-[4] and Turmezei et al. [26] support the assumption that osteophytes significantly influence the variations in the architecture of bone tissue. The current 3D FE model confirms, in both

coronal and sagittal planes, that the reduced MCA due to the presence of bone outgrowths could justify the formation of large areas of bone resorption (geodes) in correspondence of under stimulated regions and the development of highly mineralized tissue (eburnation) in overstimulated zones. Moreover, the study highlights that the region with alternated low and high values of strain coincides with the arrangement of geodes identified by Jeffery [5] in the coronal plane. In the sagittal plane, the zones with minor strain surrounded by high strain regions respect the localization criteria described by [25]. However, limited data are available in literature with regard to OA bone characteristics in the sagittal plane. Turmezei et al. [26] indicate minimum values of cortical bone thickness in correspondence of the peripheral regions of the human femur head, while in the same zone Jeffery [5] highlights the presence of geodes in advanced OA. According to our simulations, these regions are under stimulated, thus they present an appropriate mechanical behaviour for the creation of geodes. Therefore, although the sagittal plane is scarcely characterized from the point of view of bone abnormal growth in OA, we may introduce the hypothesis of the geodes presence also in the lateral peripheral regions of the human femur head sagittal slice. The agreement with clinical observations [5], [25] regarding the pattern and the location of bone sclerosis also validates the load distribution adopted in the OA model of the femur head.

As a final note, we analyse the hypothesis of linear, elastic, homogeneous and isotropic material we have adopted for the bone tissue. Although this approach is not physiologic, it is frequently used in biomechanical FEM [10] as a first attempt in investigating complex mechanically induced processes in bone [27].

IV. CONCLUSIONS

The 3D FE analysis leads to a model of the mechanical behaviour of the trabecular bone that fits the actual biomechanics measurements which predict regions of high contact pressures at the superior and superolateral femoral head [26]. The evolution to the 3D model confirms the results achieved in the 2D analysis [3]-[4] though the present model allows to more accurately assess the strain patterns within the hip joint. We suggest that the altered load distributions due to the osteophytes can influence the appearance of subchondral bone anomalies. The nature of this mechanism is however yet to be clarified and further research is required to confirm this assumption. For instance, a future enhancement of the model should consider nonlinear FE simulations. Nevertheless, in the context of the specified limitations, the FE approach presented in this work could have an impact on both OA research and could provide new insights into biomechanics of pathological joints.

REFERENCES

[1] Sharma A.R., Jagga S., Lee S. S., Nam J.S. 2013. “Interplay between cartilage and subchondral bone contributing to pathogenesis of osteoarthritis”. *Int. J. Mol. Sci.* 14, 19805-19830.

[2] Cox L.G.E., Van Rietbergen B., Van Donkelaar C.C., Ito K. 2011. “Bone structural changes in osteoarthritis as a result of mechanoregulated bone adaptation: a modelling approach”. *Osteoarthritis and cartilage*, 19: 676-682.

[3] Marinozzi F., Bini F., De Paolis A., De Luca R., Marinozzi A. 2015. “Effects of hip osteoarthritis on mechanical stimulation of trabecular bone: a finite element study”. *J. Med. Biol. Eng.*, 35 (4): 535-544.

[4] Marinozzi F., Bini F., De Paolis A., Zuppante F., Bedini R., Marinozzi A. 2015. “A finite element analysis of altered load distribution within femoral head in osteoarthritis”. *Computer Methods in Biomechanics and Biomedical Engineering: Imaging & Visualization*, 3:2, 84-90.

[5] Jeffery A. K. “Osteophytes and the osteoarthritic femoral head”. 1975. *The Journal of bone and joint surgery*, Vol 57-B n. 3.

[6] Turmezei T.D. and Poole K.E.S. 2011. “Computed tomography of subchondral bone and osteophytes in hip osteoarthritis: the shape of things to come?”. *Frontiers in endocrinology*, Vol. 2, article 97.

[7] Sanders A.P., Brannon R.M. 2011. “Assessment of the applicability of Hertzian contact theory to edge-loaded prosthetic hip bearings”. *J. Biomech*, 44(16):2802-2808.

[8] Richard F., Villars M., Thibaud S. 2013. “Viscoelastic modelling and quantitative experimental characterization of normal and osteoarthritic human articular cartilage using indentation”. *J. Mechanical behaviour of biomedical materials*. 24:41-52.

[9] Wang G., Huang W., Song Q., Liang J. 2017. “Three-dimensional finite analysis of acetabular contact pressure and contact area during normal walking”. *Asian Journal of Surgery*, 40:463-469.

[10] Van Rietbergen B, Huiskes R, Eckstein F, Ruegsegger P. 2003. “Trabecular bone tissue strains in the healthy and osteoporotic human femur”. *J Bone Miner Res*, 18(10):1781–1788.

[11] Pustoc’h, A., & Cheze, L. 2009. “Normal and osteoarthritic hip joint mechanical behaviour: A comparison study”. *Medical & Biological Engineering & Computing*, 47: 375–383.

[12] Marinozzi, F., De Paolis, A., De Luca, R., Bini, F., Bedini, R., & Marinozzi, A. 2012. “Stress and strain patterns in normal and osteoarthritic femur using finite element analysis” (pp. 247–250). *Proceedings of CompImage-computational modelling of objects represented in images III: Fundamentals, methods and applications*.

[13] Bini, F., Marinozzi, A., Marinozzi, F., & Patane`, F. 2002. “Microtensile measurements of single trabeculae stiffness in human femur”. *J. Biomech.* 35:1515–1519.

[14] Cowin S. “Bone mechanics handbook”. 2001, Boca Raton (FL): CRC Press.

[15] Miller Z, Fuchs MB, Arcan M. 2002. “Trabecular bone adaptation with an orthotropic material model”. *J Biomech.*, 35:247–256.

[16] Miyasaka D., Ito T., Imai N., Suda K., Minato I., Dohmae Y., Endo N. 2014. “Three-dimensional assessment of femoral head coverage in normal and dysplastic hips: a novel method”. *Acta Med. Okayama*, 68(5):277-284.

[17] Van der Kraan P.M., Van den Berg W.B. 2007. “Osteophytes: relevance and biology”. *Osteoarthritis and Cartilage*, 15, 237-244.

[18] Bergmann G., Deuretzbacher G., Heller M., Graichen F., Rohlmann A., Strauss J., Duda G.N. 2001. “Hip contact forces and gait patterns from routine activities”. *J Biomech* 34:859-871.

[19] Pompe B. 2003. “Gradient of contact stress in normal and dysplastic human hips”. *Med Eng Phys*. 25:379–385.

[20] Johnson, K. L. 1985. “Contact mechanics”. Cambridge: Cambridge University Press.

[21] Naghieh G.R., Jin Z.M., Rahnejat H. 1998. “Contact characteristics of viscoelastic bonded layers”. *Appl. Math. Modelling*, 22:569-581.

[22] Fang X., Zhang C., Chen X., Wang Y., Tan Y. 2015. “A new universal approximate model for conformal and non-conformal contact of spherical surfaces”. *Acta Mach*, 226:1657-1672.

[23] Hodge W.A., Fuan R.S., Carlson K.L., Burgess R.G., Harris W.H., Mann R.W. 1986. “Contact Pressure in the human hip joint measured in vivo”. *Proc. Natl. Acad. Sci. Usa*, 83:2879-2883.

[24] Genda E., Konishi N., Hasegawa Y., Miura T. 1995. “A computer simulation study of normal and abnormal hip joint contact pressure”. *Arch Orthop Trauma Surg*, 114:202-206.

[25] Landells J.W. 1953. “The bone cysts of osteoarthritis”. *The Journal of Bone and Joint Surgery*. 35B (4): 643-649.

[26] Turmezei T.D., Treece G.M., Gee A.H., Fotiadou A.F., Poole K.E.S. 2016. “Quantitative 3D analysis of bone in hip osteoarthritis using clinical computed tomography”. *Eur. Radiol.*, 26:2047–2054.

[27] Van Rietbergen B., Müller R., Ulrich D., Ruegsegger P., Huiskes R. 1999. “Tissue stresses and strain in trabeculae of a canine proximal femur can be quantified from computer reconstructions”. *J Biomech* 32:165-173

A three-dimensional biomechanical model for shoulder joint kinematics and kinetics during forearm crutch walking in post after total hip replacement patients

Marco Freddolini[1], Francesco Esposito[1,2], Leonardo Latella[1,3], Massimiliano Marcucci[1,2,3], Andrea Corvi[1,2]

[1]*Laboratorio congiunto di Analisi del Movimento, "Fondazione ONLUS: In cammino…", Fucecchio (FI), Italy.*
[2]*Dipartimento di ingegneria industriale, Università degli studi di Firenze, Firenze (FI) Italy.*
[3]*"Centro di Eccellenza Sostituzioni Articolari Toscana (C.E.S.A.T.)", Fucecchio (FI), Italy.*

***Abstract*— Crutch is prescribed to permit patients to walk safely after hip replacement. Purpose of the study was to develop a biomechanical model to evaluate influence of crutch setup on shoulder joint kinematics and kinetics. Thirty patients were randomly assigned to elbow flexed or elbow extended crutch setup and evaluated during walking. Elbow extended crutch setup reduces stress on shoulder joint. Results may help therapists in rationalizing crutch length adjustments for patients.**

***Keywords*— Shoulder joint; kinematics and kinetics model; crutch setup; total hip replacement; walking; rehabilitation.**

I. Introduction

WALKING is one of the most important activity in daily life and it plays a crucial role in the rehabilitation of THR patients [1]. For this reason, after THR surgery, a crutch is prescribed to permit the patient to walk independently immediately after surgery, increasing both tolerance to exercise, independence, and in turn accelerating recovery [2, 3].

During crutch-assisted gait, part of the body mass is borne by the upper limbs, which improves stability and reducing load on the pathologic limb [4]. On the other hand, crutch-assisted gait results in higher energy cost than normal gait [5, 6] and induces load on the upper limbs, which in some cases may be higher than body weight [4, 7, 8].

Crutch users showed prevalence of shoulder pain [9,10] and other upper limbs pathological conditions [4, 11, 12].

Although there have been a few studies exploring the effects of supported walking on the shoulder [8, 13, 14], none of them evaluated how forearm crutch setup may influence upper limb loading during gait.

Purpose of this study is to develop a biomechanical model for shoulder joint kinematics and kinetics during forearm crutch walking and to evaluate differences in these parameters due to different crutch length setups.

II. Methods

Thirty post THR surgery patients were recruited for this study and randomly assigned to two different crutch length setup groups: elbow flexed (EF) group, with length defined as the vertical distance between ground and greater trochanter, and the elbow extended (EE) group, with length defined as the vertical distance between ground and wrist crease with the arm along the side.

No significant differences were present between groups for age, BMI, VAS scales for hip and shoulder, Oxford hip and shoulder scores.

Optoelectronic motion tracking system together with two force platforms, were used to evaluate upper limbs kinematics and kinetics with reflective markers placed on the subjects before starting the trial, on the left and right acromia, xiphoid process, jugular notch, sacrum, C7 and T8 spinous processes, lateral and medial epicondyle, radial and ulnar styloid processes, on the crutch side (Figure 1).

After a familiarization protocol, subjects walked straight at their comfortable pace on the laboratory path. Each participant completed three recorded trials.

A custom-made model, as described previously by Esposito et al. [15], was used on the Smart-Analyzer software (BTS Bioengineering, Milan) to get shoulder joint kinematics, which was defined as humerus rotation relative to the thorax coordinate system (shoulder FE=flexion/extension, AA=abduction/adduction and IE=internal/external rotation angles), following Wu et al. [16] recommendations. Range of motion (ROM) was derived for all three angles.

A modified version of the model used by Esposito et al. [15] was used to obtain 3-D forces and moments acting on the shoulder joint using an inverse dynamic approach in thorax coordinate system [16].

As Esposito et al. (2017) evaluated moments and forces in a static task, we added moment of inertia and angular acceleration of the segments and linear acceleration of the centers of mass for the three planes of motion. Vertical (FshoY), medio-lateral (FshoZ) and anterior–posterior (FshoX) forces together with shoulder adduction/abduction (Maa), flexion/extension (Mfe) and internal/external rotation (Mie) planes moments were derived. Moment of inertia, masses and centre of mass positions for upper arm, forearm and hand were derived as described previously [17, 18], while angular acceleration of the segments and linear acceleration of the centers of mass were taken using markers position.

Shoulder joint forces were normalized by the body weight, while shoulder joint moments by body weight multiply by arm length [19]. Anterior (Fan), posterior (Fpo), lateral (Fla), superior (Fsu) and inferior (Fin) shoulder force peaks were

taken during crutch stance. In addition, peak-to-peak (P-P) values were taken for all shoulder joint moments. Independent T-test was used to evaluate differences between groups.

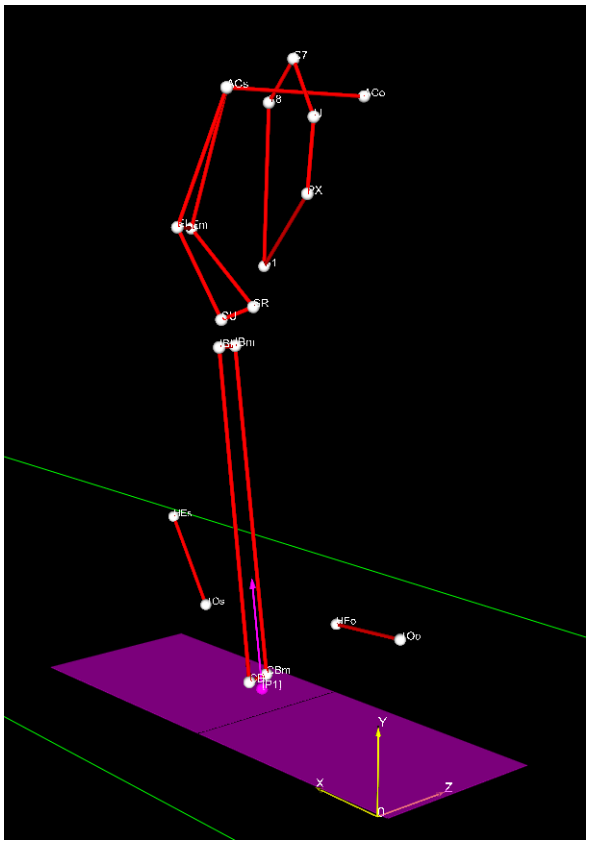

Fig. 1: Stick diagram example during crutch walking

III. Results

An example of 3-D shoulder joint kinematics and kinetics for one subject is shown in Figure 2. AA angle ROM, Fla and Fdo force peaks, Mfe, Maa and Mie P-P moments ($p<0.05$) increased significantly in the EF group when compared to EE group ($p.< 0.05$). No significant differences were found for the other ($p.> 0.05$) parameters.

IV. Conclusion

An upper extremity model was developed and implemented to evaluate possible differences in shoulder kinematics and kinetics during gait due to crutch length setup. EE setup showed reduced joint forces and moments when compared to the EF setup. Vertical, lateral force and moments in all planes of motion showed a significant increase, similar to what has been found previously during standing [15]. Several studies reported that repetitive load on the upper limbs during crutch walking, with an abnormal stress on this structure, may trigger shoulder, wrist and elbow joint disorders [4, 8,14], especially in elderly THR patients, which are at higher risk of developing upper limb conditions [20] and OA [22]. For this reason, an EE setup is suggested for post THR patients, as it reduced both shoulder external torque and weight supported by the crutch, and in turn can reduce upper limbs risks associated with higher loads due to crutch usage [14].

Results may help therapists help in rationalizing crutch length adjustments for patients after total hip replacement surgery.

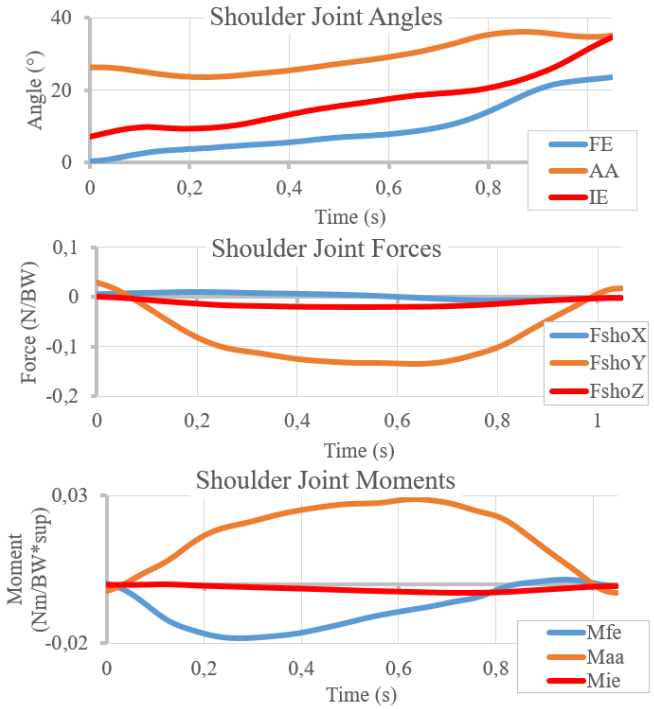

Fig. 2: -D Shoulder joint kinematics and kinetics profile examples for one subject in thorax coordinates system.

References

[1] H. Husted, Fast-track hip and knee arthroplasty: clinical and organizational aspects, Acta Orthop. Suppl. 83 (2012) 1-39.

[2] B.M. Joyce, R.L. Kirby, Canes, crutches and walkers, Am. Fam. Physician. 43 (1991) 535–542.

[3] J.W. Youdas, B.J. Kotajarvi, D.J. Padgett, K.R. Kaufman, Partial weight-bearing gait using conventional assistive devices, Arch. Phys. Med. Rehabil. 86 (2005) 394–398.

[4] K.A. Opila, A.C. Nicol, J.P. Paul, Upper Limb Loadings of Gait With Crutches, J. Biomech. Eng. 109 (1987) 285–290.

[5] S.V. Fisher, R.P. Patterson, Energy cost of ambulation with crutches, Arch. Phys. Med. Rehabil. 62 (1981) 250–256.

[6] H. Thys, P.A. Willems, P. Saels, Energy cost, mechanical work and muscular efficiency in swing-through gait with elbow crutches, J. Biomech. 29 (1996) 1473–1482.

[7] J. Fischer, C. Nüesch, B. Göpfert, A. Mündermann, V. Valderrabano, T. Hügle, Forearm pressure distribution during ambulation with elbow crutches: a cross-sectional study, J. Neuroengineering Rehabil. 11 (2014) 61.

[8] P. Westerhoff, F. Graichen, A. Bender, A. Halder, A. Beier, A. Rohlmann, G. Bergmann, In vivo measurement of shoulder joint loads during walking with crutches, Clin. Biomech. Bristol Avon. 27 (2012) 711–718.

[9] N.B. Jain, L.D. Higgins, J.N. Katz, E. Garshick, Association of shoulder pain with the use of mobility devices in persons with chronic spinal cord injury, PM R. 2 (2010) 896–900.

[10] I.H. Sie, R.L. Waters, R.H. Adkins, H. Gellman, Upper extremity pain in the postrehabilitation spinal cord injured patient, Arch. Phys. Med. Rehabil. 73 (1992) 44–48.

[11] F. Ginanneschi, G. Filippou, P. Milani, A. Biasella, A. Rossi, Ulnar nerve compression neuropathy at Guyon's canal caused by crutch walking: case report with ultrasonographic nerve imaging, Arch. Phys. Med. Rehabil. 90 (2009) 522–524.

[12] N. Venkatanarasimha, S. Kamath, G. Kambouroglou, S.J. Ostlere, Proximal ulna stress fracture and stress reaction of the proximal radius associated with the use of crutches: a case report and literature review,

J. Orthop. Traumatol. Off. J. Ital. Soc. Orthop. Traumatol. 10 (2009) 155–157.
[13] L.L. Haubert, D.D. Gutierrez, C.J. Newsam, J.K. Gronley, S.J. Mulroy, J. Perry, A comparison of shoulder joint forces during ambulation with crutches versus a walker in persons with incomplete spinal cord injury, Arch. Phys. Med. Rehabil. 87 (2006) 63–70.
[14] B.A. Slavens, P.F. Sturm, R. Bajournaite, G.F. Harris, Upper extremity dynamics during Lofstrand crutch-assisted gait in children with myelomeningocele, Gait Posture. 30 (2009) 511–517.
[15] F. Esposito, M. Freddolini, L. Latella, P. Braccio, M. Marcucci, A. Corvi, The influence of the crutch setup on stability and weight-bearing parameters in post total hip replacement surgery patients during quiet standing, Disabil. Rehabil. Assist. Technol. (2017) 1–6.
[16] G. Wu, F.C.T. van der Helm, H.E.J. (DirkJan) Veeger, M. Makhsous, P.V. Roy, C. Anglin, J. Nagels, A.R. Karduna, K. McQuade, X. Wang, F.W. Werner, B. Buchholz, ISB recommendation on definitions of joint coordinate systems of various joints for the reporting of human joint motion—Part II: shoulder, elbow, wrist and hand, J. Biomech. 38 (2005) 981–992.
[17] P. de Leva, Adjustments to Zatsiorsky-Seluyanov's segment inertia parameters, J. Biomech. 29 (1996) 1223–1230.
[18] E.M. Gutierrez, A. Bartonek, Y. Haglund-Akerlind, H. Saraste, Centre of mass motion during gait in persons with myelomeningocele, Gait Posture. 18 (2003) 37–46.
[19] A.L. Hof, Scaling gait data to body size, Gait Posture. 4 (1996) 222–223.
[20] Burner, T., Abbott, D., Huber, K., Stout, M., Fleming, R., Wessel, B., Massey, E., Rosenthal, A., Burns, E., 2014. Shoulder symptoms and function in geriatric patients. J. Geriatr. Phys. Ther. 2001 (37), 154–158.
[21] Cushnaghan, J., Dieppe, P., 1991. Study of 500 patients with limb joint osteoarthritis. I. Analysis by age, sex, and distribution of symptomatic joint sites. Ann. Rheum. Dis. 50, 8–13.

Does prosthesis design influence dynamic activities in patients following Total Knee Replacement?

Francesco Esposito[1,2], Marco Freddolini[1], Leonardo Latella[1,3], Massimiliano Marcucci[1,2,3], Andrea Corvi[1,2]

[1]*Laboratorio congiunto di Analisi del Movimento, "Fondazione ONLUS: In cammino…", Fucecchio (FI), Italy.*
[2]*Dipartimento di ingegneria industriale, Università degli studi di Firenze, Firenze (FI) Italy.*
[3]*"Centro di Eccellenza Sostituzioni Articolari Toscana (C.E.S.A.T.)", Fucecchio (FI), Italy.*

***Abstract*—Total Knee Replacement (TKR) is an effective treatment for patients with advanced osteoarthritis [1]. There are different types of prostheses available on market and in this work, we evaluated two different designs: Medial Pivot (MP) and Posterior Stabilised (PS). In vitro study demonstrated that MP design biomechanics is closer to physiological condition rather than PS design [2]. Purpose of this study is to evaluate in-vivo performance of these designs. We selected walking on flat surface and stairs climbing tasks to detect any differences in biomechanical parameters of the knee in terms of joint kinematics and dynamics [3].**

The results showed a reduction of knee flexion in MP group comparing to PS group during walking and stairs climbing. In addition, PS group showed a higher knee flexion moment during walking, respect to MP group, closer to physiological condition.

***Keywords*—Osteoarthritis, knee prosthesis design, biomechanics, gait analysis, stairs climbing, posterior stabilised, medial stabilised.**

I. INTRODUCTION

OSTEOARTHRITIS (OA) refers to clinical syndrome of joint pain that is often accompanied with functional limitation and decreased life quality. It is one of the most spread musculoskeletal condition worldwide affecting articular joint [4]. It causes a progressive degeneration of the joint cartilage with a remodelling of the adjacent bone and associated inflammation. There are different treatments available for knee osteoarthritis that include pharmacological and non-pharmacological options, but surgical treatment, in particular Total Knee Replacement, is extremely effective in improving function and reducing pain in patients. In the present work, two different kind of knee prostheses were evaluated: the posterior stabilised (PS) and medial pivot (MP). In PS design stability is guaranteed by a cam on polyethylene insert whereas in MP design the high congruence of medial compartment guarantees stability for all flexion degrees, closer to the physiological knee kinematic. Preliminary studies showed that MP prostheses reduced post-operative pain, minimize polyethylene wear, increased flexion-extension ROM and stability perception [2]. An in vivo study, which compared these two designs, demonstrated a reduction in passive flexion/extension range of motion for patients with PS design respect to MP design [5].

MP design has been implemented to improve knee joint kinematics replication, in particular the natural femoral rollback.

Knee medial compartments has been shown to function as a ball-in-socket joint, with the lateral femoral condyle translating in anteroposterior direction and rotating around the medial compartment in flexion.

MP design allows the lateral condyle to move freely in anteroposterior direction, through a deeper, highly conforming medial compartment and a less congruent lateral component.

In PS design a "paradoxical motion" is introduced, which represents a relative translation between femoral component and polyethylene insert and it has been related to an increasing of polyethylene wear.

The aim of surgical treatment is to restore functional abilities for activities of daily living in patients, whose mobility has been reduced by OA. One of the most common activity is walking on a flat surface [3]. In addition, stairs climbing is an activity with high load on the knee joint and it is used to evaluate post-surgery patient condition, absence of pain during this activity is considered a full recovery sign [6].

For our knowledge, there are no studies comparing these two designs during dynamic activities using motion analysis technique, but only fluoroscopic, radiological and questionnaires data [7-10] based studies have been found. Consequently, the purpose of the study is to detect any differences between PS and MP designs during walking and stairs climbing task.

II. MATERIALS & METHODS

A. Patients selection

Forty patients following TKR were recruited and separated in two groups according to the implanted prosthesis design: MP and PS.

We selected patients from Fucecchio C.E.S.A.T. (Centro Eccellenza Sostituzione Articolare Toscana) database with primary osteoarthritis at least one year after surgery, which were able to perform walking on a flat surface and stairs climbing. The exclusion criteria consist of BMI > 35 kg/m^2, neurologic or cardiovascular disorder, lower limb muscular disorder or pain, diabetes mellitus, osteoporosis and secondary osteoarthritis. Same surgeon and same surgery technique were used for all patients.

Furthermore, twenty Healthy Control (HC) subjects were collected.

B. Instrumentation

Optoelectronic motion tracking system (SMART DX-700, BTS Bioengineering, Milan, Italy), consisting of eight infrared cameras, was used to evaluate joint kinematics, acquiring at sampling rate of 250 Hz. Two force platforms (P6000D, BTS Bioengineering, Milan, Italy), placed on the

laboratory, were used to record GRF during walking with a sampling rate of 500 Hz.

C. Acquisition protocol

All acquisitions were performed at the C.E.S.A.T biomechanics laboratory. Before starting the acquisition, each patient was asked to sign an informed consent form. A visual analogue scale (VAS) was used to record the perceived severity of pain for both limbs [11] and an Italian version of the Oxford Knee Score (OKS) was used to evaluate functional ability of the operated knee joint [12] experienced by all patients.

Reflective markers were placed on subjects according to DAVIS protocol.

The protocol consists of two tasks and before each task we performed a training session to patients.

The first task was walking on flat surface. After standing data were collected, subjects were asked to walk straight at their comfortable pace on the instrumented laboratory walking path. A minimum of 5 walking trials were collected for each subject.

The second task was stairs climbing. Patients were asked to climb a four-step-staircase. A minimum of 6 ascent and 6 descent trials were collected for each subject.

D. Parameters selection

Three-dimensional kinematics and kinetics of knee joint were evaluated for both limbs.

Maximum knee flexion (FE) angle, maximum knee flexion moment normalised by body weight (FE Mo), walking speed, step width, stride length and time were taken for all subjects during walking. In addition, three-dimensional kinematics and kinetics were also evaluated for ankle and hip joint to understand possible compensation mechanisms.

Maximum knee flexion (FE) angle, stairs climbing speed, step width and stride time were taken for all subjects during stairs ascent and descent tasks. The results of stairs climbing were normalised on step cycle defined as two consecutive heel strikes of the same foot. For this reason, the first step started from first to third step whereas the second step started from second to fourth step.

Dominant limb was chosen for HC group evaluation whereas, for patient groups, parameters referred to operated limb.

E. Statistics and ethical approval

Independent t-test was used to evaluate differences between groups. A false discovery rate procedure was used to adjust the p-values for multiple comparisons.

The study has been approved by C.E.S.A.T. ethical committee in accordance with the guidelines stated in Declaration of Helsinki.

III. RESULTS

There were no significant differences for age, BMI, VAS and Oxford Knee Score between patient groups (TABLE I). No significant differences were found for tasks speed, step width and for both stride length and time between patient groups. No differences were found for healthy limb data, hip and ankle kinematics and kinetics on all three plans, knee data in frontal and transverse plane.

TABLE I
SUBJECTS CHARACTERISTICS

Parameter	*MP (n = 20)*	*PS (n = 20)*	*HC (n = 20)*
Age [yo]	74.9 ± 4.0	70.1 ± 4.9	32.0 ± 5.9
BMI [kg/m2]	32.8 ± 4.7	31.9 ± 4.5	23.3 ± 2.7
Involved VAS	1.4 ± 1.9	0.9 ± 1.4	n.d.
Healthy VAS	1.7 ± 2.2	1.3 ± 1.9	n.d.
OKS	43.6 ± 3.4	45.6 ± 2.5	n.d.

FE and FE Mo during walking were significantly reduced in MP group respect to PS and HC groups. No significant differences were found about these parameters between PS and HC groups (Fig. 1).

FE for both stair ascent and descent tasks were significantly reduced in MP group respect to PS and HC groups. No significant differences were found between PS and HC groups (Fig. 2).

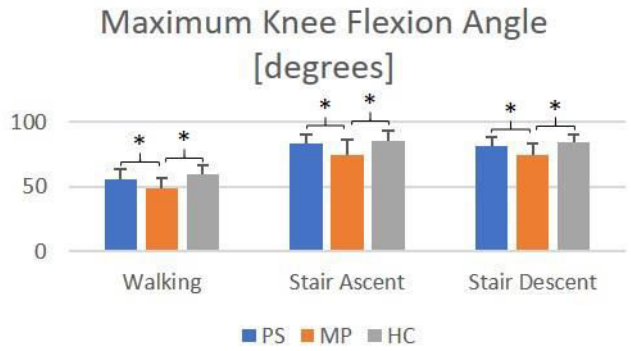

Fig. 1: Maximum knee flexion during dynamic activities (* Indicates significant differences between groups)

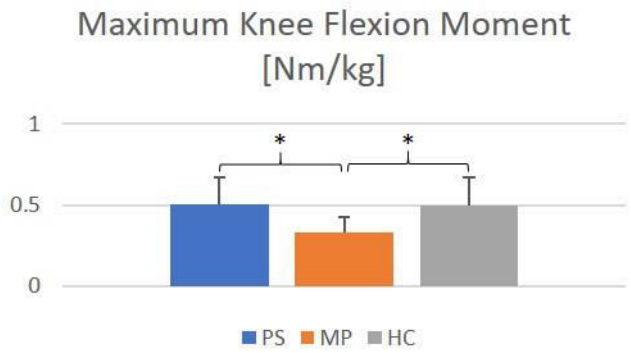

Fig. 2: Maximum knee flexion moment during walking (* Indicates significant differences between groups)

IV. CONCLUSION

Results showed how prostheses design influenced kinematics and kinetics of the knee joint. PS group had higher knee flexion angle and flexion moment during walking compared to MP group, but closer to healthy control.

The kinematics results were confirmed during stairs climbing for both ascent and descent tasks.

The reduction of knee flexion angle during both walking and stair tasks and flexion moment during walking may suggest a voluntary stiffening of the joint due to an instability «feeling» in MP group, but further investigations are needed, including electromyography analysis, to confirm this hypothesis.

ACKNOWLEDGEMENT

None.

REFERENCES

[1] J. Hutt, M. Dodd, H. Bourke, J. Bell, Outcomes of total knee replacement after patellofemoral arthroplasty, J. Knee Surg. 26 (2013) 219–223.

[2] A. Steinbrück, C. Schröder, M. Woiczinski, A. Fottner, V. Pinskerova, P.E. Müller, V. Jansson, Femorotibial kinematics and load patterns after total knee arthroplasty: An in vitro comparison of posterior-stabilized versus medial-stabilized design, Clin. Biomech. Bristol Avon. 33 (2016) 42–48.

[3] I. Komnik, S. Weiss, C.H. Fantini Pagani, W. Potthast, Motion analysis of patients after knee arthroplasty during activities of daily living--a systematic review, Gait Posture. 41 (2015) 370–377.

[4] M. Cross, E. Smith, D. Hoy, S. Nolte, I. Ackerman, M. Fransen, L. Bridgett, S. Williams, F. Guillemin, C.L. Hill, L.L. Laslett, G. Jones, F. Cicuttini, R. Osborne, T. Vos, R. Buchbinder, A. Woolf, L. March, The global burden of hip and knee osteoarthritis: estimates from the global burden of disease 2010 study, Ann. Rheum. Dis. 73 (2014) 1323–1330.

[5] F. Hossain, S. Patel, S.-J. Rhee, F.S. Haddad, Knee arthroplasty with a medially conforming ball-and-socket tibiofemoral articulation provides better function, Clin. Orthop. 469 (2011) 55–63.

[6] S. Fantozzi, M.G. Benedetti, A. Leardini, S.A. Banks, A. Cappello, D. Assirelli, F. Catani, Fluoroscopic and gait analysis of the functional performance in stair ascent of two total knee replacement designs, Gait Posture. 17 (2003) 225–234.

[7] David A. Samy, Jesse I. Wolfstadt, Iman Vaidee, David J. Backstein, A Retrospective Comparison of a Medial Pivot and Posterior-Stabilized Total Knee Arthroplasty With Respect to Patient-Reported and Radiographic Outcomes, The Journal of Arthroplasty, article in press

[8] M. Dehl∗, Y. Bulaïd, M. Chelli, R. Belhaouane , A. Gabrion , E. Havet , P. Mertl, Total knee arthroplasty with the Medial-Pivot knee system: Clinical and radiological outcomes at 9.5 years' mean follow-up Orthopaedics & Traumatology: Surgery & Research 104 (2018) 185–191

[9] Luigi Sabatini, Salvatore Risitano, Gennaro Parisi, Ferdinando Tosto, Pier Francesco Indelli, Francesco Atzori and Alessandro Massè, Medial Pivot in Total Knee Arthroplasty: Literature, Review and Our First Experience, Clinical Medicine Insights: Arthritis and Musculoskeletal Disorders Volume 11: 1–4

[10] Schmidt R, Komistek RD, Blaha JD, Penenberg BL, Maloney WJ. Fluoroscopic analyses of cruciate-retaining and medial pivot knee implants. Clin Orthop Relat Res 2003:139e47.

[11] N. Bellamy, Osteoarthritis clinical trials: candidate variables and clinimetric properties, J. Rheumatol. 24 (1997) 768–778.

[12] R. Padua, G. Zanoli, E. Ceccarelli, E. Romanini, R. bondì, A. Campi, The Italian version of the Oxford 12-item Knee Questionnaire - cross-cultural adaptation and validation, Int. Orthop. 27 (2003) 214–6.

Biomechanical analysis of the interaction phenomena between the cuff of an artificial urinary sphincter and urethral duct

A.N. Natali[1,2], C.G. Fontanella[2,3], S. Todros[1,2] , S. Carmignato[2,4], F. Zanini[4], P.G. Pavan[1,2], E.L. Carniel[1,2]

[1] *Department of Industrial Engineering, University of Padova, Padova, Italy*
[2] *Centre for Mechanics of Biological Materials, University of Padova, Padova, Italy*
[3] *Department of Biomedical Sciences, University of Padova, Italy*

***Abstract*— The present work pertains to the mechanics of urethral duct, in consideration of the adoption of artificial urinary sphincteric (AUS) devices to overcome incontinence problems. The interaction phenomena occurring between artificial sphincteric cuff and urethral duct represent a fundamental problem in the investigation of reliability and durability of devices. Experimental activity is performed on urethral tissues and also structural test are carried out on the overall urethral duct, to provide parameters definition within the constitutive formulation developed. The mechanical behaviour of the cuff of AUS is investigated using mechanical and physicochemical procedures, leading to the formulation of a model to be adopted for definition of the structural response by means of numerical approach. The cuff conformation is relieved by tomographic technique and experimental and numerical data of inflation process are compared. The results obtained are adopted for the definition of the model of the cuff. Numerical analyses were developed to evaluate the interaction between the cuff itself and the urethral duct, with reference to the lumen occlusion process for maintaining urinary continence.**

***Keywords*—urethra biomechanics, artificial urinary sphincter mechanics, experimental testing, computational biomechanics.**

I. Introduction

URINARY incontinence represents a pathology with a relevant social and economic impact [1]. Different prostheses are currently adopted for surgical treatment of incontinence. A specific artificial urinary sphincter is considered as the most effective solution at present [2],[3]. The cuff exerts a pressure field on the urethra, leading to the occlusion of the duct. However, several complications, as tissue atrophy and erosion, were observed after medium-long term implantation, leading to surgical recurrence. The interaction between artificial sphincter and urethra should be evaluated trough computational analysis.

A biomechanical analysis of urethral tissues and structure was developed, using an integrated experimental and computational approach [4]-[7]. A validation framework of urethra mechanics is defined, based on experimental investigation data, leading to virtual solid and finite element models of urethral duct. A specific hyperelastic formulation is developed to characterize the non-linear mechanical behaviour of urethral tissues. The inverse analysis of tests on a urethra samples enables to define preliminary constitutive parameters. The parameters are validated also with reference to data from inflation tests.

The cuff that provides the mechanical action addressed to duct lumen occlusion represents a fundamental component of the overall device and it is studied to evaluate the functional response. An accurate characterization of the cuff material is performed, by means of mechanical and physicochemical tests, addressed to the definition of a constitutive model of the basic material. The geometric configuration of the cuff is relieved with high accuracy by computed tomography (CT). Moreover, the measure of the deformed shape of the cuff submitted to pressure fields is performed and results are compared with the data from numerical model, aiming at a reciprocal validation between experimental and computational data. The computational model of a urethra is exploited to evaluate the mechanical response when the AUS cuff is applied, aiming at the interpretation of the surgical practice at urethral lumen occlusion.

II. Materials and Methods

A. Urethra biomechanics

A computational framework of urethra mechanics is based on experimental investigation of the mechanical properties of urethral tissues and structure.

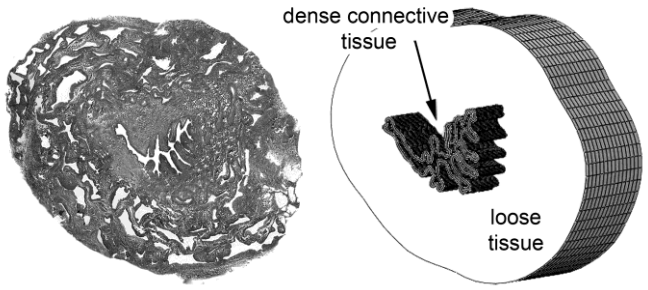

Fig. 1. Histological investigation of urethral section (a) and 3D finite element model of urethra (b).

Horse urethra samples were cut in transversal direction after a histological fixation process [8]. Masson trichrome staining was used to identify tissue morphological properties, collagen and muscular fibres amount and preferred orientation. Histological analysis showed strong similarity between horse distal urethra and human anterior urethra (Fig. 1a) and, consequently, horse urethra samples were adopted for mechanical investigation [4]-[7]. Mechanical tests on urethral tissues were performed on specimens from both distal and proximal urethra, along longitudinal and circumferential directions (Bose Corporation, ElectroForce Systems Group, Eden Prairie, MN,

USA). Inflation tests were carried out on tubular segments of the urethral duct pertaining to distal and proximal regions [9]. A specific hyperelastic formulation was developed to characterize the non-linear mechanical behaviour of urethral tissues. The inverse analysis of tests on a urethra samples enabled to define preliminary constitutive parameters, while were defined in final form also with reference to data form inflation tests. Histological images were processed to make virtual solid and finite element models of urethral duct. The geometrical sections of the urethra were imported into the finite element preprocessing software Abaqus/CAE 6.14 (Abaqus Documentation 2014, Dassault Systèmes Simulia Corp., Providence, RI) [10] and the dimensions were enlarged in scale to correct shrinkage phenomena that occurred during histological analysis [11]. Subsequently, the 3D virtual solid was provided up to a length of 20 mm. Eight nodes hexahedral elements with reduced integration were adopted to mesh the dense connective tissue layer and the loose tissue stratum. The model was composed of about nine hundred thousand nodes and elements. Inflation numerical analysis was developed to validate the numerical model of the urethra (Fig. 1b).

B. Occlusive cuff of artificial urinary sphincteric device: Computational modelling

An accurate characterization of the cuff material was performed, by means of mechanical and physicochemical tests, addressed to the definition of a constitutive model of the basic material.

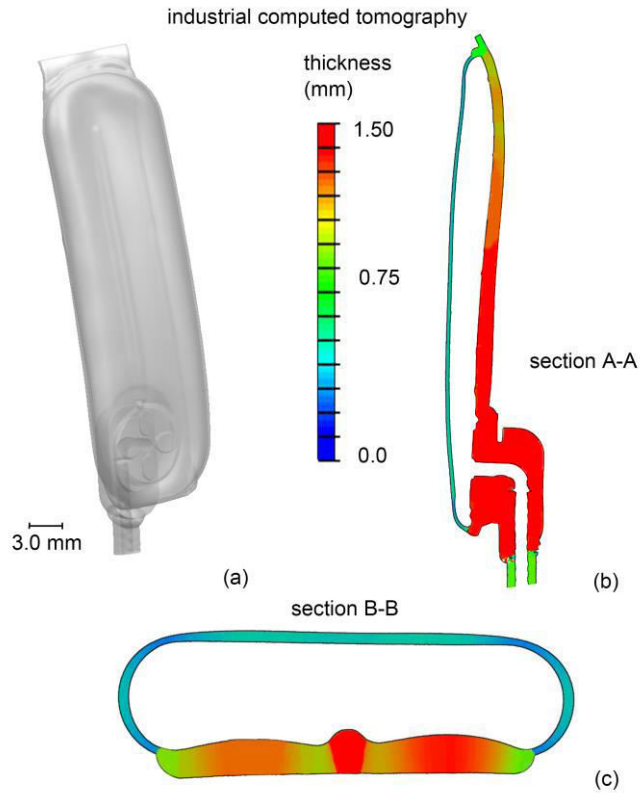

Fig. 2. Computer tomographic data (a) and different views of the geometrical model of the cuff with longitudinal section A-A (b) and transversal B-B (c) and contour of the material wall-thickness at the corresponding sections.

The same material was coupled with a reinforcing network of fibers in the region of the supporting band. Experimental tests on cuff materials and overall structure, as tensile test on samples and overall cuff inflation test, were carried out to evaluate the actual mechanical behavior, in relation with a suitable numerical model of the cuff [4].

The geometric configuration of the cuff was relieved with high accuracy by computed tomography (CT). This technique was increasingly used in geometrical metrology by non-destructive procedures to perform dimensional measurements with high accuracy and was capable for detailed three-dimensional geometrical models reconstruction [12],[13]. CT scan provided an accurate three-dimensional geometrical model of the cuff in the unloaded configuration (Fig. 2), as well as specific dimensional measurements [14]. The software VGStudio MAX was used for the evaluation of wall-thickness and internal distance between surfaces (Fig. 2). The intent was also to compare the results obtained by tomographic scanning of the cuff under pressure and the correspondent data from numerical model for a validation procedure. Consequently, several scans of the cuff has been made at different internal pressure level.

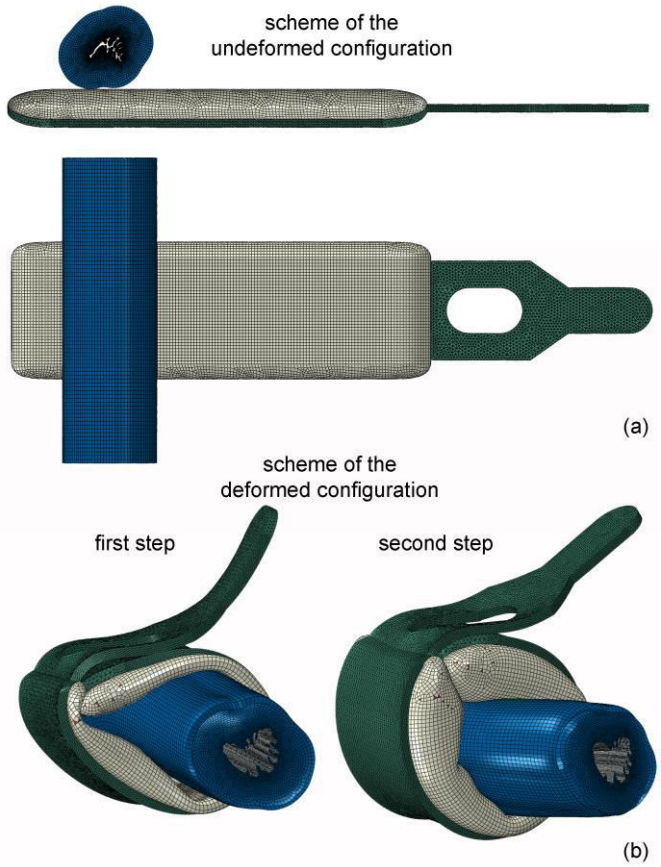

Fig. 3. Finite element models of the cuff together with the finite element model of the urethra, in the undeformed and deformed configurations.

Data relived from undeformed conformation were assumed for the definition of a solid model of the cuff as basis for the subsequent finite element model with a refined discretization into the pre-processing software Abaqus/CAE 6.14 (Abaqus Documentation 2014, Dassault Systèmes Simulia Corp., Providence, RI) [9]. For the polymeric blister, an isotropic hyperelastic formulation was assumed, considering the results from the tensile tests [14].

The mechanical response of the fiber-reinforced layer was evaluated by a hyperelastic formulation that considers contributions from the isotropic matrix and the fibers network [5]-[7]. Numerical analysis has been developed to interpret the inflation tests in order to validate the model developed by comparison with experimental data.

C. *Numerical analysis*

A specific numerical analysis has been developed to interpret the occlusion of the cuff around the urethra. Preliminary, the numerical model of the cuff was virtually closed around the urethra. In the second step, the cuff was inflated up to 50.0 cmH_2O, acoording to clinical practice (Fig. 3).

III. RESULTS

The analysis of data from experimental investigations on horse urethra, at both tissue and structure level, is the basis for the constitutive parameters identification and assessment. Model results and statistical distribution of experimental data are compared in Fig. 4, taking into account tests on tissue samples and inflation tests on tubular specimens, respectively.

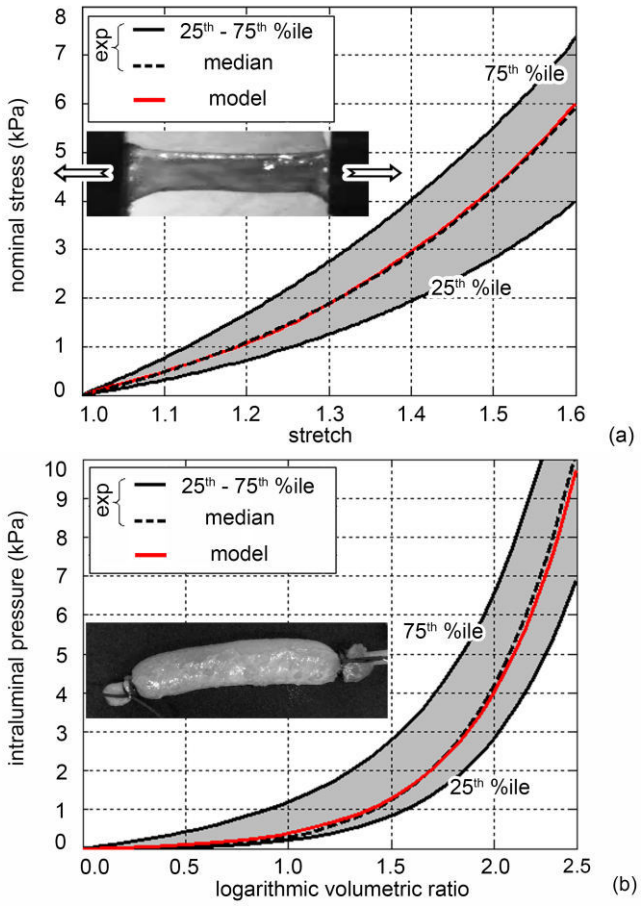

Fig. 4. Urethral tissue analysis. Results from tensile tests (a) and inflation tests (b).

The distribution of pressure and volume data of inflation test of the cuff was compared to the results from the numerical analysis (Fig. 5), showing a valid agreement. The maximum pressure condition was 50.0 cmH_2O, according to the assuemd range.

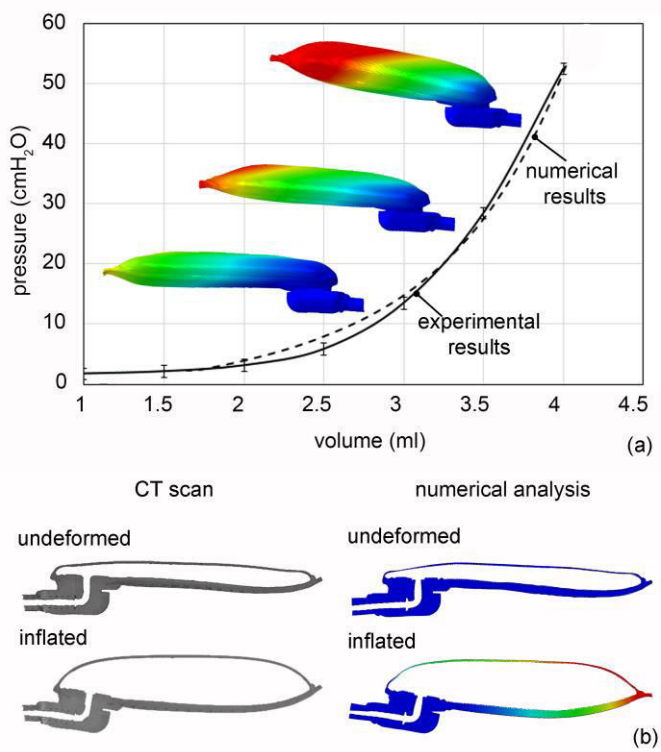

Fig. 5. Comparison of experimental data (mean±SD) and numerical results for inflation tests (a). Comparison of CT data and numerical results during the inflation tests (b).

The validation of the numerical model was obtained also comparing the numerical results with the data obtained by the CT scan at different pressures (Fig. 5).

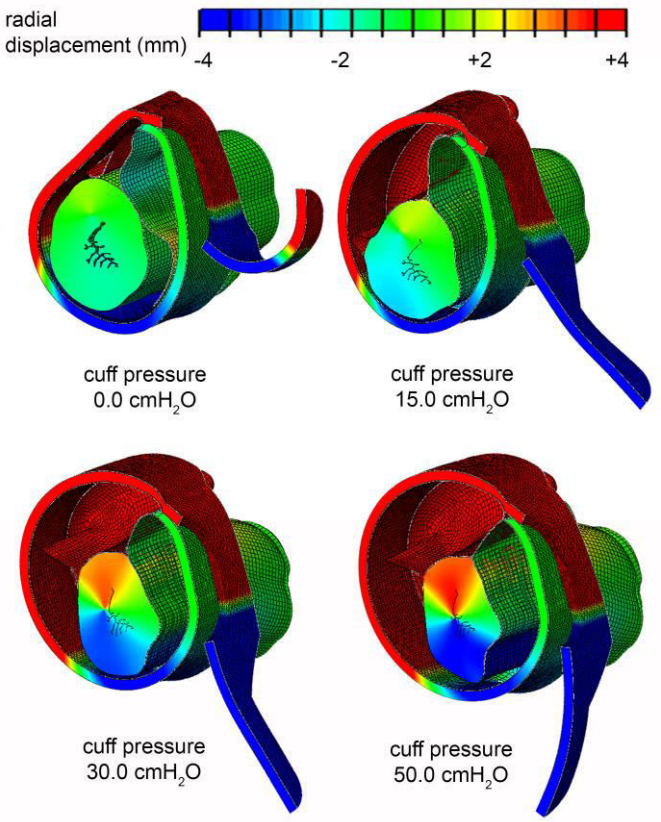

Fig. 6. Numerical analysis of lumen occlusion with AUS cuff. Displacement fields at null intraluminal pressure.

The conformation of the cuff in the numerical model was compared by the CT scan data. The maximum discrepancies between the CT data and model results were reported in terms of percentage error of the order of 2,5%. The agreement of data from tests and numerical model developed proved the reliable interpretation of the mechanical response of the cuff.

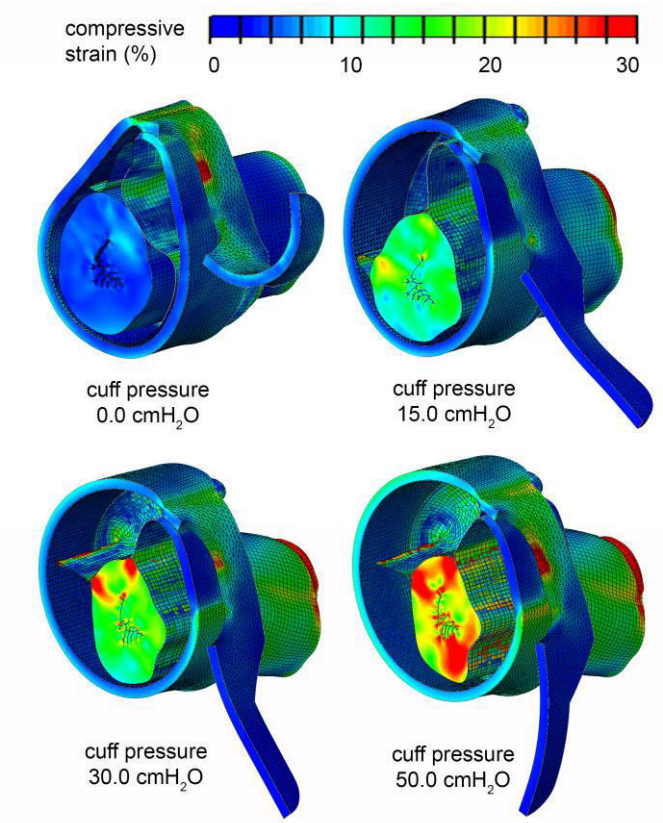

Fig. 7. Numerical analysis of lumen occlusion with AUS cuff. Compressive strain field at null intraluminal pressure.

Finally, urethral duct was investigated when external occluding action is applied by the AUS cuff. The displacement and the compressive strain (as the minimum principal strain) fields were reported for different values of the cuff pressure, while intraluminal pressure was kept at 0.0 kPa (Fig. 6 and 7).

IV. Conclusion

The present work represents a step toward the investigation of interaction phenomena occurring between the cuff of an artificial sphincteric device and the urethral duct. The development of reliable computational models of the urethral duct requires a relevant experimental effort for the characterization of the constituent tissues and structure, through histologic analysis and mechanical testing. Experimental data allow the definition of an appropriate tissues constitutive formulation and the identification of constitutive parameters. The evaluation of comparative animal and human urethra mechanical properties is not extensively discussed in the literature and was deeply investigated on the basis of histo-morphometric data. The specific characterization of human urethra is in progress by additional experimental activities on human samples.

The accurate analysis of the constitutive materials and of the geometrical characteristics is justified in the light of the complex behavior that the cuff is showing at the different inflation levels. In a subsequent investigation, already in progress, the interaction occurring with the cuff is evaluated considering the shape that the cuff is assuming during inflation in dependence on the duct biomechanical properties. In fact, experimental tests demonstrate that the cuff can assume different shapes at similar inflation pressure in dependence of the interaction occurring with the duct. This aspect stresses the relevance of an accurate knowledge of the cuff material and structural characteristics, while duct properties represent a variable datum mostly in dependence on age of the subject and of potential pathologies. A additional investigation is in progress to evaluate the interaction by using artificial ducts designed in accordance with duct variable stifffness [16] just for a mimicking of different patients conditions.

References

[1] A.D. Marklan, P.S. Goode, D.T. Redden, L.G. Borrud, K.L. Burgio, "Prevalence of urinary incontinence in men: results from the national health and nutrition examination survey," *J Urol.,* vol 184(3), pp.1022–1027, 2010.

[2] B.H. Cordo, N. Singla, A.K. Singla, "Artificial urinary sphincters for male stress urinary incontinence: current perspectives," *Med Devices (Auckl)*, vol. 9, pp.175–183, 2016.

[3] E. Chung. "A state-of-the-art review on the evolution of urinary sphincter devices for the treatment of post-prostatectomy urinary incontinence: past, present and future innovations," *J. Med. Eng. Technol.,* vol. 38(6). pp. 328-332, 2014.

[4] A.N. Natali, E.L. Carniel, A. Frigo, P.G. Pavan, S. Todros, P. Pachera, C.G. Fontanella, A. Rubini, L. Cavicchioli, Y. Avital, G.M. De Benedictis, "Experimental investigation of the biomechanics of urethral tissues and structures," *Exp. Physiol.* vol. 101, pp. 641–656, 2016.

[5] A.N. Natali, E.L. Carniel, C.G. Fontanella, S. Todros, G.M. De Benedictis, M. Cerruto, W. Artibani, "Urethral lumen occlusion by artificial sphincteric devices: a computational biomechanics approach," *Biomech. Model. Mechanobiol.,* vol. 16(4), pp. 1439-1446, 2017.

[6] A.N. Natali, E.L. Carniel, A. Frigo, C.G. Fontanella, A. Rubini, Y. Avital, G.M. De Benedictis, "Experimental investigation of the structural behavior of equine urethra," *Comput. Methods Programs Biomed.*, vol. 141, pp. 35-41, 2017.

[7] A.N. Natali, E.L. Carniel, C.G: Fontanella, A. Frigo, S. Todros, A. Rubini, G.M. De Benedictis, "Mechanics of the urethral duct: tissue constitutive formulation and structural modeling for the investigation of lumen occlusion," *Biomech. Model. Mechanobiol.* vol. 16(2), pp. 439-447, 2017.

[8] H. D. Dellmann, J. A. Eurell. "Textbook of Veterinary Histology, 5th edn," Lippincott Williams &Wilkins, Baltimore,MD, USA, 1998.

[9] E.L. Carniel, A. Frigo, C.G. Fontanella, G.M. De Benedictis, A. Rubini, L. Barp, G. Pluchino, B. Sabbadini, L. Polese, "A biomechanical approach to the analysis of methods and procedures of bariatric surgery," *J. Biomech.,.* vol. 56, pp.32-41, 2017.

[10] Abaqus Documentation, Version 6.14-2, Dassault Systémes Simulia Corp., Providence, RI, 2014.

[11] P.B. Dobrin, "Effect of histologic preparation on the cross-sectional area of arterial rings." *J Surgical Research,* vol. 61, pp. 413–415, 1996.

[12] L. De Chiffre, S. Carmignato, J.P. Kruth, R. Schmitt, A. Weckenmann, "Industrial applications of computed tomography," *CIRP Ann.-Manuf. Techn.* vol. 63, pp. 655–677, 2014.

[13] J.P. Kruth, M. Bartscher, S. Carmignato, R. Schmitt, L. De Chiffre, A. Weckenmann, "Computed tomography for dimensional metrology," *CIRP Ann.-Manuf. Techn.*, vol. 60, pp. 821–842, 2014.

[14] S. Carmignato, V. Aloisi, F. Medeossi, F. Zanini, E. Savio, "Influence of surface roughness on computed tomography dimensional measurements," *CIRP Ann.-Manuf. Techn.,* vol. 66, pp. 499–502, 2017.

[15] A.N. Natali, C.G. Fontanella, E.L. Carniel, "A numerical model for investigating the mechanics of calcaneal fat pad region," *J Mech. Behav. Biomed. Mat*., vol. 5(1), pp. 216-223, 2012.

[16] A.N. Natali, C.G. Fontanella, S. Todros, E.L. Carniel, "Urethral lumen occlusion by artificial sphincteric device: evaluation of degraded tissues effects," *J Biomech.* In Press, 2017.

CT-based non-linear finite element models of healthy and metastatic femurs

Cristina Falcinelli[1], Alessio Gizzi[1], and Giuseppe Vairo[2]
[1] *Campus Bio-Medico University of Rome*
[2] *University of Rome "Tor Vergata"*

***Abstract*—The inclusion of non-linear constitutive modelling in computed tomography-based patient-specific finite element models of healthy and metastatic femurs highlighted significant differences in the strain and stress patterns compared to linearly-elastic constitutive models. As such, a non-linear constitutive modelling may improve the femur failure understanding and characterization, opening towards the proper development of an accurate fracture risk indicator for pathological bones to be used in clinics.**

***Keywords*—Femur computational modeling, bone non-linear constitutive response, finite element formulation, metastasis modeling.**

I. Introduction

PATHOLOGICAL bones as metastatic femurs are characterized by a significant loss of mechanical integrity due to the presence of diseased tissue and thus are characterized by an increased fracture risk. In these situations, the assessment of fracture risk is crucial to decide the most appropriate therapeutic treatment and eventually preventive strategies [1]. Currently, in the clinic the fracture risk is assessed through systems based on clinical and radiological data (e.g., the Mirels scoring system) showing in most cases a low predictive power [1]. As a result, the fracture risk assessment is still a challenging task for clinicians.

It is well known that a fracture is a mechanical event that occurs when the loads acting on bone exceed a certain strength limit [2]. Thus, bone mechanical features and loads acting on bone are essential mechanical aspects that should be considered in order to have a comprehensive understanding of bone failure mechanics and thus for developing an accurate fracture risk indicator [1]. In the last decade, computational modeling approaches have been widely used to successfully study the failure mechanisms and femur fracture [3]-[7]. In detail, computed tomography (CT)-based patient-specific finite element (FE) models have been successfully developed and used to predict femur fracture load against experimental measurements and to assess the femur strength in clinical studies. Most of the FE modeling techniques treated femoral bone as an isotropic linearly elastic material, neglecting any damage and irreversible effect (e.g., yielding-like response) [8]. Nevertheless, during daily activities, the femur is mostly subjected to cyclical loadings, leading to damage accumulation. Moreover, bone stress-strain response exhibits a highly non-linear behavior characterized by a softening state beyond a certain yield level. Thus, more sophisticated modeling is required to capture the realistic bone response under functional loads. As a matter of fact, an accurate description of the bone constitutive behavior is essential for healthy and mostly for pathological bones that have an already compromised structural integrity. As such, the present work i) includes a non-linear constitutive formulation of femur based on a CT-based FE modeling strategy; ii) accounts for an accurate characterization of the bone compressive behavior in realistic scenarios; iii) compares and contrasts strain and stress patterns arising in femur structures in healthy and diseased conditions.

II. Material and methods

A. Healthy femur

The FE modeling procedure is reported in Figure 1. Femur solid model was reconstructed from patient-specific CT images through manual segmentation. The computational domain was discretized via second-order displacements-based tetrahedral elements, resulting in an unstructured mesh. Mesh size and refinement levels have been detected through a convergence analysis. Disribution of heterogeneous material properties was derived from the CT scan and mapped into the computational model. In detail, the local element-wise values of density were obtained by linearly interpolating the Hounsfield Unit (HU) values of CT voxels. Thus, the patterns of the Young's modulus (E) associated to the linear psrt of the stress-strain relationship and of the ultimate strength (S) were derived by using well-established correlations depending on the local density values, in agreement with [9]-[11]. Thereby, the bone constitutive response was described via an ideal-elastoplastic behavior until the local strain exceeds a certain threshold value (defined in terms of the strain level ε_{AB} relative to the elastic limit Figure 2). Then, the subsequent bone response was assumed to be characterized by a softening branch associsted to the plastic modulus E_p and lower-bounded in stress by the value σ_{min} (Figure 2). All the postfailure properties ($\varepsilon_{AB,}$ $E_{p,}$ σ_{min}) were described as functions of the CT-nased density pattern [11]. Finally, as it is customary in other well-established computational approaches [3]-[5] [7], an homogeneous distribution of the Poisson's ratio was assumed and equal to 0.3 [12].

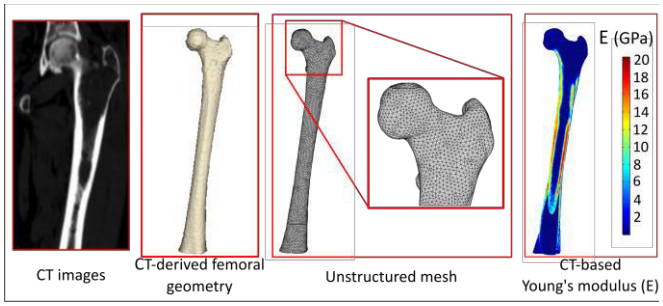

Fig. 1: CT-based FE modeling procedure. Starting from the CT scan the femoral solid model is reconstructed. Then, the domain is discretized through a tetrahedral-based unstructured mesh. Finally, the material properties were mapped onto the mesh.

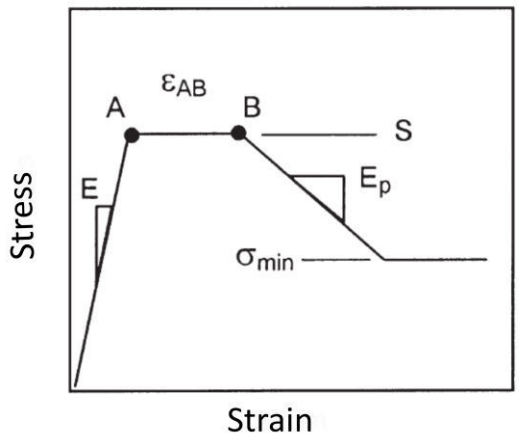

Fig. 2: Non-linear bone constitutive response. E: Young's modulus, S: material strength, ε_{AB}: ideal plastic strain level, E_p: plastic modulus, σ_{min}: plastic stress. Local elastic and plastic properties are derived from CT-based HU distributions in agreement with [11].

B. *Metastatic femur*

Most of the available studies addressing metastatic femurs have modeled metastases as voids [13]-[14]. However, such an approach does not account for the interaction between bone and metastasis, as well as for alterations in bone material properties due to the disease evolution. In this study, the metastatic bone was modeled by following the strategy described in the previous section. As a novel contribution, the computational procedure included a refined description of metastasis. In detail, the metastatic lesions were identified by using CT and magnetic resonance images (MRI) obtaining the location and contours of each metastasis region. Then, each metastasis was modeled through 3D Gaussian-like shape functions, valued in [0,1]. For the m-th metastatic region the following corresponding analytical description was employed:

$$f_m(x,y,z) = e^{(-A_{xm}(x-x_{0m})^2 - A_{ym}(y-y_{0m})^2 - A_{zm}(z-z_{0m})^2)} \quad (1)$$

where A_{xm}, A_{ym} and A_{zm}, are geometric parameters derived from a least-square fitting procedure and x_{0m}, y_{0m} and z_{0m} are the center coordinates. These functions were used to define different material properties of the metastatic lesion, allowing to enforce different continuity degrees in the transition region between healthy and diseased (namely, metastatic) tissues.

The behavior of the metastatic bone was described by coupling the non-linear constitutive formulation with a two-phase non-homogeneous porous description to account for the fluid occurence within the pores of the solid matrix. In a two-phase formulation, the local stresses are distributed between the solid and fluid phases. The second-order solid phase stress tensor can be expressed as:

$$\boldsymbol{\sigma}' = C : \boldsymbol{\varepsilon} \quad (2)$$

with C the fourth-order material tensor of the solid phase and $\boldsymbol{\varepsilon}$ the second-order solid phase strain tensor. Thus, the total stress can be recast as:

$$\boldsymbol{\sigma} = \boldsymbol{\sigma}' - pI \quad (3)$$

where I is the second-order identity tensor and p is the pore pressure. The influence of the fluid phase in pores of the solid matrix was considered with different spatial distribution of the pore pressure p. The pressure was assumed to be at the most piece-wise constant within the domain, by considering three different regions: cortical healthy region, trabecular healthy region and metastatic region. In addition, beside to assume the same constant value of p in both healthy bone and metastatic lesion, an increase of pore pressure induced by the metastasis in the bone environment around the lesion was considered, fully in agreement with the evidence provided in [15]. The two-phase porous behavior of bone has been successfully employed in [16], as well as a two-phase models have been adopted for treating metastasis regions in [17]-[18].

C. *FE calculations*

Stress and strain patterns arising in the femur under a compressive functional loading (vertically oriented and equal to 1000N) were analyzed and compared with those obtained by using a linearly-elastic constitutive model. The FE modeling and the FE analyses were performed through home-made codes implemented in Matlab (MATLAB, Natick, Massachusetts: The MathWorks Inc., 2010) and coupled with the FE solver within the Comsol Multiphysics environment (Comsol with Matlab, v.5.2. Comsol, Stockholm, Sweden).

III. Results

By using the proposed non-linear constitutive model, significant differences in strain and stress fields were obtained in comparison with the corresponding fields resulted from linearly elastic models in both healthy and metastatic femurs (Figure 3). These differences may lead to an enhanced prediction of femoral strength and thus of the fracture risk assessment.

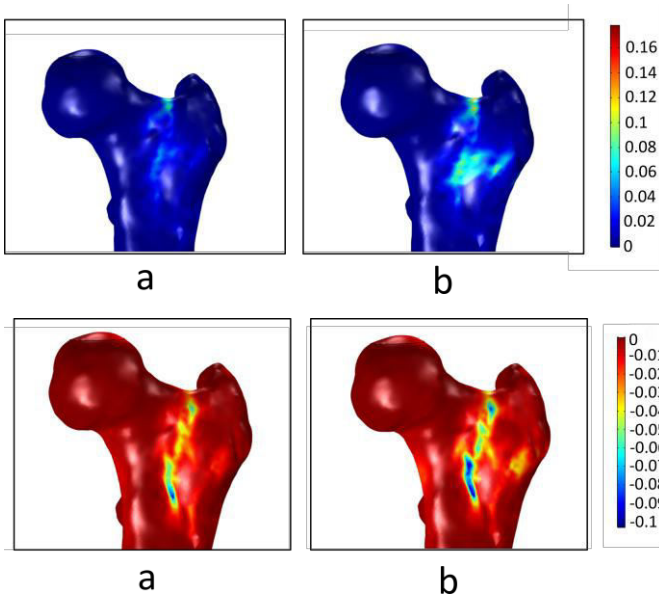

Fig. 3: Distribution of maximum (above) and minimum (below) principal strain in the proximal metastatic femur obtained by using (a) linearly-elastic constitutive model and (b) non-linear constitutive formulation with a two-phase non-homogeneous porous description.

IV. Conclusion

Preliminary results showed that the inclusion of non-linear constitutive laws might improve the understanding of the femoral failure mechanisms. This result is mostly relevant in case of pathological femurs (e.g., metastatic femurs) because a comprehensive understanding of femoral structural failure may enhance the prediction of femoral fracture load and thus may open towards an effective assessment of fracture risk, leading to an improvement of current clinical protocols and therapeutic treatments. As a matter of fact, an accurate prediction of fracture risk is an essential requirement to develop preventive treatment strategies against fracture in the presence of diseases that affect the bone mechanical competence (e.g., bone metastases).

In addition, the proposed computational approach may be used to study the growing and remodeling phenomena of the metastatic defects [19], as well as to develop multiscale models of femur mechanical response, allowing to account for bone remodeling and growth within the framework of bone physiopathology [20]-[21].

References

[1] E. Benca, J.M. Patsch, W. Mayr, D.H. Pahr and R. Windhager, "The insufficiencies of risk analysis of impending pathological fractures in patients with femoral metastases: A literature review," *Bone Rep*, vol. 5, pp. 51–56, 2016.

[2] M.L. Bouxsein, "Determinants of skeletal fragility", *Best Pract Res Clin Rheumatol*, vol. 19, pp. 897-911, 2005.

[3] J.H. Keyak, S.A. Rossi, K.A. Jones and H.B. Skinner, "Prediction of femoral fracture load using automated finite element modeling", *J Biomech*, vol. 31, pp. 125-133, 1998.

[4] E. Dall'Ara et al., "A non linear QCT-based finite element model validation study for the human femur tested in two configurations in vitro", *Bone*, vol. 52, pp.27-38, 2013.

[5] D. Dragomir-Daescu et al, "Robust QCT/FEA models of proximal femur stiffness and fracture load during a sideways fall on the hip", *Ann Biomed Eng*, vol. 39, pp. 742-755, 2011.

[6] Z. Yosibash, N. Trabelsi and C. Milgrom, "Reliable simulations of the human proximal femur by high-order finite element analysis validated by experimental observations", *J Biomech,* vol. 40, pp. 3688-3699, 2007.

[7] E. Schileo, L. Balistreri, L. Grassi, L. Cristofolini and F. Taddei, "To what extent can linear finite element models of human femora predict failure under stance and fall loading configurations?", *J Biomech*, vol. 47, pp. 3531-3538, 2014.

[8] H.S. Hosseini, D.H. Pahr and P.K. Zysset, "Modeling and experimental validation of trabecular bone damage, softening and densification under large compressive strains", *JMBBM*, vol. 15, pp, 93-102, 2012

[9] E.F. Morgan, H.H. Bayraktar, T.M. Keaveny, "Trabecular bone modulu-density relationships depend on anatomic site", *J Biomech*, vol. 36, pp. 897-904, 2003

[10] F. Taddei, A. Pancanti, M. Viceconti, "An improved method for the automatic mapping of computed tomography numbers onto finite element models", *Med Eng Phys*, vol. 26, pp. 61-69, 2004

[11] J.H. Keyak, T.S. Kaneko, J. Tehranzadeh and H.B. Skinner, "Predicting proximal femoral strength using structural engineering models", *Clin Orthop Relat Res*, vol. 437, pp. 219-228, 2005.

[12] D.C. Wirtz, N. Schiffers, T. Pandorf, K. Radermacher, D. Weichert, R. Forst, "Critical evaluation of known bone material properties to realize anisotropic FE-simulation of the proximal femur", J Biomech vol.33, pp. 1325-1330, 2000

[13] J.H. Keyak, T.S. Kaneko, H.B. Skinner and B.H. Hoang, "The effect of simulated metastatic lytic lesions on proximal femoral strength", *Clin Orthop Relat Res*, vol. 459, pp. 139-145, 2007.

[14] E. Tanck et al., "Pathological fracture prediction in patients with metastatic lesions can be improved with quantitative tomography based computer models", *Bone*, vol. 45, pp. 777-783, 2007.

[15] J.L. Sottnik, J. Dai, H. Zhang, B. Campbell and E.T. Keller, "Tumor-induced pressure in the bone microenvironment causes osteocytes to promote the growth of prostate cancer bone metastases", Cancer Res, vol. 75, pp. 2151-2158, 2015.

[16] D. Carter and W. Hayes, "The compressive behaviour of bone as two phase porous structure", *J Bone Joint Surg Am*, vol. 59, pp. 954-962, 1977.

[17] C. Whyne, S. Hu, K. Workman and J. Lotz, "Biphasic material properties of lytic bone metastases", *Ann Biomed Eng*, vol. 28, pp. 1154-1158, 2000.

[18] C.M. Whyne, S.S. Hu and J.C. Lotz, "Parametric finite element analysis of vertebral bodies affected by tumors", *J Biomech*, vol. 34, pp. 1317-1324, 2001.

[19] C.J. Cyron, J.D. Humphrey," Growth and remodeling of load-bearing biological soft tissues", *Meccanica*, vol.52, pp. 645-664 , 2017

[20] H. Gao, "Application of fracture mechanics concepts to hierarchical biomechanics of bone and bone-like materials", *Int J Fract*, vol.138, pp. 101-137, 2006

[21] H. Yao, H. Gao, "Multi-scale cohesive laws in hierarchical materials", International Journal of Solids and Structures, vol. 44, pp. 8177-8193, 2007

Influence of the diagonal branches in stenotic left anterior descending coronary

L.T. Gaudio[1], S. De Rosa[2], M.V. Caruso[1], C. Indolfi[2], P. Veltri[1] and G. Fragomeni[1]
[1] *Bioengineering Unit, Department of Medical and Surgical Sciences, Magna Graecia University of Catanzaro*
[2] *Cardiology Unit, Department of Medical and Surgical Sciences, Magna Graecia University of Catanzaro*

***Abstract*—Coronary arteries are prone to develop pathologies such as the narrowing of the vessel lumen by the accumulation of lipids. From the main coronary, there are numerous branches to terminal arterioles. This study wants to investigate the influence of lateral branches in left anterior descending (LAD) in presence of diameter stenosis of 20% to 70% severity. Reconstructions of 3D-Real coronary anatomy are used to perform a fluid-dynamic computational analysis (CFD).**

In particular, the influence of stenosis positions up and down with respect to the diagonal branches was evaluated in terms of the variation of the hemodynamic parameter of shear stress. Wall shear stress (WSS), oscillatory stress index (OSI) and relative residence time (RRT) results were considered to quantify the differences between the geometry considered with or without the side branches and the different degree of stenosis.

***Keywords*—side branches, stenosis, CFD, hemodynamic, shear stress indices.**

I. Introduction

LEFT anterior descending (LAD) raises a large area of heart muscle [1]. A significant narrowing (stenosis) of the left coronary artery, usually due to the accumulation of lipids on the arterial wall, can cause serious damage as well as myocardial infarction [1]. The evaluation of the collateral coronary flow is of importance in the presence of stenosis on the main branches [1],[2]. The LAD gives rise to septal branches and diagonal branches [1],[3]. The first and the second diagonal branches, and in quite cases the third diagonal branches, of the LAD originate from the front to sidewall of the heart [2].

In patients with coronary artery disease (CAD), the collateral circulation provides an alternative way of supplying blood to the risky myocardium [3].

In general, the presence of other adequately developed branches indicates a lower risk of mortality during the subsequent follow-up [3]. Therefore, the evaluation of the impact of the other branches has been the subject of numerous studies, as it provides useful information for a precise assessment of the patient's risk profile [4]-[7].

There are many studies that make a simplification in the geometry of the coronary not considering the presence of the branches [8]-[11].

Moreover, the presence of side branches can give rise to collateral circulation, that distorts the measure of the Fractional Flow Reserve (FFR) [2],[12],[13]. This technique is invasive to assess the functional significance of coronary stenosis [2],[12]. For this reason, we felt the need to investigate hemodynamics through other techniques, the effect of side branches in presence of stenoses.

By using Computational Fluid Dynamics (CFD) analysis, other authors before us tried to investigate blood flow through coronary arteries in presence of side branches [4]-[7]. CFD is very often used, as it allows to solve basic equations that model the flow in complex geometries using a non-invasive approach [14]-[16]. For instance, Koo et al. evaluated hemodynamics in the lesion in the side branch at different positions and diameter reduction through CFD Analysis [7]. Chiastra et al used CFD simulations to investigate the influence of the bifurcation angle of side branch lesion on intracoronary hemodynamics [6]. Using the same technique, Yingguag et al. studied the impact of side branches in the presence of coronary stenosis carrying out a hemodynamic analysis and demonstrated that the presence of side branches adds a higher level of accuracy on the results [4].

The following work is placed in this context, its aims being firstly to evaluate the impact of diagonal branches on the up and down position of the left coronary artery (LAD) stenosis compared to the model that only considers the main branch and secondly to quantify the percentage variations of shear stress indices.

II. Material and methods

A. Geometrical Model

For clinical reasons, 3D-Real coronary anatomies of LAD vessel were reconstructed from the angiography of patients. The frame corresponding to the diastolic phase was selected and the geometries of three patients were rebuilded using RHINOCEROS V.4.0 software (Robert McNeel & Associates, Seattle, WA, USA). In the first analysis the reconstruction of the LAD vessel was evaluated considering the distal segment, central segment (in which the stenosis resides), and proximal segment. Secondly is considering the main branch (LAD) and two side branches (the first diagonal branch and the second diagonal branch) were considered.

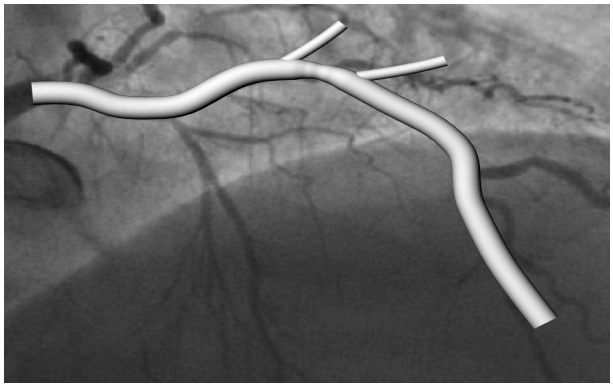

Fig. 1: LAD reconstruction

Three patients with not severe stenosis (with a diameter reduction of 20%), intermediate lesion (with a diameter stenosis of 50%) and severe stenosis (with a diameter reduction of 70%) were considered. The stenosis proximal to the origin of the diagonal branch was considered as "up lesion" and the distal was considered as "down lesion".

B. *Mathematical Model*

Fluid motion within the coronary artery geometry is assumed to be laminar. To represent blood flow models, with a density of 1060 (kg/m^3), non-Newtonian model of Carreau-Yasuda is considered in this study [14],[16]. Dynamic viscosity is defined by:

$$\mu = \mu_\infty + (\mu_0 - \mu_\infty)[1 + (\lambda\gamma)^2]^{(n-1)/2} \quad (3)$$

where μ_0 =0.056 (Pa.s) is viscosity at zero shear rate, μ_∞ = 0.0035 (Pa.s) is viscosity at infinite shear rate, γ is the shear rate (s^{-1}) , λ =3.313 (s) is relaxation time (s) and n=0.3568 is power index [14],[16].

Shear stress indices have been taken into account for their implication in being a marker of disturbed flow in coronary artery disease (CAD) [17]-[22]. First, was investigated the Wall Shear Stress (WSS), index which is responsible for the change of morphology and the orientation of the wall of the vessel [17],[18]. It is defined by:

$$WSS = \sqrt{(\tau_x)^2 + (\tau_y)^2 + (\tau_z)^2} \quad (4)$$

where τ_x, τ_y, τ_z are the viscous stress in x, y, z directions, respectively.

Second, the Oscillatory Stress Index (OSI) was considered, because it is an identifier of the regions of the vessel subjected to oscillating WSS [19]. It is defined by the following equation:

$$OSI = \frac{1}{2}\left[1 - \frac{\left|\int_0^T WSS\, dt\right|}{\int_0^T |WSS|\, dt}\right] \quad (5)$$

The OSI value can vary from 0 and 0.5, from no oscillatory of WSS vector to 180° deflection of WSS direction [19].

Finally, the Relative Residence Time (RRT) was used to identify the regions in which particle residence occurs [20]. The RRT equation is:

$$RRT = \frac{1}{(1-2*OSI)*\frac{1}{T}\int_0^T |WSS|\, dt*} = \frac{T}{\left|\int_0^T WSS\, dt\right|} \quad (6)$$

C. *CFD Analysis*

The simulations were conducted using the COMSOL 5.3a software (COMSOL Inc., Stockolm, Sweden), which by means of the finite element method (FEM), is able to solve fluid dynamic problems. The patients' specific boundary conditions were imposed on each geometry of LAD acquired through an intracoronary catheter.

At inlet boundary condition to the coronary a flow curve was imposed and in first output condition to the main coronary a pressure profile was imposed. In the second output, in the first diagonal branches considered and in the second diagonal branches the curve pressure was climbed with an adimensional parameter α. In the diagonal branches on average the pressure values vary between 104/70 (mmHg) and 108/76 (mmHg) [7].

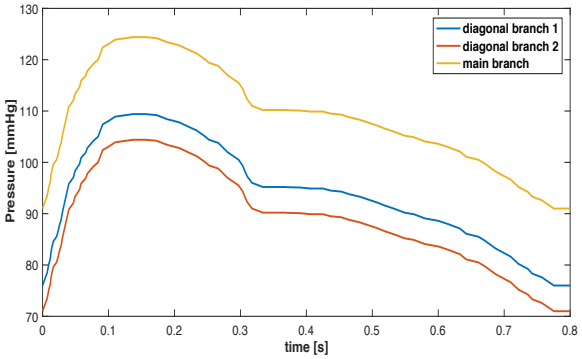

Fig. 2: Pressure curve a)main branch b)diagonal branch 1 c)diagonal branch 2

To the wall the no-slip boundary condition was applied for each coronary artery. Subsequently, the mesh was generated on the 3D domain composed of grids with tetrahedral and prismatic elements. Steady-state and transient simulation for each coronary in two cases - with and without branches - were performed using direct solver PARDISO.

III. Result and Discussion

The CFD results of three models showed the distribution of the blood flow to the coronary artery (LAD). In order to represent the result, Figures 3 and 4 were divided into 'without branches' and 'with branches' for Case A (20% stenosis), Case B (50% stenosis), Case C (70% stenosis).

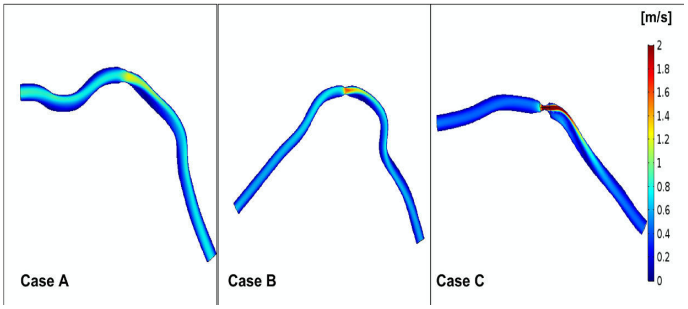

Fig. 3: Velocity result without branches A)20% B)50% C)70%

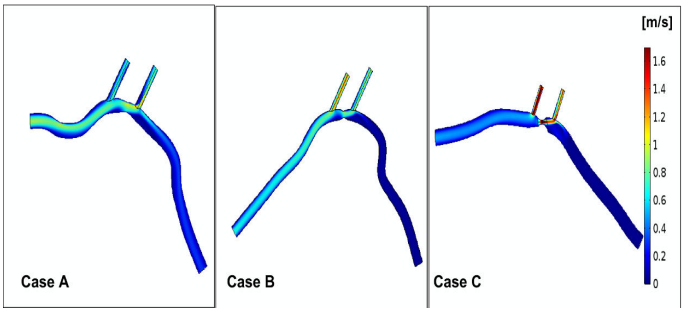

Fig. 3: Velocity result with branches A)20% B)50% C)70%

As it can be seen from Figures 3, the three cases show an increase in speed in the area of the stenoses, with a maximum value for case C of 2 (m/s), as the degree of stenosis increases when the speed value increases. The presence of the secondary branches leads to a decrease in the maximum value in the area of stenosis in case C of 1.6 (m/s). Indeed, as it was anticipated, the flow is carried in these branches, in this case of 70% of stenosis, it is possible tosee the onset of the collateral circulation in the up branch.

Secondly, the wall shear stress was evaluated. Figures 5 and 6 show the distribution of WSS during the systolic peak for cases without and with branches.

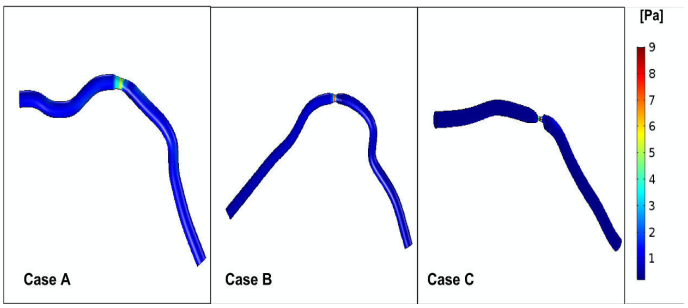

Fig. 5: WSS result without branches A)20% B)50% C)70%

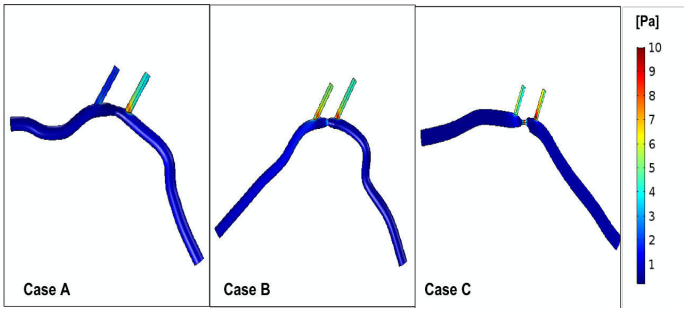

Fig. 6: WSS result with branches A)20% B)50% C)70%

As it can be seen from Fig 5, considering only the main branch, it shows high values of WSS in the area of stenosis, which may be higher in cases B and C, up to 8 (Pa), with more severe stenosis. In the case of side branches, the WSS values in the stenosis region are lower than in the case without them. Values of WSS greater than 3 (Pa) in the region of stenosis involve clotting referred to intimal thickness [17],[18]. Considering the side branches reduces the maximum value in the area of stenosis, which passes, comparing Figures 5 and 6, for case A a reduction of 34.1%, for case B a reduction of 27.8%, for case C a reduction of 22.7 %.

Subsequently, two indices - OSI and RRT - were studied. The result of OSI index shows the areas downstream of stenosis are characterized by a high value. Value of OSI greater than 0.3 induces perturbed endothelial alignment [19],[20].

On the other hand, in the same region, downstream of stenosis, there are a low value of WSS and high of OSI. In the same region is found there is a high value of the index of relative residence time, RRT. This coupling indicates the time of residence of particles at endothelium, which is an interesting predictor of the localization of atherosclerosis [19]. The results of simulations shown that the area with high OSI and RRT values becomes wider if the side branches are present. Furthermore, it is noted that area is always downstream of the stenosis but in the case of the side branches it is closer to the stenosis area.

Table I and Table II show the maximum value calculated in region after the stenosis for OSI and RRT. In the first case considering the model without the branches and in the second case with.

TABLE I
MAXIMUM VALUE OSI AND RRT WITHOUT BRANCHES

OSI (1)	*RRT (1/Pa)*
Case A: 0.39	Case A: 5
Case B: 0.46	Case B: 12.08
Case C: 0.49	Case C: 21.5

Case A)20% Case B)50% Case C)70%

TABLE II
MAXIMUM VALUE OSI AND RRT WITH BRANCHES

OSI (1)	*RRT (1/Pa)*
Case A: 0.33	Case A: 4.13
Case B: 0.42	Case B: 10
Case C: 0.43	Case C: 17,43

Case A)20% Case B)50% Case C)70%

The results of percentage variation of WSS, OSI and RRT are shown in Table III, summarizing the percentage decreases of all the shear stress indices considered for the cases studied, in the narrowing of the stenosis, compared to the same cases without considering the side branches.

TABLE III
PERCENTAGE VARIATION SHEAR STRESS INDICES WITH VS WITHOUT BRANCHES

WSS	*OSI*	*RRT*
Case A: 34.1%	Case A: 15%	Case A: 17.3%
Case B: 27.8%	Case B: 8.2%	Case B: 16.6%
Case C: 22.7%	Case C:13.3%	Case C: 18.9%

As it is displayed in the table, considering the diagonal branches leads to variations in the results of shear stress indices. Particularly in the area of the stenosis for the WSS and downstream of the stenosis for OSI and RRT consider the branches leading to the decrease of the maximum value at that point. WSS, OSI and RRT increase the total maximum value at other points in the vessel.

IV. CONCLUSION

An accurate assessment of the three shear stress indices, WSS, OSI and RRT provides a useful predictive tool for identifying the possible localization of atherosclerotic plaque in the coronary artery. Considering the diagonal branches adds more detail to the model. This study aims at quantifying the variation is made, in the parameters of shear stress, in considering the presence of the side branches or not, for different degree of stenoses.

The WSS is the parameter that is most influenced by the presence in geometry of the diagonal branches. This parameter has importance in the characterization of the critically of the stenosis. Adverse events also occur in presence of negative FFR, the results of CFD analysis of these cases can show critical WSS value [21].

Subsequent studies will be carried out with the aim of extending the case studies in order to provide a statistical model for predicting the variation of these indices subject to the presence of the branches.

REFERENCES

[1] N. Ikeda, S. Yajima, T. Asahara, and H. Sakai, "Intervention for jailed diagonal branch is not necessary while stenting the left anterior descending artery", *Journal of interventional cardiology*, *22*(3), 252-256, 2009.

[2] B.K. Koo, et al. "Physiological evaluation of the provisional side-branch intervention strategy for bifurcation lesions using fractional flow reserve." *European heart journal*29.6 (2008): 726-732.

[3] M. Cohen and K.P. Rentrop, (1986). Limitation of myocardial ischemia by collateral circulation during sudden controlled coronary artery occlusion in human subjects: a prospective study. *Circulation*, *74*(3), 469-476.

[4] Y. Li, et al. "Impact of side branch modeling on computation of endothelial shear stress in coronary artery disease: coronary tree reconstruction by fusion of 3D angiography and OCT." *Journal of the American College of Cardiology* 66.2 (2015): 125-135.

[5] S. H. Na, et al. "Evaluation of local flow conditions in jailed side branch lesions using computational fluid dynamics." *Korean Circulation Journal* 41.2 (2011): 91-96.

[6] C. Chiastra, et al. "Coronary fractional flow reserve measurements of a stenosed side branch: a computational study investigating the influence of the bifurcation angle." *Biomedical engineering online* 15.1 (2016): 91.

[7] B.K. Koo, et al. "Assessment of clinical, electrocardiographic, and physiological relevance of diagonal branch in left anterior descending coronary artery bifurcation lesions." *JACC: Cardiovascular Interventions* 5.11 (2012): 1126-1132.

[8] R. Xing, et al. "Contrast-enhanced micro-CT imaging in murine carotid arteries: a new protocol for computing wall shear stress." *Biomedical engineering online* 15.2 (2016): 156.

[9] G. Choi, et al. "Coronary artery axial plaque stress and its relationship with lesion geometry: application of computational fluid dynamics to coronary CT angiography." *JACC: Cardiovascular Imaging* 8.10 (2015): 1156-1166.

[10] A. Mahalingam, et al. "Numerical analysis of the effect of turbulence transition on the hemodynamic parameters in human coronary arteries." *Cardiovascular diagnosis and therapy* 6.3 (2016): 208.

[11] A. SC. Yong, et al. "The relationship between coronary artery distensibility and fractional flow reserve." *PloS one* 12.7 (2017): e0181824.

[12] B.K. Koo, et al. "Physiologic assessment of jailed side branch lesions using fractional flow reserve." *Journal of the American College of Cardiology* 46.4 (2005): 633-637.

[13] S. Tu, et al. "Fractional flow reserve calculation from 3-dimensional quantitative coronary angiography and TIMI frame count: a fast computer model to quantify the functional significance of moderately obstructed coronary arteries." *JACC: Cardiovascular Interventions* 7.7 (2014): 768-777.

[14] R. Mazzitelli, F. Boyle, E. Murphy, A. Renzulli G. Fragomeni "Numerical prediction of the effect of aortic Left Ventricular Assist Device outflow-graft anastomosis location." *Biocybernetics and Biomedical Engineering* 36.2 (2016): 327-343.

[15] V. Gramigna, et al. "A numerical analysis of the aortic blood flow pattern during pulsed cardiopulmonary bypass." *Computer methods in biomechanics and biomedical engineering* 18.14 (2015): 1574-1581.

[16] J.V. Soulis, et al. "Non-Newtonian models for molecular viscosity and wall shear stress in a 3D reconstructed human left coronary artery." *Medical Engineering and Physics* 30.1 (2008): 9-19.

[17] H. Samady, et al. "Coronary artery wall shear stress is associated with progression and transformation of atherosclerotic plaque and arterial remodeling in patients with coronary artery disease." *Circulation* (2011): CIRCULATIONAHA-111.

[18] J.M. Dolan, J. Kolega, and H. Meng. "High wall shear stress and spatial gradients in vascular pathology: a review." *Annals of biomedical engineering* 41.7 (2013): 1411-1427.

[19] J. Knight, et al. "Choosing the optimal wall shear parameter for the prediction of plaque location—a patient-specific computational study in human right coronary arteries." *Atherosclerosis* 211.2 (2010): 445-450.

[20] J.V. Soulis, O.P. Lampri, D.K. Fytanidis, G.D Giannoglou, "Relative residence time and oscillatory shear index of non-Newtonian flow models in aorta." *Biomedical Engineering, 2011 10th International Workshop on*. IEEE, 2011.

[21] L.T. Gaudio, S. De Rosa, C. Indolfi, M.V. Caruso, and G. Fragomeni, (2017, September). Hemodynamically non-significant coronary artery stenosis: a predictive model. In *Proceedings of the International Workshop on Innovative Simulation for Health Care* (pp. 18-20).

Computational modelling of brain tissue in neurosurgery

Daniele Bianchi and Giuseppe Vairo
Department of Civil Engineering and Computer Science, University of Rome "Tor Vergata", Italy;
email: d.bianchi@ing.uniroma2.it; vairo@ing.uniroma2.it

***Abstract*— In this study a novel computational model, formulated via a finite-element technique and based on the Biot's linear poroelasticity theory, is developed for the assessment of brain mechanical response in neurosurgery. The proposed computational framework aims to furnish a contribution towards the definition of a tool useful for surgical planning and for improving the intra-operatory accuracy of neuro-navigation systems, with specific reference to brain-shift effects. Some exemplary results are presented, highlighting the influence of a glioblastoma tumoral mass on the brain shift associated to a craniectomy surgical procedure.**

***Keywords*— Brain tissue mechanics, Biot's poroelasticity theory, Patient-specific computational models, Brain shift.**

I. Introduction

NEURONAVIGATION represents the best technique for complex brain and spinal surgeries since it is the only method allowing both minimal invasiveness and high precision during the surgical procedure [1].

Neuronavigation relies on morphological data acquired in the preoperative stage by employing Magnetic Resonance Imaging (MRI) and Computed Tomography (CT), from which patient-specific anatomy is reconstructed. Before the surgical procedure begins the neuro-navigator has to be set up in order to establish a spatial correspondence between the reference system associated to the physical space of the patient and the reference system assigned to the virtual model displayed on the monitor of the neuro-navigator. After the registration procedure and referring to brain surgery, the possible insurgence of brain shift (BS) as induced by different and coupled factors associated to surgical treatments (e.g., opening of the dura mater, high or unbalanced intracranial pressure, cerebrospinal fluid leakage, administration of drugs, dimension of craniectomy, tissue resection [2]), may induce non-negligible errors in the neuro-navigation procedure, resulting in an overall loss of accuracy and in possible ineffective surgical performance.

Different methods have been developed to correct the inaccuracy induced by the BS. One of the most used consists in acquiring new data after the change of configuration of the brain tissue, by carrying out intraoperative MRI [3] that allows the updating of the neuro-navigator set-up and thereby the recovering of a suitable accuracy degree. Nevertheless, such an approach is expensive and time consuming, and it

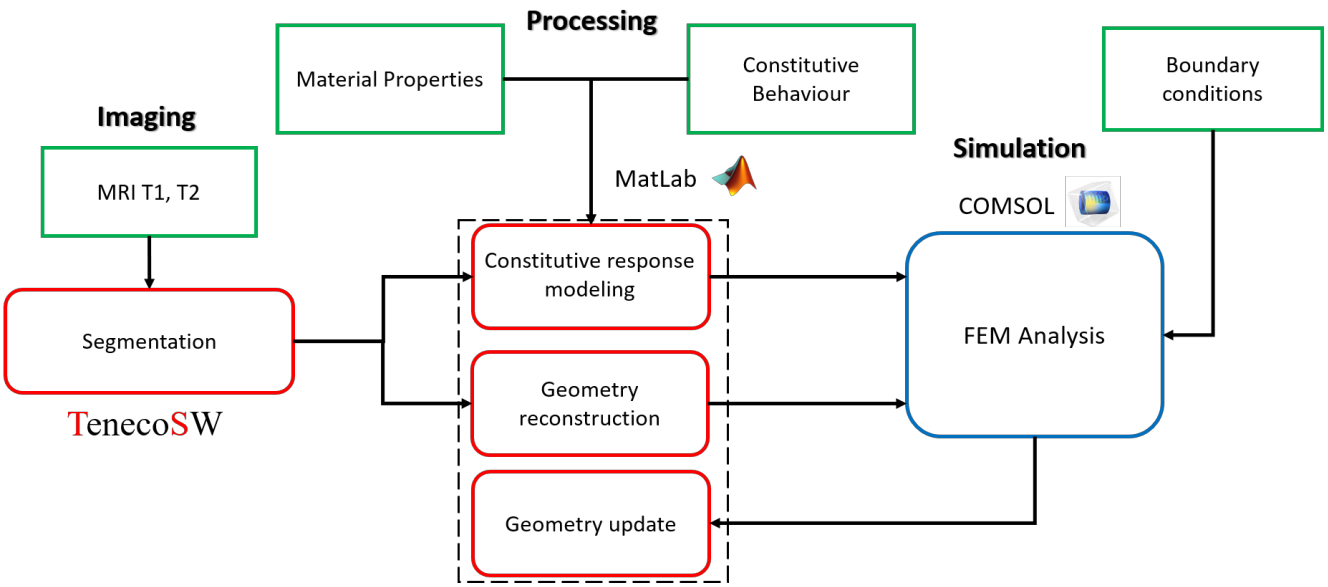

Fig. 1: FEM-based computational strategy. Patient-specific data deriving from diagnostic imaging techniques are integrated with a constitutive description accounting for histological, biophysical and biochemical features, and are adopted in non-linear finite-element simulations

generally may result incompatible with timing of neurosurgery brain treatments. Another interesting method involves ultrasound systems (US), characterized by portability features. These approaches allow for real-time data acquisition, and they are less expensive than the intraoperative MRI-based one. However, image resolution obtained in this case is usually not suitable for neuro-navigation purposes [4].

In order to contribute towards the definition of an effective computational tool, able to describe mechanical response of brain tissue during neurosurgical treatments, in this paper a novel modeling framework is established. In particular, a computational approach formulated via a finite-element technique and based on the Biot's linear poroelasticity theory, is developed and applied for some preliminary analyses focused on the assessment of brain shift in neurosurgery. The proposed computational tool opens towards the definition of a simulation-based protocol for planning and optimizing surgical procedures, as well as for improving the intra-operatory accuracy of neuro-navigation systems. Some exemplary results are presented, highlighting the influence of a glioblastoma tumoral mass on the brain shift associated to a craniectomy surgical procedure.

II. Materials and Methods

A methodology for developing three-dimensional computational models of brain and neurocranium, incorporating patient-specific geometry and biophysical data from computer tomography (CT) images and magnetic resonance imaging (MRI), is herein described (Fig. 1).

A. Geometry reconstruction and mesh generation

Input data are constituted by volumetric greyscale images in DICOM format obtained by co-registration of CT and MRI. Brain, skull, ventricles and falx cerebri have been segmented from volumetric images employing the software TenecoSW developed by SenTech (Rome, Italy), and providing a description of the geometry via a surface mesh. Segmentation errors, due to possible coarse resolution of medical devices and/or involuntary patient movements, are reduced by applying a Taubin smoothing algorithm [5], performed via a homemade Matlab code. The geometrical model has been discretized through second-order displacement-based tetrahedral elements by adopting the Comsol environment. Mesh size and local refinements have been set as the result of preliminary convergence analyses.

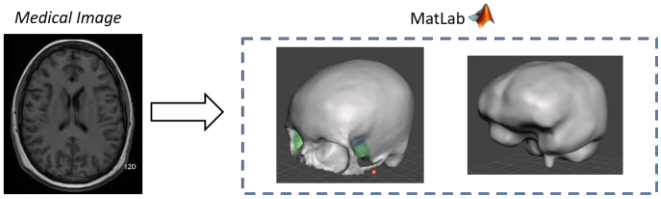

Fig. 2: Geometries reconstruction of brain and neurocranium from DICOM format images obtained by co-registration of CT and MRI

B. Biot's linear poroelastic model

As a constitutive hypothesis, brain tissue is regarded as a porous medium saturated by fluid [6], [7]. Accordingly, its mechanical behaviour has been modelled via the Biot's poroelastic linear theory [4], allowing to account for the influence of pressure within the pores on the overall stress in the porous matrix. In detail, stresses applied to the overall brain tissue are partly distributed to the solid skeleton and partly to the pore fluid. The former stresses (namely, effective stresses $\boldsymbol{\sigma}$) are responsible for tissue deformations and are expressed as:

$$\boldsymbol{\sigma} = \mathbb{C}:\boldsymbol{\varepsilon} - \alpha p\mathbf{I} \tag{1}$$

where $\mathbb{C}$ is the fourth-order constitutive tensor, satisfying minor and major symmetries, $\boldsymbol{\varepsilon}$ is the second-order infinitesimal strain tensor, $\mathbf{I}$ is the second-order identity tensor, α is the Biot's coefficient and p is the pore pressure.

C. Material properties

All tissue regions are assumed to behave as nearly-incompressible linearly elastic materials with isotropic constitutive symmetry. In detail, Poisson coefficient is assumed to be uniformly distributed and equal to 0.45. Brain tissue (namely, the porous matrix) has been described as strongly inhomogeneous, in agreement with the greyscale distribution occurring in diagnostic images and by adopting mechanical data measured in both in vivo [8] and ex vivo [9] studies. Definition of local material properties starting from medical images is performed via standard correlations and by adopting a Matlab filter. Figure 3 highlights the inhomogeneous distributions of the Young modulus deduced from diagnostic images. Possible pathological tumoral tissues have been assumed to be characterized by a higher stiffness compared with the surrounding healthy tissue and by a different distribution of Biot's coefficent [8]. In particular by denoting with $\bar{E}$ the average value of the Young modulus deduced from diagnostic images, the corresponding value in the tumoral region is considered equal to $E_t = 2\bar{E}$, as well as the Biot's coefficient within the pathological region is assumed equal to $\alpha_t = 1.5\alpha$, where $\alpha = 0.65$ is considered within the healthy tissue. Moreover, falx cerebri has been modelled by considering a Young's modulus six times greater than the average value characterizing the surrounding parenchyma [10]. Ventricles, fulfilled with cerebrospinal fluid (CSF), have been simply modelled as a soft material whose Young's modulus is about 1/10 of the average value considered for the surrounding brain tissue. Finally, skull bones are considered as rigid elements, since their stiffness is about six orders of magnitude greater than that of other tissues [11].

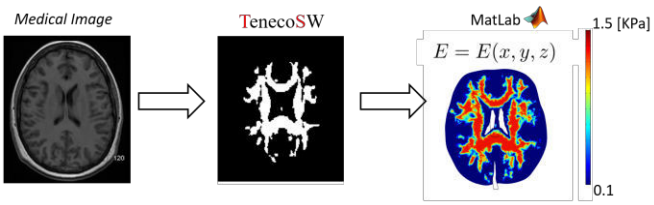

Fig. 3: Definition of local material properties starting from medical imaging

D. *Boundary conditions*

In order to simulate realistic scenarios, the boundary conditions summarized in the following have been considered (see Fig. 4).

(i) Skull-brain interaction is accounted for and it is described via a frictionless unilateral contact model, based on a penalty approach. As a result, a non-linear problem has been solved.

(ii) As it is well-known from histological evidence, falx cerebri is a fold of the dura mater, which adheres strongly to the skull. Accordingly, from a computational point of view, the upper surface of the solid region describing the falx cerebri has been considered as fully restrained [7].

(iii) Linearly elastic springs have been applied to the base of the spinal cord to simulate the interaction with surrounding spinal tissues. Elastic properties of such springs have been set on the basis of available data and in order to satisfies convergence requirements.

(iv) In order to furnish preliminary indications associated to surgical procedure related to craniectomy, the assumption that opening of dura mater determines a variation in pore pressure is enforced. In particular, the pore pressure before the craniectomy is assumed as uniformly distributed and equal to ICP, considered as a relative pressure whit respect to the external one. Accordingly, such an internal pressure acts as a loading condition since it is not counteracted at the tissue boundary side approaching the craniectomy window.

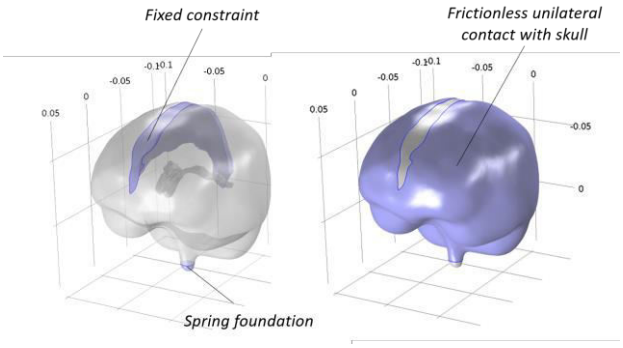

Fig. 4: Mechanical boundary conditions adopted for describing the skull-brain interaction, the spinal cord, and falx cerebri joint

III. Results

As a first case study, the brain herniation induced by craniectomy is simulated. Corresponding results are compared with available clinical evidence (see Fig. 5). Moreover, the influence on the tissue response induced by a possible tumoral glioblastoma region has been addressed. The glioblastoma has been simply described as a sphere with radius R and located in the left hemisphere, wherein the craniectomy window is considered. This latter is described by a quadrangular opening whose sides have an average length of about 10 cm. Numerical results are obtained, highlighting the coupled influence of intracranial pressure (ICP) and of tumor radius (R) on brain shift effects. Figure 6 displays some exemplary numerical results in terms of displacement spatial distribution in a frontal cross section, for different values of R and ICP.

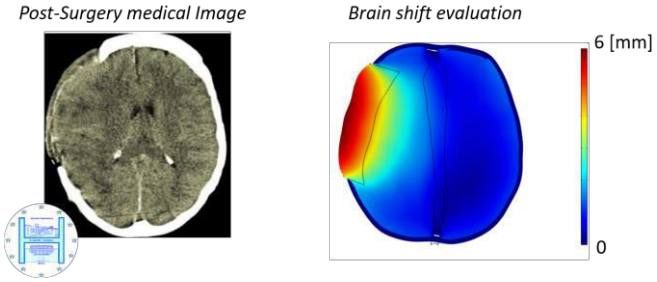

Fig. 5: Brain herniation induced by craniectomy: comparison between available clinical evidence and numerical simulation. Medical images are courtesy of Hospital San Camillo Forlanini of Rome.

IV. Conclusions

The effectiveness of the implemented model has been verified by reproducing, as a first case study, a craniectomy intervention. The results obtained show that the proposed model, allowing to reproduce brain shift process, may be a useful tool in the phases of planning and management of surgical treatments. Moreover, the effects of intracranial pressure (ICP) and tumour size on brain shift have been investigated. Finally, with the aim of providing a contribution to the current state of the art, the developed model can be

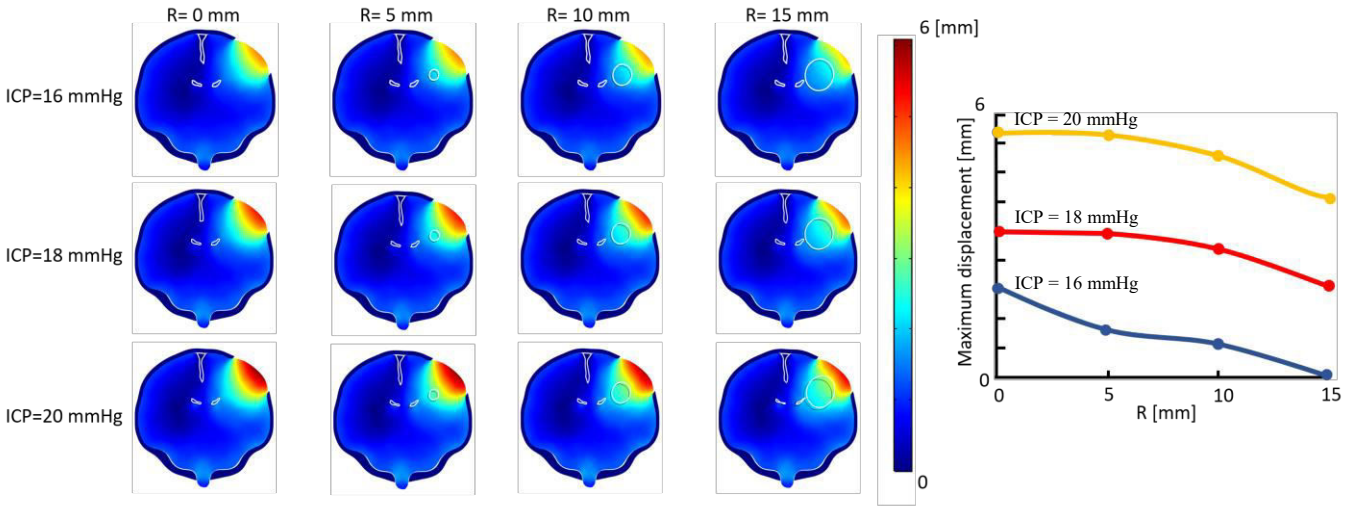

Fig. 6: Brain herniation induced by craniectomy for surgical treatment of a glioblastoma. Spatial distributions of the displacement field (on the left) and corresponding maximum values (on the right). Coupled influence of intracranial pressure (ICP) and of tumour radius (R).

retained as a first step towards the conception and realization of an advanced neuronavigation system that integrates imaging methodologies with computational biomechanical models. In this way, the integrated use of these aspects will allow to develop innovative technology in the context of biomedical instrumentation and clinical practice.

ACKNOWLEDGEMENT

D. Bianchi and G. Vairo acknowledge the Italian Minister of University and Research, MIUR (Research program: "Consolidate the Foundations 2015"; Project: BIOART; Grant number (CUP): E82F60 0 0850 0 05). Moreover, helpful cooperation given by SenTech s.r.l. is gratefully acknowledged.

REFERENCES

[1] Ian J. Gerard, Marta Kersten-Oertel, Kevin Petrecca, Denis Sirhan, Jeffery A. Hall, L. D. Collins, "Brain Shift in Neuronavigation of Brain Tumors: A review", *Medical Image Analysis*, 2017, pp 403-420.

[2] Reinges M.H., Nguyen H., Krings T., Hutter B.O., Rohde V., Gilsbach J, "Course of brain shift during microsurgical resection of supra-tentorial cerebral lesions: limits of conventional neuronavigation", A*cta Neurochirurgica*, 2004, pp 369-377.

[3] F. Esposito, F. Di Rocco, G.l Zada, G. Cinalli, H. W.S. Schroeder, C. Mallucci, L. M. Cavallo, P. Decq, C. Chiaromonte, P. Cappabianca., "Intraventricular and Skull Base NeuroEndoscopy in 2012: A Global Survey of Usage Patterns and the role of intraoperative neuronavigation", *World Neurosurgery*, 2013, pp 709-716.

[4] Kay Sun, T. S. Pheiffer, A. L. Simpson, J. A. Weis, R. C. Thompson, M. I. Miga, "Near Real-Time Computer Assisted Surgery for Brain Shift Correction Using Biomechanical Models", *IEEE Journal of Translational Engineering in Health and Medicine*, 2014.

[5] G. Taubin, 1994, Curve and surface smoothing without shrinkage, Technical Report, RC-19563, IBM-Research.

[6] L. Xiaogai, H. von Holst, K. Svein, "Influences of brain tissue poroelastic constants on intracranial pressure (ICP) during constant-rate infusion", *Computer Methods in Biomechanics and Biomedical Engineering*, 2013, pp 1330-1343.

[7] M. Biot, "General Theory of Three-Dimensional Consolidation", *Journal of Applied Physics,* 1941, pp 155-164.

[8] R. Sinkus, M. Tanter, T. Xydeas, S. Catheline, J. Bercoff, M. Fink, "Viscoelastic shear properties of in vivo breast lesions measured by MR elastography", *Magnetic Resonance Imaging*, 2005, pp 159-165.

[9] B. Rashid, M. Destrade, M. D. Gilchrist, "Hyperelastic and Viscoelastic Properties of Brain Tissue in Tension", *Proceedings of the ASME 2012 International Mechanical Engineering Congress and Exposition,* 2012.

[10] M. I. Miga, K. D. Paulsen, F. E. Kennedy, A. Hartov, D. W. Roberts., "Model-Updated Image-Guided Neurosurgery Using the Finite Element Method: Incorporation of the Falx Cerebri", *Medical Image Computing and Computer-Assisted Intervention,* 1999, pp 900-910.

[11] J. A. Motherway, P. Verschueren, G. Van der Perre, J. V. Sloten, M. D. Gilchrist., "The mechanical properties of cranial bone: The effect of loading rate and cranial sampling position", *Journal of Biomechanics,* 2009, pp 2129-2135.

Engineering viscoelasticity in biomaterials

L.Cacopardo[1], N.Guazzelli[1], R. Nossa[1], G.Mattei[1,2], and A. Ahluwalia[1]
[1] *Research Center 'E. Piaggio', Department of Information Engineering, University of Pisa, Italy;*
email:ludovica.cacopardo@ing.unipi.com; arti.ahluwalia@unipi.it.
[2] *Optics11, The Netherlands.*

***Abstract*— Hydrogels have an intrinsic viscoelastic behaviour. Although their elastic properties have been extensively studied - along with the development of different techniques to modulate their stiffness - their viscoelastic behaviour has largely been ignored. The stiffness of hydrogels is often modulated using crosslinking strategies, which however alters both elastic and viscous behaviour concomitantly. To obtain hydrogels with the same degree of crosslinking but different viscoelastic properties, agarose and acrylamide hydrogels were prepared using aqueous solutions with increasing concentrations of dextran and hence increasing viscosities. Using commercial polyurethane sponges soaked in dextran as controls, the viscoelastic properties of the different samples were characterised using the epsilon-dot method. While increasing the solvent viscosity in the controls resulted in a significant increase of the characteristic relaxation time (τ), both the instantaneous modulus (E_inst) and the equilibrium modulus (E_eq) remained almost constant. In the hydrogels however, a significant reduction of both E_inst and τ was observed. On the other hand, E_eq – an indicator of the equilibrium elastic behaviour after the occurrence of viscoelastic relaxation dynamics – was found to be independent of the solvent viscosity.**

Therefore, although the elastic and viscous components of hydrogels cannot be completely decoupled due to the chemical interaction of the liquid and solid phases, we show that their viscoelastic behaviour can be modulated by varying the viscosity of the aqueous phase. This simple-yet-effective strategy might be beneficial to the field of mechanobiology, particularly for studying cell response to substrate viscoelastic relaxation, while keeping the elastic cue (i.e. equilibrium modulus, or quasi-static stiffness) constant.

***Keywords*—viscoelasticity, biomaterials, epsilon-dot.**

I. Introduction

Soft tissues and hydrogels are characterised by a biphasic structure: a solid network, which confers elastic properties, surrounded by an aqueous solution, which is associated with its viscous behaviour [1]. Recently, the possibility to manipulate the mechanical properties of biomaterials has been of interest to scientists. Indeed, cells are responsive to mechanical cues from the extracellular matrix (ECM). The process that allows cells to sense the stiffness of their microenvironment is known as mechano-transduction. In particular, cells explore their mechanical environment mainly thanks to integrins, which are linked to the cytoskeleton and are able to modify intracellular signalling pathways (Humphrey et al., 2014). Moreover, recent works demonstrate that cells are also able to respond to time dependent properties of the substrate [2-4].

Therefore, the ability to control the mechanical properties of hydrogels could have a wide range of applications in the biomedical field, ranging from the development of pathophysiological in-vitro models to the modulation of stem cell differentiation. However, despite the intrinsic viscoelasticity of these materials, most of the studies in the literature are focused on the modulation of the elastic behaviour using different stiffening techniques (i.e. physical, chemical, enzymatic) [1]. The few reports in the literature on the modulation of viscoelasticity are based on rheological measurements. The resultant dynamic modulus reflects the (elastic storage modulus G') and viscous behaviour (loss modulus G").

For example, polyacrylamide (PAAm) gels with different viscous properties were realized adding high molecular weight linear polymers of PAAm, which results sterically entrapped in the gels [2], or simply varying the proportion of acrylamide monomer and bis-acrylamide [3]. In the first case, a G" of 200 and 500 Pa for 1.8% and 2.75% of polymer was obtained, while in the second, the values of G" were 130, 10 and 11 Pa for the following acrylamide/crosslinker ratios 15/0.0125%, 12/0.0358%, 8/0.1% respectively. Furthermore, polyethylene glycol (PEG) gels with an elastic moduli varying from 0.24 kPa to 12 kPa were obtained from Mabry and colleagues, submerging the gels for 12 min in PEG-norbornene (2 or 10mM) and PEG-thiol (2 or 10mM) solutions [5]. However, since the loss modulus was much lower than the storage modulus, the viscous behaviour of these gels was ignored. For example, The yield stress, defined as the critical applied stress after which the gel starts to flow, was studied in [6], for nanoparticles (NP) containing gels, resulting in an increasing yield stress (i.e. a stiffening of the gel) with increasing NP concentration. Moreover, as described in [7] the macroscopic viscoelastic properties of a physical hydrogel can be are reversibly modulated by tuning the microscopic hydrogen bonding interactions with pH. As a result, the yield stress of the hydrogel is greatly enhanced reducing the pH from 7.0 to 5.0, and also G′ and G″ indicate an enhanced rigidity and stability of the gel. Jay and co-workers [8] also modulated the viscoelasticity of phenylboronate (PBA) and salicylhydroxamate (SHA) gels for topical drug-delivery using pH. In particular, the mechanical properties of the gels are dominated by the viscous component at low pH (around 4.8), while the elastic components increase with increasing the pH and finally G' reaches a plateau at pH 6. Finally, Mensitieri et al. show that auto-crosslinked polysaccharide (ACP) polymers can be modulated both by varying the degree of crosslinking and the weight concentration [9]. At a fixed concentration, the elasticity can be increased by increasing the level of chemical crosslinking substantially without increasing the viscous

dissipation. A different example can be found in Mattei et al. [10], where gelatin samples were crosslinked with different glutaraldehyde (GTA) concentrations obtaining a stiffening of the gels. In particular, the viscoelastic properties of the gels were investigated using the nano-epsilon dot method [11], showing that both the instantaneous and equilibrium moduli moduli as well as the characteristic relaxation time increase with GTA concentration. Taken together, these results indicate that not only gelatin hydrogels stiffen with increasing GTA concentrations, but there is also a concomitant shift in their viscoelastic behaviour towards a more elastic one. Furthermore, Kreger and co-workers used both rheological measurements and compressive tests to study the effect of hyaluronic acid (HA) concentration on collagen matrix, showing that increasing HA concentration resulted in a decrease of shear stiffness and increase of the viscous or fluid-like behavior (decrease of G' and increase of the phase shift δ). Moreover, a significant increase of the compressive modulus (hydraulic resistance) was observed at high strains (>50%), while no significant differences were observed at low strains (<50%). Differently, varying collagen concentration altered both low and high strain compressive moduli. This suggests that HA modify the viscoelastic properties of collagen matrix acting on the physio-chemical properties of the fluid phase, thus altering the fluid flow within the matrix.

Despite the increasing interest of viscoelastic properties, to date there are only few studies focused on a specific modulation of the viscous component. Indeed, the studies present in the literature are mainly focused on the modulation of the elastic component and on the measurement of the resultant effect on both the elastic and viscous component. To address this gap, our aim is to modulate material viscoelasticity by acting on the damping component, i.e. through tuning of the liquid phase viscosity of spongiosum sample and agarose and acrylamide gels with different dextran concentrations.

II. Material and Methods

A. Sample Preparation

Polyurethane sponges were cut to obtain cubic sample (l≃10mm) and submerged with water and dextran solution at different concentration (2 and 5% w/v).

Agarose solutions were prepared at 1% w/v polymer concentration by dissolving agarose powder (Sigma A9539) in aqueous media with different viscosities, i.e. water and 2 and 5% w/v dextran (Sigma D1037) solutions. Agarose solutions were stirred until boiling and then cast into custom moulds, obtaining 13 mm diameter-8 mm height cylindrical samples.

Polycrylamide (PAAm) gels were prepared dissolving 15.6% w/v of Acrylamide monomer (Biorad) in water and 2 and 5% dextran solutions (Sigma D1037); with the addition of 0.02% w/v Bis-acrylamide (Sigma M7256), 0.084% w/v of ammonium persulfate (Biorad) and 0.056% v/v Tetramethylethylenediamine (TEMED) (Sigma T9281). All the components were mixed and the final solution was first degassed for 2 minutes and finally cast in the custom molds. The polymerization is completed in 90 minutes at room temperature.

B. Viscosity Measurements and Mechanical Testing

Dynamic viscosity of the different dextran solutions (0%, 2% and 5%) was measured with an AMVN Automated micro-viscometer (Anton Paar GmbH, Germany), three different temperatures (16°C, 21°C and 26°C), using a capillary with 1.6 mm inner diameter and a 1.5 mm diameter ball.

The sponges and gels were tested using the epsilon-dot method (Tirella et al., 2013). Unconfined bulk compression tests were performed at different constant strain rates (0.0005 – 0.001 – 0.005 and 0.01s-1) with a ProLine Z005 Zwick/Roell (Germany). The mean stress-time curves were globally fitted using the relative equation for the standard linear solid model, obtaining E1, E2 and η and consequently the equilibrium modulus (Eeq), the instantaneous modulus (Einst) and the relaxation time (τ) as described in (Tirella et al., 2013). In particular, sponges were testes both in wet and dry conditions. Finally, a 1-way ANOVA analysis was performed (GraphPad Prism) to investigate the effect of the dextran variations on viscoelastic properties.

III. Results And Discussions

As expected, viscosity increases with increasing dextran concentration (Figure 1).

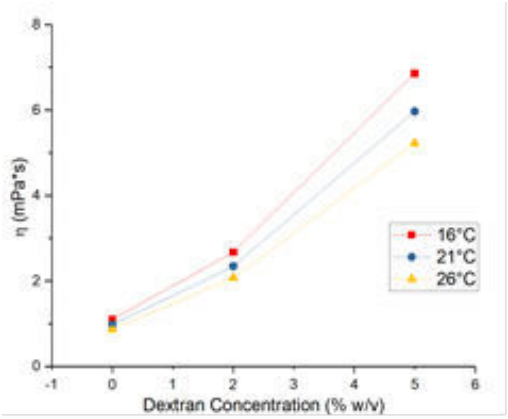

Figure 1. *Dynamic viscosity of the solutions in function of dextran concentration.*

The results of the mechanical tests for the sponges are shown in Figure 2: the relaxation time increases significantly with increasing dextran concentration; while, both Einst and Eeq do not vary significantly for the wet sponges. The dry sponges have significantly higher moduli and significantly lower τ.

Figure 3 shows the results for agarose gels: the increase of viscosity of the liquid phase is reflected in a significant reduction of both instantaneous and relaxation time, reflecting the action on the viscous component of the system (i.e. E2 and η, which are placed in series in the SLS parallel model). E_{eq} does not vary significantly between 0 and 2%, and only for 5% dextran concentration a reduction of the equilibrium

modulus is observed, suggesting that after this threshold also the properties of the solid network are altered.

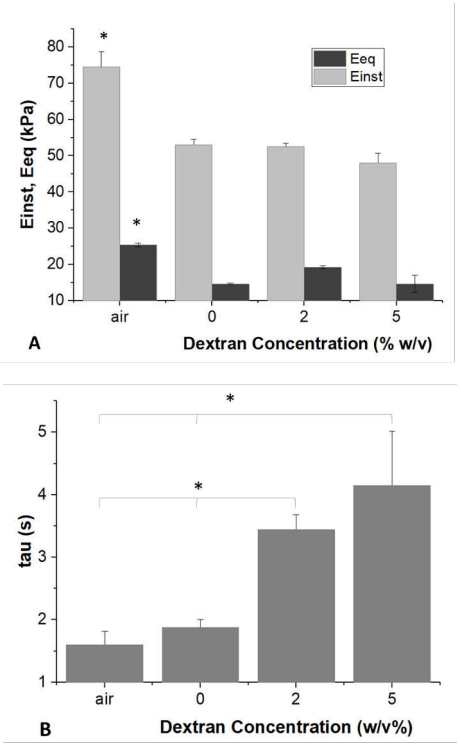

*Figure 2. Instantaneous and equilibrium moduli (a) and characteristic relaxation time (b) of sponges as a function of different dextran concentrations. *p<0.05.*

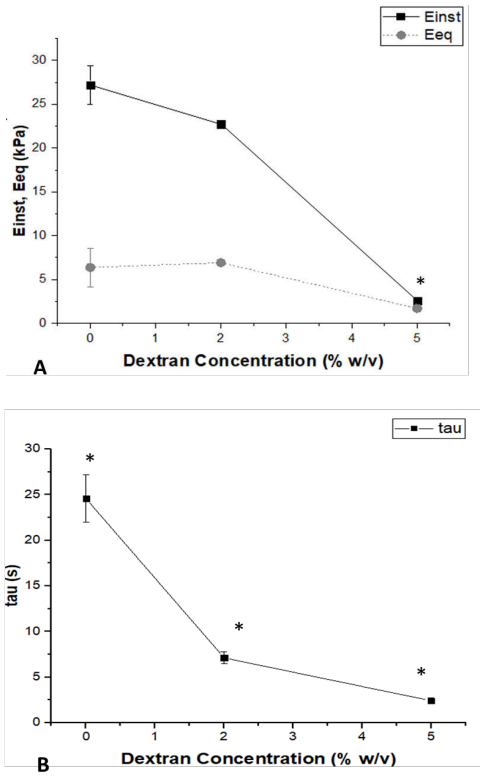

*Figure 3. Instantaneous and equilibrium moduli (a) and characteristic relaxation time (b) of Agarose samples as a function of different dextran concentrations. *p<0.05.*

In the case of PAAm gels (Figure 4), Einst and τ follow the same decreasing trend observeddescribed for agarose, while the equilibrium modulus is almost constant with increasing dextran concentration.

The ANOVA analysis shows a significant reduction of both instantaneous modulus and characteristic relaxation time.

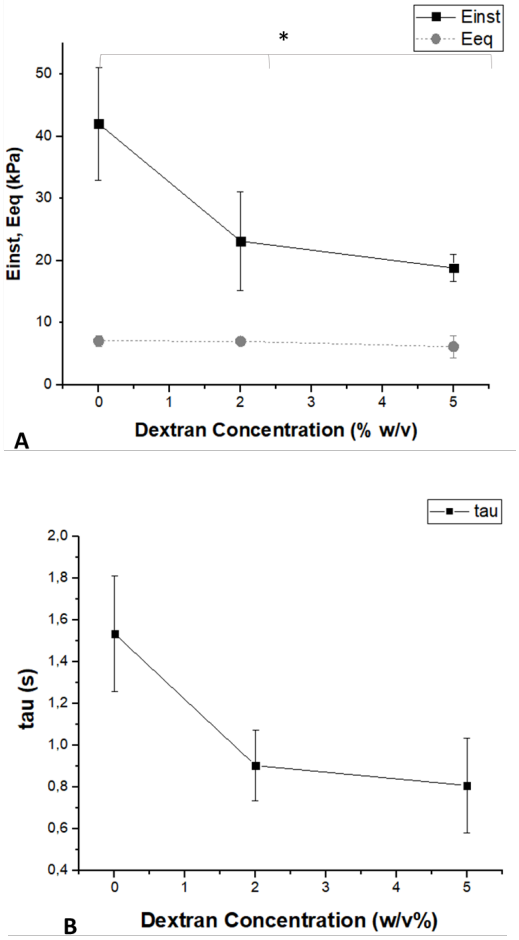

*Figure 4. Instantaneous and equilibrium moduli (a) and characteristic relaxation time (b) of PAAm samples as a function of different dextran concentrations. *p<0.05*

In hydrogels, water molecules bonds to polymeric chains, contributing to the stiffness of the gel [12]. Therefore, the addition of dextran in the liquid phase interferes with hydrogen bonding between agarose chains and water, thus resulting in a stiffness reduction. A minor quantity of entanglements causes also an enhanced sliding between the chains, which result in an increase of the damping component.

Another consideration regards the conformation of the polymer chains, which change from coil in good solvent to globular in poor ones. This effect depends from the polymer–solvent interaction that can be described with the Huggins constant k and it is related with the specific viscosity [η]. In particular, [η] increases with increasing intermolecular interaction, and decreases with increasing intramolecular interaction [13]. This can explain well the behaviour of our hydrogels. In fact, our results suggest that as dextran concentration increases, water 'needs less time to flow' (i.e. τ

decreases), which means that water is less bonded to the chains and flow easily through the network. On the contrary, in the control (0% dextran) the bond of water with the network is higher and thus it needs more time to flow (i.e. higher τ). We hypothesize that Eeq does not vary significantly because the addiction of dextran is not modifying the elastic network itself, but only the interaction between the aqueous and solid phase. On the other hand, Einst varies significantly according to the degree of water-polymer binding, i.e. the instantaneous stiffness is higher for an strong bond and lower in the case of a weak water-polymer bond. On the contrary, in the case of the sponges, there is a weak interaction between the spongiosum structure and the liquid phase, thus the only factor ruling on the flow is the viscosity of the solution. In conclusions, this suggests that when there are strong interactions between the two phases of a gel, varying the viscosity of the liquid phase adding a different compound in solution alter the interaction between the liquid and solid structure thus modifying the viscous response. In our case, dextran reduced this interaction in both agarose and PAAm gels, facilitating the liquid flow (lower relaxation time). On the contrary, when these interactions are lower, as in the case of the sponges, increasing the viscosity of the liquid phase results in an increase of τ, i.e. the time required for its flowing is higher.

IV. Conclusion

Considering the importance of the viscous component in tissues and biomaterials, in this study the viscosity of the liquid phase of sponges and agarose and polyacrylamide hydrogels was modulated by adding increasing concentrations of dextran to the aqueous medium. Mechanical tests showed that the relaxation time increases as the viscosity of the solution increases for the sponges. Since there is a low interaction between the liquid phase and the spongiosum structure, the time necessary for the liquid flow depends only from its viscosity. However, for the gels, there is a strong interaction between water and the polymeric network, thus adding dextran alters significantly the interaction of the liquid and solid phase. As a consequence, the τ is no longer related only to the solution viscosity, but, since water is less bonded to the solid network, it flows easily as the concentration of dextran increases. Moreover, while the instantaneous modulus is not altered in the sponges, it follows a decreasing trend with increasing dextran concentration for the gels. In fact, the more rapid is the flow of the aqueous phase, the less strong is its contribution to the initial compressive strength. In conclusion, this method is suitable to modulate material viscoelasticity, demonstrating that even acting only on the damping component, instead on the crosslinking of the 'elastic network', affects the whole mechanical properties and suggesting that a deeper study is necessary on the contribution of the liquid phase composition in different materials (with particular regards to the interaction between the liquid and solid phases, which is a critical element for determining the resultant viscoelastic behaviour). Indeed, an increase of viscosity of the solution not always results in an increase of the 'global viscosity of the gel' (i.e. in an increase of τ) as one could expect a priori, but the relaxation time can increase or decrease in the case of low or high solid-liquid interaction respectively.

References

[1] A. S. Hoffman, "Hydrogels for biomedical applications," *Adv. Drug Deliv. Rev.*, vol. 64, pp. 18–23, 2012.

[2] E. E. Charrier, K. Pogoda, R. G. Wells, and P. A. Janmey, "Control of cell morphology and differentiation by substrates with independently tunable elasticity and viscous dissipation," *Nat. Commun.*, vol. 9, no. 1, pp. 1–13, 2018.

[3] A. R. Cameron, J. E. Frith, and J. J. Cooper-White, "The influence of substrate creep on mesenchymal stem cell behaviour and phenotype," *Biomaterials*, vol. 32, no. 26, pp. 5979–5993, 2011.

[4] O. Chaudhuri *et al.*, "HHS Public Access," 2015.

[5] K. M. Mabry, R. L. Lawrence, and K. S. Anseth, "Dynamic stiffening of poly(ethylene glycol)-based hydrogels to direct valvular interstitial cell phenotype in a three-dimensional environment," *Biomaterials*, vol. 49, pp. 47–56, 2015.

[6] S. Bhattacharya, A. Srivastava, and A. Pal, "Modulation of viscoelastic properties of physical gels by nanoparticle doping: Influence of the nanoparticle capping agent," *Angew. Chemie - Int. Ed.*, vol. 45, no. 18, pp. 2934–2937, 2006.

[7] N. Shi, H. Dong, G. Yin, Z. Xu, and S. Li, "A smart supramolecular hydrogel exhibiting pH-modulated viscoelastic properties," *Adv. Funct. Mater.*, vol. 17, no. 11, pp. 1837–1843, 2007.

[8] J. I. Jay *et al.*, "Modulation of Viscoelasticity and HIV Transport as a Function of pH in a Reversibly Crosslinked Hydrogel," *Adv. Funct. Mater.*, vol. 19, no. 18, pp. 2969–2977, Sep. 2009.

[9] M. Mensitieri, L. Ambrosio, L. Nicolais, D. Bellini, and M. O'Regan, "Viscoelastic properties modulation of a novel autocrosslinked hyaluronic acid polymer," *J. Mater. Sci. Mater. Med.*, vol. 7, no. 11, pp. 695–698, 1996.

[10] G. Mattei, L. Cacopardo, and A. Ahluwalia, "Micro-Mechanical Viscoelastic Properties of Crosslinked Hydrogels Using the Nano-Epsilon Dot Method," *Materials (Basel).*, vol. 10, no. 8, p. 889, Aug. 2017.

[11] G. Mattei, G. Gruca, N. Rijnveld, and a. Ahluwalia, "The nano-epsilon dot method for strain rate viscoelastic characterisation of soft biomaterials by spherical nano-indentation," *J. Mech. Behav. Biomed. Mater.*, vol. 50, pp. 150–159, 2015.

[12] K. te Nijenhuis, "Agarose," in *Thermoreversible Networks, Advances in Polymer Science. vol 130*, Springer, Berlin, Heidelberg, 1997, pp. 194–202.

[13] S. Wu and R. A. Shanks, "Conformation of polyacrylamide in aqueous solution with interactive additives and cosolvents," *J. Appl. Polym. Sci.*, vol. 89, no. 11, pp. 3122–3129, 2003.

Computational modeling of the interaction of lymphatic and vascular microcirculation in uremia

L. Possenti[1], G. Casagrande[1], S. Di Gregorio[1,2], P. Zunino[2], M.L. Costantino[1]
[1] *Department of Chemistry, Materials and Chemical Engineering Giulio Natta, Politecnico di Milano, Italy*
[2] *MOX, Modelling and Scientific Computing, Department of Mathematics, Politecnico di Milano, Italy*

***Abstract*—Microcirculation has a key role in the homeostasis maintenance in physiology and uremia. Aim of the study is to develop a computational model of the interaction of a vascular network with the surrounding tissue, accounting for non-linear lymphatic contribution. The 3D/1D micro-scale finite element model results appropriate to describe microcirculation fluid balance, making possible the study of local equilibriums and effects of variations in capillary density and network morphologies.**

***Keywords*—microcirculation, fluid homeostasis, uremia, finite element model.**

I. INTRODUCTION

MICROCIRCULATION have a key role in the homeostasis maintenance in physiological and uremia conditions. Moreover, the role of microcirculation in the toxins and fluid removal from tissues during hemodialysis is largely known. Due to the complexity of such phenomena, a comprehensive approach is required accounting for: (i) capillaries-to-tissue interactions taking into consideration capillary wall permeability; (ii) hydraulic and oncotic pressures; (iii) microvasculature morphology and capillary density; (iv) blood properties along with hematocrit heterogeneity within the vessels network [1]; (v) extra vascular properties; (vi) the presence of lymphatic system. Recently, microcirculation alterations have been pointed out in uremic patients, also considering the effects of hemodialysis, in terms of worsening of peripheral perfusion and reduced capillary density [2]. Aim of this study is to develop a computational model able to describe the interaction of a vascular network with the surrounding tissue, accounting also for the contribution of lymphatic system. With this model, differences in local equilibrium peculiar of healthy and uremic subjects can be analyzed and studied at the micro-scale.

II. MODEL

A finite element model of microcirculation interactions with the surrounding interstitium has been implemented using GetFEM++ [3]. Starting from a previous work [4], the model has been improved combining different features as follow: (i) coupled capillary and interstitial flow; (ii) realistic vasculature; (iii) hematocrit dependent flow properties (Faharaeus-Lindqvist effect); (iv) prediction of Red Blood Cells (RBCs) distribution along the vasculature (simulating plasma skimming effect); (v) non-linear description of the lymphatic drainage. Then, the model has been tested and used to analyze fluid balance and hydraulic pressure at microcirculatory level in healthy and uremic subjects.

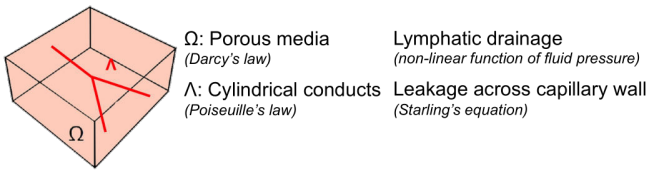

Fig. 1: Schematic view of a vessel network (Λ) and the surrounding tissue (Ω)

A. Model description

This model combines equations on two different domains, thus we defined the capillary network as a 1D domain called Λ and a 3D domain, Ω, for the interstitium. The latter is modeled as a 3D portion of an isotropic porous medium and thus it is described by means of Darcy's law with a hydraulic conductivity k and a fluid viscosity μ_t. Poiseuille's law is used to describe blood flow inside the capillaries, considered as cylinders with rigid vascular walls [3], referring to vessel radius R and a fluid viscosity μ_v. The schematic representation of the domains is shown in figure 1. The network is coupled to the interstitium, due to the capillary wall permeability. The amount of fluids that cross the vessels wall is computed employing the Starlings equation:

$$\varphi_{vessels} = 2\,\pi\,R\,L_p\,((p_v\,-\,\bar{p}_t)\,-\,(\pi_v\,-\pi_t)) \qquad (1)$$

where Lp is the hydraulic conductivity of the capillary membrane, σ is the reflection coefficient of Starling's equation, π indicates oncotic pressures and the subscripts v and t indicate vessels and tissue respectively. The term $\bar{p}_t$ denotes the averaged pressure on a cross section of the capillary wall and is computed as described in [4]. By means of a homogenized approach, lymphatic drainage is accounted as a distributed sink term in the interstitium continuity equation, as a function of tissue properties, and not including a lymphatic vessels geometry. This approach is usually employed in FEM analysis of microcirculation [5]-[7] due to difficulty in achieving the full geometrical description of lymphatic vessels (e.g large number, structure, and dimension).

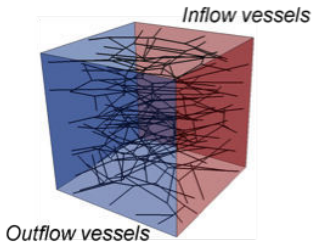

Fig. 2: Domain and boundary conditions

B. Vascular network modeling

Simulations have been carried out considering a fairly complex and realistic model of microvasculature. The network we use satisfies the following criteria: (i) its morphology respects the optimal distribution of a Voronoi tessellation; (ii) the aspect ratio of each branch (L_i/R_i) is large enough to justify the one-dimensional flow assumption; (iii) the radii of branches merging at any junction satisfy Murray's law; (iv) the surface to volume density of the capillaries satisfies the desired values of S/V. The networks have been generated by a complex (nonlinear) iterative procedure. In order to set proper boundary conditions, only 4 faces of the cube intersect network branches, whereas the 2 parallel to the network planes, do not intersect any network branches. The 4 lateral faces of the cube are subdivided in two neighboring arteriolar faces (inflow vessels) and two neighboring venular faces (outflow vessels) as in Fig. 2. The pressure drop from arteriolar to venular endpoints of the network drives the flow along the network: we enforce 32 mmHg and 15 mmHg at the arteriolar and venular endpoints respectively [8]. The developed protocol is controlled by a fairly small number of parameters, set according to the literature so as to describe healthy and uremic subjects.

C. Hematocrit dependent flow properties

Rheology of blood in such small vessels is dependent on vessel dimension and on hematocrit: this effect is known as the Faharaeus-Lindqvist effect. We adopt the equation defined by Pries et al. [9] in order to describe this phenomenon. As a consequence, in the proposed model, the viscosity of blood is not constant in different vascular branches.

D. RBCs distribution along the vasculature

In a complex network, hematocrit is not constant: indeed, in presence of bifurcations, RBCs are carried into the daughter vessels depending on their diameter and flow rate [10]. We refer to empirical relationship recently reviewed by Secomb [10]:

$$H_\alpha = FQE_\alpha \cdot H_f \cdot \frac{Q_f}{Q_\alpha} \tag{2}$$

where H is the discharge hematocrit, Q is the flow rate, the parameter FQE is computed as described in their work, and the subscripts α and f indicate a daughter vessel and the father vessel respectively. Due to these phenomena, the solution of the problem must be reached by an iterative method accounting for the interdependence of the analyzed variables: RBCs behavior at bifurcations depends on the flow rate of the vessels that is influenced by viscosity and eventually by hematocrit.

E. Lymphatic drainage description

Following the physiologic description and neglecting oncotic pressure differences in between lymph and interstitial fluid [11], the lymphatic flow rate is modeled as a sigmoid function: a non linear relationship with interstitial pressure with a saturation flow rate.

$$\varphi_{lymphatic} = \varphi_{max} - \frac{\varphi_{max} - \varphi_{min}}{1 + \exp\left(\frac{p_t - p_{50}}{slope\ factor}\right)} \tag{3}$$

To identify parameters values, we refer to Chamney et al. [12] adopting: the same increase of pressure necessary to reach the maximum lymphatic drainage from the working point; the maximum and minimum values of the lymphatic drainage scaled to obtain a volumetric term, namely the lymphatic drainage per unit of volume; the same lymphatic drainage at the working point, whereas the corresponding interstitial pressure is identified with a tiny sub-atmospheric pressure as reported in [13].

F. Simulations

Computational tests regard both physiological and pathological conditions, with reference to uremia. Two different vessel networks are considered to match physiological and pathological capillary density as reported in table 1. Considered parameters are taken from the literature; in order to simulate uremia, the following parameters are modified (table 1): (i) discharge hematocrit, directly related to blood viscosity; (ii) capillary wall properties in terms of hydraulic conductivity and reflection coefficient; (iii) oncotic pressure difference across capillary membrane; and (iv) capillary density. First, each single parameter has been varied to assess its influence on the obtained results. After the uremic conditions was simulated considering the simultaneous variation of all the parameters.

TABLE I: MODEL PARAMETERS MODIFIED TO DESCRIBE HEALTHY AND UREMIC SUBJECTS

	Healthy	(ref)	Uremic	(ref)
Ht (%)	45	[14]	35	[15],[16]
Lp ($m^2\,s\,kg^{-1}$)	10^{-12}	[4]	8.80×10^{-12}	[17]
$\Delta\pi$ (mmHg)	25	[8]	19	[15],[16]
σ (-)	0,95	[18]	0,75	[17],[18]
S/V (m^{-1})	7000	[19]	4900	[19],[20]

We remark that information at such a small scale, and especially for pathological conditions, are not easily found due to difficulties in measurement. For what concern the lymphatic drainage, no difference is reported in the literature thus we adopt the same sigmoid description for both the conditions. In both cases we address the equilibrium conditions in which fluid is not leaving the domain, meaning that all the surrounding tissue have the same mean interstitial pressure: for this reason we adopt homogeneous Neumann conditions.

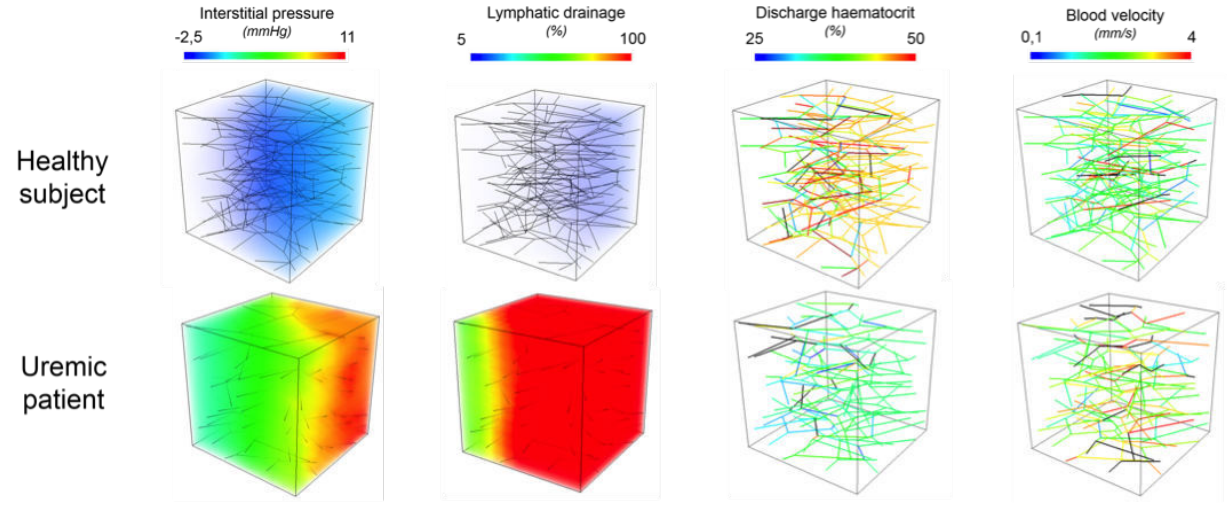

Fig. 3: Comparative results for healthy and uremic subjects in terms of interstitial pressure, lymphatic drainage, discharge hematocrit, and blood velocity

III. RESULTS

A. Vascular network

The iterative procedure results in a total of 3×10^4 configurations: the selection based on acceptable vessels radii (mean of $4\,\mu m \pm 5\,\%$ and $2\,\mu m < radius < 6 \mu m$) produce a final number of networks equal to 10^4. These networks allow us to successfully assemble geometries depicting different capillary density.

B. Interaction with the interstitium

The pressure in the network progressively decreases from the arteriolar to the venular ends of the microvasculature, as expected. The blood velocity, however, is not uniformly distributed and several network branches are crossed by a flow rate significantly lower than the average. Looking to the interaction of the microvasculature with the interstitium, we observe that the variation of pressure through the capillary bed influences the pressure in the interstitial space. In proximity of the arteriolar end of the network, an increased interstitial pressure is observed, while it decreases below average next to the venules. This pressure gradient in the vasculature induces a secondary, weaker gradient in the interstitium, generating modest flows in the interstitial volume. The hematocrit is characterized by a high spatial variability.

C. Comparison of healthy and uremic conditions

For what concerns uremic conditions, a greater interstitial pressure is reported along with a greater lymphatic drainage, as shown in figure 3. The non-linear relationship implemented for lymphatic drainage produces a strong non-linear effect near to the saturation flow rate. A gradient in interstitial pressure is present in this condition, and it is more pronounced than in physiological conditions. The heterogeneity in hematocrit and velocity is confirmed in both the conditions; in addition, velocity of blood flowing within the network is quite higher when uremia is simulated.

D. Effect of parameters alteration

The effect of each parameter variation is shown in figure 4. For both mean interstitial pressure and net filtration, the most important variations are caused by oncotic pressure difference or capillary wall properties (reflection coefficient and hydraulic conductivity). Moreover, the overall effect, namely the uremic conditions, is not equal to the sum of each parameter variation, highlighting interactions in between parameter alterations. Lastly, due to the boundary conditions set (enforcing pressure at vessels in- and end-point), the hematocrit variation produces no effect on both the variables considered in the graph but a variation of flow rate flowing in the vasculature.

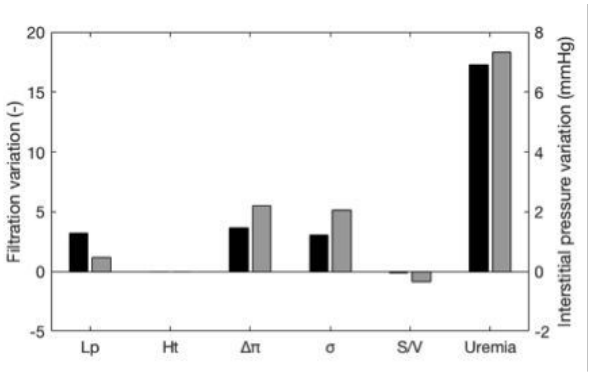

Fig. 4: Effect on the variation of a single parameter, with respect to physiological conditions, on filtration (black) and interstitial pressure (grey). Alterations are computed as follows: $NFR_{var} = (NFR_i - NFR_{physio}) \,/\, NFR_{physio}$; $p_{t,var} = (p_{t,i} - p_{t,physio})$

IV. DISCUSSION

The analysis of the results allows us to highlight the key role of the lymphatic drainage modeling, in order to properly model fluid homoeostasis at microcirculatory scale. First of all, we compare the models performance in both the considered conditions and then a comparison with the few data available in the literature is reported. The use of a non-linear approach for the description of the lymphatic drainage allows reaching

a correct description of the phenomena, considering flow from tissue to vessels, but not the opposite. For what concerns pathological conditions, as expected, the working point is shifted to higher hydraulic pressures (figure 3). The lymphatic system acts draining fluid in the whole domain with higher intensity than in physiological conditions, respecting the maximum 20-fold increase with respect to physiological condition reported in the literature [12],[14]. We remark that a non-linear modeling approach for the behavior of the lymphatic system should be used to correctly describe local phenomena both in physiological and pathological conditions [5]: indeed, the local effects are not negligible to accurately describe homoeostasis phenomena within the microenvironment. Looking at interstitial pressure, a gradient is always observed in the tissue, resulting more evident when pathological conditions are simulated.

A. Comparison with literature

Literature data about microvasculature and fluid homoeostasis at this small scale are difficult to be found and often still report a big acceptable range of variation. In order to compare results of our model with the few available data, we consider the analyzed variables: interstitial fluid pressure, net filtration rate and lymphatic drainage. For the interstitial fluid pressure values agree with those reported by Ebah and colleagues [13]: they reported for healthy volunteers an interstitial pressure of $0.9 \pm 1.3\, mmHg$ and for the pathological conditions $4.6 \pm 4.2\, mmHg$. Thus, comparing physiological to pathological conditions, the increase of interstitial pressure is correctly reproduced by the model. For NFR, the value reported for the entire body in physiological conditions is about $2\, ml/min$ [14], which is in agreement with our results ($2.09\, ml/min$). The increase of pressure is also related to greater net filtration rate from the network to the tissue with a 18-fold growth reported. Since the equilibrium condition has been addressed, the lymphatic drainage balances the net filtration in both cases, with an analogue overall 18-fold increase, that is lower than the maximum allowable as reported in literature [12],[14]. The lymphatic wall permeability is found to be in the same range usually accepted and considered by the literature [5].

B. Hematocrit

Hematocrit is characterized by a high spatial variability, in line with the observations of Figure 3. Thanks to a sophisticated mathematical formulation (3D-1D coupling), advanced numerical solvers and nonlinear description of blood rheology (Fahraeus-Lindqvist and plasma skimming effects), we are able to apply the model to fairly complex network configurations. The results obtained by the model are quantitatively consistent with the physiological values expected for healthy and uremic tissues.

V. CONCLUSION

The proposed model of fluid homeostasis in microcirculation allows us to simulate fluid balance by means of tridimensional finite element model for physiological and in particular for pathological conditions. Non-linearity included in the model is found to be necessary to accurately describe the phenomena. However, their inclusions rise the required computational time, which is still acceptable. This work shows the appropriateness of the 3D/1D micro-scale finite element approach to describe microcirculation fluid balance: with respect to current modeling approach of fluid homeostasis it allows a local description and make possible the analyses of the effects related to capillary density variations and different network morphologies (e.g.: tortuosity). Future applications of this model would allow the study of specific peripheral districts in order to better understand microcirculation worsening related to uremia. In addition, we believe that such a model, being a flexible investigation tool, could be successfully employed in different medical research areas, such as oncology, neurology and nephrology.

REFERENCES

[1] Di Gregorio; Master thesis, Politecnico di Milano, AY 2016/2017

[2] Yeh, et al.; An observational study of microcirculation in dialysis patients and kidney transplant recipients, European Journal of Clinical Investigation (2017)

[3] Getfem++ v. 5.0. getfem.org

[4] Cattaneo, Zunino, Computational models for fluid exchange between microcirculation and tissue interstitium, Networks and Heterogeneous Media 9 (1) (2014) 135159. doi:10.3934/nhm.2014.9.135

[5] Possenti, Casagrande, Costantino, Zunino; Int J Artif Organs; 40(8): 382-428, 2017

[6] Siggers, Leungchavaphongse, Ho, Repetto; Mathematical model of blood and interstitial flow and lymph production in the liver, Biomechanics and Modeling in Mechanobiology 13 (2) (2014) 363378.

[7] Sefidgar, Soltani, Raahemifar, Bazmara; Effect of Fluid Friction on Interstitial Fluid Flow Coupled with Blood Flow through Solid Tumor Microvascular Network, Computational and Mathematical Methods in Medicine (2015).

[8] Silverthorn; Human Physiology, 2010

[9] Pries et al.; Resistance to blood flow in microvessels in vivo. Circulation Research. 1994nov;75(5):904915.

[10] Secomb; Blood Flow in the Microcirculation. Annu. Rev. Fluid Mech. 2017;49(August):44361.

[11] Swartz and Fleury, Interstitial Flow and Its Effects in Soft Tissues, Annual Review of Biomedical Engineering 9 (1) (2007) 229256.

[12] Chamney et al.; Fluid balance mod- elling in patients with kidney failure, Journal of Medical Engineering and Technology 23 (2) (1999)

[13] Ebah et al.; Subcutaneous interstitial pressure and volume characteristics in renal impairment associated with edema, Kidney International 84 (5) (2013) 980988.

[14] Hall; Guyton and Hall Textbook of Medical Physiology 13th Edition, 2015

[15] Database from INTERREG IT-CH 2007-2013: DialysIS (Dialysis therapy between Italy and Switzerland) Project - Grant ID 33570710., www.dialysis-project.eu.

[16] Vito, Casagrande, Bianchi, Costantino; How to extract clinically useful information from large amount of dialysis related stored data, Proceedings of the Annual International Conference of the IEEE Engineering in Medicine and Biology Society, EMBS 2015-November (2015) 68126815.

[17] Harper, Tomson, Bates, Human uremic plasma increases microvascular permeability to water and proteins in vivo, Kidney International 61 (4) (2002) 14161422.

[18] Levick; Capillary filtration-absorption balance reconsidered in light of dynamic extravascular factors., Experimental physiology 76 (1991) 825 857.

[19] Baxter, and Jain; Transport of fluid and macromolecules in tumors. II. Role of heterogeneous perfusion and lymphatics, Microvascular Research 40 (2) (1990) 246263

[20] Amann et al; Reduced capillary density in the myocardium of uremic ratsa stereological study., Kidney international 42 (5) (1992) 10791085.

Mechanical characterization of the passive elastic behaviour of muscular fibres and bundles

P.G. Pavan[1,2], L. Marcucci[2,3], C. Reggiani[2,3] and A.N. Natali[1,2]
[1] *Department of Industrial Engineering, University of Padova, Italy*
[2] *Centre for Mechanics of Biological Materials, University of Padova, Italy*
[3] *Department of Biomedical Sciences, University of Padova, Italy*

***Abstract*— In the present work, tensile properties of human musculoskeletal tissue are experimentally evaluated in inactivated single muscle fibres, both for slow and fast isoform, and bundles. Specific exponential functions are adopted to model the tensile passive behaviour of fibres and bundles and differences emerged from experimental testing are pointed out. Numerical formulations usually adopted in the literature to mimic the tensile behaviour of musculoskeletal under passive conditions are also considered in the light of the experimental data obtained.**

It emerges that in passive conditions fast and slow fibres differ for the initial length and stiffness. Furthermore, muscular bundles are stiffer than single fibres. It is made the hypothesis that this can be attributed to a different percentage or structural characteristics of ECM within the bundle.

The mechanical characterization of ECM by means of appropriate constitutive formulations can help in investigating its role in the transmission of contractile force in musculoskeletal system. This aspect can be of interest in the case of pathologies and aging and in the evaluation of consequent effects.

***Keywords*—Musculoskeletal Tissue, Passive Behaviour, Mechanical Testing, Constitutive Modelling.**

I. Introduction

EXTRACELLULAR matrix (ECM) in musculoskeletal system is responsible for the stiffness of the tissues in passive conditions, but it can have also a role in determining the transmission of the contractile force. An alteration of the mechanical properties of ECM can be investigated as a possible reason for the observed reduction of contractile force transmission in the case of specific pathologies [1] or, simply, due to aging [2], [3].

For these reasons, it is important to include a precise characterization of this component when multiscale numerical models of large muscles, such as diaphragm [4], are developed to analyse the functional response of whole organs. However, a precise physiological characterization is still lacking. Models generally mix the passive tension component generated by the titin, a protein that interlinks actin and myosin filaments in each sarcomere to prevent overstretch in fibres, with the component generated by ECM, which acts at the bundle level [5]. This is generally due to the difficult of experimentally analyse the ECM alone.

Moreover, a common practice in finite element method (FEM) based modelling, as evident from the literature, is to scale this mixed passive tension to the maximum active tension, whereas there is no evidence that a physiological relationship between these two components exists.

In this work, we have defined a new protocol to estimate the passive component of ECM starting from the analysis of passive behaviour in single fibres, both of fast and slow isoform, and bundles. Specific constitutive equations are proposed for fibres and bundles and fitted to experimental data, while it is shown that constitutive formulations commonly adopted in the literature are not consistent with their mechanical response.

II. Materials and Methods

A. Experimental testing

Muscle fibres and bundles biopsies were taken from human subjects from *vastus lateralis* muscle with approval of the local ethical committee and informed consent of the donors. Biopsies samples were placed in ice-cold skinning solution, and segments of single fibres or groups of fibres with the surrounding ECM were dissected. Whole duration of the experiments and low temperature were aimed to preserve the sample and, in particular, to avoid proteolytic degradation. A total of 11 fibres and 11 bundles were analysed from male older adults in their 7th decade of life. The length of single fibres was in the range 500÷1,000 μm. Both the ends of the specimens were fixed through aluminium T-shaped clips, leaving 1-2 mm of free region. Each fibre or bundle was then transferred to the apparatus (Fig. 1a-b) and mounted horizontally between two hooks: one linked to the puller to control the length of the specimen and the other to the force transducer.

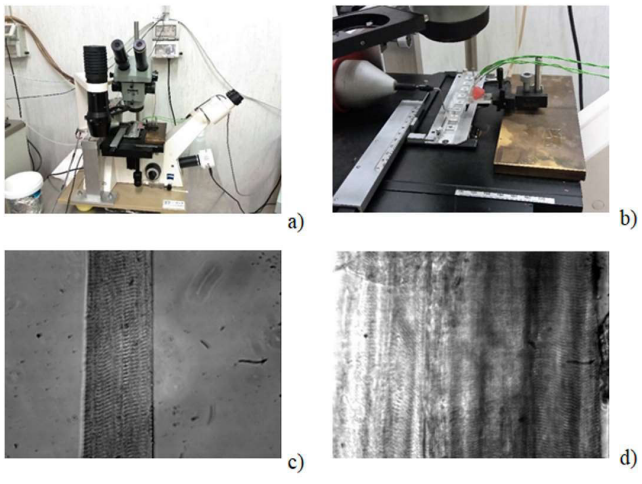

Fig. 1: Experimental setup for the mechanical testing (a, b), single fibre (c) and bundle (d).

The hooks and the specimen were placed above an aluminium plate where drops of relaxing, pre-activating and activating solutions were laid (see Doria et al. [6] for composition).

Fibres and bundles (Fig. 1c-d) were initially immersed in the drop with a relaxing solution. The sarcomere length was manually adjusted to the shorter unloaded configuration sufficient to keep the specimen straight (L_0). The length of the sarcomeres in the central portion and the specimen cross-section (d_0) were measured through an electronic image with an optical microscope (Zeiss, Axiovert 35, equipped with a digital camera Optikam B5, OPT), while the total length of the fibre or bundle L_0 with a direct observation trough an optical microscope (Konus Diamond, KONUS at 40x magnification).

Fibre area was estimated by the fibre diameter assuming a circular section. Bundle area was more difficult to be estimated because we had only the vertical view of its section. We estimated the number of fibres and measured their diameter and area. The cross sectional area of the fibres was in the range 4,000÷6,000 μm^2, while the cross sectional area of the bundles was 5 to 10 times that of single fibres. In some bundles, we tested the method comparing the estimated area with the one obtained by direct observation of a cryo-cross section of the bundle. Errors was within 10%.

The fibre or bundle was then stepwise elongated passively of about 10% of L_0 each step, to a total of about 200% of L_0. At each step, the passive force after viscous recovery were recorded as well as the length of the sarcomeres in the central region and the cross-section. Force output was recorded at a frequency of 1 kHz through a strain gauge (Strain Gauge Force Transducer AME-801; SensorOne, Sausalito, CA, connected with an A-D converter interface CED 1401 plus, Cambridge Electronic Design, Cambridge, UK) and elaborated with Spike® software. Once reached the maximum stretch, the fibres or bundles were allowed to shorten back to the length L_0 and transferred to a pre-activating solution for about 30 seconds, then to the activating solution for recording the maximum isometric active force generated. During isometric contraction, a quick shortening was applied to reduce active tension to zero, followed by a re-stretch after 5 ms.

Nominal stress was obtained as tensile force normalized to the initial undeformed cross sectional area; sarcomere, fibre and bundle stretch was obtained by considering the current length normalized to the initial undeformed length.

The tension-time trace during the isometric phase of tension redevelopment was fitted with a single exponential curve and the obtained time constant used to distinguish between fast and slow isoforms.

B. Literature constitutive modelling of passive behaviour

The three element Hill's model [7] is frequently assumed to describe the mechanical response of muscles. The model consists of a contractile element (CE) in series with an elastic element (SE). A further elastic element (PE) is coupled in parallel with the branch CE-SE to describe the tensile response under passive condition. This model is whether adopted for muscular tissue, bundles or single fibres. When applied to the muscular tissue, an isotropic term related to ECM is included as additional stress response to the one associated to the spatially oriented muscle fibres.

Different numerical formulations are proposed in the literature for PE. Tang et al. [8], for example, assume that the nominal stress in muscle tissue due to the fibres under passive condition is given by the equation:

$$P(\lambda) = 4P_0(\lambda - 1)^2 \qquad (1)$$

where $\lambda = L/L_0$ is the stretch with respect to the optimal or initial length of the fibres L_0, being L the deformed length, while the stress-like parameter P_0 is the maximum isometric stress. Alternatively, an exponential function [9], [10] is also proposed to describe the stress-stretch response of PE:

$$P(\lambda) = 2P_0 aA(\lambda - 1)exp\left[a(\lambda - 1)^2\right] \qquad (2)$$

for $\lambda > 1$, where P_0 is again the maximum isometric stress, a is a dimensionless parameter and A is a stress-like parameter. Notably, all the formulations use P_0 as a fibre characteristic parameter, despite it is recognized that the passive tension in muscle fibres is generated by different structures than active tension.

C. Proposed constitutive modelling of passive behaviour

Considering the stiffening behaviour shown by the fibres in tensile passive condition, the following numerical formulation is assumed in this work to describe the stress-length response:

$$P(L) = A\left[\exp\left(\frac{L}{L_0} - 1\right| - 1\right] \qquad (3)$$

where L is the mean current length of the sarcomeres and A and L_0 are constitutive parameters, to be determined through a fitting procedure of the previous equation to experimental data. The parameter L_0 is the initial length of a fibre and the stress-like parameter A represents its initial tangential stiffness, since the latter can be simply deduced as:

$$\left.\frac{\partial P(\lambda)}{\partial \lambda}\right|_{\lambda=1} = A \qquad (4)$$

having defined the stretch as $\lambda = L/L_0$. A multiple fitting was made on the experimental data of fast and slow fibres, separately, by minimizing the following error measure with respect to A and L_0:

$$\Xi = \sqrt{\frac{1}{n_{exp}}\sum_{i=1}^{n_{exp}}\left[P_{i,exp} - P_{num}\left(L_{i,exp}, A, L_0\right)\right]^2} \qquad (5)$$

where n_{exp} is the number of experimental data and $L_{i,exp}$, $P_{i,exp}$ are the measured values of nominal stress and sarcomere length, respectively.

The stress-length behaviour of the muscular bundles is described by assuming the following exponential function:

$$\begin{aligned} P_b(L) = {} & \alpha_f A_f\left[\exp\left(\frac{L}{L_{0f}} - 1\right| - 1\right] + \\ & + \alpha_s A_s\left[\exp\left(\frac{L}{L_{0s}} - 1\right| - 1\right] + \\ & + \alpha_b A_b\left[\exp\left(\frac{L}{L_{0b}} - 1\right| - 1\right] \end{aligned} \qquad (6)$$

In the above equation, L is the current length of the bundle, while (A_f, L_{0f}) and (A_s, L_{0s}) are the pairs of values determined in the fitting of experimental data of fast and slow fibres,

respectively. The parameters A_b and L_{0b} represent a parameter related to the initial stiffness of the bundle and its stress-free length, respectively. The dimensionless parameters α_f, α_s and α_b are the volume fraction of fast fibres, low fibres and ECM in the bundle, which respect the condition:

$$\alpha_f + \alpha_s + \alpha_b = 1 \qquad (7)$$

These values are calculated as average, by estimating the areal fraction of the different components from images of the transversal sections of the bundles, obtained with a cryo-section method. The fitting of equation (6) to experimental data is obtained minimizing a function of the type (5), where the contribution to stress of fast and slow fibres is considered only for $L > L_{0f}$ and $L > L_{0s}$, respectively.

Finally, equation (1) and (2), which have been proposed in the literature, are fitted to experimental data of single fibres to compare them with those proposed in this work.

III. RESULTS

From experimental testing of single skinned fibres, it appears the stretch of a whole fibre is generally greater than the stretch of the sarcomeres, both for fast and slow fibres (Fig. 2). In what follows, the comparison between the different isoforms of the single fibres and between single fibres and bundles is based on the evaluation of sarcomere stretch.

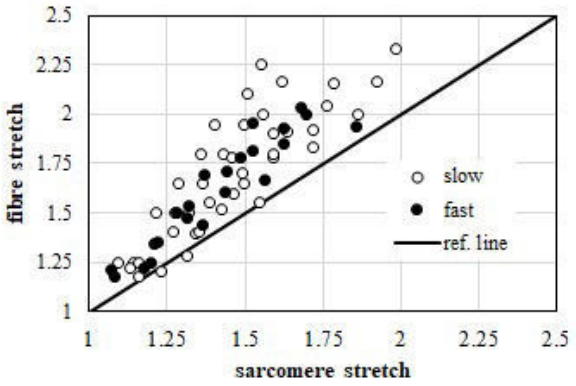

Fig. 2: Comparison of fibre stretch and sarcomere stretch for fast and slow fibres at the same level of elongation. The solid line represents the region of equivalence of the two values. Fibre stretches result greater than bundle stretches.

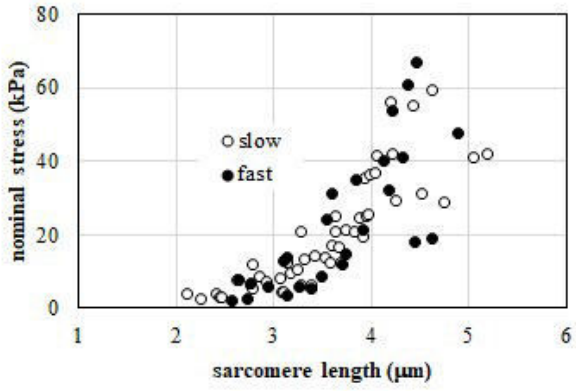

Fig. 3: Experimental values of nominal stress vs. sarcomere length for fast fibres (black circles) and slow fibres (open circles).

Experimental data of nominal stress versus sarcomere length are apparently confused for single fast and slow fibres (Fig. 3) while it emerges a larger difference in the stiffness of the bundles compared to single fibres (Fig. 4). The fitting of equation (3) to experimental data gives the pair of parameters A = 31.730 kPa and L_0 = 2.431 μm for fast fibres and A = 19.726 kPa and L_0 = 2.165 μm for slow fibres. A comparison of fitted analytical curves and experimental data for fast and slow fibres are depicted in Fig. 5, in terms of nominal stress versus stretch L/L_0 where L is the average current length of the sarcomeres and L_0 their optimal length.

The fitting of equation (6) to experimental data is obtained fixing the volume fractions as $\alpha_f = \alpha_s = 0.475$ and $\alpha_b = 0.05$. This is based on the analysis of the percentage of different isoforms in a bundle and the evaluation of the fraction areas of fibres and ECM from staining procedures applied to transversal sections of the bundles. The comparison of experimental data and numerical values are shown in Fig. 6, in terms of nominal stress versus sarcomere length. The contribution of fast and slow fibres and ECM in equation (6) are reported separately and can be compared to the whole stress of the bundles.

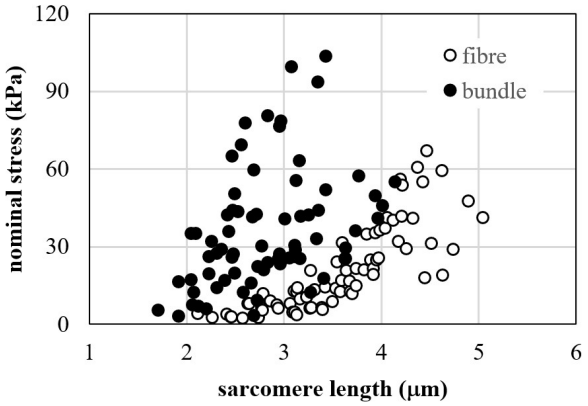

Fig. 4: Experimental values of nominal stress vs. sarcomere length for bundles (black circles) and fibres (open circles).

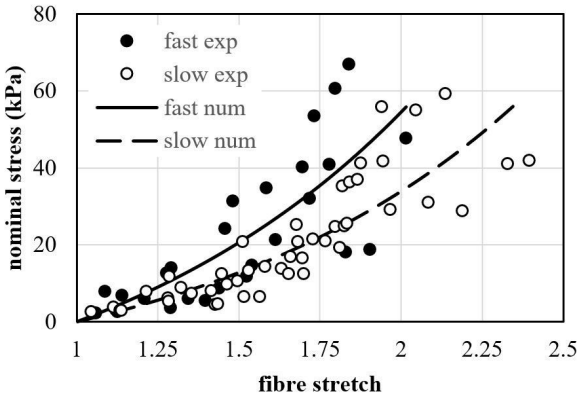

Fig. 5: Comparison of experimental data and analytical curves fitted for fast fibres (a) and slow fibres (b), in terms of nominal stress versus stretch L/L_0, being L the current length of sarcomere and L_0 its initial length.

The fitting of the equations (1) and (2) proposed in the literature and considered in this work are not reported graphically. The fitting of the equation (1) to experimental data

takes the maximum isometric stress P_0 as a free parameter – otherwise the fitting completely fails – obtaining for fast fibres P_0 = 4.035 kPa and L_0 = 1.721 μm, while for slow fibres it is obtained P_0 = 1.827 kPa and L_0 = 1.371 μm. In the fitting of equation (2) the maximum isometric stress P_0 has been set to the experimental values of 145 kPa for fast fibres and 130 kPa for slow fibres [11]. For the fast fibres it is obtained a = 0.028 and A = 6.873 and L_0 = 2.619 μm, while for slow fibres the pair of parameters a = 0.029 and A = 5.430 is found, with and initial length L_0 = 2.405 μm. These values correspond to an initial stiffness of 55.810 kPa for fast fibres and 40.942 kPa for slow fibres, which are not in line with the values calculated with the proposed equation (3).

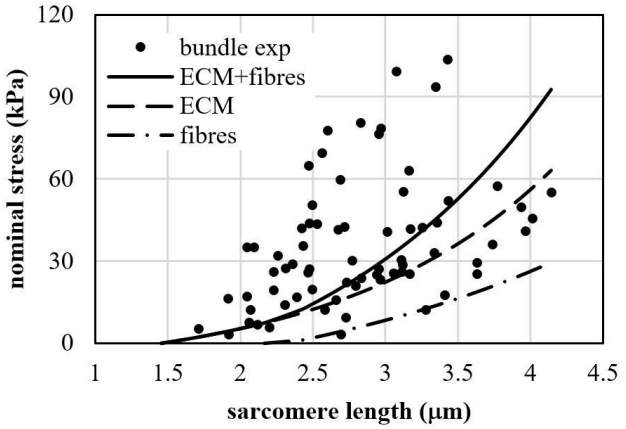

Fig. 6: Comparison of experimental data and analytical curves fitted for bundles, in terms of nominal stress versus sarcomere length. The contribution of fibres and ECM to the tensile response of bundles is shown separately.

IV. DISCUSSION AND CONCLUSIONS

With the help of the fitting of the exponential function (3) to experimental data, it is possible to estimate that fast fibres are stiffer than slow fibres. Furthermore, they have a higher value of initial length. The difference in stiffness, generally attributed to titin structures [12], clearly appears in the graph of Fig. 5, where the nominal stress is reported in terms of stretch with respect to the initial length. For the fibres considered in this work, the initial stiffness of fast fibres is about 60% greater than the stiffness of slow fibres, while the initial length of fast fibres is about 12% greater that the initial length in slow fibres.

The stiffness of slow and fast fibres by itself does not explain the passive behaviour stiffness of bundles (Fig. 6) and an additional term – that it is hypothesized given by the stiffness of ECM – must be considered to explain the stress versus sarcomere length response. In fact, even considering a bundle totally composed of fibres with equal percentage in the two isoforms (fast and slow), it is not possible to obtain the stiffness of the bundles.

Some of numerical formulations proposed in the literature to describe the passive behaviour of single fibres and bundles show to have some limits, in the light of the experimental data obtained in this work. As a way of example, an equation of the type (1) completely fails if the effective values for the maximum isometric stress P_0 are considered. On the contrary, taking P_0 as a free parameter, the best fitting of experimental data for both fast and slow fibre gives values that largely differ with respect the values usually reported in the literature [11]. On the contrary, the latter values for the maximum isometric stress can be adopted as fixed parameters in equation (2), because the pair of parameters (a, A) make it possible to find an acceptable fitting of experimental data. However, in the case of assumption of this equation, it is not rationally explained or confirmed by any experimental validation why the passive behaviour of muscular fibres – represented in the Hill's model by the element PE – should be related to the values of the maximum isometric stress.

At present it remains to explore the tensile behaviour of ECM perpendicularly to muscle fibres to asses a possible anisotropy. Similarly, the shear behaviour of ECM should be investigated to obtain a constitutive formulation capable of describing the effects of ECM in transmitting contractile forces generated by the fibres, as well as general multi-axial mechanical states.

Despite the limited number of samples tested – which will be incremented in the next – from the present work it appears that fast and slow fibres are dissimilar in their passive behaviour. Furthermore, single fibres in general are less stiff than bundles. The constitutive models proposed to describe the passive behaviour of fibres and bundles will be implemented in the framework of FEM models to investigate the role of ECM in contractile force transmission.

REFERENCES

[1] K. M. Virgilio, K. S. Martin, S. M. Peirce and S. S. Blemker, "Multiscale models of skeletal muscle reveal the complex effects of muscular dystrophy on tissue mechanics and damage susceptibility," *Interface Focus*, vol. 5(2), pp. 20140080, April 2015.

[2] L. Brocca *et al.* "Structure and function of human muscle fibres and muscle proteome in physically active older men," *Journal of Physiology*, vol. 595(14), pp. 4823–4844, July 2017.

[3] J. I. Quinlan *et al.*, "Muscle and Tendon Contributions to Reduced Rate of Torque Development in Healthy Older Males," *The journals of gerontology. Series A, Biological sciences and medical sciences*, Epub ahead of print, August 2017, doi: 10.1093/gerona/glx149

[4] M. P. Pato *et al.*, "Finite element studies of the mechanical behaviour of the diaphragm in normal and pathological cases," *Computer Methods in Biomechanics and Biomedical Engineering*, vol. 14(6), pp. 505–13, June 2011.

[5] M. Kojic, S. Mijailovic and N. Zdravkovic, "Modelling of muscle behaviour by the finite element method using Hill's three-element model," *International Journal of Numerical Methods in Engineering*, vol. 43, pp. 941–953, 1998.

[6] C. Doria *et al.*, "Improved VO_2 uptake kinetics and shift in muscle fiber type in high-altitude trekkers," *Journal of Applied Physiology*, vol. 111, pp.1597–1605, 2011.

[7] A.V. Hill, "The Heat of Shortening and the Dynamic Constants of Muscle," *Proceedings of the Royal Society of London. Series B, Biological Sciences*, vol. 126, pp. 136–195, 1938.

[8] C.Y. Tang, G. Zhang and C.P. Tsui "A 3D skeletal muscle model coupled with active contraction of muscle fibres and hyperelastic behaviour." *Journal of Biomechanics*, vol. 42, pp. 865–872, 2009.

[9] G. Zhang *et al.*, "Biomechanical simulation of thorax deformation using finite element approach," *BioMedical Engineering OnLine*, vol. 15:18, pp. 1–18, 2016.

[10] J. A. C. Martins, M. P. M. Pato and E. B. Pires, "A finite element model of skeletal muscles," *Virtual and Physical Prototyping*, vol. 1(3), pp. 159–170, September 2006.

[11] Z. H. He, R. Bottinelli, M. A. Pellegrino, M. A. Ferenczi and C. Reggiani, "ATP consumption and efficiency of human single muscle fibers with different myosin isoform composition," *Biophysics Journal*, vol. 79, pp. 945–961, August 2000.

[12] H. L. Granzier and S. Labeit, "The Giant Protein Titin," *Circulation Research*, vol. 94, pp. 284–295, 2004.

Aortic expansion induces lumen narrowing in anomalous coronary arteries: a parametric structural finite element analysis

G.M. Formato[1], M. Lo Rito[2], F. Auricchio[1], A. Frigiola[2] and M. Conti[1]
[1] *Department of Civil Engineering and Architecture, University of Pavia, Pavia, Italy*
[2] *Department of Cardio-Thoracic Surgery, IRCSS Policlinico San Donato, San Donato (MI), Italy*

***Abstract*—Anomalous origin of coronary can lead to sudden cardiac death (SCD) in young athletes, but the mechanisms underlying its occlusion during high stress conditions have still to be elucidated. To this aim, we create a parametric computer-aided designed (CAD) model of the aortic root and anomalous coronary and perform a static finite element analysis (FEA) on 10 models with different angles of take-off and intramural penetration at three different loading conditions. Results show that the anomalous coronary experiences a reduced luminal expansion when compared to the normal condition, with a mismatch that increases with pressure. Acute angles of take-off lead to elongated ostia, with an eccentricity that increases with aortic expansion. The present study provides a proof of concept of the biomechanical reasons of the lumen narrowing in anomalous coronaries during aortic expansion, promoting the role of computational simulations in elucidating the mechanisms of such a pathology.**

***Keywords*—Coronary anomaly, finite element simulation.**

I. Introduction

ANOMALOUS aortic origin of coronary artery (AAOCA) (Fig. 1) is a congenital anatomical alteration of the coronary which can result in severe prognostic implications like SCD, especially for individuals subjected to prolonged physical efforts, such as young athletes and soldiers. The challenges associated with AAOCA are two-fold: 1) a weak knowledge of both its epidemiology and pathophysiology; 2) its possible compatibility with life, which makes difficult to distinguish the cases associated with severe clinical risks from those that can allow a long and active life. The underlying mechanism of coronary compression during exercise is still unclear. While several authors attribute the cause to the interarterial course between the aorta and the pulmonary trunk, others sustain that a reasonable explanation corresponds to the intramural course, a condition in which the intussuscepted coronary is laterally compressed by the aortic wall during exertion [1]. Moreover, the identification of specific morphological features that could lead to coronary occlusion is difficult to assess. Some studies suggest that acute angles of take-off may lead to slit-like orifices during aortic expansion [1], [2]. On the other hand, Taylor and co-workers did not found any significant correlations between length of aortic intramural segment, coronary ostial size or angle of coronary take-off and SCD [3].

Given such premises, the goal of the present study is to investigate the biomechanical implications between AAOCA with intramural course and coronary occlusion, assessing the influence of the intramural inclusion and the take-off angle of the coronary on its lumen narrowing during aortic exertion. To this aim, we create a parametric geometrical model of the aortic root and anomalous coronary and performed a static FEA. This is, to the best of our knowledge, the first computer-based biomechanical study on AAOCA.

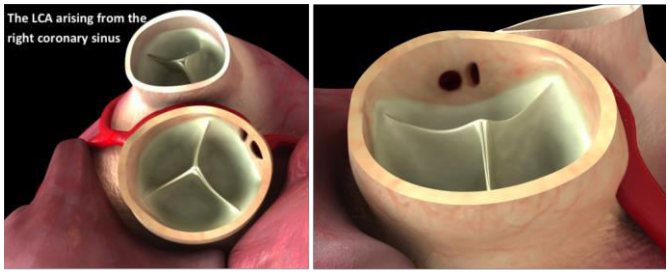

Fig. 1-Graphic representation of AAOCA: (A) the left coronary artery origins from the right coronary sinus; (B) view of the coronary ostia.

II. Materials and Methods

A. Parametric CAD model of aortic root with AAOCA

We create a geometrical model of an idealized aortic root with AAOCA with Rhinoceros v. 5.0 software integrated with the plug-in Grasshopper v. 0.9.0076 (McNeel and associates, Seattle, Washington, USA). The model has twenty-three parameters that allow to obtain an aortic root with the desired geometry and simulate the AAOCA varying the positioning of the coronary, the take-off angle (γ), the amount of intramural penetration (δ) and the length of intramural course. During structural FEA, all parameters are kept constant except γ and δ in order to study how the coronary lumen narrowing depends on the take-off angle and intramural penetration, which are considered key-factors of the anomaly [4], [5].

B. Parametric CAD model of aortic root with normal coronary

We create an idealized model of the aortic root with normal coronary, which is modeled as a pipe that origins perpendicularly from the sinus of Valsalva, with cross-sectional geometrical dimensions equal to the anomalous case.

C. Finite element analysis

Static finite strain analyses are performed with Abaqus Standard solver v. 6.16 (Dassault Systèmes, Providence, RI, USA). Both the aortic root and coronary are modelled with an isotropic, homogeneous, and linear elastic material, with Young modulus of 1 MPa and Poisson ratio of 0.45. The values of the mechanical properties are chosen to match a

distensibility for the aortic root of 0.001 $mmHg^{-1}$ [6]. The model is discretized with 58395 quadratic tetrahedral elements (element type: C3D10) having an approximate global size of 1 mm, since a preliminary mesh convergence analysis revealed that smaller size leads to a variation of the maximum coronary luminal narrowing less than 0.1%. As boundary conditions of the top and bottom cross-sections of the aortic root, we constrain the longitudinal and circumferential displacement, allowing only the radial dilatation of the root. Furthermore, a translational rigidity of 1MPa is added to the free extremity of the coronary using Abaqus spring elements Spring1 to simulate the constraint due to the surrounding heart muscle.
The pressure load is applied to the model taking the systolic peak values from the pressure waveform reported by [7]. Starting from the hypothesis that the unloaded CAD model idealizes the aortic root and the coronary at the end of the diastolic phase, (i.e., at 80 mmHg), we discharge the pre-stress due to this condition applying hydrostatic pressures of 40, 70, 100 mmHg to the inner surfaces of the aortic roots and of 10, 40, 70 mmHg to the inner surfaces of the coronaries, respectively. In this manner, we simulate the loading of the models with aortic pressures of 120, 150, 180 mmHg, which are possible pressures during exercise [8].

D. Post-processing

The inner surface of each deformed coronary is extracted as .stl file and imported in the VMTK software v. 1.3, where the centerline and the corresponding luminal cross-sections are computed. The sections at the extremities - up to almost ten mm from the ends - are excluded from the analysis to avoid outliers due to failure of the algorithm. For each model, the shape and area of the ostium is extracted separately using Rhinoceros and a corresponding eccentricity index *e* is computed.

III. RESULTS AND DISCUSSION

We firstly compare the luminal sections of normal and anomalous coronaries during aortic expansion (Fig. 2.A and Fig. 2.B). For the normal coronary (fig. 2.A) we can distinguish two zones: the ostial and proximal zone, where the coronary experiences a major expansion due to the simultaneous pressurisation of both the aortic root and coronary, and the distal tract, where the coronary experiences a minor expansion due to the effect of only the coronary pressurisation. We also report the luminal sections of the anomalous coronary γ35-δ50 during aortic exertion (Fig. 2.B). We do not find significant differences in the trend of the lumen narrowing with different intramural penetrations and take-off angles. In this case, the anomalous coronary experiences a much smaller expansion in the proximal and distal tract and even a narrowing in correspondence of the sinuses of Valsalva. These results show that even if the coronary is pressurized with increasing pressure, the presence of the anomalous course leads to a narrowing of -4.01%, -3.74%, -3.60% in correspondence of the sinuses of Valsalva, comparing to the reference case (dashed line). On the other hand, at the proximal level the anomalous coronary enlarges -5.62%, -11.74%, -20.32% less than the normal coronaries at the corresponding pressure.

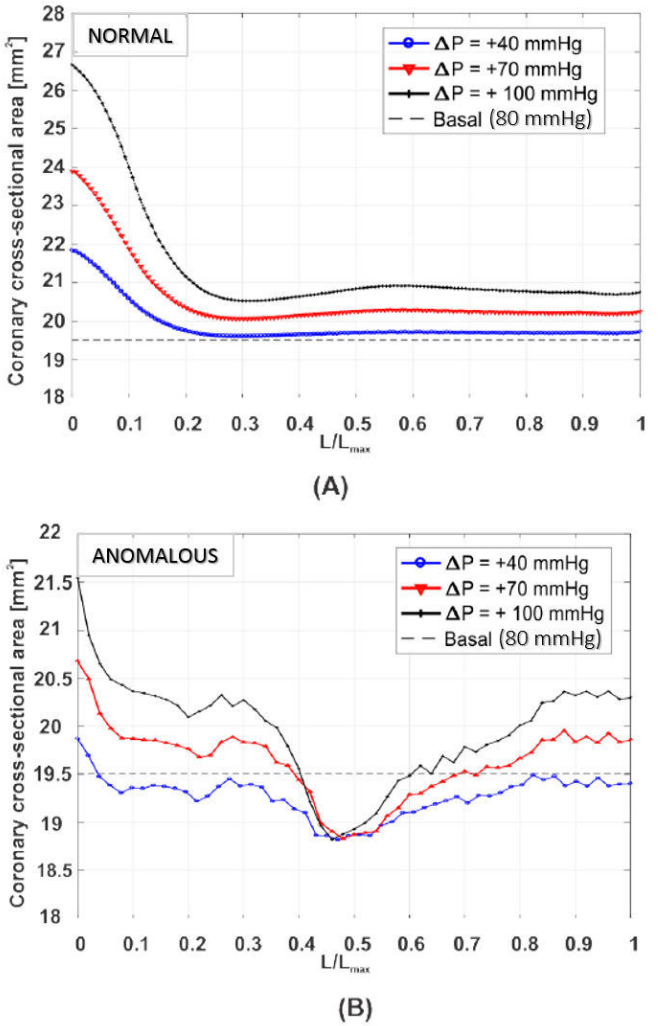

Fig. 2- (A) Luminal sections of healthy coronary at different pressure increments with respect to the basal condition (i.e. 80 mmHg): as the aortic pressure increases, the coronaric lumen enlarges along the whole length, particularly in the proximal tract (i.e. L/L_{max} =0); (B) luminal sections of the anomalous coronary γ35-δ50 (angle equal to 35°, wall penetration equal to 50%) at different pressure increments: as the aortic pressure increases, the coronaric lumen experiences a slight or null enlargement in the proximal (i.e. $L=L_{max}$ = 0) and distal (i.e. L/L_{max} = 1) tract, and a narrowing in correspondence of the sinuses of Valsalva (i.e. L/L_{max} = 0.5), which is not dependent on the pressure increment.

These results may reveal the incapability of the anomalous coronary to adapt its lumen to the increasing pressure and thus, to the increasing blood request during the critical stage of sustained physical effort. Although the lumen reduction of AAOCA has been detected by several authors, the computed reductions of the luminal areas are not matched by that found in the literature. For example, Angelini and co-workers [9] measured at systolic phase a reduction of the luminal area of 15-19%. However, the comparison between the two studies is not trivial. Angelini and co-workers perform the measures in the proximal intussuscepted tract of the coronary, where they find a 48.6% to 70.1% stenosis; therefore, the percentage reduction is much more important if computed on a smaller area. On the other hand, we do not model any initial narrowing in the intussuscepted tract due to stenosis or hypoplasia. Moreover, it is also necessary to take into account that the aortic pressures and exertions of the two studies may not coincide.

For the sake of simplicity, the reported results refer to the specific configuration of the model γ35- δ50; however, we do not find significant differences in the trend of the lumen narrowing with different intramural penetrations and take-off angles. In fact, the effect of the changes of the intramural penetration is hardly appreciable except for the case δ = 0% (i.e., extramural course), where the coronary experiences two peaks of narrowing at the sinuses of Valsalva because it courses outside the wall and, thus, is not compressed in correspondence of the junction of the sinuses (results not shown).

On the other hand, as expected, the angle of take-off influences the characteristics of the anomalous coronary only in correspondence of the ostium, which changes its shape (Fig. 3). Normal coronaries are characterized by a round ostium (e = 1.00) which slightly stretches following the aortic wall exertion, reaching a value e = 0.78 at the pressure increment of 100 mmHg. On the other hand, the decrease of the angles of take-off lead to an increasing of the ostial area on equal pressures, but also to an increasing of the eccentricity, reaching a value e = 0.49 at 100 mmHg for angles of take-off of 20°.

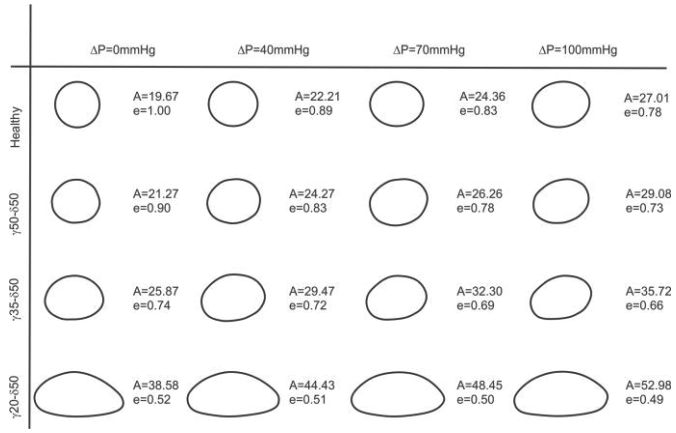

Fig. 3- Ostial sections of healthy (top line) and anomalous coronaries with fixed wall penetration and different angles of take-off at different increment pressures. Ostial sections become more eccentric during aortic dilatation and with small angles of take-off. A – ostial area [mm^2], e – eccentricity.

The tendency of the ostial and proximal tract to get on oval morphology is observed in several studies [4], [5], [10], suggesting its relation with the clinical outcomes of this pathology.

While the values of eccentricity found at the ostial level are confirmed by the work of [9], the computed ostial areas do not agree with that found in the literature. In fact, while we detect an enlargement of the ostium with acute angles of take-off, several authors sustain that one of the possible cause of myocardial ischemia during aortic expansion is the coronaric flow reduction caused by the narrowing of the anomalous coronaric ostium [11], [12]. We believe that such a disagreement is due to the missing inclusion, in our model, of a stenosis in the ostial and proximal tract of the coronary [9]. Such considerations call for the evaluation of the hemodynamic effects of the elliptical ostium and anomalous course on the coronaric flow, with the aim of assessing if the anomaly can trigger the origin and development of the atherosclerosis, which is still a matter of debate [13] [14].

IV. LIMITATIONS

At the best of our knowledge the present study represents the first computer-based structural analysis of coronary anomalies. Despite the model resamples the main geometrical features considered in the clinical practice, we acknowledge some limitations as discussed in the following.

Firstly, we assume that both the coronaric and aortic tissues can be described with the same mechanical properties. While a linear, isotropic and homogeneous material characterization is widely accepted for the aortic root [15], [16] it could not be valid for the coronaric tissue and, thus, lead to non-realistic deformations of the vessel during the aortic expansion. We think that this limitation can be neglected since, in the present study, we are interested in performing a comparative study basing only on geometrical parameters. However, in future studies, more complex constitutive models for the coronary may be used, as suggested by Karimi [17] and Lally [18].

Secondly, we perform structural finite element analyses simplifying the boundary conditions of the root extremities and neglecting the complex movement of the aortic root during the cardiac cycle and its dynamic change in the twist and tilt angle, which can have a role on coronary lumen reduction. In future studies, we can refer to clinical studies such as that of Lansac et al. [19] and adjust the boundary conditions in order to take into account the aortic root motion.

Finally, our results are inevitably influenced by the set geometry of the model. In particular, we model the coronary with a constant wall thickness along its intramural course and do not include any stenotic or hypoplasic region in the vessel, which are observed by [9]. Since the thinning of the coronary wall can promote the local buckling and the consequent luminal occlusion, in future studies we could include such features in the model and assess their role on the coronaric narrowing.

Another important limitation of our study is that we simulated a very specific case, i.e., when the coronary has a high take-off and has an intramural course around the aortic root. Therefore, our results can in principle refer only to such a particular configuration of the coronary. Even if the take-off level below or at aortic valve commissure has been found the most probable among large studies [5] in future we are going to simulate other configurations of the coronary in order to assess the impact of the specific course on the lumen narrowing.

V. CONCLUSIONS

The present study investigates the biomechanics underlying the luminal narrowing in AAOCA in an idealized geometrical model as a proof of concept for static structural finite element simulations as a mean to assess the role of specific geometrical features on coronaric narrowing.

Counter-intuitively, our simulations show that the anomalous coronary, under the investigated loading conditions, experiences a reduced luminal expansion when compared with the one in normal condition which, more obviously, enlarges proportionally to the increment of pressure with a localized enlargement at the ostium due to the expansion of the aortic root. Furthermore, the higher is the pressurization, the higher is the mismatch between the anomalous and normal condition.

The anomalous coronaries experience the maximum narrowing always in correspondence of the protrusion of the sinuses of Valsalva; if the coronary has an extramural course, the maximum narrowing is described by two peaks. Finally, acute angles of take-off of the anomalous coronaries cause an elongated ostial shape, with an eccentricity that increases with aortic expansion.

However, further studies should be made in order to increase the validity of the model. First of all, the results of the simulations could be experimentally validated with an *in vitro* model, which could be obtained by 3-D printing the CAD geometry used in the finite element simulations and putting the model in a simple hydraulic circuit with controllable pressures and flows. Secondly, the model should be validated clinically. To this aim, we are planning to use the framework here developed in a retrospective multi-patient clinical study in which the geometrical parameters of the CAD model are adjusted starting from CT images. Successively, the coronary narrowing computed with finite element simulations on the patient-specific models could be compared with clinical data in order to find critical parameters for luminal narrowing; in addition, a CFD analysis could also be performed with the goal of elucidating the hemodynamics impact of the anomaly.

ACKNOWLEDGEMENT

This study was supported by ESC Research Grant 2016.

REFERENCES

[1] S. Kaushal et al., "Intramural Coronary Length Correlates With Symptoms in Patients With Anomalous Aortic Origin of the Coronary Artery," The Annals of Thoracic Surgery, vol. 92, no. 3, pp. 986–992, Sep. 2011.

[2] R. Virmani, P. K. C. Chun, R. E. Goldstein, M. Robinowitz, and H. A. Mcallister, "Acute takeoffs of the coronary arteries along the aortic wall and congenital coronary ostial valve-like ridges: Association with sudden death," Journal of the American College of Cardiology, vol. 3, no. 3, pp. 766–771, Mar. 1984.

[3] A. J. Taylor, J. P. Byers, M. D. Cheitlin, and R. Virmani, "Anomalous right or left coronary artery from the contralateral coronary sinus: 'High-risk' abnormalities in the initial coronary artery course and heterogeneous clinical outcomes," American Heart Journal, vol. 133, no. 4, pp. 428–435, Apr. 1997.

[4] C. Gräni et al., "Hybrid CCTA/SPECT myocardial perfusion imaging findings in patients with anomalous origin of coronary arteries from the opposite sinus and suspected concomitant coronary artery disease," J. Nucl. Cardiol., vol. 24, no. 1, pp. 226–234, Feb. 2017.

[5] M. K. Cheezum et al., "Anomalous origin of the coronary artery arising from the opposite sinus: prevalence and outcomes in patients undergoing coronary CTA," European Heart Journal-Cardiovascular Imaging, vol. 18, no. 2, pp. 224–235, 2016.

[6] A. P. Patrianakos, D. Karakitsos, E. de Groot, F. I. Parthenakis, E. Daphnis, and P. E. Vardas, "Alteration of proximal aorta biophysical properties in patients with end stage renal disease," Heart, vol. 92, no. 2, pp. 228–232, 2006.

[7] T. Chaichana, Z. Sun, and J. Jewkes, "Computation of hemodynamics in the left coronary artery with variable angulations," Journal of Biomechanics, vol. 44, no. 10, pp. 1869–1878, Jul. 2011.

[8] E. J. Kroeker and E. H. Wood, "Comparison of simultaneously recorded central and peripheral arterial pressure pulses during rest, exercise and tilted position in man," Circulation Research, vol. 3, no. 6, pp. 623–632, 1955.

[9] P. Angelini, R. P. Walmsley, A. Libreros, and D. A. Ott, "Symptomatic Anomalous Origination of the Left Coronary Artery from the Opposite Sinus of Valsalva.," Texas Heart Institute Journal, vol. 33, no. 2, 2006.

[10] M. Krupiński et al., "Anomalous origin of the coronary artery from the wrong coronary sinus evaluated with computed tomography: 'High-risk' anatomy and its clinical relevance," Eur Radiol, vol. 24, no. 10, pp. 2353–2359, Oct. 2014.

[11] J. Lee, Y. H. Choe, H.-J. Kim, and J. E. Park, "Magnetic resonance imaging demonstration of anomalous origin of the right coronary artery from the left coronary sinus associated with acute myocardial infarction," Journal of computer assisted tomography, vol. 27, no. 2, pp. 289–291, 2003.

[12] M. J. Lim, M. J. Forsberg, R. Lee, and M. J. Kern, "Hemodynamic abnormalities across an anomalous left main coronary artery assessment: Evidence for a dynamic ostial obstruction," Cathet. Cardiovasc. Intervent., vol. 63, no. 3, pp. 294–298, Nov. 2004.

[13] O. Topaz, E. J. DeMarchena, E. Perin, L. S. Sommer, S. M. Mallon, and R. A. Chahine, "Anomalous coronary arteries: angiographic findings in 80 patients," International Journal of Cardiology, vol. 34, no. 2, pp. 129–138, Feb. 1992.

[14] N. Garg, S. Tewari, A. Kapoor, D. K. Gupta, and N. Sinha, "Primary congenital anomalies of the coronary arteries: a coronary arteriographic study," International journal of cardiology, vol. 74, no. 1, pp. 39–46, 2000.

[15] C. A. Conti et al., "Dynamic finite element analysis of the aortic root from MRI-derived parameters," Medical Engineering & Physics, vol. 32, no. 2, pp. 212–221, Mar. 2010.

[16] F. Sturla, E. Votta, M. Stevanella, C. A. Conti, and A. Redaelli, "Impact of modeling fluid–structure interaction in the computational analysis of aortic root biomechanics," Medical Engineering & Physics, vol. 35, no. 12, pp. 1721–1730, Dec. 2013.

[17] A. Karimi, M. Navidbakhsh, R. Razaghi, and M. Haghpanahi, "A computational fluid-structure interaction model for plaque vulnerability assessment in atherosclerotic human coronary arteries," Journal of Applied Physics, vol. 115, no. 14, p. 144702, Apr. 2014.

[18] C. Lally, A. J. Reid, and P. J. Prendergast, "Elastic behavior of porcine coronary artery tissue under uniaxial and equibiaxial tension," Annals of biomedical engineering, vol. 32, no. 10, pp. 1355–1364, 2004.

[19] E. Lansac et al., "Aortic root dynamics are asymmetric," J Heart Valve Dis, vol. 14, no. 3, pp. 400–407, 2005.

MECHANICS-BASED QUANTITATIVE TUMOR IDENTIFICATION AND CHARACTERIZATION

Antonio Candito[1], Robert L. Reuben[1], Yuhang Chen[1]
1. School of Engineering and Physical Sciences, Heriot-Watt University, Edinburgh, United Kingdom;

***Abstract*— Identification and characterization of tumor nodules in soft tissue, including their size, shape and location, provide essential information for clinical diagnosis. This study proposed a finite element based computational framework, for detecting the appearance of, and characterizing the volume fraction of, tumor nodule in the prostate, as an exemplar soft tissue, using instrumented palpation. The analysis is carried out based on the reaction forces obtained from an FE model where an idealized nodule, which depicts the presence of tumor nodule, was embedded into a tissue 'box'. The location of the nodule and its mechanical properties were varied with the aim of evaluating and quantifying the cancer heterogeneity in the palpation outcome. The results demonstrate the capability of the proposed framework in identifying the presence of the cancerous nodule in the prostate. Therefore, it presents promising potential, as a useful method associated with instrumented palpation, for primary diagnosis of prostate cancer, and potentially solid tumors in other types of soft tissues.**

***Keywords*—Tumor identification, Instrumented palpation, Prostate cancer, Tissue mechanics**

I. Introduction

A pathological condition such as the presence of cancer alters the microstructure of biological tissue. As a consequence, the mechanical behaviors between healthy and diseased tissues may be different. Therefore, parameters of such mechanical behavior can be used as indices for anomaly identification [1]. For example, the palpation devices developed for tumor identification is capable of recording the force feedback of the soft tissue when the tissue surface is subjected to instrumented palpation [2], similar to finger palpation used for primary diagnosis of prostate cancer. In general, the palpation at the location close to the tumor nodules, which often has higher elastic modulus, have a higher reaction force. However, the identification procedure could be greatly influenced by the characteristics of the tumor nodule such as its volume and elastic modulus. In this study, a computational framework will be established with the aim of identifying and quantifying the tumor nodule in soft tissue, such as in prostate, based on instrumented palpation.

II. Methods

Anatomically, the prostate in male pelvis is surrounded by bladder, rectum and other connective tissue. As mentioned, the procedure of digital rectal examination involves palpation carried out by practitioners over the reachable posterior surface of the prostate over the rectum. Similarly, iDRE and its device [3], based on the similar principle, is capable of recording the force feedback when palpating the prostate over a number of points from the posterior. A Finite Element (FE) model has been used to simulate the mechanical behavior of prostate tissue subject to instrumented palpation with simplifications to the geometries of the organ, as shown in Fig.1, where the prostate is subject to constraints at the boundaries interacting with the bladder and other tissue. The instrumented palpation is modeled using a rigid 'probe', with prescribed displacement along the posterior-anterior axis, and is repeated over a number of points.

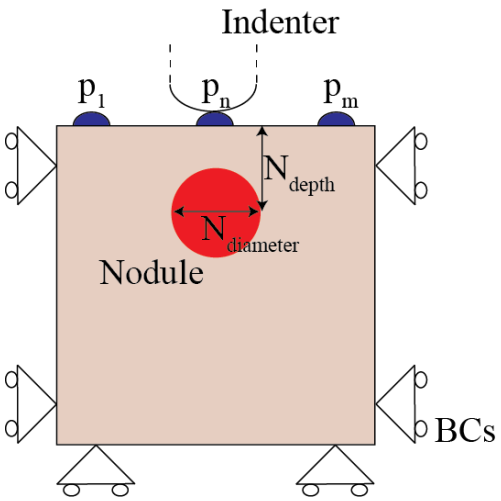

Fig. 1: Soft tissue model which involves the presence of a cancer nodule

Without loss of generality, the tumor was described as a circular nodule 2.5 times higher than the healthy one, embedded into a tissue 'box'. The size of the prostate model used here is chosen to be between 50x50 mm, although having a wider range than the size of adult prostate of 30 to 60 mm. Indentation is performed at the upper surface at 5 equally spaced locations, with depths of 3, 6 and 9 mm. It should be noted here that the number of indentations along the surface and the depths of indentation would be constrained in the clinical framework. A high number of indentation points would result in long, uncomfortable and expensive procedures. Similarly, very deep indentations would result in discomfort or pain for the patient or even damage to the organ. Therefore, a balance needs to be found between the optimal parameters for the test. The 10mm diameter probe used for performing such indentation is considered as a rigid body considering a spherical shape. A cancerous nodule is placed in the middle of the healthy sample with a vertical depth comprised between 1 and 31 mm from the upper surface of the prostate model and the center of the cancer nodule.

The diameter of the cancer nodule was varied between 2 and 18 mm which is within the range of nodule volume often found in prostate cancer patients [4].

The point-wise instrument palpation carried out for iDRE is considered to be quasi-static, with strain rate lower than $0.01s^{-1}$. To account for high local strain that may occur in FE models, neo-Hookean hyperelastic model is adopted here to model both cancerous nodule and non-cancerous tissue, and its strain energy function can be expressed as

$$W = C_1(I_1 - 3) + \frac{1}{D_1}(J_e - 1)^2 \quad (1)$$

$$D_1 = \frac{2}{K_0} = \frac{3(1-2\nu)}{\mu_0(1+\nu)} \quad and\ \mu_0 = 2C_1 \quad (2)$$

where I_1 is the first invariant of the right Cauchy-Green deformation tensor and J_e the elastic volume ratio. The remaining material parameters, $C_1\,D_1$, are related to bulk modulus (K_0), initial shear modulus (μ_0) and Poisson's ratio (ν), as shown in Eq. (2). The prostate tissue is modeled as an incompressible material [5].

The parameters used in the neo-Hookean model are fitted against the elastic properties taken from the earlier work carried out by Hoyt and coworkers [6], where the Young's moduli of the non-cancerous and cancerous tissues, measured from the ex vivo experiments, are measured to be 17 kPa and 42.5 kPa, respectively. As a result, the non-cancerous tissue has a material property of C_1 (0.00285) and D_1 (7.067) and the cancerous tissue of C_1 (0.00712) and D_1 (2.827). Furthermore, the probe is modeled as a rigid material, in a diameter of 10mm, and its contact with the prostate tissue is assumed to be frictionless [7]. The FE model is meshed with 3-node linear triangular elements and solved in ABAQUS (Dassault Systemes, VlizyVillacoublay, France).

III. Results and Discussion

The identification and characterization of the cancer parameter such as size and depth can give essential information for the purpose of diagnosis. The presence of the tumor nodule, which often has higher elastic properties, may cause distortion to the stress field when subject to mechanical probing, consequently leading to different reaction forces. When a tumor nodule is present, as discussed above, it introduces certain distortion to the stress field in tumor-free tissue. Such stress distortion can be influenced by the geometrical and mechanical properties of the cancer nodule. Furthermore, it can be 'amplified' by deeper probing, which leads to a greater difference between the tumor and tumor-free cases. To investigate and quantify the influence of the nodule depth and size in the palpation outcome an experiment was set up considering three diverse sizes of the nodule. The nodule radius was 3 mm (small), 6 mm (medium) and 9 mm (large). The cancer nodule was located considering different vertical depths in the prostate model, from 1 and 31 mm, distance between the upper surface of the prostate model and the center of the nodule for a total of 19 data points. The range covered a condition when the nodule is located close the surface and a nodule which is located deeply in the tissue. A static indentation was performed using an indentation depth of 3, 6 and 9 mm. The reaction force was recorded for each configuration of the model. The reaction force as mentioned early can be used as index to distinguish between a diseased and a healthy tissue.

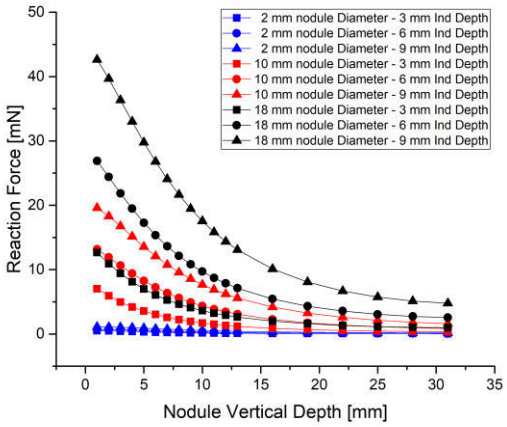

Fig. 2: Influence in the palpation outcome when the nodule depth and size is varied. The indentation was performed using three indentation depth values, 3, 6 and 9 mm

In Fig. 2 the Reaction Force was defined as difference between the one measured when the prostate model presents a cancer nodule and a model without presence of singularity (i.e. healthy). The Reaction Force has a negative trend when nodule depth decreases. When the Reaction Force values tend to zero it means that the values are equal to the force feedback measured when the tissue is healthy, i.e. tumor-free. Furthermore, if the nodule size increases, the Reaction Force values are higher, which means that in some cases also if the nodule is located deeper it is possible to detect it. However, the detectability of the palpation procedure increases significantly when the indentation depth performed is greater.

In conclusion, the influence in the palpation outcome of the cancer nodule depth and size is significant. A tumor located close to the surface and of a diameter within 10 and 18 mm can be detected, however, when the nodule is small or located over 20 mm deep in soft tissue it is not detectable using the proposed procedure. More importantly, the indentation depth values play an important role in the nodule cancer identification as the mechanical response of heterogeneous soft tissue is different when a shallow indentation is performed.

The characterization of the nodule size and depth can make the difference for the diagnosis. However, using the reaction force as index to distinguish between healthy and diseased tissue can lead to mal-diagnosis as it is not always possible to decouple the influence in the palpation outcome of those parameters. For this reason, in Fig. 3 an attempt to define a 'law' to estimate the nodule size and depth using palpation was made. In this case the ratio between nodule size and depth was considered. When this tends to zero, the Reaction Force measured have high values as the nodule size is significant or the nodule is located close to the surface. When the ratio increases, the detectability of the procedure decreases, either because the nodule has a small size, or because it is located deeply in the tissue. In addition, the mechanical properties of the cancer nodule can vary with grade and stage of the disease. For this reason, the experiment was run considering 3 different mechanical properties for the cancer nodule, i.e. a cancer

nodule with modulus 1.5, 2/5 and 3.5 times higher than the modulus of the healthy tissue. The results show how the detectability of the cancer nodule is influenced from the modulus of the cancer nodule. When the cancer modulus is 3.5 times higher, the detectability improves. The data can fit using a power function which can be used to define a law to identify if there is presence of the cancer nodule and attempt to characterize it geometrical properties such as size and depth in the soft tissue.

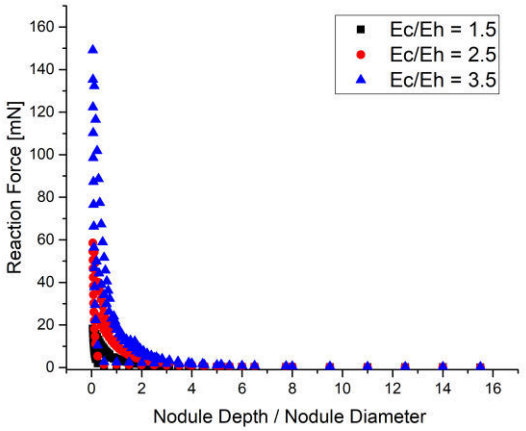

Fig. 3: Influence in the palpation outcome when the modulus of the cancer nodule was varied. The indentation was performed using an indentation depth value of 9 mm

IV. Conclusion

Despite of rapid development in novel medical devices which utilize mechanical probing as a means to detect the anomaly in soft tissue, e.g. instrumented palpation, there is a need of robust and effective methods in making sense of such mechanical data for the purpose of tumor nodule identification. In this study a diagnostic framework is proposed with the aim of quantitative identify and characterize tumor nodule in soft tissue based on instrumented palpation. The procedure provides quantitative understanding of key parameters, such as the size, depth and their sensitivity to instrumented palpation and, because of its less invasive nature, can be used as a tool for primary cancer detection. The results have shown how the detectability is influenced from the geometrical and mechanical properties of the cancer nodule. Nodules located deeply in the tissue or with a small diameter are harder to detect or characterize. Nevertheless, the sensitivity of the palpation method can improve significantly when a greater indentation depth is performed. Decoupling the influence of the cancer nodule size and depth is still a difficult task. For this reason, it has been mentioned that an attempt was made to define a law which is able to identify the ratio of the nodule size and depth. In that way, the uncertainty of the system can be quantified to suggest the potential ranges of nodule size and depth in the possible solution space. The diagnostic framework proposed can be validated experimentally using a phantom made of gelatin which mechanically mimics the prostatic tissue. The procedure will allow fabricating different samples with embedded nodules characterized with diverse mechanical properties comparing with the rest of the gelatin material to mimics the presence of cancer nodules. Besides, the nodules will be located in diverse positions and depths in the phantom gel. The indentation system - Mach-1 V500css (Biomomentum Inc, Laval, Canada) will be used to test the samples and characterize the their mechanical response. Afterward, measurements of the reaction force will be performed indenting in diverse points the gel surface.

Acknowledgement

The support under EPSRC, grant no. (EP/I019472/1 and EP/I020101/1), is greatly acknowledged.

References

[1] T.A. krouskop, T.M. Wheeler, F. Kallel, B.S. Garra, T. Hall, Elastic Moduli of Breast and Prostate Tissues Under Compression, *Ultrasonic Imaging,* 20 (1998) 260-274.

[2] J. Kim, B. Ahn, S. De, M.A. Srinivasan, An efficient soft tissue characterization algorithm from in vivo indentation experiments for medical simulation, *Int J Med Robot,* 4(3) (2008) 277-85.

[3] B. Ahn, Y. Kim, C.K. Oh, J. Kim, Robotic palpation and mechanical property characterization for abnormal tissue localization*, Med Biol Eng Comput*, 50(9) (2012) 961-71.

[4] P. Scanlan, S.J. Hammer, D.W. Good, S. Phipps, G.D. Stewart, S.A. McNeill, W. Shu, R.L. Reuben, Development of a novel actuator for the dynamic palpation of soft tissue for use in the assessment of prostate tissue quality. *Sensors and Actuators A: Physical*, 232 (2015) 310-318.

[5] W.C. Carson, G.J. Gerling, T.L. Krupski, C.G. Kowalik, J.C. Harper, C.A. Moskaluk, Material characterization of ex vivo prostate tissue via spherical indentation in the clinic. *Med Eng Phys*, 33(3) (2011) 302-9.

[6] K. Hoyt, B. Castaneda, M. Zhang, P. Nigwekar, P.A.d. Sant'Agnese, J.V. Joseph, J. Strang, D.J. Rubens, K.J. Parker, Tissue elasticity properties as biomarkers for prostate cancer. *Cancer Biomarkers*, 4 (2008) 213–225.

[7] B. Ahn, J. Kim, Measurement and characterization of soft tissue behavior with surface deformation and force response under large deformations. *Med Image Anal*, 14(2) (2010) 138-48.

Upper limb biomechanical model for orthopaedic applications: preliminary results

Vi DoTran[1,2,3], PaoloDario[1,3], and Stefano Mazzoleni[1,2]
[1] *The BioRobotics Institute, Scuola Superiore Sant'Anna, Viale R. Piaggio 34, Pontedera, Italy*
[2] *Laboratory of Rehabilitation Bioengineering, Volterra, Italy*
[3] *School of Mechanical Engineering, Tianjin University, P. R. China*

***Abstract*—In this study an upper limb biomechanical model which includes strain-adjustable ligaments of the acromioclavicular joint was developed. The model including 7 degrees of freedom is able to evaluate the movements of the shoulder, elbow and wrist. The ligaments strain can be adjusted in order to simulate different types of Rockwood acromioclavicular dislocation.**

Movements recorded from three healthy subjects are used as preliminary assessment of the proposed model.

***Keywords*—Musculoskeletal model, upper limb biomechanics, shoulder, ligament modeling.**

I. INTRODUCTION

INTERNALstructural loads and muscle activation are crucial for quantitative evaluation of human movements: unfortunately in vivo measurements are complex to be performed. Hence musculoskeletal models which provide meaningful noninvasive estimations of these variables can be used. During the last decade several upper limb musculoskeletal models have been developed, such as the Stanford VA upper limb model [1], the Garner model [2], the Delft shoulder and elbow model (DSEM) [3], the Dickerson mathematical musculoskeletal shoulder model [4] and the AnyBody shoulder model [5].

The musculoskeletal shoulder models are used to obtain a detailed biomechanical description. The DSEM model has been used for different categories of applications, such as analysis goal-directed movements [6], evaluation the performance and mechanical behavior of the arm and shoulder girdle [7] and wheelchair propulsion [8], [9]. The Swedish shoulder model was used to calculate the distribution of internal forces among a large number of shoulder structures in house painting movement [10].

In addition they can be also used to predict the influence of injuries on movements. The Stanford VA upper limb model was used to perform simulations of surgical rotator cuff repair of the supraspinatus muscle–tendon unit [11]. Recently the impact of cuff tear arthropathy on the mechanics of the deltoid during elevation in the frontal, scapular and sagittal planes was simulated by using the AnyBody shoulder model [12]. To better appreciate the possible benefit of an anatomic reduction and internal fixation, Patel et al. [13] quantified the expected deficit of a malunited clavicle fracture by using the Stanford VA upper limb model. The use of a musculoskeletal model for assessing the effects of a change in morphological structure is becoming rather common and may represent a promising reliable and valid approach.

The human shoulder joint can be considered as a group of joints which includes the sternoclavicular joint, the acromioclavicular (AC) joint, the glenohumeral joint and the scapulothoracic joint. AC joint injuries occur commonly in active persons and athletes [14], [15]. The injuries of the AC joint are graded according to the amount of injury on the acromioclavicular and coracoclavicular ligaments [16]. The Rockwood's classification divides AC injuries into six different types, from type I to type VI according to the severity of the joint dislocation.

The AC joint stability, which is maintained by a group of ligaments and muscles, is influenced by the specific dislocation injury. The analysis of the effects of the abnormal ligament on upper limb movements is still an open issue. To predict the effects of ligaments injury on upper limb movements, a biomechanical model should include adjustable strain ligaments.

In this study a biomechanical upper limb model including AC joint ligaments have been developed. The ultimate goal of this biomechanical model is to estimate the motion kinematics of the shoulder according to different types of Rockwood AC dislocation and to provide a clinical support to the evaluation of functional recovery of the patient after a treatment.

Upper limb movements recorded from three healthy subjects were recorded and analysed as preliminary assessment of the proposed model.

II. METHODS

A. Musculoskeletal upper limb model

The upper limb musculoskeletal model presented in this study was developed by using the OpenSim [17] platform version 3.3 (National Central for Simulation in Rehabilitation Research NCSRR, Stanford, CA, USA). The musculoskeletal model of the upper limb used in this study was developed from a previous upper limb model [1].The model includes 7 degrees of freedom (DOFs) such as shoulder rotation, shoulder elevation, elevation plane of the shoulder, elbow flexion, forearm rotation and wrist flexion. Fifty musculotendon actuators across these joints were also included. The model was based on the anthropometry and muscle force-generating characteristics of a 50th percentile adult male.

In addition, the trapezius muscle was added to control the moving, rotating, and stabilizing the scapula. The parameters of the trapezius muscle, including tendon slack length, optimal muscle-fiber length and peak isometric muscle force, are obtained from the DSEM [3]. This

muscle was included in order to control the shoulder elevation.

B. Acromioclavicular joint ligaments

The AC joint is stabilized by a complex of three ligaments arranged around the joint: the coracoacromial ligament, the acromioclavicular ligament and the coracoclavicular ligament.

The coracoclavicular ligament consists of the conoid ligament and the trapezoid ligament. The conoid ligament inserts into the inferior surface of the clavicle of the conoid tubercle near its posterior ridge. The trapezoid ligament runs obliquely, superiorly, and then laterally toward the trapezoid ridge to the inferior surface of the clavicle [16].

TABLE I
LIGAMENTS PARAMETERS

Ligament	*Length (m)*	*Stiffness (N/m)*
Acromioclavicular	0.0150 [21]	N/A
Coracoacromial	0.0369 [22]	51600[22]
Conoid	0.0112 [23]	70000 [23]
Trapezoid	0.0096 [23]	83000 [23]

N/A: Not available.

The ligaments were modeled under OpenSim by means of two parameters: physiological cross-sectional area and resting length, the length at which the ligament has no strain and no force is produced. The length and stiffness of ligaments in normal condition are reported in Table I.

C. Participants

To demonstrate how this model works based on the inverse kinematics problem by using experimental data, 3 healthy young volunteers were asked to perform right upper limb movements. The subject characteristics are reported in Table II.

TABLE II
SUBJECTS CHARACTERISTICS

	S1	S2	S3	Mean ± SD
Gender	M	M	M	N/A
Age	28	24	25	25.67 ± 2.08
Height (cm)	155	177	178	170.00 ± 13.00
Weight (kg)	51	62	78	63.67 ± 13.58
Clavicle (cm)	15	16	17	16.00 ± 1.00
Humerus (cm)	24	30	30	28.00 ± 3.46
Ulna(cm)	23.5	26	27	25.50 ± 1.80

N/A: Not available; S1, S2, S3: Subject 1, Subject 2, Subject 3, respectively; M: Male; SD: Standard deviation.

The subject performed shoulder flexion-extension, shoulder abduction-adduction and "hand to mouth" movement. Each movement was performed five times with a self-paced velocity (e.g., 4 seconds for bringing the hand toward the mouth and 4 seconds for returning to the original position).

The movements were recorded by a motion capture system (SMART-DT, BTS Bioengineering Corp., Milano, Italy) which is capable of recording 3D movements. There Nine markers were placed at the following body landmarks to record the upper limb movements: acromion, clavicular, C7 vertebra, bicep front, elbow lateral, elbow medial, wrist lateral, wrist medial and hand (Table III). The position of these markers has been determined according to the recommendations from a previous study [18].

TABLE III
MARKER LOCATION

Marker name	*Segment*	*Description*
C7	Thorax	Processus Spinosus of the 7th cervical vertebra
Clavicular	Clavicle	Most ventral point on the sternoclavicular joint
Acromion	Clavicle	Most dorsal point on the acromioclavicular joint
Bicep front	Humerus	5 cm from the middle of the humerus (on the bicep muscle)
Elbow lateral	Humerus	Most lateral point on lateral epicondyle
Elbow medial	Humerus	Most medial point on medial epicondyle
Wrist lateral	Radius	Distal point of the radial styloid
Wrist medial	Ulna	Ulna distal point of the olecranon
Hand	Hand	5th metacarpal (distal)

III. RESULTS

A. Biomechanical upper limb model

A schematisation of the developed musculoskeletal upper limb model is shown in Figure 1.

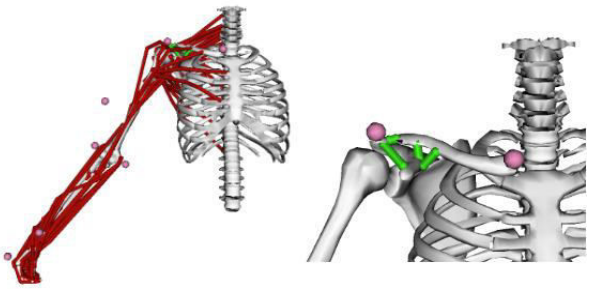

Fig. 1. Upper limb model in an anterior view (left) and acromioclavicular joint (right) where ligaments are represented as green bars.

The developed model worked well under OpenSim: no constraint or abnormal operations have been encountered. The model is formed by 63 muscle-tendon units in total.

B. Shoulder movement analysis

Based on the marker positions recorded during an experimental trial, anatomical scaling, inverse kinematics and dynamics were performed.

In order to match the anthropometric values of the generic model to the characteristics of the subject, the Scale Tool was used. The Scale Tool alters the anthropometric features of a biomechanical model so that

it matches a particular subject as closely as possible. Scaling is typically performed by comparing experimental marker data to virtual markers placed on a model [19].

Then the joints angles of each DOF of the model were obtained by means of the Inverse Kinematics OpenSim Tool. Finally the inverse dynamics was used to estimate the forces and moments that cause the motion.

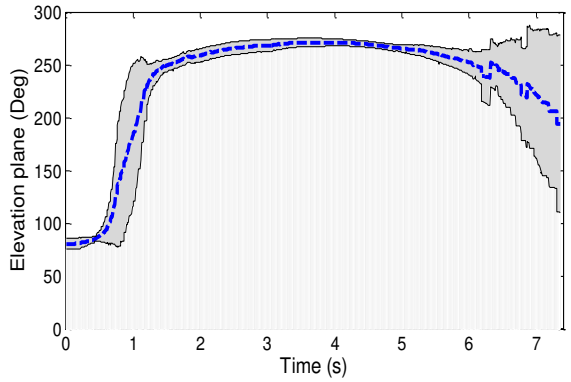

Fig. 2. Elevation plane angles in hand to mouth movement.

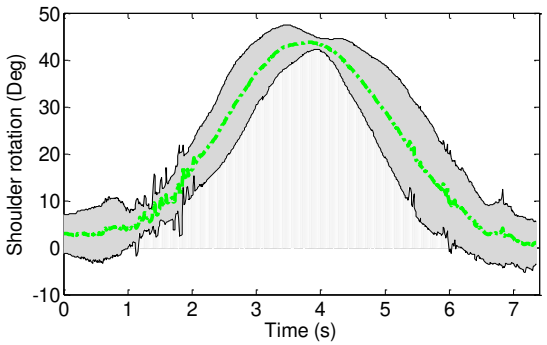

Fig. 3. Shoulder rotation angles in hand to mouth movement.

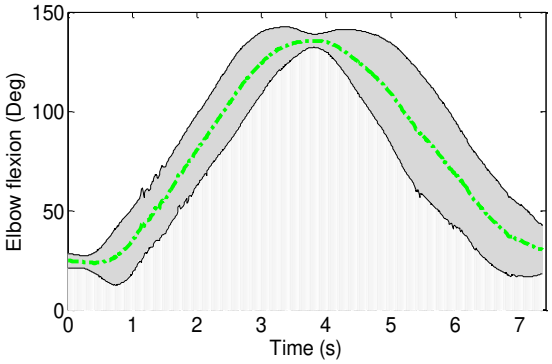

Fig. 4. Elbow flexion angles in hand to mouth movement.

Joint angles corresponding to elevation plane of the shoulder, shoulder rotation and elbow flexion during the hand to mouth movement were shown in Fig. 2, Fig. 3 and Fig. 4, respectively. The joint angles obtained from the experiment are in agreement with the literature [9].

IV. Conclusion

The developed model was tested in order to evaluate upper limb movement kinematics by means of experimental data recorded from three healthy subjects. The influence of different types of Rockwood AC dislocations can be evaluated by means of this biomechanical model.

Further analysis will be performed in order to study the effects of ligaments strain on shoulder movements. Experimental data from patients with orthopaedic surgery are needed to verify the reliability of the presented biomechanical model to evaluating the functional recovery after a treatment.

References

[1] K. R. S. Holzbaur, W. M. Murray, and S. L. Delp, "A model of the upper extremity for simulating musculoskeletal surgery and analyzing neuromuscular control," *Ann. Biomed. Eng.*, vol. 33, no. 6, pp. 829–840, 2005.

[2] B. A. Garner and M. G. Pandy, "Musculoskeletal Model of the Upper Limb Based on the Visible Human Male Dataset," *Comput. Methods Biomech. Biomed. Engin.*, vol. 4, no. 2, pp. 93–126, 2001.

[3] D. Blana, J. G. Hincapie, E. K. Chadwick, et al., "A musculoskeletal model of the upper extremity for use in the development of neuroprosthetic systems," *J. Biomech.*, vol. 41, no. 8, pp. 1714–1721, 2008.

[4] C. R. Dickerson, D. B. Chaffin, and R. E. Hughes, "A mathematical musculoskeletal shoulder model for proactive ergonomic analysis.," *Comput. Methods Biomech. Biomed. Engin.*, vol. 10, no. 6, pp. 389–400, 2007.

[5] M. Damsgaard, J. Rasmussen, S. T. Christensen, et al., "Analysis of musculoskeletal systems in the AnyBody Modeling System," *Simul. Model. Pract. Theory*, vol. 14, no. 8, pp. 1100–1111, 2006.

[6] R. Happee and F. C. T. Van der Helm, "The control of shoulder muscles during goal directed movements, an inverse dynamic analysis," *J. Biomech.*, vol. 28, no. 10, pp. 1179–1191, 1995.

[7] E. K. Chadwick, D. Blana, R. Kirsch, et al., "Real-time simulation of three-dimensional shoulder girdle and arm dynamics," *IEEE Trans. Biomed. Eng.*, vol. 61, no. 7, pp. 1947–1956, 2014.

[8] D. J. J. Bregman, S. van Drongelen, and H. E. J. Veeger, "Is effective force application in handrim wheelchair propulsion also efficient?," *Clin. Biomech.*, vol. 24, no. 1, pp. 13–19, 2009.

[9] S. Van Drongelen, L. H. Van Der Woude, T. W. Janssen, et al., "Mechanical load on the upper extremity during wheelchair activities," *Arch. Phys. Med. Rehabil.*, vol. 86, no. 6, pp. 1214–1220, 2005.

[10] B. Stenlund, L. Lindbeck, and D. Karlsson, "Significance of house painters' work techniques on shoulder muscle strain during overhead work.," *Ergonomics*, vol. 45, no. 6, pp. 455–68, 2002.

[11] K. R. Saul, S. Hayon, T. L. Smith, et al., "Postural dependence of passive tension in the supraspinatus following rotator cuff repair: A simulation analysis," *Clin. Biomech.*, vol. 26, no. 8, pp. 804–810, 2011.

[12] P. O. Lemieux, N. Nuño, N. Hagemeister, et al., "Mechanical analysis of cuff tear arthropathy during multiplanar elevation with the AnyBody shoulder model," *Clin. Biomech.*, vol. 27, no. 8, pp. 801–806, 2012.

[13] B. Patel, P. Gustafson, and J. Jastifer, "The effect of clavicle malunion on shoulder biomechanics; A computational study," *Clin. Biomech.*, vol. 27, no. 5, pp. 436–442, 2012.

[14] M. W. Mariscalco and P. Saluan, "Upper extremity injuries in the adolescent athlete.," *Sports Med. Arthrosc.*, vol. 19, no. 1, pp. 17–26, 2011.

[15] M. S. Kocher, P. M. Waters, and L. J. Micheli, "Upper extremity injuries in the paediatric athlete.," *Sports Med.*, vol. 30, no. 2, pp. 117–135, 2000.

[16] C. A. Rockwood, M. FA, W. MA, et al., *The Shoulder, 2nd Edition, Volume 1*. Philadelphia, PA: W B Saunders Co, 1998.

[17] S. L. Delp, F. C. Anderson, A. S. Arnold, et al., "OpenSim: Open source to create and analyze dynamic simulations of movement," *IEEE Trans. Biomed. Eng.*, vol. 54, no. 11, pp. 1940–1950, 2007.

[18] G. Wu, F. Van Der Helm, H. Veeger, et al., "ISB recommendation on definitions of joint coordinate systems of various joints for the reporting of human joint motion - Part II: Shoulder, elbow, wrist and hand," *J. Biomech.*, vol. 38, no. 5, pp. 981–992, 2005.

[19] OpenSim Users Guide: https://simtk-confluence.stanford.edu/display/OpenSim/.

[20] H. Gill, L. Gustafsson, L. Hawcroft, et al., "Shoulder joint range of motion in healthy adults aged 20 to 49 years," *Br. J. Occup. Ther.*, vol. 69, no. 12, pp. 556–561, 2006.

[21] B. A. Ponce, P. J. Millett, and J. J. P. Warner, "Acromioclavicular

joint instability-reconstruction indications and techniques," *Oper. Tech. Sports Med.*, vol. 12, no. 1, pp. 35–42, 2004.

[22] R. Fremerey, L. Bastian, and W. E. Siebert, "The coracoacromial ligament: anatomical and biomechanical properties with respect to age and rotator cuff disease," *Knee Surg. Sports Traumatol. Arthrosc.*, vol. 8, no. 5, pp. 309–313, 2000.

[23] R. Costic, A. Vangura, J. a Fenwick, et al., "Viscoelastic behavior and structural properties of the coracoclavicular ligaments.," *Scand. J. Med. Sci. Sports*, vol. 13, no. 5, pp. 305–10, 2003.

Thermal stabilization of the deglycating enzyme Amadoriase I by computational protein design

Federica Rigoldi[1#], Stefano Donini[2#], Alberto Redaelli[1], Emilio Parisini[2], Alfonso Gautieri[1*]*

[1]*Biomolecular Engineering Lab, DEIB, Politecnico di Milano, Piazza Leonardo da Vinci 32, 20133 Milano (Italy)*
[2]*Center for Nano Science and Technology @Polimi, Istituto Italiano di Tecnologia, Via G. Pascoli 70/3, 20133 Milano (Italy)*
 # These authors contributed equally to this work
**To whom correspondence should be addressed: Emilio.Parisini@iit.it or Alfonso.Gautieri@polimi.it*

***Abstract* - Amadoriases are a class of FAD-dependent enzymes that naturally hydrolyze single glycated amino acids. Albeit still relatively unstudied, their possible use as biocatalysts for multiple industrial applications has been hypothesized. To this end, however, one major limitation is that in their native form Amdoriases show no activity at temperatures higher than about 50°C. Through a combined rational computational design and experimental approach we obtained an engineered Amadoriase enzyme featuring a substantially increased thermal stability relative to its wild-type form. We used an in-silico strategy to identify amino acids that, once mutated to cysteines, would allow the formation of one or two disulfide bonds in the structure of Amadoriase I. We computationally evaluated a number of mutant models thus obtained and we experimentally produced the four most promising ones, leading to the identification of those mutants where the introduction of the disulfide bond(s) proved effective in increasing the thermal stability of the enzyme without affecting its activity. We also, obtained the crystal structures of the two most valuable mutants. Our approach allowed us to expedite the design and the experimental identification of four Amadoriase I mutants, two of which show a remarkable increase in thermal stability compared to the wild type enzyme. Impressively, one of the two mutants show a residual activity of ~10% at 90 °C. This work provides a novel conceptual framework for a fast and experimentally agile identification of thermally stabilized enzyme mutants.**

***Keywords*—Molecular dynamics, Thermo-stabilization, Enzyme, Protein engineering.**

I. Introduction

Amadoriases, also known as Fructosyl Amino Acid Oxidases (FAOX), are enzymes that are found in fungi and bacteria and that are able to cleave low molecular weight Amadori product (i.e., glycated amino acids) to yield a free amine, glucosone and hydrogen peroxide [1], [2].

Today, specific mutant Amadoriase enzymes are being used as molecular biosensors for the measurement of the concentration of glycated haemoglobin (HbA1c), particularly in the management of diabetes [3]. However, these numerous engineered forms of Amadoriases show relatively unsatisfactory levels of activity and partially impaired stability compared to their wild type form, which affects their conditions of use [4]. Amadoriase enzymes represent also a promising strategy for the prevention of protein glycation in biological tissues [2]. Glycation is the spontaneous, non-enzymatic and irreversible covalent addition of a sugar molecule onto some specific protein residues [5]. This process leads to numerous adverse side effects (e.g. arterial stiffening, atherosclerosis [6], nephropathy [7], retinopathy and neuropathy [8]). Clearly, owing to the buried location of their active site and to the narrow tunnel that provides access to the catalytic pocket [9], [10], native Amadoriases have no activity on intact proteins [11], [12]. A stabilized form of Amadoriase may therefore help the development of a further, more extensive engineering approach to the design of mutants that can act as enzymatic protein deglycation tools.

II. Aims of the Work

We used a novel high-throughput computational screening method based on Molecular Dynamics (MD) simulations and on the rational evaluation of a library of potentially stabilizing mutations of the Amadoriase I enzyme from *Aspergillus fumigatus* to identify a reduced number of mutants to be produced and tested experimentally. Unlike the classical directed evolution method, our approach allowed a faster and experimentally less demanding identification of thermally stabilized forms of the enzyme.

III. Materials and Methods

A. Design of disulfide bonds and MD simulation.

We applied SSBONDS [13] software in order to identify the sites where possible disulfide bonds could be introduced within the architecture of the native enzyme starting from the Amadoriase I crystal structure that we had previously solved (PDB_Id: 4WCT [14]). We applied specific constraints to designable areas (as specified in [15]), resulting in the prediction of 23 possible disulfide sites. These results are based only on geometrical and energetic constraints.

Using MD, we tested the 23 Amadoriase I variants (named SS01 to SS23), each featuring the double substitution of a couple of native residues with cysteines, and we derived the most promising putative sites where the introduction of a disulfide bond may result in improved enzyme thermostability. The protocols for building enzyme variant

models and the simulation parameters are reported in our recent published work [15]. Briefly, each systems resulted in a in ~ 50.000 atoms orthogonal box minimized and then equilibrated using the NAMD code[16]. During minimization and constant pressure equilibration, the Cα atoms of the protein were restrained to prevent protein diffusion. Finally, ACEMD software [17] was used to produce dynamic trajectories, using only a different time step increased to 4 fs. We simulated each variant for 10 ns at three different temperatures (273, 300 and 340 K).

B. Mutants screening

The Root Mean Square Fluctuation (RMSF) was used as pivotal measure for efficient quantitative screening. This computational value well-correlates with the crystallographic thermal parameter (B factor).

For each of the 23 possible disulfide mutants, the averaged RMSF (avg-RMSF) was calculated on the last 5 ns of the MD trajectory at each of the three simulated temperatures. In the calculation, we decided to exclude the N- and the C-terminus of the protein due to their intrinsically high mobility, in particular the regions from residue 1 to 9 and from residue 438 to 446.

The RMSF increases significantly in specific regions of the protein, which can represent the origin of local protein unfolding. We extracted the slope (λ) of avg-RMSF vs. temperature. In our approach, the λ value has a key role for the estimation of the different flexibility of each mutant at increasing temperatures. We assume that if, in a mutant, the λ parameter is lower than the one calculated for the wildtype enzyme, the inserted double cysteines mutation may have improved the enzyme backbone resistance to thermal stresses compared to the native form, in which case that particular disulfide bond is to be considered as stabilizing and the mutant is selected for experimental production and testing. Otherwise, the SS-variant is filtered out (Fig 1).

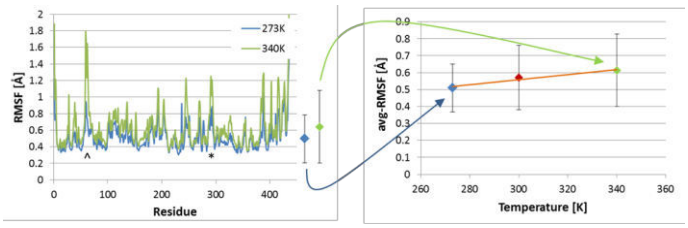

Figure 1. The avg-RMSF is the result of averaging protein RMSF over time and over the length of the protein, thus including contribution from stable regions and from more flexible loops. The increase in avg-RMSF at higher temperature is due to two major contributions: (1) an overall increase in the baseline RMSF over the whole protein and (2) a significant increase of vibration in the least stable regions

C. Proteins expression and purification

Each double-cysteine mutation was introduced by PCR in the native Amadoriase I gene cloned in a pET3a vector using the QuikChange II (Agilent) site-directed mutagenesis kit. All the resulting proteins were expressed following the same expression protocol that we developed for native Amadoriase I [14], using 0.5 mM of isopropyl 1-thio-β-D-galactopyranoside (IPTG) to induce recombinant protein expression during overnight culture at 25°C. All the resulting soluble proteins-rich fractions were purified in a 10 mM Tris buffer, pH 8.0.

D. Activity assays and characterization of the thermoresistant properties

Enzymatic activity was monitored by glucosone release detection from fructosyl-lysine at 322nm [14], using a 96 transparent polystyrene plate in a Spark10M (Tecan). After 1 minute of pre-incubation, the reaction was started adding 4.5 µg of enzyme, and the increase in absorbance at 322nm was monitored. Enzymatic activity was assayed at 25°C, and then after thermal treatment, which consisted in incubating for 10 minutes the enzyme to target temperature ranging from 25°C to 100°C (with 5°C steps) then cooling it down at 4°C until test. The reduced forms of the enzymes were obtained by supplementing the buffer with 100 mM 1,4-Dithiothreitol (DTT). After 1 h of incubation, the heat treatment and enzymatic assay are performed as for the oxidized forms. The T_{50} values, the temperature at which the enzymes lose 50% of the activity with respect to the activity at 25°C, were extrapolated by fitting the data with the Boltzman sigmoidal function using GraphPad Prism version 5.00 [GraphPad Software, La Jolla California USA].

E. Crystallization and structures solving

Crystals of both the SS03 and the SS17 mutant were obtained by the vapor diffusion method at room temperature mixing a 1 µl drop of ~ 15 mg/ml protein sample with an equal volume of a 0.1 M sodium citrate pH 5.6, 14% PEG4K, 15 % isopropanol and 0.1 M sodium citrate pH 5.6, 14% Peg4K, 5 % dimethyl sulfoxide solution respectively. Medium-size (150 x 100x 50 µm) rod-like crystals appeared within a few days. The structure was determined by molecular replacement using MOLREP[18] from the CCP4 package [19] and the free Amadoriase I structure (PDB code: 4WCT) as the search probe. Model building and refinement were carried out using REFMAC5 [20] and PHENIX[21]. The refinement of the two structures converged to a final R/R_{free} = 13.9/18.1 % for SS03 and 17.2/24.4 % for SS17.

IV. Results and Discussion

A. Computational results

SSBOND software outputs a list of 23 possible disulfide bond sites across the enzyme. We built the molecular models of these enzyme mutants (named SS01 to SS23) and we screened them computationally by means of MD simulations. The RMSF was calculated for three different temperatures (270, 300 and 340 K) and the avg-RMSF was interpolated with a linear equation. The slope (λ) represents the index that we used to discriminate the stabilized mutants (as reported in Material & Methods section). We excluded all the enzyme variants whose λ value were bigger than the λ calculated for the native enzyme, and the mutants with a poor avg-RMSF vs. temperature fitting (R^2< 97%).

At the end of this screening phase, we selected four mutants for experimental production and testing. The selected variants were: SS03 with cysteine substitutions in positions 67 and 121, SS07 in positions 106 and 150, SS11 in positions 233 and 404 and SS17 in positions 295 and 303 (Fig 2).

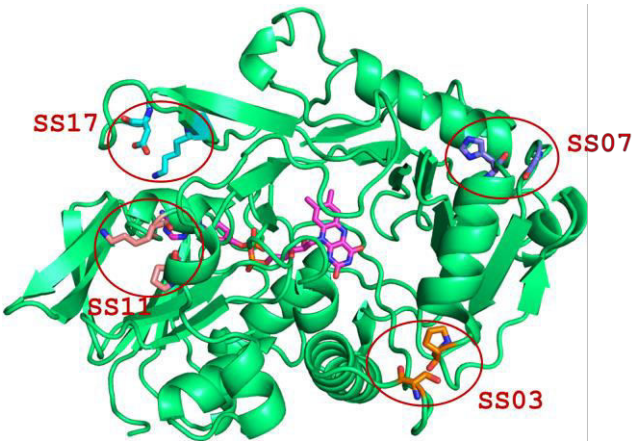

Figure 2. Crystal structure of the native Amadoriase I enzyme (PDB code 4WCT). In sticks, the original amino acids identified as possible, computationally selected, favorable disulfide locations (orange sticks for SS03, blue for SS07, pink for SS11, and cyan for SS17).

B. Experimental results

We obtained pure and active variants: SS03, SS07, SS17 mutants with an average yield of 30 mg per liter of bacterial culture. In contrast, the SS11 variant showed much lower expression levels (less than 1 mg/L) and no detectable activity suggesting that in this case the mutations highly destabilized the enzyme. The SS07 variant also showed lower enzymatic activity than the native enzyme; this suggests that these cysteine mutations introduced a structural perturbation that affects enzymatic activity or that no actual double SS bond formation occurs, thus causing a partial destabilization of the enzyme. For all enzyme variants we report the T_{50}, i.e. the temperature at which the enzymes lose 50% of the activity with respect to its activity at 25°C (Table 1).

TABLE I.
STABILITY OF ENZYME MUTANTS

Enzyme	T_{50} [°C]	ΔT_{50} [°C]
WT	50.40 ± 0.69	-
SS03	55.25 ± 3.28	+4.85
SS07	40.76 ± 1.80	-9.64
SS17	60.62 ± 0.95	+10.22

Absolute T_{50} and difference with respect to native Amadoriase I (ΔT_{50}). Data are reported as the mean of 3 replicas ± standard deviation

With the exception of the SS17 mutant, all the enzymes, including the WT, lose completely their activity at temperatures ≥60°C. the SS17 mutant retains a 50% residual activity at 60°C and shows residual activity up to 95°C (Fig 3). To confirm disulfide bond formation, we performed the same experiments also in the presence of 100 mM 1,4-dithiothreitol (DTT). Indeed, the reduced forms of all the SS-mutants lost their improved thermal resistance and behaved very similarly to the WT.

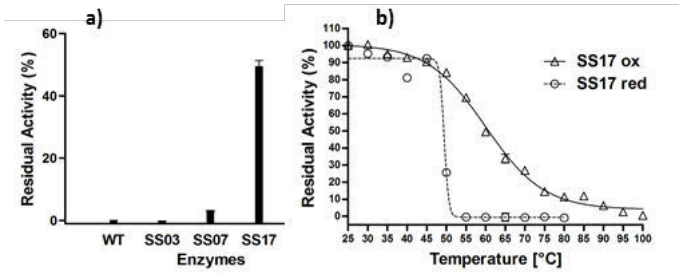

Figure 3. Panel A). Residual activity at 60°C. The histograms show that only variant SS17 retain an activity larger than 50% at that temperature. Panel B) Activity trend of SS17 in its oxidized and reduced form as function of temperature.

We solved the X-ray crystallographic structure of variants SS03 and SS17 to confirm the introduction of the designed disulfide bonds (at 2.15 and 2.85 Å resolution, respectively), and to assess any possible change that such modifications may have caused to their global molecular architecture relative to the wild-type enzyme (Fig 4).

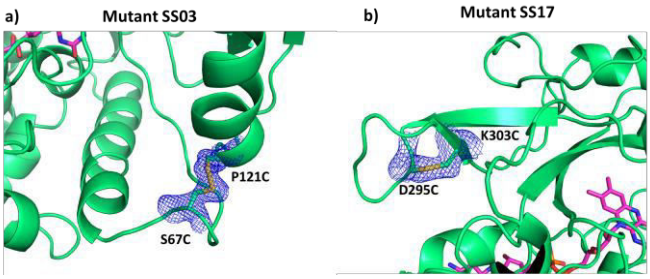

Figure 4. Electron density maps of the SS03 (panel a) and the SS17 (panel b) disulfide bonds.

The enzyme variants maintained a similar overall folding to that of the wild-type enzyme, with an RMSD for main chain atoms of less than 1 Å. No significant variation in the geometry of the catalytic pocket can be observed between the two mutants and the wild type enzyme, demonstrating that indeed the introduction of these disulfide bonds, which is intended for thermal stabilization only, does not alter the architecture of the active site of the enzyme.

In this work we provided a significant thermal stabilization to the Amadoriase I enzyme without incurring in an extensive experimental validation phase. This was achieved via the adoption of a computational high-throughput screening filter based on MD simulations, which was used to evaluate a library of mutations. For most mutants the λ index, chosen as screening filter variable, was larger than that of the native enzyme, suggesting that the introduction of those disulfide bonds may lead to local and/or global unfolding. Conversely, four mutant models featured a reduced λ value, indicating a possible stabilizing effect associated with the designed mutations. In particular, the SS03 mutant showed ~5°C higher thermostability with respect to the native enzyme, while the SS17 variant showed an increase of about 10°C in the T_{50} value and, contrary to all other tested mutants, a gradual decrease in residual activity at increasing temperatures, featuring detectable activity even after thermal treatment at 95°C.

V. CONCLUSION

By the use of a novel and rational computational method

we designed possible Amadoriase I mutants and we identified four possible thermostabilized mutated structures.

Among them, two mutants showed significantly higher thermostability properties compared to the native form.

We believe that our thermostable enzyme may represents a further step towards the development of an improved biosensor to be used for the detection of diabetes as well as a promising starting point for more invasive engineering approach to the design of a new enzyme-based therapeutic tool for pathological protein deglycation. The proposed computational screening method [Fig 5.] appears to be effective in speeding up and reducing the costs of an enzyme thermostabilization campain. The enzyme stabilization is beneficial for different reasons. In addition to allowing the use of the enzymes to higher temperature, it allows to increase the yield of protein production (reducing the cost) and it allows to increase the resistance to transport and storage. In particular, concerning glycated protein detection, stabilized enzymes may improve the typical shelf-life of the biosensors, of which the enzymes are usually the most sensitive component.

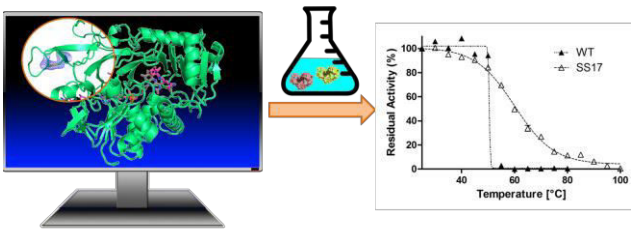

Figure 5. Graphical summary of our method. It combines MD-based screening of possible promising enzyme variants with *in-lab* production, in order to identify the ones with increased thermal stresses resistance, minimizing time and laboratory costs.

Our future work will focus on the validation of this method by further expanding our analysis to different enzymes.

ACKNOWLEDGEMENT

The authors wish to thank Istituto Italiano di Tecnologia and Fondazione Cariplo (grant 2016-0481) for funding. They also thank the X06DA-PXIII beamline personnel of the Paul Scherrer Institute, Villigen Switzerland, for help with the data collection.

REFERENCES

[1] D. R. Sell and V. M. Monnier, "Molecular basis of arterial stiffening: Role of glycation-a mini-review," *Gerontology*, vol. 58, pp. 227–237, 2012.

[2] V. M. Monnier and X. Wu, "Enzymatic deglycation with amadoriase enzymes from Aspergillus sp. as a potential strategy against the complications of diabetes and aging," *Biochem Soc Trans*, vol. 31, no. Pt 6, pp. 1349–1353, 2003.

[3] M. Hatada, W. Tsugawa, E. Kamio, N. Loew, D. C. Klonoff, and K. Sode, "Development of a screen-printed carbon electrode based disposable enzyme sensor strip for the measurement of glycated albumin," *Biosens. Bioelectron.*, pp. 1–7, 2016.

[4] H. Lin and J. Yi, "Current status of HbA1c biosensors," *Sensors (Switzerland)*, vol. 17, no. 8. 2017.

[5] R. G. Paul and A. J. Bailey, "Glycation of collagen: The basis of its central role in the late complications of ageing and diabetes," *Int. J. Biochem. Cell Biol.*, vol. 28, no. 12, pp. 1297–1310, 1996.

[6] S.-Y. Y. Goh and M. E. Cooper, "Clinical review: The role of advanced glycation end products in progression and complications of diabetes.," *J. Clin. Endocrinol. Metab.*, vol. 93, no. January, pp. 1143–1152, 2008.

[7] R. H. Nagaraj, M. Linetsky, and A. W. Stitt, "The pathogenic role of Maillard reaction in the aging eye," *Amino Acids*, vol. 42, no. 4, pp. 1205–1220, 2012.

[8] A. M. Vincent, J. W. Russell, P. Low, and E. L. Feldman, "Oxidative stress in the pathogenesis of diabetic neuropathy," *Endocr. Rev.*, vol. 25, no. 4, pp. 612–628, 2004.

[9] R. H. Stadler, I. Blank, N. Varga, F. Robert, J. Hau, P. a Guy, M.-C. Robert, and S. Riediker, "Acrylamide from Maillard reaction products.," *Nature*, vol. 419, no. 6906, pp. 449–450, 2002.

[10] E. Capuano and V. Fogliano, "Acrylamide and 5-hydroxymethylfurfural (HMF): A review on metabolism, toxicity, occurrence in food and mitigation strategies," *LWT - Food Sci. Technol.*, vol. 44, no. 4, pp. 793–810, 2011.

[11] Y. Qian, J. Zheng, and Z. L. Lin, "Loop engineering of amadoriase II and mutational cooperativity," *Appl. Microbiol. Biotechnol.*, vol. 97, no. 19, pp. 8599–8607, 2013.

[12] D. S. Mottram, B. L. Wedzicha, and A. T. Dodson, "Food chemistry: Acrylamide is formed in the Maillard reaction," *Nature*, vol. 419, no. 6906, pp. 448–449, 2002.

[13] B. Hazes and B. W. Dijkstra, "Model building of disulfide bonds in proteins with known three-dimensional structure," *Protein Eng. Des. Sel.*, vol. 2, no. 2, pp. 119–125, 1988.

[14] F. Rigoldi, A. Gautieri, A. Dalle Vedove, A. P. Lucarelli, S. Vesentini, and E. Parisini, "Crystal structure of the deglycating enzyme amadoriase i in its free form and substrate-bound complex," *Proteins*, 2016.

[15] F. Rigoldi, S. Donini, F. Giacomina, F. Sorana, A. Redaelli, T. Bandiera, E. Parisini, and A. Gautieri, "Thermal stabilization of the deglycating enzyme Amadoriase I by rational design," *Sci. Rep.*, vol. 8, no. 1, p. 3042, 2018.

[16] U. (2017) Theoretical and Computational Biophysics Group, "NAMD 2.13," p. http://www.ks.uiuc.edu/Research/namd.

[17] M. J. Harvey, G. Giupponi, and G. De Fabritiis, "ACEMD: Accelerating Biomolecular Dynamics in the Microsecond Time Scale," *J. Chem. Theory Comput.*, vol. 5, no. 6, pp. 1632–1639, 2009.

[18] A. Vagin and A. Teplyakov, "Molecular replacement with MOLREP," *Acta Crystallogr. Sect. D-Biological Crystallogr.*, vol. 66, pp. 22–25, 2010.

[19] CCLRC Daresbury Laboratory (2017), "CCP4," p. http://www.ccp4.ac.uk.

[20] G. N. Murshudov, P. Skubak, A. A. Lebedev, N. S. Pannu, R. A. Steiner, R. A. Nicholls, M. D. Winn, F. Long, and A. A. Vagin, "REFMAC5 for the refinement of macromolecular crystal structures," *Acta Crystallogr. Sect. D-Biological Crystallogr.*, vol. 67, pp. 355–367, 2011.

[21] P. D. Adams, P. V Afonine, G. Bunkoczi, V. B. Chen, I. W. Davis, N. Echols, J. J. Headd, L. W. Hung, G. J. Kapral, R. W. Grosse-Kunstleve, A. J. McCoy, N. W. Moriarty, R. Oeffner, R. J. Read, D. C. Richardson, J. S. Richardson, T. C. Terwilliger, and P. H. Zwart, "PHENIX: a comprehensive Python-based system for macromolecular structure solution," *Acta Crystallogr. Sect. D-Biological Crystallogr.*, vol. 66, pp. 213–221, 2010.

Evaluation of butanediol diglycidyl ether crosslink density along a collagen molecule

Irene Cristiani[1], Federica Rigoldi[1], and Simone Vesentini[1]
[1]*Dipartimento di Elettronica, Informazione e Bioingegneria, Politecnico di Milano*

***Abstract* — 1-4 butanediol diglycidyl ether (BDDGE) represents an innovative reagent for type I collagen cross-linking. In fact, along the collagen molecule, lysine residues are amenable binding sites for BDDGE. In this regard, a key structural parameter to be verified is if two lysine side chains would be close enough to be linked to BDDGE extremities. For this reason, molecular dynamics (MD) simulation have been performed both on the unbound BDDGE and on the collagen molecule. Results confirmed that BDDGE does not crook in the unbound state, maintaining an end-to-end length of about 0,9 nm. Within this length, 14 lysine couples represent putative sites for collagen functionalization.**

***Keywords* — Butanediol, Collagen functionalization, Molecular modelling.**

I. Introduction

COLLAGEN is the major structural protein of the animal body, from the simplest sponges to Homo sapiens. Because of its high mechanical strength, good resistance to degradation and its low antigenicity, it has been used in a wide range of products in industry and in regenerative medicine. The basic structure of collagen is very simple. The primary sequence is basically a repeating tripeptide (Gly-Xxx-Yyy) 100-400 where Xxx and Yyy are specific amino acid such as Proline, Alanine and Hydroxyproline [1]. Each peptide adopts a left-handed polyproline helix and the three chains interacts to form a right-handed triple helix. Although the family of collagen molecules forms several different types of aggregates, the majority of collagen has a fibrous structure in which the long rod-like molecules (1.5 × 300 nm) are aligned in parallel in a quarter-staggered arrangement. Collagen products can be purified from fibers, molecules reconstituted as fibers or from specific recombinant polypeptides with preferred properties. A common feature of all these biomaterials is the need to control the mechanical properties and the residence time in the body by means of a stable cross-linking agent. Chemically, this can be achieved through the use of different cross-linking agents that react with two specific amino acid residues on the collagen molecule, imparting individual biochemical, thermal and mechanical characteristics to the biomaterial. The exact location of these two amino acids and the number of couple can be evaluated precisely by in silico studies. In particular, the time evolution of a given crosslinking agent can be used to establish a geometrical/structural threshold to determine the most effective couple of amino acids along the collagen molecule.

II. Material and Methods

The fibril model, extensively described in previous works [2],[3], is solvated using the solvate plugin of VMD [4] by adding TIP3P water molecules. Since the molecule at physiological pH includes a net charge (positive net charge +34), counterions (Cl^-) are added to keep the system neutral. The final solvated all-atom system contains about 75,000 atoms, including ≈ 12,000 water molecules. The first step of energy minimization is performed by a steepest descent algorithm using the NAMD 2.9 code and the CHARMM force field to identify the most likely position of lysine couples. Full atomistic simulations are carried out using the NAMD 2.9 code. Rigid bonds are used to constrain covalent bond lengths involving hydrogen atoms, thus allowing an integration time step of 2 fs. Non-bonding interactions are computed using a cut-off for neighbor list at 1.35 nm, with a switching function between 1.0 and 1.2 nm for van der Waals interactions, while the Particle-Mesh Ewald sums method is applied to describe electrostatic interactions. The fibril model is equilibrated through 100 ns molecular dynamics simulations at a temperature of 310 K (37 °C). The structural convergence of the structure is reached within the first 30 ns, hence the remaining 70 ns are used for analysis. The 70 ns molecular dynamics trajectory of the collagen microfibril is analyzed through an in-house VMD script to find lysine–lysine pairs for which the distance between lysine Nζ atoms is below a 10 Å cutoff.

A. Chemical crosslink

Collagen, because of its highly crystalline structure, is relatively inert to chemical and enzymatic attack over a long period of time. Nonetheless, slow and detrimental degradation often occurs, but it can be mitigated by artificial covalent cross-linking reagents. The interaction of these reagents may occur with the ε-amino group of lysine residues, the carboxyl groups of glutamic and aspartic acids, or with hydroxyl groups. Nature and stability of these different chemical bonds produce a significant difference in the peculiar properties of the cross-linked product. Whit respect to other cross-linker, the advantage in using BDDGE derives from its morphological features that can be tuned by acting on its reaction parameters (mainly temperature, pH and BDDGE concentration), to obtain *ad hoc* results such as the enhancement of the final biomaterial mechanical properties For example, the use of BDDGE as type I collagen crosslinker has been proved to increase elasticity and tensile strength of the collagen scaffold, providing high stability and enhancing its resistance towards enzymatic degradation [5].

B. 1-4 Butanediol diglycidyl ether

Cyclic ethers are reactive due to the strained three-membered ether ring that can be opened by the nucleophilic attack of bases and acids. The polyepoxide 1,4-butanediol diglycidyl ether (BDDGE) has been used to cross-link dermal sheep collagen at either alkaline or acidic pH. At acid pH cross-linking is predominantly via reaction with carboxylic acid groups whilst alkaline pH results in cross-links involving amine groups [5]. The full atomistic, three-dimensional model of BDGGE is built from the chemical structure using Hyperchem 6 software, and simulated for 2 ns using the NAMD 2.9 code and the CHARMM force field. The trajectory of the simulation is used to define the average distances between the terminal carbon atoms of the molecules as well as the angle formed by these two carbons and Carbon number 5, as shown in figure 1.

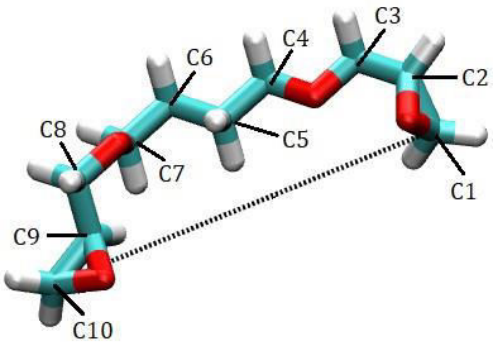

Figure 1: Reference carbons for molecular distension analysis.

In particular, the molecule obtained from Hyperchem is approximately 10 Angstrom long and has 32 atoms. After BDDG is uploaded on VMD, it is solvated using the solvate plugin and then ionized through the auto-ionize plugin. The ionization process aims at simulating a system with a neutral pH by adding 0.15 M of NaCl salt. The Final total number of atoms of the system is 10210, with 10158 TIP3W atoms, 10 SOD and 10 CLA type ions. Three simulations are run in order to obtain a stable system: first, the molecule is fixed while the surrounding environment is free to adjust according to weak forces (eg. Van der Waals) and interactions between ions and water, for 40 ps, in NPT ensemble. Then, the molecule's alpha carbon backbone is restrained from movement, allowing hydrogens atoms to tune their position for 80 ps, in NPT ensemble. Finally, a NVT simulation is run for 2 ns.

III. Results and Discussion

A. 1-4 Butanediol diglycidyl ether

After the NVT simulation, an RMSD analysis was carried out to verify that the system had come to a stable condition. As shown in Figure 2, this was the case since the trend of the RMSD curve is to reach convergence. After data from the molecular dynamics simulations were retrieved and processed, BDDGE mean length was found to be of 9.4 Angstroms.

This value, consistent with what is currently reported from literature in *in vitro* studies [6], was used as a reference to find lysine couples in the *in silico* collagen model.

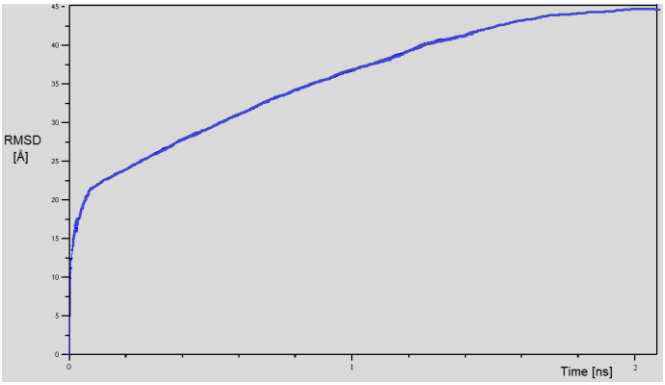

Figure 2: BDDGE RMSD during the NVT simulation of 2 ns.

Furthermore, to understand how BDDGE length varied over time at equilibrium conditions in aqueous environment, we considered the distance between the two carbons C_{10} and C_1 (figure 1) during the NVT simulation, finding no significant changes in BDGGE overall geometry. This was confirmed by the analysis performed on the internal angles of the molecule, namely the angle between carbons C10-C5-C1, C10-C7-C5 and C5-C3-C1, whose value remains stable through the simulation. In fact, angle variation during the NVT simulation is ≈ 1,3% for C10-C5-C1, ≈ 8,3% for C10-C7-C5 and ≈ 26% for C5-C3-C1.
From this qualitative analysis, results show that BDDGE has a convenient geometry for collagen crosslinking.

A. Collagen binding sites

Since BDDGE characteristic length was found to be ≈ 9 Angstroms, the goal was to locate, along the fibril backbone, lysine residues close less than 10 Angstroms, so that crosslinking collagen with BDDGE can be possible, as sketched on Figure 3.

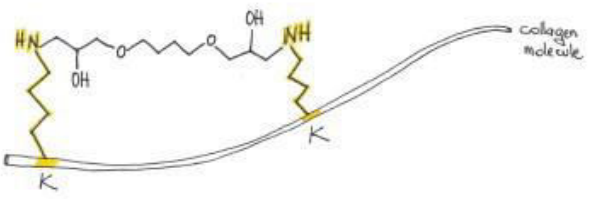

Figure 3: Sketch of a portion of the final crosslinked molecule

In order to do that, a script was implemented to systematically find the exact positions of each lysine residue. In particular, each lysine N-terminus was taken as reference to evaluate the distance between two subsequent lysine. Only the couples close less than 10 Angstroms for at least the 25% of the simulation time were considered. The mean distance between said couples was found to be of about 9 Angstroms. The total

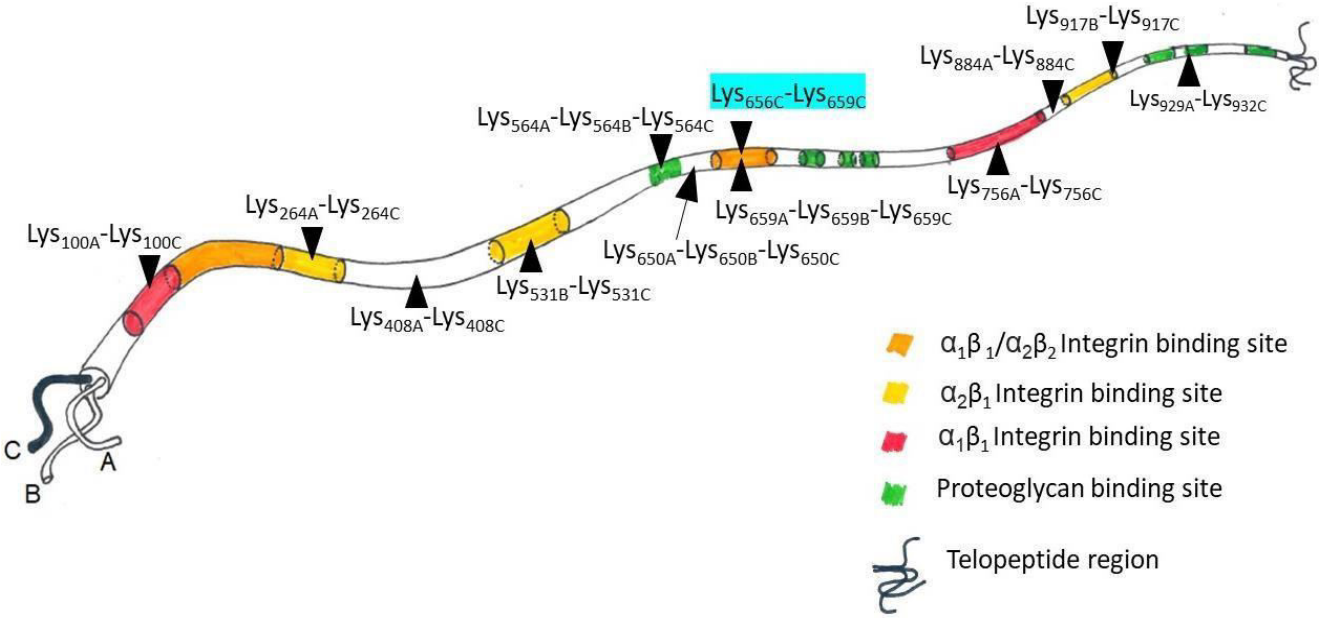

Figure 4: Qualitative location of lysine couples along a collagen molecule

number of lysine residues within the collagen fibril is 186, of which 14 couples were found consistent with requirements. The overall distribution of ligand-binding sites on type I collagen fibril are qualitatively shown in Figure 4.

Highlighted in light blue is the only lysin couple that stays close to the subsequent lysine residue of the same chain (C), rather than to a lysine of another chain. The orange, yellow and fuchsia sections represent integrins binding sites, respectively $\alpha_1\beta_1/\alpha_2\beta_2$, $\alpha2\beta_1$ and $\alpha_1\beta_1$. The green sections represent proteoglycan binding site and the doodled extremities of the molecule portray the telopeptide region. Results report just one couple of residues *intra* chain, while all the other couples are found to be *inter* chains. Furthermore, data show that some of the lysine couples (≈ 42%) fall in the region of intermolecular recognition along the collagen molecule, that is the position of the major binding sites for proteoglycans (keratan sulfate proteoglycan, and dermatan sulfate proteoglycan), collagenases, heparin, integrin and enzymatic crosslinks.

This means that functionalizing collagen in those points could lead to the modification of its interaction with other molecules such as proteoglycans, enzymes (e.g., collagenase) and cell integrins and it would lead to a decrease in substrate adhesive properties.

IV. Conclusion

In this work, a MD model of 1-4 butanediol diglycidyl ether was implemented, with the aim to study some specific nanoscale-level properties. The prospect would be to virtually crosslink the *in silico* collagen model. Furthermore, thanks to the knowledge obtained from MD simulations and the post-process analysis, it maybe be possible to create composite experimental models, by grafting BDDGE onto the collagen backbone throughout the amino group of the lateral chain of the lysine residue.

So far, this work regards the MD simulations and post-processing analysis of the two individual molecules. MD simulations were run to understand BDDGE behavior in an aqueous environment and results showed that the molecule's geometry does not change considerably over the simulation time at equilibrium, thus proving it to be a stable compound t be used for collagen crosslinking. This is just a beacon in light of the possible foreseeable applications of BDDGE as a bridge for molecular crosslinking, coupling and functionalization.

The choice of the BDGGE molecule was determined by the fact that it represents an innovative bifunctional reagent for collagen crosslinking. Nonetheless, hardly any study on reaction kinetics has been described in literature [5], not to mention MD studies. The three-dimension, full-atomistic representation of BDDGE proposed in this work is therefore a pioneering model, allowing a qualitative analysis of its molecular dynamics and leaving space for future developments.

To conclude, this study could aid the design of artificial compounds for Tissue Engineering, while the MD models can provide a reference for a variety of projects, so to deepen our understanding of the physico-chemical nature underlying molecules interactions with the environment and qualitatively improve the accuracy in predicting some behaviors such as folding or docking.

References

[1] A. Gautieri, A. Redaelli, M. J..Buehler, S. Vesentini, "Age and diabetes-related nonenzymatic crosslinks in collagen fibrils: Candidate amino acids involved in Advanced Glycation End-products", Matrix Biology, Volume 34, February 2014, Pages 89-95

[2] Nair et al., "Molecular mechanics of mineralized collagen fibrils in bone", Nature Communications, Volume 4, April 2013

[3] A.Gautieri, S. Vesentini et al., "*Hierarchical structure and nanomechanics of collagen microfibrils from the atomistic scale up.*" Nano Lett., Volume 9, February 2011, Pages 757-66

[4] Humphrey et al., "VMD: visual molecular dynamics.", J Mol Graph. Volume14, February 1996, Pages 27-8

[5] R. Zeeman, P.J. Dijkstra et al., "*Cross-linking and modifcation of dermal sheep collagen using 1,4-butanedio diglycidyl ether*" CROSSLINKING OF COLLAGEN-BASED MATERIALS, 1998 Chapter 3, Pages 43-60.

[6] A. Nicoletti, M. Fiorini, et al., "*Effects of different crosslinking conditions on the chemical-physical properties of a novel bio-inspired composite scaffold stabilised with 1,4-butanediol diglycidyl ether (BDDGE)*", 24, J. Mat. Science, Pages 17-35

On-field assessment of the rugby tackle for ACL injury prevention and technique enhancement

D. Pavan [1], F. Cibin [1], A. Guiotto [1], A. Colangelo [1], F. Spolaor [1], T. Casagrande [2], G. Sbrocco [2], A. Pavanello [2] and Z. Sawacha [1]

[1] *Department of Information Engineering, University of Padua, Italy*

[2] *Italian Rugby Federation (FIR), Rome, Italy*

***Abstract*— When considering some of Rugby game's strongholds such as gaining possession, retaining possession, creating space, penetrating, supporting play during a rugby match high-speed hits and great forces delivery are expected. The most injuring tasks have been recognized in scrummaging and tackling. Researches developed about injuries' risk assessment displayed that, although scrummage more likely injuries the participating athletes, the tackle leads to a higher number of injuries, being the most contact task performed. This study aims to assess the tackle biomechanics both in term of performance and its implication in injury prevention. Ten elite players were acquired on the field with 4 synchronized cameras and a Novel Pedar plantar pressure system. Hence three side-on tackles were elaborated to compute kinematics, ground reaction forces, joint torques and centre of mass acceleration. Results highlighted differences between the single player and the rest of the team, enabling identifying potentially dangerous behaviours for the anterior cruciate ligament (ACL) injury, while evaluating also the gesture effectiveness. The developed setup and elaboration workflow has been proved to be effective in the identification of athletes with higher risk of noncontact ACL injury, analysing a sport-specific gesture executed in its environment. The developed tool could be used as a screening to prevent ACL injuries, developing specific preventive training routines, basing on the results acquired on field.**

***Keywords*—Rugby tackle, biomechanics, on-field, injury prevention.**

I. Introduction

DUE to the hits and high forces developed during a rugby match, injury rate is likely to be higher than other non-contact sports. Body districts that have been demonstrated to have the highest injury incidence are: head, shoulder, thigh, knee and ankle [1], [2]. Connections between injuries and playing dynamics in which they are more likely to happen have been proved [1]; although the scrum is the circumstance when most serious injuries are more likely to happen [3], [4] the tackle, being a skill much more performed, is reporting a higher injury frequency, and leads to longest overall athlete's absence period from trainings and competitions [5], [6]. Injuries concerning the tackler have been recognized to mostly affect the shoulder and lower limb, especially the anterior cruciate ligament (ACL) [7].

High fitness level is essential to Rugby players, since the injury risk influencing factors in the tackle includes number of performed tackles, their impact force [8], and the reduced ability to regain speed, and thus momentum, as quick as possible in preview of the next impact [9]. Injury prevention must therefore pass through an excellent fitness state; furthermore, an in-depth technique knowledge is mandatory especially for the tackle [10], as have been reported that since young ages the athletes, even though during the training sessions focus their attention to keep a correct posture while tackling, in competition leave "Your own safety" at the 8th position of the importance chart, where "Bringing down the ball-carrier at all costs" and "Preventing the ball-carrier from gaining position" covers respectively the 1st and 2nd place [11].

High impact speed, acceleration at contact, correct body posture and great force delivery are expected to perform a dominant and safe tackle. Finally, regaining a quick standing posture after grounding is required to retrieve the ball.

Among the available on field screening methodologies, it is possible to find protocols that employ video acquisitions, evaluation scales correlating physiological parameters and risk of injury, and observational methodologies.

Physiological evaluation scales as the method developed by Myer [12]-[14], mainly based on knee joint range of motion, isokinetic tests and knee position variation on the coronal plane, they were less reliable than protocols such as the landing error scoring system (LESS) [15]-[17] which, with the aid of two cameras placed frontally and laterally to the subject, aims to quantitatively assess the postural errors during the drop-jump test. Other preventive screening protocols were even less reliable and repeatable [18], [19].

High accuracy was found in laboratory studies, which demonstrated greater repeatability in the prevention of ACL injuries. On the other hand, screening tests carried out on field proved to be more accessible for the tools and time needed, returning results aimed to identify subjects needing further investigations [19].

The development of a methodology for the evaluation of variables validated as ACL injury risk predictive, combining the use of reproducible data with the accessibility of tools and the speed of acquisition and processing, would lead to the development of a screening protocol for ACL injury prevention returning more reliable results when compared to the protocols currently present in the literature.

The aim of the present study is to develop a biomechanical based tool to assess tackling technique, directly on field, as a means for ACL injury prevention and performance optimization.

II. Methods

A. Subjects

Ten subjects participated in the study (mean ± standard deviation (SD) BMI: 29.26±4.41, age: 24.20±4.49 years). All

the athletes were members of the Benetton Rugby Treviso team: one of the two Italian clubs permanently tacking part in the Guinness PRO14 international championship.

B. Task

Subjects, after signing informed consent, performed 4 repeating tackles in the rugby field.

The tackle execution area (10 m length, 4 m width) and the instructions given, only to the ball carrier, were thought to make the tackler to replicate a gesture as close as possible to the one performed during a match.

The playing situation presented to the tackler was shaped to drive him to choose the side-on tackling technique [20], without asking him directly to perform that specific gesture.

C. Data collection and Elaboration

Video sequences and plantar pressure (PP) distribution were acquired by means of a Novel Pedar system and 4 synchronized cameras (GoPro Hero3), placed on the outer side of the playing area corners; hence peak PP, peak vertical ground reaction force (PV), hip, knee and ankle joints kinematics were determined [21], [22] and their position with respect to the tackle evaluated with purposely developed Matlab code.

Specific features were tracked bilaterally, directly on the motion sequences [22]: acromion, C7, L5, anterior iliac spine, posterior iliac spine, greater trochanter, lateral femoral epicondyle, calcaneus, two points on the shoe corresponding to the 1st and the 5th metatarsal head, lateral humerus epicondyle. Key instants were recognized as: left foot PV (PVL), right foot PV (PVR), contact between players (C). A further Matlab code was developed to calculate the knee torque in the three key instants, both in flexion/extension (FET) and varus/valgus (VVT). Tackler's centre of mass (CM) acceleration was calculated based on a 2D trajectory reconstruction; positive and negative CM acceleration peaks were identified in three phases of the task: start-contact (SC), contact-grounding (CG), and grounding-ball retrieve (GR).

The Mann-Whitney U test was finally applied to compare the single subject to the rest of the cohort, for each of the considered variables (α-level = 0,05).

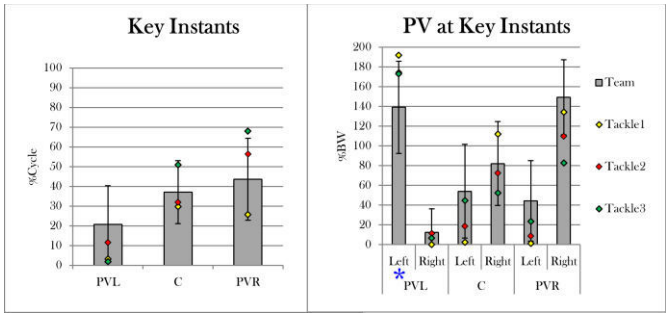

Fig. 1: Key instants during the tackle, and relative PV (*=p<0,05)

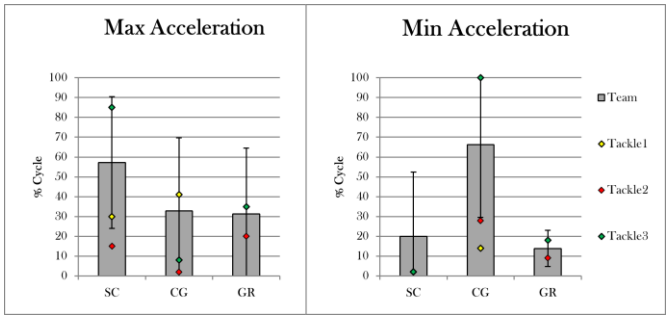

Fig. 2: Acceleration peaks during the three tackle phases.

III. RESULTS

Results here reported concern a single player's performance, compared to the rest of the cohort: the considered athlete reported behaviours strongly different from the cohort while approaching the tackle. The left leg showed a significantly higher load in term of PV, reaching the 191,9% of body weight (BW; Fig. 1), along with higher extensive moments in the three joints analysed (p<0,05) at PVL instant (Fig. 3-5). At C instant, the right limb clearly showed a higher tendency to the valgus, supported by the torque at hip, knee (-9,2±1,2% BW*height), and ankle (p<0,05); this latter one registered a higher eversion torque also at RPV. Results concerning the same variables are available for all the acquired athletes. Effective and dominant tackle attitude has been underlined in single players, as later discussed with the coaching staff, and potentially ACL-injuring behaviours, showed by three athletes (one of which presented here) have been reported to the medical and coaching staff to take action with specific, preventive training protocols.

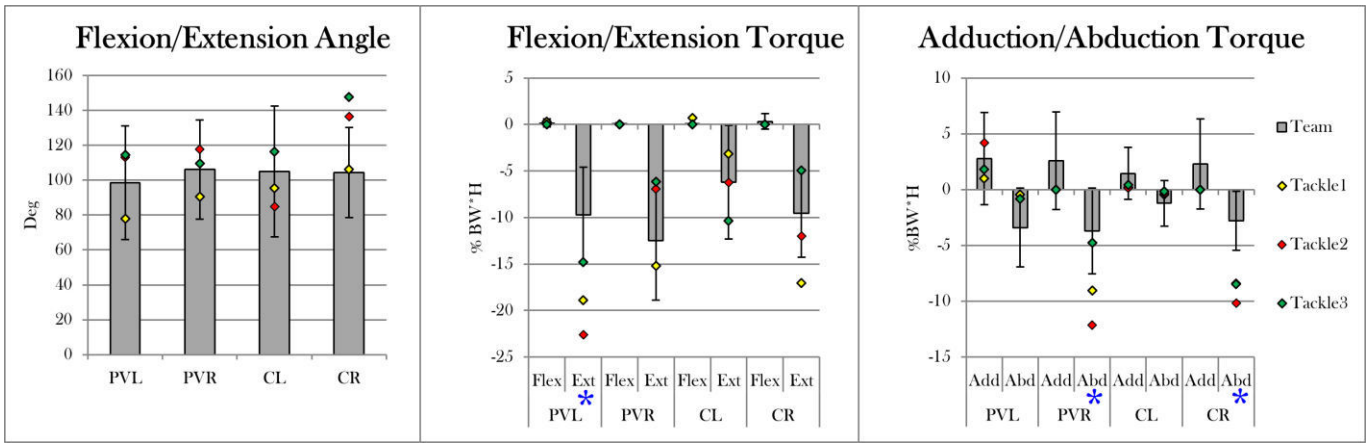

Fig. 3: Hip joint sagittal plane kinematics, coronal and sagittal plane dynamics (*=p<0,05). BW*H = Body Weight times Height.

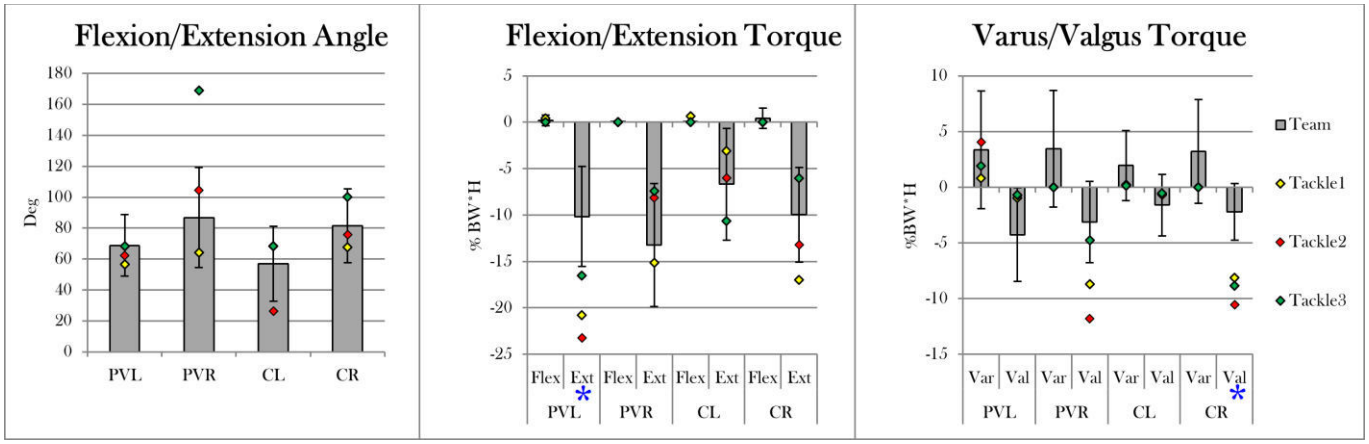

Fig. 4: Knee joint sagittal plane kinematics, coronal and sagittal plane dynamics. (*=p<0,05). BW*H = Body Weight times Height.

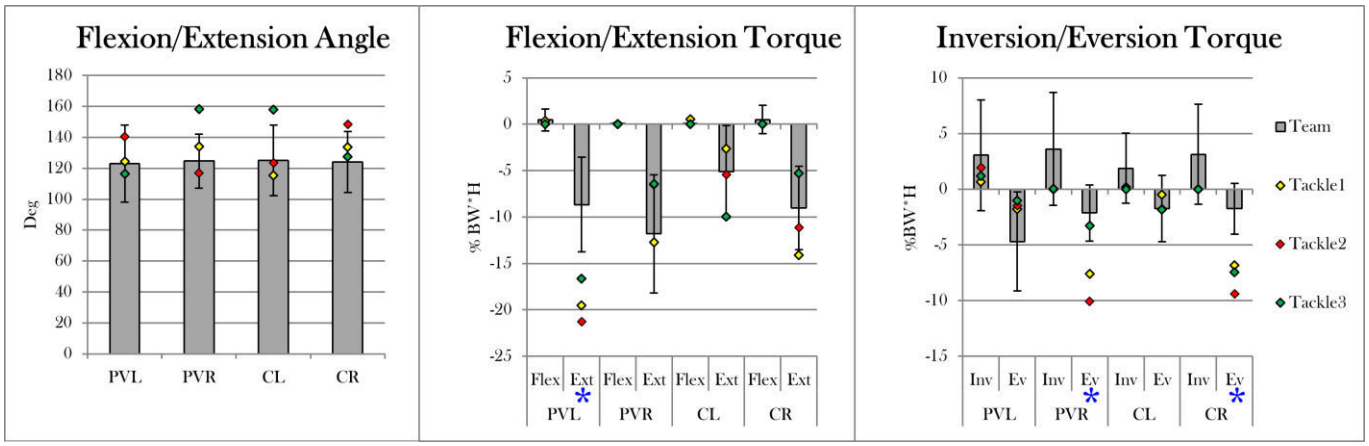

Fig. 5: Ankle joint sagittal plane kinematics, coronal and sagittal plane dynamics. (*=p<0,05). BW*H = Body Weight times Height.

IV. Discussion

The considered athlete showed higher loads on the left limb when compared to the rest of the cohort, while a significantly higher valgus moment was registered at the right knee, both in PV and C instants. As valgus torque has been proven to be related to ACL injury risk [23], [24], and valgus posture associated with low scoring in widely applied screening procedures [19], the higher loads on the counter lateral limb could be interpreted as a protection/compensation for the right leg poor posture. One trial showed a high flexion in the dominant knee, along with a contemporary low load appliance: as the knee deep flexion has been associated with ACL tensioning [25], [26], it is to be avoided during high load activities, especially in open skills gestures: a high load associated with this posture, during an open skill, will eventually lead to an injury, and is therefore to be avoided.

A relation between hip, knee, and ankle moments on the coronary plan has been noticed, leading to the belief of a poor posture in the whole low limb: hence preventive training could be useful in correcting the lower limb positioning during the specific task [27], and the same evaluation protocol could be applied to estimate the specific training effectiveness. The evaluation of a specific task gives the opportunity to investigate dynamics and kinematics of a specific gesture, performed in its environment, going beyond the potential bias given by the difference between closed and open skill, and by the gesture learning effect. Finally, CM acceleration peaks (Fig. 2), along with PV and key instants temporal displacement (Fig. 1), are useful to the coaching staff for the gesture execution assessment, in terms of technique effectiveness.

V. Conclusion

The present experimental setup and elaboration flow has allowed us to effectively assess executive quality and safety of the tackle, directly on-field. Results have been supported from the coaching staff. Further development of the study will include enhancing the sample size and to develop a complete screening tool for coaches and video analysts, while determining a complete biomechanical model for the tackle. Furthermore, the developed tool could be useful in different sport-specific gestures, with minimum adaption of the experimental setup.

Acknowledgement

The authors acknowledge the Benetton Rugby Treviso club for athletes and rugby field availability.

References

[1] J H M Brooks, C W Fuller, S P T Kemp and D B Reddin, "Epidemiology of injuries in English professional rugby union: part 1 match injuries" *Br. J. Sports Med.,* vol. 42, pp. 757-766, 2005.

[2] D T Fong, Y Hong, L Chan, P S Yung and K Chan, "A Systematic Review on Ankle Injury and Ankle Sprain in Sports" *Sports Medicine,* vol. 37, *(1),* pp. 73-94, 2007.

[3] M J Wetzler, T Akpata, W Laughlin and A S Levy, "Occurrence of cervical spine injuries during the rugby scrum" *Am. J. Sports Med.,* vol. 26, *(2),* pp. 177-180, 1998.

[4] A E Taylor, S Kemp, G Trewartha and K A Stokes, "Scrum injury risk in English professional rugby union" *Br. J. Sports Med.,* vol. 48, pp. 1066-1068, 2014.

[5] C W Fuller, J H M Brooks, R J Cancea, J Hall and S P T Kemp, "Contact events in rugby union and their propensity to cause injury" *Br. J. Sports Med.,* vol. 41, pp. 862-867, 2007.

[6] S P Roberts, G Trewartha, M England and K A Stokes, "Collapsed scrums and collision tackles: what is the injury risk?" *Br. J. Sports Med.,* vol. 49, *(8),* pp. 536-540, Apr, 2015.

[7] K L Quarrie and W G Hopkins, "Tackle injuries in professional rugby union" *Am. J. Sports Med.,* vol. 36, *(9),* pp. 1705-1716, 2008.

[8] S Hendricks and M I Lambert, "Theoretical Model Describing the Relationship between the Number of Tackles in Which A Player Engages, Tackle Injury Risk and Tackle Performance" *Journal of Sports Science and Medicine,* vol. 13, pp. 715-717, 2014.

[9] W M Garraway *et al*, "Factors influencing tackle injuries in rugby union football" *Br. J. Sports Med.,* vol. 33, pp. 37-41, 1999.

[10] C W Fuller *et al*, "Injury risks associated with tackling in rugby union" *Br. J. Sports Med.,* vol. 44, *(3),* pp. 159-167, Feb, 2010.

[11] S Hendricks, E Jordaan and M Lambert, "Attitude and behaviour of junior rugby union players towards tackling during training and match play" *Saf. Sci.,* vol. 50, *(2),* pp. 266-284, 2012.

[12] J Goetschius *et al*, "Application of a clinic-based algorithm as a tool to identify female athletes at risk for anterior cruciate ligament injury: a prospective cohort study with a nested, matched case-control analysis" *Am. J. Sports Med.,* vol. 40, *(9),* pp. 1978-1984, 2012.

[13] G D Myer, K R Ford, J Khoury, P Succop and T E Hewett, "Development and validation of a clinic-based prediction tool to identify female athletes at high risk for anterior cruciate ligament injury" *Am. J. Sports Med.,* vol. 38, *(10),* pp. 2025-2033, 2010.

[14] G D Myer, K R Ford and T E Hewett, "New method to identify athletes at high risk of ACL injury using clinic- based measurements and freeware computer analysis" *Br. J. Sports Med.,* vol. 45, *(4),* pp. 238, 2011.

[15] D A Padua *et al*, "Reliability of the landing error scoring system-real time, a clinical assessment tool of jump-landing biomechanics" *J. Sport Rehab.,* vol. 20, *(2),* pp. 145-156, 2011.

[16] D A Padua *et al*, "The Landing Error Scoring System (LESS) Is a valid and reliable clinical assessment tool of jump- landing biomechanics: The JUMP- ACL study" *Am. J. Sports Med.,* vol. 37, *(10),* pp. 1996, 2009.

[17] H C Smith *et al*, "A prospective evaluation of the Landing Error Scoring System (LESS) as a screening tool for anterior cruciate ligament injury risk" *Am. J. Sports Med.,* vol. 40, *(3),* pp. 521-526, 2012.

[18] J M Dallinga, A Benjaminse and K A Lemmink, "Which Screening Tools Can Predict Injury to the Lower Extremities in Team Sports?" *Sports Medicine,* vol. 42, *(9),* pp. 791-815, 2012.

[19] A S Fox, J Bonacci, S G McLean, M Spittle and N Saunders, "A systematic evaluation of field-based screening methods for the assessment of anterior cruciate ligament (ACL) injury risk" *Sports Medicine,* vol. 46, *(5),* pp. 715-735, 2016.

[20] W Viljoen, P Treu and B Swart, *Safe and Effective Techniques in Rugby - Practical Guidelines.* South African Rugby Union, 2009.

[21] F A Magalhães *et al*, "Performance of an automatic tracking software for underwater motion analysis" *Journal of Sports Science and Medicine, (12),* pp. 660-667, 2013.

[22] Z Sawacha *et al*, "Biomechanical assessment of balance and posture in subjects with ankylosing spondylitis" *Journal of Neuroengineering and Rehabilitation,* vol. 9, *(1),* pp. 63, 2012.

[23] C S Shin, A M Chaudhari and T P Andriacchi, "The effect of isolated valgus moments on ACL strain during single-leg landing: A simulation study" *J. Biomech.,* vol. 42, *(3),* pp. 280-285, 2/9, 2009.

[24] C S Shin, A M Chaudhari and T P Andriacchi, "Valgus plus internal rotation moments increase anterior cruciate ligament strain more than either alone" *Med. Sci. Sports Exerc.,* vol. 43, *(8),* pp. 1484-1491, 2011.

[25] C O Dyrby, M K toney and T P Andriacchi, "27 Relation between knee flexion and tibial-femoral rotation during activities involving deep flexion," *Gait & Posture,* vol. 5, *(2),* pp. 179, 1997.

[26] T Nagura, C O Dyrby, E J Alexander and T P Andriacchi, "Mechanical loads at the knee joint during deep flexion" *Journal of Orthopaedic Research,* vol. 20, *(4),* pp. 881-886, 2002.

[27] D R Bell, D C Oates, M A Clark and D A Padua, "Two-and 3-dimensional knee valgus are reduced after an exercise intervention in young adults with demonstrable valgus during squatting" *Journal of Athletic Training,* vol. 48, *(4),* pp. 442-449, 2013.

Patient-Specific CFD modelling in the Thoracic Aorta through a Least-Square 3-Element Windkessel approach

R.M. Romarowski[1], A. Lefieux[2], S. Morganti[1], A. Veneziani[2], and F. Auricchio[1]
[1] *Department of Civil Engineering and Architecture, University of Pavia, Italy*
[2] *Department of Mathematics and Computer Science, Emory University, USA*

***Abstract*— Computational fluid dynamics in the aorta is currently a well established methodology. Authors describe many possibilities to prescribe boundary conditions, all of them based on the availability of data. In this article we propose a tuning method for 3-Element Windkessel based on constrained optimization. Flow data is extracted from PC-MRI whereas pressure wave is adopted from literature. We conclude that this method performs better than using data usually available in literature.**

***Keywords*—computational fluid dynamics, thoracic aorta, boundary conditions, lumped parameter models.**

I. Introduction

Patient-specific modeling of cardiovascular diseases has been consolidating over the last two decades as a tool for quantitative analysis to elucidate pathological dynamics or even to design new therapies. Computational Fluid Dynamics (CFD) simulations customized in geometries retrieved from patient's images are moving from a proof-of-concept stage to the clinical practice.

The customized treatment of boundary data still requires specific investigations due to its major impact in numerical results. On the one hand, one would like to retrieve from specific measures all the data needed by the mathematical model, so to maximize the adherence of the numerical model to the patient-specific data. On the other hand, this is not possible nor appropriate for physical or practical limitations of the measurement process. Devices have limited time and space resolution and measures are typically affected by noise and inconsistencies, so they are not complete and trustworthy. In addition, clinical needs require referring to non-invasive and possibly already approved protocols.

Different pathologies, diseases, vascular districts and ultimately available measures in this respect lead to different strategies and the identification of the optimal approach for different problems (and different purposes) is far from being reached. In particular, treatment of boundary conditions shows a wide variety of approaches from an extremely simplified stress free approach in the outflow boundaries to sophisticated data assimilation techniques such as Kalman filtering.

The aim of this article is to present and test an algorithm for calibrating boundary conditions in thoracic aortic simulations based on the so called 3-Element Windkessel model (3WK) and a minimization approach as proposed by [1]. A recent article [2], though using a different calibration strategy, has confirmed the strength of using 3WK circuits as outflow boundary conditions against other methodologies.

We illustrate our novel calibration technique for the parameter identification together with its validation. Special focus is done on possible approaches for the reliable prescription of defective (or missing) data. Then we test it in one patient within the framework of a Computer Aided Clinical Trial dedicated to the investigation of aortic pathologies, and CFD results are compared with parameter calibration techniques proposed by other authors.

II. Methods

One patient with an aneurysm in the aortic arch was selected from our database. Aortic geometry was reconstructed from thin-cut angioCT from the annulus to the diaphragm including the proximal part of the three supraortic vessels. Volume meshing was performed with VMTK [3], resulting in a mesh of 4.5 million tetrahedral elements. All simulations were run with lifeV finite element library [4].

In addition contrast MRI (PC-MRI) was retrospectively reviewed in order to collect flow data in all the aforementioned boundaries.

To test our hypothesis, we run four sets of simulations with different boundary conditions each: BC1, where both inflow and 3WK parameters were retrieved from literature [5,6]; BC2, where the inflow wave was patient-specific and the outflow parameters were, again, retrieved from literature; BC3 and BC4, where both inflow wave and outflow 3WK were patient specific.

In order to tune the resistances and capacitance in the outlets, we used a constrained optimization procedure as described in [1]. Since the pressure wave required for the procedure was missing because no catheterization was performed, we assumed a standard one as described in [7] and then adapted to match each patient's mean and pulse pressures.

Conservation of mass was not respected neither instantaneously nor by integrating an entire heart beat. In order to account account for this difference in our simulations the 3WK parameters in the descending aorta of BC3 were tuned by subtracting the supraortic flow to the ascending aortic flow. In BC4, the tuning in the descending aorta was made directly with the flow wave retrieved from PC-MRI within its slice.

Velocity and WSS fields were compared qualitatively. Pressure and flow waves in the outputs were compared against their reference counterpart.

III. Results

Figure 1 shows the velocity field at the systolic peak considering all the boundary condition strategies.

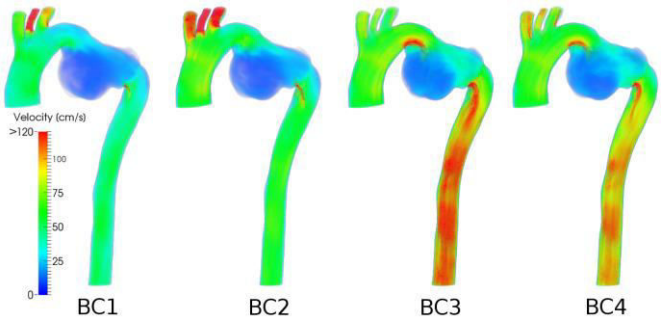

Figure 1: Velocity volume rendering in our patient. Each set of boundary conditions results in a different hemodynamic behaviour.

Higher velocities towards the supraortic vessels are seen in BC1 and BC2. Conversely, when using patient-specific data, flow is mostly diverted towards the descending aorta (BC3/BC4).

This is confirmed in Figure 2, where flow distribution is significantly different among tuning strategies. BC3 and BC4 show the closest agreement in terms of flow in most of the vessels. Pressure is better estimated by BC3.

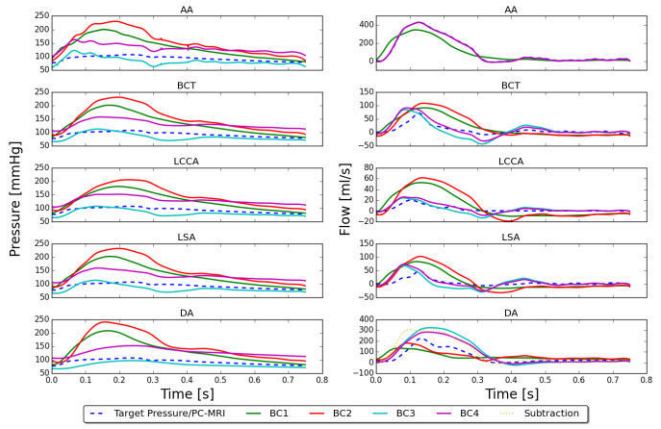

Figure 2: Flow and pressure profiles in all the outlets.

IV. Discussion

Boundary conditions for computational hemodynamics is an active area of research. The complexity of choosing a boundary condition scheme is intrinsically related to the availability of the data.

Historically, lumped models have been primarily used to assess physiological parameters such as vessel compliance, cardiac output, and peripheral resistance. Then, only in the last decades, lumped models were adapted as boundary condition systems for CFD. Because of their relevance in the clinical practice, most of the literature has focused on the quality of the parameter estimation with different methodologies.

In this work, we pick a lumped model known to be a good approximation of the physical system (i.e., the 3-element Windkessel model for aortic flow) and we find its parameters in a least-square fashion rather than relying in their formal definition.

Additionally with this method, we also account for the diastolic and systolic pressure, which can be easily known from patient-specific data. As expected, results show that the use of patient-specific data under the optimization strategy work much better than the use of literature data. Furthermore, we found that modifying flow waves a-priori in order to satisfy the conservation of mass, which is one of the modelling assumptions, leads to much better results than using the raw data, even though the mathematical model does not require it.

V. Conclusion

To systematically perform CFD simulations in diseased thoracic aortas, we faced the challenge of assimilating an important quantity of measured data such as PC-MRI flow measurements at the inlet and all the outlets of the domain, as well as the cuff pressure. At a first analysis, retrieved flow data did not satisfy one of our modelling assumptions, which is the conservation of mass.

For this reason, we used a 3D/0D multiscale modelling (i.e., 3D incompressible Navier-Stokes equations with rigid wall and 3-element Windkessel models). Additionally, we used a non-linear Least-Square approach to evaluate the Windkessel parameters (also known as beat-to-beat parameter estimation).

In conclusion, this surrogate method for data assimilation and boundary condition enforcement has the advantage to be extremely cheap with respect to alternative robust methods such as via a Kalman filter approach. This study also stresses, again, the importance of clinical and patient-specific data for running computational hemodynamics studies.

References

[1] Toorop, G. P., Westerhof, N, & Elzinga, G. (1987). Beat-to-beat estimation of peripheral resistance and arterial compliance during pressure transients. *American Journal of Physiology-Heart and Circulatory Physiology*, *252*(6), H1275-H1283.

[2] Pirola, S., Cheng, Z., Jarral, O. A., O'Regan, D. P., Pepper, J. R., Athanasiou, T., & Xu, X. Y. (2017). On the choice of outlet boundary conditions for patient-specific analysis of aortic flow using computational fluid dynamics. *Journal of biomechanics*, *60*, 15-21.

[3] Antiga, L., Piccinelli, M., Botti, L., Ene-Iordache, B., Remuzzi, A., & Steinman, D. A. (2008). An image-based modeling framework for patient-specific computational hemodynamics. *Medical & biological engineering & computing*, *46*(11), 1097.

[4] Passerini, T., Quaini, A., Villa, U., Veneziani, A., & Canic, S. (2013). Validation of an open source framework for the simulation of blood flow in rigid and deformable vessels. *International journal for numerical methods in biomedical engineering*, *29*(11), 1192-1213.

[5] Morbiducci, U., Ponzini, R., Rizzo, G., Cadioli, M., Esposito, A., De Cobelli, F., ... & Redaelli, A. (2009). In vivo quantification of helical blood flow in human aorta by time-resolved three-dimensional cine phase contrast magnetic resonance imaging. *Annals of biomedical engineering*, *37*(3), 516.

[6] Kim, H. J., Vignon-Clementel, I. E., Figueroa, C. A., LaDisa, J. F., Jansen, K. E., Feinstein, J. A., & Taylor, C. A. (2009). On coupling a lumped parameter heart model and a three-dimensional finite element aorta model. *Annals of biomedical engineering*, *37*(11), 2153-2169.

[7] Stergiopulos, N., Westerhof, B. E., & Westerhof, N. (1999). Total arterial inertance as the fourth element of the windkessel model. *American Journal of Physiology-Heart and Circulatory Physiology*, *276*(1), H81-H88

Effect of nichoid substrates on the morphology of adhering mesenchymal stem cells.

E. Jacchetti[1], R. Osellame[2], G. Cerullo[2] and M.T. Raimondi[1]

[1] Department of Chemistry, Materials and Chemical Engineering "Giulio Natta", Politecnico di Milano, Milano, Italy

[2] Istituto di Fotonica e Nanotecnologie (IFN)-CNR and Department of Physics, Politecnico di Milano, Milano, Italy;

Abstract—

In recent years, it has been demonstrated that substrates influence the lineage specification and cell properties in stem cells. It has also been shown that application of mechanical stress on the cells cytoskeleton or directly on the cell nuclei influences gene expression and cell functionality. We developed an innovative 3D culture substrate named "nichoid", nanoengineered via two-photon laser polymerization. The nichoid limits the cell adhesion sites inducing a morphological modulation.

In this work, we studied the adhesion and the nuclear morphology of rat bone marrow mesenchymal stem cells seeded into the nichoid and on standard flat glass substrates.

Our results show that the 3D micro-lattice structure reduces the cell adhesion site and restricts the formation of the actin cytoskeleton to the cortical part. This is translated into a reduction of the nuclear semi-axes and the nuclear envelope surface.

Future work will be focalized on the study of the cell functionality modulation induced by the nichoid with respect to the standard culture substrates.

Keywords—**Two-photon polymerization, 3D microstructure, mesenchymal stem cells, nuclear deformation.**

I. Introduction

The cellular environment is complex and plays an important role in cellular processes such as cell adhesion, proliferation, gene expression and therefore the cellular fate [1], [2], [3].

From literature is widely known that mesenchymal stem cells (MSCs) differentiate to specific lineages if subjected to mechanical forces induced by adhesion to a scaffold, with extreme sensitivity to topography and mechanical stiffness [4], [5]. Since the maintenance of the cell stemness has been correlated with the cell spatial organization [6], in the last few years, there is an increasing interest in the development of scaffolds that mimic aspects of the three-dimensional (3D) architecture and structural role of the extracellular matrix [7] to modulate the behaviour of stem cells in culture.

By using the 2-photon polymerization technique, we developed a 3D artificial scaffold (the nichoid), fabricated in a hybrid organic–inorganic silicon–zirconium composition (the SZ2080), to mimic the native stem cell niche. It was previously demonstrated that this substrate is able to guide spontaneous homing and colonization of mesenchymal stromal cells by the presence of synthetic microniches, and that it preserves the cell stemness during their expansion [8], [9]. The aim of this work is to quantify the modulation of MSC nuclear morphology induced by cell adhesion to the nichoid (Fig. 1) with respect to the nuclear morphology of MSC grown on a standard glass substrate.

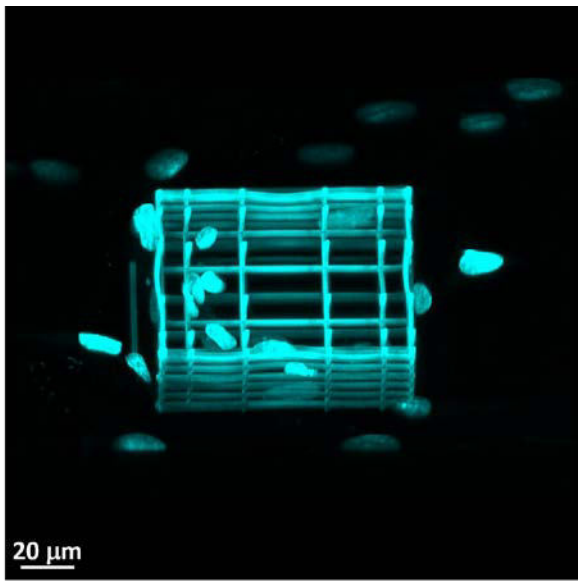

Figure 1. 3D rendering of a *z*-stack of the nichoid. Into the 3D micro-lattice are grown rat bone mesenchymal stem cells. Their nuclei are stained with the fluorescent dye Hoecst 33342.

II. Materials and Methods

3D microstructured substrates

3D structures, the nichoids, were fabricated into a 8-well chambered coverglass Nunc Lab-Tek II (Thermo Scientific, Italy) using an organic-inorganic photoresist (SZ2080) by two-photon laser polymerization, as already described [8]. Briefly, in each chamber, three niches were positioned in a triangular pattern, at a distance around 200µm. The Niches sizes are $90\times90\times30\mu m^3$. They consisted of a lattice with interconnected lines, composing a structure with pores of graded size (Fig. 1). The structure is composed by 3 horizontal planes (spaced 15 µm) and, in the vertical direction, a graded spacing of 10, 20 and 30µm. Each nichoid was surrounded by outer confinement walls, formed by horizontal rods, which allow the diffusion of nutrients, but prevent the cells escape outside from the structure. Before cell seeding, the chambers were treated with poly-L-lysine to improve cell adhesion both on the nichoids and on the surrounding glass bottom flat surface.

Cell culture and seeding.

MSCs were isolated from the bone marrow of adult rats provided from IRCCS-Istituto di Ricerche Farmacologiche "Mario Negri" (Bergamo, Italy) [10] and cultured in alpha-MEM medium supplemented with 20% fetal bovine serum,

1% L-glutamine (2mM), penicillin (10 units/ml), and streptomycin (10 µg/ml) at 37°C and in 5% CO_2 (Euroclone, Italy). Culture medium was changed every 2-3 days and cells were used at passages 1-6 after thawing.
For the experiments, in each well 10^4 MSC cells were seeded. Cells adhered on the glass coverslip around the nichoids were used to study the morphology of cells grown on 2D flat substrate.

Immunofluorescence assay.

To visualize the actin stress fibers distribution and the organization of focal contacts, one day after seeding, cells were fixed for 15 min in 4% paraformaldehyde, rinsed with phosphate buffered saline (PBS, Euroclone, Italy) and permeabilized with 0.25% Triton X-100 (Sigma Aldrich, Italy) in PBS for 15 min at room temperature, and processed for indirect immunofluorescence analysis.
Cells were first incubated for 4h in PBS 2% BSA (bovine serum albumin, Sigma Aldrich, Italy) and then incubated with mouse monoclonal anti-Vinculin antibody (dilution 1:400,Sigma Aldrich, Italy) at 4°C.
The day after samples were wash three times with PBS and then incubated for 45 min at room temperature with 1 µg/ml phalloidin-FITC and 2 µg/ml of donkey anti-mouse IgG H&L Alexa Fluor 647 (Abcam, United Kindom). Cell nuclei were labeled by 1 µg/ml of Hoecst 33342 (Thermo Fischer Scientific, Italy) in PBS and then washed three times. Fixed and stained cells were imaged using a confocal microscopy setup.

Live Cell staining.

MSC nuclei were incubated with 1µM Hoecst-33342 fluorescent probe (ThermoFisher, Italy) ten minutes before the experiments. Later, the cell culture medium was replaced with DMEM w/o phenol red medium supplemented with 10% fetal bovine serum, 1% L-glutamine (2mM), penicillin (10 units/ml), and streptomycin (10 µg/ml) (Euroclone, Italy).

Confocal microscopy.

Fixed samples maintained in PBS were imaged using a confocal microscope (Olympus Fluoview FV10i) equipped with four diode lasers (emission wavelength 405, 473, 559, 635 nm), with a 60x water immersion objective, 1.2 N.A. (Image size 212.13x212.13 µm^2). The pinhole was set to 1 Airy Unit. *Z*-stack images were acquired on "spread" cells grown on the 2D glass substrate (the acquisition depth was approximatively 10 µm) and "roundish" cells grown into the 3D microstructure (the acquisition depth was approximatively 40 µm) with 1 µm step.
The image analysis was carried out with the open source software ImageJ (ttps://imagej.nih.gov/ij/index.html, USA).

Cellular parameter analysis.

The rendering of *z*-stacks in Fig. 2 shows that the shape of the nuclei, in both spread and roundish cells, can be modeled as an ellipsoid. To evaluate the semi-axes *a, b* and c, a z-projection and an y-projection of the z-stack images acquisitions was performed like in Fig. 2a. For each cell, the nuclear region was then manually selected as the region of interest (ROI) and fitted with an ellipse. This solution corresponds to the identification of the biggest *xy* and *xz* nuclear sections.

For each cell the *a* and *b* semi-axes values were organized in descending order, so that *a*>*b*.

Nuclear surfaces, *S,* and the nuclear volume, *V,* were calculated by using the scalene ellipsoid formulae

$$S = 4\pi \sqrt[p]{(ab)^p (ac)^p (a)c^p} \qquad (1)$$

$$V = \frac{4\pi}{3} abc \qquad (2)$$

where p =1.6075.

Statistical analysis.

All the experiments were independently repeated four times for each reported dataset (roundish and spread cells). The number of analyzed cells is 28 (roundish) and 66 (spread). Results are shown as mean ± stadard deviation. Data were statistically analyzed using the commercial software OriginLab. For parametric data (after Shapiro-Wilk normality test), One-Way Anova with Tukey's post-test or two sample t-test analysis was used. The statistical significance refers to $P < 0.05$.

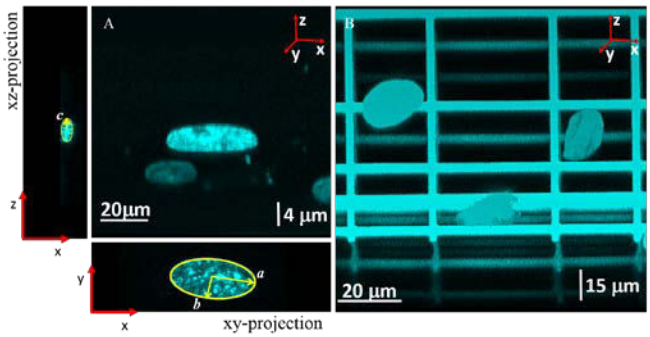

Figure 2. Method adopted to estimate the geometry of cell nuclei in cells grown on flat substrates and in the nichoid. 3D rendering of nuclei of spread (A) and roundish (B) cells. In blue are represented the cell nuclei stained with the fluorescent dye Hoecst33342 and the nichoid, which is autofluorescent. In panel A are shown the *xy* and the *xz* projections of the *z*-stack acquisition (left and bottom panel). The yellow region of interest (ROI) underline the edge of the projection. Semi-axes *a, b* and *c* were calculated by fitting the ROIs with scalene ellipses.

III. RESULTS

A qualitative analysis of the protein displacement in MSC seeded on 2D and 3D substrates was performed by using the immunofluorescence assay.
Fig. 3 is an immunofluorescence acquisition of MSC seeded on a flat substrate (A) and into a nichoid (B). It shows the nuclei (blue), actin filaments (green) and vinculin proteins (red). The focal adhesion sites results in orange/yellow as result of the co-localization of actin and vinculin.
The two images suggest that the nuclei of roundish cells are smaller than the spread cell nuclei. In spread cells (Fig. 3A), actin filaments are visible at the cells edge (the cortical cytoskeleton) but it is also present a strong cytoskeletal organization inside the cells. Mature focal adhesions are displaced at the edge of the cells but other smaller focal adhesions are shown in the bottom plasmatic membrane, near the nuclei.
The cytoskeletal organization of roundish cells (Fig 3B) is mainly composed from the cortical actin networks and the focal adhesions are evident only at the cell edge.
The observation of the nuclear shape (Fig. 2 and Fig. 3) shows that in the 2D spread configuration (A) the shape of the nuclei tends to be very elongated while in cells grown in 3D in nichoids (B) is quite roundish. In any case, all the images suggest that cell nuclei can be modeled with an ellipsoid.

The nuclear shape and its morphological parameters were calculated as described above (see materials and methods, paragraph cellular parameter analysis). The obtained parameters are summarized as mean and standard deviation in Tab 1. The ratio between roundish cells versus spread cells is shown in Fig. 4.

Results confirm that in both cellular configurations the nuclei assume a scalene ellipsoidal shape (the value of the three semi-axes is statistically significant $a \neq b \neq c$).

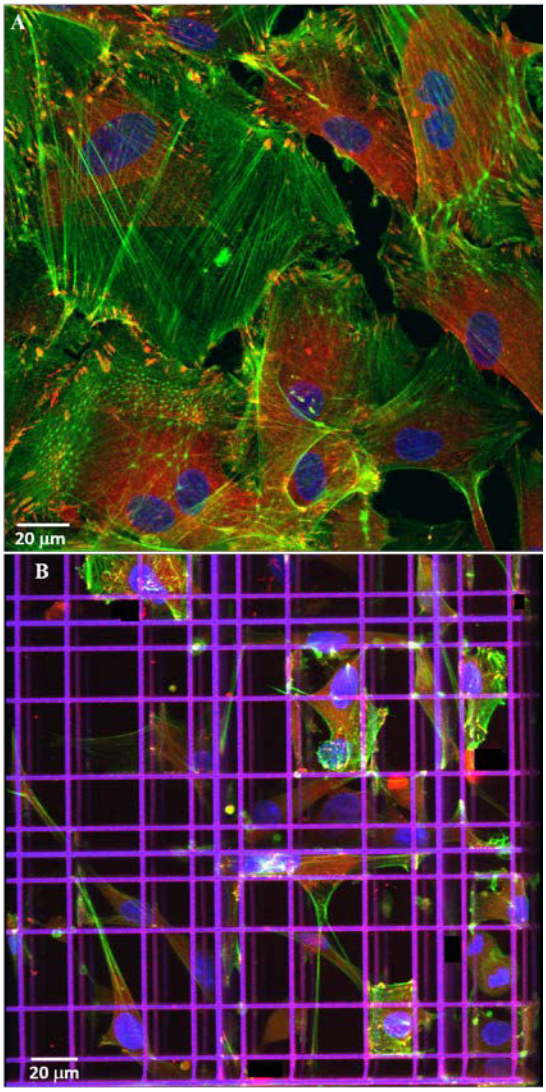

Figure 3. Results of immunofluorescence assays. Confocal images of MSCs. In blue the nuclei, in green the actin filaments, in red vinculin. The focal adhesion sites result in yellow. (A) Projection of a *z*-stack of MSC grown on a flat substrate. (B) 3D rendering of a *z*-stack acquisition of MSC grown in the nichoid. From the image is evident that the nichoid is autofluorescent in all the acquired channels (blue, green and red).

The size of the *a* and *b* semi-axis is smaller (around 20%) in the roundish cells than in the spread cells; instead, the length of the third semi-axis *c* is doubled for cells grown in 3D configuration.

Calculating the surface of the nuclei and their volume from the *a, b* and *c* parameters, it is possible to observe that the 3D cell configuration presents a 28% and 17% reduction of the nuclear surface and volume, respectively.

TABLE I
CHARACTERIZATION OF THE CELL NUCLEAR SHAPE

Sample	*a(µm)*	*b(µm)*	*c(µm)*	*S (µm²)*	*V (µm³)*
Roundish cells	*7.4 ± 1.9*	*4.5 ± 1*	*3.3 ± 0.9*	*633 ± 233*	*486 ± 275*
Spread cells	*9.5 ± 2.4*	*6 ± 1.7*	*2.2 ± 0.8*	*883 ± 464*	*586 ± 457*

Table 1. Results of the characterization of nuclear shape by estimation of the semi-axes of roundish and spread cells. The nuclei can be represented with a scalene ellipsoid. For each population($N_{Roundish}$=28 cells, N_{Spread}=66 cells), the semi-axes are statistically significant at 5% (ANOVA test). The calculation of the nuclear surface and volume was performed by using the formulae (1) and (2) declared in materials and methods. For each population, the surface values are statistically significant at 5% (t-test).

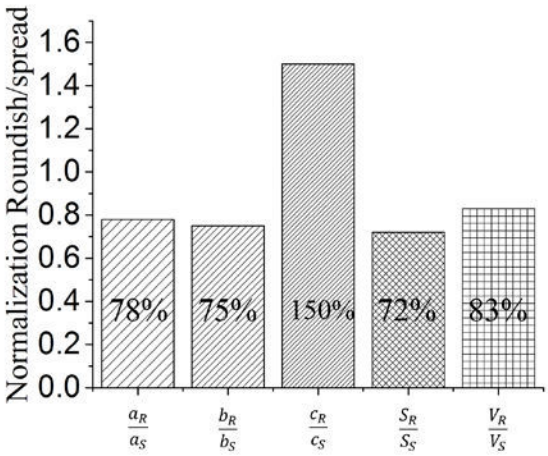

Figure 4. Comparison between the parameters of roundish (*R*) and spread (*S*) cells. Result show that apart from the cell elongation along the *z* axis, *c*, all the other parameters (semi-axes a and b, surface and volume) are about 20% smaller in the roundish cells adhering to the nichoid with respect to the spread ones.

IV. DISCUSSION

MSCs are a subset of non-hematopoietic adult stem cells originating from the mesoderm. They possess great potential for therapies in regenerative medicine to restore the function of injured cells, tissues and organs, mainly because of their self-renewal ability, multilineage differentiation and limited immunogenicity. MSCs exist in almost every tissue and are easily isolated, for example from the bone marrow, because they are adherent cells. This means that these cells interact with the environment binding to it with integrin proteins, then forming focal adhesions and re-organizing the actin cytoskeleton as a consequence of intra-cellular traction forces developed. This interaction therefore modulates the cell shape and aspects of cell function including proliferation, differentiation and cytoskeletal organization [2], [9], [11], [12].

Therefore in this work we started to observe qualitatively, by using immunofluorescence assay, the MSC cytoskeleton organization comparing the result obtained on cells grown on a 2D glass flat substrate (spread cells) and cells grown into a 3D micro-structured scaffold called nichoid (roundish cells).

Figure 3 shows that in spread cells (Fig. 3A) the mature focal adhesions (in orange/yellow) are localized at the cell edge, but other smaller focal adhesions are localized also below the cell, at the interface between the cell and the glass substrate near the nucleus. From focal adhesions, actin fibres elongate, forming the cortical cytoskeleton at the cell edge and a mesh

of stress fibres that covers the nucleus regulating its shape and cell contractility as declared in [13]. Focal adhesions in cells grown in the 3D nichoid (Fig. 3B) are strictly localized at the cell edge, where they adhere to the micro-lattice structure in presence only of the cortical cytoskeleton, suggesting a possible modulation of the cell motility [14]. The immunofluorescence images also suggest that the roundish cells present nuclei smaller in size respect to the spread cells.

As a matter of fact, from literature is widely known that changes in the cytoskeletal architecture induce modifications of nuclear shape, playing a crucial role in mechanotransduction and stem cell fate determination [15], [16], [17], [18]. We focused our attention on the nuclear shape of MSC grown on 2D flat glass substrate and into 3D nichoids shaped as micro-lattices. From 3D rendering of *z*-stack acquisitions, we observed that both type of cells present an ellipsoidal nuclear shape (Fig. 2) and we calculated some parameters that describe these ellipses. From our results, we observed that the nichoid reduces the semi axes dimension along the *xy* plane of 20%, increasing instead the length of the semi axis along the *z* direction by twice. This fact results in a diffuse arrangement of the cells in the environment in which they are grown and a different geometry of the nucleus, resulting in a nuclear surface reduced by 20% in the round cells compared to the spread ones. The cell volume are not significantly affected by the 3D geometry of the nichoid.

In this work, the results are affected by errors due to: 1) overestimation of the semi axes (calculated as the maximum projection of the nuclei along the two *xy* and *xz* planes); 2) neglection of the case of roundish cells with the semi-axes diagonally arranged with respect to the nichoid. Despite these limitations, our results are aligned with similar estimations presented in [19]. These results demonstrate that the 3D microscaffold named nichoid induces a modulation of the entire cell cytoskeleton. This result implies the possibility by using the nichoid to control nuclear shape to obtain, by using only physical cues, the modulation of crucial cell functions such as cell motility and the nuclear envelope permeability. In future work, to check if the control of cell adhesion is dependent only on the 3D structure, similar experiments will be performed with 3D scaffold characterized by a different pore size and also with the nichoid subjected to a chemical functionalization, e.g. with zwitterionic moieties [20], or growth factor and RGD-containing peptides. [21], [22]. Furthermore, we will also focalize our efforts towards the description of how the MSC cytoskeletal organization in cells cultured in the nichoid affects cell migration, fluxes of transcription factors through the nuclear pore complexes and the regulation of gene expression.

V. CONCLUSION

One of the goal in regenerative medicine is to be able to control and modulate cell functionality like proliferation, migration and gene expression. We developed an innovative 3D micro-structured culture substrate to seed and grow MSC. Our results show that this pioneering substrate is able to modulate cell morphology at the single-cell level, consistently with our previous observations of an increased homing behavior [8] and proliferation speed [23] of MSC cultured inside these structures, compared to flat monolayer culture. The results of this work are at the basis of a new “physical” strategy to guide the fate of stem cells and they are also driving us in understanding the tasks of process that regulate cellular functions.

ACKNOWLEDGEMENT

We acknowledge funding by the ERC, project NICHOID, Grant Agreement No. 646990.

REFERENCES

[1] D. Discher, P. Janmey, Y.L. Wang; “Tissue cells feel and respond to the stiffness of their substrate”. Science 310: 1139–1143, 2005.

[2] D. Discher, D. Mooney, P. Zandstra, “Growth factors, matrices, and forces combine and control stem cells”. Science 324: 1673–1677, 2009.

[3] F. Guilak *et al*, “Control of stem cell fate by physical interactions with the extracellular matrix”. Cell Stem Cell 5: 17–26, 2009.

[4] M. Nikkhah *et al*, “Engineering microscale topographies to control the cell– substrate interface”. Biomaterials 33: 5230–5246, 2012.

[5] A.J. Engler *et al*, “Matrix elasticity directs stem cell lineage specification”. Cell 126: 677–689, 2006.

[6] P. Rompolas, K.R. Mesa, V. Greco, “Spatial organization within a niche as a determinant of stem cell fate”, Nature 502(7472): 513–518, 2013.

[7] T. Kraehenbuehl, R. Langer, L. Ferreira, “Three-dimensional biomaterials for the study of human pluripotent stem cells”. Nature Methods 8: 731–736, 2011.

[8] M.T. Raimondi *et al*, “3D structural niches engineered via two-photon laser polymerization promote stem cell homing”. Acta Biomaterislis 9: 4579–4584, 2013.

[9] M.M. Nava *et al*, “Synthetic niche substrates engineered via two-photon laser polymerization for the expansion of human mesenchymal stromal cells”. Journal of tissue engineering and regenerative medicine 11: 2836–2845, 2017.

[10] C Zoja *et al*, “Mesenchymal stem cell therapy promotes renal repair by limiting glomerular podocyte and progenitor cell dysfunction in adriamycin-induced nephropathy”. American Journal of Physiology. Renal Physiology 303: F1370–F1381, 2012.

[11] J. Wang, B. Thampatty, “Mechanobiology of adult and stem cells.” International Review of Cell and Molecular Biology 271:301–346, 2008

[12] E. Hadjipanayi, V. Mudera, R. Brown, “Guiding cell migration in 3D: a collagen matrix with graded directional stiffness”. Cell Motility and the Cytoskeleton 66:121–128, 2009.

[13] S.B. Khatau *et al,* “A perinuclear actin cap regulates nuclear shape”. PNAS 106 (45) 19017-19022, 2009.

[14] E. Jacchetti, C. Di Rienzo, S. Meucci, F. Nocchi, F. Beltram, M. Cecchini. “Wharton's Jelly human mesenchymal stem cell contact guidance by noisy nanotopographies”. Scientific Reports 4, 3830:1-9, 2014.

[15] M. Bao, J.Xie, A. Piruska and W.T.S. Huck. “3D microniches reveal the importance of cell size and shape”. Nature Communication 8(1), 1962: 1-12, 2017.

[16] K. Dahl, A. Ribeiro, J. Lammerding, “Nuclear shape, mechanics and mechanotransduction”. Circulation Resource 102(11):1307–1318, 2008.

[17] S. Dupont *et al*, “Role of YAP/TAZ in mechanotransduction”. Nature 474(7350):179–183, 2008.

[18] S. Gupta, N. Marcel, A. Sarin, G. Shivashankar, “Role of actin dependent nuclear deformation in regulating early gene expression”. PLoS One 7(12):e53031, 2012.

[19] M.M. Nava, R. Fedele, M.T. Raimondi, “Computational prediction of strain-dependent diffusion of transcription factors through the cell nucleus”. Biomechanics and Modeling in Mechanobiology 15(4):983-93. 2016.

[20] A.B. Lowe *et al*. “Well-defined sulfobetaine-based statistical copolymers as potential antibioadherent coatings”. Journal of Biomedical Materials Researc 52,1:88-94, 2000.

[21] L. More *et al*. “Tethered growth factors on biocompatible scaffolds improve stemness of cultured rat and human neural stem cells and growth of oligodendrocyte progenitors”. Methods 133:54-64, 2018.

[22] U. Hersel, C. Dahmen, H. Kessler. “RGD modified polymers: biomaterials for stimulated cell adhesion and beyond”. Biomaterials 24(24):4385-4415, 2003.

[23] M.T. Raimondi, et al. " Optimization of Femtosecond Laser Polymerized Structural Niches to Control Mesenchymal Stromal Cell Fate in Culture". Micromachines 5(2):341-358, 2014.

Age and risk factors promote abnormal hemodynamics and differentially influence aortic calcification

Rodrigo M. Romarowski[1], Michele Conti[1], Ferdinando Auricchio[1], Simone Morganti[1], and Alexey V. Kamenskiy[2]
[1] *Department of Civil Engineering and Architecture, University of Pavia, Italy*
[2] *Department of Surgery, University of Nebraska – Medical Center, USA*

***Abstract*—Aortic geometry changes with age by increasing its diameter and tortuosity. Consequently, hemodynamics become affected and move towards an atherogenic pathway. We measured calcium in 122 healthy individuals ranging from 5 to 90 years-old and computed Wall Shear Stress in one representative geometry of each age group. Results show that atherogenic zones increase with age and are closely correlated with calcium development.**

***Keywords*—aorta, calcification, computational fluid dynamics**

I. Introduction

Aging is associated with arterial stiffness and morphological changes in vascular anatomy that involve increased arterial diameter and tortuosity. These conditions lead to altered hemodynamics and result in low Wall Shear Stress (WSS), flow recirculation, and stagnation that are sensed by the endothelium and can trigger pathology through complex mechanobiological pathways. Arterial calcification is one measure of such pathology that can be quantified using clinical imaging [1]. The aim of this work was to investigate the relations between aging, hemodynamics, and vascular calcification.

II. Methods

3D reconstructions of vascular anatomy were performed in 122 subjects 5-93 years old (mean age 47±24 years, 64M/58F). Vascular volumes and calcification percentages were measured in five vascular zones spanning from the ascending thoracic aorta to the femoral bifurcation. Computational fluid dynamics simulations were performed in geometries representing each of the nine age groups, and Time Averaged WSS (TAWSS), and Oscillatory Shear Index (OSI) were computed to characterize atherogenic (TAWSS<4 dyne/cm^2, OSI>0.3) and atheroprotective (TAWSS>15 dyne/cm^2) areas [2,3]. Calcification in each vascular zone was analysed in the context of demographics, risk factors, and hemodynamic variables.

III. Results

Calcification appears after the fifth decade of life and first involves distal vasculature. At the age of 65 years all subjects had identifiable calcium, with age and coronary artery disease having the strongest positive effects, and dyslipidemia affecting calcification negatively. Mean TAWSS decreased with age in all vascular segments, resulting is larger areas of atheroprone TAWSS and OSI and smaller areas of atheroprotective TAWSS (all $p<0.05$), particularly after the age of 50 years (Figure 1). Calcification burden positively correlated with atherogenic TAWSS ($r=0.88$, $p<0.01$) and high OSI ($r=0.70$, $p=0.04$), and negatively with average TAWSS ($r=-0.88$, $p<0.01$) and atheroprotective TAWSS ($r=-0.85$, $p<0.01$).

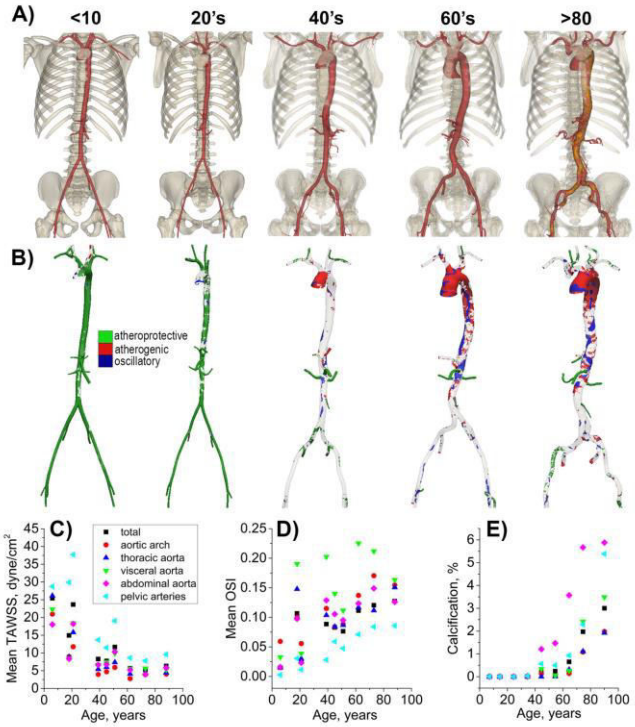

Figure 1: A) Vascular anatomies of subjects from five age groups demonstrating increase in arterial diameter and tortuosity with age; B) CFD simulations showing regions of atheroprotective (>15 dyne/cm^2) and atherogenic (<4 dyne/cm^2) TAWSS, and areas of oscillatory flow (OSI>0.3). Changes in average TAWSS, OSI, and calcification with age are presented in panels C), D), E) respectively for different segments of the vasculature.

IV. Discussion

Vascular tree remodels with age demonstrating increased diameter, tortuosity, and stiffness. These changes appear to be associated with pathologic flow patterns and higher incidence of calcification that may further promote pathologic remodelling. Understanding the hemodynamic conditions associated with aging and calcification can help explain clinical correlations between calcification and higher incidence of cardiovascular events, aid in better understanding of disease pathophysiology, and help develop better prevention and treatment strategies.

ACKNOWLEDGEMENT

Computational simulations were performed thanks to the LISA 2017 initiative under the project B-BeST at CINECA.

REFERENCES

[1] Harbaoui, Brahim, et al. "Aorta calcification burden: towards an integrative predictor of cardiac outcome after transcatheter aortic valve implantation." *Atherosclerosis* 246 (2016): 161-168.

[2] Malek, Adel M., Seth L. Alper, and Seigo Izumo. "Hemodynamic shear stress and its role in atherosclerosis." *Jama* 282.21 (1999): 2035-2042.

[3] Morbiducci, Umberto, et al. "In vivo quantification of helical blood flow in human aorta by time-resolved three-dimensional cine phase contrast magnetic resonance imaging." *Annals of biomedical engineering* 37.3 (2009): 516.

Dynamic torsional behaviour of native ACL and grafts commonly used in surgical reconstruction: setup definition and preliminary results

M. Berni[1], G. Marchiori[1], S. Zaffagnini[1], N. Lopomo[1,2]

[1] *Rizzoli Orthopaedic Instituite, Bologna, Italy; matteo.berni@ior.it*

[2] *University of Brescia, Brescia, Italy.*

***Abstract*— Anterior cruciate ligament (ACL) rupture is a common and serious knee joint injury, currently treated by reconstructing the ligament with biological and/or synthetic graft, which performances are crucial in restoring knee biomechanics, but still partially unexplored. In this study we developed and implement a dynamic torsional protocol able to compare the behaviour - through complex shear modulus analysis - of native ACL with that of the grafts commonly used in surgical reconstruction.**

***Keywords* — Anterior Cruciate Ligament; Dynamic Mechanical Analysis; Torsional behaviour.**

I. Introduction

ANTERIOR cruciate ligament (ACL) represents, among the major knee joint anatomical structures, one of the most subjected to lesion, especially during pivoting sport practice: the common kinetic scenario of injury report internal twisting of the tibia relative to the femur or combined multi-axial stresses [1]. Generally, in order to mimic the native ligament behaviour, a torn ACL is replaced by a biological graft or by introducing synthetic augmentations made of different materials, particularly by polymers [2]. Despite biocompatibility is the most investigated aspects of these grafts, even their mechanical performances are fundamental, particularly in determining and predicting knee biomechanics [3]. A complete characterization of ligaments/graft still remains incomplete [4,5], especially for what concerns their behaviour under torsional stress, which is particularly detrimental for these tissues [6]. For this reason, aim of the present study was to develop and implement a testing protocol able to compare the torsional behaviour of native ACL with the most common grafts used in ACL surgical reconstruction, e.g. the hamstring tendon [7].

II. Materials and Methods

After thawing, fresh-frozen soft tissue samples were tested on a multi-axis mechanical tester (Mach-1, Biomomentum Inc. Canada), with the adoption of "ad hoc" designed clamping devices (Fig.1). Identified testing protocol combined a pre-conditioning cyclic phase addressing ligaments/tendons [8] followed by a Dynamic Mechanical Analysis (DMA) approach [9]. During DMA, cyclic angular displacements within the physiological 20° range of internal-external knee rotation [10] were applied following the typical gait frequencies (e.g. 0.41 and 1 Hz, as in [11]). Bovine tendon was used to preliminary validate the procedure.

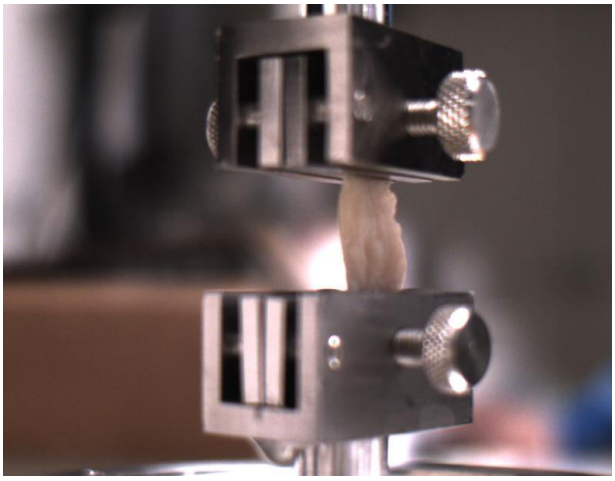

Fig. 1. Human ACL loaded in multi-axis Mach-1 Biomomentum.

III. Results and Discussion

Preliminary validation highlighted the typical ellipsoidal shape of the torque (Tz) vs angle (theta) curve (Fig. 2), allowing us to estimated complex shear modulus with storage (Modulus') and loss (Modulus'') components.

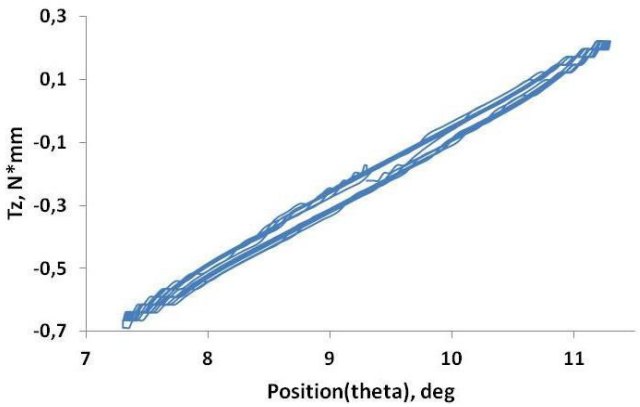

Fig. 2. Typical ellipsoidal shape concerning the torque (Tz) vs angle (theta) curve resulting from torsional test.

At 1 Hz cyclical torsion, they resulted 0.730 MPa and 0.038 MPa for bovine tendon, coherently with literature [5]. As it happens in physiological context [12], torsional loading induced also tension stresses on the specimens.

IV. CONCLUSION

The designed protocol allows to perform a comparative analysis concerning soft tissue behaviour under torsional loading. Specifically, the focus was the evaluation of native ACL and common substituting grafts as a function of loading dynamics, after inducing a physiological loading history [12]. With the aim of highlight the strict relation between structural patterns and mechanical response of ligaments/grafts, future developments will integrate mechanical testing with a morphological and microstructural analysis.

V. ACKNOWLEDGEMENT

We thank the “Italian Ministry of Health” financier of the project GR-2011-02351803.

VI. REFERENCES

[1] E. G. Meyer, R. C. Haut, "Anterior cruciate ligament injury induced by internal tibial torsion or tibiofemoral compression", J Biomech, 2008; 41 (16) : 3377 - 83.

[2] C. Legnani, A. Ventura, C. Terzaghi, E. Borgo, W. Albisetti, "Anterior cruciate ligament reconstruction with synthetic grafts. A review of literature", Inter Orth (SICOT), 2010, 34: 465-471.

[3] J. W. Freeman, A. L. Kwansa, "Recent Advancements in Ligament Tissue Engineering: The Use of Various Techniques and Materials for ACL Repair", Recent Patents on Biomedical Engineering, 2008, 1-1 (6): 18-36.

[4] S. G. McLean, K. F. Mallet, E. M. Arruda, "Deconstructing the anterior cruciate ligament: what we know and do not know about function, material properties, and injury mechanics", J Biomech Eng, 2015, 137(2): 020906.

[5] L. M. Marin, C. P. Buckley, A. B. Zavatsky, "An experimental platform for measuring the mechanical behavior of tendons in torsion", 2015.

[6] Y. K. Oh, D. B. Lipps, J. A. Ashton-Miller, E. M. Wojtys, "What strains the anterior cruciate ligament during a pivot landing?", Am J Sports Med, 2012, 40(3):574-83.

[7] C.P. Charalambous, T. A. Kwaees, "Anatomical considerations in hamstring tendon harvesting for anterior cruciate ligament reconstruction", Muscles Ligaments Tendons J., 2012, 2(4):253-257.

[8] R. Zdero, M. Olsen, S. Elfatori, T. Skrinskas, H. Nourhosseini, C. Whyne, E. H. Schemitsch, H. von Schroeder, "Linear and torsional mechanical characteristics of intact and reconstructed scapholunate ligaments", J Biomech Eng, 2009, 131 (4): 041009GE.

[9] Mach-1-Dynamic Mechanical Testing, Biomomentum procedure MA056-SOP04-D.

[10] P. Imbert, C. Belvedere, A. Leardini, "Knee laxity modifications after ACL rupture and surgical intra- and extra-articular reconstructions: intra-operative measures in reconstructed and healthy knees", Knee Surg Sports Traumatol Arthrosc, 2017, 25:2725-2735.

[11] J. Nilsson, A. Thorstensson, "Adaptability in frequency and amplitude of leg movements during human locomotion at different speeds", Acta Physiol Scand, 1987, 129 (1):107-14.

[12] F. Mollica, M. Ventre, F. Sarracino, L. Ambrosio, L Nicolasi, "Mechanical properties and modelling of a hydrophilic composite used as a biomaterial", Composites Science and Technology, 2006, 66(1):92-101.

Carotid restenosis risk via hemodynamic and morphometric analysis: a 5 year follow-up

D. Gallo[1], M. Domanin[2], D. Iommi[1], C. Vergara[3], and U. Morbiducci[1]
[1] *PolitoBIOMed Lab, Department of Mechanical and Aerospace Engineering, Politecnico di Torino*
[2] *Department of Clinical Sciences and Community Health, University of Milan*
[3] *MOX Dipartimento di Matematica, Politecnico di Milano*

***Abstract*— The risk of carotid restenosis after endarterectomy is predicted by assessing bifurcation hemodynamic and geometric features in 13 patients. Bifurcation expansion and tortuosity of the tract proximal to the bifurcation are quantified and correlated with hemodynamic descriptors of disturbed shear and with restenosis severity after 5 years, expressed as the percentage reduction of lumen diameter. Multiple linear regression revealed a significant correlation between geometric features and the exposure to disturbed shear (R^2=0.68, p<0.05). Restenosis risk stratification through the combination of bifurcation expansion and tortuosity showed a promising correspondence with clinically-measured restenosis severity, correctly identifying those patients who developed a >50% restenosis or a relevant intimal thickening at 5 years. The role of the bifurcation expansion is underlined and potential for risk stratification is demonstrated.**

***Keywords*— Endarterectomy, Computational fluid dynamics, Geometric risk.**

I. Introduction

RESTENOSIS, i.e. the re-occurrence of carotid lumen narrowing at the same site of a previous carotid endarterectomy (CEA), is an important complication affecting CEA outcomes. The overall incidence of restenosis, defined as a 50% reduction in the lumen diameter measured by Doppler ultrasound (DUS), is 5.8% with only 8% of patients having symptoms [1]. While restenosis in the first two years after surgery is characterized by the development of myointimal hyperplasia, intermediate (2 to 5 years) and late (>5 years) restenosis are more similar to primary atherosclerotic lesions [1].

To minimize restenosis risk, the insertion of a patch graft (PG) for the closure of the longitudinal arteriotomy gained considerable success as an alternative to primary closure (PC). However, debate still exists: PG avoid restenosis in early postoperative period, when PC technical defect might result in lumen narrowing. However, PG angioplasty involves longer operating time, risks of graft infection and pseudoaneurysm development. According to the current guidelines, the choice between PG or PC is based on the measure of some simple geometric features [2], PG being preferred for smaller carotid. Although the simple measurement of carotid diameters can be easily implemented into the clinical practice, this approach could result in inaccurate selection criteria. In fact, several studies demonstrated that specific geometric attributes of the carotid bifurcation promote hemodynamic disturbances leading to primary atherosclerotic lesions [3] or restenosis [4]. Challenged by these suggested links, we here aim to establish whether the immediately post-CEA geometry of the carotid bifurcation can predict the risk of restenosis in a cohort of 13 carotid bifurcations submitted to CEA with PG or PC closure technique. To do so, we quantified by a morphometric analysis the bifurcation expansion and the tortuosity of the tract proximal to the bifurcation, which were previously linked to hemodynamic flow disturbances [3]. In addition, we paralleled the morphometric analysis with a computational hemodynamic analysis. Hemodynamic disturbances were quantified, with particular reference to wall shear stress (WSS), due to its role in the restenosis process [4]. After demonstrating the relationship between geometric bifurcation features and WSS disturbances, we matched the results of the morphometric and hemodynamic analyses with clinical and ultrasonographic outcomes at 5 years follow up.

II. Methods

A. Patient population data

Thirteen carotid bifurcations with a stenosis greater than 70% were submitted to CEA in 12 patients. According to the guidelines, PG angioplasty was performed in 9 cases (PG1-9) using 6x75 mm polyester collagen-coated patch (Ultra-thin Intervascular®, Mahwah, U.S.A), tailored and distally trimmed to give a smoothly tapered transition, while PC was performed in 4 cases (PC1-4). Two patients died respectively for myocardial infarction (PG4), and pancreatic carcinoma (PG8) at three years. All the patients have been submitted to 3 months and 2 years DUS follow-up without detection of any relevant restenosis. After 5 years, all eligible patients have been submitted to a third DUS follow up. The study has been approved by the I.R.C.C.S. Fondazione Policlinico Ethics Committee.

B. Geometry reconstruction and Morphometric analysis

MRI acquisitions were performed immediately after surgery with a Siemens 1.5T Avanto MR scanner as detailed elsewhere [4]. From the acquired set of images, the three-dimensional geometry of the carotid bifurcations was reconstructed with a level-set segmentation method by using Vascular Modeling Toolkit (VMTK, www.vmtk.org).

The morphometric analysis is based on the definition of the vessel centreline **C,** defined as the locus of the centers of the maximal inscribed spheres along the vessel. An analytical representation of the centerline was obtained through 3D free-knots regression splines [5,6]. To delimit the bifurcation region, sections located at 3, 5 and 2 maximally inscribed spheres radii along the common, internal and external carotid (CCA, ICA and ECA, respectively) were used (CCA3, ICA5

and ECA2, Figure 1). Geometric descriptors previously defined to predict the underlying hemodynamics were then calculated automatically [3]. These "hemodynamic-informed" descriptors quantify flare (i.e., the expansion at the carotid bulb), and planar tortuosity. As shown in Figure 1A, the carotid flare was evaluated by considering the ratio between the maximum cross-sectional area at the CCA branch (CCA_{max}) and the CCA3 area (FlareA). Tortuosity was defined as L/D-1, where L is the curvilinear distance between two points and D is the Euclidean distance between them. As illustrated in Figure 1B, the two points were the centerline point lying on CCA3 cross-section, and the so-called "inflection point", that is the point proximal to the flow divider where the typically sigmoidal-shaped CCA-ICA centerline reverses its concavity. Taking into consideration fluid mechanics theory demonstrating that planar curvature promotes centrifugal forces leading to secondary flows production, the projected centerline segment between CCA3 and the inflection point was fitted using a least square method with a plane, where tortuosity (Tort2D) was calculated.

The prediction of the burden of disturbed hemodynamics for each carotid from geometric descriptors was then distilled into a simple relationship combining flare and tortuosity. This relationship summarized that a larger expansion promotes flow disturbances, that can be limited by a curved or tortuous upstream tract thanks to the beneficial helical flow generation [5,7]. In this study, the mentioned relationship was adopted to define a Geometric Risk Factor (*GRF*):

$$GRF = FlareA - C \times Tort2D \quad (1)$$

where C was set equal to 34 [3,8]. *GRF* was used to stratify the patients in tertiles according to the predicted geometric risk, to test whether the geometric analysis successfully identify patients characterized by the worst 5-years follow up.

C. Computational Hemodynamics

Hemodynamics was modelled by assuming blood as a homogeneous Newtonian fluid. The incompressible Navier-Stokes equations was solved under laminar and rigid wall assumptions with the finite elements library LifeV (http://www.lifev.org), as detailed elsewhere [4]. In detail, velocity data from DUS acquisitions were used to estimate flow rates [5], which were prescribed by means of Lagrange multipliers as boundary conditions at the CCA and ICA. At the ECA, a zero-stress condition was imposed. Regarding the spatial discretization, P1 bubble finite elements were used for the velocity, and P1 finite elements for the pressure. A grid refinement sensitivity study was carried out [4]. Regarding the time discretization, we used the backward Euler method with a time step size of 0.01s.

From the instantaneous WSS distribution, the WSS-based descriptor Relative Residence Time (RRT) was calculated, quantifying low and oscillatory WSS and proven to promote myointimal hyperplasia and restenosis [4]. To determine objective thresholds for disturbed WSS, WSS data in the bifurcation region from all cases were pooled to identify the 80th percentile value for RRT. The burden of disturbed WSS was quantified by the surface area exposed to RRT above its threshold value, and divided by the respective model surface area. This descriptor is denoted as %RRT.

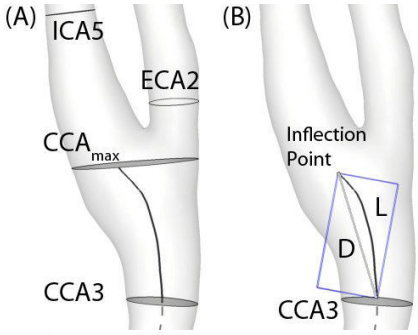

Fig. 1: A) Maximum CCA section (CCAmax) and CCA3 define FlareA. ECA2 and ICA5 are also shown. B) The projection of the centerline between CCA3 and the inflection point on a fitted plane is used to calculate Tort2D.

III. Results and Discussion

From the quantitative morphometric analysis, higher flare values were found for PG patients (PG: 2.59±1.43, PC: 1.55±0.36), while tortuosity values were similar among the two groups (PG: 0.037±0.015, PC: 0.036±0.017). The exposure to low and oscillatory WSS in all models in Figure 2 shows high RRT concentration at the carotid bulb. Quantitatively, the surface area exposed to low and oscillatory WSS was higher for PG patients. Additionally, the prediction of disturbed hemodynamics by the considered geometric factors was verified by performing a multiple linear regression, that yielded a coefficient of determination R^2 equal to 0.68 (p-value<0.05).

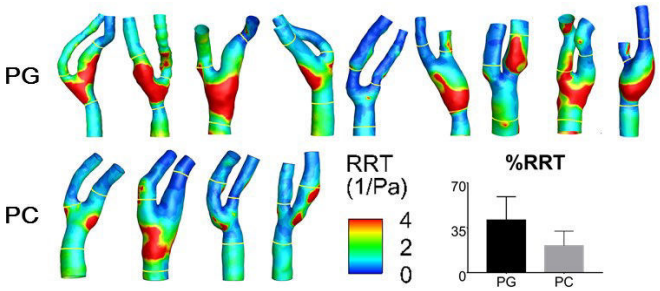

Fig. 2: Exposure to low and oscillatory WSS in all models, as given by RRT. Quantitative analysis of %RRT in terms of mean and standard deviation is shown in the histogram.

The highest value of *GRF* (and FlareA) were found for PG1 and PG2 (Figure 3), where the most severe restenosis occurred in the follow-up, based on DUS. In particular, PG1 developed >70% restenosis (Figure 3, mid and right panels), while PG2 developed >50% restenosis, highlighting the beneficial effect of a higher Tort2D value (and of helical flow generation, promoted by tortuosity). PG9, showing a high *GRF*, did not show any significant restenosis, although a relevant intimal thickening was evident in the area of high RRT (not shown). Among patients with intermediate *GRF* values, we observed a significant intimal thickening for PG3 and PG6, whereas a moderate restenosis process was found for PC2. Although the biological or systemic risk factors (e.g. hypertension, age, etc.) involved in the restenosis processes were not taken into account, we demonstrate here that hemodynamic disturbances can be encoded in simple geometric quantities for restenosis risk stratification.

Pragmatically, such geometric quantities can be easily and robustly measured in a clinical setting and could be used to classify risk and identify patients at greater susceptibility for restenosis at the carotid bifurcation after CEA, offering evident practical advantages in large-scale in vivo studies.

In conclusion, this analysis shows that (1) PG should be used avoiding an artificial flaring, that we here demonstrate to be linked with restenosis via the generation of flow disturbances, and that (2) stratification of the risk for carotid restenosis after CEA, based on robust image-based morphometric analysis that can be easily integrated in the clinical practice, is promising.

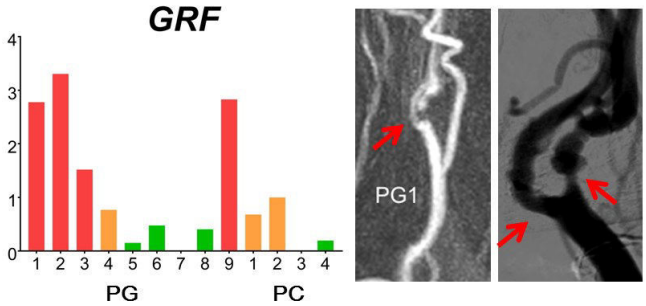

Fig. 3: Left: *GRF* for all models, where the color indicates high/medium or low risk (respectively, red, orange and green) according to the group tertile. Mid and right: clinical evidences of restenosis for PG1.

REFERENCES

[1] R. Kumar, A. Batchelder, A. Saratzis, A.F. AbuRahma, P. Ringleb, et al., "Restenosis after carotid interventions and its relationship with recurrent ipsilateral stroke: a systematic review and meta-analysis", *Eur J Vasc Endovasc Surg*, vol. 53, pp. 766-775, 2017.

[2] A.R. Naylor, J.B. Ricco, G.J. de Borst, S. Debus, J. de Haro, et al., "Management of atherosclerotic carotid and vertebral artery disease: 2017 clinical practice guidelines of the ESVS", *Eur J Vasc Endovasc Surg,* vol. 55, pp. 3-81, 2018.

[3] P.B. Bijari,L. Antiga, D. Gallo, B.A. Wasserman, and D.A. Steinman,"Improved prediction of disturbed flow via hemodynamically-inspired geometric variables". *J Biomech*, vol. 45, pp. 1632-1637, 2012.

[4] B. Guerciotti, C. Vergara, L. Azzimonti, L. Forzimonti, A. Buora, P. Biondetti, and M. Domanin, "Computational study of the fluid-dynamics in carotids before and after endarterectomy", *J Biomech*, vol. 49, pp. 26-38, 2016.

[5] D. Gallo, D.A. Steinman, and U. Morbiducci, "An Insight into the mechanistic role of the common carotid artery on the hemodynamics at the carotid bifurcation", *Ann Biomed Eng*, vol. 43, pp. 68-81, 2015.

[6] D. Gallo, O. Vardoulis, P. Monney, D. Piccini, P. Antiochos, J. Schwitter, N. Stergiopulos, and U. Morbiducci, "Cardiovascular morphometry with high-resolution 3D magnetic resonance: First application to left ventricle diastolic dysfunction", *Med Eng Phys*, vol. 47, pp.64-71, 2017.

[7] D. Massai, G. Soloperto, D. Gallo, Y.Xu, and U. Morbiducci, "Shear-induced platelet activation and its relationship with blood flow topology in a numerical model of stenosed carotid bifurcation", *Eur J Mech/B Fluids*, vol. 35, pp. 92-101, 2012.

[8] S.W. Lee, L. Antiga, J.D. Spence, and D.A. Steinman, "Geometry of the carotid bifurcation predicts its exposure to disturbed flow", *Stroke*, vol. 39, pp. 2341-2347, 2008.

MicroCT-traction apparatus to follow anterior cruciate ligament fibrous structure under strain

G. Marchiori[1], A. Parrilli[2], N. Sancisi[3], M. Conconi[3], M. Berni[1], L. Luzi[3], R. Calzoni[3], G. Cassiolas[1], Milena Fini[2], S. Zaffagnini[1] and N. Lopomo[1,4]

[1] *Laboratory of Biomechanics and Technology Innovation, Rizzoli Orthopaedic Institute, Bologna, Italy*
[2] *Laboratory of Preclinical and Surgical Studies, BITTA Laboratory, Rizzoli Orthopaedic Institute, Bologna, Italy*
[3] *Industrial Engineering Department, University of Bologna, Bologna, Italy*
[4] *Department of Information Engineering, University of Brescia, Brescia, Italy*

***Abstract*—Anterior Cruciate Ligament (ACL) typically exhibits non-linear stress-strain characteristics related to its fibers behavior and distribution, which intrinsically define its functional properties. Aim of this study was to design and test a dedicated setup able to acquire the volumetric fibrous microstructure in ACL samples, under increasing mechanical strain, thus to obtain useful information for the definition of an optimal graft to be used during its reconstruction.**

***Keywords*—MicroCT, ACL, fibres, tensioning device**

I. Introduction

ANTERIOR cruciate ligament (ACL) plays a fundamental role in the stability of human knee joint and control of its laxity. For this reason, it is also highly susceptible to injuries, above all during pivoting sport activities. A torn ACL is usually reconstructed by using a biological graft or augmented by implementing a synthetic solution, that should mimic the function of the native ligament. Ideally such a function is obtained when the graft - once implanted - undergoes a process of integration and "ligamentization" [1], i.e. tissue remodelling to optimally respond to the new role. Unfortunately, common grafts used today often do not complete that process in such a time to avoid permanent alterations of joint biomechanics, which can lead – for instance – to the early development of osteoarthritis (OA) [2]. Main reasons of this limitation lie into a too high initial gap between the mechanical characteristics of the native tissue and substituting material [3]. Furthermore, also a still partial knowledge of the micro-structure and function of these tissues can contribute to a sub-optimal choice of the graft [4].

Dense fibrous tissues, such as ACL, typically present nonlinear stress-strain characteristics related to collagenous fibres uncrimping, reorienting and tensioning, which inherently define their peculiar functional properties.

Until now, few studies reported specific data on microstructural volumetric changes of soft tissues under strain. ACL fibres behaviour was already investigated under load, but considering only external surface by using polarization imaging technique [5]. On the other hand, a 3D investigation of fibrous structure was performed by microCT, but considering only artificial scaffolds and without loading [6].

Main aim of this study was to design and test a dedicated setup able to acquire the volumetric fibrous microstructure of ACL samples, under increasing mechanical strain, thus to give important information for the choice and development of optimal grafts.

II. Materials and Methods

The designed testing setup had to integrate ACL micro-structure imaging and mechanical straining. Design implementation combined a commercial microCT system for imaging and a custom-made traction apparatus for straining.

A. MicroCT System

MicroCT was selected because of its resolution potentially able to give reliable information about the microstructure of the tissue, including fibres bundles. A specific microCT system (Bruker Skyscan 1176) was considered for this development, whose overall internal dimensions were considered (Fig. 1) and served as design input of the hosted mechanical setup.

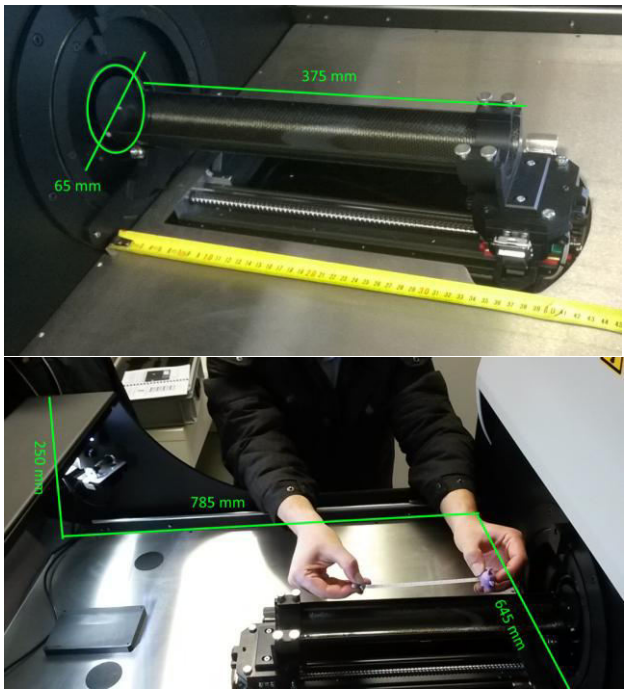

Fig. 1: Dimensions of the microCT system measured to host the mechanical apparatus

B. Traction apparatus design

Because tissue fibres are primary able to resist tensile loading [7], an experimental setup for traction test was

implemented and coupled to the microCT. Its design was performed using PTC Creo 4.0 software. Ergal, an alloy of aluminium and zinc, was used for the structural non-commercial components instead of stainless-steel, because characterized by a lower density (2.81 g/cm³), a good mechanical resistance and a lower x-ray attenuation. The final equipment (Fig. 2) is a device consisting in an actuation and support side and in a measuring side. The former is fixed to the microCT scanner basement and consists in a cylindrical tube (1) and a cube-shaped support (2) that contains a linear guide (3) driven by a manually operated threaded rod (0.75 mm pitch) (4) to impose axial elongation to the ligament sample. The measuring side consists in three coaxial cylindrical tubes (5) that surround two clamps (6) for ligament tensioning and a load cell (7) to measure the axial load. Each clamp is composed of two flat surfaces (red and green in Fig. 2) covered by sandpaper and tightened at each ligament end by a screw. One clamp is connected to the linear guide and the other to the aluminum tube. The measuring side is divided into three cylinders to allow i) mounting and demounting of the ACL sample, ii) reduction of tube thickness in the measuring section, without reducing overall resistance due to buckling. In particular, the central tube has a 0.5 mm thickness calibrated to minimize x-ray attenuation but still resisting up to a 1000 N compression force which represents the full scale of the load cell inside the machine (Burster Italia; resolution 1 N). The load cell signal is acquired and interfaced to a computer display.

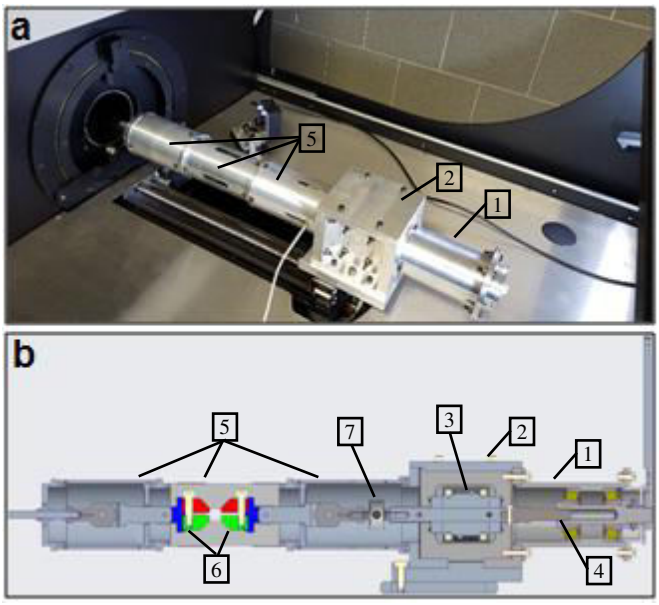

Fig. 2: a) Custom-made ligament tensile system and b) its schematic section

C. *Experimental testing*

The implemented custom-made apparatus was tested by an experimental protocol designed to visualize fibres' reaction in ACL under strain. Specifically, fresh frozen ACL samples were harvested from patients that underwent surgery for total knee replacement. The study was approved by the local ethics committee and patient consent. After thawing, ACL was stained following a defined protocol to highlight the collagen fibers during microCT scan. This process is due to the necessity to improve the X-ray contrast of the ACL fibrous structure. For this reason, first it was tested which contrast agent could be considered as optimal to enhance the identification of the fibres bundles. Different contrast stain formulations (iodine or phosphotungstic acid PTA solutions), concentrations and protocols were assessed. The specimen was then clamped and its elongation was manually imposed by acting on the threaded rod, whereas reaction force was measured by the load cell. ACL was first subjected to a cyclic preconditioning to reduce the effects of freezing [8], then it underwent increasing percentages of deformation (1, 2, 4, 6 and 8%) to highlight the toe- and linear region of the strain-stress curve [9]. After each elongation of the ACL, it was waited for 12 minutes to relax the sample stress before microCT scanning. A source voltage of 50 kV and a source current of 500 µA were applied for the acquisitions. The nominal resolution used for the images was set at 9 µm (pixel size). At each elongation of the ACL, a microCT dataset was acquired with a 14 minutes scanning. The images (2672x4000 pixels) were then reconstructed with NRecon program (version 1.7.1.6, Bruker) to obtain the microCT sections in bmp format (4000x4000 pixels, maintaining the relative pixel size). In addition to the specific alignment, slight beam hardening and reduction of ring artifact were used as correction factors in the reconstruction process.

III. RESULTS

The optimal contrast enhancement protocol resulted in staining human ACL in a 2% PTA solution in H_2O overnight. In a preliminary test, sample initial length was measured maintaining a preload of 22 N, then it was subsequently subjected to 1-2-3-4-6-8% strains and relative microCT scans. Force-strain behaviour (Fig. 3) was in fair agreement with the literature [10], even if some of the test conditions may have partially altered the native mechanical behaviour.

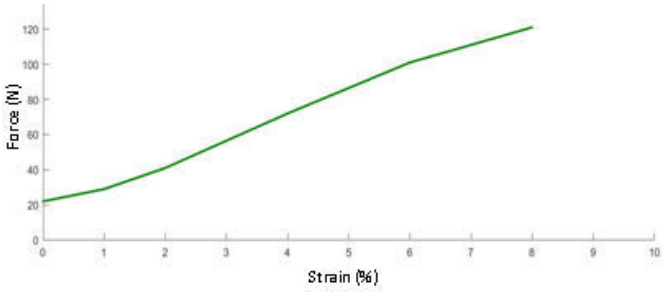

Fig. 3: interpolated strain-force curve on an ACL sample

The microCT images relative to 0% and 8% of deformations are shown in Fig. 4.

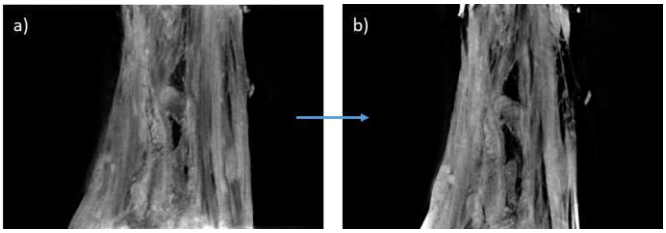

Fig. 4: coronal microCT sections of the ACL at 0% (a) and 8% of deformation (b)

IV. Conclusion

The specific microCT procedure, with a nominal resolution of 9 μm used to visualize the ACL volume under progressive elongation, was able to detect the hierarchical structure at the level of the fibre bundles (Fig. 5). At present, images are being processed in order to perform a 3D morphometric analysis of the fibre bundles' changes in relation to the quantified mechanical behaviour by exploiting image correlation analysis. In the future, the evolution of the proposed experiment can be exploited to compare structure and mechanics of native ligament and natural/artificial grafts, considering more loading conditions such as torsion.

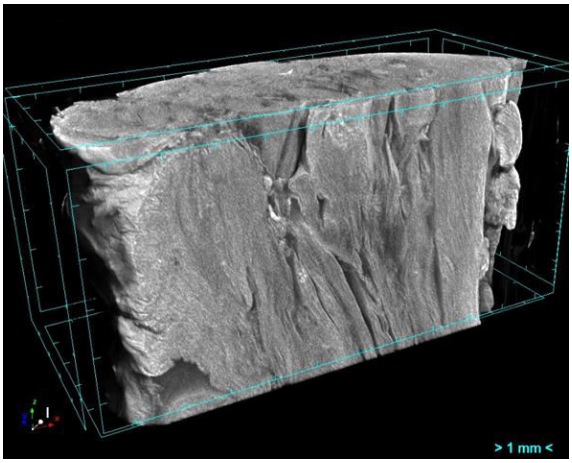

Fig. 5: 3D CTVox model of the fibre bundles of the ACL

Acknowledgement

We thank the "Italian Ministry of Health", funding the project GR-2011-02351803.

References

[1] S. Claes, P. Verdonk, R. Forsyth, J. Bellemans, "The "ligamentization" process in anterior cruciate ligament reconstruction. What happens to the human graft? A systematic review of the literature", *The American journal of sports medicine*, vol. 39(11), pp. 2476-2483, November 2011.

[2] P. M. Vacek, J.R. Slauterbeck, T.W. Tourville, D. R. Sturnick, L.A. Holterman, H.C. Smith, S.J. Shultz, R.J. Johnson, K.J. Tourville, B.D. Beynnon, "Multivariate analysis of the risk factors for first-time noncontact ACL injury in high school and college athletes: a prospective cohort study with a nested, matched case-control analysis", *The American journal of sports medicine*, vol. 44(6), pp. 1492-1501, June 2016.

[3] J.W. Freeman, A.L. Kwansa, "Recent Advancements in Ligament Tissue Engineering: The Use of Various Techniques and Materials for ACL Repair", *Recent Patents on Biomedical Engineering*, vol. 1(1), pp. 18-23, January 2008.

[4] S. G. McLean, K. F. Mallet, E. M. Arruda, "Deconstructing the Anterior Cruciate Ligament: what we know and do not know about function, material properties, and injury mechanics", *Journal of Biomechanical Engineering*, vol. 137(2), pp. 020906-19, February 2015.

[5] R.M. Castile, N.W. Skelley, B. Babaei, R.H. Brophy, S.P. Lake, "Microstructural properties and mechanics vary between bundles of the anterior cruciate ligament during stress-relaxation", *Journal of Biomechanics*, vol. 4;49(1), pp. 87-93, January 2016.

[6] A. Sensini, C. Gualandi, L. Cristofolini, G. Tozzi, M. Dicarlo, G. Teti, M. Mattioli-Belmonte, M.L. Focarete, "Biofabrication of bundles of poly(lactic acid)-collagen blends mimicking the fascicles of the human Achille tendon", *Biofabrication*, vol. 8;9(1), pp. 015-025, March 2017.

[7] J.A. Weiss, J.C. Gardiner, B.J. Ellis, J.L. Trevor, N.S. Phatak, "Three-dimensional finite element modeling of ligaments: technical aspects", *Medical Engineering & Physics*, vol. 27(10), pp. 845-861, December 2005.

[8] J. Hashemi, N. Chandrashekar, J. Slauterbeck, "The mechanical properties of the human patellar tendon are correlated to its mass density and are independent of sex", *Clinical Biomechanics*, vol. 20(6), pp. 645-652, July 2005.

[9] J.W. Freeman, M.D. Woods, C.T. Laurencin, "Tissue Engineering of the Anterior Cruciate Ligament Using a Braid-Twist Scaffold Design", *Journal of Biomechanics*, vol. 40(9), pp. 2029-2036, November 2006.

[10] J.S. Bach, F. Detrez, M. Cherkaoui, S. Cantournet, D.N. Ku, L. Cortè, "Hydrogel fibers for ACL prosthesis: Design and mechanical evaluation of PVA and PVA/UHMWPE fiber constructs", Journal of biomechanics, vol. 46(8), pp. 1463-1470, May 2013.

Structure and mechanosensing response of the nuclear pore complex

F. Donnaloja[1], E. Jacchetti[1], M. Soncini[2], M. T. Raimondi[1]

[1] *Department of Chemistry, Materials and Chemical Engineering "G. Natta", Politecnico di Milano, 20133 Milano, Italy;*

[2] *Dipartimento di Elettronica, Informazione e Bioingegneria, Politecnico di Milano, 20133 Milano, Italy;*

***Abstract*— The nuclear pore complexes are large multiprotein channels spanning the nuclear envelope whose main function is to mediate the nucleocytoplasmic transport of selected molecules. In this review, we gather all the literature supporting the hypothesis that the cargoes transport may be controlled by mechanical external stimuli transmitted to the pore through cytoskeletal filaments and the linker of nucleoskeleton and cytoskeleton binding domain (LINC) complex. In this context, mechanotransduction may influence the pore architecture altering both the molecules transport and the gene expression control via the pore chromatin binding domain.**

***Keywords*—Nuclear pore complex, mechanical model, mechanotransduction.**

I. INTRODUCTION

IN eukaryotic cells, nuclear and cytoplasmic compartments are separated by the nuclear envelope, a coat protecting the genome material that embeds 2000-5000 nuclear pore complexes (NPCs) per nucleus [1], [2]. NPCs are large protein assemblies (110 MDa) which control the bidirectional nucleocytoplasmic transport inducing a selective transport of thousands of molecules per second (~100 MDa/s; transport process is complete in 5 ms) [3], [4], [5], [6]. The pore central channel consists of effective mesh size of 4–5 nm composed by FG-nucleoporins which restrict passive diffusion to molecules up to 40 kDa (9nm) in size and allows selective transport of the only larger molecules (up to 25 MDa, 39 nm) characterized by nuclear localization signal or nuclear export signal [4], [7]. These cargoes domains are bound by soluble nuclear transport factors that shuttle between the nucleus and the cytosol (and *vice versa*), via their affinity with the protein of the mesh (FG Nups).

Cryo-electron microscopy and Cryo-electron tomography images have revealed the global features of the pores complexes consisting of an eight-fold symmetric central framework (see the green part in Fig.1), eight cytoplasmic filaments (~35-50 nm) (see the yellow part in Fig.1) and eight nucleoplasmic filaments (~40-75 nm; 3-6 nm in diameter) co-joined in a distal ring [3], [8], [5], [9], [10], [11], [12].The nucleoplasmic protrusions form a structure named nuclear basket (Fig.1) (see the grey part in Fig.1).

II. NPC STRUCTURE

Based on scanning electron microscopy data, it is assumed that NPC is characterized by an eight-fold rotational symmetry [5] whose function seems to be maximizing the bending stiffness of each of the eight NPC spokes [13]. This maximization would both guarantee structural stability during the large cargoes transport and allow for the massive NPC to be built upon a comparatively small number of nucleoporins [13]. Indeed, NPCs are comprised of only about 30 different proteins called nucleoporins (Nups) which occur in a copy number of eight or multiples of eight to give a total of ~1000 Nups/NPC [4], [9]. The Nups are often categorized as:

- transmembrane nucleoporins, or pore-membrane proteins, which anchor the NPC in the nuclear envelope forming the so called membrane ring [14] (orange in Fig.1);
- structural nucleoporins (~1/2 of all Nups) which form the NPC scaffold (green in Fig.1);
- channel nucleoporins (~1/3 of all Nups) rich of phenylalanine-glycine repeats (FG-Nups) (red in Fig.1);
- nuclear-basket nucleoporins (grey in Fig.1);
- cytoplasmic-filament nucleoporins (yellow in Fig.1) [9], [15].

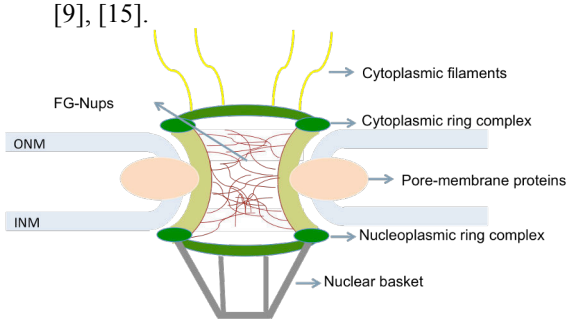

Fig.1: Structural architecture of NPCs. NPCs span the nuclear envelope at sites where the outer nuclear membrane (ONM) and inner nuclear membrane (INM) are fused. The core scaffold (green) is bound to the nuclear envelope through the Pore membrane proteins (orange) and contains multiple binding sites for the FG-Nups (red) which fill the central channel. Filaments extend from the NPC core into both the cytoplasm (cytoplasmic filaments in yellow) and nucleoplasm (nuclear basket in grey).

A. NPC scaffold

The NPC central framework (also called scaffold) is dominated by α-solenoid domains which guarantee flexibility to the structure allowing conformational changes without breaking protein-protein interactions during nucleocytoplasmic transport [16]. Three connected rings compose the scaffold: the cytoplasmic ring complex and the nucleoplasmic ring complex sandwich (dark green in Fig.1) the inner ring complex, also called spoke ring (~90 nm in length) (light green in Fig.1) [4], [16].

Cryo-Electron tomography analysis indicated that both nucleoplasmic and cytoplasmic ring complexes are characterized by so-called Y subcomplexes (0.5-0.75 MDa), consisting of a stem base which joins the two arms in a central hub element [16], [5]. Their structures are made from a total of 32 Y complexes assemble into two eight-membered concentric, reticulated rings which are stacked with a slight offset and differ only [10]slightly in diameter [5], [17], [15]. Individual Y-shaped complexes are head-to-tail arranged [18], [11]. Instead, the spoke ring is composed by eight similar "spokes" that stabilize the sharply bent nuclear

envelope [9]. Some of Nup93 complex's domains (localized in the inner ring complex) have showed homology to Y complex members and tomographic studies have revealed possible locations of 32 copies of some inner ring complex Nups (Nup155 and Nup205 or Nup188). So it, it has been supposed that simple and highly similar organizational principles govern the architecture of the inner and outer rings of the NPC [19]. The spoke ring harbours the central transport channel which exhibits an hourglass shape (~50 nm wide in the middle and expands to ~70 nm at its edges [3]).

B. Central channel

Anchored to the central channel inner wall there are many unstructured and intrinsically disordered nucleoporins (~1mM of concentration) which contain hydrophobic sequences rich in phenylalanine-glycine repeats (such as FG, FxFG, GLFG) [20], [4]. Through their FG-repeats, the nucleoporins can interact with one other guaranteeing a compact morphology counteracted by repulsive charged amino acids [4]. Although the morphology of the FG-Nups in the central channel is essential for the selective transport, the mechanism is not yet well understood and several models have been proposed so far to explain the structure of the NPC's interior. According to the "virtual gate model", the FG-Nups form an entropic barrier at the NPC periphery that repels non-specific cargo [2], [3], [22], [26]. The "polymer brush model" proposes that FG-Nups form extended brush-like polymer with inter-linked bristles that reversibly collapse upon nuclear transport factor binding [3], [21], [23]. Instead, the "selective phase" model suggests that FG-FG hydrophobic interactions in the central channel form a sieve-like hydrogel meshwork, which is reversibly dissolved by nuclear transport factors allowing cargo to permeate the channel [2], [21], [24] . In contrast, the "reduction of dimensionality" model supposes that a layer of FG-motifs lines the NPC interior and nuclear transport factor slides on the surface of FG motifs according to a 2D random walk [2], [3], [21], [25]. The "forest model" features two separate channel's zones: the interior of the NPC seems a hydrogel and the periphery is brush-like [3], [21]. More than one configuration can exist in parallel for an FG-domain, and they might also be in dynamic equilibrium [20].

Nevertheless, the Cryo-electron tomography studies revealed an ordered ring-like structure (named central channel ring) attached to the inner ring complex [18] which assume an open configuration during large cargoes passage as revealed in NPC by electron microscopy data [26], [27]. In this context, it's been proposed a new model based on two channel Nups (Nup54 and Nup58) which can be rearranged to form a midplane ring in constricted or dilated conformations (~20 nm ~40 nm respectively) corresponding to high or low nuclear transport factor's concentration respectively [26], [28]. In addition, Nup54 interacts with Nup62 forming "finger"-shaped triple helices before splitting into "unstructured" appendages characterized by FG-repeat motifs [28].

C. Nuclear basket

The nuclear basket is a structure appended to the nucleoplasmic sides of the NPC which harbours Nup153, Tpr and Nup50 [29]: it has been proposed Tpr to be the basket central architectural element linked to the NPC via direct binding to the Nup153. In this context, the basket fibres would be formed by Tpr dimers folded back onto themselves with both N and C termini at distal ring, forming shorter but thicker fibers. Folding of Tpr dimer would occur at the NPC binding domain upon binding the Nup153 and the intradimer interactions would take place between the first two third of Tpr's rod domain. The last domain constitutes the distal ring [12], [30]. The Nup153 is characterized by N-teminal domain close to the membrane, a central domain consisting of four zinc fingers at the distal ring and a C-terminal domain containing ~30 FXFG-repeats detected all over the nuclear basket and occasionally on the cytoplasmic side too [10], [11], [31], [32]. NPCs lacking the Nup153 have shown more mobility within the nuclear envelope with consequent redistribution, ([10], [33]) altered nuclear lamina, cytoskeleton and SUN1 organization ([11], [34]) and several Nups lost from nuclear basket (such as Nup93, Nup98 and Tpr) [10].

III. STRUCTURAL BIOLOGY OF THE CONNECTION BETWWEN THE NPC AND ITS ENVIRONMENT

A. Linkage with lamin and LINC complex

Evidences suggested that NPCs are fixed in space by stable tethering to its environment. In vertebrates, there are three different Nups named pore-membrane proteins (Pom152, Pom34 and Ndc1) which anchor the NPC inside the nuclear envelope forming the so called membrane ring (or luminal ring) [14]. In addition to the pore-membrane proteins, there are other connections between NPC and its environment. For instance, the Nup153 exhibits multiple lamin-binding domains at both its N- and C-terminal domain which induce altered nuclear lamina organization in Nup153-depleted cells [31], [34], [35]. As described in nuclear basket section, Nup153 has a dynamic nature which seems to suggest other Nups involvement in maintaining NPC-nuclear envelope stable interaction. In that respect, studies have revealed connection with LInker of Nucleoskeleton and Cytoskeleton (LINC) complex which avoids NPCs clustering, affect cytoskeletal organization and define nuclear size and architecture (Fig. 2) [33], [36].

The LINC complex is constituted of SUN domain proteins (primarily inner nuclear membrane proteins) (Sad1-UNC-84 homology [37]) and nesprins KASH domain (primarily outer nuclear membrane proteins) (Klarsicht, ANC-1, and Syne homology [37]) which interact in the intramembrane lumen of the nuclear envelope [38], [33]. The SUN proteins are transmembrane proteins connected with the nuclear lamina, chromatin and other "nucleoskeletal" structures at their N-terminal [38] [39]. SUN1 and SUN2 are more widely expressed SUN proteins and are connected to Nesprin 1/2 which in turn bind actin at their actin binding domain [33], [37], [40], [41], [42]. Structural and biomechemical SUN-KASH domain complexes characterization shows that three KASH proteins can bind to a SUN trimer [37], [43], [41]. Even if NPC-LINC connection has not been formally proven yet [39], some evidences seem to verify it: Sun1 (not Sun2) co-localizes with Nup153 and Nup153 depletion alters Sun1 localization (and *vice versa*) [44], [33], [34], [45]. The hypothetical connection with SUN1 would provide an indirect coupling between the pore and the cytoskeleton elements, resulting in NPCs exposure to cytoskeletal forces [39]. On the other hand, due to SUN1 interaction with lamin A, it could function as an adaptor between the nuclear lamina

and the pore [44]. Finally, other linkage could be found in Nup358 N-terminal region which seems to interact with interphase microtubules via motor proteins such as dynein and kinesins [39], [33], [46].

B. *Linkage with chromatin*

In addition to lamin connection, Nup153 is considered as chromatin-binding proteins (Fig.2): it binds to 25% of the genome in continuous domains termed nucleoporin-associated regions, which demarcate regions of open chromatin and transcriptional activity. The wide-spread transcriptional changes (e.g. activated genes re-localization at the nuclear periphery) revealed in Nup153 depletion cells seemed to prove Nup153 role in open chromatin environment formation and gene expression control [47], [11], [48].
Even if the gene localization to the NPC is clearly correlated with transcription, the underlying mechanism has not yet been realized [49], [48]. So that, even if it has been shown that NPCs may be involved in gene regulations, their role remains elusive [50].

IV. MECHANOSENSING RESPONSE

The cells respond to extracellular environment changes with both chemical-based signal (25-50 s/50 um) and mechanical-based signal transmission (2us/50 um) [51]. During cell-extracellular matrix adhesion, the cytoskeleton rearrangement transmits tensile forces to the Nesprins which in turn transfer the physical force propagation to SUN proteins [40], [52]. The LINC complex is supposed to bind to both NPC (via only SUN1 protein) and chromatin, enabling the entire cell to function as a single mechanically coupled system [51], [52]. Given that, the external stimuli transmission via LINC complex may act on NPC inducing its distortion in size (likely through basket distortion), altered NPC transport rate and gene activities [51]. On the other hand, mechanical load induces rapid chromatin stretching, which subsequently results in increase of transcription proportional to the magnitude of chromatin stretching [53]. In summary, it could be taught that any applied force leading to nuclear deformation elicits an open chromatin state, upregulating transcription which may be enlarged by NPC distortion due to its chromatin connection [53] (Fig.2).

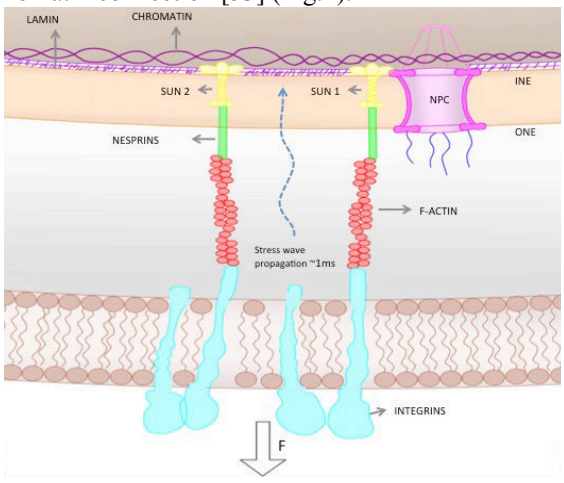

Fig.2: A possible model of stretch activation for the NPC.

V. MODELLING APPROACH

Even if progress in imaging techniques in combination with X-ray crystallography has improved knowledge of NPC structure and organization, some domains have remained elusive. The NPC is involved in several cellular processes such as bidirectional nucleocytoplasmic exchange, cell cycle regulation, kinetochore organization, regulation of gene expression and its functionality seems to be mechanically sensitive. Considering the several NPC connections with nuclear envelope, chromatin and other transmembrane proteins, it is reasonable to suppose that nuclear deformations could affect directly or indirectly, NPC structure too. As reported in the previous sections, the main linker between the environment and the pore seems to be the basket nucleoporin Nup153. In that respect, we hypothesise that the mechanical force transmission may primarily affect the basket conformation with two possible effects on transcription variation: changes in basket structure could both alter molecules passages through it, and influence the open chromatin state via Nup153 connection. Indeed, several evidences showed that the nuclear basket is determinant for chromatin structure modulation and gene expression, whose alteration may be linked to various types of diseases such as cancer, autoimmune disease, aging and laminopathies [48], [19]. Indeed, mutations in the LMNA gene (lamin A encoding gene associated to laminopathies), have been observed in correlation with a decrease in Nup153 at the nuclear envelope [11]. Furthermore, in high-speed atomic force microscopy analysis the distal ring showed either opened and closed states but the triggering signals remain so far elusive [54].
In future work, we plan to conduct biophysical and computational studies to validate or negate such hypothesis. In this context, we are developing an homology structures analysis to predict a possible arrangement of Nup153-SUN1 complex based on similar structures observed in different proteins. This analysis would allow us to simulate the most favourable configuration of the complex using molecular dynamics software. We will validate the obtained computer structures by solving the SUN1-Nup153 interaction complex by X-ray crystallography. In addition we will implement a model to evaluate the external force transmission and its effects on the nuclear pore complex structure. This engineering approach, already explored by our group [55], should lead to a more quantitative understanding of basket structure alteration and its effect on transcription and disease.

ACKNOLEDGEMENT

This study is funded by the European Research Council (ERC) under the European Union's Horizon 2020 research and innovation program (G.A. No. 646990 - NICHOID).

REFERENCES

[1] S. R. Wente, "Gatekeepers of the Nucleus," *Science (80-.).*, vol. 288, no. 5470, pp. 1374–1378, 2000.
[2] K. S. Lingling Miao, "Transport-Related Structures and Processes of the Nuclear Pore Complex Studied Through Molecular Dynamics," vol. 17, no. 3, pp. 449–459, 2010.
[3] R. Moussavi-Baygi, Y. Jamali, R. Karimi, and M. R. K. Mofrad, "Biophysical coarse-grained modeling provides insights into transport through the nuclear pore complex," *Biophys. J.*, vol. 100, no. 6, pp. 1410–1419, 2011.
[4] G. J. Stanley, A. Fassati, and B. W. Hoogenboom, "Biomechanics of the transport barrier in the nuclear pore complex," *Semin. Cell Dev. Biol.*, vol. 68, pp. 42–51, 2017.
[5] K. E. Knockenhauer and T. U. Schwartz, "The Nuclear Pore Complex as a Flexible and DynamicGate ," *Cell* , vol. 164, no. 6, pp. 1162–1171, 2016.
[6] C. Y. Chen *et al.*, "Accumulation of the inner nuclear envelope

protein Sun1 is pathogenic in progeric and dystrophic laminopathies," *Cell*, vol. 149, no. 3, pp. 565–577, 2012.

[7] L. C. Tu, G. Fu, A. Zilman, and S. M. Musser, "Large cargo transport by nuclear pores: Implications for the spatial organization of FG-nucleoporins," *EMBO J.*, vol. 32, no. 24, pp. 3220–3230, 2013.

[8] T. R. Lezon, A. Sali, and I. Bahar, "Global motions of the nuclear pore complex: Insights from elastic network models," *PLoS Comput. Biol.*, vol. 5, no. 9, 2009.

[9] S. Wälde and R. H. Kehlenbach, "The Part and the Whole: Functions of nucleoporins in nucleocytoplasmic transport," *Trends Cell Biol.*, vol. 20, no. 8, pp. 461–469, 2010.

[10] T. C. Walther, M. Fornerod, H. Pickersgill, M. Goldberg, T. D. Allen, and I. W. Mattaj, "The nucleoporin Nup153 is required for nuclear pore basket formation, nuclear pore complex anchoring and import of a subset of nuclear proteins," *EMBO J.*, vol. 20, no. 20, pp. 5703–5714, 2001.

[11] V. Duheron and B. Fahrenkrog, "The nuclear pore complex: structure and function," *Atlas Genet. Cytogenet. Oncol. Haematol.*, no. 5, pp. 355–375, 2017.

[12] B. B. Sandra Krull, Johan Thyberg and and V. C. C. Hans-Richard Rackwitz, "Nucleoporins as Components of the Nuclear Pore Complex Core Structure and Tpr as the Architectural Element of the Nuclear Basket," *Mol. Biol. Cell*, vol. 16, no. 1, pp. 1–13, 2004.

[13] C. Wolf and M. R. K. Mofrad, "On the octagonal structure of the nuclear pore complex: Insights from coarse-grained models," *Biophys. J.*, vol. 95, no. 4, pp. 2073–2085, 2008.

[14] F. Alber *et al.*, "The molecular architecture of the nuclear pore complex," *Nature*, vol. 450, no. 7170, pp. 695–701, 2007.

[15] J. S. André Hoelz and and M. B. . Glavy, "Towards the atomic structure of the Nuclear Pore Complex: When top down meets bottom up," vol. 23, no. 7, pp. 624–630, 2016.

[16] A. Von Appen and M. Beck, "Structure Determination of the Nuclear Pore Complex with Three-Dimensional Cryo electron Microscopy," *J. Mol. Biol.*, vol. 428, no. 10, pp. 2001–2010, 2016.

[17] A. Von Appen *et al.*, "In situ structural analysis of the human nuclear pore complex," *Nature*, vol. 526, no. 7571, pp. 140–143, 2015.

[18] M. Eibauer, M. Pellanda, Y. Turgay, A. Dubrovsky, A. Wild, and O. Medalia, "Structure and gating of the nuclear pore complex," *Nat. Commun.*, vol. 6, no. May, pp. 1–9, 2015.

[19] J. Kosinski *et al.*, "Molecular architecture of the inner ring scaffold of the human nuclear pore complex," *Science (80-.).*, vol. 352, no. 6283, pp. 363–365, 2016.

[20] E. A. Lemke, "The Multiple Faces of Disordered Nucleoporins," *J. Mol. Biol.*, vol. 428, no. 10, pp. 2011–2024, 2016.

[21] R. Gamini, W. Han, J. E. Stone, and K. Schulten, "Assembly of Nsp1 Nucleoporins Provides Insight into Nuclear Pore Complex Gating," *PLoS Comput. Biol.*, vol. 10, no. 3, pp. 8–10, 2014.

[22] M. P. Rout, J. D. Aitchison, A. Suprapto, K. Hjertaas, Y. Zhao, and B. T. Chait, "The yeast nuclear pore complex: Composition, architecture, transport mechanism," *J. Cell Biol.*, vol. 148, no. 4, pp. 635–651, 2000.

[23] L. Miao and K. Schulten, "Probing a structural model of the nuclear pore complex channel through molecular dynamics," *Biophys. J.*, vol. 98, no. 8, pp. 1658–1667, 2010.

[24] K. Ribbeck and D. Görlich, "The permeability barrier of nuclear pore complexes appears to operate via hydrophobic exclusion," *EMBO J.*, vol. 21, no. 11, pp. 2664–2671, 2002.

[25] R. Peters, "Translocation through the nuclear pore complex: Selectivity and speed by reduction-of-dimensionality," *Traffic*, vol. 6, no. 5, pp. 421–427, 2005.

[26] J. Koh and G. Blobel, "Allosteric regulation in gating the central channel of the nuclear pore complex," *Cell*, vol. 161, no. 6, pp. 1361–1373, 2015.

[27] S. Au and N. Panté, "Nuclear transport of baculovirus: Revealing the nuclear pore complex passage," *J. Struct. Biol.*, vol. 177, no. 1, pp. 90–98, 2012.

[28] S. R. Solmaz, G. Blobel, and I. Melcak, "Ring cycle for dilating and constricting the nuclear pore," *Proc. Natl. Acad. Sci.*, vol. 110, no. 15, pp. 5858–5863, 2013.

[29] N. Mészáros, J. Cibulka, M. J. Mendiburo, A. Romanauska, M. Schneider, and A. Köhler, "Nuclear Pore Basket Proteins Are Tethered to the Nuclear Envelope and Can Regulate Membrane Curvature," *Dev. Cell*, vol. 33, no. 3, pp. 285–298, 2015.

[30] D. A. Byrd *et al.*, "Tpr, a large coiled coil protein whose amino terminus is involved in activation of oncogenic kinases, is localized to the cytoplasmic surface of the nuclear pore complex," *J. Cell Biol.*, vol. 127, no. 6 I, pp. 1515–1526, 1994.

[31] T. Al-Haboubi, D. K. Shumaker, J. Köser, M. Wehnert, and B. Fahrenkrog, "Distinct association of the nuclear pore protein Nup153 with A- and B-type lamins.," *Nucleus*, vol. 2, no. 5, pp. 500–509, 2011.

[32] J. R. Ball and K. S. Ullman, "Versatility at the nuclear pore complex: Lessons learned from the nucleoporin Nup153," *Chromosoma*, vol. 114, no. 5, pp. 319–330, 2005.

[33] M. W. Goldberg, "Nuclear pore complex tethers to the cytoskeleton," *Semin. Cell Dev. Biol.*, vol. 68, pp. 52–58, 2017.

[34] L. Zhou and N. Panté, "The nucleoporin Nup153 maintains nuclear envelope architecture and is required for cell migration in tumor cells," *FEBS Lett.*, vol. 584, no. 14, pp. 3013–3020, 2010.

[35] A. C. Rowat, J. Lammerding, and J. H. Ipsen, "Mechanical properties of the cell nucleus and the effect of emerin deficiency," *Biophys. J.*, vol. 91, no. 12, pp. 4649–4664, 2006.

[36] A. J. Engler, S. Sen, H. L. Sweeney, and D. E. Discher, "Matrix Elasticity Directs Stem Cell Lineage Specification," *Cell*, vol. 126, no. 4, pp. 677–689, 2006.

[37] Z. Zhou *et al.*, "Structure of Sad1-UNC84 homology (SUN) domain defines features of molecular bridge in nuclear envelope," *J. Biol. Chem.*, vol. 287, no. 8, pp. 5317–5326, 2012.

[38] S. Gay and M. Foiani, *Nuclear Envelope and Chromatin, Lock and Key of Genome Integrity*, vol. 317. Elsevier, 2015.

[39] Z. Jahed, M. Soheilypour, M. Peyro, and M. R. K. Mofrad, "The LINC and NPC relationship – it's complicated!," *J. Cell Sci.*, vol. 129, no. 17, pp. 3219–3229, 2016.

[40] Z. Jahed, H. Shams, M. Mehrbod, and M. R. K. Mofrad, *Mechanotransduction pathways linking the extracellular matrix to the nucleus*, 1st ed., vol. 310. Elsevier Inc., 2014.

[41] B. A. Sosa, A. Rothballer, U. Kutay, and T. U. Schwartz, "LINC complexes form by binding of three KASH peptides to domain interfaces of trimeric SUN proteins," *Cell*, vol. 149, no. 5, pp. 1035–1047, 2012.

[42] D. A. Starr and H. N. Fridolfsson, "Interactions Between Nuclei and the Cytoskeleton Are Mediated by SUN-KASH Nuclear-Envelope Bridges," *HHS Public Access*, pp. 421–444, 2014.

[43] S. Nie *et al.*, "Coiled-Coil Domains of SUN Proteins as Intrinsic Dynamic Regulators," *Structure*, vol. 24, no. 1, pp. 80–91, 2016.

[44] Q. Liu *et al.*, "Functional association of Sun1 with nuclear pore complexes," *J. Cell Biol.*, vol. 178, no. 5, pp. 785–798, 2007.

[45] L. Wang, "SUN1 silencing inhibits cell growth through G0 / G1 phase arrest in lung adenocarcinoma," pp. 2825–2833, 2017.

[46] Jomon Joseph and Mary Dasso, "The nucleoporin Nup358 associates with and regulates interphase microtubules," *FEBS*, vol. 582, no. 2, pp. 190–196, 2008.

[47] J. M. Vaquerizas, R. Suyama, J. Kind, K. Miura, N. M. Luscombe, and A. Akhtar, "Nuclear pore proteins Nup153 and megator define transcriptionally active regions in the Drosophila genome," *PLoS Genet.*, vol. 6, no. 2, 2010.

[48] C. Ptak, J. D. Aitchison, and R. W. Wozniak, "The multifunctional nuclear pore complex: A platform for controlling gene expression," *Curr. Opin. Cell Biol.*, vol. 28, no. 1, pp. 46–53, 2014.

[49] L. Texari and F. Stutz, "Sumoylation and transcription regulation at nuclear pores," *Chromosoma*, vol. 124, no. 1, pp. 45–56, 2015.

[50] M. Capelson, Y. Liang, R. Schulte, W. Mair, U. Wagner, and M. W. Hetzer, "Chromatin-Bound Nuclear Pore Components Regulate Gene Expression in Higher Eukaryotes," *Cell*, vol. 140, no. 3, pp. 372–383, 2010.

[51] N. Wang, J. D. Tytell, and D. E. Ingber, "Mechanotransduction at a distance: Mechanically coupling the extracellular matrix with the nucleus," *Nat. Rev. Mol. Cell Biol.*, vol. 10, no. 1, pp. 75–82, 2009.

[52] K. N. Dahl, A. J. S. Ribeiro, and J. Lammerding, "Nuclear shape, mechanics, and mechanotransduction," *Circ. Res.*, vol. 102, no. 11, pp. 1307–1318, 2008.

[53] Y. A. Miroshnikova, M. M. Nava, and S. A. Wickström, "Emerging roles of mechanical forces in chromatin regulation," *J. Cell Sci.*, vol. 130, no. 14, pp. 2243–2250, 2017.

[54] Y. Sakiyama, R. Panatala, and R. Y. H. Lim, "Structural dynamics of the nuclear pore complex," *Semin. Cell Dev. Biol.*, vol. 68, pp. 27–33, 2017.

[55] Garcia A, Rodriguez Matas JF, Raimondi MT. Modeling of the mechano-chemical behaviour of the nuclear pore complex: current research and perspectives. Integr Biol (Camb). 2016 Oct 10;8(10):1011-1021.

Local vascular remodeling and hemodynamic changes of patient-specific arteriovenous fistulae for hemodialysis

M. Bozzetto[1], P. Brambilla[2], S. Rota[3], B. Ene-Iordache[4], D. Curtò[3], S. Sironi[2], G. Remuzzi[3,4] and A. Remuzzi[5]

[1]*Department of Engineering and Applied Sciences, University of Bergamo, Dalmine (BG), Italy;*
[2]*USC Radiologia Diagnostica per Immagini 1, ASST Papa Giovanni XXIII - Universitá Milano-Bicocca, Italy*
[3]*Unit of Nephrology and Dialysis, ASST Papa Giovanni XXIII, Bergamo, Italy*
[4]*Department of Bioengineering, IRCCS-Istituto di Ricerche Farmacologiche "Mario Negri", Bergamo, Italy;*
[5]*Department of Management, Information and Production Engineering, University of Bergamo, Italy;*

***Abstract*— Arteriovenous fistula (AVF) is the preferred vascular access for hemodialysis, but maintaining its patency is challenging. Convincing evidence supports a key role of local hemodynamics in AVF failure, therefore longitudinal studies with repeated evaluations of structural and hemodynamic changes over time are needed. In the present investigation we explored the feasibility of coupling contrast-free MRI and high-resolution CFD to relate local hemodynamics to vascular remodelling after AVF creation.**

***Keywords*—arteriovenous fistula, contrast-free MRI, computational fluid dynamics, hemodialysis.**

I. Introduction

NATIVE arteriovenous fistula (AVF) is the preferred vascular access for hemodialysis, but it still has high rate of non-maturation and early failure due to vascular stenosis, mainly caused by neointimal hyperplasia [1], [2]. Convincing evidence supports a key role of local hemodynamics in vascular remodelling [3], therefore longitudinal studies with repeated evaluations of local hemodynamic conditions and vascular changes over time are needed to investigate the relationship between disturbed flow and vascular stenosis formation. These studies require reliable and non-invasive investigations to obtain patient-specific 3D AVF geometrical models to perform CFD simulations and to evaluate vessel structural changes over time. To avoid the use of any contrast agent, that may be toxic in patients with advanced renal failure [4], contrast-free magnetic resonance imaging (MRI) protocols should be adopted. The aim of our study was to explore the feasibility of coupling a contrast-free MRI protocol with high-resolution CFD to relate local hemodynamic changes to vascular wall remodeling after AVF creation.

II. Methods

A. MRI acquisition

We acquired contrast-free MRI in 2 patients with radio-cephalic side-to-end AVF. The acquisition was obtained on a 1.5 T scanner (GE, Optima 450w GEM) using a flexible 16-channel phased array medium coil and was cardiac gated using peripheral pulse gating. We firstly acquired a three planes scout sequence for anastomosis localization. We then performed 3D fast spin echo T1-weighted imaging with variable flip angles using CUBE sequence [5], with the parameters reported in Table I. Magnetic resonance examination was performed 1 week after AVF creation and repeated 5 weeks later, after AVF maturation.

TABLE I
MR IMAGING PARAMETERS

Acquisition duration	5-10 mins
Acquisition plane	Axial
Slice thickness	2 mm
Slice spacing	0 mm
Echo time	14-19 ms
Echo train length	24 ms
Repetition time	2340-2470
Matrix	256 x 256

Contrast-free magnetic resonance imaging protocol

B. 3D model reconstruction and mesh generation

Patient-specific 3D surface was generated using the Vascular Modelling Toolkit (VMTK) [6]. Briefly, AVF lumen with its limbs, the proximal artery (PA), the distal artery (DA), the juxta-anastomotic vein (JAV) and the outflow vein, were digitally segmented using ImageJ (Fig. 1 A-B). A polygonal surface was generated using a gradient-based level set method [7] followed by marching cubes [8] (Fig. 1C). Straight cylindrical flow extensions were then added at the inlet and outlet of every vessel to ensure fully developed flow inside the computational domain. Starting from the surface model, the internal volume was discretized using foamyHexMesh mesher [9] (Fig. 1D). We obtained high-resolution meshes with dominant-hexahedral core cells characterized by low orthogonality and predominant alignment to the vessel surface. Two thin boundary layers were generated near the wall in order to capture the sharp velocity gradients in this region.

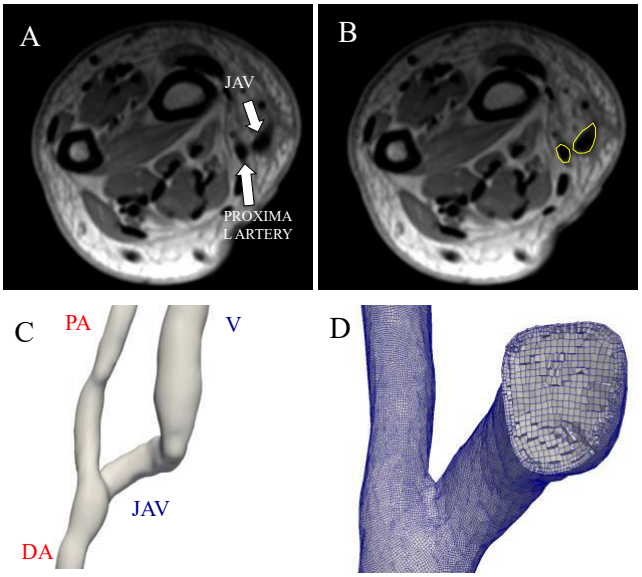

Fig. 1: Pipeline to obtain the computational grid for CFD. Abbreviations: PA, proximal artery; DA, distal artery; V vein; JAV, juxta-anastomotic vein.

C. CFD simulations of blood flow

Transient Navier-Stokes equations were solved using OpenFoam, an open-source CFD-toolbox based on the finite volume method [9]. Volumetric flow waveforms, obtained from US examinations [10], were prescribed as boundary conditions at the inlet of the PA and at the outlet of the DA, while traction-free condition was set at the vein outflow. Vessel walls were assumed to be rigid and blood rheology was modelled using Bird-Carreau. We used pimpleFoam, a transient OpenFOAM solver for incompressible flows, set with second order spatial and time integration schemes. The time step was adjusted automatically by the solver, based on a maximum Courant-Friedrichs-Lewy (CFL) number set to 1, resulting in very small time-steps. Three cardiac cycles were solved to avoid start-up transients and only the third cycle was used for post-processing with 1,000 time steps. The most important parameters of CFD simulations are presented in Table II.

TABLE II
CFD SIMULATION DATA

CFD parameter	*Patient 1 1 week*	*Patient 1 6 weeks*	*Patient 2 1 week*	*Patient 2 6 weeks*
Mesh cells (x 10^3)	1055	1099	1098	1098
Delta t (x 10^{-3})	15	18	22	16
PA (mL/min)	511	774	268	576
Q DA (mL/min)	-233	-262	-65	-101
Q V (mL/min)	744	1063	333	668
Re PA	728	1010	843	1239

Characteristics of the CFD simulations. Abbreviations: Q, blood volumetric flow; PA, proximal artery; DA, distal artery; V, vein; Re, Reynolds number. Note: delta t, blood flows and Reynolds numbers are expressed as time-average values over the pulse cycle. Negative values indicate retrograde flow.

D. Analysis structural and hemodynamic changes over time

To characterize the structural changes between 1-week and 6-week AVF models, we applied a rigid co-registration of the two AVF models using the iterative closest point (ICP) registration algorithm [11] available in VMTK suite [6]. Vascular lumen cross-sections of proximal artery and vein were obtained along the vessel centerline at 0.5 mm intervals and cross-sectional areas were calculated.

We characterized the AVF blood flow phenotype using localized normalized helicity (LNH), descriptor of changes in the direction of the rotation of flow (Eq. 1).

$$LNH = \frac{(\nabla \times \vec{v}) \cdot \vec{v}}{|\nabla \times \vec{v}| \cdot |\vec{v}|} \qquad (1)$$

Post-processing of CFD results was performed using the data analysis and visualization program Paraview [12].

III. RESULTS

Contrast-free CUBE T1 yielded high-resolution images, suitable for reliable segmentation of the vascular lumen and the generation of patient-specific AVF 3D models. Figure 2 shows local changes in vessel cross-sectional areas from 1-week to 6-week after surgery. In both patients, luminal cross-sectional areas showed an overall increase along the investigated length both for the proximal artery and for the vein. We found a homogeneous dilatation in the proximal artery of both patients, with a moderate dilatation in Patient 1 and a more significant increase of arterial lumen in Patient 2. In the venous segment of both patients we observed a dilatation in most of the investigated vessel length, with a more pronounced increase in the venous outflow segment as compared to the JAV.

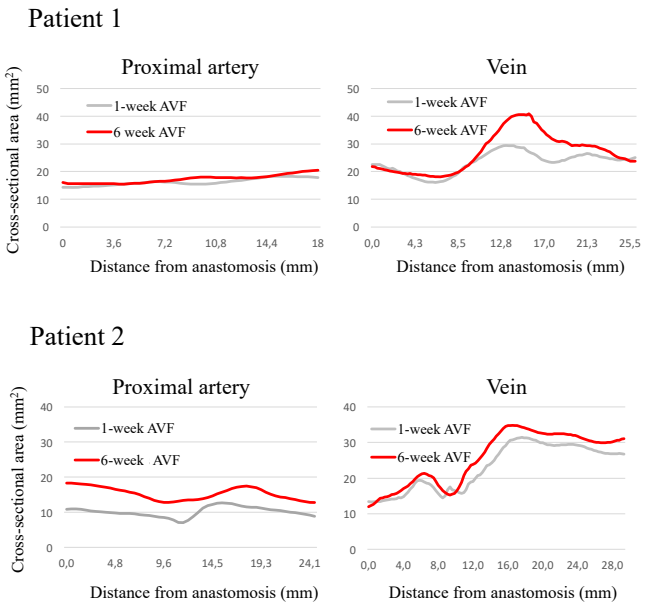

Fig. 2: Representation of venous and arterial cross-sectional area changes over time.

Figure 3 shows LNH isosurfaces at 1 week and 6 weeks after surgery. One week after surgery, the volume of the vein segment is distributed in approximately equal shares among clockwise (red) and counter-clockwise (blue) structures. On the contrary, 6 weeks after surgery one direction of the rotation of flow becomes predominant. In Patient 1 blue helical structures occupy 10% of the volume of the vein as compared to the red ones that occupy only the 3% of the segment. In Patient 2 blue structures are predominant as well, with a volume occupation of 12% as compared to 3% of the red colored ones. The regularization of the hemodynamics over time suggests that structural modifications in the AVF accommodate the flow to a helical pattern.

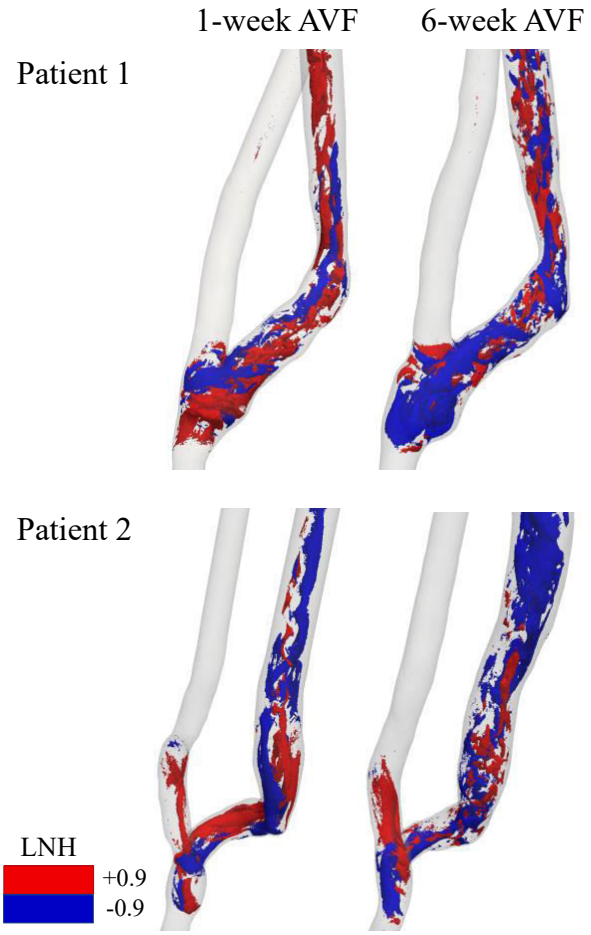

Fig. 3: LNH isosurfaces representative of the peak-systolic timepoint. Threshold values of LNH (±0.9) are used for the identification of clockwise and counter-clockwise rotation of the helical structures

IV. Discussion

Our MRI investigation provided high-resolution images that allowed detailed reconstruction of the vessel lumen surface and the characterization of the structural and hemodynamic changes that occurred within 6-week after AVF surgery. Even if preliminary, our results suggest that vascular remodelling accommodate the flow to a more stable and helical pattern during AVF maturation. We have to acknowledge that CFD simulations did not account for the effect of the vessel wall compliance. This issue could be addressed in future studies by conducting fluid-structure interaction (FSI) analysis, although its higher computational cost renders its use still challenging. We also have to mention that this investigation includes only one patient. However, as the patient selected in this study represents a fairly typical radio-cephalic AVF, we do believe that we showed a robust pipeline that can be used for future prospective clinical studies on the role of hemodynamics in AVF failure.

V. Conclusion

Our promising approach allows the detailed study of blood flow field in AVF at the patient-specific level and may help to elucidate the role of hemodynamic conditions on vascular remodelling and stenosis formation, with the final aim of improving AVF clinical outcome, both in terms of complications immediately after surgery and in terms of long-term patency. This achievement, besides entailing a significant reduction in medical costs, may significantly improve the patients' quality of life.

Acknowledgment

We acknowledge Dr. Valentina Portalupi and Dr. Carmela Condemi for their precious help in patient management and MRI planning. We also thank Luca Soliveri for assisting with US velocity curve digitalization.

References

[1] T. Lee, S. Misra. "New Insights into Dialysis Vascular Access: Molecular Targets in Arteriovenous Fistula and Arteriovenous Graft Failure and Their Potential to Improve Vascular Access Outcomes". *Clin J Am Soc Nephrol*, 2016. 11:1504–12.

[2] P. Roy-Chaudhury, Y. Wang, M. Krishnamoorthy, J. Zhang, R. Banerjee, R. Munda, et al. "Cellular phenotypes in human stenotic lesions from haemodialysis vascular access". *Nephrol Dial Transplant*, 2009. 24:2786–91.

[3] A. Remuzzi, B. Ene-Iordache. "Novel paradigms for dialysis vascular access: upstream hemodynamics and vascular remodeling in dialysis access stenosis". Clin J Am Soc Nephr. 2013; 8(12):2186-93.

[4] S. Haneder, W. Kucharczyk, S.O. Schoenberg, H.J. Michaely. "Safety of magnetic resonance contrast media: a review with special focus on nephrogenic systemic fibrosis". *Top Magn Reson Imaging,* 2015; 24:57–65.

[5] J.P. Mugler. Optimized three-dimensional fast-spin-echo MRI. *J Magn Reson Imaging*, 2014;39:745–67.

[6] L. Antiga, M. Piccinelli, L. Botti, B. Ene-Iordache, A. Remuzzi, D.A. Steinman. "An image-based modeling framework for patient-specific computational hemodynamics". *Med Biol Eng Comput,* 2008; 46:1097–112.

[7] J.A. Sethian. "Level set methods and marching cubes methods: evolving interfaces in computational geometry, fluid mechanics, computer vision and materials science". Camb Camb Univ Press 1999, Vol. 3.

[8] W.E. Lorensen and H. E. Cline. "Marching cubes: a high resolution 3D surface construction algorithm". Comput Graph, 1987; 21:163–169.

[9] OpenFoam T. The OpenFOAM Foundation. ⟨http://www.openfoam.org⟩ 2014.

[10] A. Remuzzi, B. Ene-Iordache, L. Mosconi, S. Bruno, A. Anghileri, L. Antiga, et al. "Radial artery wall shear stress evaluation in patients with arteriovenous fistula for hemodialysis access". *Biorheology*, 2003; 40:423–30.

[11] Z. Zhang. "Iterative Point Matching for Registration of Free-Form Curves and Surfaces". *Int J Comput Vis,* 1993. 13:2, 119-152

[12] http://www.paraview.org

An *in vitro* system for the mechano-electrical characterization of excitable cells

I. Pulsoni[1], G. Carlini[1], P. Farisello[1] and R. Raiteri[1,2]

[1] *University of Genova, Dept. of Informatics, Bioengineering, Robotics and System Engineering, Via Opera Pia 13, 16145, Genova, Italy*

[2] *CNR - Institute of Biophysics, Via De Marini, 6, 16149, Genova, Italy*

***Abstract*-The aim of this study is to investigate the behavior of excitable cells and their mechano-electrical response to mechanical stimuli induced by an atomic force microscope (AFM) probe.**

To achieve this goal, an integrated system composed by an AFM, an optical microscope, a MicroElectrode Array (MEA), and a custom circuitry has been developed. This circuitry allows optical microscopy, electrical recording and *in situ* mechanical stimulation of the cells by AFM.

Here we focus our attention on murine neurons which are patterned over the MEA, thus allowing also the investigation of the connectivity emerging from neuronal networks with imposed topologies.

***Keywords*—mechanical stimulation, electrical response, cell pattern.**

I. Introduction

An increased attention has been given recently to the role of biomechanical forces in neural development, as these have been shown to influence a variety of functions, ranging from gene expression to structural modification at both the micro- and macro-scale. Both micro- and nano-technology have been employed in order to understand the effects that these forces might have on both brain development as well as its disorders [1]. Even so, due to a lack of appropriate methods to investigate the microstructural elements of the brain, the investigation on the precise roles these forces play has produced limited results so far.

A growing number of recent studies have been focusing on neuronal development and homeostasis, attempting to understand the interaction of biomechanical forces that allow neurons to respond to mechanical stimulation [2]. It has been observed that these forces influence neurotransmitter release [3] and neuronal gene expression [4], as well as connectivity [5] and neurite outgrowth [6], which emphasize the importance of a study of the mechanisms involved in these changes at the single cell level.

The role of mechanical forces on the human brain is subtly evident by observing the response of the brain to the effects of these environmental forces at the microscale level, wherein they contribute to the regulation of various aspects of neuronal functions. An example of these would be the hemodynamic forces generated by each heartbeat that are capable of displacing neuronal tissue by several micrometers [7]. On an even smaller scale, the changes of the plasma membrane at the nanoscale heavily influence both the intercellular and intracellular environment, affecting processes such as ion channel exchanges [8], neurotransmitter release [9], and vesicle clustering [10]. The science of neuro-mechanobiology represents an integration of neuroscientific discoveries with mechanobiology techniques and can improve our understanding of the interactions between mechanical forces and signal transduction pathways that regulate the growth of neuronal tissue. Studies in neuro-mechanobiology can also provide greater insights into the primary consequences associated with neuronal viscoelasticity changes in traumatic brain injuries, such as concussive ones [2].

II. Materials and Methods

A. Setup description

Figure 1 shows a schematic representation of the acquisition and stimulation system, starting from the electronic board, consisting of precision JFET amplifiers AD8643 that were chosen to optimize the dimensions in the amplification stage. The MEA device is connected by spring contacts that match the MEA pads structure and is placed on an aluminum heating plate that keeps the cells cultured on the microelectrodes at 37°C (fig. 2).

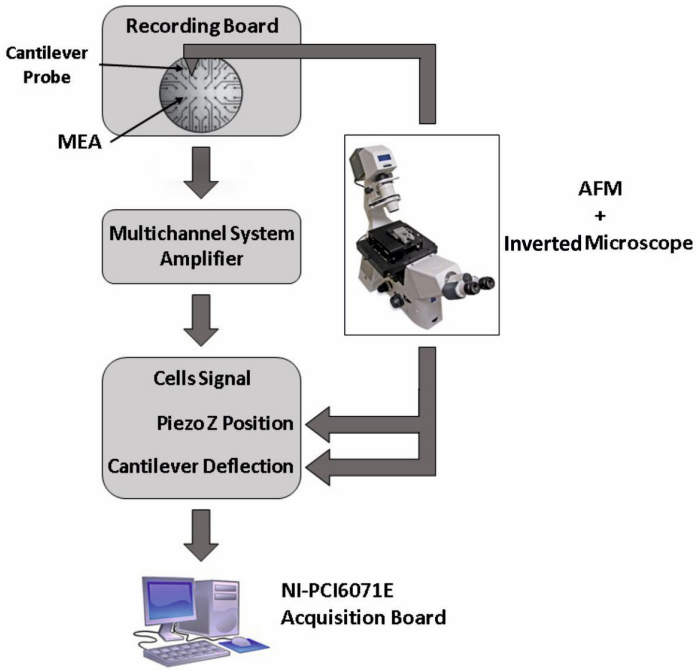

Fig1: The schematic of the acquisition and stimulation system.

Three flat cables were employed to carry the electrode amplified signals: they were chosen to minimize the cable weight burden and the transmission of mechanical noise, since they connect with the sample stage which is magnetically attached to a commercial AFM head, equipped with a closed-loop scanner (Keysight Technologies, model 5500ILM, 9μm vertical working range). The signals probed by the interface board require additional amplification and filtering in order to

be digitalized with high enough signal-to-noise ratio. In order to achieve this goal, an array of differential amplifiers was employed; in particular, we used a custom Multichannel System 64 channel system, with a band pass of 10-3000 Hz and a gain of 1000 V/V. The abovementioned flat cables are then connected through the use of zif connectors to another electronic board that is a bypass board between the interface board and the Multichannel filter amplifier. This board is also responsible for adjusting the channels' disposition so that it may fit the commercial Multichannel Systems SCSI connector. The AFM signals consist of the vertical (Z-axis) piezo position and the cantilever deflection. The former is read from the vertical displacement sensor integrated in the AFM scanner which is notch filtered, to eliminate 50 Hz noise, and amplified with a 50 V/V gain. The cantilever deflection signal is directly acquired from the AFM breakout box and does not need further conditioning. Both MEA and AFM signals are then connected to a bypass board to match the pinout of the acquisition board (model NI-PCI6071E, National Instruments).

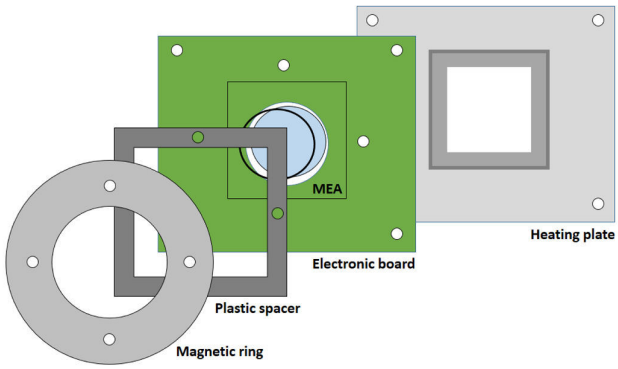

Fig2: The schematic of the integrated system consisting of: a magnetic ring that allows the board to be magnetically attached to the AFM stage; a plastic spacer to separate the ring and the upper part of the spring contacts; the electronic board and the MEA chip; the aluminum plate to provide heat transfer to the MEA chip, and to house heating elements and temperature sensor (the aluminum plate contains a central hole to allow MEA visualization in an inverted light microscope).

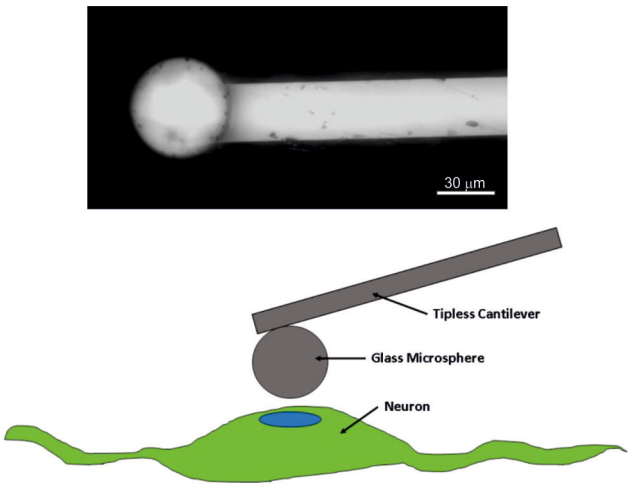

Fig3: On the top, an optical image of the AFM HQ:CSC38/Tipless/CR-AU microcantilever and the 40µm diameter glass microsphere attached on the end of it; on the bottom, the schematic of the interface between this particular probe and a cell.

In order to use a recording probe that is dimensionally similar to the excitable cells, a glass microsphere measuring 40µm in diameter was attached to a tipless cantilever (HQ:CSC38/Tipless/CR-AU) to function as the mechanical stimulation probe, as shown in figure 3.

B. Neural network preparation

To obtain a stable spontaneous neuronal network activity, MEAs were sterilized and treated with adhesion molecules (laminin and poly-D-lysine, both from Sigma Aldrich) to favor the cell adhesion and growth. Murine tissue was obtained through the removal of 18-day embryos (E18) by caesarean section. The experimental protocol was approved by the European Animal Care Legislation (2010/63/EU), by the Italian Ministry of Health in accordance with the D.L. 116/1992 and by the guidelines of the University of Genova (Prot. N. 24982, October 2013).

Cell culture: hippocampus and cortex were removed from murine embryos and their tissue were at first enzymatically dissociated in 0.125% of Trypsin/Hank's solution containing 0.05% DNAse (Sigma Aldtrich) for 18-20 min at 37°C and then mechanically dissociated with a fire-polished Pasteur pipette. Cells were plated on the MEA chips at a density of about 1000 cells/mm^2 in a solution containing Neurobasal™ Medium with 1% Glutamax, 2% B-27 supplemented, 1% penicillin–streptomycin (all from Invitrogen Life Technologies). MEAs were then incubated in a humidified 5% CO2 atmosphere at 37 °C and half-volume medium was replaced every week. Measurements of electrical activity were performed after 21 Days In Vitro (DIV).

C. Cell patterning

A technique utilized for the implementation of this study is the combined use of bio-patterning technologies to spatially control neuronal network growth and microelectrode arrays in order to realize a long-term, non-invasive neuro-electronic interface. As shown by a recent study [11], the network activity of an organized cellular culture and its overall development are not significantly altered when compared to random control cultures. It has been shown that an imposed grid topology that matches the position of the electrodes can reinforce the connectivity in the directions of interest. For these reasons, an ulterior aim of this project is to realize a strong and reproducible cell patterning protocol on MEAs.

To achieve this goal, we employed two strategies: the first one is based on micro-contact printing technique, which consists in transferring a pattern of adhesion molecules onto the MEA substrate through PDMS stamps, made with the Replica Molding technique obtained through the use of an SU-8 master on a silicon wafer as mold. In particular, the adhesion molecules pattern consists of stripes that are 40µm wide 1,2mm long and spaced 200µm (fig. 4 and fig. 6), and it matches with the 60MEA100/10iR-Ti electrodes layout.

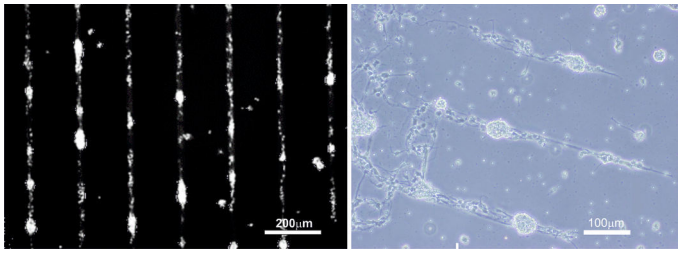

Fig4: Different neuronal patterns on glass. A fluorescence image (on the left) of phalloidin-labeled hippocampal neurons at 7 DIV, and a phase contrast image (on the right) of cortical neurons at 14 DIV.

The second approach is based on the use of PDMS masks to confine cell seeding and growth to better discriminate the effects of the mechanical stimulation. We used two different geometries for the masks, the first one (fig. 5, A and C) consisting of two compartments interconnected by microchannels (300µm x 10µm, spaced 50µm), and the second one (fig. 5, B and D) consisting of one compartment (900µm x 500µm). No significant differences were evidenced in terms of cell morphology or viability between the two geometries.

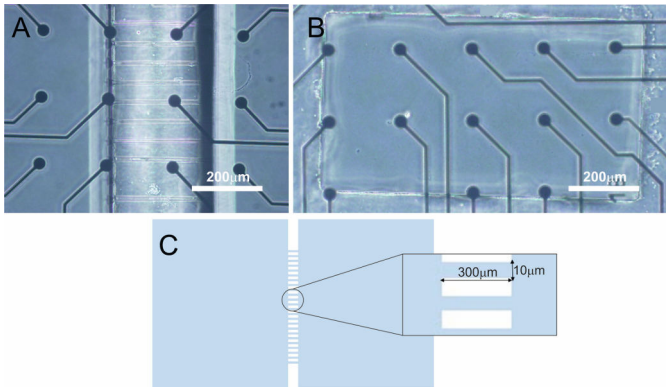

Fig5: A) PDMS mask consisting of two compartments and the microchannels upon the MEA surface; B) PDMS mask consisting of one compartment upon MEA surface; C) Schematization of the two compartments geometry.

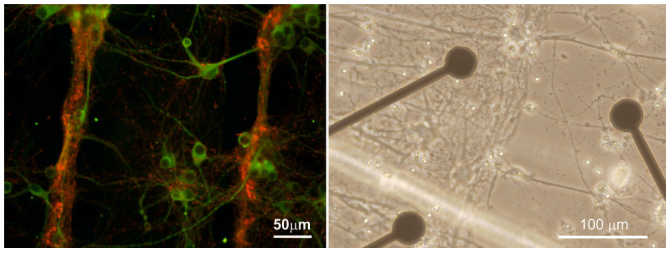

Fig6: On the left, a fluorescence image of immune-labeled neurons for the MAP-2 dendritic protein (in green) and for the synapsin protein (in red), patterned on glass using micro-contact printing technique at 18 DIV; on the right, neuronal pattern on MEA obtained using the PDMS mask with the two compartments and the microchannels, and it is possible to distinguish lines of axons grown inside the microchannels, 21 DIV.

III. RESULTS

The electrophysiological recording obtained with the custom board was compared to the one obtained with a commercial system (Multi Channel System, model MEA2100-60-System), in order to verify whether the signal-to-noise ratio of the custom system resulted in consistent neuronal network activity.

We recorded the electrical activity of the culture using the custom board with a custom-made MEA signal probing software, and we recorded the cell activity with the system provided by MEA2100-60-System, using the commercial MC_Rack software. All the data analyses were performed using SPYCODE [12]. By comparing the mean signal-to-noise ratio values (SNR) obtained in each recording channel of the custom board to those obtained by the Multi Channel System (MCS), it was observed that the SNR is reduced by 32% in the custom board.

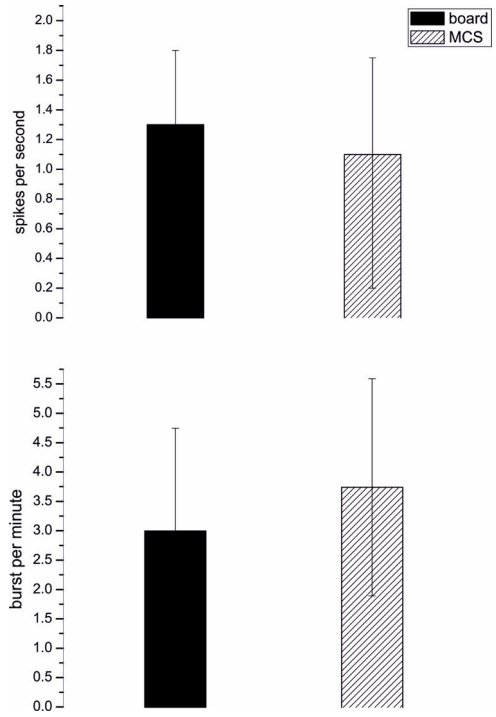

Fig7: Comparison of mean firing rate or MFR (mean spikes per second, on the top), and mean bursting rate or MBR (mean burst per minute, on the bottom) values, measured using the custom board and the MEA2100-60. The similarity of the values is evident, which proves the reliability of the board as a recording system.

Consequently, an appropriate noise thresholding procedure could be used to improve the accuracy of the spike detection algorithm. Figure 7 shows the mean firing and bursting rate values recorded using both the custom-made and the commercial system; the differences between these two were negligible.

This system was validated for the electrical recordings of the spontaneous activity of neurons, and presently data are being collected to evaluate the effects of the mechanical stimulation on the firing rate of cells.

REFERENCES

[1] Andy Tay, Felix E. Schweizer and Dino Di Carlo, Micro- and nano-technologies to probe the mechano-biology of the brain, Lab Chip 16, 1962-1977 (2016).

[2] William J. Tyler, The mechanobiology of brain function, NATURE REVIEWS NEUROSCIENCE 13, 867-878 (2012).

[3] Scott Siechen, Shengyuan Yang, Akira Chiba and Taher Saif, Mechanical tension contributes to clustering of neurotransmitter vesicles at presynaptic terminals, Proc. Natl. Acad. Sci. USA 106, 12611-12616 (2009).

[4] E. Brouzés and E. Farge, Interplay of mechanical deformation and patterned gene expression in developing embryos, Curr. Opin. Genet. Dev. 14, 367-374 (2004).

[5] Sarit Anava, Alon Greenbaum, Eshel Ben Jacob, Yael Hanein and Amir Ayali, The regulative role of neurite mechanical tension in network development, Biophys. J. 96, 1661-1670 (2009).

[6] Phillip Lamoureux, Gordon Ruthel, Robert E. Buxbaum and Steven R. Heidemann, Mechanical tension can specify axonal fate in hippocampal neurons, J. Cell Biol. 159, 499-508 (2002).

[7] John C. Kucewicz, Barbrina Dunmire, Daniel F. Leotta, Heracles Panagiotides, Marla Paun and Kirk W. Beach, Functional tissue pulsatility imaging of the brain during visual stimulation, Ultrasound Med. Biol. 33, 681-690 (2007).

[8] Arnadottir, J. & Chalfie, M., Eukaryotic mechanosensitive channels, Annu. Rev. Biophys. 39, 111-137 (2010).

[9] Chen, B. M. & Grinnell, A. D., Integrins and modulation of transmitter release from motor nerve terminals by stretch, Science 269, 1578-1580 (1995).

[10] Scott Siechen, Shengyuan Yang, Akira Chiba and Taher Saif, Mechanical tension contributes to clustering of neurotransmitter vesicles at presynaptic terminals, Proc. Natl Acad. Sci. USA 106, 12611-12616 (2009).

[11] Emanuele Marconi, Thierry Nieus, Alessandro Maccione, Pierluigi Valente, Alessandro Simi, Mirko Messa, Silvia Dante, Pietro Baldelli, Luca Berdondini and Fabio Benfenati, Emergent Functional Properties of Neuronal Networks with Controlled Topology, Plos One 7 (2012).

[12] Luca Leonardo Bologna, Valentina Pasquale, Matteo Garofalo, Mauro Gandolfo, Pieter Laurens Baljon, Alessandro Maccione, Sergio Martinoia and Michela Chiappalone, Investigating neuronal activity by SPYCODE multi-channel data analyzer, Neural Networks 23, 685-697 (2010).

MRI T_2 mapping of knee cartilage status and multi-body simulation of joint loads in anterior cruciate ligament reconstruction

G. Cassiolas[1], M. Bontempi[1], N. Lopomo[1,2], G. Marchiori[1], M. Berni[1], G. Valente[1], C. Signorelli[1], L. Bragonzoni[3], S. Zaffagnini[1]

[1] *Istituto Ortopedico Rizzoli, Bologna, Italy; giorgio.cassiolas@ior.it*

[2] *Università degli Studi di Brescia, Brescia, Italy; @ior.it*

[3] *Università degli Studi di Bologna, Bologna, Italy; @ior.it*

***Abstract* — Rupture of anterior cruciate ligament (ACL) is a common injury, widely treated by reconstruction surgery. To clarify which factors can compromise the long-term success of this procedure, the aim of the study was to investigate ACL transtibial reconstruction effects on overall knee biomechanics and articular cartilage, by integrating dynamic radio-stereophotogrammetry, inferior limb multi-body modelling and MRI T_2 mapping, thus to correlate knee joint loads to its physiopathological status.**

***Keywords*— Multi-body modelling, dynamic RSA, ACL reconstruction, MRI T2 mapping, joint cartilage.**

I. Introduction

A clear correlation between alterations of joint biomechanics and physiopathological status of the articular tissues has long being described in literature [1-3]. Such alterations are due primary to pathologic or traumatic events and secondary to their sub-optimal treatments. This is specifically important for the anterior cruciate ligament (ACL), one of the main ligaments of the knee, which is commonly involved in serious knee injuries and whose lesion can negatively affect daily life of people, with joint pain and instability. There are many ways to treat the ACL rupture but, due to the unsatisfactory outcomes of conservative treatments, reconstruction surgery remains the preferred approach, above all in young patients who want to maintain an active life style [4]. Nevertheless, the optimal surgical technique is a still highly demanding clinical issue in orthopaedic research [5]. In general, this procedure requires the substitution of the torn native ligament by a biological graft or the augmentation of its function by synthetic graft [6]. Ideally the final goal is to restore the original knee stability and functionality, preserving the articular tissues from non-physiological stresses. Instead, mainly due to not expected rearrangements of loads acting inside the joint, the physiological conditions of articular tissues like cartilage are modified after treatment, increasing the risk of developing degenerative pathologies. In this perspective, many radiographic studies document that early osteoarthritis (OA) after ACL-reconstruction occurs between 10% and 90% of the cases [7]. Therefore, in order to improve and optimize the reconstructive surgical procedure, it appears fundamental to know and control the effect of the knee loading on the articular tissues after ACL reconstruction. Accordingly, the aim of this study was to investigate if the evolution of the knee cartilage physiopathological condition can be related to the joint biomechanics induced by the ACL reconstruction. Thus, a specific clinical trial was developed, involving ACL-reconstructed patients which underwent innovative gait analysis and magnetic resonance imaging of the knee.

II. Materials and Methods

Forty-two patients (age = 25.7 ± 8.3 years), with ACL rupture underwent reconstruction by transtibial technique. For each patient, pre- (baseline) and 18 months post-surgery (FU 18) magnetic resonance (MR) images were acquired via 1.5 T apparatus and gait analyses performed by dynamic radiostereophotogrammetric analysis (RSA). MR images were exploited both to observe the cartilage status and as base for the virtual reconstruction of femoral and tibial models at the knee level.

Specifically to the cartilage assessment, a SAG T_2 sequence was adopted due to the strict relation between T_2 relaxation time and cartilage status: in the earliest stages of OA, the cartilage matrix begins to break down, becoming more permeable to water and causing an elevation of the T_2 value [8]. SAG T_2 sequences, resulting from both baseline and follow-up acquisitions, were imported into the open-source DICOM viewer software (OsiriX, Pixmeo Sarl, Bernex, Switzerland), firstly to obtain their specific range of repetition (RT) and echo (TE) time, secondly to define the cartilage regions of interest. Each sequence was divided on a slice-by-slice basis and by anatomical markers, specifically by the menisci of the knee [9]. The mid-sagittal slice through the centre of each condyle, composed by eight differents echo images, was selected for the T_2 evaluation [10]. MR images were then processed using a dedicated software (MRI Processor Toolbox, ImageJ, Bethesda, MD). According to literature [11], the investigation focused on articular cartilage regions able to significantly highlight the arise of early OA, namely posterior lateral tibial (LT), central medial tibial (LT) and central medial femoral condyle (MFC). The contours of each ROI were manually outlined on the mask obtained by overlaying the starting slice to the corresponding region in each T_2 mapping image [10].

T_2 values of more than 200 msec were considered outliers and automatically excluded from the analysis because more

than double of the highest expected mean T_2 values of healthy cartilage [12], [13]. Finally, patients were clustered by k-means algorithm in "better/stable" (when the T_2 signal in post-surgery is lower or comparable to the one before ACL reconstruction in all the investigated regions) and "degenerated" (T_2 signal increases) groups.

Specifically to the virtual reconstruction of the bones, an MRI SAG PD Cube sequence was used and the scans were imported into an open-source software (3DSlicer) for model generation: segmentations of femur, tibia and fibula were carried out in order to obtain STL surfaces to be used as building blocks for subject-specific virtual reconstruction of the inferior limb; since a MRI of the foot was not available, a generic STL model (scaled according to patients' anthropometry) was taken to include the foot segment. The dynamic skeletal model was built by means of a dedicated software (nmsBuilder [14]) with the following features: the inertial properties for the body segments were adapted accordingly to patients' anthropometry from a 10 segments, 23 degrees-of-freedom (dof) model developed by Anderson and Pandy [15]; the ankle joint was modelled as a 1 dof hinge joint (only the flexion-extension movement was permitted)[15]; the knee joint was modelled as a free joint (6 dof) in order to appreciate all forces and torques. The open-source software of biomechanics simulation OpenSim [16] was exploited to carry out inverse kinematics and dynamics analyses. The kinematic data for the simulations derived from a dynamic radio-stereophotogrammetric analysis (RSA) based on the bone models, optimized in radiological dose and performed with a data-rate of 8 Hz [17]. Since the field of vision was focused around the knee joint, no kinematic data for the foot were available: in order to consider ankle movement, data from literature [18] were inserted in the simulations. The ground reactions forces – necessary for the dynamic analysis – were acquired at 400 Hz and derived from a force platform (BTS), registered with the RSA acquisition volume.

For each patient, changes in the knee rotations and moments between pre- and post-surgery were evaluated and consequently inserted in the relative "better/stable" or "degenerated" group, thus to correlate joint mechanics and cartilage status.

III. Results and Discussion

The analysis of SAG T_2 sequence allowed to evaluate the variation in the cartilage status between pre- and post-surgery. T_2 values mapped in the analyzed ROIs were coherent with the literature [10], [19]. On average, the cartilage medial compartment showed an increase in T_2 relaxation time from baseline to FU 18; an opposite trend was instead highlighted by the lateral one. However, no statistical differences were founded in any ROI between pre and post-surgery T_2 values. Concerning clustering results (Fig. 1), the medial compartment of the "better/stable" group showed a slight increase in T_2 relaxation time after ACL reconstruction, while the lateral one even a decrease. For the "degenerated" group instead, the increase of T_2 value between baseline and FU 18 was common to all the compartments and strongly more relevant than the "better/stable" condition (Fig. 1).

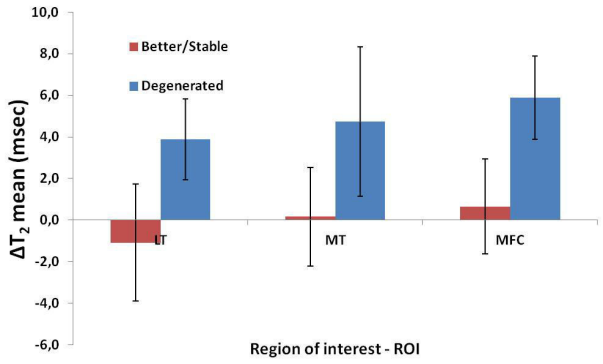

Fig.1. T_2 relaxation time variations between pre- and 18 months post-surgery in "better/stable" and "degenerated" groups.

Multi-body modelling of the lower limb allowed to estimate knee rotation angles and torques, which were coherent with the results of literature [20]–[23]. Preliminary outputs about the dynamic analysis highlighted an increase, after ACL reconstruction, both for peak and impulse for the internal abduction moment (normalized to patient's mass and height) during the stance phase, both for a "degenerated" subject (Fig.2) and a "better/stable" (Fig.3) subject. The peak augmentation from baseline to follow-up resulted higher for the "better" subject rather than the "degenerated" one, but, if absolute values were considered, peak magnitude was higher for the degenerated patient (Table I). Furthermore, the onset of the moment occurred sooner in both cases respect to their baseline.

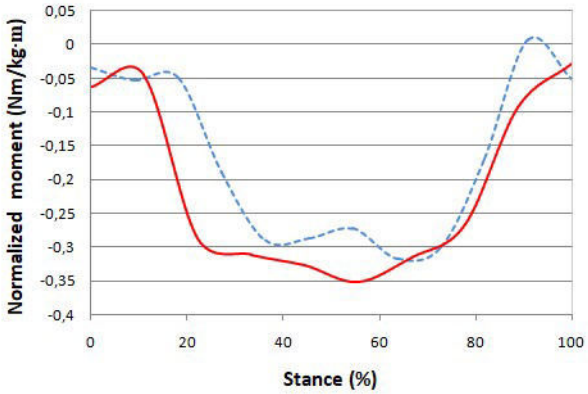

Fig.2 knee moment for a patient clustered as "degenerate" before (dot curve) and after ACL reconstruction (solid curve).

The knee outcome of our analysis resulted very slightly influenced by the ankle kinematics, thus the choice of a medium ankle movement from literature was thought to be a good compromise in first instance.

Our work gives the possibility to explore the variation of moments between pre-surgery condition and post-rehabilitation status, giving an integration to the few available data in this field [24]. In fact, limited to our knowledge, the relationship between injured and post-reconstruction dynamic conditions and has not been profoundly investigated: several studies exploited as comparator for the evaluation of gait parameters healthy control groups [20], [25], [26], or the uninjured contralateral limb [25], [26]. The possibility to investigate different kinetic and kinematic aspects of the ACL reconstruction constitutes a

central issue, because, although big efforts have been made in the last years in order to understand a precise relationship between altered biomechanics and the development of knee OA, the findings remain controversial: as example, some studies hypotized that the cause of OA occurrence may be induced by an increase in knee moments [26]; others that may be related to lower moments [24], [25].

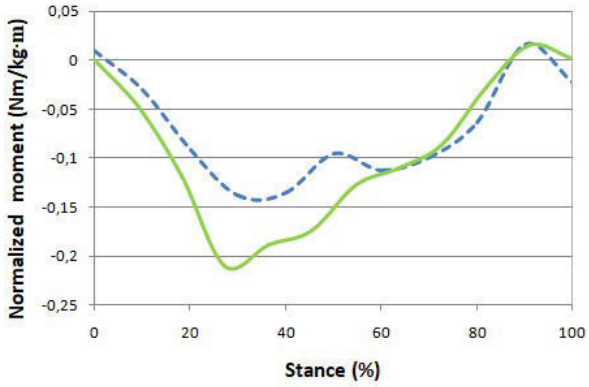

Fig.3. Internal abduction moment for a patient clustered as "better/stable" before (solid curve) and after ACL reconstruction (dot curve).

Potentially, thanks to its congruence with literature, our study was able to evaluate absolute knee moments, thereby to make a comparison between gait parameters of healthy control groups and other reconstructed groups of other studies. Furthermore, through the correlation with T2 mapping in absolute and relative terms, it could permit to provide some conclusions on knee moments and compare them with literature.

TABLE I
PRELIMINARY OUTCOMES

	Better/stable patient	*Degenerated patient*
Max baseline moment peak	-0.14	-0.32
Max FU 18 moment peak	-0.21	-0.35
Δ% Peak	33%	9%
Δ% Impulse	30%	4%
ΔT2map	8.17	1.58

Tab I. .Preliminary outcomes of the study. The differences are intended between the follow up condition and the pre-surgery condition.

IV. CONCLUSION

ACL reconstruction aims to restore the knee pre-injured biomechanics, but, since the patient generally undergoes diagnosis and laboratory evaluations only after the traumatic event, in most of the cases the subject-specific native condition is not precisely known. Evidence of altered biomechanics has been demonstrated for ACL injured and ACL reconstructed subjects [24], but to date no strong relationship has been demonstrated.

This work, thanks to the combination of bone based RSA, multi-body modeling and quantitative MRI in the injury state and 18 months after surgery, may provide a potentially useful instrument to lead non-invasive investigations on how the ACL reconstruction affects knee loads and cartilage physiopathological status, with the perspective to investigate the correlation between biomechanics and cartilage damages.

The innovative combination of T2 mapping and dynamic analysis can pose the basis for a "prognostic" approach and for guiding the treatment since, tuned on patient measures, target knee biomechanics can be predicted and guide both ACL reconstruction and rehabilitation to preserve articular tissues from early degeneration.

V. ACKNOWLEDGEMENTS

We thank the "Italian Ministry of Health" financier of the projects RF-2010-2312173 and GR-2011-02351803.

VI. REFERENCES

[1] T. Nishii, k. Kuroda, Y. Matsuola, T. Sahara, H. Yoshikawa, Change in Knee Cartilage T2 in Response to Mechanical Loading. J Magn Res Imag 2008, 28:175-180

[2] T. Nishii, T. Shiomi, H. Tanaka, Y. Yamazaki, K. Murase, N. Sugano, Loaded Cartilage T2 Mapping in Patients with Hip Dysplasia. Radiology 2010, 256 (3): 955-65.

[3] K. Amano, V. Pedoia, F. Su, R. B. Souza, X. Li, C. Benjamin, Persitent Biomechanical Alterations After ACL Reconstruction Are Associated With Early Cartilage Matrix Changes Detected by Quantitative MR. Orthop J Sports Med 2016, 4(4) : 232596711664421.

[4] CL. Ardern, NF. Taylor, JA. Feller, KE. Webster, Fifty-five per cent return to competitive sport following anterior cruciate ligament reconstruction surgery: an updated systematic review and meta-analysis including aspects of physical functioning and contextual factors. Br J Sports Med. 2014;48:1543–1552.

[5] Brophy, R.H., Pearle, A.D. Single-bundle anterior cruciate ligament reconstruction: a comparison of conventional, central, and horizontal single-bundle virtual graft positions. Am. J. Sports Med. 2009;37:1317–1323.

[6] Fu FH, Bennett CH, Ma CB, Menetrey J, Lattermann C. Current trends in anterior cruciate ligament reconstruction. Part II. Operative procedures and clinical correlations. Am J Sports Med. 2000; 28:124–130.

[7] B. Barenius, S. Ponzer, A. Shalabi, R. Bujak, L. Norlén, K. Eriksson. Increased Risk of Osteoarthritis After Anterior Cruciate Ligament Reconstruction A 14-Year Follow-up Study of a Randomized Controlled Tria. Am. J. S. Med. 2014, 42 (5), 1049-1057.

[8] S. Van Rossom, CR. Smith, L. Zevenbergen, DG. Thelen, B. Vanwanseele, D. Van Assche, I. Jonkers, Knee Cartilage Thickness, T1ρ and T2 Relaxation Time Are Related to Articular Cartilage Loading in Healthy Adults. PLoS ONE 2017, 12(1): e0170002.

[9] R. Gupta, W. Virayavanich, D. Kuo, F. Su, T. Link, B. Ma, X.Li. MR T1ϱ quantification of cartilage focal lesions in acutely injured knees: correlation with arthroscopic evaluation. Magnetic Resonance Imaging (2014), 32, 1290-1296.

[10] H. Nishioka, J. Hirose, E. Nakamura, N. Okamoto, T. Karasugi, T. Taniwaki, T. Okada, Y. Yamashita, H. Mizuta, Detecting ICRS grade 1 cartilage lesions in anterior cruciate ligament injury using T1ρ and T2 mapping. Eur J Radiol 2013, 82(9):1499-505.

[11] F. Su, JF. Hilton, L. Nardo, S. Wu, F. Liang, TM. Link, CB. Ma, X. Li. Cartilage morphology and T1ρ and T2 quantification in ACL-reconstructed knees: a 2-year follow-up. Osteoarthritis Cartilage. (2013) 21(8), 1058-1067.

[12] TC. Dunn, Y. Lu, H. Jin, MD. Ries, S. Majumdar. T2 relaxation time of cartilage at MR imaging: comparison with severity of knee osteoarthritis. Radiology, 2004, 232(2) : 592-598.

[13] M. F. Koff, K. K. Amrami, K. R. Kaufman. Clinical evaluation of T2 values of patellar cartilage in patients with osteoarthritis. Osteoarthritis and Cartilage (2007) 15, 198-204.
[14] Valente G, Pitto L, Testi D, Seth A, Delp SL, Stagni R, Viceconti M, Taddei F, Are Subject-Specific Musculoskeletal Models Robust to the Uncertainties in Parameter Identification? PLoS ONE 2014, 9(11):e112625.
[15] Anderson F.C., Pandy M.G.: A dynamic optimization solution for vertical jumping in three dimensions. Computer Methods in Biomechanics and Biomedical Engineering 2:201-231, 1999.
[16] Delp SL, Anderson FC, Arnold AS, Loan P, Habib A, John CT, Guendelman E, Thelen DG. OpenSim: Open-source Software to Create and Analyze Dynamic Simulations of Movement. IEEE Transactions on Biomedical Engineering. (2007).
[17] Bonanzinga T , Signorelli C , Bontempi M , Russo A , Zaffagnini S, et al. Evaluation of RSA set-up from a clinical biplane fluoroscopy system for 3D joint kinematic analysis. Joints 2016, 4(2), 121-125.
[18] G. Bovi, M. Rabuffetti, P. Mazzoleni, M. Ferrarin. A multiple-task gait analysis approach: Kinematic, kinetic and EMG reference data for healthy young and adult subjects. Gait & Posture 33 (2011) 6-13.
[19] X. Li, D. Kuo, A. Theologis, J. Carballido-Garmio, C. Stehling, TM. Link, C. Benhamin Ma, S. Majumdar, Cartilage in Anterior Cruciate Ligament–Reconstructed Knees: MR Imaging T1ρ and T2—Initial Experience with 1-year Follow-up. Radiology 2011, 258(2):505-514.
[20] M. Patterson, E. Delahunt, B. Caulfield, Peak knee adduction moment during gait in anterior cruciate ligament reconstructed females. Clinical biomechanics 2013 (Bristol, Avon).
[21] Butler RJ, Barrios JA, Royer T, Davis IS. Frontal-plane gait mechanics in people with medial knee osteoarthritis are different from those in people with lateral knee osteoarthritis, Physical Therapy 2011; 91(8): 1235-1243.
[22] Wang H, Fleischli JE, Hutchinson ID, Zheng N. Knee moment and shear force are correlated with femoral tunnel orientation after single-bundle anterior cruciate ligament reconstruction. Am J Sports Med. 2014 July; 42(10):2377-2385.
[23] Hall M et al. Does meniscal pathology alter gait knee biomechanics and strength post-ACL reconstruction? Knee Surg Sports Traumatol Arthrosc (2016) 24:1501-1509.
[24] Wellsandt E. et al. Decreased Knee Joint Loading Associated With Early Knee Osteoarthritis After Anterior Cruciate Ligament Injury. Am J Sports Med. 2016 January; 44(1): 143-151.
[25] Zabala ME, Favre J, Scanlan SF, Donahue J, Andriacchi TP. Three-dimensional knee moments of ACL reconstructed and control subjects during gait, stair ascent, and stair descent. J Biomech. 2013; 46:515–520.
[26] Hart HF et al. Knee kinematics and joint moments during gait following anterior cruciate ligament reconstruction: a systematic review and meta-analysis. Br J Sports Med 2016;50:597-612.

Left ventricle dysfunctions in post-ischemic cardiomyopathy: an integrated methodological approach based on 4D Flow CMR

S. Pozzi[1], F. Piatti[2], A. Camporeale[3], G. Di Giovine[4], S. Castelvecchio[3], L. Menicanti[3], A. Greiser[5], E. Votta[2], A. Redaelli[2], M. Lombardi[3]

1. *Department of Mathematics, Politecnico di Milano, Milan, Italy*
2. *Department of Electronics, Information and Bioengineering, Politecnico di Milano, Milan, Italy*
3. *Multimodality Cardiac Imaging, IRCCS Policlinico San Donato, Milan, Italy*
4. *Division of Cardiology, Azienda Ospedaliera-Universitaria "Maggiore della Carità", Novara, Italy*
5. *Siemens Healthcare GmbH, Erlangen, Germany*

***Abstract*— Post-ischemic dilated cardiomyopathy (DCM) is characterized by adverse LV remodeling, with impairment of systolic and diastolic function, which can be assessed through MRI. The purpose of this work was to integrate standard MRI measurements and 4D Flow analysis, to characterize *in vivo* flow patterns in terms of WSS and diastolic vortices. Preliminary results confirmed the potential of 4D Flow in describing LV impairments, aiming at elucidating the fluid-dynamic determinants of post-ischemic DCM.**

***Keywords*—Dilated cardiomyopathy, 4D Flow cardiac MRI, Ventricular fluid-dynamics.**

I. Background

Myocardial infarction (MI) represents one of the main causes of death in the world. The mechanism of MI often involves the complete occlusion of a coronary artery, caused by the formation of an atherosclerotic plaque [1]. If untreated, this can lead to the damaging of cell membranes and necrosis of the myocardial tissue, with the formation of scar tissue. Post-ischemic dilated cardiomyopathy (DCM) is a complex clinical condition that arises following an ischemic event. This pathology is characterized by adverse left ventricular (LV) remodeling, including chamber dilation, aneurysm formation and increased wall stresses, with impairment of LV systolic and diastolic function [2]. Morphological and functional changes in the ventricle affect not only the site of ischemia, but can damage the fraction of healthy myocardium, named remote myocardium.

Different features of DCM can be assessed through cardiac magnetic resonance (CMR) modalities. Standard analyses assess LV volume and function through CINE-CMR, and location and extension of the ischemic scar through late gadolinium enhancement (LGE) images. Recently, it was proposed to characterize *in vivo* intraventricular flow patterns through 4D Flow MRI sequences [3], a technique suitable to obtain a real time acquisition of three-directional velocity data in a volume of interest.

However, the information yielded by these modalities is typically not integrated in the clinical practice. The aim of this work was to integrate standard clinical measurements, coming from bidimensional imaging data (CINE and LGE MRI), with 4D Flow analysis to aid the potential for comprehensive understanding of DCM pathophysiology.

II. Methods

Study population included 19 patients (all males, age 66±10) with post-ischemic DCM and severe LV dysfunction (EF < 35%).

CMR studies (CINE, LGE and 4D Flow) were performed with a 1.5T Magnetom Aera scanner (Siemens, Erlangen, Germany). CINE images were acquired through retrospective ECG-gating during breath-hold at maximum expiration. 4D Flow images were acquired through prospective ECG-gating with free-breathing subjects and respiratory navigator. For every acquisition an appropriate value of VENC was set for each of the 3 encoding directions, and delta phase images were reconstructed.

Scar transmurality and wall kinetics scores were available from clinical data, derived from CINE and LGE sequences.

A. Image segmentation

Left ventricle geometry was outlined on CINE short axis images, during the whole cardiac cycle, using an in-house automatic algorithm. The procedure combined a thresholding operation [4] with a region-growing algorithm to define a three-dimensional region of interest (ROI). Misaligned CINE slices were semi-automatically repositioned along the ventricle axis.

Telediastolic (EDV) and telesystolic (ESV) volumes were computed from the ROI. Stroke volume (SV) and ejection fraction (EF) were computed as in Eq. (1) and (2), respectively.

$$SV = EDV - ESV \quad (1)$$

$$EF = \frac{SV}{EDV} \cdot 100 \quad (2)$$

B. 4D Flow imaging analysis

The three-dimensional mask of the LV was used to select velocity information from the 4D Flow volume, after operations of spatial registration and temporal synchronization between the CINE and 4D Flow datasets.

Three potentially relevant features of LV hemodynamics were quantified using custom in-house algorithms: transmitral blood flow, intraventricular vortical structures [5], and wall shear stress distribution on the endocardium.

For the computation of transmitral blood flow, the mitral

plane was created by selecting four reference points from long axis CINE images. The mitral orifice was selected manually or outlined automatically by the tool. The blood flow rate Q was computed as:

$$Q = A_P \cdot \sum_{i=1}^{n_{points}} vel_{norm}(i) \qquad (3)$$

where A_P was the area of each pixel, obtained as the lumen area A divided by the number of pixels n_{points}, and vel_{norm} were the velocity components normal to the mitral plane.

Diastolic vortices were extracted using the *lambda2* method [6]. The structure of the vortices was analysed qualitatively by visual inspection and quantitatively by computing two parameters (Fig. 1): the distance d_v reached by the vortex along the long axis of the ventricle, and the angle α formed between the vortex and the long axis.

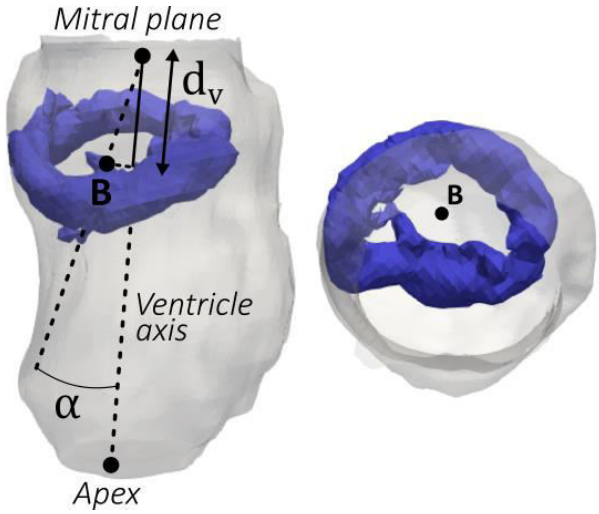

Fig. 1: Geometrical parameters computed for vortical structures.

Wall shear stress (WSS) was computed on the endocardium using a Newtonian model, under the assumption of a linear dependence between shear rate and shear stress [7]. A complete formulation for an incompressible fluid was used:

$$WSS = 2\mu\dot{\varepsilon} \cdot \overrightarrow{n_n} \qquad (4)$$

where μ was the blood dynamic viscosity (equal to 3 cP), $\overrightarrow{n_n}$ was the unit vector normal to the ventricle wall and $\dot{\varepsilon}$ was the strain tensor, obtained from the partial derivatives of the velocity, computed using three-dimensional Sobel filters.

III. Results

Values of ESV and EDV, normalized by body surface area (ESV/BSA = 106 ± 39 ml/m^2 and EDV/BSA = 147 ± 40 ml/m^2) were above the physiological ranges (25 ± 5,5 ml/m^2 and 76 ± 9 ml/m^2 respectively [8]). SV values (77 ± 15 ml were below the physiological range (100 ± 14 ml). EF values (29,3% ± 9,6) were compatible with the diagnosis of moderate to severe left ventricle disfunction [9].

Mitral flow rate curves showed non-physiological morphologies [9], caused by the presence of a single peak or by a higher A peak with respect to the E peak. These anomalies were reflected in the morphology of the diastolic vortices: the E vortex formed in 18 patients (94%), while the A vortex formed in only 5 (26%). The shape of the vortex was visually inspected in all subjects. In some patients the vortex formed a compact ring, while in others the ring created an open conformation or a jagged shape. On average the A vortex reached a lower distance along the axis of the ventricle with respect to the E vortex (6,6 % ± 5 and 13,9% ± 8 respectively), while the angles formed with the ventricle axis were comparable (7° ± 5 for the E vortex, 6° ± 2 for the A vortex). Fig. 2 shows the morphology of the diastolic vortices for two patients. The intraventricular flow of blood at the E peak is displayed through streamlines.

By comparing these results with data in healthy subjects [6], the discrepancies appear mainly regarding the A vortex, which in a healthy population appears in a much bigger percentage of subjects, and reaches a much higher distance along the axis of the ventricle.

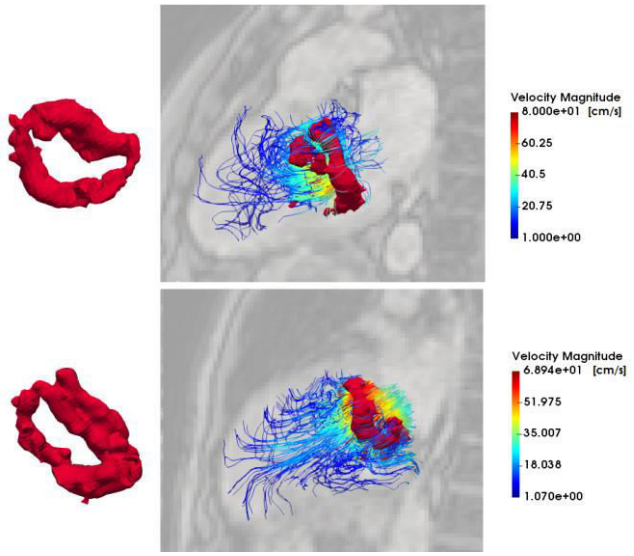

Fig. 2: Diastolic vortex at the instant of peak E wave, shown for two patients. Intraventricular flow is shown by velocity streamlines.

Regional analysis of WSS on the endocardium wall showed the presence of a gradient between the basal and apical regions: WSS was higher in basal segments (0,07 ± 0,02 Pa) with respect to medial (0,05 ± 0,01 Ps) and apical segments (0,04 ± 0,01 Pa). This result was compatible with the higher velocity flows acting on the basal region [10].

Statistical analysis of WSS values was performed on healthy and pathologic segments: the comparison was made between segments occupied by remote myocardium and by scar tissue, and between segments that show a normal and abnormal kinetics (hypokinetic, akinetic or dyskinetic). The results (Tables I and II) showed a statistically significative difference between remote myocardium and scar tissue, and between segments with normal and abnormal kinetics. On average WSS was lower on segments occupied by scar tissue with respect to remote myocardium (Fig. 3), and lower on abnormal kinetic segments with respect to normal kinetic segments.

TABLE I
MEAN AND SD VALUES OF WSS IN SEGMENTS OCCUPIED BY REMOTE MYOCARDIUM OR BY SCAR TISSUE.

WSS [Pa]	*Remote myocardium*	*Scar tissue*	*p-value*
WSS max	0.88 ± 0.22	0.61 ± 0.26	0.0080
WSS mean	0.06 ± 0.02	0.05 ± 0.02	0.0251

TABLE II
MEAN AND SD VALUES OF WSS IN SEGMENTS WITH NORMAL OR ABNORMAL KINETICS.

WSS [Pa]	*Normal kinetics*	*Abnormal kinetics*	*p-value*
WSS max	0.84 ± 0.28	0.56 ± 0.30	0.0096
WSS mean	0.06 ± 0.02	0.05 ± 0.03	0.0294

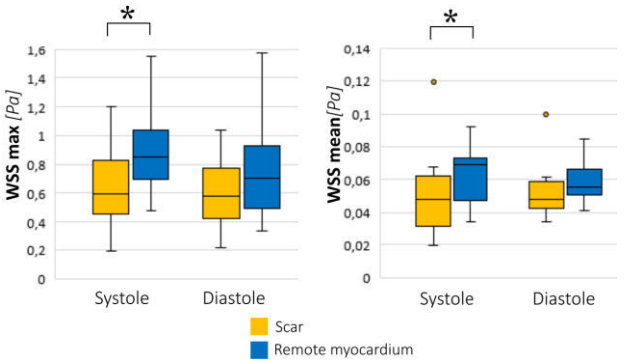

Fig. 3: Mean and maximum WSS values. * highlights a statistically significant difference between WSS in healthy (remote myocardium) and pathologic (scar) segments.

IV. CONCLUSIONS

To our knowledge, our work represents the first analysis of 4D Flow MRI data applied to a population affected by post-ischemic DCM, a pathology that causes several morphological and functional changes in the ventricle, which in turn influence the intraventricular fluid-dynamics. Through the analysis of novel features and integration with clinical parameters, preliminary results confirm the potential of 4D Flow CMR: DCM patients showed abnormal and heterogeneous vortical structures, and WSS was significantly altered in presence of scar tissue of dyskinetic segments. Ongoing studies aim at elucidating on the fluid-dynamic determinants of post-ischemic DCM.

REFERENCES

[1] F. Zannad, N. Agrinier, *Heart failure burden and therapy*. Europace, 11, 2009.

[2] M. A. Konstam, D. G. Kramer, "Left ventricular remodeling in heart failure: current concepts in clinical significance and assessment", *JACC Cardiovascular Imaging*, 4:98–108, 2011.

[3] R. J van der Geest, P. Garg, "Advanced analysis techniques for intra-cardiac flow evaluation from 4D Flow MRI", *Current Radiology Reports*, 4(7):1–10, 2016.

[4] N. Otsu, "A threshold selection method from gray-level histograms", *IEEE Transactions on Systems, Man, and Cybernetics*, 9(1):62–66, 1979.

[5] J. Jeong, F. Hussain, "On the identification of a vortex", *Journal of Fluid Mechanics*, 285:69–94, 1995.

[6] M. S. M. Elbaz, B. P. F. Lelieveldt, J. J. M. Westenberg, "Automatic extraction of the 3D left ventricular diastolic transmitral vortex ring from 3D whole-heart phase contrast MRI using Laplace-Beltrami signatures", *Statistical Atlases and Computational Models of the Heart. Imaging and Modelling Challenges*, 204–211, 2013.

[7] A. F. Stalder, M. F. Russe, A. Frydrychowicz, J. Bock, J. Hennig, and M. Markl, "Quantitative 2D and 3D phase contrast MRI: optimized analysis of blood flow and vessel wall parameters", *Magnetic Resonance in Medicine*, 60:1218–1231, 2008.

[8] N. Kawel-boehm, A. Maceira, E. R. Valsangiacomo-buechel, J. Vogelclaussen, E. B. Turkbey, et al., "Normal values for cardiovascular magnetic resonance in adults and children", *Journal of Cardiovascular Magnetic Resonance*, 17(29), 2015.

[9] S. F. Nagueh, C. P. Appleton, "Recommendations for the evaluation of left ventricular diastolic function by echocardiography", *Journal of the American Society of Echocardiography*, 2:107–133, 2009.

[10] M. S. Arefin, T. S. Morsi. "Fluid structure interaction (FSI) simulation of the left ventricle (LV) during the early filling wave (E-wave), diastasis and atrial contraction wave (A-wave)", *Australasian Physical & Engineering Sciences in Medicine*, 2014.

A non-local approach to model blood flow in small arterial vessels

G. Alotta[1], E. Bologna[2], and M. Zingales[1,2]
[1]Bio/NanoMechanics for Medical Sciences Laboratory, ATeN-Center, Università di Palermo, Palermo 90128, Italy.
[2]Department of Civil, Environmental, Aerospace, Materials Engineering,Università di Palermo, Palermo 90128, Italy.

***Abstract*— It is widely known that the rheological behaviour of blood is quite complex because of its multiphase nature. Among all existing rheological models, the Casson law is considered the most suitable for the blood behaviour. In this work an alternative approach, taking into account long-range interactions in the fluid particles, is proposed. It is shown that the proposed model is able to reproduce experimental velocity profiles of blood.**

***Keywords*—Blood flow, non-local forces, red blood cells.**

I. Introduction

THE rheological behaviour of blood is an important topic in biomechanics since the characteristic of blood flow inside vessels strongly affects stresses that are transmitted by the blood to the vessels; in biomechanics context, stresses on the vessels may be determinant for some arterial widespread diffused diseases such as aneurism or arterial stenosis. For these reasons, a deep knowledge of the real mechanical characteristics of blood and analytical models that are able to accurately predict the main features of blood flow inside human arteries are essential in order to better understand mechanism of appearance of aneurisms and consequence in blood supply downstream the aneurism or stenosis; moreover, an accurate description of blood flow may be useful in the future in order to set up medical protocols capable to predict whether an aneurism is going to break or not on the basis of medical images.

The well-known Hagen-Poiseuille law [1] is derived by assuming Newtonian fluid and provides parabolic profile of velocity across the diameter of a circular vessel; this model has proven to be reliable for large arterial vessels [1]-[2]. For capillary arterial vessels experimentally measured profiles of velocity are not parabolic [3], hence the Hagen-Poiseuille model fails to reproduce the real features of blood flow. Indeed for small capillary vessels the Casson model is used in place of Newton law; this law assumes a non-linear relationship between shear stress and shear strain rate that leads to non-linear governing equations and piecewise profile of velocity across the vessel diameter. The use of Casson law provides results that are in good agreement with experimental measurements, however the model is not constructed on a mechanical basis and mathematical manipulations are not straightforward because of the non-linearity.

For the above-mentioned reasons, in this paper an alternative mesoscale approach is proposed. The model is based on the Hagen-Poiseuille law enriched with non-local forces [4]-[5] aimed to represent the interactions between non-adjacent fluid elements that is due to the presence of relatively large cells, mainly Red Blood Cells (RBC), inside capillary vessels. These long range interactions are thought as volume viscous forces weighted by an attenuation function that scales the forces mutually exerted by two non-adjacent volume elements as the distance between them increases. As a results in the governing equation an integral representing this additional forces appears. However the governing equation remains linear and comparison with experimental measurements of velocity profiles across capillary vessels shows very good agreement, with lower root mean square error in comparison with Casson model. Finally, as the diameter of the vessel increases, non local term becomes negligible and the proposed model reverts to the classical Hagen-Poisueille model.

II. Recalls on classical models

In this section the Hagen-Poisueille model and the Casson model are recalled for the sake of clarity of the comparisons between these models and the proposed model. The Hagen Poiseuille model is recalled also because the proposed approach is a generalization of it.

The analysis is referred to the stationary laminar flow of blood inside a cylindrical vessels with radius R and length L (see Fig. 1); for this geometry, the problem can be studied as axialsymmetric. The hypothesis of stationarity is perfectly fulfilled in small arterial vessels since the pulsatile part of the blood flow does not reach vessels with such small dimensions (diameter in the order of tens of μm); the hypothesis of laminar flow, instead, is satisfactory for the simple geometry of the considered problem.

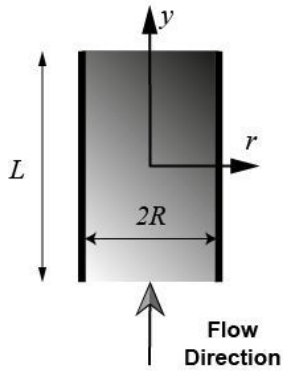

Fig. 1: Blood vessel model.

Under the above-mentioned assumptions the governing equation of the fluid flow is a very simple ordinary differential equation, that is

$$\frac{\Delta p}{L} = \frac{1}{r}\tau(r) + \frac{d\tau(r)}{dr} \tag{1}$$

where Δp is the pressure drop and $\tau(r)$ is the tangential stress between two adjacent fluid elements. Eq. (1) is

specialized depending on the assumed rheological behaviour, as will be shown in the next sections.

A. The Hagen-Poiseuille model

The Hagen-Poiseuill model assumes that the fluid is Newtonian, hence the shear stress $\tau(r)$ is linearly dependent on the shear strain rate $\dot{\gamma}(r)$:

$$\tau(r) = \mu \frac{dv(r)}{dr} = \mu \dot{\gamma}(r) \tag{2}$$

where μ is the dynamic viscosity and $v(r)$ is the velocity of the generic fluid element. Substitution of Eq. (2) into Eq. (1) leads to the following governing equation:

$$\frac{\Delta p}{L} = \mu \left(\frac{1}{r} \frac{dv(r)}{dr} + \frac{d^2 v(r)}{dr^2} \right) \tag{3}$$

The solution of Eq. (3) is straightforward and consists of a parabolic profile of velocity across the vessel diameter:

$$v(r) = \frac{r^2 - R^2}{4\mu} \frac{\Delta p}{L} \tag{4}$$

As already mentioned in the Introduction, this velocity profile is accurate for blood flow in large arterial vessels; this basically means that the presence of cells dispersed in the blood plasma is not determinant at this scale, indeed the largest of them, i.e. RBCs, have an average dimensions of 8 μm. For arterial vessels with smaller diameter, the presence of RBCs is no longer negligible in the macroscopic behaviour of blood and then its behaviour is no longer Newtonian.

B. The Casson model

For narrow arterial vessels at low shear rate the velocity profiles are no longer parabolic; moreover, researchers of the field have observed an increase in viscosity of blood at low rates of shear that is justified by the tendency of RBCs to aggregate into Rouleaux form [2]. This increase in viscosity is believed to be responsible for the flattened parabolic velocity profile rather than the pure parabolic velocity profile of a Newtonian fluid. Another cause of velocity profiles flattening may be the Fahraeus-Lindqvist effect [6], which implies that RBCs migrates towards the central axis of the vessels.

In order to capture the behaviour of blood in capillary vessels, the Casson model introduces the concept of yield stress in the rheological behaviour of blood that is believed to depend on fibrinogen concentration and on hematocrit [2]. As a consequence, the Casson rheological model is characterized by two parameters, the viscosity μ and the shear yield stress τ_0 [7]:

$$\tau(r)^{1/2} = \tau_0^{1/2} + \mu^{1/2} \left(\frac{dv(r)}{dr} \right)^{1/2} \tag{5}$$

By inserting Eq. (5) into equilibrium equation (1) the following nonlinear governing equation is obtained

$$\frac{\Delta p}{L} = \frac{1}{r} \left[\tau_0 + \mu \frac{dv(r)}{dr} + 2\sqrt{\tau_0 \mu} \left(\frac{dv(r)}{dr} \right)^{1/2} \right] + \\ + \frac{d^2 v(r)}{dr^2} \left[\mu + 2\sqrt{\tau_0 \mu} \left(\frac{dv(r)}{dr} \right)^{-1/2} \right] \tag{6}$$

The solution of Eq. (6) is a piecewise velocity profile across the diameter that can be written as

$$v(r) = \frac{R^2}{4\mu} \left\{ \frac{\Delta p}{L} \left[1 - \left(\frac{r}{R} \right)^2 \right] + \right. \\ \left. - \frac{8}{3} \left(\frac{2\tau_0}{R} \frac{\Delta p}{L} \right)^{1/2} \left(1 - \frac{r}{R} \right)^{3/2} + \frac{2\tau_0}{R} \left(1 - \frac{r}{R} \right) \right\} \qquad r > r_y \tag{7a}$$

$$v(r) = v(r_y) \qquad r \le r_y \tag{7b}$$

where

$$r_y = 2\tau_0 \frac{L}{\Delta p} \tag{8}$$

In the mechanics of the laminar stationary flow of a Casson fluid, the shear stress τ_0 is not reached in the region $r < r_y$, hence in this region the velocity is constant. Although the Casson model is satisfying in the reproduction of experimentally measured velocity profiles, it has the disadvantage to be nonlinear, hence mathematical manipulations are not straightforward except that for simple problems (see e.g. [2]); moreover the concept of shear yield stress, in the authors opinion, does not reflect the real mechanical reason that make flat the velocity profiles at the center of narrow vessels. For these reason, in the next section an alternative approach is proposed.

III. NON-LOCAL BLOOD FLOW MODEL

In this section the non-local blood flow model is introduced starting from simple observation regarding the mechanics of blood. In particular two main facts are taken into account:

- the blood is multiphase material, which contain a fluid part, the plasma, and many different solid parts, such as RBCs that are the larger and more influent cells;
- the blood is strongly heterogeneous, indeed the Rouleaux and the Fahraues-Lindqviust effects make the concentration of RBCs larger at the center of the vessels than at the sides; as a consequence if the dimensions and the position of a representative volume are changed, different situations may be found.

In order to take into account of these peculiarities without really modelling all the phases contained in the blood, it is possible to adopt a *mesoscale approach*. In this manner, the blood is considered as a homogeneous fluid and the presence of RBCs and fibrinogen is taken into account by inserting in the governing equations long range forces mutually exerted by non-adjacent fluids elements.

The reason to introduce these forces is readily understandable if Fig. 2 is closely inspected.

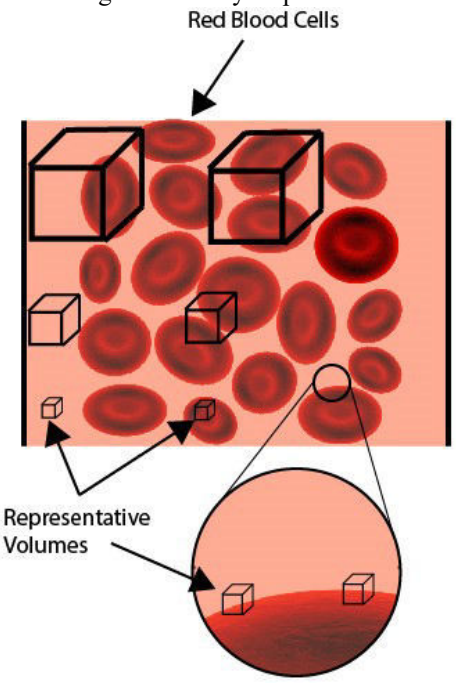

Fig. 2: Heterogeneity and multiphase nature of blood. In the circle, two non-adjacent fluid elements mutually exchange forces because of the presence of the RBC.

If two small volume elements are taken on the boundary of a RBC, it is reasonable to think that they interact because of the presence of the RBC itself, and their interaction is modelled here as non-local viscous forces.

In particular non-local forces are thought as linearly depending on the product between the two interacting volumes and their relative velocity; moreover the long-range forces are weighted by an attenuation function that decreases the force magnitude as the distance between the two elements increases. Under these assumptions the force mutually exerted by two non-adjacent volume elements may be written as follows (see Fig. (3)):

$$F_{ki} = \mu_{ki}\Delta V_k \Delta V_i (v_i - v_k) \tag{9}$$

where $\mu_{ki} = \mu_{NL} g(d_{ki})$, being $g(\bullet)$ the attenuation function.

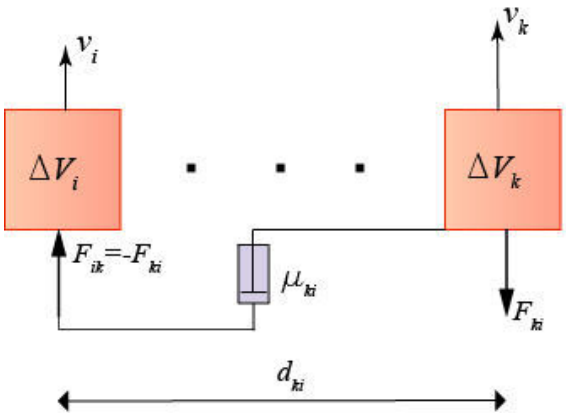

Fig. 3: Non-local forces mutually exerted by the two volume elements *i* and *k* in a one-dimensional problem.

The resultant of non-local forces on the element *k* may be written as follows

$$F_k = \mu_{NL}\Delta V_k \sum_{i=1}^{N} \Delta V_i \, g(\mathrm{d}_{ki})(v_i - v_k) \tag{10}$$

being μ_{NL} non-local viscosity parameter. If we refer to the two dimensional domain of Fig. (4) in axial symmetric conditions, the resultant of non-local forces may be written as

$$F_k = \mu_{NL} \sum_{i=1}^{N_r} \Delta V_k \sum_{j=1}^{N_\vartheta} \Delta V_{ij} \, g(\mathrm{d}_{k,ij})(v_{ij} - v_k) \tag{11}$$

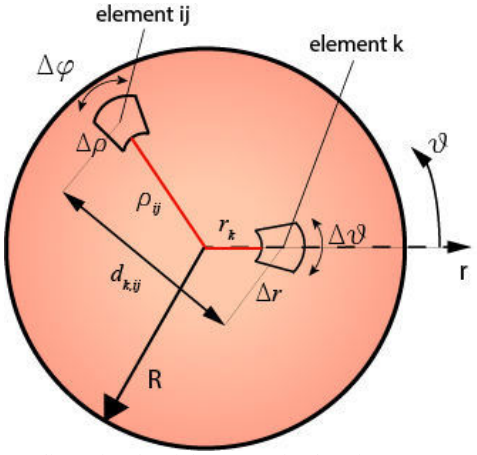

Fig. 4: Two dimensional axial symmetric domain (cross section of the circular vessel).

where

$$\Delta V_k = r_k \Delta r \Delta \vartheta L \qquad \Delta V_{ij} = \rho_{ij} \Delta\rho \Delta\varphi L \tag{12}$$

are the volumes of the two considered fluid elements. By taking the limits for $\Delta V_k \to 0$ and $\Delta V_{ij} \to 0$, the double sum reverts to a double integral; by considering both non-local forces and Newtonian local forces, the governing equation is obtained as

$$\frac{\Delta p}{L} = \mu\left(\frac{1}{r}\frac{dv(r)}{dr} + \frac{d^2 v(r)}{dr^2}\right) + \\ +\mu_{NL} L \int_0^R \int_0^{2\pi} g(d_{r\vartheta,\rho\varphi})\big(v(r,\vartheta) - v(\rho,\varphi)\big)\rho \, d\varphi \, d\rho \tag{13}$$

which may be labelled as *Non-local Hagen-Poiseuille law*. As for the attenuation function $g(\bullet)$, a typical form is exponential

$$g(d) = \exp(-\frac{d}{\lambda}); \qquad \lambda > 0 \tag{14}$$

where λ is an internal length parameter that determines the way the attenuation function decays. The Non-local Hagen-Poisueille law has three mechanical parameters. In the next section it is shown that the proposed model is able to reproduce accurately experimentally measured velocity profiles.

IV. Best Fitting of Model Parameters

In [3] velocity profiles have been measured on arterioles of rabbit mesentery. The measurement has been performed on arterioles with diameters size in the range 17-32 μm. In this paper a measurement on a 32 μm diameter vessels (Figure (3) of Reference [3]) has been taken into consideration in order to tune parameters of the Hagen Poiseuille model, the Casson model and the proposed non-local model. Results of the best fitting are reported in Table I and theoretical curves are contrasted with experimental data in Fig. (5).

TABLE I
PARAMETERS OBTAINED BY BEST-FITTING PROCEDURE

Model	μ *(MPa s)*	τ_0 *(MPa)*	μ_{NL} *(N s/mm^6)*	λ *(μm)*
Hagen-Poisueille	$1{,}23\ 10^{-8}$	--	--	--
Casson	$2{,}45\ 10^{-9}$	$1{,}79\ 10^{-6}$	--	--
NL Hagen-Poisueille	$6{,}79\ 10^{-9}$	--	4,04	7,3

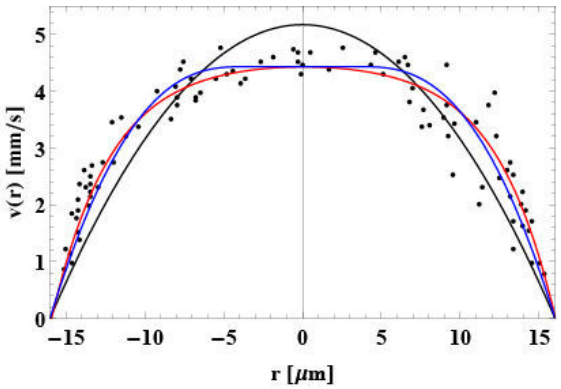

Fig. 5: Comparison between theoretical velocity profile and experimental data (black dots). Hagen Poisueille model black line, Casson model blue line, non-local Hagen Poiseuille model red line.

From Fig. (5) it is evident that the classical Hagen-Poiseuille model is not suitable to model behaviour of blood in small arterial vessels; the Casson and the proposed non-local model are capable of reproducing the characteristics flattened velocity profiles that are experimentally observed. Comparison between the Casson and the non-local model shows that while the former has two different behaviours in along the diameter, the latter provides a velocity profile that varies very gradually. In order to assess the accuracy of the three models, the root mean square error (RMSE) is used; the RMSE is defined as

$$RMSE = \sqrt{\frac{\sum_i \left(v_T(x_i) - v_{m,i}\right)^2}{n}} \qquad (15)$$

where n is the number of velocity data along the diameter, v_T is the theoretical velocity and v_m is the measured velocity. In Table II the RMSEs of the three models are compared .

TABLE II
COMPARISON BETWEEN RMSES

Model	*RMSE*
Hagen-Poisueille	0,6644
Casson	0,4486
NL Hagen-Poisueille	0,4012

From Table II it can concluded that the proposed non-local model represents an improvement of results obtained with the Casson model. The proposed non-local model is a linear model that is able to capture an apparent non-linearity in the blood behaviour. Moreover, it can be easily verified that another desirable feature of the proposed model is that as the diameter of the vessel increases, non-local forces become negligible and the model reverts to the classical Hagen-Poiseuille model.

V. Conclusion

In this paper a non-local model for the blood behaviour has been introduced. The model has proved to be very efficient in reproducing experimental velocity profiles without the need of non-linearity in the rheological behaviour. In the future the model maybe applied to more complicated problems and implemented in a CFD context.

References

[1] Y.C. Fung. (1997). Biomechanics – Circulation, Springer-Verlag, New York.

[2] J. Venkatesan, D.S. Sankar, K. Hemalatha, Y. Yatim, "Mathematical Analysis of Casson Fluid Model forBlood Rheology in Stenosed Narrow Arteries", *Journal of Applied Mathematics*, vol. 2013, pp. 1–13, 2013.

[3] G.J. Tangelder, D.W. Slaaf, A.M.M. Muijtjens, T. Arts, M.G.A. Egbrink, R.S. Reneman, "Velocity profiles of blood platelets and red blood cells flowing in arterioles of the rabbit mesentery", *Circulation Research*, vol. 59(5), pp. 505-514, 1986.

[4] M. Di Paola, M. Zingales. "Physically-based approach to the mechanics strong non-local linear elasticity theory", *Journal of elasticity*, vol. 97(2), pp. 103-130, 2009.

[5] G. Alotta, G. Failla, M. Zingales. "Finite element method for a non-local Timoshenko beam model", *Finite element in analysis and design*, vol. 89, pp. 77-92, 2014.

[6] S.Kim, "A Study of Non-Newtonian Viscosity and Yield Stress of Blood in a Scanning Capillary-Tube Rheometer", PhD Thesis, Drexel University, 2002.

[7] Y.I. Cho, J.M. Jung. "New method of hematocrit correction of whole blood viscosity", *International Communications in Heat and Mass Transfer*, vol. 57, pp. 221-227, 2014.

Patient-specific aortic root FE models biomechanics: impact of leaflets thickness distribution and discretization approach

G. Rossini[1*], M. Sabbatini[1*], F. Sturla[1], A. Della Corte[2], C. Bancone[2], S. Dellegrottaglie[3,4], A. Redaelli[1], E. Votta[1]

[1] *Department of Electronics, Information, And Bioengineering, Politecnico di Milano, Italy; email: giovanni.rossini@polimi.it*

[2] *Department of Cardiothoracic and Respiratory Sciences, Second University of Naples, Napoli, Italy*

[3] *Department of Advanced Biomedical Sciences, Federico II University, Napoli, Italy*

[4] *Division of Cardiology, Ospedale Medico-Chirurgico Accreditato Villa dei Fiori, Acerra, Napoli, Italy*

* *these two authors contributed equally to this work*

***Abstract*— Finite element models (FEMs) have been widely used to quantify aortic root (AR) biomechanics and its role in several pathologies. Among these, the progression of aortic valve calcification represents a particularly relevant condition which has been recently linked to altered patterns in the mechanical stimuli (e.g. mechanical stress) on the valve leaflets.**

In this context, the discretization of the valve leaflets and the distribution of the leaflet thickness have a key role; in the literature, shell elements are typically used, but a more reliable computation of leaflet stresses might be obtained through the use of solid elements with an appropriate region-dependent leaflet thickness distribution.

To compare these two discretization approaches and investigate the impact of the local leaflet thickness, we implemented a semi-automated tool for the generation of image-based aortic root FEMs; the tool allows for discretizing the valve leaflets using shell or solid hexahedral elements, and for setting space-dependent patterns of leaflets thickness for solid leaflets. The ARs of three healthy subjects were modeled, and their biomechanics throughout the cardiac cycle were computed.

Results highlighted that the use of solid elements leads to a more reliable quantification of leaflets stresses and that the local leaflet thickness strongly influences stresses patterns.

***Keywords*— Finite element biomechanical model, aortic root, cMRI, aortic valve leaflets**

I. Introduction

THE aortic root (AR) is the functional and anatomical unit connecting the outlet of left ventricle to the ascending aorta. It includes the aortic valve (AV), the Valsalva sinuses, the aortic annulus, the sino-tubular junction (STJ), the interleaflets triangles and the proximal ascending aorta. To better understand AR structural mechanics and its role into AR pathophysiology, different finite element models (FEMs) have been proposed in the scientific literature. Most of these use shell elements to discretize the geometry of AV leaflets, although this approach likely limits the detailed insight into leaflet stress distribution and into its role in the progression of clinically relevant pathological conditions, such as calcific AV disease. The discretization of AV into solid elements was proposed only by few numerical studies, and its impact on computed leaflet stresses was never investigated. Moreover, those model were limited by a homogeneous leaflet thickness distribution, while human leaflets thickness varies strongly throughout different regions of the cusps.

In this scenario, we generated the FEM of a small set of healthy ARs based on medical imaging, and computed AR biomechanics throughout the cardiac cycle. For each FEM, three variants were generated, which were characterized by 1) the use of shell elements, 2) solid elements with homogeneous thickness and 3) solid elements with a region-dependent thickness respectively, to discretize AV geometry.

II. Material and Methods

A. Acquisition of cMRI data and segmentation

Cardiac MRI was performed on 3 healthy volunteers. T1-weighted cine-cMRI sequences were acquired on 18 planes evenly rotated around the axis passing through the center of the annulus and the center of the sino-tubular junction. Acquisitions were performed on a 1.5 T Achieva scanner (Philips Healthcare Medical System, Irvine, Calif). In-plane spatial resolution and slice thickness were 1.1 mm and 7 mm, respectively. Thirty frames/cardiac cycle were acquired with R-wave triggering. In the first systolic frame, when the transvalvular pressure acting on AV leaflets was considered negligible [2], AR substructures were manually traced through in house Matlab© scripts.

B. Reconstruction and discretization of AR geometry

Through in house Matlab© scripts, AR 3D geometry was obtained a point-cloud, which was filtered to eliminate noise effects. A 3D surface for each AR structure was created and discretized with quadrangular shell elements.

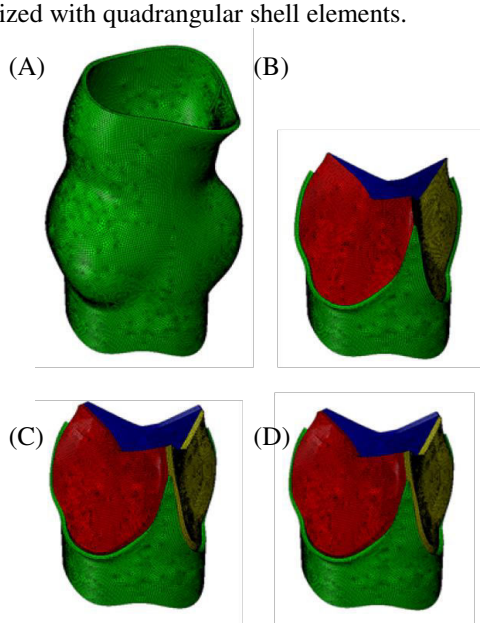

Fig. 1: A) Full volume mesh of the aortic wall, B) AV shell model, C) AV homogeneous thickness solid model D) AV region-dependent thickness solid model. Data are shown for subject 1.

The full volume mesh for the aortic wall was created by extruding the shell element along the local outward normal to generate three layers of hexahedral solid elements with a cumulative thickness of 1.0 mm (Figure 1A).
The mesh for the aortic valve leaflets were obtained in a different way for each of the three variant of the models:
1) the shell model was generated by assigning a virtual homogeneous thickness of 0.8 mm to the leaflet shell elements;
2) the homogeneous thickness solid model was obtained through a complex extrusion process to obtain three layers of hexahedral solid elements with a homogeneous cumulative thickness of 0.8 mm (Figure 1C).
3) the region-dependent thickness solid model was derived tuning the extrusion process of model b), in order to obtain a thickness of 1.2 mm for the attachment edge and the free margin regions, and a thickness of 0.3 mm for the belly region, as in [3].

C. *Tissues mechanical properties*

The mechanical response of the aortic wall was assumed linear, elastic and isotropic, with a 2 MPa Young's modulus and a 0.45 Poisson's ratio to reproduce the almost incompressible behavior of the real tissue [4]. AV leaflets tissue was described as a transversely anisotropic and hyperelastic material using the following strain energy function

$$U = \frac{C}{2}\left(e^{Q} - 1\right) + K\left(\frac{J^2 - 1}{2} - \ln J\right) \quad (1)$$

with the expression of Q as in the model originally proposed by Guccione [4] to mimic the passive response of myocardial tissue

$$\begin{aligned} Q = {} & 2b_1 tr(E) + b_2 E_{ff}^2 + \\ & + b_3\left(E_{ss}^2 + E_{nn}^2 + E_{sn}^2 + E_{ns}^2\right) \\ & + b_4\left(E_{nf}^2 + E_{fn}^2 + E_{fs}^2 + E_{sf}^2\right) \end{aligned} \quad (2)$$

where E_{ij} are the components of the Green-Lagrange tensor (with f the fiber direction, s the cross-fiber direction and n the normal direction) and b_1, b_2, b_3 and b_4 the model parameters which were identified by least square fitting of experimental data from biaxial tensile tests by Billiar and Sacks [5] [6]. The constitutive model was implemented into a VANISOHYPER_STRAIN subroutine for the commercial solver ABAQUS/Explicit©.

D. *Computation of aortic wall pre-stresses*

The initial configuration of the AR was defined at early systole, when AV leaflets are approximately unloaded, but the aortic wall is pressurized to 80 mmHg. Consistently, aortic wall pre-stresses were computed through the iterative process described in detail in a recent work by Votta [7]; briefly, the stress-free AR configuration was pressurized by applying a pressure load of 82mmHg to the inner surface of the aorta and of the aorto-ventricular junction; then, the computed nodal displacement field was checked for the entire aortic wall; if the peak value of displacement magnitude did not exceed the in-plane resolution of cMRI, that inflated configuration was considered equivalent to real configuration related to the cMRI, and the corresponding Cauchy true stress field characterizing the aortic wall was considered the pre-stresses field to be applied when simulating AR biomechanics throughout the cardiac cycle. Otherwise, the stress-free AR configuration was updated and set equal to inflated configuration just obtained, and the pressurization simulation was performed again.

E. *Computation of AR biomechanics*

The structural response of the pre-stressed AR over two consecutive cardiac cycles was computed; to this aim, physiological time-dependent ventricular and aortic pressures were applied to the aortic wall upstream from and downstream of the AV, respectively, and a consistent trans-valvular pressure drop was applied to the AV leaflets.

III. RESULTS AND DISCUSSION

AV kinematics as computed by the three model's variant were compared. When shell elements were used (model variant 1), leaflets were allowed for wide local rotations at their insertion onto the aortic wall, which behaved as a sort of spherical joint. When solid elements were used (model variant 2 and 3), the connection behaved as a deformable encastre, preventing from free rotations. In systole, this effect reflected into a reduced outward motion of the solid leaflet, and hence into a smaller orifice area at peak systole for both solid elements models compared to the shell elements model (Figure 2A-C). At peak diastole, this effect reflected into a different leaflets profile: when shell elements were used, AV leaflets tended to prolapse (Figure 2D).

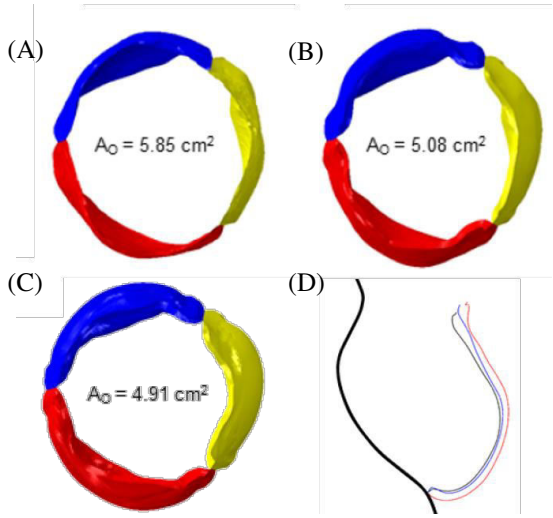

Fig. 2: A) Shell model, B) homogeneous thickness solid model and C) region-dependent thickness solid model orifice area at peak systole; D) left coronary leaflet profile at peak diastole (red = shell, blue = solid homogeneous thickness, black = solid region-dependent thickness). Data are shown for subject 1.

AV mechanical response during the cardiac cycle was evaluated through the analysis of the circumferential stresses on the ventricular and atrial side of the leaflets, as well at their mid-section. Shell models (Figure 3, first line) showed a patchy distribution, in particular on the two AV sides, without a clear separation between the belly region and the cooptation

area, and marked differences, up to 981 kPa, were detected between the ventricular and aortic sides (Table I).

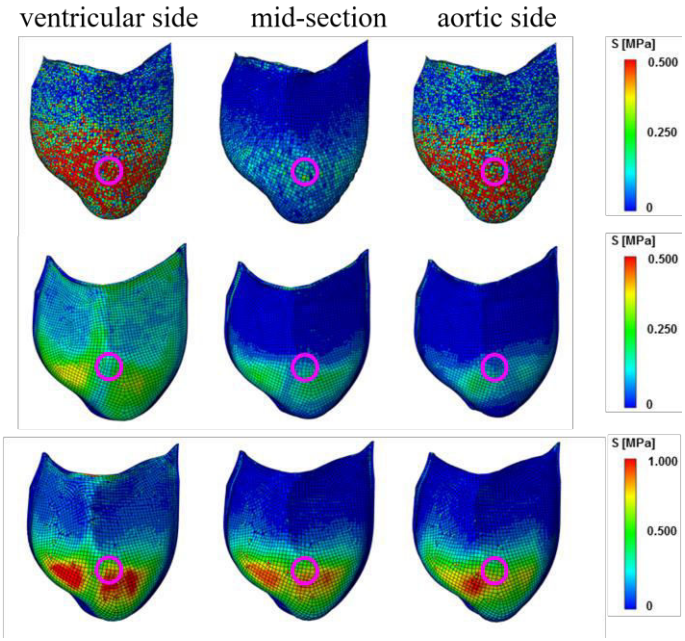

Fig. 3: Circumferential stress patterns on the ventricular side, mid-section and aortic side for the shell model (first line), homogeneous thickness solid model (second line) and region-dependent solid thickness solid model (third line). Data are shown for subject 1. The pink circles highlight the region where values in Table 1 were obtained.

CIRCUMFERENTIAL STRESSES IN THE BELLY REGION

Subject 1			
location	*shell*	*solid homogeneous thickness*	*solid region-dependent thickness*
V side	0.526	0.229	0.770
Mid-section	0.096	0.170	0.640
A side	0.169	0.135	0.548
Subject 2			
location	*shell*	*solid homogeneous thickness*	*solid region-dependent thickness*
V side	0.480	0.259	0.851
Mid-section	0.078	0.154	0.758
A side	0.351	0.091	0.682
Subject 3			
location	*shell*	*solid homogeneous thickness*	*solid region-dependent thickness*
V side	1.054	0.321	1.108
Mid-section	0.073	0.237	0.995
A side	0.497	0.169	0.909

In Table I, circumferential stresses (MPa) in the belly region. Values were obtained through averaging over the region highlighted in Figure 3.

Conversely, in the solid elements models (Figure 3, second and third line) the distribution was much smoother and a gradual trend over the three considered layers was visible. Computed stresses values also proved the strong impact of the thickness modulation; in particular, max principal, radial and circumferential stresses were notably increased in the solid thinned belly region of region-dependent thickness models as compared to the corresponding value for constant thickness solid models.

IV. Conclusion

Computed results highlighted that the use of solid elements has a major impact on AV kinematics, and leads to a more reliable quantification of leaflet stresses and of the associated variations through the leaflet thickness. Moreover, it was evident that leaflet stresses strongly depend on the local leaflet thickness, thus suggesting that in the context of patient-specific modeling a reliable quantification of the patient-specific tissue thickness distribution should be mandatory. Hence, the most important improvement concerns the imaging technique as cMRI cannot provide any information about the patient leaflets' thickness distribution and a higher resolution imaging technique, e.g. 3D ultrasound imaging, have to be considered in order to be able to trace also the patient-specific tissue thickness distribution.

References

[1] C. A. Conti et al., "Dynamic FE analysis of the aortic root from MRI derived parameters", in Medical Engineering and Physics, 2010.
[2] K.J. Grande-Allen, R. P. Cochran, P. G. Reinhall, K.S. Kunzelman, "Stress variations in the human aortic root and valve: the role of anatomic asymmetry", in Annals of Biomedical Engineering, 1998.
[3] J. M. Guccione, A. D. McCulloch, L. K. Waldman, "Passive material properties of intact ventricular myocardium determined for a cylindrical model", in Journal of Biomechanical Engineering, 1991.
[4] Conti CA et al. "Dynamic finite element analysis of the aortic root from MRI-derived parameters". In: Medical Engineering and Physics 2010.
[5] M. S. Sacks, K. L. Billiar, "Biaxial mechanical properties of the native and glutaraldehydetreated aortic valve cusp: part I, experiment results", in Journal of Biomechanical Engineering, 2000.
[6] M.S. Sacks, K. L. Billiar, "Biaxial mechanical properties of the native and glutaraldehydetreated aortic valve cusp: part II, a structural constitutive model", in Journal of Biomechanical Engineering, 2000.
[7] E. Votta et al., "A novel approach to the quantification of aortic root in vivo structural mechanics", in International Journal for Numerical Methods in Biomedical Engineering, 2016.

Image-based analysis of tricuspid valve biomechanics: towards a novel approach integrating *in vitro* 3D echocardiography and finite element modelling

M. Selmi[1,2], O.A. Pappalardo[2,1], A. Aversa[2], E. Careddu[2], M. Jaworek[2], R. Vismara[2], G.B. Luciani[1], G. Faggian[1], A. Redaelli[2] and E. Votta[2]

[1] *Division of Cardiac Surgery, Department of Surgery, Università di Verona, Italy*

[2] *Department of Electronics, Information and Bioengineering, Politecnico di Milano, Italy*

***Abstract*—Tricuspid valve (TV) realistic finite element (FE) models could aid the design of novel devices and solutions.**

Through a circulatory mock loop, real-time 3D-echocardiography was performed and manual segmentation of TV geometry was accomplished. Numerical simulations were run accounting for dynamic boundary conditions and realistic mechanical properties.

Based on obtained results, the proposed method will provide a predictive tool for the biomechanical evaluation of novel TV surgical repair.

***Keywords*—tricuspid, finite element, echocardiography, biomechanics.**

I. Introduction

TRICUSPID valve (TV) has recently gained a growing interest, as proved by the increasing number of new minimally-invasive solutions for its surgical treatment [1]. In this scenario, TV realistic finite element (FE) models could aid the design and the optimization of novel devices and solutions as well as being crucial in the surgical decision-making process. Nevertheless, in the literature only one and highly idealized TV FE model is present [2], due to the lack of information about the anatomical features and tissue mechanical properties of this valve.

We propose a method to obtain anatomically detailed TV FE models accounting for dynamic boundary conditions and for realistic TV tissue mechanical properties [3]. To develop and test our method, we integrated FE modelling with *in vitro* experiments, so to obtain input data under repeatable conditions and to be able to compare numerical results vs. experimental evidence.

II. Materials and Methods

A. 3D echocardiographic imaging

Through a circulatory mock loop (CML) [1], real-time 3D-echocardiography (3DE, Philips iE33) was performed on three TVs under pulsatile conditions. In particular, an *ad-hoc* protocol was defined:

i) a TEE probe (X7-2t) was used directly placed on the epicardium, found as the best position in minimizing the artifacts and shadowing effects;

ii) a ECG-gated acquisition on four cardiac cycles was set to have a good trade-off between spatial and temporal resolution.

B. From geometry reconstruction to finite element model

Obtained 3DE data were firstly navigated through the open-source software 3D Slicer, getting the position of both the commissures and the papillary muscles (PMs), using the septal insertion of the CML pump connector as a reference point to be able to distinguish the relative position of such points.

Secondly, by using custom software developed in MATLAB (The MathWorks Inc., USA), 3DE data were navigated and interpolated to generate 18 planes evenly rotated around the long axis of the valve (Fig. 1). At end-diastole (ED), on each plane annulus, leaflets and, where visible, papillary muscles were manually traced (Fig. 1A). The annulus was traced also at each time point until mid-systole (MS).

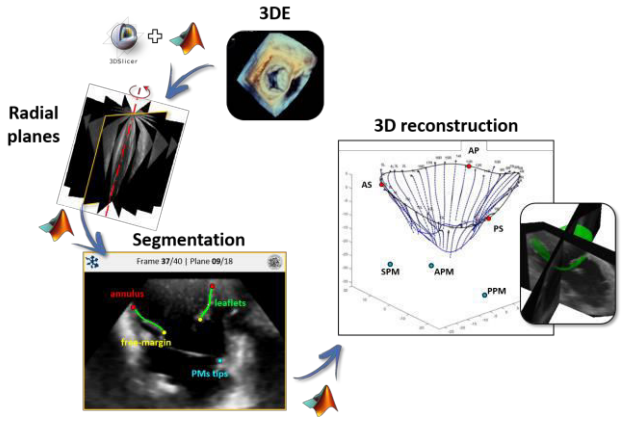

Fig. 1: TV reconstruction workflow.

TV 3D geometry at ED was automatically reconstructed through cubic-spline interpolation of the traced points, and complemented by a paradigmatic chordal apparatus, whose branched structure was defined according to *ex vivo* findings [2] and to the anatomical description presented by Silver et al [4].

In the FE model, leaflets' triangulated surface (uniform thickness 0.46 mm) and chordae tendineae (section area 0.09 mm^2 for the main branches) were modelled as plane-stress 3-nodes shell elements (S3) and truss elements (T3D2), respectively. CML-derived transvalvular pressure curve and image-based annular kinematic were imposed as boundary conditions to simulate the systolic closure, adopting a friction contact algorithm to model leaflets coaptation.

C. *Mechanical properties definition*

The markedly non-linear and transversely isotropic behaviour of TV leaflets was described through the hyperelastic model proposed by Lee [5], with the following invariant-based strain energy function:

$$\boldsymbol{W} = c_0(I_1 - 3) + c_1\left[(1-\beta)e^{c_2(I_1-3)^2} + \beta e^{c_3(I_4-1)^2} - 1\right] \quad (1)$$

where $I_1 = trace(\boldsymbol{C})$, $I_4 = N \cdot \boldsymbol{C} \cdot N$ are respectively the first and fourth invariants of the Cauchy-Green strain tensor **C** and N is the direction of the fibres in the unloaded configuration, assumed circumferentially oriented along the commissure-commissure direction. The constitutive parameters of the model, i.e. $c_0, c_1, c_2, c_3, \beta$ were identified by fitting the equi-biaxial tensile tests data acquired by Pham et al. from human TV leaflets [3] (Table I).

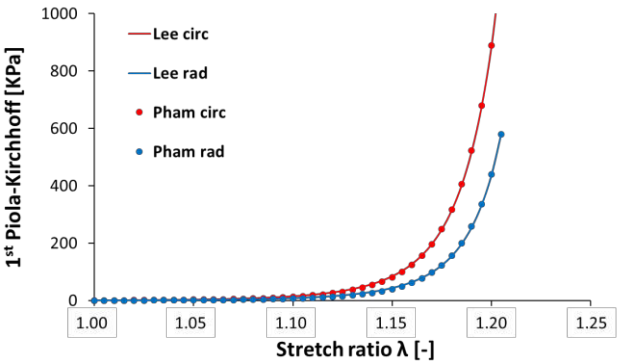

Fig. 2: Fitting of the experimental data from equi-biaxial test (dot) with Lee strain energy function (line). Stress are expressed as Piola-Kirchhoff 1st tensor; *circ* and *rad* depict the circumferential and radial direction, respectively.

TABLE I
CONSTITUTIVE PARAMETERS

c_0 [MPa]	c_1 [MPa]	c_2	c_3	β
0.0004	0.0017	19.14	22.79	0.06

The mechanical response of the chordae tendineae was considered non-linear isotropic and was described through a second order polynomial strain energy function. The constitutive parameters were evaluated from the experimental tensile data on human chordae provided by Lim et al [5], supposing lower tension acting on the basal chordae, compared to the rough and commissural ones, as reported in literature [6].

D. *Experimental campaign*

In parallel, experimental measurements were performed. All the three valves were excised in order to quantitatively describe their morphological features, measuring characteristic dimensions, such as annular perimeter, as well as leaflet length and height to be subsequently used as reference ground-truth data to investigate possible approximation introduced by the reconstruction procedure.

III. RESULTS AND DISCUSSION

A. *Morphological results*

Table II shows the comparison between direct and 3DE-based measurements of the TVs geometry. annular perimeter and leaflets lengths are not notably affected by the approximations introduced with the TV reconstruction process. On the contrary, while leaflets lengths are border-line towards the maximum experimental value, commissural heights considerably exceed the direct measurements. Such kind of overestimation is probably due to double reason: i) commissure actual position exactly in between two consecutive radial planes and ii) free-margin not so clearly detectable as the annulus in the images.

TABLE II
3DE-BASED VS DIRECT MEASUREMENTS

Measurement [mm]	*Direct*	*3DE-based*
Perimeter	150±9	149±5
Anterior Leaf height	20±5	24±8
Septal Leaf height	18±6	23±5
Posterior Leaf height	19±8	19±4
AS commissure height	5±2	21±7
PS commissure height	7±3	15±6
AP commissure height	8±3	17±7

The annular dynamics evaluation showed almost the same pattern for the three valves, leading to a paradoxical enlargement in the annulus dimensions from end-diastole towards the systolic peak. However, this is consistent with the benchmark working condition: the heart is passive and the *in vivo* muscle contraction is lacking.

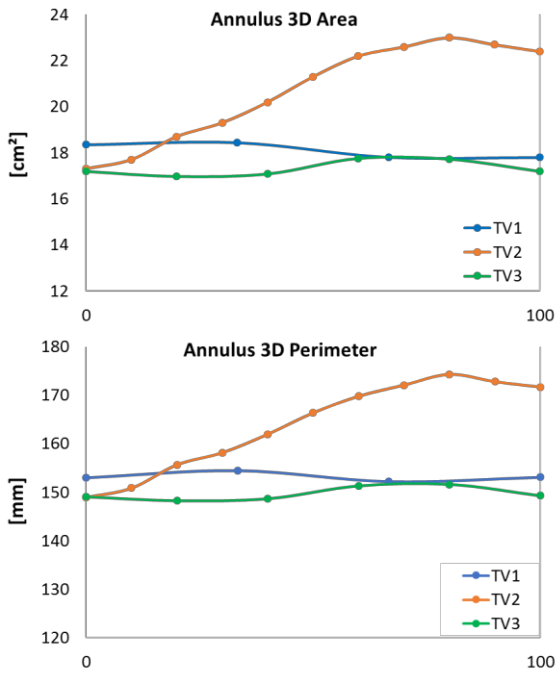

Fig. 3: Results from annular dynamics derived from segmentation of the imaging data along the cardiac cycle (in the horizontal axis, 0 and 100 represent end-diastole and mid-systole, respectively).

B. *Biomechanical results*

For the sake of clarity, result of the biomechanical analysis are depicted in Figure 4 only for one of the three valves, considered the one which experienced the "average" behaviour.

Even from the biomechanical standpoint, all the three TVs yielded the same resulting trend, achieving a non-complete coaptation of the leaflets at the systolic peak (Figure 4-a).

The analyses of leaflets motion along the closing phase, as well as of the strain and stress distributions over the leaflets at systolic peak suggested that the incomplete leaflets coaptation is likely due to an excessive tethering effect exerted by the chordae tendineae, owing to the shape of the leaflets free margin next to chordal insertions. So, for this main reason, the chordae may be too short and, consequently, excessively stiff. Furthermore, given the relative position of papillary muscles and chordal insertions, in some cases the leaflet is pulled not only downwards and radially outwards, but also circumferentially, thus hampering the effectiveness of leaflet motion in terms of orifice occlusion.

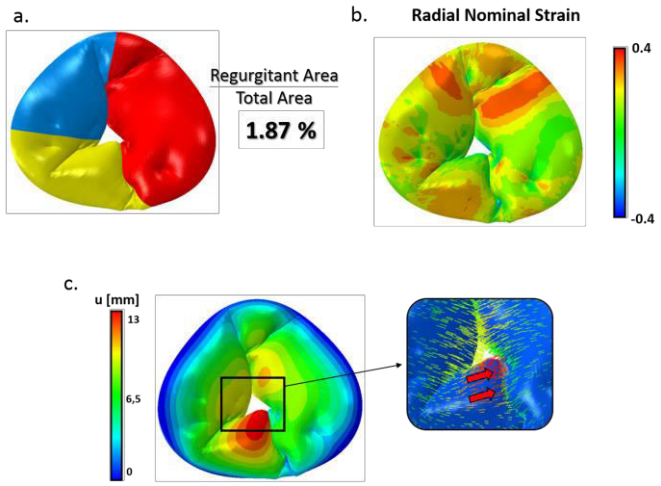

Fig. 4: Results from biomechanical analysis: a) non-complete coaptation expressed as the ratio between orifice and total area; b) radial nominal strain distribution; c) displacement magnitude pattern on the leaflets.

This explanation is even corroborated by the quantitative assessment of both the strain and the stress fields over the TV leaflets surface. Maximum principal strains were mostly aligned with the radial direction, associated with the hypomobility of the leaflets' free margin, experiencing smaller values as compared to previous data [2]. Peak values of about 35% were detected at the chordal insertions, proving the tethering effect induced by chordal apparatus (Figure 4-b). This trend is confirmed in the stress distribution, with peak values around 400 kPa exactly nearby the insertions.

Of note, the described features are likely exacerbated by the combination of applied kinematic boundary conditions, namely the enlargement of the annulus, due to the paradoxical ventricle passive movement, and the fixed position of the papillary muscles throughout the simulation, whose in vitro movement was neglected.

IV. Conclusion

As compared to the only previously published TV FE model [2], the one herein proposed represents a great step forward. The presented study has still some limitations, mainly related to a not always suitable quality of the imaging acquisition as well as to the segmentation accuracy. The latter strictly depends on some issues related to the manual tracing of the leaflets, such as the identification of their free-margin. Moreover, the morphological outcomes depict that the profiles' reconstruction strategy is markedly influenced by the approximation algorithm (namely 4th order Fourier function) exploited, suggesting that an interpolating one could be probably better (e.g. cubic spline), especially regarding the commissural zones.

Nevertheless, this work has to be considered pivotal in moving towards reliable and accurate modelling of TV biomechanics. Indeed, the integration of FE modelling with in vitro experiments allowed to test the proposed method and will provide robust guidance for further refinements. The final goal would be to pave the way towards a quantitative and predictive tool for the biomechanical evaluation of surgical solutions for TV repair; this is something encouraging since the proposed method can be exploited even on *in-vivo* image-based volumetric data (e.g. 3D-Echo, CT).

Acknowledgement

We kindly thank the ForCardiolab ONLUS for giving us the opportunity and the facilities to perform the experimental part of the study

References

[1] R. Vismara, G. Gelpi, S. Prabhu, P. Romitelli, L.G. Troxler, et al, "Transcatheter Edge-to-Edge Treatment of Functional Tricuspid Regurgitation in an Ex Vivo Pulsatile Heart Model" in *J. Am. Coll. Cardiol.*, 68(10), 2016, pp. :1024-33.

[2] M. Stevanella, E. Votta, M. Lemma, C. Antona, A. Redaelli, "Finite element modelling of the tricuspid valve: A preliminary study" in M*ed. Eng. Phys.*, 32(10), 2010, pp. :1213-23.

[3] T. Pham, F. Suleimani, E. Shin, D. Wang, W. Sun, "Quantification and comparison of the mechanical properties of four human cardiac valves" in *Acta Biomater.*, 54, 2017, pp. :345-355.

[4] M.D. Silver, J.H. Lam, N. Ranganathan, E.D. Wigle, "Morphology of the human tricuspid valve" in *Circulation*, 43(3), 1971, pp. :333-48.

[5] K.O. Lim, D.R. Boughner, D.G. Perkins, "Ultrastructure and mechanical properties of chordae tendineae from a myxomatous tricuspid valve" in *Jpn. Heart J.*, 24(4), 1983, pp. :539-48.

[6] J.H. Jimenez, D.D. Soerensen, H.E. Zhaoming, J. Ritchie, A.P. Yoganathan, "Mitral valve function and chordal force distribution using a flexible annulus model: An in vitro study" in *Ann. Biom. Eng.*, 33(5), 2005, pp. :557-66.

Simulation of Mitral valve function: quantitative comparison between mass-spring and finite element approach

O.A. Pappalardo [1, 2], F. Sturla [3], F. Onorati [2], G. Puppini [4], M. Selmi [2, 1], G.B. Luciani [2], G. Faggian [2], A. Redaelli [1] and E. Votta [1]

[1] Department of Electronics, Information and Bioengineering, Politecnico di Milano, Italy
[2] Division of Cardiac Surgery, Department of Surgery, Università degli Studi di Verona, Italy
[3] 3D and Computer Simulation Laboratory, IRCCS Policlicnico San Donato, San Donato Milanese, Italy
[4]Radiology, Università degli Studi di Verona, Italy

Abstract

Patient-specific finite element (FE) models can assess the impact of mitral valve (MV) repair on the complex MV anatomy and function. However, FE excessive time requirements hamper their use for surgical planning; mass-spring models (MSMs) represent a more approximate approach but can provide almost real-time simulations. On this basis, we implemented MSMs of three healthy MVs from cardiac magnetic resonance (cMR) imaging to simulate the systolic MV closure, including the in vivo papillary muscles and annular kinematics, and the anisotropic and non-linear mechanical response of MV tissues. Data on MSMs time-efficiency and data from the comparison of MSMs vs. FE models suggest that MSMs could represent a suitable trade-off between almost real-time simulations and reliability when computing MV systolic configuration, with the potential to be used in a clinical setting either as a support to the decisional process or as a virtual training tool.

***Keywords*—Mitral valve, Mass-spring model, Finite element model, Heart valve repair.**

I. Introduction

Mitral valve (MV) physiologic function requires the correct interplay of its components: annulus, leaflets, papillary muscles (PMs), which originate from the ventricular myocardium, and chordae tendineae, which connect the leaflets to the PMs [1]. When this mechanism is altered, mitral regurgitation (MR) occurs.

The only effective treatment for MR is surgery, MV repair being the procedure of choice over MV replacement owing to lower surgical mortality and better long-term preservation of left ventricular function [2,3]. However, the anatomical and functional complexity of the MV makes surgical repair technically demanding, requiring longer learning curves and expertise in the selection of the most effective techniques for a given scenario [4]. Moreover, in open heart surgery the intraoperative evaluation of the surgical outcome is performed on a motion-less and almost flaccid heart, making it difficult to correctly predict the actual post-operative MV function [5].

In order to help identifying more robust criteria to select and tune MV repair techniques in different clinically relevant scenarios, and to test novel concepts, different research groups have proposed computational models to simulate the post-operative MV function based on its baseline pre-operative conditions [6-9]. However, the vast majority of these models are based on the finite element (FE) approach and are far too time-demanding to be used in a real clinical setting [10]

Mass-spring models (MSMs), which differ from FE models in that they describe a continuum structure as a discrete cloud of nodal masses connected through a mesh of springs, were used to simulate the effects on MV dynamics of chordae tendineae surgical modification [11] and of annuloplasty [12] almost in real- time.

On this basis, we implemented the image-based MSM of three healthy MVs, applied it to the simulation of their systolic closure, and compared its capability to correctly compute the systolic configuration of the considered MVs vs. state-of-the-art subject-specific FE models. In this process, we also quantified the computational expense related to the use of proposed MSM modelling approach.

II. Material and Methods

Following a well-established protocol [13], cardiac magnetic resonance (cMR) imaging was performed on three healthy subjects through a 3.0T TX Achieva system (Philips Medical Systems, Irvine, Calif). Cine-sequences with 1.25 mm in-plane resolution and 8 mm slice thickness were acquired. Through in-house software implemented in Matlab® (MATLAB, The MathWorks Inc, Natick, Mass), MV annulus, leaflets and PMs were manually traced in the tele-diastolic frame, i.e., the last frame preceding transient leaflets closure, when the MV was assumed stress-free. Data yielded by manual tracing were automatically filtered and used to reconstruct the 3D geometry of annulus and leaflets, whose non-uniform and compound curvature was accounted for [14], and for the 3D position of PMs tips. The boundary conditions of annulus and PMs were defined segmenting along the systolic phase from the tele-diastolic to the systolic-peak frame.

Firstly, the physiologic closure of an anatomically detailed MV was simulated through finite element (FE) modelling as in [15] the hyperelasticity and anisotropy of the MV tissue.

FE simulations were parallelized on 16 CPUs on a scientific workstation (Intel Xeon 2.93 GHz, 16 CPUs, 100 GB RAM).

For each MV, the leaflet mesh generated for the FE model was subsampled through Meshmixer (Autodesk, Inc, San Rafael, CA, USA) to obtain three different model with different levels of spatial resolution were: coarse, intermediate and fine. The implementation of the MSM-based simulator

required:

- Modelling leaflet tissue anisotropic and non-linear mechanical response by defining spring stiffness k as a function of the spring orientation in space (Fig. 1) and of the spring current elongation. The stress-strain curves was defined approximating May Newman data [16] with a piecewise function in which the initial portion was fitted with a straight line and the second one with an exponential function (Fig. 2).
- Definition of chordae tendineae according to ex vivo findings [17]
- Modelling of chordae tendineae non-linear mechanical properties by defining spring stiffness k as a function of the spring current elongation. The fitting of stress-strain curves were obtained using the experimental data yielded by Kunzelman [17]. In particular marginal and structural chordae were fitted with a polynomial function of degree 3 while the second order chordae were approximated with a parabolic function.
- Development of a penalty contact algorithm to handle the coaptation of valvular leaflets.
- MV closure was simulated applying a physiological pressure and the entire system was solved using Euler forward numerical scheme.

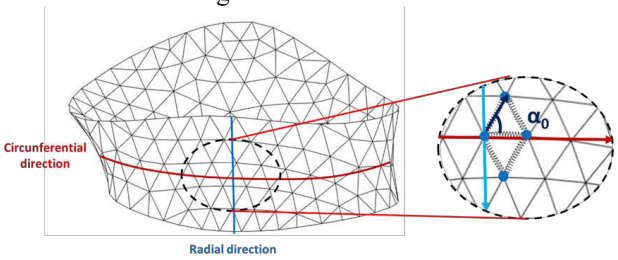

Fig. 1: Detail of the leaflet mesh depicting two triangular elements sharing a spring, which connects two point masses.

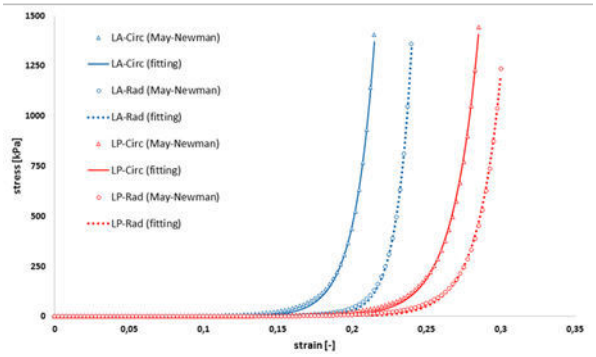

Fig. 2: Experimental stress-strain data and fitting functions used for the leaflets and chordae material model.

In order to evaluate the accuracy of the MSM, for each MSM simulation the computed MV configuration at peak systole was compared to the one yielded by a FEM of the same MV in terms of local node-to-node distance.

III. Results and Discussion

Differences in leaflets' configuration as obtained through FE models and MSMs were quantified. The Euclidean node-to-surface distance between MSM leaflet nodes and the corresponding FE leaflet surface was computed (Fig. 1). Peak distances were always within 4 mm, and were located at P2, P3 and A3 for sub- jects 1, 2 and 3, respectively. For each simulated MV, no relevant effect of the mesh refinement level in the MSMs was observed on the distance distribution over the leaflets. At 120 mmHg of pressures, the distribution of the Euclidean node-to-surface distances between MSM leaflet nodes and the corresponding FE leaflet surface was analysed. No statistically significant differences between different MSM mesh refinement levels were found (Kruskal–Wallis test), the 75th of the distance distribution was lower than 2 mm, and the 95th of the distance distribution was lower than 3 mm.

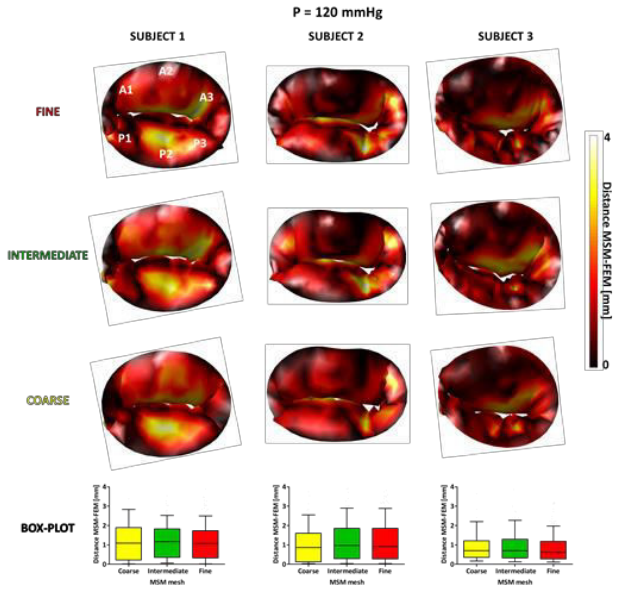

Fig. 3: Heat map and Boxplots of the distribution of the node-to-surface distance between MSM nodes and the corresponding FE model surface of the MV leaflets at peak systole (transmitral pressure P = 120 mmHg).

FE simulations required 73–98 min. Simulations run through MSMs required less than 10 min when coarse meshes were used, and up to 37–61 min when fine meshes were used (Table 1). This increase in computational expense is mostly due to contact modelling, which requires 3–4 min for coarse meshes, and 26–49 min for fine meshes. On the opposite, the modelling of tissues' non-linear mechanical properties only marginally affects the computational expense of MSMs, independently of the mesh refinement level.

Computational Cost					
		Total Time [min]	Contacts Time [%]	Non-Linearity Time [%]	Time of the other Characteristic [%]
Subject 1	fine	36.67	71.86	8.09	20.05
	intermediate	16.47	55.57	11.23	33.2
	coarse	9.25	40.36	12.97	46.67
Subject 2	fine	56.45	79.24	6.52	14.23
	intermediate	24.12	64.89	9.61	25.5
	coarse	8.8	39.58	13.26	47.16
Subject 3	fine	60.77	80.17	6.23	13.6
	intermediate	26.6	67.23	9.27	23.5
	coarse	9.85	43.15	12.69	44.16

Table I: Computational expense of the simulations performed through MSMs. The percentage expense associated to the modeling of contact and of tissues' non-linear mechanical properties is highlighted.

IV. Conclusion

The present work showed a MV MSM based on in vivo

images able to combine the modelling of both PMs and annulus motion with the different anisotropic and non-linear mechanical properties of MV leaflets

The deformed configuration of MV leaflets as computed by MSMs was compared vs. the corresponding configuration obtained through FE modelling. Mismatches by less than twice the in-plane resolution of cMR data were detected over 75% of the leaflets' surface (Fig. 3), independently of the mesh refinement and of the specific MV considered. Somewhat counterintuitively, for every simulated MV such mismatch was smallest when the configuration obtained through MSMs with an intermediate level of mesh refinement was considered. Altogether, data on MSMs computational performance and data from the comparison of MSMs vs. FE models suggest that, as long as the focus of the analysis is computing the MV configuration at high systolic pressure values, MSMs with intermediate or coarse meshes can be as reliable as state-of-the-art FE models, while reducing computational expense to few minutes even when a standard laptop is used.

Hence, MSMs could represent a suitable trade- off between almost real-time simulations and reliability, with the potential to be used in surgical planning or in virtual surgical training. In the context of surgical planning, MSMs could be exploited to simulate different surgical options [18], e.g., neochordoplasty, annuloplasty, leaflet resection, and their potential combination, to compare the corresponding systolic MV configurations in terms of those geometrical indexes that are indicators of repair durability, such as coaptation length and tenting height [19,20].

REFERENCES

[1] Yacoub M . Anatomy of the mitral valve, chordae and cusps. In: Kalmanson D, editor. The mitral valve. London: Edward Arnold; 1976. p. 15–20 .

[2] Nishimura RA, Otto CM, Bonow RO, Carabello BA, Erwin JP III, Guyton RA, et al. 2014 AHA/ACC guideline for the management of patients with valvular heart disease: a report of the American College of Cardiology/American Heart Association Task Force on Practice Guidelines. YMTC 2014;148:e1–e132.

[3] Vahanian A, Alfieri O, Andreotti F, Antunes MJ, Barón-Esquivias G, Baumgart- ner H, et al. Guidelines on the management of valvular heart disease (version 2012). Eur Heart J 2012.

[4] Drake DH, Zimmerman KG, Hepner AM, Nichols CD. Echo-guided mitral repair. Circ Cardiovasc Imaging 2014;7:132–41.

[5] Anyanwu AC, Adams DH. Etiologic classification of degenerative mitral valve disease: Barlow's disease and fibroelastic deficiency. Semin Thorac Cardiovasc Surg 2007;19:90–6.

[6] Votta E, Maisano F, Bolling SF, Alfieri O, Montevecchi FM, Redaelli A. The geo- form disease-specific annuloplasty system: a finite element study. Ann Thorac Surg 2007. doi:

[7] Kunzelman KS , Reimink MS , Cochran RP . Flexible versus rigid ring annulo- plasty for mitral valve annular dilatation: a finite element model. J Heart Valve Dis 1998;7:108–16.

[8] Votta E , Maisano F , Soncini M , Redaelli A , Montevecchi FM , Alfieri O . 3-D com- putational analysis of the stress distribution on the leaflets after edge-to-edge repair of mitral regurgitation. J Heart Valve Dis 2002;11:810–22 .

[9] Avanzini A , Donzella G , Libretti L . Functional and structural effects of percu- taneous edge-to-edge double-orifice repair under cardiac cycle in comparison with suture repair. Proc Inst Mech Eng H 2011;225:959–71 .

[10] Sturla F, Votta E, Onorati F, Pechlivanidis K, Pappalardo OA, Gottin L, et al. Biomechanical drawbacks of different techniques of mitral neochordal implan- tation: when an apparently optimal repair can fail. J Thorac Cardiovasc Surg 2015.

[11] Hammer PE, Sacks MS, Del Nido PJ, Howe RD. Mass-spring model for sim- ulation of heart valve tissue mechanical behavior. Ann Biomed Eng 2011. doi: 10.1007/s10439- 011- 0278- 5.

[12] Hammer PE, Del Nido PJ, Howe RD. Anisotropic mass-spring method accurately simulates mitral valve closure from image-based models. Lect Notes Comput Sci (including Subser Lect Notes Artif Intell Lect Notes Bioinform) 2011.

[13] Tenenholtz NA, Hammer PE, Fabozzo A, Feins EN, Del Nido PJ, Howe RD. Fast simulation of mitral annuloplasty for surgical planning. Lect Notes Comput Sci (including Subser Lect Notes Artif Intell Lect Notes Bioinform) 2013.

[14] Sturla F, Redaelli A, Puppini G, Onorati F, Faggian G, Votta E. Functional and biomechanical effects of the edge-to-edge repair in the setting of mi- tral regurgitation: consolidated knowledge and novel tools to gain insight into its percutaneous implementation. Cardiovasc Eng Technol 2015.

[15] Sturla F, Votta E, Onorati F, Pechlivanidis K, Pappalardo OA, Gottin L, et al. Biomechanical drawbacks of different techniques of mitral neochordal implan- tation: when an apparently optimal repair can fail. J Thorac Cardiovasc Surg 2015.

[16] May-Newman K , Yin FC . Biaxial mechanical behavior of excised porcine mitral valve leaflets. Am J Physiol 1995;269:H1319–27 .

[17] Kunzelman KS , Cochran RP . Mechanical properties of basal and marginal mitral valve chordae tendineae. ASAIO Trans 1990;36:M405–8 .

[18] Adams DH, Anyanwu AC, Rahmanian PB, Filsoufi FC, Adams AC, Anyanwu PB, Rahmanian F, Filsoufi DH. Current concepts in mitral valve repair for degener- ative disease. Hear Fail Rev 2006;11:241–57.

[19] Calleja A, Poulin F, Woo A, Meineri M, Jedrzkiewicz S, Vannan MA, et al. Quan- titative modeling of the mitral valve by three-dimensional transesophageal echocardiography in patients undergoing mitral valve repair: correlation with intraoperative surgical technique. J Am Soc Echocardiogr 2015;28:1083–92.

[20] [43] Ciarka A, Braun J, Delgado V, Versteegh M, Boersma E, Klautz R, et al. Pre- dictors of mitral regurgitation recurrence in patients with heart failure under- going mitral valve annuloplasty. AJC 2010;106:395–401.

Passive beating heart platform for transcatheter tricuspid valve treatments evaluation

M. Jaworek[1], M. Piola[1], F. Lucherini[1], G. Gelpi[2], C. Romagnoni[2], C. Antona[2], G.B. Fiore[1], R. Vismara[1].

[1] *Department of Electronics, Information and Bioengineering, Politecnico di Milano, Milan, Italy*
[2] *Cardiovascular Department, 'Luigi Sacco' General Hospital, Milan, Italy*

***Abstract*—Tricuspid valve (TV) treatment is challenging and new transcatheter techniques are emerging. We developed an in-vitro beating heart platform housing a porcine heart and featuring a model of functional tricuspid regurgitation. The platform was employed in evaluation of two TV treatments (transcatheter edge-to-edge technique and papillary muscle approximation) and provided quantitative hemodynamic parameters and enabled direct visualization of TV in pathological and post-treatment conditions.**

***Keywords*—tricuspid valve, in-vitro, mock loop, transcatheter.**

I. Introduction

FUNCTIONAL tricuspid regurgitation (FTR) involves tricuspid valve (TV) annulus dilation in antero-posterior direction and right ventricular papillary muscle displacement. All currently available TV treatments are annulus-level based only. Hence, gold-standard treatment, TV annuloplasty, was associated with recurrence risk in long-term due to unaddressed progressing right ventricular dilation [1]. Moreover, TV surgical treatment is debated and considered challenging as TV open heart surgery has high in-hospital mortality rate (10-25%) [2] and the population is aging. In this scenario, TV transcatheter treatments can be an attractive alternative and currently they are an absolute novelty. Considering also the complex biomechanical interaction between the transcatheter devices and TV apparatus, not only new treatments techniques should be developed, but also new specifically tailored platforms where these treatments can be assessed preclinically are needed.

The aim of this study was to (i) develop a passive beating heart platform housing porcine right heart and featuring controllable FTR experimental model and to (ii) employ the platform in evaluation of FTR treatments. Following treatments were tested: (a) transcatheter edge-to-edge (TE2E) technique (the most common transcatheter mitral valve repair technique, recently translated to TV) and (b) papillary muscle approximation (PMA) technique (a novel subvalvular treatment concept addressing ventricular dilation).

II. Methods

A. Passive beating heart platform

The general scheme of the system is presented in Fig. 1. It comprised a swine right heart (Fig. 1, a) actuated by a positive-displacement piston pump that reciprocated fluid (saline solution at room temperature) to and from the right ventricle by a trans-septal access (Fig. 1, b). The pulmonary artery was connected to the pulmonary impedance system (PIS) (Fig. 1, c), which outflow was in turn connected to an open-to-air chamber acting as a preload (Fig. 1, d). Direct visualization was enabled by a fiberscope (Fig. 1, e). The pulmonary impedance was modelled by a 3-element Windkessel, comprising characteristic resistance, peripheral resistance and compliance and was preliminarily dimensioned using analytical approach.

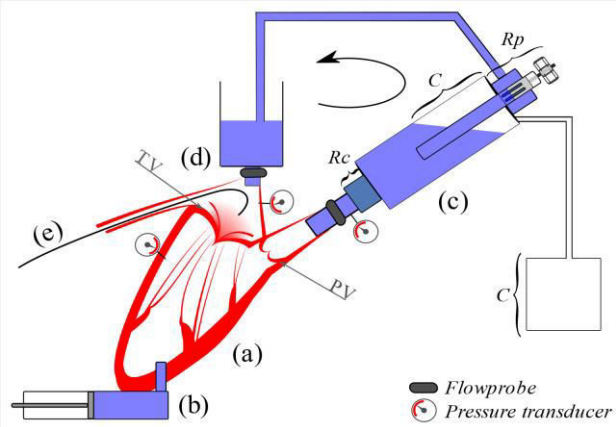

Figure 1 Scheme of passive beating heart platform: a: right porcine heart, b: pumping system, c: pulmonary impedance system, d: preload, e: fiberscope. The arrow indicates direction of fluid flow. R_C: Characteristic resistance, C: Compliance chamber (divided in two compartments), R_P: Peripheral resistance with adjustment mechanism. PV: pulmonary valve, TV: tricuspid valve.

B. FTR model

The experimental procedure for inducing the FTR exploited the tendency of the right ventricle and TV annulus to dilate under pressure in the experimental setup. Two adjustable bands, one placed at the level of the papillary muscles, the second one placed at the TV annulus level, could allow the control of the papillary muscle dislodgement and annulus dilation, thus adjusting TV functioning.

C. Treatments assessment

Porcine heart samples were housed in the passive beating heart platform and the pump was set to reproduce heart rate of 60 bpm and stroke volume of 70 mL. The two treatments were evaluated independently by comparing data obtained in pathological and post-treatment conditions. Treatments effects were evaluated in terms of hemodynamics (cardiac output, pulmonary artery pressure and mean systolic pressure drop across tricuspid valve).

TE2E was performed in 5 heart samples by clip placement between two TV leaflets at medial position (three possible grasping combinations: postero-septal, antero-posterior, antero-septal) – see Fig. 2.

PMA (see Fig. 3) was simulated in 6 heart samples by placing a surgical stitch in between posterior and anterior papillary muscles and reducing of the distance between the septal and free right ventricular wall by 60% in a controllable manner using an ad-hoc designed and 3D printed device.

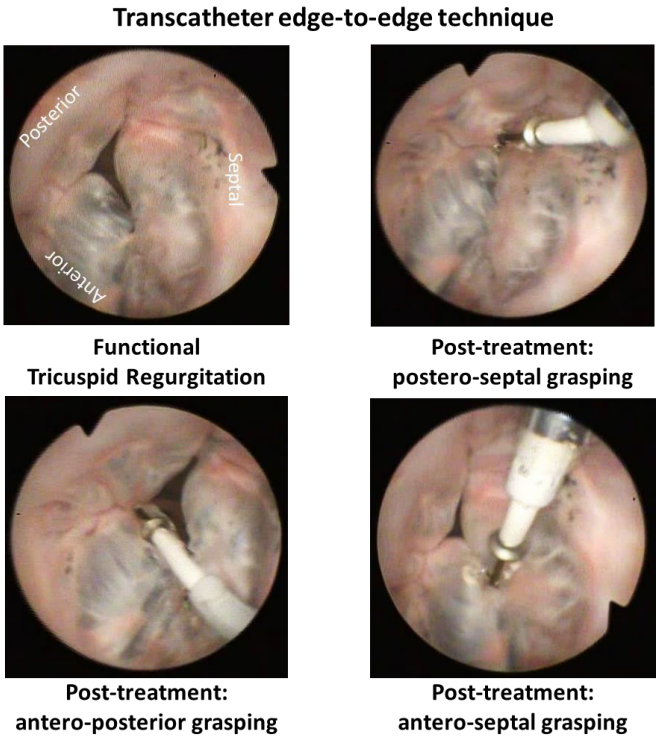

Figure 2 Direct visual feedback on tricuspid valve in mid systole (atrial view) and the evaluated clip grasping locations during transcatheter edge-to-edge treatment. Reduction of regurgitation area can be seen when the clip grasping engaged the septal leaflet.

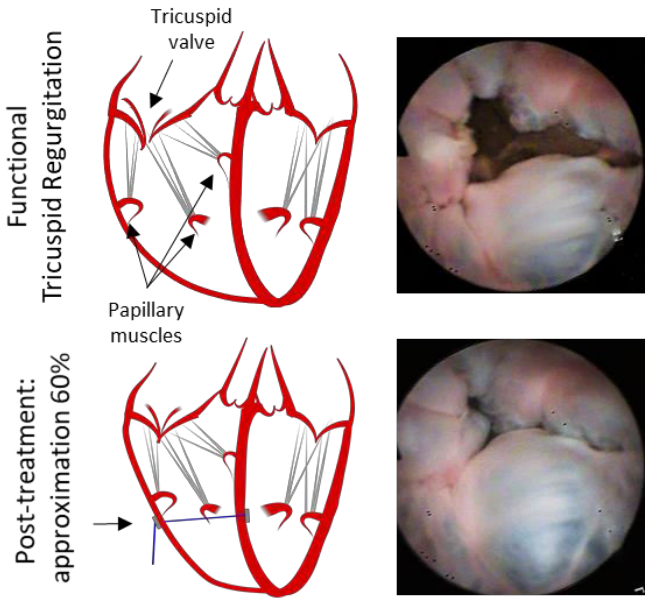

Figure 3 The concept of the papillary muscle approximation technique (first column) and direct fiberscopic visualization of tricuspid valve in mid systole in the atrial view (second column) at pathological (upper row) and post-treatment (lower row) conditions.

III. Results

A. TE2E technique

Grasping of septal leaflet along with either anterior or posterior leaflet resulted in significant increase in cardiac output ($p<0.05$), whereas antero-posterior grasping did not alter the hemodynamics. The treatment did not induce any significant increase of mean diastolic transvalvular pressure drop. Detailed results are reported in Table I.

TABLE I
TE2E TECHNIQUE

Parameter	FTR	Post-treatment		
		A-P	A-S	P-S
Cardiac Output, L/min	1.6±0.2	1.9±0.3	2.4±0.5 *	2.2±0.5 *
Mean pulmonary artery pressure, mmHg	20.8±1.4	21.5±2.6	23.1±2.7	22.3±4.1
Mean diastolic pressure drop across TV, mmHg	2.0±0.8	1.8±0.6	1.3±1.0	1.6±1.1

Hemodynamic assessment of transcatheter edge-to-edge (TE2E) treatment technique: Comparison between pathological (FTR) and post treatment conditions after clip placement in between anterior and posterior (A-P), anterior and septal (A-S) and posterior and septal (P-S) tricuspid valve leaflets. * statistical significance vs. FTR ($p<0.05$).

B. PMA technique

The treatment induced statistically significant changes in cardiac output after 60% of PMA ($p<0.05$) and did not cause any significant increase of pressure drop across TV. Detailed results are reported in Table II.

TABLE II
PMA TECHNIQUE

Parameter	FTR	Post-treatment
Cardiac Output, L/min	2.4±0.7	3.0±0.7 *
Mean pulmonary artery pressure, mmHg	15.4±3.1	18.3±3.7
Mean diastolic pressure drop across TV, mmHg	1.4±0.8	1.0±1.1

Hemodynamic assessment of right ventricular papillary muscle approximation (PMA) technique: comparison between pathological (FTR) and post treatment conditions. * statistical significance vs. FTR ($p<0.05$).

IV. Conclusion

The developed experimental platform provided a unique setting tailored for TV transcatheter approaches evaluation. It enabled realistic assessment of upcoming FTR treatments in a controllable and reliable manner. Moreover, the performed treatment evaluations provided valuable insights with a translational potential to the clinic.

The treatments were feasible and effective in an in-vitro model. It was confirmed that TE2E procedural success can be expected when the septal leaflet is involved in the grasping. It agrees with the biomechanical point of view as one of the TV leaflets (posterior or anterior) involved in TV annulus and ventricular dilation was grasped along with the septal one which is proximal to mechanically constrained septum. The treatment did not increase significantly the diastolic pressure drop across TV. PMA proof-of-concept results demonstrated

that this technique can address ventricular dilation and can restore TV coaptation by reducing the tethering of TV leaflets. It encourages to develop a dedicated transcatheter device.

ACKNOWLEDGEMENT

This work was supported by the European Commission within the Horizon 2020 Framework through the MSCA-ITN-ETN European Training Networks (project number 642458) and by Fondazione per la Ricerca in Cardiochirurgia ONLUS, Milano, Italy. The authors would like to thank P. Romitelli (Abbott Vascular International) for the technical support.

REFERENCES

[1] S. Fukuda, et al., "Determinants of recurrent or residual functional tricuspid regurgitation after tricuspid annuloplasty", Circulation, 114(1Suppl), pI582-7, 2006

[2] M.Taramasso, et al. "The growing clinical importance of secondary tricuspid regurgitation", *Journal of American College of Cardiology* 59(8), p703-710, 2012

Internal fixation of spinal metastasis: a finite element analysis of a new technique

L. La Barbera[1], A. Ferrari[1], A. Cianfoni[2,3], D. Distefano[2], G. Bonaldi[4], and T. Villa[1]
[1] *LaBS, Dept. of Chemistry, materials and Chemical Engineering "G. Natta", Politecnico di Milano, Milan, Italy*
[2] *Dept. of Neuroradiology, Neurocenter of Southern Switzerland, Lugano, Switzerland*
[3] *Dept. of Neuroradiology, Inselspital; UniBern, Bern, Switzerland*
[4] *Neuroradiology, Pope John XXIII Hospital, Bergamo, Italy*

***Abstract*— The surgical treatment of severe spinal metastasis is directed at the stabilization of the affected vertebra restoring its load bearing capability and minimising the risk of vertebral collapse. While very invasive posterior fixation is considered the preferred option, a new internal fixation technique has been recently proposed based on vertebral body stents, cannulated pedicle screws and bone cement injection.**

The present finite element study describes the biomechanical effects due to the presence of a lithic defect involving an increasing amount of vertebral volume on surrounding bony structures. Moreover, the new internal fixation technique is successfully compared to the clinical gold standard, to evaluate the biomechanical implications and potential advantages.

***Keywords*—Spine biomechanics, Spine metastasis, Internal fixation, Finite element model.**

I. Introduction

THE metastatic stage of tumour evolution often involves the formation of lithic regions within the vertebral bone, where the healthy tissues degenerate towards a fibrotic structure. In this condition, the quality of life of the patients', already severely invalidated by heavy and periodic chemotherapical treatment, could be furtherly impacted by the occurrence of very likely vertebral fractures.

Although very invasive, posterior external fixation represents the first surgical option to shield the metastatic vertebra, otherwise highly exposed to collapse. A new internal fixation technique has been recently proposed, based on vertebral body stents, bone cement injection to prevent vertebral collapse and a monolateral cannulated pedicle screw anchoring the anterior column to the neural arch (Fig. 1). The new technique promises to shorten hospitalization stays and the recovering time after surgery, surely improving the patients' quality of life.

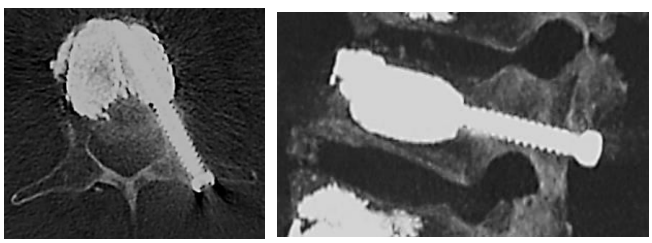

Top view *Lateral view*

Fig. 1: Clinical CT images of a lumbar vertebra treated with the new internal fixation technique (Courtesy of A.C.). Transversal (left) and sagittal (right) slices.

The first aim of the current study was to investigate how the biomechanics of an intact spine segment is altered due to the presence of a lytic defect. The second aim was to compare whether the new internal fixation technique can restore the strain on the surrounding bony structures compared to traditional posterior fixation for the treatment of highly unstable lithic vertebrae.

II. Materials and Methods

A. Metastatic models

A non-linear finite element model (FEM) representing L1-S1 spine segment of a healthy human male (age 40) without any spinal pathology nor defects was used [1]. The model, complete of vertebral bodies, intervertebral discs and ligaments, has already been validated by comparison with experimental in vitro measurements both regarding the kinematics, the overall compressive stiffness and the strains reached on the bony parts [2].

In order to exclude any influence of the boundary condition on the vertebra level of interest, the lithic defect was simulated in L3 as a low-modulus (5 MPa) linear elastic isotropic region [3] involving different bony structures:

a) 2/3 of the middle part of the vertebra (Fig. 2.a),

b) 2/3 of the middle part of the vertebra with involvement of the right pedicle (Fig. 2.b),

c) 100% of the trabecular bone with involvement of the right pedicle (Fig. 2.c),

d) 100% of the trabecular bone with cortical bone disruption,

e) 100% of the trabecular bone with cortical bone disruption with involvement of the right pedicle.

a) *b)* *c)*

Fig. 2: Representation of the metastatic models (a-c) highlighting the lithic defect (red) obtained assigning poor material properties to specific elements within L3 vertebra.

B. Models of alternative surgical techniques

To restore the load bearing capacity of the segment with lithic defect at L3 different surgical scenario were considered (Fig. 3):

b.1) model b with low-volume (7ml) of bone cement filling,

assumed to have a 2.5 GPa elastic modulus and a monolateral (right side) titanium pedicle screw (2B1 SRL, Milan, Italy). The result of bipedicular cement injection around the cannulated screw was assumed to have a roughly cylindrical distribution according to intraoperative imaging (Fig. 1).

c.1) model c with high-volume (about 20ml) of bone cement assuming optimal endplate-to-endplate filling and bipedicular bone cement injection with a monolateral titanium pedicle screw (2B1 SRL, Milan, Italy),

b.f) model b.1 with rigid posterior fixation,

c.f) model c.1 with rigid posterior fixation,

f) rigid posterior fixation of model b with pedicle screws spanning L2 and L4 vertebrae and a 5.5mm titanium spinal rod (standard clinical treatment).

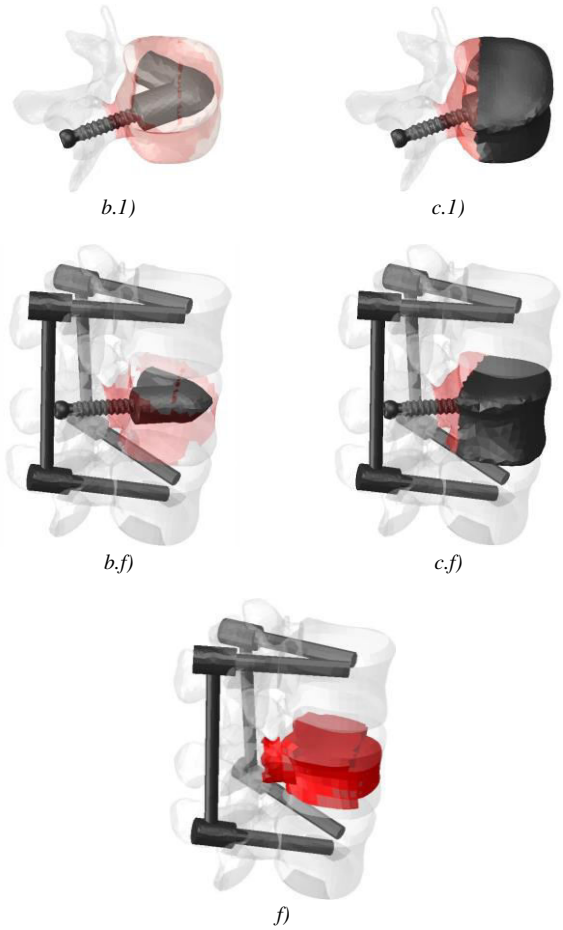

Fig.3: Representation of the models of alternative surgical techniques highlighting the injected cement (grey) within the lithic regions of L3 (shaded red) and details of the new unipedicular screw approach first without (b.1 and c.1) and then with posterior fixation from L2 to L4. For the sake of comparison stand-alone posterior fixation of the metastatic vertebra (red) is also considered (f). Surrounding structures are represented in all pictures (shaded light grey).

All models were loaded with: (i) an axial follower load of 500N representative of standing [4], and (ii) a 1175N load exceeding the physiological condition, well below the static strength of a metastatic spine segment [5]. Regarding the model's boundary conditions, the lower part of S1 vertebra was considered to be encastred.

The axial stiffness of the lithic vertebra was calculated to evaluate the loss of stability due to the presence of a lithic defect involving different structures, as well as the capability of each surgical technique in restoring adequate stability.

The principal strains distribution predicted on centrally-located element-sets on the bony structures (superior and inferior endplates, posterior and anterior cortical walls) were analysed in terms of point clouds and median values. Principal strain criterion was considered as a reliable estimate of fracture risk on cortical bone [6].

To compare alternative surgical approaches (i.e. b, b.1, b.f, f and c, c.1, c.f and f), a non-parametric Wilcoxon paired-samples test was used to determine statistical difference in median values (a significance level p of 0.05 was assumed).

III. Results and Discussion

A. *Metastatic models*

i) The intact vertebra exhibited an axial stiffness of 12.8kN/mm and the median strains remained relatively low on every bony structure (range: -0.016 to 0.004%).

A lithic defect involving 2/3 of the trabecular volume and the pedicle (b) dramatically decreased the stiffness of L3 vertebra to 4.1kN/mm; while the strains slightly increased on the endplates (range: -0.052 to 0.055%), on the posterior wall (-0.041 to 0.023%), as well as on the anterior cortical wall (-0.020 to 0.009%). A lithic defect involving 100% of the trabecular volume (c) furtherly decreased the stiffness of L3 vertebra to 3.3kN/mm; while the strains significantly increased on the endplates (range: -0.064 to 0.070%), on the posterior wall (-0.043 to 0.026%), as well as on the anterior cortical wall (-0.027 to 0.064%). The disruption of the cortical shell (d, e) produced a dramatic loss of vertebral stability (287N/mm) with a general strain increase beyond the bone strength (0.8%). Involvement of one pedicle (b, e) produced negligible variations on variables of interest.

ii) The predicted axial stiffness values are in agreement with the range of values measured by Groenen et al. [5], who tested until failure human thoracolumbar spine segments, both as intact and after the creation of an artificial bony defect.

B. *Models of alternative surgical techniques*

The new internal fixation technique effectively restored the axial stiffness of L3, especially with the higher cement injection (7.8 and 33.9kN/mm, respectively with 7 and 20ml); posterior fixation shielded the lytic vertebra, resulting in a lower axial displacement than with the internal fixation. The new technique with low-injected volume (b.1) was effective in reducing the strains on the superior EP and the posterior wall (-0.025 to 0.015%) with a percentage reduction of median values of 72% and beyond 39%, respectively ($p<0.05$, Fig. 4).

The new technique with high-injected volume (c.1) was effective in reducing the strains on every bony structure (-0.015 to 0.005%, $p<0.05$) with a percentage reduction of median values beyond 94% for the superior EP, beyond 64% for the anterior wall and beyond 65% for the posterior one ($p<0.05$, Fig. 4).

The supplementation of the new technique with posterior fixation (b.f) lead only to a further marginal decrease up to 10% on the superior EP and to 24% on the posterior cortical wall considering the low-cement injection (Fig. 4).

Particularly with the high-volume injection, the new

technique produced significantly lower strain values compared to posterior fixation alone (range: -0.043 to 0.044%, $p<0.05$, Fig. 4).

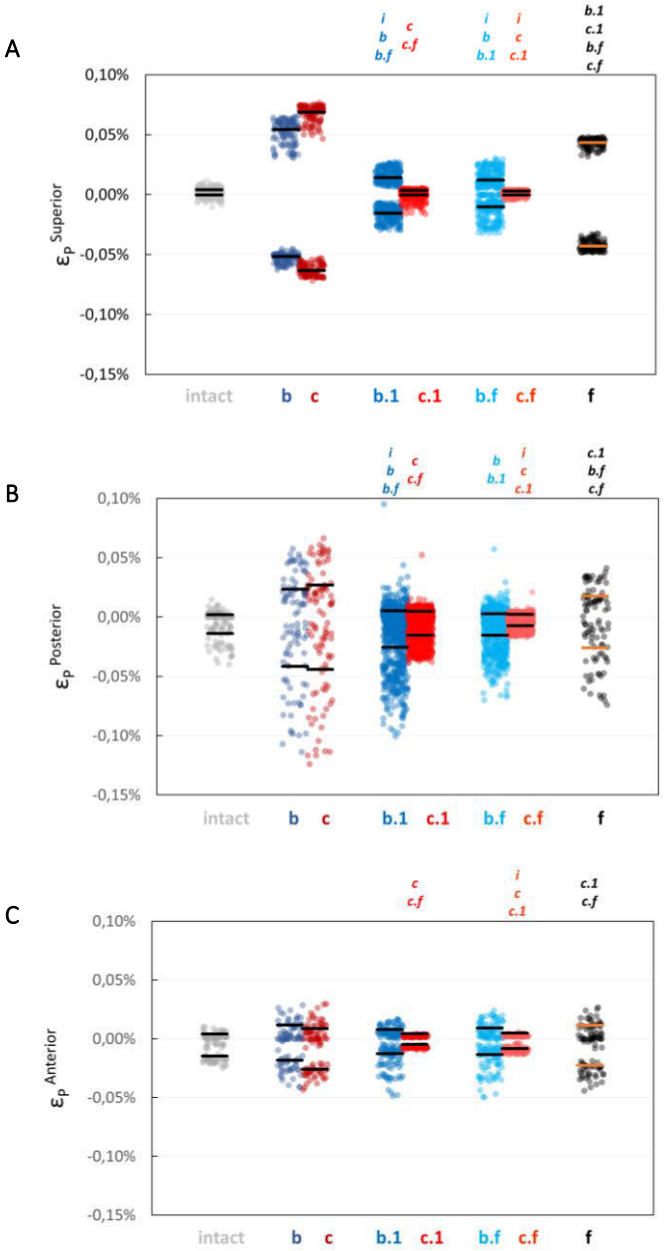

Fig.5: Point clouds of principal strains distributions on the superior end-plate of L3 (A), on the posterior (B) and anterior cortical (C) walls. The black line highlights the median value of each distribution, while significant difference ($p<0.05$) both on tensile and compressive values compared to the indicated groups is reported on top of each graph (e.g. "b" on top of the strains distribution predicted for the superior EP in model b.1 indicates a significant difference compared to model "b").

C. *Limitations*

It is important to remind that the current approach does not catch inelastic phenomena and failure modes related to vertebral body collapse. Moreover, the shape/volume of L3 vertebra were assumed to be equal to the intact condition. This choice, may more closely represent a preventive treatment of the vertebra, instead of a partially collapsed condition. Nevertheless, the current approach has the advantage to finely control specific study parameters (e.g. defect volume, material parameters, loading condition), that may present a wide variability in a real clinical setting and may imply a confounding effect on the results.

IV. Conclusion

The new internal fixation technique was effective in restoring the load bearing capacity of the lithic vertebra, while significantly reducing the strain on the surrounding bony structures. High injected cement volumes seemed to have the most beneficial effects. The present study provided a solid rationale to support the usage of the new internal fixation technique for the treatment of highly unstable lithic vertebrae. In addition, posterior fixation alone demonstrated to be less effective than the new minimally invasive technique, while not being justified as an integration of cement injection.

Acknowledgement

The authors gratefully acknowledge Fondazione per la Ricerca Ospedale Maggiore (FROM, Bergamo, Italy) who funded the present study.

References

[1] Ottardi C, Galbusera F, Luca A, Prosdocimo L, Sasso M, Brayda-Bruno M, Villa T. Finite element analysis of the lumbar destabilization following pedicle subtraction osteotomy. Med Eng Phys 2016. 38(5):506-9. doi: 10.1016/j.medengphy.2016.02.002.

[2] Ottardi C, Ph.D. Thesis. Politecnico di Milano. December 2015.

[3] Whyne CM, Hu SS, Lotz JC. Parametric finite element analysis of vertebral bodies affected by tumors. J Biomech. 2001 Oct;34(10):1317-24.

[4] Rohlmann A, Zander T, Rao M, Bergmann G. Applying a follower load delivers realistic results for simulating standing. J Biomech. 2009 Jul 22;42(10):1520-6. doi:10.1016/j.jbiomech.2009.03.048.

[5] Groenen KHJ, Janssen D, van der Linden YM, Kooloos JGM, Homminga J, Verdonschot N, Tanck E. Inducing targeted failure in cadaveric testing of 3-segment spinal units with and without simulated metastases. Med Eng Phys. 2018 Jan; 51:104-110. doi:10.1016/j.medengphy.2017.11.007.

[6] Schileo E, Taddei F, Cristofolini L, Viceconti M. Subject-specific finite element models implementing a maximum principal strain criterion are able to estimate failure risk and fracture location on human femurs tested *in vitro*. J Biomech 2008; 41:356-367. doi:10.1016/j.jbiomech.2007.09.009.

Biomechanical analysis of different treatments for Kienböck's disease

A. Aimar[1], E. Camus[2], C. Bignardi[3], A. Audenino[3],F. Schuind[4], B. Innocenti[1]
[1] *BEAMS Department (Bio Electro and mechanical Systems), Universitè Libre de Bruxelles, Brussels, Belgium*
[2] *SELARL Chirurgie de la Main, polyclinique du Val de Sambre, Maubeuge, France*
[3]*DIMEAS Department, Politecnico di Torino, Torino, Italy*
[4]*Orthopedic department Höpital Erasme, Universitè Libre de Bruxelles, Brussels, Belgium*

***Abstract*— The *Kienbock's disease* is a condition in which one of the small bones of the wrist, the Lunate, loses its blood supply and dies, causing pain and stiffness with wrist motion. In the late stages of the disease, the bone collapses, shifting the position of other bones in the wrist. This shifting eventually leads to degenerative changes and osteoarthritis in the joint. While the exact cause of this uncommon disease isn't known, a number of treatment options are available with different clinical result. This study proposes a biomechanical analysis of seven current surgical treatments for Kiemböck's disease on a full 3D patient-specific finite element model of the wrist.**

Each model, representing a different surgical treatment for the pathology underwent the same physiological load and the stress distributions, contact areas and contact forces between the carpal bones were analysed and compared among the different treatments and with respect to the physiological wrist.

The results clearly show that two of the seven techniques analysed are advantageous treatments for different reasons: the Capitate and Hamate shortening osteotomy lead to a condition in which the Lunate is unloaded; the Camembert-Sennwald osteotomy is the one closest to a physiologic configuration regarding the contact forces distribute between each bone considered. From a biomechanical point of view such treatment are suggested with respect to the other.

***Keywords*- Wrist, Kiemböck, FEM, Patient specific.**

I. INTRODUCTION

The anatomy of the wrist joint is extremely complex, probably the most complex of all the joints in the body. The wrist is actually a collection of many joints and bones. These joints and bones let us use our hands in lots of different ways. For this reason the wrist must be extremely mobile to give our hands a full range of motion and at the same time the wrist must provide the strength for heavy gripping. The wrist is made of eight separate small bones, called the *carpal bones*. The *lunate* is one of these bones.

The Kienböck's disease is a rare and debilitating wrist condition that can lead to chronic pain and dysfunction. It happens when the lunate bone becomes damaged. Doctors have not determined exactly what causes Kienböck's disease. A number of factors seem to be involved. Usually the patient has injured the wrist. The injury may be a single incident, such as a sprain, or a repetitive trauma. But the injury alone does not seem to cause the disease.

The way that blood vessels supply the lunate is thought to play a role in Kienböck's disease. A bone with a limited blood supply may be more at risk of developing the disease after an injury and may became damage.

In addition, other bones around the lunate may play a role in the disease too. The length of the ulna, the bone of the forearm on the opposite side of the thumb, may be a factor. When the ulna is shorter than the radius, the lunate bone absorbs more force when the wrist is used for heavy gripping activities. Over time, this extra force may make it more likely for a person to develop Kienböck's disease. The extra forces make a person more likely to injure the lunate or the blood vessels around it as a result.

Kienböck's disease is also sometimes found in people with other medical conditions that are known to damage small blood vessels of the body. Whatever the cause, the lunate bone develops a condition called *osteonecrosis*. In osteonecrosis, the bone dies, usually because it's not getting enough blood.
The primary symptoms of Kienböck's disease are pain in the wrist and limited wrist motion. Pain may vary from slight discomfort to constant pain. In the early stages there may be pain only during or after heavy activity using the wrist. The pain usually gets slowly worse over many years. The wrist may swell. The area over the back of the wrist near the lunate bone may feel tender. You may not be able to move your wrist as much as normal or grip objects as well.

There are different treatment options that include operations designed to decompress the lunate bone. Doing this may allow the bone to heal and revascularize, or it may at least slow the progression of the disease. Only few biomechanical studies are currently available for the analysis of different surgical techniques, aimed to treat the Kiemböck's disease, but they analysed only few treatments or a limited wrist region or used simplified bi-dimensional model [2,3]. This analysis aims to develop a three-dimensional patient specific model for the physiologic wrist and each surgical technique to compare different osteotomies and depending on the outcomes knows which is more advantageous and efficient to reduce the disease.

II. MATERIAL AND METHOD

A. Geometry

A 3D patient-specific model of a wrist was developed based on CT scans of a healthy patient (ScanIP, Simpleware). During the segmentation process different masks were used in order to recognize each bone taken in account in the study.
Apart of the native model, seven different osteotomies models were defined:

- Neutral shortening of the Radius: 2-3 mm length shortening in front of the Lunate and Scaphoid;

- Radial shortening of the Radius: 2-3 mm lateral closing wedge osteotomy;
- Ulnar shortening of the Radius: 2-3 mm medial closing wedge osteotomy;
- Capitate shortening: 2 mm shortening of the Capitate;
- Capitate and Hamate shortening: 2 mm shortening of the Capitate and the Hamate;
- Camembert shortening: 2-3 mm shortening of the Radius in front of the Lunate from the ulnar side, proximally to the distal radioulnar joint, distally to the scapholunate crest of the radial glenoid;
- Camembert-Sennwald shortening: in case the ulnar variance is neutral or positive (the length of the Ulna is equal or major than the Radius one) the Camembert shortening is associated to a metaphysal ulnar oblique shortening.

Each model replicates a different surgical treatment, defined according to surgical practice (yellow parts in figure 3 show the different techniques).
The analysis was performed using finite element modeling (Abaqus, Dassault).

B. *Materials*

Materials were defined according to previous literature studies [1,2,3]. The mechanical properties of the materials are reported in Table I.

TABLE I
MATERIALS

Materials	*Young's Modulus*	*Poisson's coefficient*	*Density*
Subchondral bone bone	1000 MPa	0.2	1.75 g/cm^3
Cortical bone	18000 MPa	0.2	1.8 g/cm^3
Cancellous bone	500 MPa	0.2	1.3 g/cm^3
Cartilage	15 MPa	0.4	1.1 g/cm^3
Triangular fibrocartilagineous complex	52 MPa	0.4	1.25 g/cm^3

The complex configuration of ligaments was modelled, according to the literature, as springs [4]. Totally 47 ligaments were insert in the different models to reproduce the stability of the wrist joint (Fig.1). They were characterised with a low stiffness to reduce as much as it possible the stresses in compression to the bones. In Table II the modelling of the ligaments.

TABLE II
MATERIALS

Materials	*Stiffness*
Ligament	1 N/m

Fig.1 Ligaments representation.

C. *Load and Boundary conditions*

Load and boundary conditions were defined according to previous literature studies [5].

Fig.2 Loads and constraints representation.

In particular, were applied five different loads on the transverse surface of each Metacarpal bone as follow:

- 1st Metacarpal load: 12 N;
- 2nd Metacarpal load: 20 N;
- 3rd Metacarpal load: 25 N;
- 4th Metacarpal load: 25 N;
- 5th Metacarpal load: 20 N.

The Radius and Ulna bones were keep fixed. Both the configuration of loads and the fixation of Radius and Ulna aimed to simulate the compressive action of the wrist tendons, which imposed a proximal traction movement to the metacarpal bones that made in compression the rest of the carpal bones, especially the Lunate.

Fig.3 Loads and constraints representation.

D. *Bones contact and regions of interest definition*

To simulate the interaction between all the carpal and metacarpal bones considered in the model a general contact was defined. Later different surfaces were identified, equally in each model, with respect to the contact taken in account for the analysis. On these surfaces the contact area and contact force were extracted.

E. *Mesh*

A quadratic mesh was defined with different sizes according to the regions of interest. The Fig.4 shows the mesh characterization of the physiologic wrist model.

Fig.4 Mesh of the Native wrist model.

F. *Simulation*

A dynamic explicit simulation was chosen due to the fact that the computational power needed in a static one was too high. The simulation period of 1.2 second was divided in two steps: in the first one the loads applied to the metacarpal bones linearly increased from 0 N to the value previously defined (from the beginning to 1 second simulation); in the second one the loads were kept constant and the bones were free to position according to the limit imposed by the ligaments (from 1 second to the end).

III. Results

In this study, the bones contact area, bone contact force and stress distribution were extracted and compared among the different models.

A. *Comparison between different models result*

Results, reported only for contact forces, demonstrate that, with respect to the control configuration (physiological, red box in figure 5), all the osteotomies induce a change in the wrist biomechanics (both in term of contact area/force and bone stress). Among the different treatments, the Capitate and Hamate cut (green box in figure 5) and the Camembert-Sennwald cut (blue box in figure 5) induce a lower force and stress on the Lunate bone and, therefore, could be beneficial for the treatment of the Kienböck's disease. However, the Camembert-Sennwald cut, in addition to reducing more the force and stress on the Lunate than the Capitate and Hamate cut, it also preserves more the interaction between the carpal bones. In fact, the major risk of the Capitate and Hamate cut is to generate sharp edge after the osteotomy that during the movement of the wrist could damage the nearby bones and cartilages.

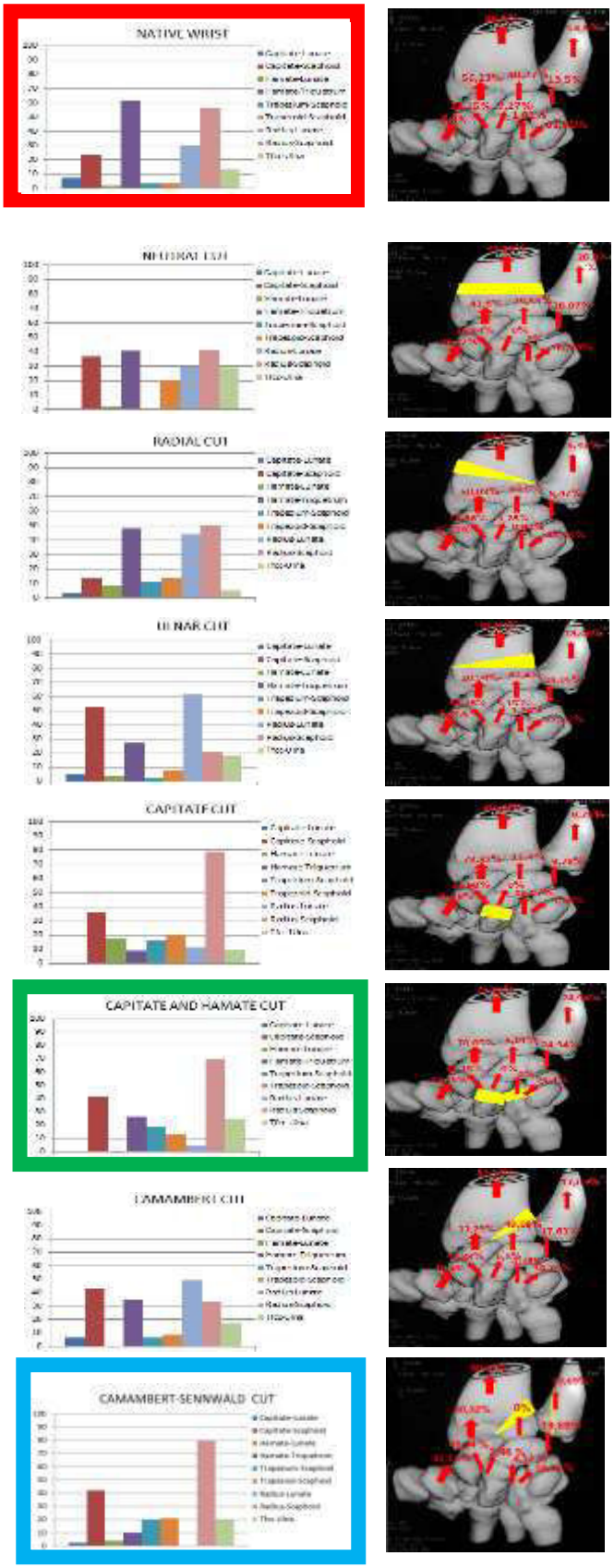

Fig.5 Contact forces distribution in each model.

IV. CONCLUSION

Different surgical procedures are currently available to treat the Kienböck's disease. In this study we demonstrate that all these treatments induce a change on wrist biomechanics, both in terms of contact force and area and bone stress. Results show that the Capitate and Hamate cut and the Camembert-Sennwald cut induce the lower stress on the Lunate bone. However, the risk to alter more the interactions between the nearby bones and the one involved in the osteotomy is higher for the Capitate and Hamate cut than the Camembert-Sennwald cut.

The results obtained from the study are also in agreement with clinical findings [6-7]. The patients follow-ups show the decreasing of the wrist illness and the complete healing of the Lunate bone. This may represent a possible way to validate this study.

The Camembert-Sennwald osteotomy is finally preferable in terms of wrist biomechanics.

V. LIMITS AND FURTHER IMPROVEMENTS

This study aimed to be a starting point for knowing the effectiveness of different treatments for the Kienböck's disease during a dynamic simulation. Testing different position configurations of the wrist (ex. different flexion angle of the joint) or different dynamic movements, like the flexion-extension of the wrist, could be interesting to better know how the wrist reacts to different treatments, how the stress distribution changes according to the positions and the ligaments reaction.

Finally, another improvement of the model could be reached in a more accurate estimation of materials involved with experimental tests: in this model, for example, all the ligaments were modelled as springs with all the same stiffness. An experimental tensile test based on cadaver specimens could be useful to recognise the differences between the contribution of each ligaments for the wrist stability and to obtain a more precise estimation of their mechanical properties. It's important to remember that the ligaments mechanical properties are highly dependent to the patient specific.

It's clear that lots of improvements can be adopt in the model in order to reach a configuration every time closer to the physiological one.

REFERENCES

[1] Modifications to the mechanical behaviour of the wrist after fracture of the scaphoid. Modeling by finite element analysis, P. Ledoux, D. Lamblin, R. Targowsky.
[2] A finite element analysis of Kienböck's disease, P. Ledoux, D. Lamblin, A. Wuilbaut, F. Schuind.
[3] Finite element analysis of osteotomy treatment for Kienbock's disease, G. Yang, K.A. Partridge, A. Abdel-Mohti, A.J. McMullen, H. Shen.
[4] Three-Dimensional imaging of the carpal ligaments, Mitsuhiko Nanno, Rita M. Patterson, Steven F. Viegas.
[5] Assessing finger joint biomechanics by applying equal force to flexor tendons in vitro using a novel simultaneous approach, T. Yang, S. Lu, W. Lin, K. Zhao, C. Zhao, K. An, I. Jou, P. Lee, L. Kuo, F. Su.
[6] Surgical Technique of a Radial Wedge "Camembert" Osteotomy in Kienböck Disease, E. J. Camus, L.V. Overstraeten.
[7] Clinical and MRI evaluation of Kienböck Disease treated by ''Camambert'' radial osteotomy, E. J. Camus, L.V. Overstraeten.

Towards non-invasive assessment of human aortic tissue microstructure: Diffusion Tensor Imaging for collagen fiber detection

E. Vignali[1,2], N. Martini[3], P. Losi[4], K. Capellini[1], D. Della Latta[3], F. Di Bartolo[1,2], L. Landini[2], V. Positano[1] and S. Celi[1]

[1] *BiocardioLab, Bioengineering Unit, Fondazione Toscana "G. Monasterio", Heart Hospital, Massa*

[2] *Department of Information Engineering, University of Pisa, Pisa*

[3] *Bioengineering Unit, Fondazione Toscana, "G. Monasterio", Heart Hospital, Massa*

[4] *Biomaterial laboratory, Institute of Clinical Phisiology, IFC-CNR, Pisa*

***Abstract*—Diffusion Tensor Imaging (DTI) is a non-invasive imaging technique that provides information on the tissue microstructure by evaluating the diffusion of water molecules. This technique allows to investigate the organization of fibers that compose a biological tissue, thus permitting to obtain information on tissue microstructure in-vivo non-invasively. In this work, five fresh human aortic samples of dilated ascending aorta were imaged in 3T scanner with a diffusion weighted sequence. In order to analyse the DTI images, firstly different commercial software have been compared in term of usability, data processing and information extraction capability; secondly, a specific custom workflow has been developed. Different scan parameters on various DTI indices have been tested and compared in terms of sensibility with respect to histological investigation. This study points out the feasibility to use DTI technique with a whole body Magnetic Resonance Imaging (MRI) machine to study fibre orientation and distribution in cardiovascular diseases.**

***Keywords*—DTI, Tissue Micromechanics, Aorta.**

I. INTRODUCTION

The arterial wall consists of extracellular matrix (ECM) and several types of cells organized into different layers [1]. Collagen is the major structural compound of the ECM, its potential to form complex microstructures is pivotal to grant the vessel mechanical characteristics [2]. Given this, defining the collagen microstructure in human aorta using a non-invasive method might be the key to better understand aortic tissue mechanics. In literature, small-angle scattering (SALS) methods have been used as an alternative to the light microscopy [3]. Small-angle X-ray scattering (SAXS) seems to be capable to reveal a relation between fibers orientation and external load in nano-scale [4]. SALS method has also been employed for micro-scale investigations of collagen organization in a tissue [5]. It should be noted that techniques of nonlinear optics such as multi-photon excited fluorescence (MFM) may also be engaged in histomorphometrical analysis of arterial wall. Wang et al. [6] combined MFM with coherent anti-Stokes Raman scattering, which allows chemically selective imaging in carotid artery extracellular matrix inspection. Also Zoumi et al. [7] reported MFM to be suitable within histological analysis of coronary arteries. Recently, the Magnetic Resonance Imaging (MRI) with the Diffusion Tensor Imaging has been proposed as a suitable imaging method for studying the fibrous structure of the aorta non-invasively [8], [9], [10]. Currently, only one DTI study is reported on human aorta [11].

Diffusion tensor imaging (DTI) is an imaging modality that provides information on the directional anisotropy of water diffusion through the evaluation of a diffusion matrix [12]. The water molecules motion is normally random and isotropic, but the presence of fibers generates preferential diffusion directions parallel to the fiber orientation. According to this assumption, the diffusion matrix eigenvector with the largest eigenvalue is considered to represent the local diffusion direction, corresponding to the fiber orientation. The aim of this study is to evaluate the accuracy of DTI technique on human ex-vivo samples by using a whole-body MRI machine and by investigating the influence of different scan parameters.

II. MATERIALS AND METHODS

A. Sample Preparation, DTI Protocol and histology

Whole fresh samples of dilated ascending aorta were collected from five patients undergoing elective surgical repair. Samples have been stored in physiological solution at 4° after excision and scanned within 3 hours. During the DTI acquisition samples were placed into a custom-designed chamber filled with physiological hydrogel. In order to avoid translation and rotation under the effect of the self weight, the external borders of the sample were sutured to the chamber.

MRI acquisitions were performed on a 3T Philips Ingenia MRI scanner. First, an anatomical T1-weighted dataset was acquired with a 3D gradient echo (GRE) sequence with TE/TR 3.4/7.8, flip angle 8°, 90 slices, matrix 128x128, voxel size 0.5x0.5x0.5 mm^3. Then, DTI images were acquired using a fat-saturated multi-shot echo planar imaging (EPI) sequence to reduce T2* blurring and Nyquist ghosting effects. Eight slices were acquired orthogonal to the vessel.

To investigate the influence of different acquisition parameters, four DTI protocols were adopted by varying: spatial resolution, sensitivity parameter (b-value), number of diffusion gradient directions (NDD) and number of signal averages (NSA) as

reported in Table I.

TABLE I: Parameters for DTI protocols

	Res $[mm]$	*B-Value* $[mm^2/s]$	*NDD*	*NSA*	*Scan Time*
P_1	0.65x0.65x1.5	1000	15	16	$2H59'$
P_2	0.65x0.65x1.5	500	32	8	$2H36'$
P_3	0.75x0.75x2	500	32	8	$2H02'$
P_4	0.75x0.75x2	1000	15	16	$2H32'$

To obtain a qualitative assessment of the tissue compaction, aortic tissue were evaluated by histology after the DTI scan process. Two strips were harvested from anterior and posterior region. Samples were fixed in 3.7% formaldehyde in phosphate buffered saline. Subsequently, the strips were detached from the frame and embedded in paraffin transversely. Tissues were sectioned at 10 μm and stained with Haematoxylin and Eosin (H&E, Sigma, USA) to visualize the general tissue morphology, with with Masson's trichrome to highlight fibrillar collagen and Van Gieson to highlight elastin. The staining was visualized under a Zeiss light microscope (Carl Zeiss). Magnification was set to 600. Images from the Pico Sirius Red-stained sections were acquired using appropriate polarizing optics.

B. Custom Workflow

The DTI data processing platform was developed in Python and it presented a graphical user interface in order to perform an entire DTI workflow, from the import of diffusion images to the fiber tracking, in a simple and fast way. The developed software platform allowed not only a qualitative analysis (such as visualization of fiber tracking results), but also a quantitative analysis of some parameters estimated from the fiber distribution. The platform is composed by 6 modules, each one performing a particular step of the DTI pipeline, as follows:

1) conversion from DICOM to NIfTI format;
2) eddy current distortion correction;
3) automatic segmentation;
4) diffusion tensor calculation with display of scalar maps;
5) fiber tractography;
6) quantitative and statistical analysis on the fiber tracking results.

C. Data Analysis

DTI data were postprocessed after acquisition. In order to analyze the fiber orientation, the coordinates were converted from the image reference system to a cylindrical coordinate system and quantitative assessment of the four different protocols was carried out by evaluating: the SNR of the images without diffusion gradients (b0-images), the SNR of diffusion-weighted (DW) images, the fractional anisotropy (FA). Fiber tractography was performed on the DTI data by a custom-developed software program based on maximum eigenvalue evaluation. A deterministic algorithm reporting the number of detected fibers was implemented with the following stopping criteria for fiber identification: minimum FA equal to 0.1, max angle change of 45° and minimum fiber length to 10 mm. As reported in literature [13], areas with low FA and fiber length are assumed to be characterized by no coherent population.

D. Statistical Analysis

Protocol performances have been evaluated in terms of SNR and FA. Non-parametric statistical tests have been imposed to assess the significance of the differences. Additionally, a fitting with a linear combination of two Gaussian distributions has been imposed to evaluate the dispersion of the angle measurement according to protocol variation. The fitted coefficient of variation (CoV), defined as the median-standard deviation ratio, has been used as a parameter for measurement dispersion evaluation. Non-parametric statistical tests have been imposed to assess the significance of the difference between the different protocols in terms of measurement dispersion.

E. Software Evaluation

Our software performances have been evaluated through a comparison with common software available for DTI image processing. The comparison has included medInria (med.inria.fr), TrackVIs (trackvis.org), DiffusionKit (diffusionkit.readthedocs.io) and 3D Slicer (www.slicer.org). Two qualified technical users performed the comparison between the software and associated a numeric value ranging from 1 to 3, according to six different scores:

1) *Operative System* - operative system compatibility (Windows, Linux and MacOSx);
2) *Pre-processing* -availability of pre-processing operations such as automatic/manual ROI definition, filtering and similar (yes, partial and no);
3) *Data Access* - intermediate results and data accessibility (yes, partial and no);
4) *Import/Export File Format* - flexibility of image file format for the software (yes, partial and no);
5) *Field of Application* - the possibility to use the software with cardiovascular images (yes, partial and no);
6) *Easiness of use* - the level of ease for the user interface (yes, partial and no).

The score has been assigned assuming *yes* = 3, *partial* = 2 and *no* = 1. For the operative systems (OS), the score stands for the number of options available for the software (single OS = 1; two OSs = 2; all OSs = 3).

III. RESULTS

Figure 1 depicts the results of the four DTI protocols. In all cases a good image quality without significant artifacts was obtained. The SNR of the b0-images is explained by the different voxel resolution (0.63 mm^3 for $P_1 - P_2$, 1.12 mm^3 for $P_3 - P_4$) and NSA. As expected, the SNR of DW

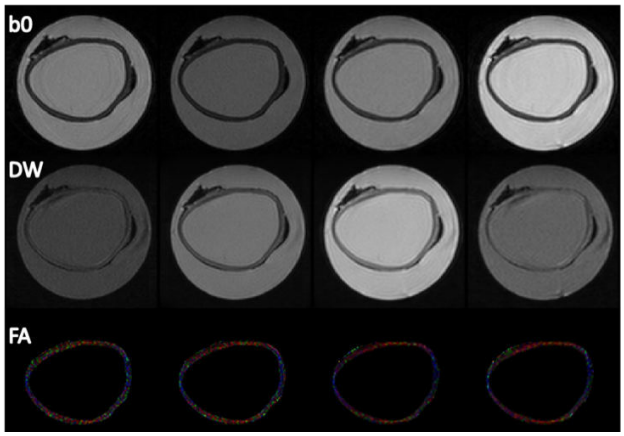

Fig. 1: Example of b_0 image, trace image (DWI) and FA anisotropy in RGB and results of the tractography for the four protocols (red (x direction), green (y direction) and blue (z direction)).

images increased for lower b-values ($P_2 - P_3$). Mean FA values were found to be lower for scan protocols with lower spatial resolution ($P_3 - P_4$). Color-coded FA maps showed similar pattern of the predominant diffusion direction, mainly distributed on the in-plane directions. Fiber trajectories are color-coded based on their directions: red (x direction), green (y direction) and blue (z direction).

In Figure 2 quantitative analyses of the different DTI protocols in terms of SNR for b0 and for DW images is reported. By comparing the four protocols, the P_3 (higher resolution and a low b-value) was chosen as the best one in terms of SNR parameter (24.7 $\pm$ 0.04 a.u.), reduced scan time and measurement dispersion.

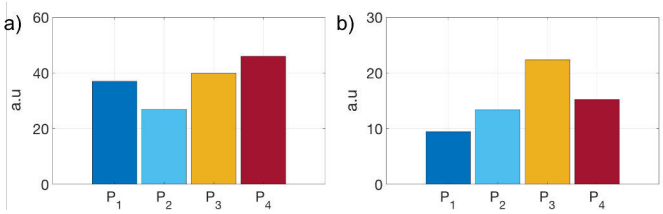

Fig. 2: Quantitative analyses of the different DTI protocols in terms of SNR for b0 images (a) and for DW images (b). Y-scale is expressed in arbitrary units (a.u.).

Figure 3 depicts the tractography results of the four DTI protocols for one sample.

The tractography statistical analysis has revealed that protocols P_2 and P_3 have the highest score in terms of measurement dispersion (with average CoV of 27% $\pm$ 0.7 % and 22% $\pm$ 0.66 % respectively). A significant difference with the other protocols emerged (p-value < 0.01) from the non-parametric tests. Both P_2 and P_3 protocols have exhibited a fiber angle distribution with a typical symmetric behaviour with two dominant angles. In Figure 4 we can observe the post-process result of the P_3 protocol. As we can observed the fibres are predominantly oriented in the circumferential direction and the median angle distribution of each fiber is 40°.

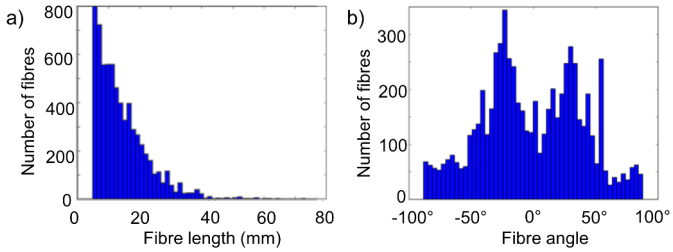

Fig. 4: Fiber distribution in terms of fiber length (a) and fiber angle after P_3 data processing for sample 1 (b).

A qualitative agreement was found between the DTI process with tractography and the histological analysis in term of fibre continuity and fibre density al local level. In particular, areas in which the collagen fibers were well organized and aligned have been identified with both the DTI tractography and histological investigation. Moreover, the regions in which cystic degenerations and lamellar openings have been detected by histology revealed low fractional anisotropy scores according to tractography.

The comparison between the available software is presented. The corresponding scores have been reported in Table II. The scores reveal differences in the software evaluated. In particular, most of these packages revealed partial pre-processing tools. They are typically black-box tools: once the input is set, only the final output is provided. As a consequence, intermediate results are not available for all packages. Only the DiffusionKit and 3D Slicer allow intermediate data access that can be used for further and different analysis. Moreover, it is important to point out that all the mentioned software have been developed primarily for white matter cerebral imaging and not for cardiovascular dataset without the integration with additional external codes.

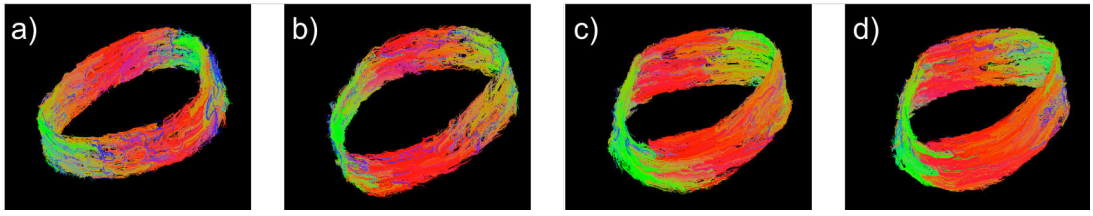

Fig. 3: Tractography results at different DTI protocols (from P_1 to P_4, from left to right)

TABLE II: Comparison of software for DTI analysis

	Operative System	*Pre-processing*	*Data Access*	*Imp./Exp. File Format*	*Field of application*	*Easiness of use*	*Total score*
medInria	3	2	2	2	2	3	14
TrackVIs	3	2	1	1	1	2	10
DiffusionKit	2	3	3	2	1	2	13
3D Slicer	3	3	3	2	1	2	14
Custom SW	3	3	3	3	3	2	17

IV. CONCLUSION

The collagen fibers three-dimensional architecture has a strong influence on the mechanical behaviour of biological tissues. To understand the mechanical behaviour of the artery, it is crucial to get insight into the arterial structure and particularly into collagen organization. Several different techniques have been presented in literature to assess arterial fibre orientation based on harvested tissue. Our results are in good agreement with data reported in literature [10]. This evidence confirms the previous results on DTI feasibility to determine the fibre orientation in the aorta. In this study we proposed for the first time a workflow able to investigate ex-vivo human fibre distribution by means of a whole body 3T MRI scanner. For the DTI analysis, we have implemented a specific code due to the fact that all the commercial DTI software are designed to study brain regions and their workflow is optimized for this kind of district. An optimal acquisition protocol was established for obtaining the fiber distribution of the aortic tissue. Our software has shown a high efficiency in terms of performance and flexibility with respect to the available packages.

Some of the limitations encountered in the present study can be overcome with further analyses able to compare at quantitative level DTI results with histological findings. The capability to visualize the entire 3D fiber architecture in a non-destructive way could provide novel and valuable information on the pathological state of the vessel wall. Moreover, this full non invasive characterization opens different possibilities in the world of tissue modeling in the landscape of Finite Element simulations, which have acquired a growing importance in the world of clinical planning. However, further investigation is necessary to correlate quantitative DTI results with histological analysis and mechanical modeling.

ACKNOWLEDGEMENT

This work was supported by the VALVETECH (by Regione Toscana) and VIVIR (PE-2013-02357974) projects.

REFERENCES

[1] G. A. Holzapfel, T. C. Gasser, R.W. Ogden, “Comparison of a multi-layer structural model for arterial walls with a Fung-type model, and issues of material stability”, Journal of Biomechanical engineering, vol. 126 n. 2, pp 264-275, Apr 2004

[2] J. D. Humphrey, *Cardiovascular solid mechanics: cells, tissues, and organs*, Springer Science and Business Media, 2013

[3] P. B. Canham, H. M. Finlay, D. R. Boughner, “Contrasting structure of the saphenous vein and internal mammary artery used as coronary bypass vessels”, Cardiovascular Research, vol. 34 n. 3, pp 557-567, Jun 1997

[4] F. Schmid et al., “*In situ* tensile testing of human aortas by time-resolved small-angle X-ray scattering”, Journal of Synchrotron Radiation, vol. 12 n. 6, pp 727-733, Nov 2005

[5] M. S. Sacks, D. B. Smith, E. D. Hiester, “A small angle light scattering device for planar connective tissue microstructural analysis”, Annals of Biomedical Engineering, vol. 25 n. 4, pp 678-689, Jul 1997

[6] H.-W. Wang, T. T. Le, J.-X. Cheng, “Label-free imaging of arterial cells and extracellular matrix using a multimodal CARS microscope”, vol. 281 n. 7, pp 1813-1822, Apr 2008

[7] A. Zomui, X. Lu, G.S. Kassab, B. J. Tromberg,“Imaging coronary artery microstructure using second-harmonic and two-photon fluorescence microscopy”, Biophysical Journal, vol. 87 n. 4, pp 2778-86, Oct 2004

[8] V. Flamini, C. Kerskens, K. M. Moerman, C. K. Simms, C. Lally, “Imaging arterial fibres using diffusion tensor imagingfeasibility study and preliminary results”, EURASIP Journal of Advances in Singal Processing, 2010

[9] V. Flamini, C. Kerskens, C. Simms, C. Lally, “Fibre orientation of fresh and frozen porcine aorta determined non-invasively using diffusion tensor imaging”, vol. 35 n. 6, pp 765-776, Jun 2013

[10] V. Flamini, A.P. Creane, C. M. Kerskens, C. Lally, “Imaging and finite element analysis: a methodology for non-invasive characterization of aortic tissue”, Medical engineering and physics,vol. 37 n. 1, pp 48-54, Jan 2015

[11] N. Martini et al., “Diffusion tensor imaging of the human aortic wall: an ex-vivo study”, International Society for Magnetic Resonance in Medicine, (ISMRM-2014), 2014, 3780

[12] P. J. Basser, J. Mattiello, D. Lebihan, “Estimation of the effective self-diffusion tensor from the NMR spin echo”, Journal of Magnetic Resonance B, vol. 103 n. 3, pp 247-254, Mar 1994

[13] P. Mukherjee, J. Berman, S. W. Chung, C.P. Hess, R. G. Henry , “Diffusion tensor mr imaging and fiber tractography: theoretic underpinnings”, AJNR Am J Neuroradiol, vol. 29 n. 4, pp 632-641, Apr 2008

Transcatheter aortic valve repair performances in elliptic annuli: Corevalve versus Portico

A. Finotello[1], S. Morganti[2], N.Brambilla[3], R. Gorla[3], F. Bedogni[3], and F. Auricchio[4]
[1] *Department of Experimental Medicine, University of Genoa, Genoa, Italy*
[2] *Department of Electrical, Computer, and Biomedical Engineering, University of Pavia, Pavia, Italy*
[3] *Department of Cardiology, IRCCS Policlinico San Donato, San Donato MI, Italy*
[4] *Department of Civil Engineering and Architecture, University of Pavia, Pavia, Italy*

***Abstract*—In the last few years, the use of computational simulations has been proposed to investigate transcatheter aortic valve implantation (TAVI) and to predict TAVI adverse events. In this work, the behavior of two self-expandable devices (Medtronic CoreValve and St. Jude Medical Portico) has been investigated in idealized aortic root models and different degrees of aortic annulus eccentricity are tested.**

***Keywords*—thanscatheter aortic valve implantation, finite element analysis, stent design.**

I. INTRODUCTION

Aortic stenosis, the most common form of valvular heart disease in the developed countries, is a degenerative disease of the aortic valve complex, compromising its function of regulating bood flow from the heart (left ventricle) to the aorta, with significant consequences on patients' mortality, thus representing a relevant clinical problem [1]. In the last years, transcatheter aortic valve implantation (TAVI) has recently become the new standard medical treatment for patients affected by severe aortic valve stenosis who are not eligible for open-heart surgery [2]. However, there are still some complications related with TAVI (e.g. paravalvular leakage, prosthesis migration, aortic root rupture) [3], most of them related to the mutual interaction between the device and the aortic root wall. In this context, computational simulations could represent a powerful tool [4] which may help to obtain predictive information about the behavior of the device during transcatheter delivery and its post-operative performances. Aim of the work is to compare the performance of two different self-expandable devices (CoreValve (Medtronic, Minneapolis, MN, USA) and Portico (St.Jude Medical, Minneapolis, MN, USA)) implanted in an idealized aortic root with elliptical-shape annulus. Three different annulus eccentricities are tested and the device performances are compared.

II. MATERIALS AND METHODS

A. Simulation framework

Two different devices are compared: CoreValve size 26 and Portico size 25. Both the devices are recommended for native annulus diameters 21-23 mm.
The geometrical models of the CoreValve and Portico devices are reconstructed from micro-CT scans of real device samples. For each device, the reconstructed STL file is imported in Rhinoceros 5.0 (McNell, WA, USA) where the CAD model of one elementary unit is built. Then Matlab software (Mathworks Inc, Natick, MA, USA) is used to replicate in polar series the elementary unit in order to obtain the entire description of the device. A structured mesh of first-order hexahedral solid elements with a reduced integration scheme is defined for the device model (C3D8R elements). The two reconstructed stent models are depicted in Figure 1. Material properties of the Nitinol alloy are considered according to the model proposed by Auricchio et al. [5]. The density is set to $6.5e^{-9}Tmm^3$. We assumed the same material properties for both the devices. In this work only the stent of the prosthetic valve is considered because the valve is not visible from CT images and we reasonably assume that the post-operative configurations of the stent and of the native aortic root are not influenced by the prosthetic leaflets.

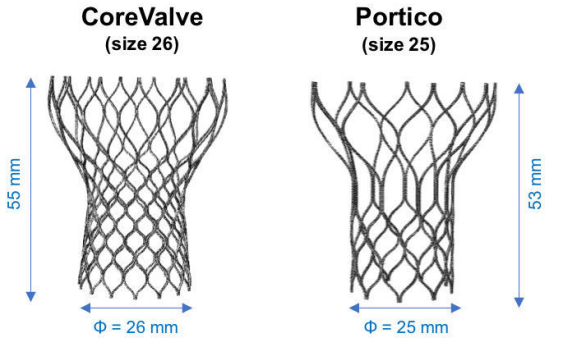

Fig. 1: Reconstructed stents geometries: CoreValve (left) and Portico (right).

A cylindrical surface, in the following labeled as the catheter, is built and used in the numerical analysis to position the stent within the aortic valve and to reproduce the crimping technique. The catheter is defined through a surface obtained by sweeping a cylindrical section and meshed using quadrilateral surface elements with reduced integration (SFM3D4R). It is modeled as a rigid material with a density equal to $6.7e^{-9}Tmm^3$.
An idealized aortic root model composed of three regions (Left ventricular outflow tract -LVOT-, Valsalva sinuses -VS- and

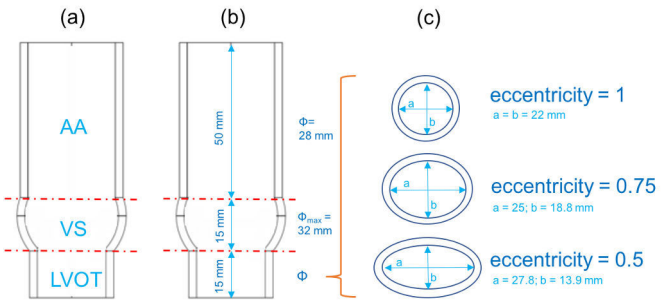

Fig. 2: Schematic representation of the idealized aortic root models.

Ascending aorta -AA-) is conceived (see Figure 2(a)-(b)).

As depicted in Figure 2(c), three different idealized models, corresponding to three different LVOT eccentricities (eccentricities 1, 0.75, and 0.5), are modeled. In detail, the axes dimensions (a and b) are varied as a function of the eccentricity value, keeping the annulus perimeter constant. The eccentricity e is defined as $e = b/a$ where a and b are the lengths of the major and the minor axes, respectively.
The CAD model is generated in Rhinoceros 5.0 and then meshed within the finite element software Abaqus (v. 6.14, Simulia, Dassáult Systems, Providence, RI, USA) using three-dimensional hexahedral elements (C3D8R). In accordance with a previous work [6], a non-linear isotropic hyperelastic six-order reduced polynomial constitutive model was adopted. The aortic tissue is assumed to be nearly incompressible and a Poisson's ratio ν of 0.475 is considered.
These idealized aortic root models are used as the initial geometries for finite element simulation of TAVI. The simulation setup is composed of two steps: crimping of the stent and expansion of the stent within the aortic root model. The steps are performed in two different simulations to save time. In the first step both the CoreValve and the Portico stents are crimped inside the catheter. Then, the stent inside its catheter is positioned inside the idealized aortic root. The progressive sliding of the constraining catheter from the bottom to the top allows the stent self-expansion inside the aortic root wall. More details about the simulation procedure are given in [7].

B. Simulation post-processing

Device performances are measured in terms of:

- stent-root interaction area: measure of the expanded device footprint onto the inner wall of the aortic root;
- Von Mises stress distribution: measure of the stress induced by device expansion onto the inner wall of the aortic root;
- paravalvular leakage: measure of the area of the orifices generated (after stent expansion) between the device and the inner aortic wall;
- stent eccentricity: measure of the device deformation due to the expansion within the aortic root.

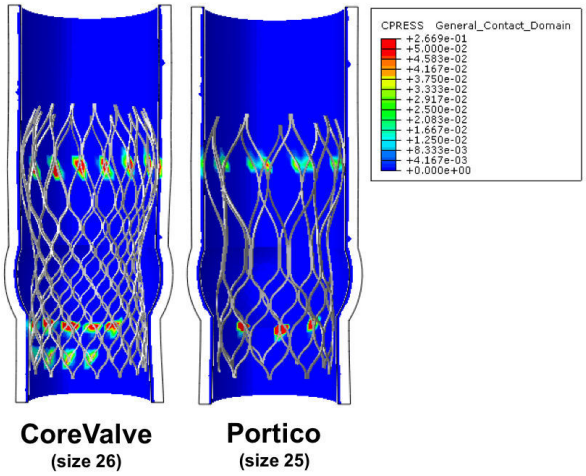

Fig. 3: Stent-root interaction area: comparison between CoreValve (left) and Portico (right) devices. The case with eccentricity 0.75 is shown.

III. Results

All the simulations are performed using Abaqus Explicit solver on 8 CPUs. In total, two crimping simulations (CoreValve and Portico) are performed and, for each device, three different aortic root models are analyzed.
Then, each simulated configuration has been post-processed to extract quantitative measures of:

- *Stent-root interaction area.* The measure of the stent-root contact area may represent an indication of the device anchoring and adesion to the wall. It is computed as the sum of the areas of the elements with contact pressure different from zero. An example is given in Figure 3. In Table I quantitative values are reported. As shown, significantly higher values of contact area are observed for the CoreValve device if compared to the Portico stent. In addition, the Portico device is less sensitive to annulus eccentricity variations.

- *Von Mises stress distribution.* The average (σ_{av}) and maximum (σ_{max}) stress values on the LVOT are reported in Table I (for each of the three aortic root configurations and for both the devices) with the aim of obtaining information about the device anchoring, the localization of the stress peaks, and the potential risk of inflammation and LVOT rupture. As highlighted in Table I when the eccentricity is inferior to 1, similar values of σ_{max} are obtained meaning that the LVOT wall stress is comparable. However, σ_{av} is higher in the CoreValve with regard to the Portico device meaning higher global anchoring force, more evenly distributed. As shown in Figure 4, where the aortic root configuration with eccentricity 0.75 is depicted, the Portico shows localizations of high stress in the LVOT if compared to the CoreValve device.

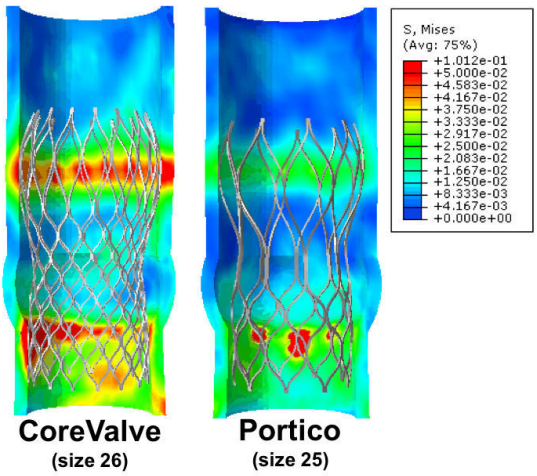

Fig. 4: Stress distribution (MPa) on the aortic root internal wall after stent implantation. CoreValve (left) and Portico (right) devices are compared. The case with eccentricity 0.75 is shown in both cases.

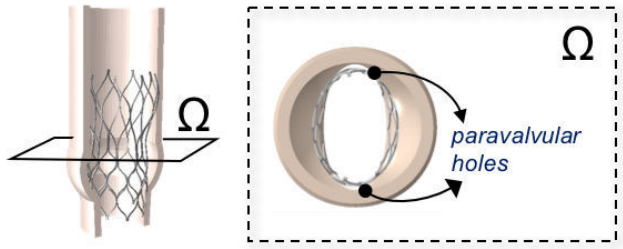

Fig. 5: The grade of paravalvular leakage is taken considering a plane Ω correspondent to the sino-tubular junction (left). On the right an example of the cross-section of the valve at the level of the plane Ω.

- *Paravalvular leakage.* The grade of paravalvular orifice area between the expanded stent and the internal aortic root wall surface is measured in the plane correspondent to the sino-tubular junction (Ω in Figure 5). Quantitative values are reported in Table I. As shown, the CoreValve device seems to exhibit improved performance with regard to the Portico when the LVOT eccentricity is not too much pronounced (e=0.75). In contrast, the Portico shows better performance in the worst case scenario (in terms of LVOT eccentricity, e=0.5).

- *Stent eccentricity.* Measurements of the elliptic shape of the implanted device are used to evaluate stents deformation. Twenty-two equally spaced cross-sections of the implanted devices are considered and the eccentricity values are plotted against the stent longitudinal axis. As shown Figure 6, Portico and Corevalve devices exhibit very similar behavior. As expected, for both the devices, the portion of the stent that deforms more is the proximal one (i.e., placed in the LVOT). In addition, as shown in both the graphics, the more the LVOT eccentricity, the greater is the device deformation.

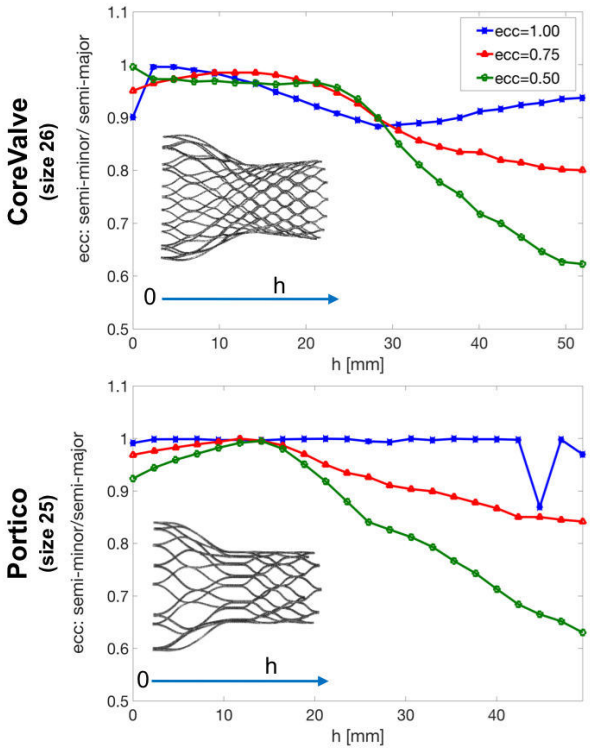

Fig. 6: Measure of stent cross-section eccentricity for the Corevalve (top) and the Portico (bottom) devices for each simulated aortic root configuration.

TABLE I: Simulation post-processing: quantitative results

Eccentricity	Corevalve	Portico
	Stent-root interaction area $[mm^2]$	
e=1	741.5	236.8
e=0.75	834.3	380.5
e=0.5	570.2	284.0
	σ_{av}/σ_{max} [kPa/kPa]	
e=1	29 / 134	10 / 74
e=0.75	36 / 107	19/ 104
e=0.5	103/ 416	38 / 367
	Paravalvular orifice area $[mm^2]$	
e=1	0	0
e=0.75	0	6.2
e=0.5	11.7	8.6

Quantitative results, for each simulated configuration are presented. The performances of the two devices (CoreValve and Portico) are compared.

IV. Discussion

The prediction of TAVI adverse outcomes remains a significant challenge when the pre-operative planning is based on medical images only. Following a strong need directly coming from clinicians, in this work we have focused on two self-expandable devices (Medtronic Corevalve and St.Jude Portico) with the aim of comparing their performances with different annulus eccentricities.

Our results indicate that the two devices exhibit a different behavior both in terms of stent-root interaction area and Von Mises stress distribution. As concerns the stent-internal aortic root wall interaction area, we have seen that, for all the eccentricity configurations of the aortic root, the contact area exerted from the CoreValve is at least 2X times that of the Portico.

Another important factor when evaluating the performances of the percutaneous procedures is the occurrence of aortic regurgitation. Such an aortic root wall-device mismatch has been quantitative evaluated in terms of paravalvular orifices. Our results show that, the CoreValve device seems to exhibit better performances with circular annuli (eccentricity ≥ 0.75). On the contrary, for elliptic annuli the use of the Portico device may be preferable.

In this work we consider a simplified aortic root model and calcification are not included. However, future studies will involve the inclusion and comparison between different calcifications patterns. Moreover, the present work could be extended by performing fluid-structure interaction simulations to analyze how the fluid domain is influenced by eccentricity changes.

Acknowledgement

The authors would acknowledge the Interdisciplinary Research Center on Biomaterials of the University of Naples Federico II (Professors Netti and Ventre) and the Orthopedic Institute Rizzoli of Bologna for the Micro-CT scans.

References

[1] K. Maganti, V.H. Rigolin, M.E. Sarano, and R-O. Bonow, Valvular heart disease: diagnosis and management. In Mayo Clinic Proceedings. Ed. Elsevier, 2010, Vol. 85, No. 5, pp. 483-500.

[2] M.B. Leon, C.R. Smith, M. Mack, D.C. Miller, J.W. Moses, et al, Transcatheter aortic-valve implantation for aortic stenosis in patients who cannot undergo surgery. New England Journal of Medicine 2010, 363.17 :1597-1607.

[3] S. Neragi-Miandoab, and R.E. Michler, A review of most relevant complications of transcatheter aortic valve implantation. ISRN cardiology, 2013.

[4] P. Vy, V. Auffret, P. Badel, M. Rochette, H. Le Breton, et al, Review of patient-specific simulations of transcatheter aortic valve implantation. International Journal of Advances in Engineering Sciences and Applied Mathematics 2016, 8.1: 2-24.

[5] F. Auricchio, and R.L. Taylor, Shape-memory alloys: modelling and numerical simulations of the finite-strain superelastic behavior. Computer Methods in Applied Mechanics and Engineering 1997, 143.1-2: 175-194.

[6] A. Finotello, S. Morganti, F. Auricchio, Finite element analysis of TAVI: impact of native aortic root computational modeling strategies on simulation outcomes. Medical Engineering and Physics 2017, 47: 2-12.

[7] S. Morganti, M. Conti, M. Aiello, A. Valentini, A. Mazzola, et al, Simulation of transcatheter aortic valve implantation through patient-specific finite element analysis: two clinical cases. Journal of biomechanics 2017, 47.11: 2547-2555.

Bidomain simulations of ventricular tachycardia in presence of infarct scars

S. Scacchi[1], P. Colli Franzone[2], V. Gionti[3] and L. F. Pavarino[2]
[1] *Department of Mathematics, University of Milan, Italy*
[2] *Department of Mathematics, University of Pavia, Italy*
[3] *Istituto di Cura Città di Pavia, Italy*

***Abstract*—We investigate by means of numerical simulations the role of repolarization properties of scar tissue border zones (BZs) on the genesis of ventricular tachycardia. The simulations are based on the Bidomain model, a reaction-diffusion system of Partial Differential Equations, discretized by finite elements in space and implicit-explicit finite differences in time. The computational domain considered is an idealized left ventricle affected from an infarct scar with a sub-epicardial BZ channel.**

***Keywords*—Bidomain model, venctricular tachycardia, re-entrant arrhythmias, parallel numerical simulations**

I. INTRODUCTION

Currently, echocardiographically assessed left ventricular ejection fraction (LVEF) is the only established criteria for implantable cardioverter defibrillator (ICD) implantation in primary prevention in ischemic and non-ischemic cardiomyopathy [1]. However, LVEF $< 30-35\%$ has been shown to be a non-specific and non-sensitive criterion for risk evaluation of ventricular tachycardia (VT) [21], [15]. There are several studies concerning the cardiac electrical remodeling (see e.g. [14], [20]), which could lead to refractoriness and conduction abnormalities contributing to arrhythmogenicity and to high variability of time to first ventricular arrhythmias; see also [13], [26]. Previous simulation studies on ventricular arrhythmias in presence of infarct scars have mainly considered the simplified Monodomain model of electrocardiology and have focused on the influence of geometric properties of the scar on the induction of re-entry, see e.g. [2], [3], [11]. The aim of this study is to investigate by means of Bidomain numerical simulations the role of repolarization properties of scar tissue border zones on the genesis of re-entrant ventricular arrhythmias.

II. METHODS

A. Mathematical models

To model the electrical current flow through the myocardium, we assume the Bidomain representation of the cardiac tissue, see [24], [10]. Let H denote a three-dimensional portion of myocardium, subdivided into an infarct scar S and a region Ω constituted by the infarct border zone (BZ) and the healthy tissue, thus $H = \Omega \cup S$. We assume that the scar can be electrically modeled as a passive conducting isotropic medium. The evolution of the transmembrane potential $v(\mathbf{x}, t)$, extracellular potential u_e, scar potential u_b, gating variables $\mathbf{w}(\mathbf{x}, t)$ and ionic concentrations $\mathbf{c}(\mathbf{x}, t)$ in a time interval (0,T) is described by the macroscopic Bidomain model:

$$\begin{cases} c_m \partial_t v - \operatorname{div}(D_i \nabla(v + u_e)) + i_{ion}(v, \mathbf{w}, \mathbf{c}) = i_{app} & \text{in } \Omega \times (0,T) \\ \partial_t w - R_w(v, \mathbf{w}, \mathbf{c}) = 0, \quad \partial_t c - R_c(v, \mathbf{w}, \mathbf{c}) = 0 & \text{in } \Omega \times (0,T) \\ -\operatorname{div}(D_i + D_e)\nabla u_e = \operatorname{div} D_i \nabla v & \text{in } \Omega \times (0,T) \\ \mathbf{n}^T D_i \nabla(v + u_e) = 0 & \text{on } \partial\Omega \times (0,T) \\ \mathbf{n}^T D_e \nabla u_e = 0 & \text{on } \partial\Omega \setminus \partial S \times (0,T) \\ -\operatorname{div} \sigma_b \nabla u_b = 0 & \text{in } S \times (0,T) \\ u_e = u_b & \text{on } \partial S \cap \partial\Omega \times (0,T) \\ \mathbf{n}^T D_e \nabla u_e = \mathbf{n}^T \sigma_b \nabla u_b & \text{on } \partial S \cap \partial\Omega \times (0,T) \\ \mathbf{n}^T \sigma_b \nabla u_b = 0 & \text{on } \partial S \setminus \partial\Omega S \times (0,T) \end{cases} \tag{1}$$

with appropriate initial conditions on $v(\mathbf{x}, 0), \mathbf{w}(\mathbf{x}, 0)$ and $\mathbf{c}(\mathbf{x}, 0)$. Here c_m and i_{ion} denote the capacitance and the ionic current of the membrane per unit volume, i_{app} represents the applied current per unit volume, $D_{i,e}$ are the intra- and extracellular transversely isotropic conductivity tensors and σ_b is the scar conductivity.

Assuming transversely isotropic properties of the intra- and extracellular media, the conductivity tensors are given by

$$D_{i,e} = \sigma_t^{i,e}\ I + (\sigma_l^{i,e} - \sigma_t^{i,e})\mathbf{a}_l \otimes \mathbf{a}_l, \tag{2}$$

where $\sigma_l^{i,e}$, $\sigma_t^{i,e}$ are the conductivity coefficients of the intra- and extracellular media measured along the fiber direction $\mathbf{a}_l$ and any cross fiber direction, respectively.

The ionic current is given by $i_{ion} = \chi I_{ion}$, where χ is the membrane surface to volume ratio and the ionic current per unit area of the membrane surface I_{ion} is given by the ten Tusscher membrane model (TP06) [22], [23], available from the cellML depository (models.cellml.org/cellml). The TP06 ionic model also specifies the functions $R_w(v, \mathbf{w})$ and $R_c(v, \mathbf{w}, \mathbf{c})$ in the ordinary differential equations (ODEs) system, consisting of 17 ODEs modeling the main ionic currents dynamics.

B. Numerical methods

The space discretization is performed by employing hexahedral isoparametric Q_1 finite elements, while the time discretization is based on the following double operator splitting

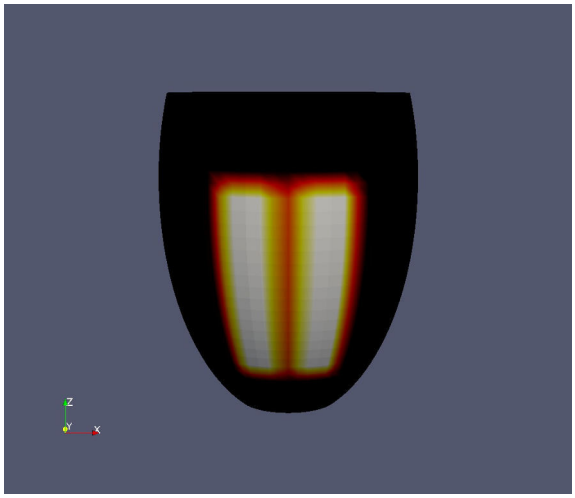

Fig. 1: Left ventricle (LV) computational domain with scar (white) and border zone (BZ) channel (red), epicardial view.

procedure: a) split the ODEs from the PDEs and b) split the elliptic PDE from the parabolic one; for further details see [9]. This operator splitting strategy yields two large linear systems of algebraic equations that must be solved at each time step. In order to ensure parallelization and portability of our Fortran code, we use the PETSc parallel library [6], a suite of data structures and functions for building large-scale parallel scientific applications, based on the MPI communication library. The parallel strategy employed assigns each subdomain to one processor and the information associated with the interior of the subdomain is uniquely owned by that processor. The processor stores all subvectors and a block of the matrices (mass, stiffness) associated to each overlapping subdomain. Our parallel code employs different DA (Distributed Arrays) PETSc objects for representing v on the non-scar domain Ω (tissue) and for u_e, u_b on the entire cardiac domain H (non-scar and scar tissue). The two large linear systems at each time step are solved by a parallel conjugate gradient method, preconditioned by the Multilevel Additive Schwarz preconditioner, developed in [17], for the ill-conditioned elliptic system and the Block Jacobi preconditioner for the well conditioned parabolic system. These preconditioners are based on the multilevel PETSc objects PCMG (MultiGrid) with ILU(0) local solvers. The simulations are run on 256 cores of the MARCONI-KNL Linux Cluster of CINECA laboratory (www.cineca.it).

C. Simulation setup

Computational domain. The computational domain H is the image of a cartesian periodic slab using ellipsoidal coordinates, yielding a truncated ellipsoid modeling a left ventricle (LV) geometry, described by the parametric equations

$$\begin{cases} x = a(r)\cos\theta\cos\phi & \phi_{min} \le \phi \le \phi_{max}, \\ y = b(r)\cos\theta\sin\phi & \theta_{min} \le \theta \le \theta_{max}, \\ z = c(r)\sin\theta & 0 \le r \le 1, \end{cases}$$

where $a(r) = a_1 + r(a_2 - a_1)$, $b(r) = b_1 + r(b_2 - b_1)$, $c(r) = c_1 + r(c_2 - c_1)$, and $a_1 = b_1 = 1.5$, $a_2 = b_2 = 2.7$, $c_1 = 4.4$, $c_2 = 5$ (all in cm) and $\phi_{min} = -\pi/2$, $\phi_{max} = 3\pi/2, \theta_{min} = -3\pi/8$, $\theta_{max} = \pi/8$. We will refer to the inner surface of the truncated ellipsoid ($r = 0$) as endocardium and to the outer surface ($r = 1$) as epicardium. In all LV computations, a structured grid of $512 \times 256 \times 48$ hexahedral isoparametric Q_1 finite elements of size $h \approx 0.02\ cm$ is used in space, for a total amount of 6 447 616 mesh nodes. Fibers rotate transmurally, linearly with the depth and counterclockwise from epicardium to endocardium, for a total amount of 120^o. The dimension of the scar is of about $2 \times 3.5 \times 1\ cm^3$ (see Fig. 1) and it develops along the entire transmural thickness, from endocardium to epicardium. The BZ consists of the sub-epicardial channel located at the center of the scar (see Fig. 1) of dimension $0.5 \times 3.5 \times 0.3\ cm^3$. In indicating the size of the scar region and of the BZ channel, we used the notation $circumferential\ size \times longitudinal\ size \times transmural\ size$.

Parameter calibration. The values of the transversely isotropic conductivity coefficients in (2), that we use in all the numerical tests for the healthy tissue, are $\sigma_l^i = 3$, $\sigma_t^i = 0.31525$, $\sigma_l^e = 2$, $\sigma_t^e = 1.3514$, all expressed in $m\Omega^{-1}cm^{-1}$. These values, coupled with the TP06 membrane model, predict conduction velocities of about 0.061 and 0.027 cm/ms for excitation wavefronts propagating along and across the fiber direction, respectively. We remark that these conduction velocities are within the physiological range, see e.g. [18], [8]. The membrane surface to volume ratio is $\chi = 10^3\ cm^{-1}$ and the membrane capacitance per unit volume is $c_m = \chi C_m$, where $C_m = 1\ \mu F/cm^2$ is the membrane capacitance per unit area. To the scar conductivity σ_b is assigned the value $0.02\, m\Omega^{-1}cm^{-1}$. In all simulations, following [3] (see also [5], [11], [16]), we model the BZ by implementing a 60% reduction of fast sodium current conductance g_{Na}, 70% reduction of L-type calcium current conductance g_{CaL} and 75% reduction of cross fiber intracellular conductivity coefficient σ_t^i. Moreover, the potassium currents conductances g_{Kr} and g_{Ks} are modified in the BZ as detailed below. Indeed, we have considered the following two settings, depending on potassium currents conductances:

- **LV1**: 70% reduction of g_{Kr}, 80% reduction of g_{Ks};
- **LV2**: no reduction of g_{Kr} and g_{Ks}, same values as in healthy tissue;

Stimulation protocol. In both **LV1** and **LV2** simulations, S1 stimuli of $250\, mA/cm^3$ amplitude and $5\, ms$ duration are applied simultaneously at four endocardial apical locations, while S2 stimuli of $1250\, mA/cm^3$ amplitude and $5\, ms$ duration are applied at an epicardial site located close to the apical entrance of the BZ channel.

In both simulations settings, the tissue is first paced in the S1 stimulus location for $2000\, ms$ and a basic cycle length of $400\, ms$. In the following, we will denote as S1-S2 coupling interval the time interval between the S1 and the S2 stimulations.

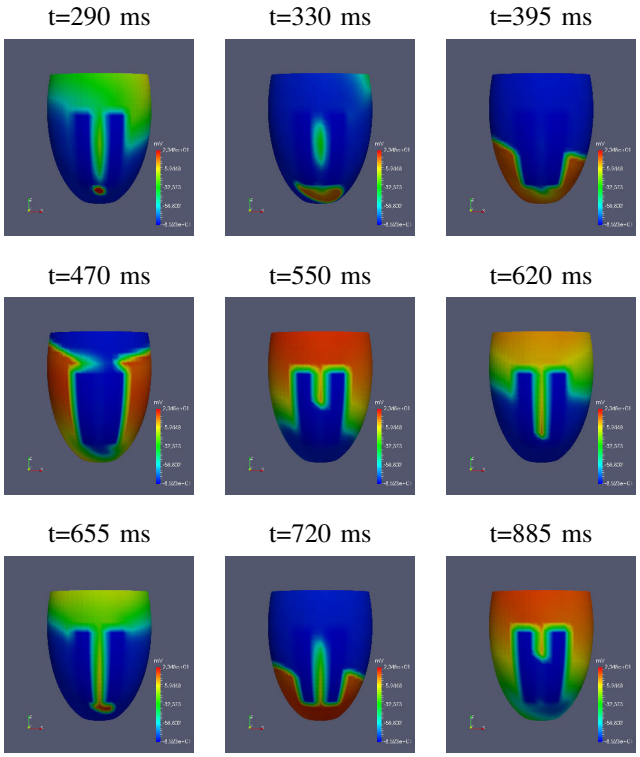

Fig. 2: LV1 simulation. Snapshots of epicardial transmembrane potential distribution.

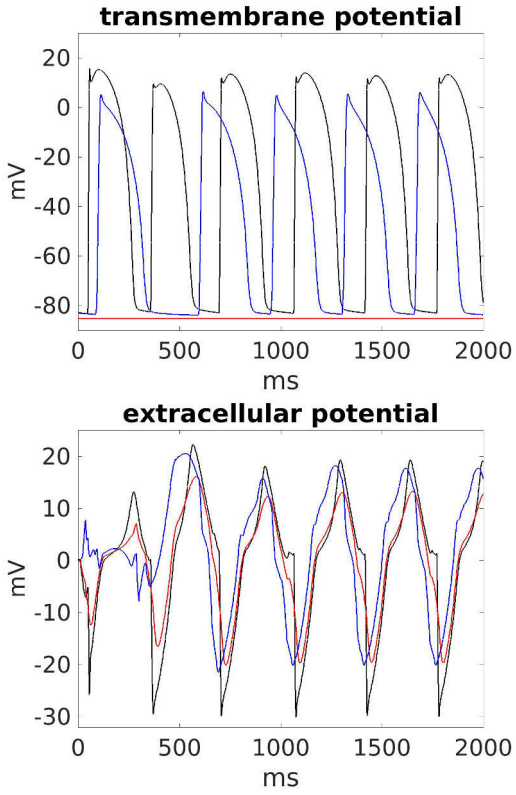

Fig. 3: LV1 simulation. Transmembrane and extracellular potential waveforms in three selected points: normal tissue (black), scar tissue (red), BZ channel (blue).

III. RESULTS

In the **LV1** setting, a premature S2 stimulus delivered at an S1-S2 coupling interval of $290\,ms$ does not propagate inside the bottom entrance of the BZ channel (see Fig. 2, $t = 290\,ms$ and $t = 330\,ms$), because the BZ tissue is still refractory, but it propagates around the scar (see Fig. 2, $t = 395\,ms$ and $t = 470\,ms$). When the activation wavefront reaches the top entrance of the BZ channel, the BZ tissue has completely recovered and the action potential propagates downwards through the channel (see Fig. 2, $t = 550\,ms$ and $t = 620\,ms$). Eventually, the excitation exits from the bottom gate of the channel into the healthy tissue and propagates again around the scar, leading to a stable VT (see Fig. 2, $t = 655\,ms$, $t = 720\,ms$ and $t = 885\,ms$). Indeed the potential distribution at $t = 885\,ms$ has the same pattern of that at $t = 550\,ms$, confirming the onset of a re-entrant wave. We report in Fig. 3 the time evolution of the transmembrane and extracellular potential waveforms in three selected points in normal tissue, scar tissue and BZ channel. The first two action potentials in Fig. 3 (top panel) correspond to the last S1 and S2 stimulations, while the later four spikes are due to the stable re-entrant wave.

In the **LV2** setting (see Fig. 4), the refractoriness of the BZ is almost the same as in the healthy tissue, and reentry does not occur at any S1-S2 coupling interval, because the activation wavefront elicited by the S2 stimulus always enters

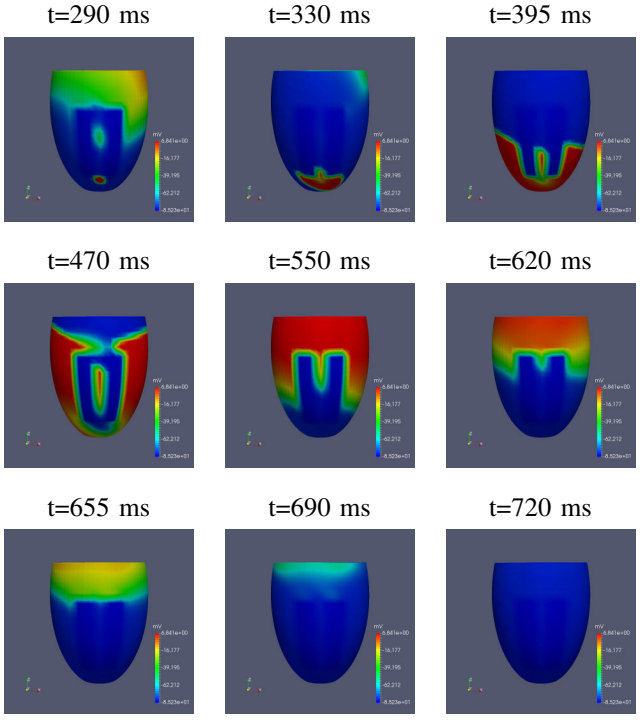

Fig. 4: LV2 simulation. Snapshots of epicardial transmembrane potential distribution.

through the bottom gate of the BZ channel.

IV. DISCUSSION

Growing research interest has been aroused by the so-called border zone because of an alleged correlation with ventricular arrhythmias, appropriate ICD discharge and cardiovascular mortality [12], [27]. Recently, it was shown that Late Gadolinium Enhancement MRI driven infarct tissue heterogeneity is associated with mortality [27] and VT [19]. Histological studies have shown that the border zone is composed of an heterogeneous mix of viable myocardium and necrotic scar [4]. These regions have isolated/late, low voltage and fractionated bipolar potentials during sinus/paced rhythm and this activation pattern reflects local slow conduction of these myocytes bundles [7]. These electrophysiologic features, together with dispersion of repolarization, could cause conduction blocks giving rise to re-entrant circuits, [20], [25]. In our study repolarization property of the BZ channel shows a fundamental role in the genesis of re-entrant VT because of its propensity to give functional blocks and slow conductions. Such results contribute to better identify the mechanisms at the origin of VT in presence of infarct scars.

Limitations. The BZ channel orientation in the scar has been chosen arbitrarily and, probably, it plays also a role because it affects the critical relation between the conduction time in outer loop of the circuit and the time of cell potential recovery. Our study does not consider border zone around the scar in outer loop to simplify the model and because we suppose that its effect is to accentuate the role of scar dimension in the time delay to reach the opposite side of the channel. Future works should also investigate how the thickness of the channel influences the genesis of VT and consider realistic patient-specific, instead of idealized, geometries.

REFERENCES

[1] 2016 ESC guidelines for the diagnosis and treatment of acute and chronic heart failure: the task force for the diagnosis and treatment of acute and chronic heart failure of the European Society of Cardiology (ESC). Europ. Heart J., vol. 37, 2016, pp. 2129–2200.

[2] H. Arevalo, G. Plank, P. Helm, H. Halperin and N. A. Trayanova. Tachycardia in Post-Infarction Hearts: Insights from 3D Image-Based Ventricular Models. PLoS ONE, vol. 8 (7), 2013, e68872.

[3] H. J. Arevalo, F. Vadakkumpadan, E. Guallar, A. Jebb, P. Malamas, K. C. Wu and N. A. Trayanova. Arrhythmia risk stratification of patients after myocardial infarction using personalized heart models. Nature comm., vol 7, 2016, 11437.

[4] H. Arheden, M. Saeed, C. B. Higgins, D. W. Gao, P. C. Ursell, L. Bremerich, R. Wyttenbach, M. W. Dae and R. F. Wendland. Reperfused rat myocardium subjected to various durations of ischemia: estimation of the distribution volume of contrast material with echo-planar MR imaging. Radiology, vol. 215 (2), 2000, pp. 520–528.

[5] S. Baba, W.Dun, C.Cabo and P. A. Boyden. Remodeling in cells from different regions of thereentrant circuit during ventricular tachycardia. Circulation, vol. 112, 2005, pp. 2386–2396.

[6] S. Balay, S. Abhyankar, M. F. Adams, J. Brown, P. Brune, K. Buschelman, L. Dalcin, V. Eijkhout, W. D. Gropp, D, Kaushik, M, G. Knepley, L. C. McInnes, K. Rupp, B. F. Smith, S. Zampini, H. Zhang and H. Zhang. PETSc users manual. Tech. Rep. ANL-95/11 - Revision 3.7, Argonne National Laboratory, 2016.

[7] F. Bogun, B. Bender, Y. G. Li, G. Groenefeld, S. H. Hohnloser, F. Pelosi, B. Knight, S. A. Strickberger and F. Morady. Analysis during sinus rhythm of critical sites in reentry circuits of postinfarction ventricular tachycardia. J. Interv. Card. Electrophysiol., vol. 7, 2002, pp. 95–103.

[8] P. Colli Franzone, L. Guerri and B. Taccardi. Modeling ventricular excitation: Axial and orthotropic effects on wavefronts and potentials. Math. Biosci., vol. 188, 2004, pp. 191–205.

[9] P. Colli Franzone, L. F. Pavarino and S. Scacchi. A comparison of coupled and uncoupled solvers for the cardiac bidomain model. ESAIM Math. Mod. Numer. Anal., vol. 47, 2013, pp. 1017–1035.

[10] P. Colli Franzone, L. F. Pavarino and S. Scacchi. Mathematical Cardiac Electrophysiology. Springer, MSA vol. 13, New York, 2014.

[11] A. Connolly and M. J. Bishop. Computational Representations of Myocardial Infarct Scars and Implications for Arrhythmogenesis. Clin. Med. Insights: Cardiology, vol. 10 (S1), 2016, pp. 27–40.

[12] S. de Haan, T. A. Meijers, P. Knaapen, A. M. Beek, A. C. van Rossum and C. P. Allaart. Scar size and characteristics assessed by CMR predict ventricular arrhythmias in ischaemic cardiomyopathy: comparison of previously validated models. Heart., vol. 97, 2011, pp. 1951–1956.

[13] A. G. Kleber and Y. Rudy. Basic mechanisms of cardiac impulse propagation and associated arrhythmias. Physiol. Rev., vol. 84, 2004, pp. 431–488.

[14] S. C. Latet, V. Y. Hoymans, P. L. Van Herck and C. J. Vrints. The cellular immune system in the post-myocardial infarction repair process. Int. J. Cardiol., vol. 179, 2015, pp. 240–247.

[15] A. J. Moss, H. Greenberg, R. B. Case, W. Zareba, W. J. Hall, M. W. Brown, J. P. Daubert, S. McNitt, M. L. Andrews and A. D. Elkin. Long–term clinical course of patients after termination of ventricular tachyarrhythmia by an implanted defibrillator. Circulation, vol. 110 (25), 2004, 3760–3765.

[16] S. Nattel, A. Maguy, S. Le Bouter and Y. H. Yeh. Arrhythmogenic Ion-Channel Remodeling in the Heart: Heart Failure, Myocardial Infarction, and Atrial Fibrillation. Physiol. Rev., vol. 87, 2007, pp. 425–456.

[17] L. F. Pavarino and S. Scacchi. Multilevel additive Schwarz preconditioners for the Bidomain reaction-diffusion system. SIAM J. Sci. Comput., vol. 31, 2008, pp. 420–443.

[18] D. E. Roberts, L. T. Hersh and A. M. Scher. Influence of cardiac fiber orientation on wavefront voltage, conduction velocity, and tissue resistivity in the dog. Circ. Res., vol. 44, 1979, pp. 701–712.

[19] S. D. Roes, C. J. W. Borleffs, R. J. van der Geest, J. J. M. Westenberg, N. A. Marsan, T. A. M. Kaandorp, J. H. Reiber, K. Zeppenfeld, H. J. Lamb, A. de Roos, M. J. Schalij and J. J. Bax. Infarct tissue heterogeneity assessed with contrast-enhanced MRI predicts spontaneous ventricular arrhythmia in patients with ischemic cardiomyopathy and implantable cardioverter-defibrillator. Circ. Cardiovasc. Imaging., vol. 2 (3), 2009, pp. 183–190.

[20] J. Sjoberg and M. Kanje. The initial period of peripheral nerve regeneration and the importance of the local environment for the conditioning lesion effect. Brain. Res., vol. 529 (1–2), 1990, pp. 79–84.

[21] E. C. Stecker, C. Vickers, J. Waltz, C. Socoteanu, B. T. John, R. Mariani, J. H. McAnulty, K. Gunson, J. Jui and S. S. Chugh. Population–based analysis of sudden cardiac death with and without left ventricular systolic dysfunction: two-year findings from the Oregon Sudden Unexpected Death Study. J. Am. Coll. Cardiol., vol. 47 (6), 2006, pp. 1161–1166.

[22] K. H. W. J. ten Tusscher, D. Noble, P. J. Noble and A. V. Panfilov. A model for human ventricular tissue. Am. J. Phys. Heart Circ. Physiol., vol. 286, 2004, pp. H1573–H1589.

[23] K. H. W. J. ten Tusscher and A. V. Panfilov. Alternans and spiral breakup in a human ventricular tissue model. Am. J. Phys. Heart Circ. Physiol., vol. 291, 2006, pp. H1088–H1100.

[24] L. Tung. A bidomain model for describing ischemic myocardial D.C. potentials. Ph.D. dissertation M.I.T., Cambridge, MA, 1978.

[25] M. Vaseghi, W. Zhou, J. Shi, O. A. Ajijola, J. Hadaya, K. Shivkumar and A. Mahajan. Sympathic innervation of the anterior left ventricular wall by right and left stellate ganglia. Heart Rhythm, vol. 9 (8), 2012, pp. 1303–1309.

[26] A. L. Wit and M. J. Janse. The Ventricular Arrhythmias of Ischemia and Infarction: Electrophysiological Mechanisms. Mount Kisco, NY: Futura Publishing Company, 1993.

[27] A. T. Yan, A. J. Shayne, K. A. Brown, S. N. Gupta, C. W. Chan, T. M. Luu, M. F. Di Carli, H. G. Reynolds, W. G. Stevenson and R. Y. Kwong. Characterization of the peri-infarct zone by contrast-enhanced cardiac magnetic resonance imaging is a powerful predictor of post-myocardial infarction mortality. Circulation, vol. 114 (1), 2006, pp. 32–39.

Ex vivo vascular human-based models: new strategies to limit the use of animal models in vascular diseases studies

Marco Piola, Simona Seminati, Monica Soncini, and Gianfranco Beniamino Fiore
Dipartimento di Elettronica, Informazione e Bioingegneria, Politecnico di Milano, Milano, Italy

***Abstract*— The present contribution reviews our recent efforts to limit the use of animal models in the study of vascular diseases. In particular, this work presents the progress in the design of ex vivo vascular human-based models used to mimic arterial hemodynamic and biochemical conditions in human vascular grafts.**

***Keywords*—ex vivo models, vascular diseases, human tissue, saphenous vein.**

I. Introduction

CURRENT methodologies to study vascular diseases involve *in vitro* cell cultures and animal models [1]. Although standard *in vitro* cell cultures have undoubted advantages (i.e., to study cell-cell interactions, and cell migration when cytokines are used; low cost and ease of use), they suffer from several limitations (the lack of physiological 3D environment, physical stimuli and realistic environmental conditions, e.g. oxygen gradients). Conversely, animal models offer the possibility to study the physiological and pathological mechanisms in a more realistic scenario [2], [3], but the animals immune system is different from that of humans, thus animals may react to therapies in a different way [1]. Hence, human-based tissue models enabling the possibility to culture viable native tissues in controlled conditions within ad hoc ex vivo culture systems are mandatory to provide an actual and comprehensive knowledge of the mechanisms at the basis of human vascular physiology and/or pathology.

In the field of reliable *ex vivo* models with human-derived vascular tissue, remarkable results have been obtained by our group, among others. In particular, in the last years, in line with the 3Rs spirit, our group developed several *ex vivo* vessel culture systems [4], [5], [6], [7] hosting human-derived vessels. The novelty of the proposed approach is the possibility to have simple and easy-to-use culture chambers for hosting native tubular vessels coupled with control and fluidic systems enabling realistic post-implant hemodynamical and biochemical conditions.

Our most exploited models were designed to study the pathological evolution of human saphenous veins (hSVs) after coronary artery bypass grafting (CABG) and were conceived to mimic the post-surgery hydrodynamics and biochemical environment.

These approaches allowed the investigation of the human tissue mal-adaptation in a tightly controlled environment, and in perspective they will allow us to test pharmacological treatments to avoid or at least limit the vein graft pathological evolution.

After grafting, the hSVs are exposed to:

i) pulsatile pressure (80-120 mmHg) and wall stress/strain;
ii) pulsatile flow (mean flow: 150-170 ml/min) and wall shear stress (0.75–2.25 Pa);
iii) luminal/adventitial oxygen imbalanced distribution, with arterial oxygen level in the luminal side and low oxygen regimen in the adventitial region.

Considering this new environment, we developed human-based models, conceived for 7-14 days ex vivo culture conditioning, and ensuring tissue viability and sterility over time.

II. Ex vivo human-based models

A. Design specifications

The design of our *ex-vivo* models took into account the general specifications of bioreactors for tissue-engineering applications [8], with particular emphasis on the easiness of assembly under laminar flow hoods and the safety of use in a cell culture laboratory.

Specifically, the following basic requirements were addressed:
i) biocompatibility of materials;
ii) transparency of the culture chambers, to ensure visual inspection for air bubble formation and/or medium colour changes;
iii) compatibility with sterilization processes, e.g. via autoclaving and/or ethylene oxide (EtO) sterilization;
iv) minimization of priming volume, in order to limit the cost of soluble culture medium compounds and factors, and in perspective also of drugs used to test pharmacological treatments;
v) easiness of vessel accommodation and handling during the system assembly.

B. Design strategies

The layout of our system comprises:
i) culture chambers, hosting human vascular sample up to 5.5 cm in length;
ii) the use of commercial/ disposable falcon tubes;
iii) peristaltic pumps to ensure medium sterility;
iv) purpose-developed hydraulic circuits and actuators.

Human samples are cannulated at both ends, using polypropylene barbed fittings, and secured to the chamber using extensible vessel loops as elastic tourniquets.

Several ports through the culture chamber cap ensure the chamber's connection to the outside.

Luer connectors are used to guarantee hydraulic leak-free connections and facilitate circuit assembly under the laminar flow hood.

C. Ex vivo model for the pulsatile pressure stimulation of human saphenous veins

Description of the model - This model is designed to apply a cyclic CABG-like pressure stimulus, i.e. a pulsed pressure oscillating between a diastolic minimum and a systolic maximum (e.g., 80–120 mmHg) or a steady flow venous perfusion (e.g., 5 ml/min) within a controlled environment [4],[5]. A picture of the pulsatile culture system is shown in Fig.1A-C. During culture, SV grafts are hosted in a culture chamber accommodated inside an incubator and connected to a hydraulic circuit and actuators to apply pressure stimulation to the human vessels or to allow the medium to recirculate within the vessel (Fig.1D). This system is managed by a programmable control system, which operates via a pressure-based feedback loop.

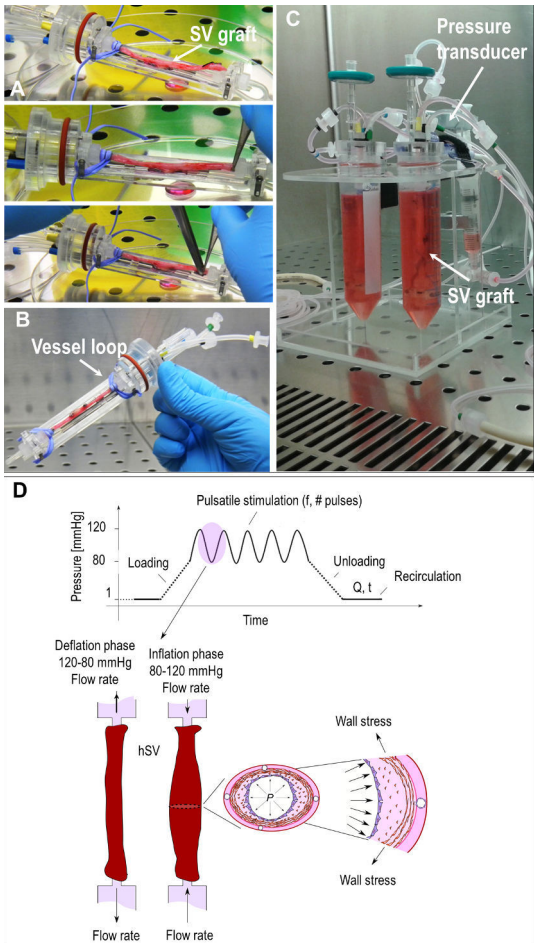

Fig. 1: *Ex vivo* model for the pulsatile pressure stimulation of hSVs. The hSV sample is mounted in the housing (A), secured via vessel loops (B), inserted within the 50-ml falcon tube and connected to the hydraulic circuit (C). The single pressure stimulation cycle (D) consists of: *i)* a loading phase (the luminal pressure reaches 80 mmHg); *ii)* a pulsatile stimulation phase (pressure oscillates between 80–120 mmHg at a desired pulse rate); *iii)* an unloading phase (pressure is lowered to zero); and *iv)* a recirculation phase with a constant flow rate allowing a metabolic supply to the vessel. During the inflation phase the cells covering the lumen (i.e., endothelial cells) and those embedded in the medial layer (smooth muscle cells) are subjected to circumferential stress and strain typical of the arterial circulation.

Results - This compact and automated system appears to be a well-suited system able to reproduce the wall strain conditions typical of the coronary circulation. The system maintains optimal tissue viability, operates under sterility and performs vessel stimulation in a low-volume culture chamber (35 ml). For these enhanced characteristics, this platform is a simple and reliable laboratory-orientated tool that can be useful for carrying out *in vitro* culture campaigns under strictly controlled hemodynamics conditions and dissecting the contribution of different biomechanical factors involved in vein graft disease.

In particular, the model allowed us to estimate the effect of the wall stress/strain on the hSV wall mal-adaptation. 7 days experiments on hSV segments showed wall thickness reduction, luminal perimeter enlargement and rupture of the endothelial layer.

D. Ex vivo model for the full mimicking of the coronary hemodynamic

Description of the model - This compact and low-priming volume pulsatile simulator enables stimulating hSVs with pressure and flow patterns of the coronary circulation (a sphygmic pulsatile pressure in counter-phase with a pulsatile flow rate) [6]. A picture of the system is shown in Fig. 2A.

This system comprises three main components (Fig. 2B):
i) a peristaltic pump equipped with a low-pass hydraulic filter for dampening its cyclical peristaltic disturbance;
ii) a service impedance;
iii) a coronary-like time-dependent impedance.

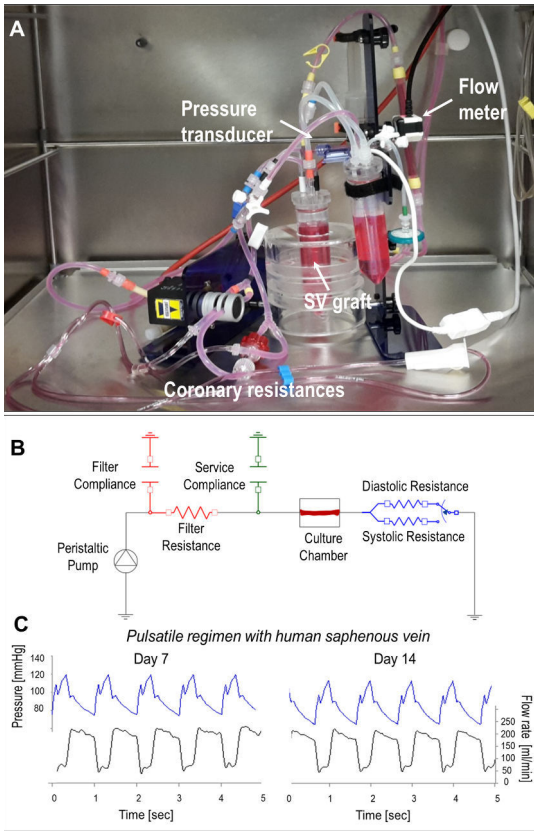

Fig. 2: Ex vivo model for the full mimicking of the coronary hemodynamic. Picture of the system posed inside the incubator (A). Lumped parameter model of the system: the hydraulic filter was implemented with an RC-low pass filter (red), the service impedance as a compliance element (green), and the coronary impedance as a time-switched parallel of two resistances (blue) (B). Pressure and flow rate data acquired during experiments in pulsatile conditions with hSV segments at 7 and 14 days (C).

While the coronary-like impedance acted as an afterload, placed in line with the SV culture chamber, the service impedance was placed in parallel, dynamically acting to yield the desired pressure-flow behavior in the SV hydraulic line (Fig. 2C). This system has been recently upgraded enabling multiple samples conditioning in parallel and semi-automatic medium change.

Results - The adopted approach enabled us to investigate *ex vivo* the effects of the altered flow and pressure conditions experienced by the hSV after CABG using a novel pulsatile model, specifically conceived for *ex vivo* culture experiments. Data revealed decrease of the intima and media thickness, partial endothelial denudation, and cell apoptosis.

E. Ex vivo model to recapitulate the oxygen milieu after human saphenous vein grafting

Description of the model - This model is designed to reproduce the imbalanced oxygen distribution in the arterialized vein after transplantation in the coronary environment (Fig. 3A) [7]. A double-compartment chamber includes two commercial reservoirs (the inner and the outer chamber) and a purpose-developed vessel housing chassis, which is integrated with the reservoir cap. The chamber is coupled with a compact de-oxygenator. The de-oxygenator consists of oxygen-permeable silicone tubing rolled up a tubing support made with polymethylmethacrylate, and hosted in a commercial 50-ml falcon tube. The system allowed the establishment of an inside-out oxygen gradient by setting (Fig. 3B):

i) a low oxygen level (5% pO_2) at the adventitial side, and an arterial oxygen level (21% pO_2) at the luminal side;

ii) an arterial oxygen level (21% pO_2) at the adventitial side and luminal side.

Results - The device proved to be a versatile, easy to use and functional system that did not cause major damages to the vessels over the time of the cultures. Also, it is compatible with the best standards for good laboratory practice and a valuable alternative to bubbling a gas mixture in the culture medium, or unwieldy and expensive oxygen-controlled cell culture incubators. The bioengineering approach employed in the present study enabled an *ex vivo* investigation of the effects induced by differential oxygen level on adaptive changes occurring in arterialized vein conduits. Data demonstrated a massive adventitial neo-vascularization, a factor known to predispose the arterialized veins to restenosis.

III. Conclusion

We strongly believe that integrating vascular biology with bioengineering and biomechanics design/modelling facilitates the understanding of vascular diseases and, in perspective, will speed up the development of new-lifesaving treatments.

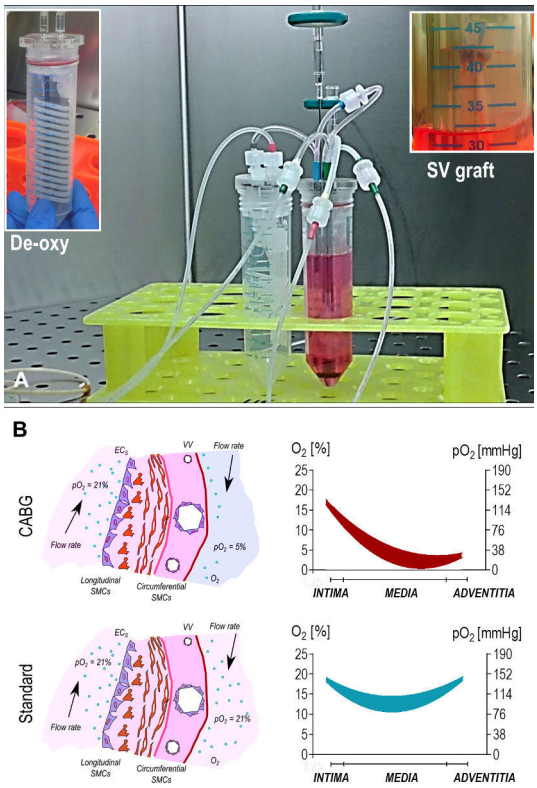

Fig. 3: Ex vivo model to recapitulate the oxygen milieu after hSV grafting. Image of the system connected to the de-oxygenator module and to the hydraulic circuit. Insets: de-oxygenator module (left) and zoomed image of the double-compartment chamber with hSV (A). Simplified representation of the oxygen levels in the vascular tissue in CABG (Luminal O_2: 21%; Adventitial O_2: 5%) and standard conditions (Luminal O_2: 21%; Adventitial O_2: 21%). The graphs show the theoretical oxygen saturation (%) and partial pressure (mmHg) pattern within the vein wall in both the tested conditions (B).

References

[1] J. Jeremy et al., "Animal Models for Studying Neointima Formation" in *Current Vascular Pharmacology,* 2010, pp. 198–219(22).

[2] S. Katsuki et al., "Nanoparticle-mediated delivery of pitavastatin inhibits atherosclerotic plaque destabilization/rupture in mice by regulating the recruitment of inflammatory monocytes" in *Circulation* 2014, pp. 896-906.

[3] S. Nakashiro et al., "Pioglitazone-Incorporated Nanoparticles Prevent Plaque Destabilization and Rupture by Regulating Monocyte/Macrophage Differentiation in ApoE-/- Mice" in *Arteriosclerosis Thrombosis Vascular Biology,* 2016, pp. 491-500.

[4] M. Piola, et al., "A compact and automated ex vivo vessel culture system for the pulsatile pressure conditioning of human saphenous veins" in *Journal of Tissue Engineering and Regenerative Medicine,* 2016, pp. E204-15.

[5] F. Prandi et al., "Adventitial vessel growth and progenitor cells activation in an ex vivo culture system mimicking human saphenous vein wall strain after coronary artery bypass grafting" in *PLoS One* 2015, pp. e0117409.

[6] M. Piola, et al., "Full Mimicking of Coronary Hemodynamics for Ex-Vivo Stimulation of Human Saphenous Veins" in *Annals of Biomedical Engineering* , 2017, pp. 884-897

[7] M. Piola, et al., "Human Saphenous Vein Response to Trans-wall Oxygen Gradients in a Novel Ex Vivo Conditioning Platform" in *Annals of Biomedical Engineering*, 2016, pp. 1449-61

[8] I. Martin, et al., "The role of bioreactors in tissue engineering" in *Trends Biotechnology*, 2004 pp. 80–86.

A novel method for slippage detection with tactile sensors

R. A. Romeo[1], A. Davalli[2], R. Sacchetti[2], E. Guglielmelli[1], and L. Zollo[1]
[1] *Research Unit of Biomedical Robotics and Biomicrosystems, Università Campus Bio-Medico di Roma, Rome 00128, Italy*
[2] *Centro Protesi INAIL, Budrio, Italy.*

***Abstract*— The perception of slippage is one of the distinctive abilities of human tactile sensing. The sense of touch allows recognizing a wide set of properties of a grasped object, such as shape, weight and dimension. Based on such properties, the applied force can be regulated accordingly, and slippage of the grasped object can be avoided. Despite the great importance of tactile sensing for humans, biomechatronic hands are rarely endowed with tactile feedback. In this paper, a new method for slippage detection is described. The algorithm can work with just a monoaxial force information and was previously validated on a biomimetic fingertip including four MEMS tactile sensors. Here, the application on a Force Sensitive Resistor (FSR) sensor mounted on a prosthetic finger is shown. The experimental results confirm the possibility to generalize the use of the proposed method for slippage detection to different categories of tactile sensors.**

***Keywords*—Slippage, Tactile, Robotics, Prosthetics.**

I. Introduction

TACTILE sensing is a crucial property of human skills. Objects with disparate shapes, surfaces and weights can be grasped and manipulated by the human hand in such a fine manner that is not paralleled by any other biological system. By exploiting different kinds of sensing units, the sense of touch allows humans to recognize a great quantity of properties of an object: roughness, shape, dimension, weight, hardness, humidity, temperature. Based on this set of properties, the hand is able to regulate the applied force of each finger when grasping an object. This provides the hand with the possibility to carry out a fundamental action, i.e. to avoid slippage when the contact condition modifies disadvantageously. Motor commands can adjust grip force in less than 100 ms since the onset of a disturbance [1].

These skills are still quite difficult to reproduce into artificial systems. Robotic and mechatronic manipulators rarely rely on tactile data [2], as artificial tactile sensors have a number of drawbacks. For instance, hysteresis and non-linearity are highly common. As a result, artificial manipulators are principally found in structured environments, relying on a priori knowledge rather than on active tactile sensing.

Further, the combination of static and dynamic sensing is not straightforward. In fact, the detection of dynamic events, such as slippage, often requires the exploitation of a dedicated sensing unit resorting on a different transducing principle w.r.t. the one employed for static contact force measurement. A direct consequence is the difficulty to endow artificial end effectors with slippage sensors, as their encumbrance can be problematic if added to the presence of e.g. a force sensor.

Nonetheless, improving tactile information with the inclusion of algorithms for slippage detection can predispose the robots towards a more natural behaviour, allowing e.g. reactions to unexpected events and situations. Sensory feedback from tactile sensors would be of great help in many robotic domains, such as robotic manipulation and prosthetics. Unfortunately, the current state of the art regarding commercial prosthetic hands reports only one case of device provided with tactile sensors employed for slip control [3]. This confirms that tactile sensing technologies, including slip detection, are not easily applicable to prosthetic systems yet, despite the considerable efforts of the last years.

The literature proposes a huge number of tactile sensors and techniques for slippage detection. The main approach used until the end of last century relied on the calculation of the static friction coefficient from normal and tangential force measurements [4]. This requires a multiaxial force sensor in order to measure forces at least along two axes (including the normal one). As an alternative, tangential forces can be analyzed in the frequency domain [5] by resorting to Fast Fourier Transform (FFT), and Power Spectrum Density (PSD). Discrete Wavelet Transform (DWT) gained consideration in the last years as well, as it is applicable to both normal and tangential forces [6] without loss of time information as in the case of FFT. A widespread solution is to combine more sensing units for static and dynamic information. To this purpose, force sensors can be jointly used with piezoelectric (such as Polyvinylidene fluoride (PVDF) or lead zirconate titanate (PZT)) sensors for slip management [7]. The employment of accelerometers as slippage sensors was also proved [8].

Further techniques exploit the derivative function of the normal component of the estimated force [9], or else, the vibrations in a fluid sealed into the core of a biomimetic sensor [10]. This is the case of the commercial sensor BioTac (by SynTouch, Montrose, CA, USA), which is able to provide slippage information by means of a band-pass filtered signal of a fluid pressure measurement in the 10–1040 Hz range.

All the reported works present sensors and/or techniques for the detection of slippage often resorting to force measurement on more axes. Multiaxial sensors are generally more expensive than monoaxial ones. In some cases, monoaxial force is sufficient for slip identification. Nonetheless, very limited attention was traditionally paid to the correct distinction between true positives (i.e., the actual slip event) and false positives (i.e., dynamic events such as contact with an object, which may be misled as slip events).

In this paper, a new method [11] for the detection of slippage

events is proposed; it provides an ON/OFF slip information thanks to online processing of a force sensor output. Simple operations such as digital filtering, rectification and envelope of the input signal are cascaded in order to generate the ON/OFF slip signal. The method was previously validated with a biomimetic fingertip providing sixteen monoaxial outputs from four MEMS tactile sensors [12]. Tested surfaces had ridged patterns with known pace. Here, the method application was assessed on Force Sensitive Resistors (FSR) sensors and the tested surfaces had roughness typical of objects handled in everyday life. The algorithm yielded successful performance with just one force component (e.g. normal), and correctly allows discarding false positives.

II. Description of the Algorithm

The method consists of three main blocks, which are put in cascade. Single axis information is enough for estimating applied force and for detecting slip events. This is possible thanks to the idea that the force signal (i.e., the voltage), which is characterized by high amplitude and low frequencies, carries a higher frequency content when the sensor is slid over a surface, or vice-versa. Such a content can be extracted by means of adequate filtering operations. At this point, a low amplitude, high frequency signal is generated; the presence of dense fluctuations indicates that the relative movement is happening between the object and the sensor. The low frequencies due to application of static load are filtered out from the voltage signal, privileging the faster variations produced by slip. The filtering operation is followed by a rectification of the signal, which is in turn followed by an enveloping phase. An ON/OFF signal relative to the onset of a slippage event is then generated.

The proposed method for slip detection works properly taking as input either the FSR raw piezoresistive voltage or the calibrated force value. The FSR basically behaves as a varying electrical resistance. By means of an appropriate circuit, such a variation can be transduced into a voltage. In this paper, the so obtained voltage served as input for the proposed algorithm. Though, using the estimated force leads to equivalent results, as its trend and variations are the same. The algorithm blocks are described in detail below; a block scheme of the whole algorithm is depicted in Fig. 1, whereas the schematic diagram of the circuit is shown in Fig. 2.

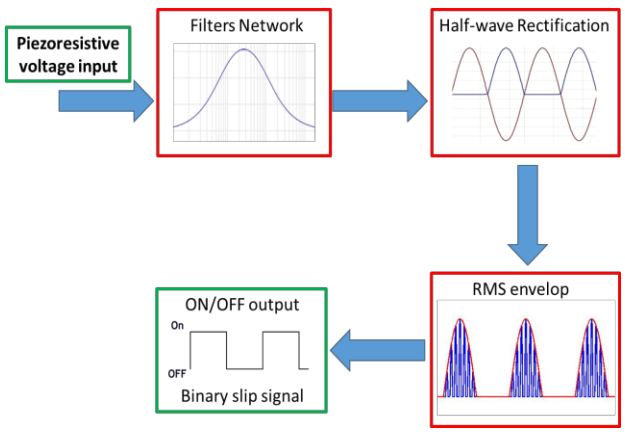

Fig. 1: Block diagram of the algorithm.

Differently from [12], the algorithm was this time implemented through a hardware solution. A dedicated PCB was printed in order to receive the piezoresistive input and to perform the operations of the various algorithm blocks, with the only exception of the ON/OFF signal generation; the latter was done through a Matlab mathscript embedded into a LabVIEW code. The choice of a high passband, e.g. above 500 Hz, allows more effective elision of false positives due to contact and/or release of the sensor during the interaction with the object. Notwithstanding, by excluding all the frequencies below 10 Hz (which dominate in the static force signal), it is still possible to get a generalized filtering block for each type of resistive sensor.

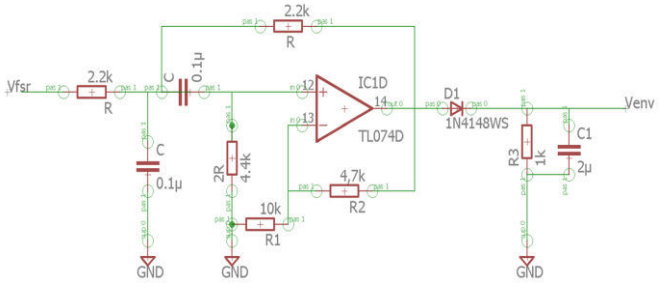

Fig. 2: Schematic diagram of the whole circuit.

A. Filters

A second-order bandpass filter was realized to extract the slip content. The Sallen-Key topology was selected, and according to the chosen values of capacitors and resistors, the transfer function is expressed in the Laplace domain by:

$$H(s) = G\frac{\omega_m s}{s^2+\frac{\omega_m}{Q}s+\omega_m^2}, \quad (1)$$

where $\omega_m=1/RC$ is the mid-frequency of the filter, i.e. the frequency at which $H(s)$ reaches its maximum, and $Q=1/(3-G)$ is the quality factor of the filter. The gain G is given by $1+R2/R1$ and was equal to 1.5 as $R1=10\ k\Omega$ and $R2=4.7\ k\Omega$. The quality factor Q determines how selective the filter is. That is, the higher the Q, the narrower is the bandpass, which is centered at $f_m=\omega_m/2\pi$. In the present case, a Q lower than 1 was considered appropriate, though higher values offer better performance. Considering that $C=0.1\ \mu F$ and that $R=2.2\ k\Omega$, the mid-frequency f_m was set to around 724 Hz. A graphical representation of the filter response is omitted for sake of brevity. Sallen-key topology allows controlling the gain G of the filter independently from the mid-frequency f_m

B. Rectification

Immediately after the filtering stage, a rectification stage is built; in this case, it was a half-wave rectification, consisting of a diode (1N4148) in series to the said filter network and a resistor (R3) between the diode and the ground. The filtering stage provides a high frequency signal, but still characterized by a bipolar nature. The rectification can improve the capability of the signal to overcome a given threshold. By converting the polarity of the negative spikes, the time window within which the signal can be ON (i.e., above

threshold) can be longer than in the case of a bipolar signal. Thus, a full-wave rectification comes to be desirable. Anyway, at least a half-wave rectification, consisting in erasing one of the two polarities spikes, has to be executed; it is needed for allowing an easier accomplishment of the next operation (i.e., envelope). Full-wave rectification would possible by realizing a diodes bridge in place of the single diode used in the current approach, yet a half-wave rectification was deemed to be sufficient for an initial hardware implementation.

C. *Envelope and ON/OFF generation*

The RMS of the signal was achieved through a supplementary stage. The addition of a capacitor in parallel to R3 gives way to an actual low-pass filter, which produces an envelope of the high frequency rectified signal. The envelope generates a continuous curve starting from the peaks of the rectified signal. This facilitates the threshold overcoming of the signal for a longer time interval. At this point, the ON/OFF slip signal can be obtained with a threshold mechanism executed with the above mentioned mathscript in the LabVIEW code. The time window for the ON/OFF calculation was chosen as large as 40 ms. In this way, a real-time functioning is achievable as demonstrated in a previous work [13]. There is no theoretical limit for the window width: it can be chosen as narrow (or large) as desired. A time window of 1 ms, or even smaller, is also possible, depending on the sampling frequency (e.g., sampling at 2 kHz implies the smallest window to be 0.5 ms): though, false positives will be inevitably comprised in the ON/OFF signal.

III. Experiments and Results

A. *Experimental set-up*

The experimental set-up used for testing the method with the FSR sensors consisted of an FSR sensor placed on a plastic distal phalanx of the IH2 hand, which was purposely removed from the robotic hand. The phalanx was covered with a silicon cap (Figure 3), simulating the prosthetic cover of a common prosthetic hand. The so obtained fingertip was interfaced to a 7 DoF robot (namely KUKA-LWR 4+) by means of a thin, cylindrical plastic segment. The robot moved the fingertip itself upon the test surfaces, releasing it after a sliding movement of 2 cm.

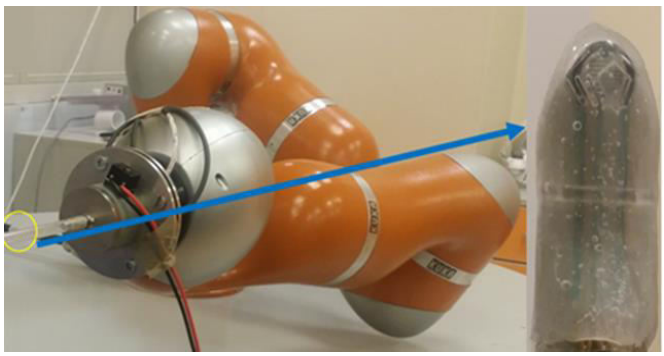

Fig. 3: KUKA-LWR 4+ robot with end effector. On the right, detail of the prosthetic finger provided with an FSR and covered with a silicone material.

Thus, the exploration was “active”, whereas a passive exploration would imply the translation of the surface under the fingertip kept still. Three trials per each tested surface were performed with the FSR sensors. Tested surface had the following roughness values: 0.2 µm, 0.8 µm and 3.2 µm. Of the three trials per surface, one was executed with a velocity equal to 2 cm/s, one with a velocity of 4 cm/s, and the last one with 8 cm/s. All the data were acquired at a sampling frequency of 2000 Hz.

B. *Results*

Fig. 4 and Fig.5 show some representative results of the algorithm application. The voltage, which is linked to the exerted force, exhibits negative variations as the amplifier configuration in the FSR conditioning circuit (not shown) was inverting, thus with negative gain. As a consequence, lower voltages are associated with higher forces.

Figure 4 relates to a trial executed on the roughest available surface, i.e. 3.2 µm, at a speed of 4 cm/s. The ON/OFF signal covers all the duration of the induced slippage, without presence of any false positive. Figure 5 illustrates instead a trial executed at a velocity of 2 cm/s, this time on the 0.8 µm roughness surface. Clearly, the smaller is the velocity, the harder is to detect slip. Nonetheless, slip event was correctly recognized in this case as well; the ON/OFF signal is not continuous but, once the onset of the slip event was recognized with an acceptable delay, this was no longer an issue. In this trial, the voltage level appears to change at the contact phase, differently from the precedent trials. Small signal peaks can be observed during contact and release phases, though they are properly excluded by the ON/OFF threshold mechanism.

Note that the force was applied by the robotic arm with random values. For this reason, in Fig. 4 and Fig. 5 the force level after contact and before slippage is different. In Fig. 4, it seems that the FSR cannot perceive any pressure until the fingertip is translated. In Fig. 4 the applied force is much less than in Fig. 5 and a clear variation is noticeable only as the slip occurs (black bars). Hence, the vertical scale in the two figures is diverse.

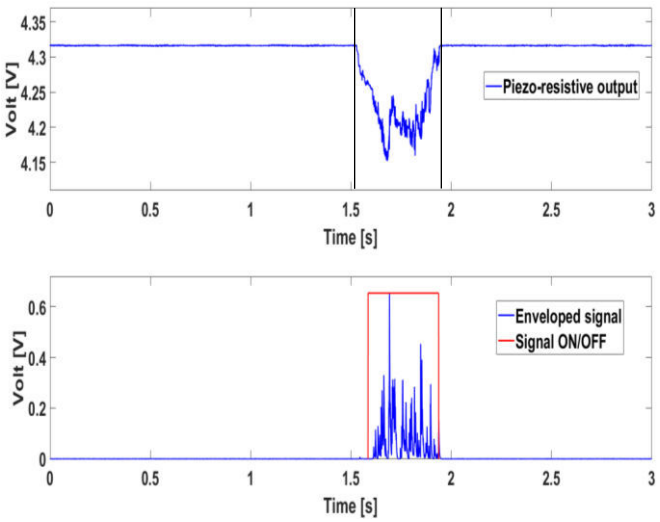

Fig. 4: FSR raw voltage signal (top) and algorithm output (bottom). Test surface: 0.2 µm roughness. Velocity: 4 cm/s.

Note also how the slippage duration changes according to the velocity of the experiment. The trial in Fig. 5 includes a contact phase around one second prior to the slip event. No false positive is evident; the same applies to the release phase of all trials.

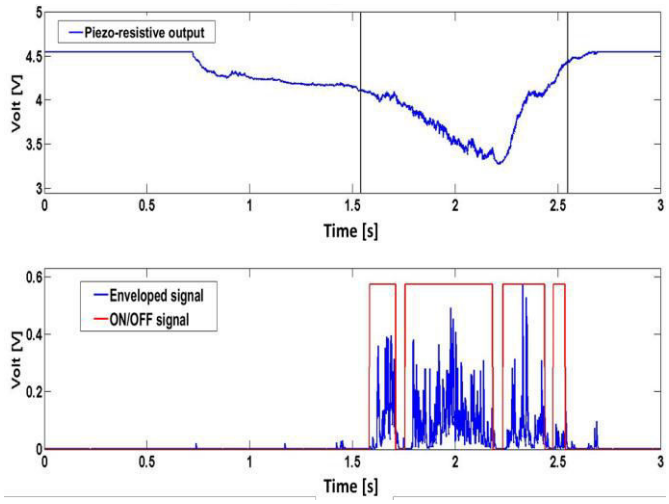

Fig. 5: FSR raw voltage signal (top) and algorithm output (bottom). Test surface: 0.8 µm roughness. Velocity: 2 cm/s.

TABLE I
MEAN DELAYS FOR DIFFERENT EXPERIMENTAL CONDITIONS

Velocity	*0.2 µm*	*0.8 µm*	*3.2 µm*
2,4, 8 cm/s	*35.44 ms*	*31.89 ms*	*25.71 ms*

IV. CONCLUSION

In this paper, a novel method for detection of slippage events with prosthetic hands was proposed. Said method was presented through a description of its sub-blocks, which include simple operations such as filtering, rectification and envelope of the input signal. Such sub-blocks are cascaded in order to generate the ON/OFF signal. The method was previously validated on piezo-resistive MEMS sensors [12], and was now assessed on FSR sensors. An ad hoc automated set-up was conceived for this purpose. The employed sensors were mono-axial, providing only the normal component of the applied force. This represents the main advantage of the algorithm, that is it can yield an ON/OFF slip information resorting on a single-axis force component. It is not necessary to employ the force value to apply the method on: the raw output voltage (relating to the force) can be used, retrieving the force value and generating the ON/OFF signal as parallel operations rather than consecutive. Besides, the ON/OFF signal can be integrated into online prosthesis control systems, as demonstrated in [13]. No false positives were detected during contact and release phases.

Although the slippage detection method proposed herein was validated with more sensors typologies, experimental tests have concerned piezoresistive sensors only; a reasonable step is to extend the validation tests on different technologies, such as capacitive, optical et., augmenting the already good generality of the method. Further optimization can be done in the choice of parameters such as the time window of the ON/OFF calculation.

ACKNOWLEDGEMENT

This work was supported by the National Institute for Insurance against Accidents at Work (INAIL) with PPR2 project "Control of upper-limb prosthesis with neural invasive interfaces" (CUP: E58C13000990001), with PPR AS 1/3 project "Implantable System for the control of an upper-limb prosthesis with invasive wireless neural interfaces" and PCR 1/2 project "New methods in the treatment of limb amputation, finalized to the application of bionic prostheses" (CUP: E57B16000160005).

REFERENCES

[1] R.S. Johansson, G. Westling, "Roles of glabrous skin receptors and sensorimotor memory in automatic control of precision grip when lifting rougher or more slippery objects," *Exp. Brain Res.*, vol. 56, pp. 550-564, 1984.

[2] R. S. Dahiya, P. Mittendorfer, M. Valle, G. Cheng, V. J. Lumelsky, "Directions toward effective utilization of tactile skin: A review." *IEEE Sens. J.*, vol. 13, pp. 4121-4138, 2013.

[3] A.L. Ciancio, F. Cordella, R. Barone, R. A. Romeo, A. Bellingegni-Dellacasa, R. Sacchetti, A. Davalli, G. Di Pino, F. Ranieri, V. Di Lazzaro, E. Guglielmelli and L. Zollo, "Control of prosthetic hands via the peripheral nervous system," *Front. Neurosci.* vol. 10, pp. 1–17, 2016.

[4] A. Mingrino, A. Bucci, R. Magni, P. Dario, "Slippage Control in Hand Prostheses by Sensing Grasping Forces and Sliding Motion," in *1994 Proc. IEEE/RSJ/GI Int. Conf.*

[5] R. Fernandez, I. Payo, A.S. Vazquez, J. Becedas, "Micro-Vibration-Based Slip Detection in Tactile Force Sensors," *Sensors*, vol. 14, pp. 709–730, 2014.

[6] Y. Wang. K. Xi and D. Mei, "Slip Detection in Prosthetic Hand Grasping by using the Discrete Wavelet Transform Analysis," in *2016 Proc. AIM conf.*

[7] B. Choi, S. Kang, and H. Choi, "Development of Fingertip Tactile Sensor for Detecting Normal Force and Slip," in *2005 Proc. ICCAS conf.*

[8] M. R. Tremblay, M. R. Cutkosky, "Estimating Friction Using Incipient Slip Sensing During a Manipulation Task", in *1993 Proc. IEEE ICRA conf.*

[9] C.F. Pasluosta, A. W. Chiu, "Evaluation of a Neural Network-Based Control Strategy for a Cost-Effective Externally-Powered Prosthesis," *Assist. Technol.*, vol. 24, pp. 196–208, 2012.

[10] J. A. Fishel, G. E. Loeb, "Sensing Tactile Microvibrations with the BioTac—Comparison with Human Sensitivity," in *2012 Proc. IEEE RAS/EMBS conf.*

[11] R.A. Romeo, L. Zollo and E. Guglielmelli, "Method for Detection of Slippage with Force Sensors and Apparatus Thereof," IT Patent 102016000105302, October19, 2016.

[12] R. A. Romeo, C. M. Oddo, M. C. Carrozza, E. Guglielmelli and L. Zollo, "Slippage detection with piezoresistive tactile sensors," *Sensors*, vol. 17, 2017.

[13] R. Barone, A. L. Ciancio, R.A. Romeo, A. Davalli, R. Sacchetti, E. Guglielmelli, and L. Zollo, "Multilevel control of an anthropomorphic prosthetic hand for grasp and slip prevention," *Adv. Mech. Eng.*, vol. 8, pp. 1–13, 2016.

A mathematical model of healthy and dystrophic skeletal muscle biomechanics

M. Stefanati[1], C. Villa[2], Y. Torrente[2] and J. F. Rodriguez Matas[1]
[1] *Department of Chemistry, Materials, and Chemical Engineering "Giulio Natta", Politecnico di Milano, Italy*
[2] *Stem Cell Laboratory, Department of Pathophysiology and Transplantation, Università degli Studi di Milano, Italy*

***Abstract*—Neuromuscular (NM) disorders as Duchenne Muscular dystrophy (DMD) affect muscle fibers and/or the central and peripheral nervous system and the NM junction that control the muscle fibers. At present, these disorders are often incurable. As life expectancy rises, the prevalence of late-onset disorders causing chronic muscle weakness increases. Muscle symptoms can manifest from midlife onward, leading to a drastic functional decline with social and economic burdens. A better understanding of the mechanisms underlying the pathogenesis of muscle atrophy and wasting associated with DMD represents an important first step for the development of novel therapeutic approaches. In this work, we develop a three-dimensional chemo-mechanical mathematical model of skeletal muscle for Duchenne Muscular Dystrophy (DMD). The model is inspired on the biophysics of the muscle and studies of changes in muscle fiber structure and interaction aiming to shade light into the biophysical mechanisms regulating muscle contraction and develop novel and more effective pharmacological approaches. Results demonstrate the ability of the model to describe passive and active behaviour of both the healthy and pathologic muscle.**

***Keywords*—skeletal muscle model, mathematical model, mice diaphragm muscle, Duchenne muscular dystrophy.**

I. Introduction

DUCHENNE muscular dystrophy (DMD) is a devastating muscle degenerative disease caused by a mutation in the dystrophin gene [1]. Dystrophin is a cytoskeletal protein essential for the stability of multinucleated myofiber membrane in skeletal muscle [2], whose lack results in increased fragility of the sarcolemma [3]. DMD patients suffer from progressive loss of muscle function to paralysis and death in the third decade of life [4]. In normal muscle healing after an acute/moderate injury, normally quiescent satellite cells (muscle stem cells) become activated and prone to proliferate and differentiate into myoblasts that fuse at the damage site to form new myofibers. On the contrary, dystrophic muscle shows homeostasis impairment of satellite cells [5], and also features structural defects, enzymatic and epigenetic modifications leading to skeletal muscle wasting and necrosis accompanied by inflammatory cells infiltration. The chronic nature of the disease with continuous cycles of muscle degeneration/regeneration determines unsuccessful muscle regeneration, typically characterized by persistent myofiber degeneration, inflammation and fibrosis, which is essentially an excessive accumulation of ECM components contributing to muscle weakness.

Significant advances in the mathematical model of skeletal muscle have been produced in the last two decades [6–11]. These models simulate the dynamic behavior of muscles with mathematical equations inspired by muscle contractile processes (cross-bridge mechanisms), coupling chemical reaction equations governing cross-bridge kinetics with cross-bridge distortion responsible for the active force generation. However, these mathematical models have been developed for healthy muscle, with little efforts regarding the application to DMD skeletal muscle. Current modelling on dystrophic muscle is limited to study the relationship between microstructural disease adaptations and modifications in the mechanical properties of muscle (passive) and strain in the cell membrane, not accounting for chemo-mechanical interactions, and ignoring the active response of the muscle [12].

The aim of this work is building a comprehensive chemo-mechanical model of muscle-skeletal tissue amenable for modeling dystrophic skeletal muscle. The model accounts for the contribution of individual muscle fibers and the extracellular matrix (ECM). The main supported hypothesis behind is that, the myosin function, as well as the single fiber mechanics, do not underlie the weakness of the dystrophic muscle [13,14] and, consequently, the muscle active part (myofibril) is not seriously affected by the dystrophic disease. So, it is hypothesized that the loss of isometric contraction force and isotonic concentric contraction stretch velocity is a mechanical problem resulting from increase of muscle matrix stiffness, loss of number and density fiber, decrease of lateral transmission force efficiency [15] and muscle fibers non-uniformity [16].

II. Mathematical Model

The mathematical model of skeletal muscle is based on the stiffness-distortion sarcomere model presented by Campbell et al. [17]. The model is formed of two parts: i) the myofilament [Ca^{2+}] kinetics (see Fig. 1a), and ii) the mechanical model of the muscle composed of the cross-bridge force generation and the passive response of the extracellular matrix (see Fig. 1b).

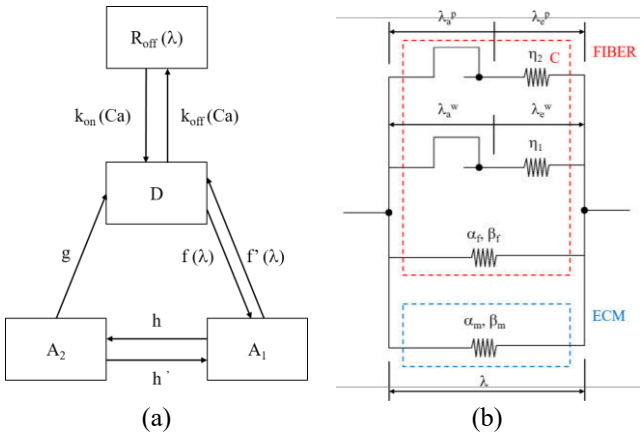

(a) (b)

Fig. 1: Myofilament kinetics.

The myofilament [Ca^{2+}] kinetics is described by a reduced

three state model (see Figure 1a). A state in which the myosin heads are detached from actin filament (D), a state in which the myosin heads are attached to actin filament in a weak load bearing condition (pre-power stroke A_1), and a state in which the myosin heads are attached to actin filament in a power load bearing condition (post-power stroke A_2). This model is described by a set of three non-linear ordinary differential equations given in [17].

The cross-bridge force generation are derived from a distortional balance that accounts for distortion entering and leaving due to cross-bridge cycling and for distortion imposed by shear motion between thick and thin filaments in both the weak and power stroke states A_1 and A_2. This translates mathematically into two first order nonlinear differential equations for the cross-bridge cycling governing the active stretches λ_a^w (pre-power stroke), and λ_a^p (post-power stroke) associated with the muscle fiber (see Fig. 1b). Let $s_1 = \log \lambda_a^w$, and $s_2 = \log \lambda_a^p$,

$$\begin{aligned} \frac{ds_1}{dt} &= \left(f\frac{D(t)}{A_1(t)} + h'\frac{A_2(t)}{A_1(t)}\right)(\log\lambda - s_1 - s_r^w), \\ \frac{ds_2}{dt} &= h\frac{A_1(t)}{A_2(t)}(\log\lambda - s_2 - s_r^p), \end{aligned} \tag{1}$$

where f, h, h' are rate constants given in [17], and s_r^w, s_r^p are the cross-bridge deformation in steady state conditions.

The muscle stress-strain relation is derived by postulating the existence of a strain energy function taken to be a function of the macroscopic deformation of the muscle, λ, and the cross-bridge active stretches λ_a^w and λ_a^p defined in terms of s_1 and s_2 [8,9]. The strain energy function, W, is decoupled into a strain energy function related to skeletal fiber, W_f, and a strain energy function related to skeletal muscle extracellular matrix, W_{matrix}. According to the model shown in Fig. 1b, for a one-dimensional case, the strain energy function reads

$$W(\lambda, \lambda_a^w, \lambda_a^p) = W_{matrix}(\lambda) + CW_f(\lambda, \lambda_a^w, \lambda_a^p), \tag{2}$$

where C is a constant associated with the density of muscle fibers present in the muscle. The matrix is assumed to be isotropic and described by a first order Ogden strain energy function

$$W_{matrix} = 2\frac{\alpha_m}{\beta_m}\left(\lambda^{\beta_m} + 2\lambda^{-\frac{\beta_m}{2}}\right), \tag{3}$$

where α_m and β_m are material parameters identified from passive stress-strain tests of the whole muscle.

The strain energy function for the fiber is also split into a passive and an active contribution as

$$W_f(\lambda, \lambda_a^w, \lambda_a^p) = W_{f,p}(\lambda) + W_{f,a}(\lambda, \lambda_a^w, \lambda_a^p). \tag{4}$$

As for the extracellular matrix, the passive component of the muscle fiber is modelled with a first order Ogden strain energy function

$$W_{f,p}(\lambda) = 2\frac{\alpha_f}{\beta_f}\left(\lambda^{\beta_f} + 2\lambda^{-\frac{\beta_f}{2}}\right), \tag{5}$$

where α_f and β_f are material parameters identified from passive stress-strain tests of the muscle fiber. The active strain energy function for the muscle fiber is defined as

$$\begin{aligned} W_{f,a}(\lambda, \lambda_a^w, \lambda_a^p) = \; & \hat{\eta}_1 A_1 \tfrac{1}{2}(\log\lambda - s_1)^2 + \\ & \hat{\eta}_2 A_2 \tfrac{1}{2}(\log\lambda - s_2)^2, \end{aligned} \tag{6}$$

where $\hat{\eta}_1$ and $\hat{\eta}_2$ are elastic constants for the pre- and post-power stroke states, which are identified from isometric force-velocity curves.

Passive and active muscle Cauchy stress can be readily derived from the strain energy function as

$$\sigma = \lambda\frac{\partial W}{\partial \lambda}. \tag{7}$$

The resulting model has a total of seven parameters to fit, two associated with the extracellular matrix (α_m and β_m), and five associated with the muscle fiber (C, α_f, β_f, $\hat{\eta}_1$ and $\hat{\eta}_2$).

III. Specialization of the Model

The proposed model can be used to model muscle-skeletal tissue in general. However, since we are interested in studying mechanisms associated with DMD, the model has been specialized to healthy and dystrophic (mdx) mice, one of the mostly used animal models of DMD [18]. In particular, the attention has been fixed to the diaphragm (DIA), which exhibits significant fibrosis as well as greatly impaired contractile function from an early age, and is regarded as a close phenotype to the human dystrophic muscle [19].

Since experimental observations support that, the myosin function, as well as the single fiber mechanics, do not underlie the weakness of the dystrophic muscle [13,14], the myofilament kinetics (Fig. 1a) of dystrophic mouse has been assumed to remain unaltered to the healthy mouse. We have adopted rate constants reported in [17]. In addition, we have assumed $s_r^w = 0.0002$, s_r^p=0.0091.

The passive fiber model parameters, α_f and β_f, were obtained from fitting uniaxial tensile test curves for sarcomeres reported by Granzier et al. [20] and were assumed equal for healthy and dystrophic muscle. Material parameters of the extracellular matrix, α_m and β_m, for healthy and dystrophic muscle were obtained by fitting uniaxial stress-strain curves for healthy and mdx DIA performed in our laboratory and shown in Fig. 2.

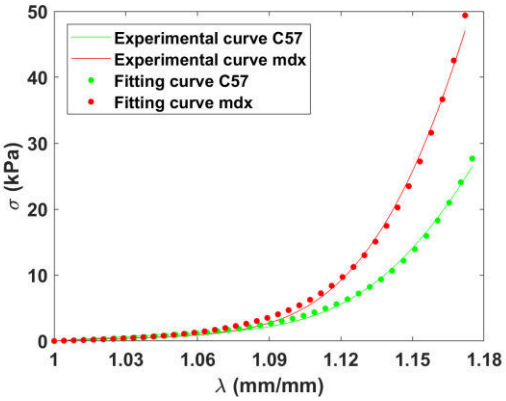

Fig. 2: Experimental passive stress-stretch for healthy and mdx DIA.

The remaining model parameters C, $\hat{\eta}_1$ and $\hat{\eta}_2$, for healthy and dystrophic muscle were found by means of a nonlinear

least square minimization of normalized specific force-stretch velocity curve for healthy and MDX mouse DIA [21], while constraining isometric contraction force [14] and isotonic concentric contraction stretch velocity [21,22] within the range reported in the literature. The constrained optimization problem was solved in Matlab.

TABLE I
MECHANICAL PARAMETERS FOR THE HEALTHY AND DYSTROPHIC DIA

PARAMETERS		*Healthy muscle*	*Dystrophic muscle*
C	(-)	1.00	0.33
α_m	(kPa)	0.039	0.068
β_m	(-)	35.865	37.046
α_f	(kPa)	0.369	0.369
β_f	(-)	7.852	7.852
$\hat{\eta}_1$	(MPa)	22.19	41.95
$\hat{\eta}_2$	(MPa)	168.3	168.3

Table 1 summarizes the model parameters identified in the fitting process for the healthy and dystrophic DIA. Figure 3 shows the normalized specific force-stretch velocity curve predicted by the model against the experimental curve reported in [21]. Figure 4 shows the overall response predicted by the model in isometric, concentric and eccentric simulations with the optimized parameters.

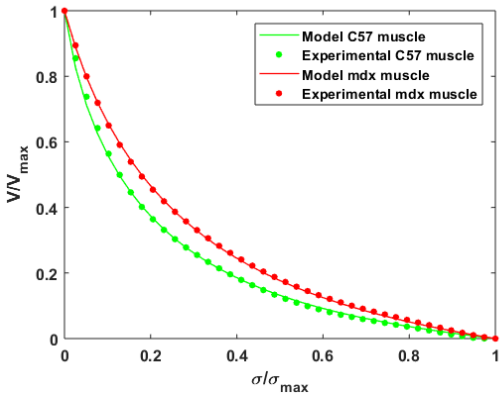

Fig. 3: Normalized force-velocity curves for dystrophic (red curve) and healthy (green curve) diaphragm muscle obtained in isometric and concentric contraction simulations.

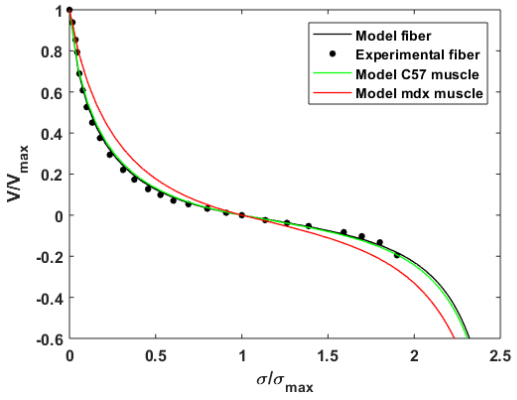

Fig. 4: Normalized force-velocity curves for single fiber (black curve), dystrophic (red curve) and healthy (green curve) diaphragm muscle obtained in isometric, concentric and eccentric contraction simulations. In eccentric condition, the muscle is stretched up to a fixed stretch equal to 1.014 μm/μm with different deformation velocities.

Results show that the model is able to reproduce experimental behaviour for the healthy and dystrophic DIA in both passive and active scenarios. For the parameters in Table I, the maximum isometric force was found to be 67.72 kPa and 22.64 kPa for the healthy and dystrophic muscles respectively, both within the range of 67.69±10.79 and 22.56±0.98 kPa reported in literature [14] for healthy and dystrophic muscles respectively. In addition, the maximum contraction velocity predicted by the model for the whole muscle was 1.21 and 0.85 mm/mm/s for healthy and dystrophic muscle respectively, both within the range of 1.235±0.035 and 0.91±0.06 mm/mm/s reported in literature [21,22] for healthy and dystrophic muscles respectively.

A positive aspect of the model is the ability to reproduce experimental eccentric contraction data with the identified parameters, an indicator of its potential predictive capabilities. However, the most remarkable finding is that the main difference between the model parameters for healthy and dystrophic models is found in the value of parameter $\hat{\eta}_1$ and C, related to the stiffness of the active element and the density of the muscle fibers respectively. The fiber density C was found to be significantly larger in the healthy muscle with respect to dystrophic muscle. These results are in good agreement with reported data on mice that show a reduction in the percentage of muscle fibers with the progression of the pathology [23,24]. In addition, the large value of $\hat{\eta}_1$ found for the dystrophic muscle with respect to the healthy case indicates that, the muscle fibers in the dystrophic muscle will be subjected to a larger active stress, favoring the onset of inflammatory process leading to cell dead and a subsequent generation of fibrosis[25,26]. Both findings are in good agreement with what is reported in the literature regarding the DMD pathology confirming the soundness of the proposed formulation.

IV. CONCLUSION

The resulting model represents a novel approach to study DMD pathogenesis by providing insights into the biophysical mechanisms regulating muscle contraction associated with the impaired muscle functionality. Moreover, it is an innovative and promising potential tool for researchers to predict muscle response under conditions that are not possible to explore in the laboratory and shade light into the biophysical mechanisms regulating muscle contraction. At last, the model can be an important step towards a new paradigm of in-silico trials that will allow identifying novel therapies implementing and bypassing the use of animal models.

However, the current model is not exempt from limitations. First, the present model does not include specific aspects of the muscle microstructure that could play a significant role on the mechanical response of the dystrophic muscle. Future investigations will study the fiber-ECM interaction by looking onto changes in the microstructure of the muscle during monoaxial loading when subjected to controlled mechanical deformation. These observations will allow to formulate a much more accurate model of the tissue, as well as to determine potential mechanisms of damage that compromise muscular functioning in DMD.

Another limitation is that the passive strain energy function

of the ECM obtained by fitting the experimental uniaxial stress-strain curves could be affected by bias arising from the different number of muscle fibers presented in the healthy and dystrophic DIA. To overcome this limitation, mechanical characterization of the only ECM can be performed from uniaxial tests on decellularized samples harvested from healthy and mdx DIA. Decellularization of muscle tissue through enzymatic processes and detergent washes allows to remove the muscle fibers, maintaining the overall architecture of the ECM, while preserving the biomechanical properties nearly identical to those of intact muscles [27]. The decellularization approach could be useful to investigate the role of the only ECM in normal and dystrophic tissue, excluding the bias that arises from the different number of muscle fibers presented in either condition.

Further improvements of the model will consider including fast and slow contracting fibers, which allows for a more accurate description of the muscle contractions, but also on the identification of potential mechanisms behind the loss of muscle functioning. Last but not least, the extension of the current three-dimensional chemo-mechanical mathematical model of the dystrophic muscle coupled with a mathematical model of the immune response in DMD muscle. This model could represents a novel approach to study DMD pathogenesis as well as to identify and evaluate potential therapeutic targets as anti-inflammatory therapies. Furthermore, this model could focus on identifying new dynamic changes taking place in specific pathways of immune system and its contribution to inflammation, fibrosis, stiffness, weakness and normal versus pathological muscle repair.

REFERENCES

[1] E. P. Hoffman, R. H. Brown, and L. M. Kunkel. “Dystrophin: The protein product of the duchenne muscular dystrophy locus.” Cell, 51(6):919–928, 1987.

[2] M. Durbeej and K. P. Campbell. “Muscular dystrophies involving the dystrophin glycoprotein complex: an overview of current mouse models.” Current Opinion in Genetics & Development, 12(3):349–361, 2002.

[3] B. J. Petrof, J. B. Shrager, H. H. Stedman, A.M. Kelly, and H. L. Sweeney. “Dystrophin protects the sarcolemma from stresses developed during muscle contraction”. PNAS, 90(8): 3710–3714, 1993.

[4] A. E. H. Emery. “The muscular dystrophies”. The Lancet, 359 (9307): 687–695, 2002.

[5] S. Messina, D. Altavilla, M. Aguennouz, P. Seminara, L. Minutoli, et al. “Lipid peroxidation inhibition blunts nuclear factor-b activation, reduces skeletal muscle degeneration, and enhances muscle function in mdx mice.” The American journal of pathology, 168(3):918–926, 2006.

[6] M. Böl and S. Reese. “Micromechanical modelling of skeletal muscles based on the finite element method.” Computer methods in biomechanics and biomedical engineering, 11(5):489–504, 2008.

[7] J. Grasa, A. Ramirez, R. Osta, M. J. Muñoz, F. Soteras, and B. Calvo. “A 3d active-passive numerical skeletal muscle model incorporating initial tissue strains validation with experimental results on rat tibialis anterior muscle.” Biomechanics and modeling in mechanobiology, 10(5):779–787, 2011.

[8] B. Hernández-Gascón, J. Grasa, B. Calvo, and J. F. Rodríguez. “A 3d electro-mechanical continuum model for simulating skeletal muscle contraction.” Journal of theoretical biology, 335:108–118, 2013.

[9] T. Heidlauf and O. Röhrle. “A multiscale chemo-electro-mechanical skeletal muscle model to analyze muscle contraction and force generation for different muscle fiber arrangements.” Frontiers in physiology, 5(498), 1–14, 2014.

[10] K. M. Virgilio, K. S. Martin, S. M. Peirce, and S. S. Blemker. “Multiscale models of skeletal muscle reveal the complex effects of muscular dystrophy on tissue mechanics and damage susceptibility.” Interface focus, 2015.

[11] A. S. Jarrah, F. Castiglione, N. P. Evans, R. W. Grange, and R. Laubenbacher. “A mathematical model of skeletal muscle disease and immune response in the mdx mouse.” BioMed research international, 2014.

[12] B. J. Petrof, H. H. Stedman, J. B. Shrager, J. Eby, H. L. Sweeney, and A. M. Kelly. “Adaptations in myosin heavy chain expression and contractile function in dystrophic mouse diaphragm.” American Journal of Physiology-Cell Physiology, 265(3):C834–C841, 1993.

[13] O. Friedrich, M. Both, C. Weber, S. Schrmann, M. D. H. Teichmann, et al. “Microarchitecture is severely compromised but motor protein function is preserved in dystrophic mdx skeletal muscle.” Biophysical journal, 98(4):606–616, 2010.

[14] G. Bates, S. Sigurdardottir, L. Kachmar, N. B. Zitouni, A. Benedetti, et al. “Molecular, cellular, and muscle strip mechanics of the mdx mouse diaphragm.” American Journal of Physiology - Cell Physiology, 304(9):C873–C880, 2013.

[15] K. S. Ramaswamy, M. L. Palmer, J. H. van der Meulen, A. Renoux, T. Y. Kostrominova, et al. “Lateral transmission of force is impaired in skeletal muscles of dystrophic mice and very old rats.” The Journal of Physiology, 589(5):1195–1208, 2011.

[16] S. S. Blemker, P. M. Pinsky, and S. L. Delp. “A 3d model of muscle reveals the causes of nonuniform strains in the biceps brachii.” Journal of biomechanics, 38(4):657– 665, 2005.

[17] K. B Campbell, M. V Razumova, R. D. Kirkpatrick, and B. K. Slinker. “Myofilament kinetics in isometric twitch dynamics.” Annals of biomedical engineering, 29(5):384–405, 2001.

[18] T. Kumamoto, S. Fujimoto, T. Ito, H. Horinouchi, H. Ueyama, et al. “Proteasome expression in the skeletal muscles of patients with muscular dystrophy.” Acta neuropathologica, 100(6): 595–602, 2000.

[19] H. H. Stedman and H. L. Sweeney. “The mdx mouse diaphragm reproduces the degenerative changes of duchenne muscular dystrophy.” Nature, 352(6335): 536–539, 1991.

[20] H. L. Granzier and T. C. Irving. “Passive tension in cardiac muscle: contribution of collagen, titin, microtubules, and intermediate filaments.” Biophysical Journal, 68(3):1027–1044, 1995.

[21] C. Coirault, B. Pignol, R. N. Cooper, G. Butler-Browne, P. E. Chabrier, et al. “Severe muscle dysfunction precedes collagen tissue proliferation in mdx mouse diaphragm.” Journal of Applied Physiology, 94:1744–1750, 2003.

[22] C. Coirault, F. Lambert, S. Marchand-Adam, P. Attal, D. Chemla, et al. “Myosin molecular motor dysfunction in dystrophic mouse diaphragm.” American Journal of Physiology - Cell Physiology, vol. 277, p. C1170–C1176, 1999.

[23] J. M. Boer, E. J. de Meijer, E. M. Mank, G. B. van Ommen, and J. T. den Dunnen. “Expression profiling in stably regenerating skeletal muscle of dystrophin-deficient mdx mice," Neuromuscular Disorders, vol. 12, Supplement, pp. S118–S124, 2002.

[24] A. Farini, C. Sitzia, L. Cassinelli, F. Colleoni, D. Parolini, et al. “Inositol 1,4,5-trisphosphate (ip3)-dependent ca2+ signaling mediates delayed myogenesis in duchenne muscular dystrophy fetal muscle.” Development, vol. 143, p. 658–669, 2016.

[25] W. Klingler, K. Jurkat-Rott, F. Lehmann-Horn, and R. Schleip. “The role of fibrosis in duchenne muscular dystrophy.” Acta Myologica, vol. 31, pp. 184–195, 2012.

[26] A. Farini, M. Meregalli, M. Belicchi, M. Battistelli, D. Parolini, et al. “T and B lymphocyte depletion has a marked effect on the fibrosis of dystrophic skeletal muscles in the scid/mdx mouse.” Journal of Pathology vol. 213, pp. 229–238, 2007.

[27] A. Porzionato, M. M. Sfriso, A. Pontini, V. Macchi, L. Petrelli, et al. “Decellularized human skeletal muscle as biologic scaffold for reconstructive surgery.” International journal of molecular sciences, vol. 16, no. 7, pp. 14808–14831, 2015.

Mechanical X'talk between Stem Cells and ECM

S. Fusco[1], V. Panzetta[1], and P.A. Netti[1,2]
[1] Interdisciplinary Research Centre on Biomaterials (CRIB), University of Naples Federico II, Naples, Italy
[2] Center for Advanced Biomaterials for Health Care@CRIB, Istituto Italiano di Tecnologia, Naples, Italy

***Abstract*—The importance of extracellular matrix (ECM) mechanical properties in controlling cell functions and responses it's well established .We investigated the behaviors of adult mesenchymal stem cells when interacting with two types of synthetic matrices presenting different time-dependent mechanical behaviors. Differences in terms of cell biophysical parameters, such as spreading, cytoskeleton assembly and forces generations were found and presented.**

***Keywords*— Stem Cell, ECM Mechanical Properties, Mechanosensing, Mechanotransduction.**

I. Introduction

Recreate an "in vitro" ECM equivalent for stem cells that generates a correct cascade of signals and triggers a self-sustaining tissues morphogenesis is today one of the fundamental challenge of tissue engineering [1]. It is well established that key role of three biophysical features of the ECM to control the cell behavior: surface chemical functionalization, topography and mechanical properties. In particular, thanks to the mechanosensing machinery, the cell recognizes ECM elastic properties and transduces them by the activation of its internal molecular machinery which, in turn, determines differences in cell functions and behaviors such as spreading, cytoskeleton assembly/disassembly, acto-myosin activity, proliferation and differentiation. On the other hand, the mechanical remodeling of ECM is a phenomenon that cells continuously actuate when in contact with the substrate. Such remodeling might change the macroscopic and microscopic characteristics of the ECM, including the surface decoration (in terms of density), topography and mechanical response. ECM, indeed, reacts to the cell remodeling of cytoskeleton-generated forces, thanks to its overall mechanical properties. Therefore, depending on the time dependent nature of the material constituting the ECM equivalent, the interplay between cell and material might trigger different mechanisms of inside-out and outside-in signaling during mechanosensing and mechanotransduction phenomena. Many reports in literature deal with the behavior of stem cells interacting with purely elastic materials [2-3] whereas only few recent reports start to investigate the time dependency of mechanical response [4-5], being this point crucial in the design of a cell instructive material. In this work we investigated the behaviors of adult mesenchymal stem cells interacting with two types of materials, presenting both different stiffness's and time-dependent mechanical behaviors, in terms of cell biophysical parameters such as spreading, cytoskeleton assembly and forces generations.

II. Materials and Methods

Poliacrylamide (PA) hydrogels were fabricated, by modulating the monomer/crosslinker ratio to obtain an elastic gel. Polydimethylsiloxane (PDMS) was used as viscoelastic substrate. Their elastic moduli ranged between 9-13 kPa (SOFT) and 28-30 kPa (STIFF). Substrates were superficially decorated with a short peptide, RGD that was spatially equalized between samples to avoid mechanical decoupling and tethering effects. Human adipose-derived stem cells (ASCs) were cultured in alpha-MEM supplemented with 10% MSC-qualified FBS, L-glutamine 2 mM, GA-1000 (1 ul/ml) and seeded at a starting density of 3000 cells/cm^2. Cells were fixed, stained with Alexa 568-phalloidin to quantify the spreading area and immunostained with Alexa-488 anti-paxillin antibody to evaluate FA areas. Mechanical analyses were conducted by measuring the energy consumption of cells during adhesion and spreading by using traction force microscopy (TFM). This technique measures the field of displacements of nanometric probes embedded in the materials. Measurements were carried out in three steps 1) a snapshot of substrates was collected before cells culture to record the initial positions of embedded beads ii) a snapshot was acquired 24 h after cells seeding to determine the effective substrates remodeling by cells; iii) last frame were captured after cells trypsinization to evaluate the elastic and non-elastic deformations of the substrates.

III. Results

TFM experiments underlined the diverse mechanical crosstalk between cells and substrates with different mechanical properties either in term of forces, remodeling activity and energy consumption. On elastic matrices (PA gels), the displacement fields measured before and after cell trypsinization were coincident both on soft and stiff cases, confirming the global elastic behavior of this material. In addition, the stresses applied on stiff substrate were greater than on the soft one. On the viscoelastic substrates (PDMS) the displacement fields measured for cells still attached to the substrate resulted higher and composed of two contributions, the first represented by elastic and then recovered displacements after cell detachment, the other one made by non-elastic displacements due to the viscous behavior of the material.

We further analyzed spreading areas and focal adhesion (FA) size and density of ASCs on elastic and viscoelastic matrices (Fig. 1). FA size increased passing from the soft to the stiff substrate and no significant statistical differences

were found for PA and PDMS when comparing the same stiffness. The spreading area of ASC showed a trend with stiffness only for elastic materials, while on viscoelastic ones the values resulted similar passing from soft to stiff substrate. These results suggested that the mechanosensing and mechanotansduction machinery could be influenced by the viscoelastic nature of the ECM and by the resulting crosstalk with cells. In particular, we found a time dependent mechanosensing process that induces different short-time cell behaviors (in terms of biophysical parameters) preluding divergent lineage induction in cell differentiation. Additional studies have to be conducted in the future.

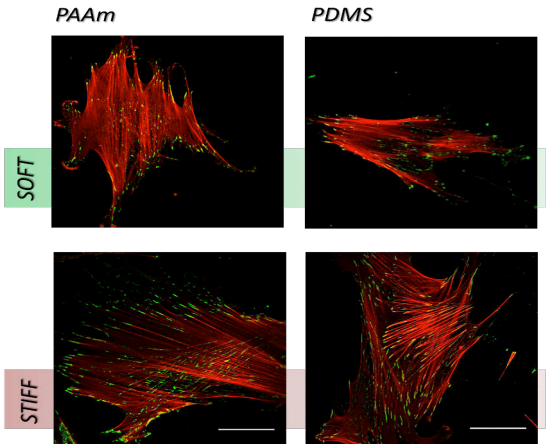

Figure 1 – ASC cultured on elastic Poliacrylamide (PA) and viscoelastic Polydimethylsiloxane (PDMS) with different stiffness (SOFT: 9-13 kPa; STIFF: 28-30 kPa). Immunosstaining: red-actin; green-paxillin.

IV. Conclusion

In this study we investigated the behaviors of adult mesenchymal stem cells when interacting with two types of synthetic matrices presenting different time-dependent mechanical behaviors: elastic and viscoelastic. Differences in terms of cell biophysical parameters, such as spreading, cytoskeleton assembly and force generations were found. In particular, we found that such time integrating cell mechanosensing may trigger divergent lineage early induction in cell differentiation, suggesting an additional role of viscoelasticity in short and long-term mechanotransduction.

References

[1] Vogel, Viola. "Unraveling the Mechanobiology of the Extracellular Matrix." Annual review of physiology 80.1**, 2018.**

[2] Engler, Adam J., et al. "Matrix elasticity directs stem cell lineage specification." Cell 126.4: 677-689, **2006**.

[3] Wen, Jessica H., et al. "Interplay of matrix stiffness and protein tethering in stem cell differentiation." Nature materials 13.10: 979, **2014**.

[4] Chaudhuri, Ovijit, et al. "Hydrogels with tunable stress relaxation regulate stem cell fate and activity." Nature materials 15.3: 326, **2016**.

[5] Fusco, Sabato, et al. "Crosstalk between focal adhesions and material mechanical properties governs cell mechanics and functions." Acta biomaterialia 23: 63-71, **2015.**